Preface

Studies of materials at low temperatures have had a tremendous impact upon the development of physics and science in general, and they played a significant role in the emergence and formulation of the quantum theory at the beginning of the 20th century. The earliest attempts at producing low temperatures in the laboratory relied on the cooling effect resulting from the dissolution of crystalline solids in water. This method was also employed by Sir Humphry Davy and Michael Faraday, who, in research started in 1823, succeeded in liquefying a variety of gases and can thus be viewed as pioneers of cryogenic research. Studies of gases at low temperatures and the observation that their pressure decreases linearly with temperature led Kelvin in 1848 to interpret temperature in terms of kinetic energy. He introduced the concept of an absolute scale, where zero corresponds to the temperature at which the constituent atoms and molecules lose all their kinetic energy.

A convenient path to cryogenic research was opened up in 1850s by the observation by Joule and Thompson that gases expanding adiabatically into vacuum have to overcome the weak attractive forces between their atoms or molecules, which results in their cooling. This method was used around 1877 by Cailletet and Pictet to condense a number of hard-to-liquefy gases, including oxygen, nitrogen, and carbon monoxide, work which in turn kindled the interest of Dewar in cryogenic research. Among his accomplishments, besides invention of the familiar ''Dewar flask'' was the demonstration that oxygen is paramagnetic; he also succeeded, in 1898, in liquefying, and a year later, in solidifying hydrogen gas.

An important step in further development of the field was the construction of the first cyclically operating refrigerators based on the Joule–Thompson effect, by Linde around 1895. This made possible the large-scale liquefaction of air with distilative separation of its components, and greatly facilitated cryogenic research. Finally, helium was liquefied in 1908 by Kamerlingh Onnes, who cooled it by liquid hydrogen below its inversion temperature prior to an adiabatic Joule–Thompson expansion.

The history of low-temperature physics is intimately intertwined with the history of rare gases. Lord Rayleigh, while making accurate measurements of molecular weights (he wanted to check Prout's hypothesis that the atoms of various elements are built from hydrogen, and therefore have weights that are integral multiples of that of the hydrogen atom) noted that nitrogen obtained from atmospheric air has a different weight than that made chemically. The mystery was solved by Ramsay, who in 1894 was able to show that atmospheric nitrogen contains a new element, the rare gas argon. Ironically, argon was not the first of the rare gases to be discovered. Some 25 years earlier Lockyer observed during a solar eclipse a strong yellow spectral line, which he could not attribute to any known element. Janssen then concluded that this line is due to a new chemical element, presumably present only on the sun, and suggested therefore to name it helium. One year after the discovery of argon, in 1895, Ramsay was able to isolate helium on earth by heating the mineral cleveite, where it forms due to radioactive decay of uranium. These first two members of the ''inert'' gas family were soon followed by neon, krypton, and xenon, all produced by fractionating liquefied air.

Interestingly, the realization of that rare gas solids and other condensed gases may provide a suitable medium for spectroscopic studies followed very shortly after their discovery. Vegard, at the university of Leiden, at that time, the Mecca of low-temperature research, started back in the early 1920s a series of studies which would clearly fall into the area which today is called matrix isolation. He investigated luminescence from condensed gases irradiated by x rays or electrons, in the hope of gaining understanding of the origin of the Aurora Borealis and other atmospheric and stratospheric phenomena. Using this method, he was, for instance, the first one to observe the $a_u^{3+} X_g^{1+}$ phosphorescence from the lowest triplet state of molecular nitrogen, which is today known as the Vegard–Kaplan bands.

After essentially a gap of some thirty years, interest in spectroscopic studies of solid rare gases resurfaced in the early 1950s, which is when Pimentel coined the phrase ''matrix isolation'' and when deliberate, systematic studies of species isolated in rare gas solids started. The major goal of matrix isolation studies at that time was the observation and characterization of highly reactive radicals and other reaction intermediates. Such species, which otherwise under normal conditions have only a very ephemeral existence, could be stabilized in a rigid, inert solid and then studied at leisure by spectroscopic means. Over the next decade, hundreds of free radicals, molecular ions, clusters, and similar transient species were generated, detected, and their molecular constants and other properties determined in rare gas matrices.

Condensed rare gases are characterized by weak interatomic interactions and are therefore usually found to perturb only weakly the isolated ''guest'' species of interest. Furthermore, the guest spectra in low-temperature solids are invariably greatly simplified, since in most cases the molecular rotation is quenched, so that the entire rotational structure collapses into a sharp zero-phonon line. Furthermore, at low temperatures typically only the vibrationless level of the ground state of the guest is populated, so that the ''hot bands'' and ''sequence bands'' that often clutter gas-phase spectra are absent.

After an initial rapid development of the matrix isolation field, in the 1970s alternative techniques were developed for studies of transient species, which completely avoid the medium perturbations inherent in the condensed-phase technique. For instance, ions, clusters, or radicals could be produced in electric discharges, by photolysis, or by laser

vaporization, cooled to a few K by an adiabatic expansion, and investigated by laser spectroscopic techniques in the gas phase. In addition to eliminating the medium perturbation problem, such investigations also have the advantage of providing the rotational information which is in general lost in the nonrotating matrix-isolated species, and for a while they seemed to spell doom for the matrix isolation technique.

In spite of that, however, if judged by the number of publications and by the frequency of and attendance at conferences on low-temperature spectroscopy in solid matrices, one finds that the technique is still very much alive and well, only the emphasis and goals of the matrix studies have in many instances changed. Very often, the perturbations and interactions of the guest with the solid host, which were in the early works viewed as bothersome drawbacks of the technique, now become the main object and emphasis of the study. A wide range of phenomena and elementary excitations specific to condensed samples, such as phonons, librons, excitons, and neutral or charged solute solvation become available for study. The low temperatures and weak interatomic interactions in van der Waals solids tend to slow down the various relaxation processes, making them accessible to experimental study. The dynamics of many processes are not obscured here by the much stronger forces present in the more conventional solids, which makes them easier to study experimentally and model theoretically.

We have mentioned above that the early experimental studies in condensed rare gases originated in Leiden and that matrix isolation was developed by George Pimentel, in California. On the other hand, many key contributions towards understanding of the spectroscopy and physical properties of impurities and defects in solids originated in the countries of Eastern Europe, including, for instance, Ukraine, Russia, Estonia, and others. It is therefore perhaps appropriate that this collection of papers appears as a special issue of *Low Temperature physics*, a journal which was founded at the B. Verkin Institute for Low Temperature Physics and in which many of these early important contributions first appeared. The contributions in this issue were selected to give what we hope is a fair cross section of the current activities in this field and to demonstrate the breadth of its applications.

Most of the early matrix isolation studies employed absorption spectroscopy, predominantly in the infrared range, to characterize the samples, but nowadays a much broader repertory of investigation techniques has become available. The samples can be studied over a wide range of wavelengths both in absorption or emission, and they can be excited by tunable or fixed-frequency lasers in the infrared, visible, or UV and by x rays or electrons. Using picosecond or femtosecond laser techniques, many processes whose dynamics could previously only be indirectly inferred from spectroscopic observations can now be investigated in real time, as exemplified in the contribution by Chergui. Synchrotron radiation is a particularly useful, widely tunable photon source that is increasingly being applied for matrix studies, as exemplified by the nice EXAFS investigation by Roubin *et al.* or by the work of Kerins *et al.* on high-lying states of Mg atoms in matrices.

The applications of matrices today extend over an extremely wide range of different fields, ranging from single molecules and microscopic properties of solids to bulk properties of solids, or investigation of reactions occurring in interstellar space. The matrix method is useful in static studies of defects and impurities and their effect upon the solid-state properties, as well as in studies of dynamics on time scales ranging from days to femtoseconds. It yields information about diffusion processes, chemical reactions, and charge localization and charge transfer. The information gained from these studies is useful in various fields, extending from purely basic science to technologically important fields such as chemical catalysis, semiconductor technology, or laser physics.

Several of the papers included deal with the traditional goal of matrix isolation—identification of new species—but novel methods are now often employed for their efficient generation, such as vaporization by lasers, which were not available to the early pioneers in the field. Here one could name the papers by Andrews *et al.* or by Lammers *et al.* Besides optical spectroscopy, EPR has also traditionally been a very useful technique, used to investigate open shell radicals and their reactions, as nicely demonstrated in the present issue by the manuscript by Misochko *et al.* Another infrared work exemplifying application to species of astrophysical or atmospheric interest is the infrared investigation of the photolysis of ozone by Chaabouni *et al.*

While the traditional matrix materials were most commonly argon or nitrogen, for a variety of reasons much interest is currently shifting to other solids, for instance solid hydrogen or helium, and several of the manuscripts in this issue deal with these hosts. In the first place, in these very light, so-called ''quantum'' hosts the zero-point motion is not negligible compared with the lattice constants and separations of the host atoms, and consequently a variety of ''quantum effects'' not present in the conventional solids can be observed and studied. In this issue the papers by Ganshin *et al.*, Kiselev *et al.*, and Galtsov *et al.* deal with such quantum solids. An additional advantage, particularly in the case of parahydrogen, are the very sharp, high-resolution spectra which can often be observed. In this collection, for instance, the papers by Miki and Momose or by Tam and Fajardo take advantage of this fact. The possibilities of producing ''high-energy-density'' materials and, for example, increasing the specific impulse of rocket fuels by stabilizing atoms and reactive intermediates in solid hydrogen have also been widely discussed and increase the interest in solid hydrogen or deuterium, and the study by Danilychev and coworkers is relevant in this context.

The specific nature of the trapping site, its symmetry, geometry, and its effects upon the guest properties and spectroscopy are most often quite unknown, and several of the contributions selected, for instance the works by Roubin *et al.* or Lorenz *et al.*, explore this question. Conversely, the spectra of an atomic or molecular guest whose spectroscopy is well known in the gas phase may be greatly affected by the host when isolated in a condensed matrix. In this way the guest atom or molecule may be used as a ''spy,'' yielding information, for instance, about the changes in the trapping site size and local symmetry and thus about the structural changes and phase transitions occurring in the host solid ma-

trix, as nicely demonstrated here in the paper by Minenko *et al.*

Inclusion of even very minor concentrations of impurities can often have a profound effect upon the optical, structural, and thermodynamic properties of solids, and this topic and the detailed understanding of such effects are of key importance in many technologically important areas, such as the semiconductor industry, solid-state lasers, and many others. Rare gases, with their relatively simple structure, provide a very suitable medium for investigating these effects. Such applications are exemplified by the thermal conductivity measurements of matrices doped with a rotating impurity, such as methane in the article by Dudkin *et al.*, or by the sound propagation study by Kiselev *et al.*, and also by study Freiman *et al.* on the effect of oxygen impurities upon the thermal and magnetic properties of cryocrystals can be mentioned in this context.

Besides being a very convenient systems for solid-state theoretical modeling, the rare gases themselves have many potentially very useful characteristics. For example, their optical properties and, in particular, their transparence, extending from the far infrared into the vacuum ultraviolet range, besides enhancing their usefulness as a medium for spectroscopic matrix isolation studies, potentially also makes them a suitable material for solid-state lasers, in particular, for the far-ultraviolet region. This consideration makes the questions of optical gain, stimulated emission, and lasing in rare gas solids, as investigated, for instance, in the contribution by Chabbi *et al.*, particularly interesting.

One of the drawbacks of the early matrix studies was due to the fact that most methods of generating transient species are not selective, but one typically obtains a complex mixture of products, among which the individual carriers have to be subsequently identified, for instance by a series of laborious isotopic substitution experiments. This problem can be solved if the product of interest is mass-selected prior to deposition into the matrix. While such deposition of mass-selected species at sufficient yields and concentrations for spectroscopic characterization represents a nontrivial task, in the last few years several groups have made considerable advances in this field, and in this issue the papers by Fang *et al.* and by Lorenz *et al.* describe experiments in this direction.

While rare gases were chosen as suitable matrix-isolation ''solvents'' for their chemical inertness, it is now well known that they are not really inert, but under suitable conditions display a relatively rich chemistry. Since the early days in Pimentel's laboratory, rare gas matrices have also proved to be a convenient reactive medium for the production, stabilization, and identification of rare gas compounds. In the last few years there has been a resurgence of activity in this field, and a wealth of novel rare gas compounds has recently been described, with the paper Lundell *et al.* exemplifying this nice work.

As already noted above, the current range of activities in matrix isolation is quite broad, in fact, so broad that a single special issue cannot do it justice. Even the selection of topics and techniques represented here is far from exhaustive. In spite of these limitations and shortcomings, we hope that this issue will demonstrate that even seventy-five years after its earliest beginnings, and some fifty years after its rebirth in Pimentel's laboratory, matrix isolation remains a very useful, versatile technique, with a wide scope of applications. Most likely it will also easily survive the next fifty years and most of its current practitioners as well, and that future generations of chemists and physicists will, like George Pimentel always used to recommend, try to ''keep it cool.''

V. E. Bondybey and E. V. Savchenko

Medium effects on the spectroscopy and intramolecular energy redistribution of C_{60} in cryogenic matrices

M. Chergui*

Institut de Physique de la Matiére Condensée, Faculté des Sciences, BSP, Université de Lausanne, CH-1015 Lausanne-Dorigny, Switzerland

(Submitted March 22, 2000)
Fiz. Nizk. Temp. **26**, 863–873 (September–October 2000)

We review some of our works on the absorption, excitation and emission spectra of C_{60} embedded in rare gas matrices while stressing the role of the environment. The gas phase resonant two-photon ionization spectrum of C_{60} is reanalysed in the light of our previous work and the energy of the lowest three excited singlet states is determined with precision. In matrices, the visible absorption bands are red-shifted by an amount ranging from $\sim$30 cm^{-1} in Ne matrices to $\sim$330 cm^{-1} in Xe matrices. The observed reversal of state ordering of the lowest two singlets states (T_{1g} and T_{2g}) between Ne and Ar matrices (in emission) and in Ne matrices, between the absorption and emission spectra, is attributed to different Stokes shifts of the T_{1g} and T_{2g} states and to the small energy splitting ($\sim$50 cm^{-1}) between them. Finally, a detailed picture of the intramolecular energy redistribution processes is obtained thanks to a combination of picosecond fluorescence experiments and femtosecond pump–probe transient absorption experiments. The intramolecular relaxation processes among the pure electronic levels of the lowest three singlet states are found to be strongly medium dependent. Medium effects are manifest even on the very short time scale of the internal conversion in the singlet vibronic manifold.
[S1063-777X(00)00209-7]

1. INTRODUCTION

Ever since the large-scale production of fullerenes, there has been a tremendous upsurge of studies concerning them because of their potential applications in different fields. For example, the idea to encapsulate atoms or molecules in fullerenes, i.e., to make endofullerenes, is attractive because of the remarkable properties such systems should exhibit. So far attempts to produce endofullerenes have all been based on ''brute force'' methods—high-intensity laser excitation of metal-coated graphite,[1] high-temperature ovens[2] or high-velocity collisions between fullerene ions and a target gas.[3] None of these methods is selective and efficient. A selective approach would be to use lasers. This, however, requires knowledge of the energetics and the energy redistribution processes in these molecules. These data are also of importance in other applications such as optical limiting or the use of fullerenes as saturable absorbers in ultrafast optics.[4–6]

According to theory,[7,8] the lowest three electronic excited singlet states of C_{60} are the T_{1g}, T_{2g}, and G_g states, whose transitions with the A_g state are dipole-forbidden. However, these transitions may be vibronically induced by nontotally symmetric modes as a result of Herzberg–Teller (H–T) and Jahn–Teller (J–T) couplings. The detailed description of these modes and their calculations has mainly been done by Negri and co-workers.[7–11] This raises an additional interesting aspect to fullerenes, which is the possibility of combining the experimental data with these high quality quantum-chemical calculations.[7–11] As such, C_{60} and C_{70} appear as ideal test systems for improving and refining the quantum chemical calculations of large polyatomic systems.

The ideal situation for determining the energetics would be to study fullerenes in the gas phase. however such studies are impossible due to the high temperatures needed to vaporize fullerenes and to the resulting hot-band contributions which arise. Therefore, most of the spectroscopic studies of on fullerenes have mainly been carried out in organic solvents,[12,13] in low-temperature organic matrices[14–16] and in the pure solids.[17,18] In all these media the relatively strong interaction of the molecule with the environment leads to a broadening of bands, strong site effects, and shifts of the energy levels, which make a clearcut assignment of the spectroscopy difficult. Despite this, the first attempt to present a complete assignment of the C_{60} absorption spectrum from the visible to the UV was made by Leach *et al.*[12] on the basis of data recorded in hexane solvents. In organic Shpolskii matrices sharp spectra were reported, but the large distribution of sites has made a clearcut assignment of bands difficult.[14–16] Another approach is to use molecular beams, which would allow one to have cold, noninteracting molecules, but surprisingly, to our knowledge there has only been one such study, in the early days of research on fullerenes.[19] The authors reported on the two-photon resonance enhanced multiphoton ionization of C_{60} and C_{70} in the 600 nm and 400 nm regions, but no assignment was proposed for the rich structures therein contained. An alternative approach is to embed the fullerenes in rare gas matrices. The matrix-isolation technique offers a number of advantages.

1) The media are cold (typically $<$10 K), so that hot-band contributions are suppressed, rotation is hindered, and thus the density of occupied states is lowered.

2) The media are chemically inert, so that the fullerene

molecules interact weakly with them. In the lightest, Ne, matrix one should in principle approach the frozen gas phase situation.

3) The rare gas matrix offers a ''physical'' environment which is ideal for investigating the coupling of the impurity optical transitions to the lattice.

The first study on C_{60} in Ar matrices was undertaken by Gasyna *et al.*,[20] who reported absorption and MCD spectra. Over the past four years, we have undertaken a systematic spectroscopic study of C_{60} and C_{70} in rare gas matrices.[21–24] More recently, we have also looked at their energy redistribution process.[25,26] Another very promising approach consists in embedding C_{60} in He nano-droplets.[27] This yields absorption (excitation) spectra with richer details than in rare gas matrices, which makes a complete assignment more difficult.

In this contribution, we will review our work on the spectroscopy of C_{60} using the matrix-isolation method with an emphasis on medium effects. We will concentrate, however, on new aspects deriving from either as-yet unpublished results or a revised interpretation of already published data. The experimental set-ups and procedures have already been described in Refs. 21–24 and will not be repeated here.

In Sec. 2 we will mainly discuss the absorption spectrum of C_{60} in the visible region. In Sec. 3 we will present and discuss the steady-state fluorescence spectrum of C_{60} in Ne and Ar matrices. This will be completed in Sec. 4 by the time-resolved fluorescence spectroscopy. Section 5 deals with the phosphorescence, and Sec. 6 concerns the conclusions.

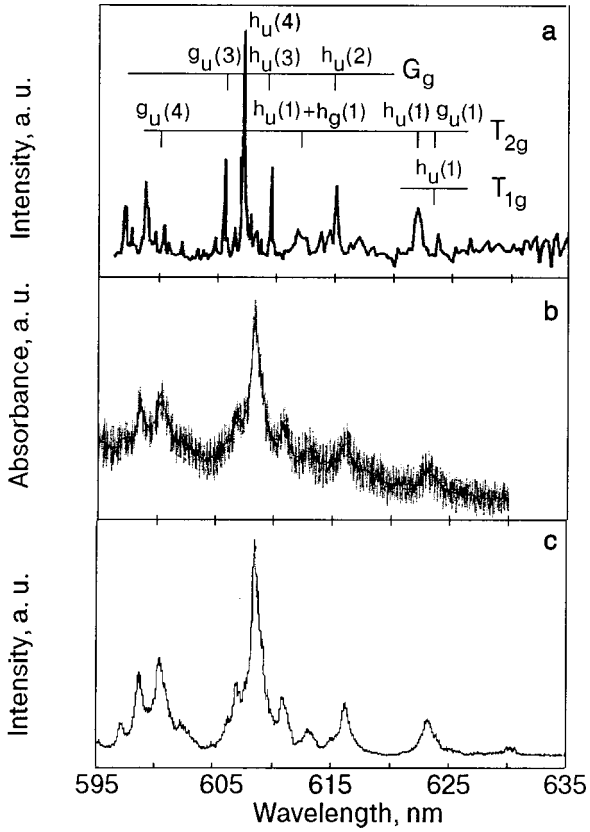

FIG. 1. Comparison the gas phase resonant two-photon ionization spectrum of C_{60} from Ref. 18 (a) with the absorption (b) and excitation (c) spectra of C_{60} in Ne matrices at 4 K.

2. ABSORPTION SPECTROSCOPY

Figure 1 compares the resonant two-photon ionization spectrum of C_{60} in molecular beams from Ref. 19 with our excitation and absorption spectra in Ne matrices. The spectra exhibit the same spectroscopic features, except for a red shift and a broadening of the bands in going from the gas phase to Ne matrices. The same holds for the spectra recorded in heavier matrices (not shown here). In addition, the close resemblance between excitation and absorption spectra suggests that all the absorbing levels lead to fluorescence with the same quantum efficiency. The broadening of the bands is mainly due to inhomogeneous broadening (the resolution was ~ 1 cm^{-1} in these spectra). The red shift increases from Ne to Xe as shown in Table I (the shifts are averages of those measured on the main bands in Fig. 1).

In Ref. 22 the fluorescence spectrum of C_{60} in Ar and Ne matrices was precisely assigned, thanks to the high-quality calculations of the vibronic modes and their oscillator strengths in the Jahn–Teller and Herzberg–Teller couplings. The mirror image which we obtained between the excitation spectrum and the fluorescence spectrum in Ar matrices allowed us also to assign the excitation spectrum. However, it was noted that in using a common, purely electronic origin for all the excitation bands, the frequencies of the vibronic modes associated to the G_g electronic state were shifted by ~ 60 cm^{-1} to lower energies than their value in the fluorescence spectrum. We recall that these values were in remarkable accord with the calculated values.[22] Given that such a change of mode frequencies between ground and excited state is unlikely (but not ruled out), we proposed that the G_g state should lie ~ 60 cm^{-1} above the T_{1g} and T_{2g} states. The hypothesis of a G_g state lying ~ 50–100 cm^{-1} higher than the T_{1g} and T_{2g} states had already been proposed by Negri *et al.*[9] In their case, the assignment of the gas phase spectrum considered only modes associated with the T_{1g} and G_g states. More recently, an energy splitting of ~ 100 cm^{-1} between these states was independently found in temperature-dependent studies of the C_{60} fluorescence in low-temperature decalin/cyclohexane matrices.[16]

We can now be more precise as, knowing exactly the mode frequencies from the fluorescence spectra and their assignment to the T_{1g}, T_{2g} and G_g states,[22] we can trace back the electronic origin of these three states in the gas phase spectrum and the matrix data. The analysis of the gas phase spectrum is given in Table II, and the attribution of bands is shown in Fig. 1. The gas phase energies of the electronic origin obtained from such a procedure imply that the T_{1g} state is the lowest, with an energy of 15632 cm^{-1}, T_{2g} is the next one above, at 15681 ± 10 cm^{-1}, and G_g is the third, with an energy 15738 ± 10 cm^{-1}. The uncertainty is due to the dispersion of mode frequencies and the pinpointing of ener-

TABLE I. Gas-to-matrix shifts measured on the main bands in the visible absorption spectrum of C_{60} in rare gas matrices.

Rare gas	Neon	Argon	Krypton	Xenon
ΔE, cm^{-1}	35 ± 5	160 ± 10	230 ± 20	330 ± 30

TABLE II. Band wavelengths and energies of the phase resonant two-photon ionization spectrum of C_{60} from Ref. 19. The assignments are based on the matrix data of Refs. 21 and 22.

Wavelength	Energy	Mode	Mode frequency (Ref. 22)	Electronic state
623.66	16034	$h_u(1)$ /$h_u(1)$	345–352/402	T_{2g} /T_{1g}
621.7	16085	$h_u(1)$	402	T_{2g}
617.2	16027.3			
614.8	16265.4	$h_u(2)$	525–536	G_g
~ 612	16340	$h_u(1)+h_g(1)$	668	T_{2g}
609.4	16409.6	$h_u(3)$	668	G_g
607.1	16471.7	$h_u(4)$	743–738	G_g
605.3	16520.7	$g_u(3)$	776	G_g
604.65	16538.5	$h_u(2)+h_g(1)$	791–802	G_g
601.9	16614			
600.3	16658.3	$g_u(4)$	962	T_{2g}
598.8	16700			
596.9	16753			

gies in the published gas phase spectrum. In the case of the lowest state and since only one vibronic band can be assigned to it (Fig. 1), we could not give error bars. However, in line with Refs. 9 and 16, we find that the $T_{1g}-G_g$ splitting is indeed $\sim$100 cm^{-1}.

The region of the electronic origin in Ne matrices is shown in Fig. 2. Recently, much less noisy contours of the threshold region were obtained for C_{60} in He_n nanodroplets,[27] which confirm our results in Fig. 2. The striking feature of this threshold region, as compared to the higher-lying vibronically induced bands, is that the latter are sharp and typically represent zero-phonon lines with no detectable phonon sideband. On the other hand, the threshold region consists of broad structureless features suggestive of a significant electron–phonon coupling for these transitions. Furthermore, as the pure electronic transitions are dipole-forbidden, they must be dynamically induced by the participation of nonototally symetric modes of the cage. The absence of a zero-phonon line for the threshold region and the fact that the bands therein are broad, implies a significant structural rearrangement prior to emission, accompanied by an absorption–emission Stokes shift. In Ref. 21 we reported a Stokes shift of $\sim$30 cm^{-1} in Ne matrices and $\sim$50 cm^{-1} in Ar matrices, measuring it from the maximum of the absorption threshold to the maximum of the emission origin.

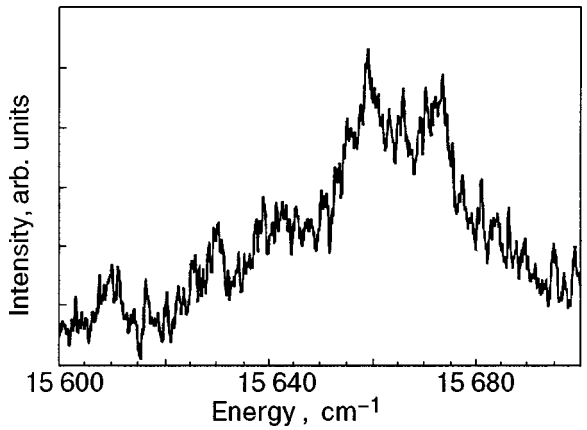

FIG. 2. Threshold region (purely electronic origin) of the visible absorption of C_{60} in Ne matrices.

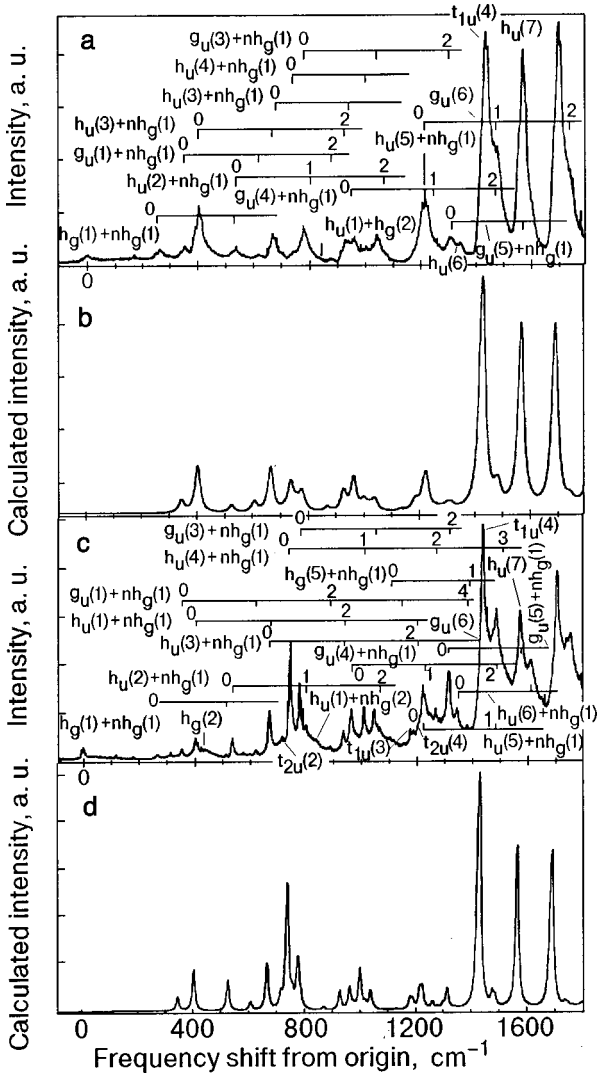

FIG. 3. Fluorescence spectrum of C_{60} in Ne matrices as a function of frequency shift from origin in the 0 to 1600 cm^{-1} region (a); simulation of the fluorescence spectrum based on computed oscillator strengths (Ref. 22). The contribution of the T_{1g}, T_{2g}, and G_g symmetry characters states to the emission is 36, 56, and 8%, respectively (b); same as (a) but for Ar (c); same as (b) but the contribution of the T_{1g}, T_{2g}, and G_g symmetry characters to the emission is 50, 25, and 25%, respectively (d).

The resemblance between the gas and the matrix data in Fig. 1 shows that the different environments do not affect the oscillator strengths of the different vibronically induced transitions in absorption. In the next Section, we will see that this is not the case for the fluorescence.

3. FLUORESCENCE SPECTRA

Figure 3 shows the experimental and simulated fluores-

cence spectra of C_{60} in Ne and Ar matrices which were already presented and discussed in detail in Ref. 22, along with the assignment of bands. This assignment was based on the fact that only one single electronic origin appears in the spectra and that the mode frequencies for all three lowest-lying electronic states inferred from this origin are in remarkable agreement with the calculated ones. Since the fluorescence spectrum contains vibronically induced transitions which are characteristic of the lowest three electronic states, the S_1 state responsible for the emission has to be a state of mixed T_{1g}, T_{2g}, and G_g character. From the simulated spectra, the weighting based on intensities was $T_{1g}:T_{2g}:G_g = 36\%:56\%:8\%$ in Ne matrices and 50%:25%:25% in Ar matrices.[22]

The near-mirror image between excitation and fluorescence spectra in Ar matrices suggests that the three states responsible for the absorption (see above) may also appear in emission with the same oscillator strengths and relative intensities as in absorption. Yet, aside from being unlikely, this idea is ruled out on the fact that, as mentioned above, our emission spectra clearly show one single electronic origin, i.e., it stems from only one single emitting state. This is also confirmed by the time-resolved picosecond fluorescence measurements as we will see in Sec. 4. Therefore, even though it helped us assign the excitation (absorption) spectrum in Ref. 22, the resemblance between emission and excitation spectra in Ar matrices is, we believe, fortuitous. Coming back to the differences between the Ne and Ar emission spectra, it is remarkable to note how dramatic is the effect of such supposedly ''weakly interacting'' media. Indeed, the weighting of intensities implies that the dominant character of the S_1 emitting state switches from T_{1g} in Ar matrices to T_{2g} in Ne matrices, whereas the absorption spectra indicate that the T_{1g} state is the lowest-lying state (Sec. 2). This points to a reversal of state ordering in going from Ar to Ne and in going from absorption to emission. The sole possibility for this to happen is by different absorption–emission Stokes shifts of the T_{1g} and T_{2g} states in the two matrices. As mentioned in the previous Section, the purely electronic transitions at the origin are characterized by multiphonon bands implying a sizeable Stokes shift, which brings the energy of the state to lower values. If, for a reason that still needs to be clarified, the Stokes shift is stronger in Ne for the T_{2g} state as compared to that of the T_{1g} state, then the T_{2g} state may end up at an energy slightly lower than the energy of the C_{60} state, which would explain the reversal of state ordering between the two matrices and between absorption and emission.

The origin of the different mixing ratios between the three lowest purely electronic states may be due to one or a combination of the following factors:

— in going from one matrix to the other, there is a differential shift of ~ 100 cm^{-1} (see Table I) which will modify the resonance conditions between the lowest three singlet states and the nearby triplet state manifold. This might give rise to singlet–triplet couplings which can alter the singlet–singlet mixing among the S_1 to S_3 states. However, if this were the case, then an intersystem crossing from S_2 or S_3 to the T_n states could take place, a hypothesis that is excluded on the basis of the time-resolved data presented in Sec. 4;

— mixing by static symmetry effects: even if we have no idea of the local symmetry of the trapping site, it is clear that it changes in going from Ne to Ar. Indeed, a simple estimate based on Lennard-Jones radii of C_{60} and rare gas atoms shows that 18 Ne atoms and 12 to 13 Ar atoms are needed to cover the surface of C_{60}. This means that there is a lowering of symmetry in going from the gas phase (I_h group symmetry for C_{60}) to Ne to Ar matrices. The lower the symmetry, the higher the likelihood of inducing state mixings;

— mixing by dynamical symmetry effects: as was mentioned in Sec. 2 in order to lift the forbidden character of the purely electronic transitions, nontotally symmetric modes of the cage have to be involved. Likewise, nontotally symmetric modes (having *gerade* character) can mix the lowest three singlet states with each other and give rise to a mixed character of the S_1 state, particularly in view of the small energy gaps between them, typically of one phonon energy.

4. TIME RESOLVED FLUORESCENCE SPECTRA

In order to identify the intramolecular relaxation pathways leading to the lowest singlet emission and, from there, to the population of triplet states, we carried out picosecond fluorescence measurements in Ne and Ar matrices. The description of the apparatus is given in Ref. 25 along with a detailed presentation of the results. Here, we emphasize the medium effects in the light of the above.

Figure 4 shows typical results in the case of C_{60} in Ar matrices and represents a set of time-gated fluorescence spectra along with a spectrum recorded under steady state conditions (Fig. 4e) as discussed in Sec. 3. In Fig. 4e, the high-frequency region of the spectrum is dominated by a group of bands around 14750 cm^{-1}, which are due to the $h_u(3)$, $h_u(4)$, and $g_u(3)$ modes of the molecules (all have frequencies around 700 cm^{-1}),[22] characteristic of the G_g emitting character. On the other hand, the bands at $\sim$14040 cm^{-1} and $\sim$13800 cm^{-1} are due to the $t_{1u}(4)$ and $t_{1u}(4) + h_g(1)$ modes, typical of the T_{1g} emitting character. Finally, the band at $\sim$13900 cm^{-1} is due to the $h_u(7)$ mode, which is to more than 80% due to the T_{2g} emitting character. If we now consider the time-gated fluorescence spectra (Fig. 4a–4d), one can see that the spectrum at 30 ps (Fig. 4a) exhibits a series of broad features of almost equal intensities in the 14800–13900 cm^{-1} region. This means that compared to the steady-state spectrum, the bands at frequencies $>$14100 cm^{-1} (most being characteristic of the G_g emitting character) are significantly enhanced as compared to those due to the T_{1g} and T_{2g} emitting characters. In addition, the bands characteristic of the latter two are also of comparable intensity (compare, e.g., the 13900 cm^{-1} band with the 14040 cm^{-1} band). However, the situation changes rapidly, as already at 90 ps (Fig. 4a) the bands characteristic of T_{1g}/T_{2g} dominate the spectrum, while all the bands tend to sharpen and by $\sim$200 ps the spectrum reproduces most of the features of the steady-state spectrum. A line narrowing also occurs, which corresponds to a change of linewidth by a factor of 2 between 30 and 150 ps.

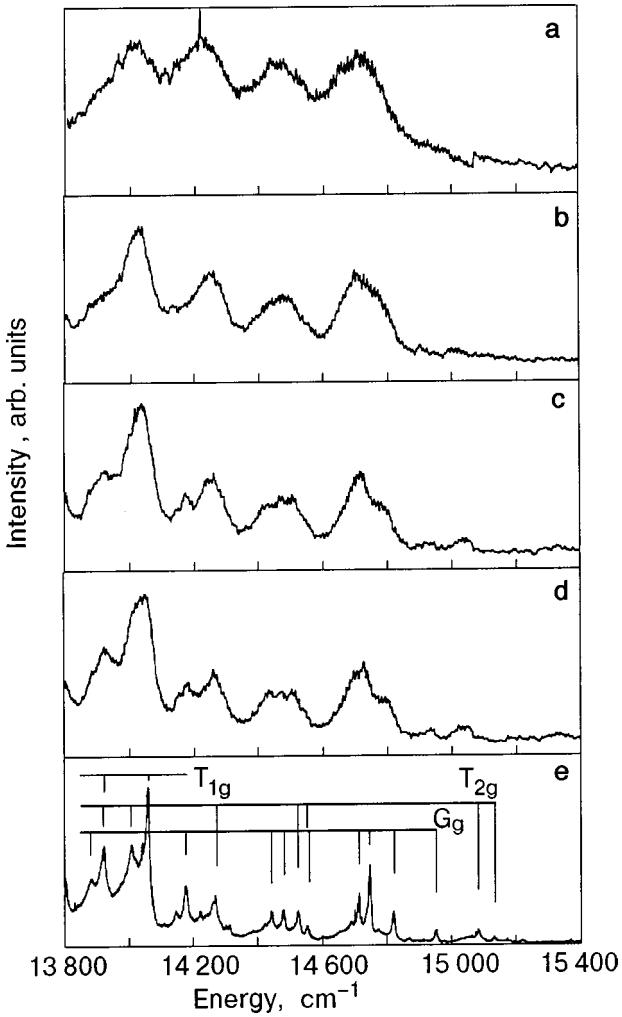

FIG. 4. Time-gated fluorescence spectra of C_{60} in Ar matrices at different τ, ps: 30 (a), 90 (b), 150 (c), 210 (d) and under steady-state conditions (e).

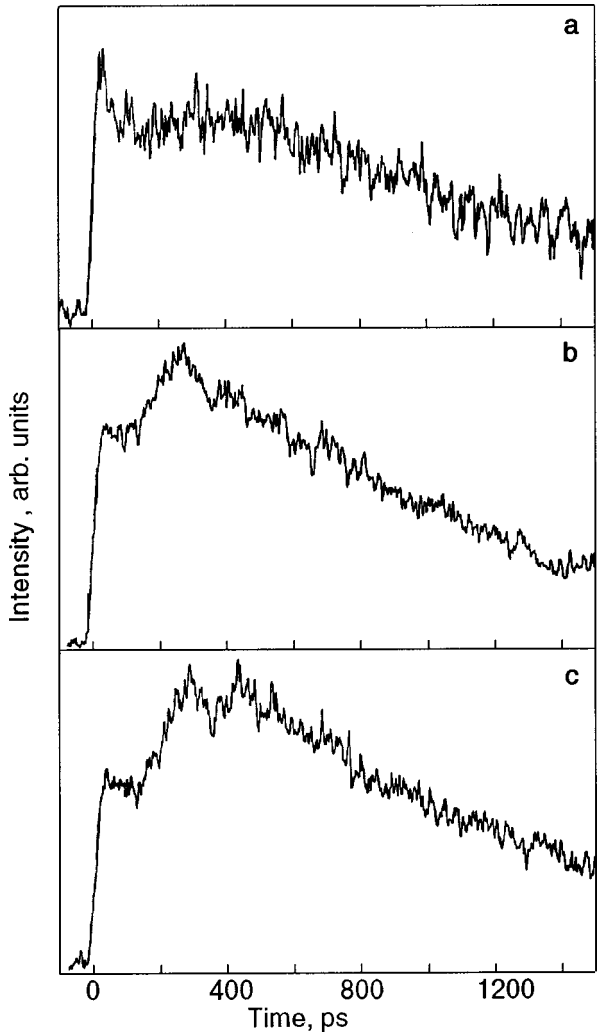

FIG. 5. Time-resolved fluorescence decay of the fluorescence bands of C_{60} in Ar matrices belonging to the different emitting characters: $h_u(4)$ of the G_g character (a); $t_{1u}(4)$ of the T_{1g} character (b), and $h_u(1)$ of the T_{2g} character (c).

This description of the time-gated fluorescence spectra shows that the bands associated with the G_g and the T_{1g}/T_{2g} characters exhibit nonidentical behaviors in the short-time domain (~200 ps). This is better visualized by plotting the time-resolved fluorescence decay curves at given emission wavelengths (i.e., looking at a band or group of bands). Time-resolved fluorescence decay curves of C_{60} in Ar matrices are given in Fig. 5, for selected fluorescence bands belonging to each emitting character. The structure at very early times (most visible in Fig. 5c) is due to the scattered laser light and the response of the detection system, as checked by recording the time profile of the emitted light at a position where no emission band occurs (e.g., at ~15400 cm^{-1}). It can be seen that the fluorescence associated to the G_g character (Fig. 5a) is characterized by a biexponential decay, with a short component having a decay constant of ~70 ps and a long one with a decay constant of ~1500 ps. On the other hand, the fluorescence bands associated to the T_{2g} and T_{1g} emitting character (Fig. 5b and 5c) show a short rise followed by a long decay. The rising component has a time constant of ~70 ps, while the long decay component has a time constant of ~1500 ps also. In the case of Ne matrices, we observe a similar behavior except that the time constants are different. The time constants, given by a fit with a biexponential function, are given in Table III for both matrices. It is clear that the decay times of the long component are identical for all vibronic bands attributed to the three different emitting characters. Therefore, the hypothesis of a single emitting S_1 state which consists of a mixed T_{1g}, T_{2g}, and G_g character is further confirmed. On the other hand, the short-time behavior suggests the existence of a short-lived transient fluorescence of a dominant G_g character that feeds the S_1 fluorescence. This point is discussed further below.

In summary, our results show that:

a) all emission bands exhibit the same decay rate of ~0.9 ns in Ne and ~1.5 ns in Ar, indicating that only one emitting S_1 state, of mixed T_{1g}, T_{2g}, and G_g character, is responsible for the steady-state fluorescence spectra;

b) in the 30–100 ps time domain, the fluorescence bands belonging to the G_g emitting character are enhanced in Ne and Ar, relative to later times. However, in Ne, they remain weaker than the bands belonging to the T_{2g} and T_{1g} emitting characters, while in Ar at 30 ps, they are equally as strong;

c) the observations in b) are corroborated by the time-resolved fluorescence spectra of the various bands. In Ne and Ar matrices, the bands belonging to the G_g emitting charac-

TABLE III. Time constants of the different components of the time-resolved fluorescence spectra of C_{60} in neon and argon matrices. τ_1 represents a decay time in the case of the G_g emitting character, and a rise time in the case of the T_{1g}/T_{2g} emitting characters.

Emitting character	Vibronic bands	τ_1 , ps	τ_2 , ps	Vibronic bands	τ_1 , ps	τ_2 , ps
	Neon			Argon		
T_{1g}	$t_{1u}(4)$ $t_{1u}(4) + h_g(1)$	205 ± 30	900 ± 150	$t_{1u}(4)$ $t_{1u}(4) + h_g(1)$	90 ± 20	1455 ± 150
T_{2g}	$g_u(6)$, $h_u(7)$ $h_u(7) + h_g(1)$ $h_u(1)$	170 ± 30	875 ± 120	$g_u(4)$, $h_u(5)$ $g_u(4) + h_g(1)$ $h_u(7)$	60 ± 20	1690 ± 200
G_g	$g_u(5)$ $g_u(5) + h_g(1)$	130 ± 30	935 ± 150	$h_u(3)$, $h_u(4)$ $g_u(3)$, $h_g(6)$ $g_u(5)$	60 ± 20	1490 ± 200

ter are characterized by a short decaying component having a time constant $\sim 170 \pm 40$ ps for Ne and $\sim 70 \pm 20$ ps in Ar (Table III). Those belonging to the T_{1g} and T_{2g} emitting characters exhibit, on the other hand, a rising component having a similar time constant in the respective matrices;

d) there is a significant narrowing of the spectral lines within the first 100 ps or so, but the linewidths become essentially constant beyond ~200 ps in Ne and ~90 ps in Ar.

The ultrafast relaxation from the initially excited state S_n to the S_3 level has in the meantime been measured in the femtosecond domain using pump–probe transient absorption. It was found to occur in ~500 fs in Ar matrices.[26] The similarity between the absorption and excitation spectra (Fig. 1) clearly suggests that this process is an internal conversion (IC) involving only the excited singlet vibronic states. However, differences between Ne and Ar matrices for this ultra-

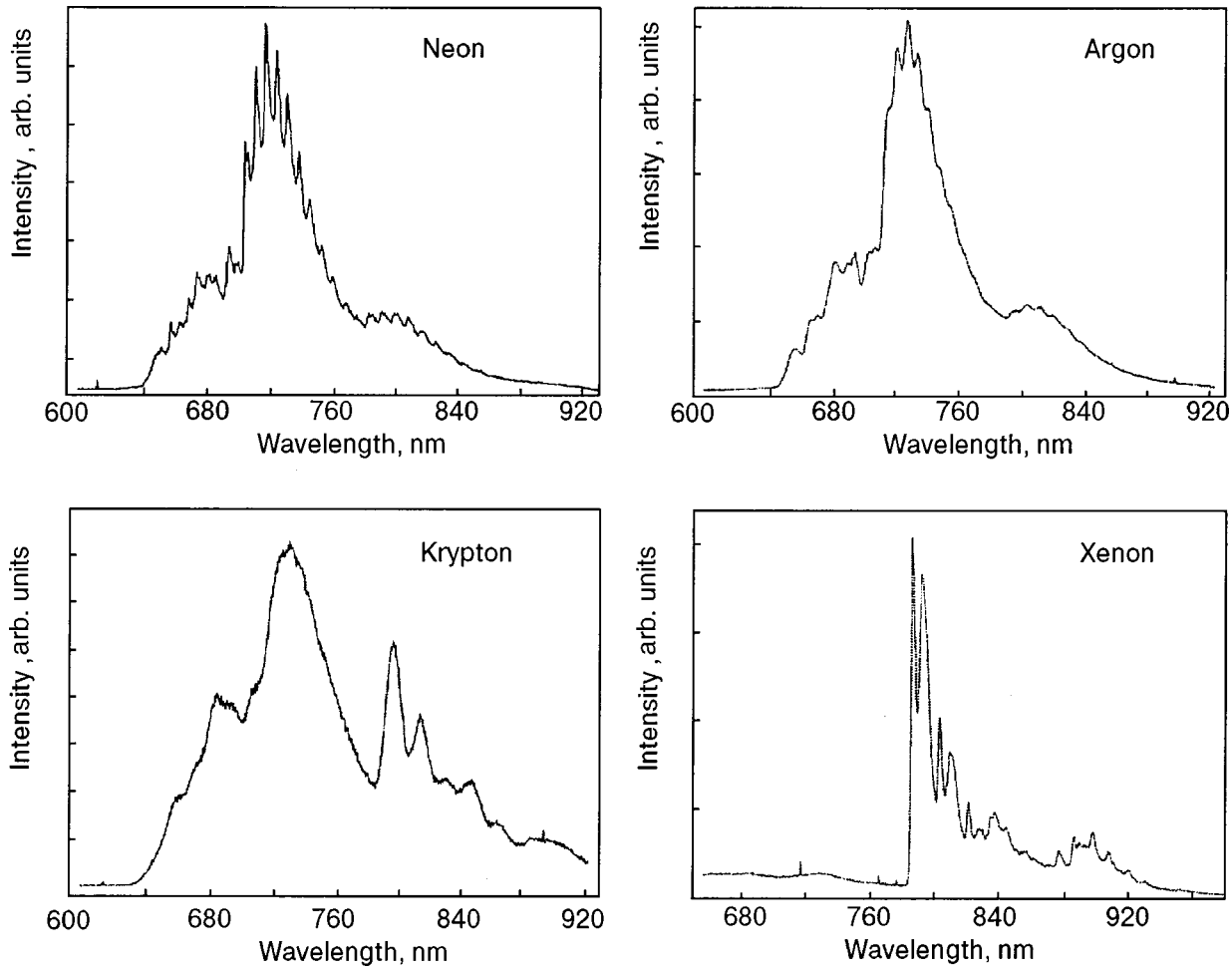

FIG. 6. Overview of low-resolution emission spectra of C_{60} in Ne, Ar, Kr and Xe. Note the broadening of the fluorescence bands and the appearance of new bands on the red side of the spectrum, in going to heavier matrices.

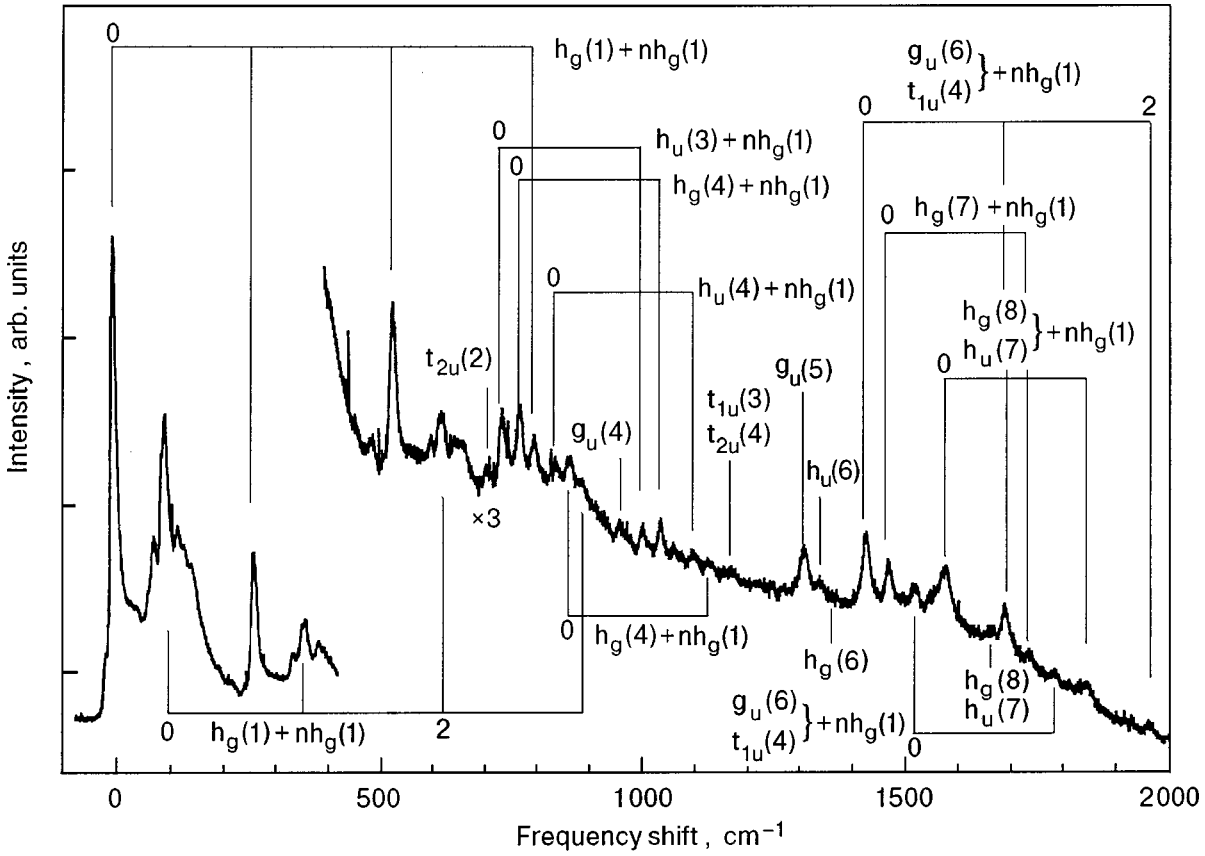

FIG. 7. High-resolution ($\Delta\lambda = 2$ Å) phosphorescence spectrum of the 780–950 nm region of C_{60} in Xe matrices ($\lambda_{exc} = 500$ nm), plotted as a function of the frequency shift from the first band at 786.5 nm. The top assignments are those of the 786.5 nm progression (site I in Table IV) and the bottom assignments are those of the 792.5 nm progression (site II in Table IV).

fast IC relaxation process have been found and are being investigated in more detail at present.[28] Coming back to the relaxation processes between the lowest three singlet states, the time-resolved data were discussed in Ref. 25, where we assumed that the S_3 state, of a predominant G_g character, relaxes to the nearly degenerate S_1/S_2 states, having predominant T_{2g} and T_{1g} characters. The latter depends on the matrix, as discussed in the preceding paragraph. We assumed the S_3 state to lie $\sim$50 cm^{-1} above the S_2/S_1 state on the basis of the absorption data only; however, in line with the above discussion (see Sec. 2), a value of $\sim$100 cm^{-1} would be more realistic. Nevertheless, the quantitative details of the relaxation process are not important. What is crucial here is that, in line with the discussion in Sec. 3, static crystal-field effects and/or nontotally symmetric modes of the cage need to be involved in order to couple the G_g state with the T_{1g} and T_{2g} states. Consistent with the steady-state fluorescence data, the time-resolved data confirm that such effects are stronger in Ar than in Ne matrices, probably because of the lower local cage symmetry in Ar.

On the basis of our picosecond fluorescence data and our preliminary femtosecond transient absorption measurements, we may already draw a general picture of the ultrafast intramolecular energy redistribution. Following excitation of the S_n state (or group of states) by the UV pump pulse, intramolecular $S_n - S_3$ relaxation occurs on an ultrafast time scale of a few hundred femtoseconds. This is a remarkably short time scale for the dissipation of over 1 eV of energy by internal conversion. We stress once more that in this picture, coupling of the singlet vibronic levels with resonant levels of the triplet manifold or the ground state is excluded. In the first case, the intersystem crossing time of about 1 ns for the S_1 state shows that it is a very inefficient process to compete with IC. In the second case, the Franck–Condon overlap integrals of the singlet vibronic levels with the ground state vibrational levels should be negligibly small.[7–11] Finally, such processes are state selective, and the similarity between the absorption and excitation spectra (Fig. 1) rules out such a selectivity. From S_3, the population decays to S_2/S_1 in tens of picoseconds, as it is mediated only by lattice phonons. From S_1, intersystem crossing then occurs on the time scale of 1 ns. Note, however, that even in this case, we also see a medium dependence (Table III), which should, in our opinion, be due to resonance conditions of S_1 with the triplet levels and/or to the changing dominant symmetry character of S_1. Internal conversion within the triplet manifold should again proceed on an ultrafast time scale followed by a tens of μs radiative decay to the ground state[25] (see Sec. 5).

5. PHOSPHORESCENCE SPECTRA

In going to heavier matrices, such as Kr or Xe, the medium effects become more striking. The singlet emission bands broaden significantly and tend to decrease in intensity at the expense of new emission bands on the red side, as seen in Fig. 6. These new emission bands are phosphorescence bands which are attributed to the triplet states of C_{60}. A detailed discussion and assignment was presented in Ref. 24

in the case of Xe matrices. We found that site effects are dramatic in such media, resulting in energy differences of $\sim$100 cm^{-1} between trapping sites. Furthermore, these sites are stable against annealing up to 50 K, and lifetimes of $\sim$15 μs are measured in both.

A detailed analysis of the phosphorescence spectra in Xe matrices was carried out, which is presented in Fig. 7 and in Table IV. The spectrum shows two groups of bands belonging to different sites. If we consider the progression with an origin at 786.5 nm which is due to the main site and on the basis of the mode frequencies determined from the fluorescence spectra of C_{60} in Ne and Ar matrices,[22] we can assign all the peaks to H–T modes of g_u, h_u, t_{1u}, or t_{2u} symmetry, in addition to the dominant J–T $h_g(1)$ mode, and to combination modes with the latter. With the T_{1g} symmetry of the spin–orbit operator, all these modes can vibronically induce phosphorescence from any of the lowest three triplet states $^3T_{1g}$, $^3T_{2g}$, and ^3G_g, to the ^1A_g ground state. According to Negri *et al.*[6] and László *et al.*[29] the lowest triplet state is the $^3T_{2g}$ state, whereas the $^3T_{1g}$ and ^3G_g states lie about 0.3 eV and 0.6 eV higher in energy, respectively. This assignment of the lowest triplet state seems to allow a consistent interpretation of the triplet–triplet absorption spectra.[30] In our phosphorescence spectra, the absence of a_u modes (expected for the $^3T_{1g}$ state) and of g_g modes (expected for the ^3G_g state) support the assignment of the lowest triplet state as $^3T_{2g}$.

The energy ordering of the triplet states as T_{2g}, T_{1g}, G_g is in line with the ordering of singlet states in the emission spectrum in Ne matrices, but differs from that observed in Ar. It also differs from the ordering observed in the absorption spectra of the singlet states (Sec. 2). In the case of C_{70} in Ne matrices, for which we could clearly separate the different origins of the lowest singlet electronic states, we observed that the ordering of state symmetries between S_1 and S_2 (separated by $\sim$260 cm^{-1}) was the same in absorption and in emission.[23] Furthermore, the energy splittings between the S_1 and S_2 states and ordering of states was found to be the same for the lowest two triplet states, T_1 and T_2. Therefore in C_{60} either the ordering of the triplet states differs from that of the singlet states, as suggested by theory,[28,29] or, as discussed in Sec. 3 for the singlet states, it would seem that the lowest triplet state also undergo a reversal of state ordering. The reversal in the case of C_{60} in rare gas matrices is probably due to the small energy splitting between the lowest electronic states ($\sim$50 cm^{-1}), which is of the order of the absorption–emission Stokes shift they undergo.

It is interesting to note that contrary to fluorescence, phosphorescence is dominated by the Jahn–Teller $h_g(1)$ mode while, all the other J–T or H–T bands are weaker by at least one order of magnitude. This suggests that a coupling mediated by these modes is probably very weak due to the fact that the surfaces associated to them are strongly shifted with respect to the equilibrium position of the $^3T_{2g}$ surface.

TABLE IV. Wavelengths, frequencies and frequency shifts from the origin of the bands belonging to the 786.5 nm progression (Fig. 7, Site I), and to the 792.5 nm progression (Fig. 7, Site II), together with the assignment and frequencies from Ref. 22.

λ, nm	ν, cm^{-1}	Δν, cm^{-1}	Assignment	Ref. 22
		Site I		
786.5	12714	0	origin	–
803.3	12448	266	$h_g(1)$	262
820.9	12182	532	$2h_g(1)$	–
833.1	12004	710	$t_{2u}(2)$	714
834.9	11977	737	$h_u(3)$	743
837.3	11943	771	$h_g(4)$	776
839.2	11916	798	$3h_g(1)$	–
842.2	11873	841	$h_u(4)$	832
850.7	11755	959	$g_u(4)$	961
854.2	11707	1007	$h_u(3) + h_g(1)$	1003
856.4	11667	1037	$h_g(4) + h_g(1)$	1042
861.2	11612	1102	$h_u(4) + h_g(1)$	–
866.4	11542	1172	$t_{1u}(3)$, $t_{2u}(4)$	1204, 1185
877.0	11402	1312	$g_u(5)$	1310
879.0	11376	1338	$h_u(6)$	1342
885.8	11289	1425	$g_u(6)$, $t_{1u}(4)$	1426, 1433
889.2	11246	1468	$h_g(7)$	1477
896.8	11151	1573	$h_g(8)$, $h_u(7)$	1567
906.8	11028	1686	$g_u(6)/t_{1u}(4) + h_g(1)$	–
910.7	10980	1734	$h_g(7) + h_g(1)$	–
919.5	10875	1839	$h_g(8)/h_u(7) + h_g(1)$	–
929.9	10754	1960	$g_u(6)/t_{1u}(4) + 2h_g(1)$	–
		Site II		
792.5	12618	0	origin	–
809.3	12357	261	$h_g(1)$	262
827.1	12091	527	$2h_g(1)$	–
844.1	11847	771	$h_g(4)$	776
863.6	11580	1038	$h_g(4) + h_g(1)$	–
884.4	11307	1272	$h_g(6)$	1265
893.0	11198	1420	$g_u(6)$, $t_{1u}(4)$	1426, 1433
904.7	11054	1564	$h_g(8)$, $h_u(7)$	1567
914.7	10932	1686	$g_u(6)/t_{1u}(4) + h_g(1)$	–

6. CONCLUSIONS

In this contribution, we have reviewed our results on the spectroscopy and intramolecular energy relaxation processes of C_{60} in rare gas matrices, while presenting new data and revising or improving some of our previous interpretations. Emphasis has been put on medium effects, which turn out to

be important both in the static and the time-re-solved data. This, in itself, is quite remarkable given the size of C_{60} and its large number of degrees of freedom.

In particular, we have confirmed our previous assignments[22] of the splitting between the lowest three singlet states in absorption and proposed a precise value for their purely electronic origins in the gas phase. In fluorescence, we have discussed the drastic differences between the Ne and Ar data and, in particular, the change in dominant emitting character from T_{1g} in Ar to T_{2g} in Ne, as well as a similar change between the absorption and the fluorescence data. This was reconciled by assuming different Stokes shifts for the two states, which bring T_{2g} at an energy lower than T_{1g} before emission. A similar situation could occur for the phosphorescence transition to account for the dominant $^3T_{2g}$ character of the phosphorescence data in Xe matrices. We note however that theory predicts it as the lowest triplet state. Both the static and time-resolved fluorescence data indicate strong mixing between the lowest three singlet states, in agreement with their small energy differences. The time-resolved data confirm the nearly degenerate character of the S_1 and S_2 states, while the S_3 state stands slightly higher (in the gas phase we inferred an S_1-S_3 splitting of $\sim$100 cm^{-1}). In the free molecule, the purely electronic T_{1g}, T_{2g}, and G_g levels cannot undergo mixing. Such mixings are induced in the matrix either by static or dynamic crystal-field effects which break the I_h symmetry of the molecule. The ultrafast internal conversion process in the singlet state manifold is a remarkable process which deserves further attention, and work toward this aim is in progress.

I would like to thank all my co-workers that have been involved in this work: A Sassara, G. Zerza, M. T. Portella-Oberli, B. Deveaud, J-D. Ganiere. I am also grateful to R. Blades and Z. Al Rahbani for inspiring ideas. This work was supported by the Swiss NSF via contracts 53811.98.

*E-mail: majed.chergui@ipmc.unil.ch

[1] Y. Chai, T. Guo, C. Jin, R. E. Haufler, L. P. F. Chibante, J. Fure, J. M. Alford, and R. E. Smalley, J. Phys. Chem. **95**, 7564 (1991).
[2] B. A. DiCamillo, R. L. Hettich, G. Guichon, R. M. Compton, M. Saunders, H. A. Jimenez-Vazquez, A. Khong, and R. J. Cross, J. Phys. Chem. **100**, 9127 (1996) (References cited).
[3] H. Sprang, A. Mahlkow, and E. E. B. Campbell, Chem. Phys. Lett. **227**, 91 (1994).
[4] L. W. Tutt and A. Kost, Nature (London) **356**, 225 (1992).
[5] K. Dou, J. Y. Du, and E. T. Knobbe, J. Lumin. **83**, 241 (1999).
[6] V. M. Farzdinov, Yu. E. Lozovik, Yu. A. Matveets, A. G. Stepanov, and V. S. Letokhov, J. Phys. Chem. **98**, 3290 (1994).
[7] F. Negri, G. Orlandi, and F. Zerbetto, Chem. Phys. Lett. **144**, 31 (1988).
[8] F. Negri, G. Orlandi, and F. Zerbetto, J. Chem. Phys. **97**, 6496 (1992).
[9] F. Negri, G. Orlandi, and F. Zerbetto, J. Phys. Chem. **100**, 10849 (1996).
[10] F. Negri and G. Orlandi, J. Phys. B **29**, 5049 (1996).
[11] C. Cepek, A. Goldoni, S. Modesti, F. Negri, G. Orlandi, and F. Zerbetto, Chem. Phys. Lett. **250**, 537 (1996).
[12] S. Leach, M. Vervloet, A. Despres, E. Bréheret, J. P. Hare, T. J. Dennis, H. W. Kroto, R. Taylor, and D. R. M. Walton, Chem. Phys. **160**, 451 (1992).
[13] Y.-P. Sun, P. Wang, and N. B. Hamilton, J. Am. Chem. Soc. **115**, 6378 (1993).
[14] D. J. van den Heuvel, G. J. B. van den Berg, E. J. J. Groenen, J. Schmidt, I. Holleman, and G. Meier, J. Phys. Chem. **99**, 11644 (1995).
[15] D. J. van den Heuvel, I. Y. Chan, E. J. J. Groenen, M. Matsushita, J. Schmidt, and G. Meijer, Chem. Phys. Lett. **223**, 284 (1995).
[16] X. L. R. Dauw, M. V. Bronsveld, A. Kruger, J. B. M. Warntjes, M. R. Witjes, and E. J. J. Groenen, J. Chem. Phys. **109**, 9332 (1998).
[17] J. Feldmann, R. Fischer, E. O. Gobel, and R. Schmitt-Rink, Phys. Status Solidi **173**, 339 (1992).
[18] M. Muccini, R. Danieli, R. Zamboni, C. Taliani, H. Mohn, W. Muller, and H. U. van ter Meer, Chem. Phys. Lett. **245**, 107 (1995).
[19] R. E. Haufler, Y. Chai, L. P. F. Chibante, M. R. Froehlich, M. R. Weisman, R. F. Curl, and R. E. Smalley, J. Chem. Phys. **95**, 2196 (1991).
[20] Z. Gasyna, P. N. Schatz, J. P. Hare, T. J. Dennis, H. W. Kroto, R. Taylor, and D. R. M. Walton, Chem. Phys. Lett. **183**, 283 (1991).
[21] A. Sassara, G. Zerza, and M. Chergui, J. Phys. B **29**, 4997 (1996).
[22] A. Sassara, G. Zerza, M. Chergui, F. Negri, and G. Orlandi, J. Chem. Phys. **107**, 8731 (1997).
[23] A. Sassara, G. Zerza, and M. Chergui, J. Phys. Chem. A **102**, 3072 (1998).
[24] A. Sassara, G. Zerza, and M. Chergui, Chem. Phys. Lett. **261**, 213 (1996).
[25] A. Sassara, G. Zerza, M. Chergui, V. Ciulin, J.-D. Ganiere, and B. Deveaud, J. Chem. Phys. **111**, 689 (1999).
[26] A. Sassara, G. Zerza, V. Ciulin, M. T. Portella-Oberli, J.-D. Ganiere, B. Deveaud, and M. Chergui, J. Lumin. **83/84**, 29 (1999).
[27] J. D. Close, F. Federmann, K. Hoffmann, and N. Quaas, Chem. Phys. Lett. **276**, 393 (1997).
[28] M. T. Portella-Oberli, A. Spiridon, F. Vigliotti, A. Sassara, and M. Chergui (work in progress).
[29] L. László and L. Udvardi, Chem. Phys. Lett. **186**, 418 (1987).
[30] R. V. Bensasson, T. Hill, C. Lambert, E. J. Land, S. Leach, and T. G. Truscott, Chem. Phys. Lett. **201**, 326 (1993).

This article was published in English in the original Russian journal. Reproduced here with stylistic changes by the Translation Consultant.

Sound propagation in liquid He in impurity–helium solids

S. I. Kiselev, V. V. Khmelenko,* and D. M. Lee

Laboratory of Atomic and Solid State Physics, Cornell University, Ithaca, NY 14853-2501, USA
(Submitted April 6, 2000)
Fiz. Nizk. Temp. **26**, 874–883 (September–October 2000)

The observed features of the attenuation of ultrasound in Im–He samples created after the introduction of impurity particles (D_2,N_2, Ne, Kr) in a volume of helium II show that a porous substance consisting of a loosely interconnected continuous network is created. It is formed by impurity particles encapsulated in solidified helium. The propagation of ordinary sound in these porous samples is similar to the fast sound mode in light aerogels. The temperature dependence of the attenuation for different Im–He samples is investigated. It is established that the character of the attenuation in D_2–He samples is considerably different from that in heavier Im–He solids (Im=N_2, Ne, Kr). Analysis of the attenuation leads to the conclusion that Im–He samples have a wide distribution of pores, from 8 nm to 800 nm. The study of ultrasound in helium in Im–He samples near the λ point shows the presence of broadening in the attenuation peak as compared with bulk liquid helium. The suppression of T_c is very small, $\leqslant$ 0.2 mK. © *2000 American Institute of Physics.* [S1063-777X(00)00309-1]

1. INTRODUCTION

The investigation of neutral atoms and clusters in liquid and solid helium is a rapidly developing research field.[1–4] Much progress has been achieved in studies of the spectral characteristics of single atoms or molecules trapped in matrices of solid helium or dissolved in liquid helium, from which information about the structure of the helium surrounding these impurities was found.

The impurities can be divided into two classes according to the sign of chemical potential inside the helium matrix. Particles with a positive potential tend to form bubbles, while atoms with a negative potential create snowballs. In the latter case, after introducing the impurity particles into liquid helium, we can produce stable impurity–helium (Im–He) clusters, which make it possible to create macroscopic Im–He samples consisting of impurity atoms isolated in liquid or solid helium. At first these systems were obtained by injecting atoms and molecules such as nitrogen, deuterium, neon and krypton[5–7] into superfluid helium. These metastable systems are of fundamental interest. For example, there is the possibility of observing collective effects caused by the interaction of stabilized impurity particles in helium and also the opportunity to create new materials with high energy density stored in them.[8] A very high relative concentration of nitrogen atoms in solidified helium (N:He=4%) has already been achieved by injecting the products of a nitrogen–helium discharge into a volume of superfluid helium.[6,9] For this case, the density of the chemical energy stored in these samples ($\sim 5\times 10^3$ J/gm) is close to that of the best chemical explosive materials. Another interesting aspect of Im–He systems is the possibility of chemical reactions in a solid matrix when the state of the low-temperature matrix is mostly determined by zero-point motion.[10–12] Investigations of atoms and molecules of hydrogen isotopes stabilized in superfluid helium have revealed tunneling reactions resulting in the exchange of hydrogen and deuterium atoms between the atomic state and the bound molecular state.[5]

Investigations of macroscopic solid samples formed by injecting impurities into superfluid helium have opened the possibility for the creation of metastable solid phases built from coalescing clusters of solid helium surrounding the impurity particles. Later it was shown that the centers of the these clusters might consist of either single impurity particles or small clusters of impurities.[13,14] At the same time the structure of these Im–He solids is not fully determined. Recently x-ray spectroscopy showed that the impurities (surrounded by a few layers of solid helium) formed porous structures in superfluid helium.[15] The characteristic size of the constituent building blocks of this porous material is 6 nm. The density of impurity particles can be as high as 10^{20} atoms/cm^3 (with a volume fraction $\sim$ 0.5%).

We briefly summarize the present state of knowledge regarding the Im–He solids. The preponderance of evidence suggests that macroscopic samples of the Im–He solid phase are built from aggregations of small Im–He clusters. Furthermore, we believe that these aggregates form extremely porous solids into which liquid helium can easily penetrate. They consist of a loosely connected continuous network of impurities or clusters of impurities, each of which is surrounded by one or two layers of solidified helium. Therefore we have a unique opportunity to investigate the properties of superfluid helium in porous structures formed by particles with a well-known potential of interaction with helium.

A great deal of effort has recently been dedicated to the investigation of superfluid helium in porous materials. We cite here a recent review article describing the specific features of helium in various porous structures.[16] The importance of these studies is now discussed. Superfluidity of helium in restricted geometries has been the object of much theoretical and experimental interest in recent years. Helium has long provided a testing ground for theories of phase transitions. Bulk helium exhibits three-dimensional (3D) critical

behavior near lambda transitions, while helium films on flat substrates are 2D, with a vortex-inhibiting transition of the Kosterlitz–Thouless type.[17] When helium is adsorbed in a porous medium either as a film or completely filling the pores, its behavior may be changed in a number of ways. Finite size effects might shift or even smear out the phase transition, the multiply-connected substrate geometry may change the effective dimensionality, or disorder induced by the porous material may change the nature of the transition. The superfluid density ρ_s near the lambda point vanishes according to the power law

$$\rho_s(t)=\rho_{s0}|t|^{\zeta}, \tag{1}$$

where t is a reduced temperature ($t=(T-T_c)/T_c$, with the transition temperature T_c). The superfluid-density exponent ζ is found to be 0.6705 for bulk helium,[18] for helium in Vycor glass,[19] and for helium in porous gold.[20] For a particular aerogel it is significantly larger—0.81.[19] For aerogels of different porosity it varies from 0.71 to 0.81.[21] At the same time, the superfluid transition temperature is suppressed down to 1.955 K in Vycor. For porous gold (which contains larger pores) $T_c=2.1691\pm 5\times 10^{-5}$ K, and for aerogels of different porosity the suppression is very small: $T_c=(2.16985\pm 3)\times 10^{-5}$ (in 95% aerogel), $T_c=(2.1717\pm 1)\times 10^{-5}$ (in 99.5% aerogel).[21] In the light of these previous studies, the problem of investigating the critical behavior of helium near the lambda point in the new class of porous material discussed here arises quite naturally. There are experimental difficulties in combining the method of preparing impurity–helium solids with precise heat capacity or torsional oscillator techniques. On the other hand, ultrasonic velocity and attenuation measurements[22,23] can be easily applied to investigate superfluid helium in Im–He solids. The sound velocity in porous media can provide information about the superfluid density as well as the density and elastic properties of the solid matrix. The sound attenuation reflects the dissipation in the system, and its frequency dependence is related to the characteristic pore size.[24] Also, if the sound speed in a ''dry'' sample (a sample with the liquid helium removed) could be measured, we could then determine the effective density of the Im–He solid. This turns to be extremely difficult and has not as yet been accomplished.

The motion of a fluid in a porous medium during acoustic measurements depends on the pore size and the fluid's properties. In liquid ^{4}He the viscous penetration depth is

$$\delta_{\rm visc}=(2\eta/\omega\rho_n)^{1/2}, \tag{2}$$

where η is the viscosity of ^{4}He, ρ_n is the density of the normal component, and ω is the frequency of ultrasound. At low sound frequencies, $\delta_{\rm visc}$ is bigger than the pore size, so the entire normal component is viscously locked to the solid matrix. Therefore the main effect of the fluid is to change the effective density of the porous medium. At high frequencies, only a thin surface layer is dragged along with the solid. The effective density of the porous material then is much smaller, and the sound is strongly attenuated by the viscous losses in the surface layer. To use sound for probing the structure of porous material, one should vary $\delta_{\rm visc}$ over as large a range as possible. Superfluid helium gives us this unique opportunity. Between 1.0 and 2.17 K the normal fluid density fraction varies from zero to one, causing $\delta_{\rm visc}$ to change by an order of magnitude from 1500 nm to 100 nm for 5 MHz sound. Biot created a basic theoretical framework for sound propagation in porous materials.[25,26] He considered the flow of the viscous fluid under an oscillatory pressure gradient in elastic porous solids. In the low-frequency regime his theory predicted that the attenuation changes as[24]

$$\alpha\propto\rho_n^2\omega^2/\eta. \tag{3}$$

For high-frequency sound, the corresponding attenuation is

$$\alpha\propto\sqrt{\eta\rho_n\omega}. \tag{4}$$

In this paper we report results of ultrasound measurements of the velocity and attenuation of longitudinal waves in helium-filled porous Im–He solids. Some of the results have been published in our previous paper.[27] It was found that the speed of sound in this material is close to that of first sound in bulk liquid helium and decreases more rapidly with temperature than does the latter, similar to the behavior observed in aerogel.[28] There was no clear explanation, however, for the way the attenuation of ultrasound changes with temperature in helium-filled Im–He solids. Here we present the results of more-detailed investigations of the speed and attenuation of sound, particularly near the lambda point. One goal of this work was to check a possible T_c suppression. We also performed the measurements at different frequencies (1, 3, 5 MHz) to help us to understand the mechanism of attenuation. Moreover we investigated the stability of different Im–He samples between 1 and 4.2 K.

2. EXPERIMENTAL METHOD

2.1. Preparation of porous impurity-helium solids

The technique for creating impurity-helium solids in a volume of He II was similar to that developed by the Chernogolovka group.[6,29] A gas jet of helium containing a small fraction (0.5–1%) of impurity atoms or molecules impinged on superfluid helium contained in a small Dewar beaker sitting in the main helium glass Dewar. The helium vapor pressure in the Dewar was maintained at 1–5 Torr by a high speed rotary pump. The gas entered through a quartz capillary of diameter about 0.7 mm, near the end of which was a region containing a high power rf (60 MHz) discharge for dissociation of molecules. In this series of experiments most of the Im–He samples were created by introducing into He II a gas jet not subjected to the action of the rf discharge. When there was no need to dissociate molecules we used a stainless-steel capillary with inner diameter of 1.6 nm surrounded by a vacuum jacket with a heater at the bottom end. As in all of our previous setups, the diameter of the hole at the end of the capillary was 0.7 mm. The nozzle of the capillary was located 2 cm above the surface of the superfluid helium in the small quartz Dewar mentioned above, which acted as the collection beaker. To prevent the freezing of impurities in the nozzle we heated the end of the capillary by an annular heater ($R\sim 10\,\Omega$). In order to keep the level of helium in the beaker constant, a continuously operating fountain pump was used. When the gas mixture jet impinged on the surface, a macroscopic snowflake-like semitransparent material was created. This fell down through the liquid and

then congealed, forming a porous impurity–helium solid between the transducers of the ultrasound cell. The centers of the transducers were ~ 5 cm below the level of helium in the beaker. For more effective collection of the sample in the cell we used a quartz funnel with two side plates which were placed between the end plates of the cell. On some occasions, in order to compress the sample at low temperatures we used a small Teflon cylinder which could be moved up and down. We could monitor the presence of the sample in the cell and its homogeneity visually through slits on the sides of the glass Dewars. In these experiments the impurities used were Kr, Ne, and molecular D_2 and/or N_2. Gas mixtures of Im:He = 1:100 were used to dilute the impurity particles and therefore prevent them from congealing as they passed from the source to the surface of the liquid helium. The total flux of the gas mixtures was $(4-6)\times 10^{19}$ particles/s. Samples with a visible volume between 1.2 and 1.7 cm^3 were usually used.

2.2. Ultrasound cell

In our experiments were used two different ultrasound cells. In the first cell two *x*-cut gold plated quartz transducers (5 MHz fundamental) were used.[27] The crystals were 1 cm in diameter. Each of these was pushed against the parallel walls of the cell by two springs, one of which served as a central electrode. The ground was provided by the brass body of the cell. The path length was determined at room temperature with a micrometer, with a correction being made for the contraction upon cooling. The value for the path length used in the experiments was (1.572 ± 0.005) cm. In our second cell we used two $LiNbO_3$ transducers with fundamental frequency ~ 1 MHz (Fig. 1). The odd harmonics were also used (3 and 5 MHz). The transducers were 1.3 cm in diameter. Otherwise the design of the second cell was similar to the first one except that the distance between transducers was (1.470 ± 0.005) cm.

2.3. Spectrometer

The ultrasonic measurements were made using a homodyne phase-sensitive spectrometer (Fig. 2). A continuously operating oscillator was gated to provide a transmitted pulse of 4–12 μsec. The amplitude of the input signal could be varied from 1 to 100 V at the resonant frequency or at the odd harmonics of the transmitting crystal. The ultrasonic pulse was received by the second crystal, amplified, and split in two parts, one of which was used to directly measure the attenuation by recording the amplitude of the signal on a TEK460 digital oscilloscope. The second part was split again in two parts to obtain the 0° and 90° components, A_{0° and A_{90°. They were used to determine the phase φ of the signal:

$$\tan(\varphi) = A_{0^\circ}/A_{90^\circ}. \tag{5}$$

Once the initial speed of sound was measured at the temperature T_0 from the pulse transit time τ_0, changes in velocity were calculated from the phase of the received signal:

$$\Delta v = l\left(\tau_0 + \frac{\varphi(T)-\varphi(T_0)}{\omega}\right)^{-1}, \tag{6}$$

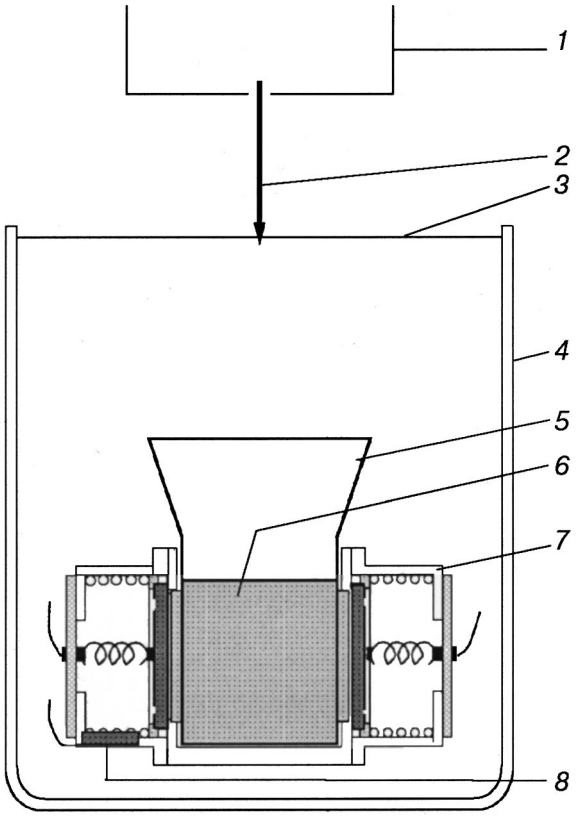

FIG. 1. Experimental cell: *1*—atomic and molecular source; *2*—impurity-helium jet; *3*—surface of liquid helium; *4*—quartz Dewar; *5*—quartz funnel; *6*—impurity-helium solid; *7*—ultrasound cell; *8*—germanium thermometer.

where l is the length of the cell. With typical samples, changes in velocity of a few parts per million could be resolved. A second oscilloscope was used to display the signal on a longer time scale. It registered up to 12 echoes of the signal in the first cell but only 3 echoes in the second one.

2.4. Thermometry

For the temperature measurements a calibrated Lake Shore germanium resistor was used. The thermometer was located inside the base of the cell just outside the path of the ultrasonic pulses, so that the effect of the temperature difference between the thermometer site and the sound path is

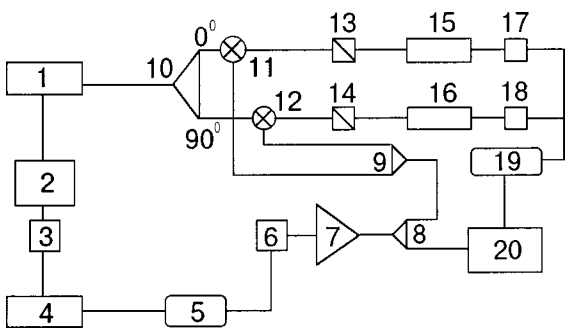

FIG. 2. Ultrasound spectrometer: *1*—HP8656B signal generator; *2*—MATEC310 gated amplifier; *3*, *6*—step attenuators (0–100 dB); *4*—ENI325LA power amplifier (+50 dB); *5*—ultrasound cell; *7*—amplification stage (+70 dB); *8*, *9*—power splitters; *10*—hybrid power splitter; *11*, *12*—mixers; *13*, *14*—low pass filters; *15*, *16*—PAR160 box car integrators; *17*, *18*—multimeters; *19*—computer; *20*—TEK TDS460 oscilloscope for peak-peak and time of flight measurement.

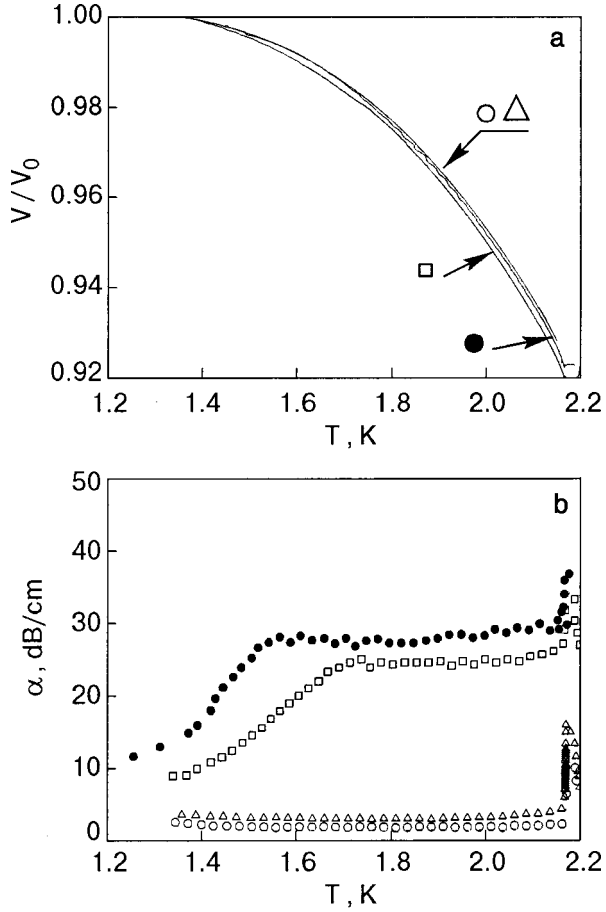

FIG. 3. The velocity (a) and attenuation (b) of 4.96 MHz sound in liquid helium: in bulk (○), in D_2–He solid (△), in Ne–He solid (□), in Kr–He solid (●). V_0 is the ultrasound velocity at initial temperature for these measurements, $T=1.362$ K.

minimized. After the lowest temperature (1.0–1.1 K) was achieved through pumping by both the rotary pump and a Roots blower, the initial speed of sound was measured. In the next stage, by closing the pumping line down, the temperature was allowed to increase by $\sim 10^{-4}$ K/s. Near the lambda point the rate was decreased to about 10^{-6} K/s. During the warmup, the fountain pump was constantly supplying helium into the Dewar beaker up to the lambda point. After the superfluid transition, the warmup rate increased to 10^{-4} K/s, but boiling in the inner Dewar did not occur.

3. EXPERIMENTAL RESULTS

Figure 3 shows the results of 5 MHz ultrasound measurements (in the first cell) at $T=1.1-2.2$ K in different Im - He solids (Im=D_2, Ne, Kr) just after preparation. Here and in later figures we show for comparison the velocity and attenuation of sound in bulk helium which were measured in each experiment before accumulating the sample. The attenuation of sound in the presence of Im–He samples (for such heavy impurities as Ne and Kr) is larger than in bulk helium at low temperatures and increases rapidly with temperature, after which it reaches a plateau, and at the λ point it goes through a maximum. Whereas heavy Im–He samples all have similar characteristic features, the D_2–He solid behaves quite differently. In the latter case, we do not observe any measurable effect on the speed of sound, and the attenuation has a behavior similar to that of bulk liquid helium, although slightly (~1 dB/cm) higher. The samples produced with heavy impurities are much denser than the ones with the D_2 impurity. In the case of the heavy impurities, investigations become impossible above temperatures in the neighborhood of 1.4 K because of an extremely high attenuation. We could have increased the signal by decreasing the distance between the transducers, but the method of collecting the sample did not allow us to do that. Therefore, in a series of experiments we introduced pulses with very large (up to 100 V) values of the input amplitude. From an analysis of the attenuation in different Im–He samples it became clear that D_2-(heavy Im)-He samples are, in fact, the most suitable ones for investigations of the mechanisms of attenuation, because they have a relatively small attenuation. In this work we compare three samples: N_2–He, D_2–He and mixed D_2–N_2–He. We investigated the stability of these samples and also the frequency dependence of ultrasound attenuation. Measurements were performed between 1.0 K and 4.2 K, with special attention to the region near the λ point. Figure 4 shows the characteristic temperature dependence of the attenuation for these three samples. The behavior of the attenuation in the D_2–N_2–He solid repeats that of the D_2–He solid and bulk helium up to $T\sim 1.75$ K. On warming up further, it becomes closer to the behavior of the N_2–He solid, i.e., the attenuation increases and then reaches a plateau.

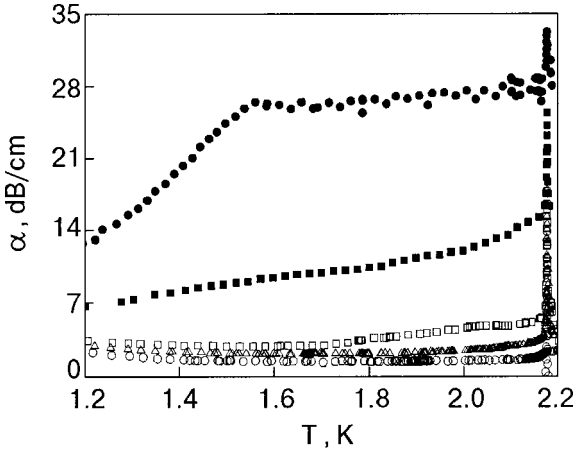

FIG. 4. The attenuation of 5 MHz ultrasound in liquid helium: in bulk (○), in D_2–He solid (△), in D_2–N_2–He solid (prepared without discharge (□), with discharge (■)), in N_2–He solid (●).

3.1. Stability of the structure of Im–He solids

In this section we discuss the factors affecting the structural stability of Im–He samples. Changes in the structure should lead to changes in the attenuation of ultrasound. Earlier it was discovered that compression of the samples results in an increased attenuation.[27] In this series of experiments we show the impact of a warmup from 1.0 K to 2.2–4.2 K on the structure of our samples. Figure 5 presents the results of ultrasound measurements for the three samples mentioned above as they were warmed up in the temperature ranges below or above T_λ. We can see that as the sample was heated up to $T_{max}<T_\lambda$ and then cooled again, there was no change in attenuation, and therefore the structure did not change. Crossing T_λ always led to the small transformations

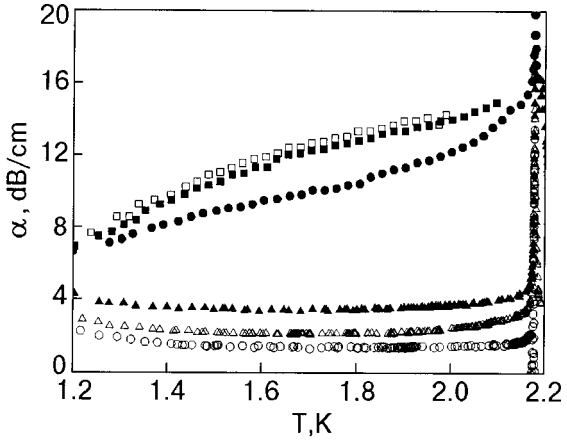

FIG. 5. The attenuation of ultrasound in liquid helium: in bulk (○), in D_2–He solid [after preparation of solid (△), after crossing λ-point and cooling down (▲)], D_2–N_2–He solid prepared with discharge [after preparation (●), after crossing λ-point and cooling down (■), after warming up to 2.1 K and cooling down (□)].

in the structure, registered by a slight increase of sound attenuation. The attenuation preserved its characteristic features, nevertheless.

Figure 6 shows the attenuation of ultrasound in liquid helium filled D_2–N_2–He solid during warmup from 1 K to 4.2 K. It was found that a sudden drop in attenuation takes place at 3.4–3.5 K, which is attributed to the change of structure of this solid. Below this temperature, the sample occupied the whole cell, but at $T \sim 3.5$ K a significant compression of the solid by a factor of 12 was observed. This is the first observation of a spontaneous macroscopic change of structure of an Im–He sample in liquid helium. For N_2–He without D_2, these changes were not observed.

3.2. Frequency dependence of the sound attenuation

Figure 7 presents the frequency dependence of the attenuation of ultrasound in the N_2–He sample. Decreasing the frequency leads to a lower attenuation and also shifts the point where the attenuation levels off to a plateau to higher temperatures. Figure 8 shows the measured frequency dependence of the attenuation in a D_2–N_2–He sample at 3 and 5 MHz. It significantly differs from the frequency dependence

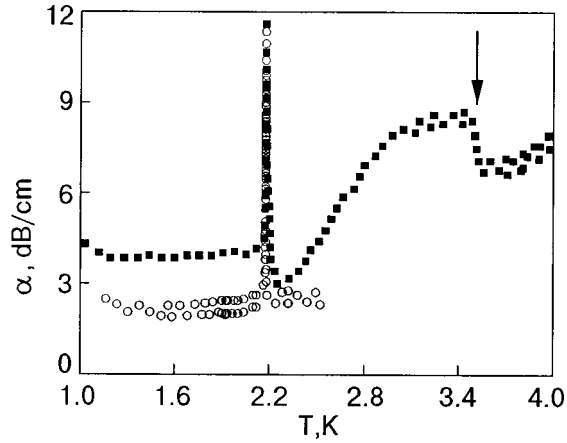

FIG. 6. The attenuation of 3.16 MHz ultrasound in liquid helium: in bulk (○), D_2–N_2–He solid (■).

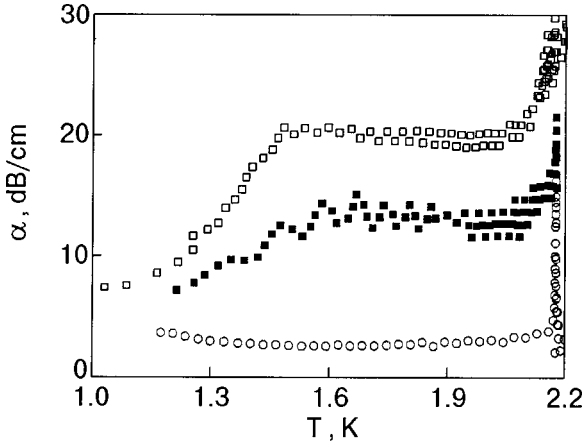

FIG. 7. The attenuation of ultrasound in liquid helium: in bulk (○), in N_2–He solid at 3.16 MHz (■), at 5.33 MHz (□).

observed in heavy Im–He samples (like N_2–He). For the first time, for the D_2–N_2–He solid, we detected a steady and steep monotonic increase in the attenuation up to the λ point without the occurrence of a plateau for 5 MHz sound. This might be explained by the purely high-frequency behavior of the attenuation in this sample. For the 3 MHz attenuation we observed only a slow linear increase in the same temperature range.

3.3. The behavior of the sound attenuation and the speed of sound near T_c.

The results of measurements near the λ point for N_2–He solids are shown in Fig. 9. Different symbols represent different samples. The maxima of the attenuation near the λ point for N_2–He samples are much broader than for liquid helium, making the precise determination of the position of the maxima impossible. We can conclude from this data that there is no significant shift of the λ point for helium-filled porous N_2–He solids.

Figure 10 shows the attenuation of ultrasound (only 5 MHz data are presented) in the mixed D_2–N_2–He solids. The width of the attenuation peak near the λ point is only slightly broader than that for pure helium. That makes it possible to determine a more precise position of the center of the peak. It

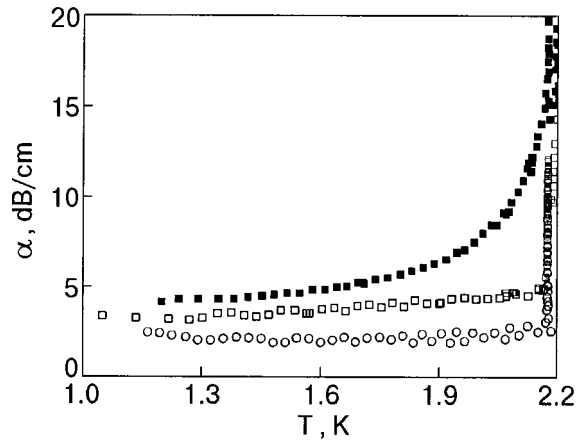

FIG. 8. The attenuation of ultrasound in liquid helium: in bulk (○), in D_2–N_2–He solid at 3.16 MHz (□), at 5.33 MHz (■).

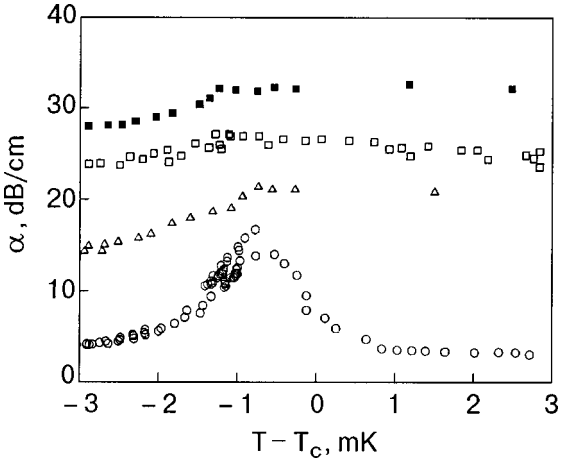

FIG. 9. The behavior of attenuation of 4.96 MHz sound in liquid helium near λ-point: in bulk (○), in different N_2–He solids (△, □, ■). For N_2–He solids the attenuation is shifted by 0, 5 and 10 dBm/cm, correspondingly.

appears that the shift of peak with respect to bulk helium is ~ 0.2 mK, but at the same time the reproducibility of the measurements of the sound attenuation maximum in liquid helium from run to run is about ~ 0.1 mK. Therefore, based on these experiments we can say that if the shift does exist, it is less than or on the order of 0.2 mK. Note that Fig. 10 reflects the fact that the attenuation peak in bulk helium is ~0.8 mK below the λ point.[30]

4. DISCUSSION

4.1. Velocity of sound in Im–He solids

Before performing this series of experiments, it was impossible to predict the characteristics of sound propagation in Im–He samples created by introducing impurities into superfluid helium. According to the existing model, these Im–He solids represent metastable phases formed by coalescing Im–He clusters, in which helium is solidified as a result of large attractive van der Waals interactions between helium atoms and a central impurity particle. Therefore, under conditions of compact packing of these clusters one would expect an increase in elastic modulus for this material and also

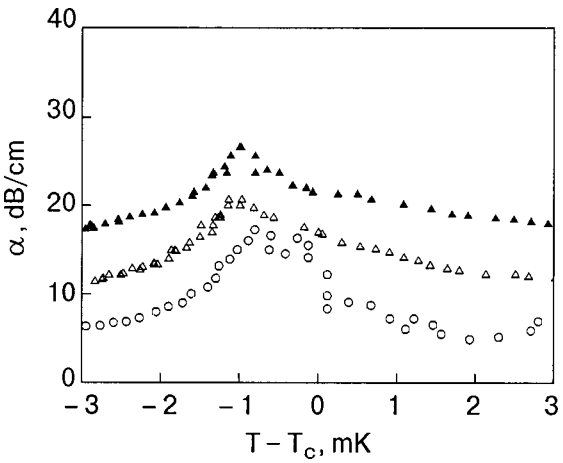

FIG. 10. The behavior of attenuation of ultrasound in liquid helium near λ-point: in bulk (○), in different D_2–N_2–He solids (△, ▲). For D_2–N_2–He solids the attenuation is shifted by 5 and 10 dBm/cm, correspondingly.

an increase of the speed of sound with respect to pure bulk liquid helium. Discovery of this effect was one of the first goals of this experiment. However, we were not able to produce samples for which we could detect an increase in the speed of sound, although we used our standard methods for creation of Im–He solids.[6,7] On the contrary, we observed a lower speed of sound than in superfluid helium. The only exception were D_2–He samples, for which the sound velocity was the same as in helium to great precision. The observed decrease in the speed of sound can be explained by the creation of a porous structure of solid helium around the impurity particles. This is also supported by the fact that the behavior of the speed of sound resembles the fast sound mode in porous aerogel.[28] This mode is intermediate between first and fourth sound. Here the normal component is locked in a very compliant solid matrix, so that the liquid and the aerogel fibers move together under mechanical and thermal gradients. McKeena *et al.*[28] developed a theory explaining the behavior of sound modes in aerogel, taking into account the coupling between the normal component and the aerogel and its elasticity. The same features are observed in Im–He samples.

4.2. Attenuation of sound in Im–He solids

As we pointed out before, the behavior of the attenuation of sound in different heavy Im–He solids has the same characteristic features. We observe the transition from the plateau with a small attenuation to the plateau with a bigger one, which ends with a maximum at the λ point. This can be explained by the structure of this porous material, which is characterized by a wide distribution of pore sizes. Among these pores there are large channels in which the behavior of the helium is close to bulk helium. The existence of these pores is realistic, especially if we take into account the method of collecting Im–He solids. This is a highly nonequilibrium process in which the impurity particles cooled by the helium vapor enter the superfluid helium, where they stick together after random collisions with each other. So in this process, as the model of aggregation of the small particles into clusters predicts,[31] highly ramified fractal structures are created.

The accumulation of Im–He sample is characterized by the existence of a convective flow of helium, which moves parts of the created condensate from the location where the impurity particles first hit the surface of the helium to the bottom and to the walls of the cell. Later these small pieces of porous material stick together to form the Im–He solid. They do not coalesce homogeneously, however. Therefore macroscopic voids might be created between them, which can lead to the formation of large channels in the final condensate. We should notice that this Im–He solid preserves its form unless removed from the helium. Then it compresses by 60%.[9]

Qualitatively the behavior of sound attenuation in samples with this structure can be explained as follows: At the lowest temperatures the normal component of helium is locked to the solid matrix, and the attenuation is small. Warming leads to a decrease of the viscous penetration depth δ_{visc}, so that, when it is comparable to the pore size R of our solid, the decoupling of a portion of the normal fluid occurs.

TABLE I. Values of T_1 and T_2 (see text) for different Im-He solids and corresponding pore sizes.

Sample	T_1, K	R_1, nm	T_2, K	R_2, nm
Kr–He	1.20	530	1.56	210
Ne–He	1.35	320	1.73	150
N_2–He	1.10	860	1.58	210
D_2–N_2–He	1.75	140	2.05	110
D_2–He	2.05	110		

Therefore sound attenuation caused by the friction of the layers of normal fluid as they become unlocked from the solid matrix starts to increase rapidly. Let us call the temperature at which this occurs, T_1. Continuous warmup leads to decoupling of helium in a greater number of pores. We define T_2 as the temperature at which the sound propagates only in the large channels. There the helium is almost like bulk helium and does not feel the effect of the walls. In addition, sound can propagate through the smallest pores formed at the earliest stage of the creation of the sample. The helium in these pores is still locked to the solid matrix, and attenuation is low and almost independent of temperature. This resembles the behavior of attenuation in bulk superfluid helium.

By calculating the viscous penetration depths for T_1 and T_2 we can find the corresponding pore size ($\delta_{\rm visc}=R$). These results, inferred from Figs. 3a and 4, are shown in Table I. Samples produced by injecting heavy impurities in superfluid helium are characterized by the presence of pores of large size—from 150 nm to 820 nm. On the other hand, the D_2–N_2–He sample has smaller pores—100 nm to 140 nm. It should be pointed out that from the analysis of the lowest-temperature part of the attenuation we can estimate only the pores of larger size, for which a large attenuation is observed. Information about the smallest pores is much harder to obtain, because after T_2, sound propagates not only through them but also through the large channels.

This model is supported by investigation of sound attenuation in the same sample but at different frequencies. Figure 7 shows that a decrease in frequency leads to a decrease of attenuation. Also T_2 shifts to the higher temperature. For both frequencies $\delta_{\rm visc}(T_2=1.48\,{\rm K}$ at 5 MHz) is equal to $\delta_{\rm visc}$ ($T_2=1.6\,{\rm K}$ at 3 MHz), which has a value of 240 nm.

Im–He samples formed in our experiments have a variety of different volume ratios between the porous part and the large channels. Compressing these samples leads to a decrease in the volume of the large channels, which in turn increases the attenuation, as was detected in the previous experiments.[27] The comparison of attenuation in freshly prepared samples and in those recycled above T_λ showed that crossing the λ transition always gives a somewhat larger attenuation, caused by compactification of the Im–He solids. A much larger effect was observed in the D_2–N_2–He sample during warmup to 3.4–3.5 K, where a sudden drop in attenuation was observed. In addition, it was seen visually that the sample volume changed from 1.7 cm^3 to 0.14 cm^3. We did not observe a similar effect in N_2–He samples. Hence this change of attenuation is ascribed to the collapse of the porous structure formed by deuterium molecules. It seems as if

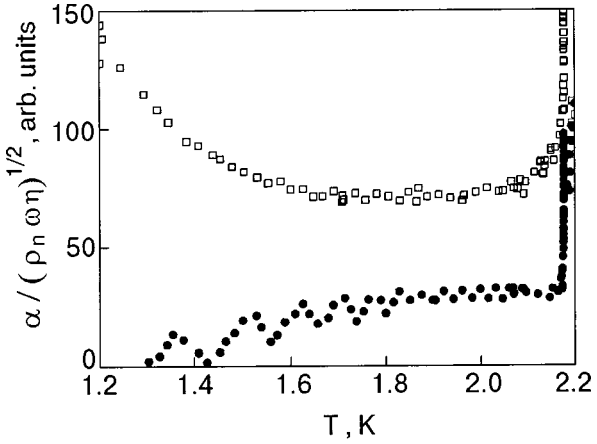

FIG. 11. Temperature dependence of ultrasound attenuation for 5.43 MHz (□) and 3.16 MHz (●).

a similar effect was detected in the work of Gordon *et al.*,[32] where a significant decrease of the concentration of deuterium atoms contained in a D_2–Ne–He sample was registered during warmup from 1.8 K to 4.2 K.

Analysis of sound propagation in Im-He solids shows that a distribution of the channels in superfluid helium is present, including very large channels, in which the helium behavior is close to that of bulk helium. Although the speed and attenuation of sound did not reveal any substantial suppression of T_c in N_2–He samples, we discovered a very small shift in D_2–N_2–He samples, on the order of 0.2 mK, which is similar to that in a very light aerogel. In addition, a small broadening of the attenuation peak was detected for the N_2–He solid near the λ point. The width of these peaks gives us information about the smallest pores in the samples. Using Josephson's relation[33] for helium in the channels of Im–He solids, namely

$$\xi(t)=\xi_0|t|^{-\zeta}=\frac{k_B T_c m^2}{\hbar^2 \rho_s(t)}, \tag{7}$$

we can find the correlation length at the temperature where the broadening of the attenuation peak starts. At this temperature T, the superfluidity in the pores (where the pore radius $R=\xi(T)$) starts breaking up. In Eq. (7) m, k_B, and $\hbar$ are the mass of a helium atom, Boltzman's constant, and Planck's constant, respectively. From Fig. 7 we can say that the onset of broadening of the attenuation peak is at $T\sim 2.1\,{\rm K}$, which gives the characteristic size of the pores from the argument above as $R\sim 8$ nm. This is reasonably close to (6 ± 2) nm, the size of the clusters from which our Im-He solids are built.[15]

Under certain favorable circumstances we were able to produce samples without any of the large channels, and in that case we did not observe the plateau in the temperature dependence of the attenuation (see Fig. 8). This idea was checked by plotting the attenuation divided by $(\rho_n \omega \eta)^{1/2}$ as shown in Fig. 11. The constant straight line above $T\sim 1.6\,{\rm K}$ describes the high-frequency behavior of helium in this particular porous sample, which implies that the energy loss is occurring on the entire surface in a thin layer of thickness $\delta_{\rm visc}$. At a lower frequency this behavior starts at a higher temperature because the viscous penetration length is

larger. If we compare the temperatures at which the graph in Fig. 11 levels off to a straight line, we get the same value of $\delta_{visc} \sim 180$ nm for 3 and 5 MHz ultrasound.

5. SUMMARY

Im–He solids have opened up a variety of intriguing possibilities for experimental investigations of the quantum properties of helium, as well as for studying atoms, molecules and small clusters stabilized in solidified helium. These studies provide a new perspective for matrix isolation in solidified helium. The big advantage of the Im–He solids is that a large variety of atoms or molecules can be used to build the ''backbone'' of the Im–He samples. It also appears that, depending on the preparation conditions, samples with different nanostructures can be prepared. To understand the properties of the Im–He samples it is necessary to determine their microscopic structure.

In this work investigations of the velocity and attenuation of ultrasound were used to study the characteristics of Im–He samples formed by introducing different impurities in the volume of superfluid helium. For helium in Im–He samples the speed of sound is a little smaller than in bulk helium, and its temperature dependence is close to the fast sound mode in light aerogel.[28] The character of the attenuation of ultrasound in helium in Im–He samples is different from that in other porous materials like Vycor, porous gold, and aerogel. The temperature dependence of ultrasound attenuation in D_2–He samples is close to that in bulk helium, whereas it is considerably different from the attenuation in heavy Im–He samples. This allows us to grow mixed solids, such as D_2–N_2–He, in which the attenuation can be regulated by the content of the gasous mixture. For these mixed samples we produced and investigated the most ''perfect'' porous solids, which do not contain large channels of bulk helium.

From the analysis of attenuation of ultrasound in Im–He samples, we conclude that they have a wide distribution of pore sizes between 8 nm and 800 nm, as well as large channels in which the behavior of helium is close to that of bulk liquid helium.

We investigated the behavior of the velocity and attenuation of ultrasound in Im–He samples near the λ point, where a broadening of the λ peak is observed. The broadening increases with increasing sample density. A small shift of the transition temperature (~0.2 mK) was observed for D_2–N_2–He samples.

For a better understanding of the microscopic structure of Im–He samples, a study of low-angle x-ray scattering might be very helpful. The similarity between the behavior of ultrasound in Im–He samples and in aerogel suggests the possibility of a fractal structure for Im–He solids. For studies of the critical behavior of helium in Im–He samples, investigations of second sound (low-frequency sound) are the most appealing. We believe that this will allow the observation of a slow sound mode similar to the one observed in aerogel[28] and also the determination of the critical exponent for different Im–He solids.

We would like to thank NASA for its support through Grant NAG 8-1445. We also wish to thank Drew Geller, John Beamish, Jeevak Parpia, and John Reppy for very useful suggestions and discussions.

*E-mail: khmel@ccmr.cornell.edu

[1] B. Tabbert, H. Gunter, and G. zu Putlits, J. Low Temp. Phys. **109**, 653 (1997).
[2] J. P. Toennies, and A. F. Vilesov, Annu. Rev. Phys. Chem. **49**, 1 (1998).
[3] S. I. Kanorsky and A. Weis, Adv. At., Mol., Opt. Phys. **38**, 87 (1998).
[4] E. B. Gordon and A. F. Shestakov, Fiz. Nizk. Temp. **26**, 5 (2000) [Low Temp. Phys. **26**, 1 (2000)].
[5] E. B. Gordon, A. A. Pelmenev, O. F. Pugachev, and V. V. Khmelenko, JETP Lett. **37**, 282 (1983).
[6] E. B. Gordon, V. V. Khmelenko, E. A. Popov, A. A. Pelmenev, and O. F. Pugachev, Chem. Phys. Lett. **155**, 301 (1989).
[7] E. B. Gordon, V. V. Khmelenko, A. A. Pelmenev, E. A. Popov, O. F. Pugachev, and A. F. Shestakov, Chem. Phys. **170**, 411 (1993).
[8] B. Palaszewski, L. S. Ianovski, and Patrick Carrik, J. Propul. Power **14**, 641 (1998).
[9] R. E. Boltnev, E. B. Gordon, I. N. Krushinskaya, A. A. Pelmenev, E. A. Popov, O. F. Pugachev, and V. V. Khmelenko, Fiz. Nizk. Temp. **18**, 819 (1992) [Sov. J. Low Temp. Phys. **18**, 576 (1992)].
[10] R. E. Boltnev, E. B. Gordon, V. V. Khmelenko, I. N. Krushinskaya, M. V. Martynenko, A. A. Pelmenev, E. A. Popov, and A. F. Shestakov, Chem. Phys. **189**, 367 (1994).
[11] R. E. Boltnev, E. B. Gordon, I. N. Krushinskaya, M. V. Martynenko, A. A. Pelmenev, E. A. Popov, V. V. Khmelenko, and A. F. Shestakov, Fiz. Nizk. Temp. **23**, 753 (1997) [Low Temp. Phys. **23**, 567 (1997)].
[12] R. E. Boltnev, I. N. Krushinskaya, A. A. Pelmenev, D. Yu. Stolyarov, and V. V. Khmelenko, Chem. Phys. Lett. **305**, 217 (1999).
[13] R. E. Boltnev, E. B. Gordon, V. V. Khmelenko, M. V. Martynenko, A. A. Pelmenev, E. A. Popov, and A. F. Shestakov, J. Chim. Phys. (France) **92**, 362 (1995).
[14] L. P. Mezhov-Deglin and A. M. Kokotin, JETP Lett. **70**, 11 (1999).
[15] V. Kiryukhin, B. Keimer, R. E. Boltnev, V. V. Khmelenko, and E. B. Gordon, Phys. Rev. Lett. **79**, 1774 (1997).
[16] J. D. Reppy, J. Low Temp. Phys. **87**, 205 (1992).
[17] J. M. Kosterlitz and D. J. Thouless, J. Phys. C **6**, 1131 (1973).
[18] L. S. Goldner, N. Mulders, and G. Ahlers, J. Low Temp. Phys. **93**, 131 (1993).
[19] M. H. W. Chan, K. I. Blum, S. Q. Murphy, G. K. S. Wong, and J. D. Reppy, Phys. Rev. Lett. **61**, 1950 (1988).
[20] J. Yoon and M. H. W. Chan, Phys. Rev. Lett. **78**, 4801 (1997).
[21] J. Yoon, D. Sergatskov, J. Ma, N. Mulders, and M. H. W. Chan, Phys. Rev. Lett. **80**, 1461 (1998).
[22] K. L. Warner and J. R. Beamish, Phys. Rev. B **36**, 5698 (1987).
[23] N. Mulders and J. R. Beamish, Phys. Rev. Lett. **62**, 438 (1989).
[24] K. Warner and J. R. Beamish, Phys. Rev. B **50**, 15896 (1994).
[25] M. A. Biot, J. Acoust. Soc. Am. **28**, 168 (1956).
[26] M. A. Biot, J. Acoust. Soc. Am. **28**, 179 (1956).
[27] S. I. Kiselev, V. V. Khmelenko, D. A. Geller *et al.*, J. Low Temp. Phys. **119**, 357 (2000).
[28] M. J. McKenna, T. Slawecki, and J. D. Maynard, Phys. Rev. Lett. **66**, 1878 (1991).
[29] E. B. Gordon, L. P. Mezhov-Deglin, O. F. Pugachev, and V. V. Khmelenko, Cryogenics **9**, 555 (1976).
[30] C. E. Chase, Phys. Fluids **1**, 3 (1958).
[31] P. Meakin, Annu. Rev. Phys. Chem. **39**, 237 (1988).
[32] E. B. Gordon, A. A. Pelmenev, O. F. Pugachev, and V. V. Khmelenko, Fiz. Nizk. Temp. **11**, 563 (1985) [Sov. J. Low Temp. Phys. **11**, 307 (1985)].
[33] B. D. Josephson, Phys. Lett. **21**, 608 (1966).

This article was published in English in the original Russian journal. Reproduced here with stylistic changes by the Translation Consultant.

Properties of solid ^{3}He inclusions embedded in a crystalline ^{4}He matrix at ultralow temperatures

A. Ganshin, V. Grigor'ev, V. Maidanov,* N. Mikhin, A. Penzev, A. Polev, E. Rudavskii, and A. Rybalko

B. Verkin Institute for Low Temperature Physics and Engineering, National Academy of Sciences of Ukraine, 47 Lenin Ave., 61164, Kharkov, Ukraine
(Submitted June 22, 2000)
Fiz. Nizk. Temp. **26**, 884–888 (September–October 2000)

A study is made of the kinetic properties of the quantum systems formed in dilute solid mixtures of ^{3}He in ^{4}He at ultralow temperatures as a result of the first-order phase transition known as phase separation. The system is a crystalline matrix of almost pure ^{4}He in which small solid inclusions of almost pure ^{3}He are embedded. Data on the inclusion growth kinetics, which is governed by diffusion processes in the matrix, are obtained using precise pressure measurements at constant volume. It is shown that impuriton quantum diffusion is the main process causing the inclusion growth at $T>100$ mK. At lower temperatures a strong suppression of quantum diffusion is discovered. This suppression can be associated with the elastic strains induced by the large difference in molar volume between the matrix and inclusions. The magnetic relaxation processes in such two-phase crystals are also investigated using a pulsed NMR technique. The spin–lattice and spin–spin relaxation in the inclusions are found to be practically independent of temperature. This can be described by exchange processes associated with the ^{3}He tunneling motion. The values of the relaxation times are in good agreement with the corresponding times for pure bulk ^{3}He. In contrast with the case of pure solid ^{3}He, the exchange plateau region extends down to lower temperatures. The nuclear magnetic relaxation in the matrix can be described by the Torrey model, which is based on ^{3}He–^{4}He tunneling exchange. The concentration dependence of the relaxation times coincides with that observed for homogeneous dilute mixtures of ^{3}He in ^{4}He. [S1063-777X(00)00409-6]

1. INTRODUCTION

Helium isotopes and their solid mixtures are the most typical examples of the not numerous but very interesting (in their scientific aspect) class of substances called quantum crystals (QCs). The influence of the zero-point motions of the atoms on the properties of QCs is a characteristic feature of these objects which becomes decisive at rather low temperatures.

The zero-point motions are manifested especially expressively in the behavior of impurities and defects inside QCs. As has been shown by Andreev and Lifshits,[1] the point defects in this case delocalize and turn into quasiparticles (QPs), which can move inside the crystal almost freely. This gives rise to the quantum diffusion (QD) phenomenon, which is characterized by a very unusual nature of the diffusive motion. The diffusion coefficient (DC) is either independent of temperature, if the motion of the QPs is restricted by their mutual collisions, or even rises with cooling, if the interaction with phonons plays the main role. Such regularities have been reliably established for ^{3}He impurities in hcp ^{4}He crystals (see, for example, Ref. 2) using NMR measurements of spin diffusion (SD). The main parameters characterizing the QD of impurity QPs in this system were also found.

However, a number of peculiarities of the diffusive motion could not be studied in the SD measurements. In particular, the regularities of mutual mass diffusion realized in the presence of a finite concentration gradient still remain unclear. In this case, one would expect a significant change in the role of mutual QP collisions, which may be effective only in proportion to the *U*-process probability. In ordinary classic crystals the self-diffusion coefficient is usually measured using the radioactive isotope technique, which cannot be implemented in solid helium. Nonetheless, its general idea (measurement of the penetration rate of an impurity into a matrix) can be used even in this case. Using the known DC values for solid helium, one can estimate the distance to which the impurity would penetrate for a reasonable duration of the experiment. For a duration of several hours ($\sim 10^4$ s) this distance is about 10^{-2} cm for mixtures with a ^{3}He concentration of 10^{-2}–10^{-3}, where the DC is 10^{-9}–10^{-8} cm^2/s. Measurement of the impurity concentration distribution in a helium crystal at such distances is a rather complicated problem. NMR tomography, for example, allows one to measure only DCs$>10^{-7}$ cm^2/s.[3,4]

From this point of view the study of another peculiar phenomenon in QCs, the so-called isotopic phase separation at low temperatures, is very promising. As has been established in experiment,[5] homogeneous mixtures of the helium isotopes separate into two phases below 0.38 K. If the initial mixture is dilute enough, a system consisting of isotopic impurity inclusions in a matrix of the other isotope is formed at $T\to 0$. Such a system is rather convenient for investigating mass diffusion in helium crystals. Experiments[6] have given

an inclusion size of about 10^{-4} cm at low temperatures. Therefore, the distance between inclusions at an initial concentration of 10^{-2} is about 10^{-3} cm. A change in temperature of the phase-separated mixtures causes a change in the equilibrium concentration in both the matrix and inclusions formed, so it is accompanied by diffusive mass transfer. In accordance with the estimate given above, the diffusion paths are such that characteristic times of variations in the concentration are about 10^2-10^3 s, well acceptable for measurement. It should be noted that in this case one can determine *in situ* the DC of ^{4}He, which cannot be measured by the NMR method at all and on which reliable data are now lacking.

The system under consideration is also interesting from the standpoint of clearing up another poorly known aspect of QD, namely the diffusive motion under conditions of a stressed state of the sample. The point is that a phase with a molar volume significantly different from that of the matrix appears upon phase separation. As a result, strains arise near the inclusions and may influence the diffusive mobility of QPs. The influence of strains on diffusion has not been adequately studied in the classic case. Besides, an additional mechanism involving the energy level shift between neighboring lattice sites appears in QCs. This leads to a decrease of the probability of tunneling, a breakdown of the coherent motion of QPs, and a corresponding decrease of DC.

The quantum nature of helium crystals is clearly manifested in their magnetic properties, too. The large amplitude of the helium atom zero-point motion gives rise to a strong exchange interaction, which causes a tunneling atom motion and may change the magnetic relaxation processes. This problem has been investigated in detail only in monophase crystals, namely solid ^{3}He and homogeneous ^{3}He–^{4}He mixtures.[7–9] As to the above mentioned two-phase crystal, consisting of ^{3}He inclusions in a ^{4}He matrix, such investigations have just started.[6,10] The matrix of almost pure ^{4}He may significantly after the nuclear magnetic relaxation at ultralow temperatures. On the one hand, being chemically inactive and nonmagnetic, the matrix excludes the familiar wall mechanisms of relaxation. On the other hand, the transition region between the hcp matrix and the bcc inclusions is supposed to contain a great number of defects, which may be collectors for magnetic excitations of the Zeeman reservoir.[7] We present experimental data both on the phase separation kinetics of solid ^{3}He–^{4}He mixtures and the corresponding diffusion processes and on the magnetic properties of solid ^{3}He inclusions in ^{4}He matrix in a millikelvin temperature region.

2. FORMATION KINETICS OF ^{3}He–^{4}He MIXTURE TWO-PHASE CRYSTAL AND FEATURES OF ^{3}He IMPURITY MASS DIFFUSION

The phase separation kinetics of solid ^{3}He–^{4}He mixtures was studied by precise pressure measurements at a constant volume. The method is based on the excess molar volume V_E emerging during the phase separation of the two-component mixtures, and for solid helium isotopes it is[11]

$$V_E = 0.4x(1-x)[\mathrm{cm}^3/\mathrm{mol}], \tag{1}$$

where x is the concentration of the mixture.

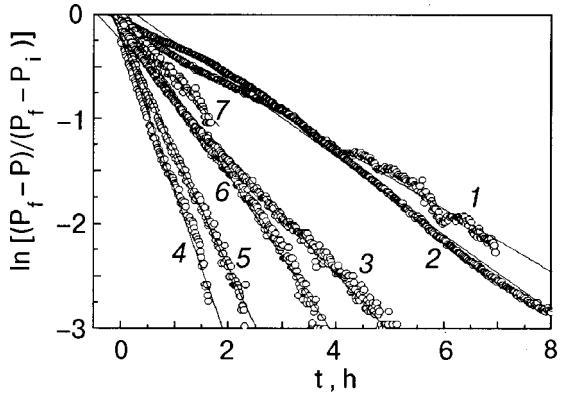

FIG. 1. The time dependence of the relative change in pressure for a sample with a molar volume of 20.27 cm^3/mol on a logarithmic scale. Solid lines are fits to (2) for different final temperatures, mK: 151 (*1*); 136 (*2*); 121 (*3*); 105 (*4*); 96 (*5*); 80.3 (*6*); 61.6 (*7*).

As the experiments were carried out at a constant volume, the phase transition produces a change in pressure ΔP, which is proportional to V_E and, for small concentrations, to the change in the concentration Δx.

The cell is a flat cylinder 9 mm in diameter and 1.5 mm in height, described in detail in Ref. 12. Samples with an initial ^{3}He concentration x_0 of $\approx$2.05% were grown using the capillary blocking technique. The annealing of the crystals was carried out for a day at a temperature close to the melting curve. The sample temperature was cycled many times in the two-phase region after annealing. As a result of this procedure, the crystal quality was improved, namely, the phase separation time constant became reproducible and the crystal pressure decreased.[13] The measurements were made in a temperature range of 50–300 mK for a molar volume of 20.27 cm^3/mol, corresponding to a pressure of 35.99 bar at the phase separation temperature T_{ps}.

The phase separation was initiated by the step-by-step cooling of the solid ^{3}He–^{4}He mixture below T_{ps}, followed by a long temperature stabilization. The equilibrium pressure in the crystal established by the exponential law

$$P(t) = P_f - (P_f - P_i)\exp(-t/\tau), \tag{2}$$

where τ is the characteristic time governing the kinetics of phase separation after cooling by ΔT; P_i is the initial pressure in the sample, and P_f is the final equilibrium pressure for the given temperature.

Figure 1 shows the time dependence of the relative change in pressure on a logarithmic scale for each cooling step. According to (1), the slope of the lines corresponds to the time constant τ. As is clearly evident from Fig. 1, the characteristic times of phase separation decrease with temperature (lines *1–4*), but they start to increase (lines *5–7*) below some temperature ($\approx$110 mK). The time constants τ determined in such a way can be associated with the effective diffusion coefficient, which provides a ^{3}He atom transfer to the new phase inclusions. The average size of the ^{3}He inclusions was measured most reliably by the confined diffusion NMR technique[6] and is about 4.5 μm.

The relation between D_{eff} and τ was found by solving the corresponding diffusion problem.[14] It is worthwhile to compare the estimated values of the mass diffusion coeffi-

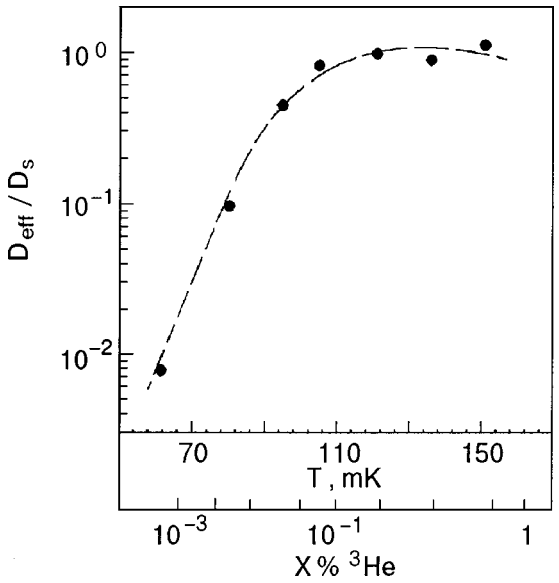

FIG. 2. The ratio D_{eff}/D_s vs temperature (concentration) for a crystal with a molar volume of 20.27 cm^3/mol.

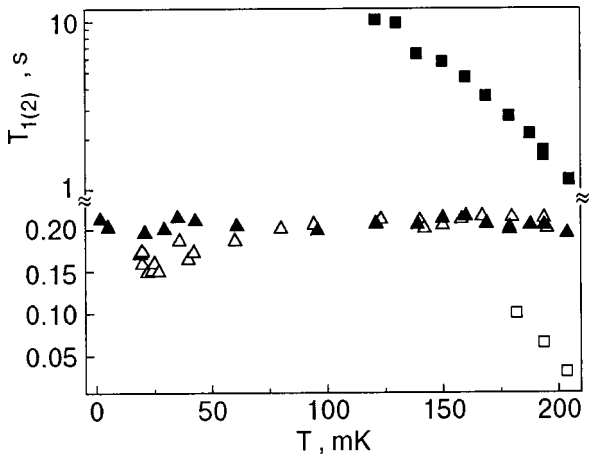

FIG. 3. Temperature dependence of the spin–lattice (■–T_1^d, ▲–T_1^c) and spin–spin (□–T_2^d, △–T_2^c) relaxation times.

cient with the self-diffusion coefficient of impuritons D_s, measured earlier in NMR experiments for solid ^{3}He–^{4}He mixtures of the same concentration by the spin-echo method.[15] In Fig. 2 we present the ratio of D_{eff}/D_s as a function of temperature (concentration). As the measurements were carried out along the phase separation curve, a mutual conformity between temperature and concentration takes place. One can see that D_{eff} and D_s practically coincide at high temperatures. This means, that the quantum diffusion under such conditions is the main mechanism which provides the ^{3}He inclusion growth in the ^{4}He matrix. However, as the temperature goes down, D_{eff} becomes much less than D_s, and the difference is more than two orders of magnitude at the lowest temperatures. As follows from Fig. 2, the impuriton quantum diffusion from the matrix to the inclusions is strongly suppressed in the low-temperature region. The most probable reason for this effect is the influence on diffusion of the elastic fields that appear in the matrix during nucleation and growth of new phase inclusions with a molar volume much higher than that of the matrix. Under such conditions the diffusion flux density can be written as follows:[16]

$$j = -\frac{Dx}{w}\left(\frac{\nabla x}{x} + \frac{\nabla U}{kT}\right), \tag{3}$$

where w is the atomic volume, ∇x is the concentration gradient, and ∇U is the potential gradient characterizing the inhomogeneous stress field. A significant decrease of mass transfer may take place at low temperatures on the condition that ∇x and ∇U have opposite directions and comparable values. The elastic force gradient appearing during the solid ^{3}He inclusion growth in the ^{4}He matrix can strongly influence the QD, slowing it down through either the action of a direct force or an energy level shift of neighboring lattice sites.

Thus the ^{3}He mass transfer in the system formed during phase separation and consisting of ^{3}He inclusions in a solid ^{4}He matrix differs significantly from that in a homogeneous mixture. Further experimental and theoretical work is needed to explain the facts described.

3. MAGNETIC RELAXATION IN A PHASE SEPARATED DILUTE ^{3}He–^{4}He MIXTURE

Cylindrical samples of solid ^{3}He–^{4}He mixtures, 4 mm in diameter and 20 mm long, were grown from an initial gaseous mixture containing 3.18% ^{3}He by the capillary blocking method in an experimental cell[17] cooled with a nuclear demagnetization refrigerator. After annealing for a day near the melting temperature, the molar volume of the samples was (20.3 ± 0.05)cm^3/mol. The 250 kHz pulsed NMR spectrometer was used to measure the spin-lattice (T_1) and spin-spin (T_2) relaxation times and spin diffusion coefficient D_s.

The difference between spin-lattice relaxation times in the matrix, with a low ^{3}He concentration, T_1^d, and in the concentrated dispersed phase, T_1^c, made it possible to separate the NMR signals from the two phases after phase separation. Consequently, the spin-lattice and spin-spin relaxation times were measured in both the matrix and inclusions of concentrated ^{3}He.

The temperature dependences of T_1 and T_2 are shown in Fig. 3. The times T_1^c and T_2^c for the concentrated phase inclusions are seen to be practically independent of temperature. This allows us to propose that in this case the main relaxation mechanism is connected with the Zeeman–tunnel interaction. This is supported by the coincidence of our experimental T_1^c value of 200 ms with the theoretical results given in Ref. 7. As in this experiment the Larmor frequency is much less than the tunneling exchange frequency ω_E, the times T_1 and T_2 in solid ^{3}He almost coincide in the ''exchange plateau'' region and are given as follows:[7]

$$(T_1^c)^{-1} \approx (T_2^c)^{-1} \approx \frac{10}{3}\left(\frac{\pi}{2}\right)^{1/2}\frac{M_2}{\omega_E}, \tag{4}$$

where M_2 is the second Van Vleck moment.

Besides, the values obtained for T_1^c are equal to the known values for bulk solid ^{3}He in the ''exchange plateau'' region under the same conditions.[7] The main difference is that the exchange plateau for solid bulk ^{3}He exists at tem-

peratures above 0.25 K, but at lower temperatures a sharp increase of T_1 occurs. This increase is due to a weakening of the bond between the exchange reservoir and the lattice. This bond in bulk samples is provided by both vacancion and impuriton relaxation mechanisms.[7] Meanwhile, temperature independence of T_1^c for the ^{3}He inclusions in the ^{4}He matrix obtains over the temperature region in question down to 1.5 mK.

The disagreement may be due to the small inclusion sizes and a considerable amount of ^{4}He in the inclusions, at least near T_{ps}. However, the mechanism that provides the strong bond between the exchange reservoir and the lattice under such conditions is unclear.

As is clearly evident from Fig. 3, T_2^c is temperature independent in the region 50–200 mK and equals (0.21 ± 0.02) s. The temperature independence of T_2^c and its coincidence with both the experimental values[7] of T_2 for bulk pure ^{3}He and the calculations according to (4) allows us to suppose that the spin-spin relaxation mechanism is determined by the ^{3}He–^{4}He tunneling exchange frequency, independent of temperature. Nevertheless, the T_2^c time tends to decrease down to 0.15 s below ~50 mK (see Fig. 3).

The decrease of T_2 is usually considered as being due to a reduction in D_s.[18] Our measurements show that D_s is $(7 \pm 2\times10^{-8})$cm^2/s in the inclusions down to 1.5 mK. This value of D_s is close to that for pure bulk ^{3}He of the same density.[7]

As expected, in the hcp matrix both the spin-spin relaxation time T_2^d and T_1^d depend on temperature in proportion to the ^{3}He concentration change, which is determined by the phase separation diagram.

The concentration dependences of T_1 and T_2 are shown in Fig. 4 alongside the well-known experimental data for homogeneous solid ^{3}He–^{4}He mixtures under the same conditions. All the experimental data can be explained solely by a dependence which conforms with the Torrey nuclear relaxation model.[19] This implies that the main mechanism of spin–spin and spin–lattice relaxation is due to the ^{3}He–^{4}He tunneling exchange.

Thus all the data obtained in this study (T_1, T_2, and D_s) testify to the similarity of the properties of separated phases and those of bulk solid helium. The reasons for the extending of the T_1 ''exchange plateau'' to ultralow temperatures and the decrease in T_2 at $T<50$ mK are unclear.

*E-mail: maidanov@ilt.kharkov.ua

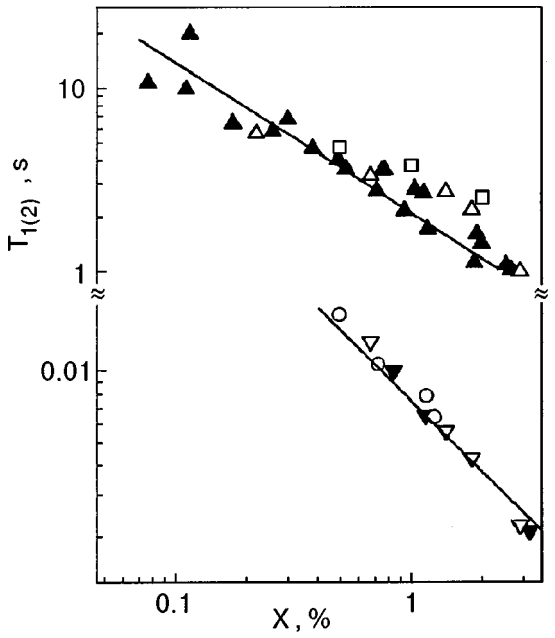

FIG. 4. Concentration dependence of the spin-lattice T_1 (▲) and spin-spin T_2 (▼) relaxation times in the dilute hcp matrix. The experimental results obtained in Ref. 8 (□, ▼), Ref. 9 (△), and Ref. 6 (○) were normalized to our experimental conditions. The solid lines correspond to dependences $T_1 \sim x^{-0.88}$ and $T_2 \sim x^{-1}$.

[1] A. F. Andreev and I. M. Lifshits, Zh. Éksp. Teor. Fiz. **56**, 2057 (1969) [Sov. Phys. JETP **29**, 1107 (1969)].
[2] V. N. Grigor'ev, Fiz. Nizk. Temp. **23**, 5 (1997) [Low Temp. Phys. **23**, 1 (1997)].
[3] I. Schuster, E. Polturak, Y. Swirsky, E. J. Schmidt, and S. G. Lipson, J. Low Temp. Phys. **103**, 159 (1996).
[4] V. L. Vvedenskii, JETP Lett. **24**, 132 (1976).
[5] D. O. Edwards, A. S. McWilliams, and J. D. Daunt, Phys. Lett. **1**, 218 (1962).
[6] S. C. J. Kingsley, V. Maidanov, J. Saunders, and B. Cowan, J. Low Temp. Phys. **113**, 1017 (1998).
[7] R. A. Guyer, R. C. Richardson, and L. I. Zane, Rev. Mod. Phys. **43**, 532 (1971).
[8] A. S. Greenberg, W. C. Thomlinson, and R. C. Richardson, J. Low Temp. Phys. **8**, 3 (1972).
[9] Y. Hirayoshi, T. Muzisaki, S. Maekawa, and A. Hirai, J. Low Temp. Phys. **30**, 137 (1978).
[10] N. P. Mikhin, A. V. Polev, E. Ya. Rudavskii, and V. A. Shvarts, Fiz. Nizk. Temp. **23**, 607 (1997) [Low Temp. Phys. **23**, 455 (1997)].
[11] W. J. Mullin, Phys. Rev. Lett. **20**, 254 (1968).
[12] A. N. Gan'shin, V. A. Maidanov, N. F. Omelaenko, A. A. Penzev, E. Ya. Rudavskii, and A. S. Rybalko, Fiz. Nizk. Temp. **24**, 815 (1998) [Low Temp. Phys. **24**, 611 (1998)].
[13] A. N. Ganshin, V. N. Grigor'ev, V. A. Maidanov, N. F. Omelaenko, A. A. Penzev, E. Ya. Rudavskii, A. S. Rybalko, and Yu. A. Tokar, Fiz. Nizk. Temp. **25**, 796 (1999) [Low Temp. Phys. **25**, 592 (1999)].
[14] B. Ya. Lyubov, *Diffusion Processes in Heterogeneous Solid Media* [in Russian], Nauka, Moscow (1981).
[15] V. A. Mikheev, N. P. Mikhin, and V. A. Maidanov, Fiz. Nizk. Temp. **9**, 901 (1983) [Sov. J. Low Temp. Phys. **9**, 467 (1983)].
[16] V. V. Slezov, Fiz. Tverd. Tela **36**, 557 (1994) [Phys. Solid State **36**, 308 (1994)].
[17] A. A. Golub, V. A. Goncharov, V. R. Litvinov, V. A. Mikheev, E. Ya. Rudavskii, Yu. A. Tokar, A. M. Usenko, and V. A. Shvarts, Fiz. Nizk. Temp. **21**, 974 (1995) [Low Temp. Phys. **21**, 751 (1995)].
[18] A. Abragam, *The Principles of Nuclear Magnetism* (Claredon Press, Oxford, 1961).
[19] H. C. Torrey, Phys. Rev. **92**, 962 (1953); **96**, 690 (1954).

This article was published in English in the original Russian journal. Reproduced here with stylistic changes by the Translation Consultant.

Observation of the high-resolution infrared absorption spectrum of CO_2 molecules isolated in solid parahydrogen

S. Tam and M. E. Fajardo*

Propulsion Directorate, U.S. Air Force Research Laboratory AFRL/PRSP, Bldg. 8451, Edwards AFB, CA 93524-7680

(Submitted February 17, 2000; revised May 4, 2000)
Fiz. Nizk. Temp. **26**, 889–898 (September–October 2000)

We report the observation of high-resolution (0.008 cm^{-1}) infrared absorption spectra of CO_2 molecules isolated in solid parahydrogen (pH_2) matrices at $T=2.4$ to 4.8 K. Several extremely sharp (0.01 to 0.04 cm^{-1} full-width-at-half-maximum) absorption features appear in the 2343.5 to 2345 cm^{-1} region. We assign the three strongest peaks to the v_3 mode of isolated CO_2 molecules. The spectra are consistent with trapping of the CO_2 molecules in three distinct double-substitutional sites in hcp and fcc regions of the pH_2 solid. We offer several hypotheses as to the origins of the numerous weaker absorption features. © *2000 American Institute of Physics.* [S1063-777X(00)00509-0]

1. INTRODUCTION

This manuscript is a status report on our continuing effort to observe and analyze vibrational spectra of molecular dopants isolated in cryogenic solid parahydrogen (pH_2) hosts. As detailed below, our investigation of the microscopic structures and dynamics underlying many of these spectra is at a preliminary stage. Despite this, we believe the experimental observations themselves merit being reported at this time. We hope that these new high-resolution data will stimulate interest in the rigorous testing of theoretical models of vibrational spectroscopy of impurities in condensed phases.

The suitability of solid pH_2 as a host for high-resolution ($\Delta v/v \sim 10^{-6}$) vibrational spectroscopy was discovered by Oka and co-workers[1–5] and was further investigated by Shida, Momose, and co-workers[6–10] and by Winnewisser and co-workers.[11–14] The favorable properties of solid pH_2 contributing to this phenomenon have been discussed in detail.[2,3,9] Here we note simply that solid pH_2 is very ''forgiving'' of highly nonequilibrium sample preparation techniques such as direct gas-to-solid condensation. Structural defects in such samples may be less numerous, and/or have a smaller influence on dopant vibrational spectra, than in other vapor deposited cryogenic van der Waals solids traditionally employed as hosts for matrix isolation spectroscopy (MIS).

Our work on solid pH_2 is supported by the U.S. Air Force's High Energy Density Matter (HEDM) program;[15] our project's ultimate objective is to demonstrate practical energy storage in cryogenic solids for use as advanced chemical rocket propellants. Thus our attention is focused on the problems of (a) trapping large concentrations of isolated energetic dopants, (b) scaling-up sample quantities beyond the thin films typically encountered in MIS studies, (c) rigorously characterizing the chemical identities, concentrations, and trapping site structures of the incorporated energetic species, and (d) evaluating the thermal and chemical stabilities of these prototypical ''cryosolid'' propellants. These last two tasks motivate our interest in the spectroscopy of dopants in solid pH_2.

Our new ''rapid vapor deposition'' technique produces easily doped, millimeters-thick pH_2 solids of remarkable optical clarity.[16,17] The compatibility of this method with most MIS dopant trapping schemes enables the isolation in solid pH_2 of a wide variety of previously inaccessible chemical species. The excellent transparency of rapid vapor deposited samples is unusual for pH_2 solids produced by vapor deposition onto a substrate-in-vacuum[18] and enables their characterization by optical methods.

Our early work on doped cryogenic hydrogen solids employed medium-resolution ultraviolet/visible and infrared (IR) diagnostics.[19–21] However, we recently added a high-resolution IR capability and were repaid by the observation of very sharp (~0.01 cm^{-1} full-width-at-half-maximum, FWHM) vibrational absorption features for dopants in rapid vapor deposited samples. Moreover, high-resolution IR spectra of several (presumably) simple molecular dopants in solid pH_2 exhibit amazingly rich structure. Not only are the vibrational transition energies often more precisely defined than for the same dopants in rare gas solid (RGS) hosts, but such spectra also typically include a larger number of distinct, well-resolved features. The increased precision and complexity of these spectral measurements may require extraordinary efforts for their complete assignment, but the reward should be a deeper and more quantitative understanding of dopant trapping site structures and vibrational dynamics in solid pH_2 than has been achieved to date by MIS in RGS hosts.

We are in the process of surveying high-resolution IR absorption spectra for a variety of dopants in solid pH_2. A substantial database of such spectra should help to determine which physical effects dominate the vibrational spectroscopy of different classes of dopants in solid pH_2. For example, the spectra of CH_4/pH_2 solids,[6,7,9,10,22] a case in which the spherical-top dopant fits easily into a single-substitutional trapping site, accordingly show line spacings and intensity progressions commensurate with slightly hindered rotors.[6,22–27] Structurally, the spectra demonstrate that in as-

prepared rapid vapor deposited $p\mathrm{H_2}$ solids some of the $\mathrm{CH_4}$ molecules are initially trapped in face-centered cubic (fcc) regions, and that these regions convert irreversibly to hexagonal close-packed (hcp) upon annealing.[22] The polarization dependences of the $\mathrm{CH_4}/p\mathrm{H_2}$ transitions further indicate that annealing also results in improved alignment of the hcp crystallites' *c*-axis orientations with the deposition substrate surface normal.[22] Dynamically, all the $\mathrm{CH_4}/p\mathrm{H_2}$ spectra can be rigorously assigned by considering the rotational–vibrational dynamics of $\mathrm{CH_4}$ at the center of static external fields having D_{3h} (Ref. 6) and O_h (Ref. 22) symmetries. Thus a satisfactory explanation of these transition energies does not require consideration of constrained rotational–translational coupling (RTC) in a rigid trapping site[28–31] or of more general RTC interactions within a dynamic trapping site structure.[32–37] These lessons learned from the $\mathrm{CH_4}/p\mathrm{H_2}$ studies provide an excellent starting point for the assignment of our recently observed highly structured $\mathrm{CO}/p\mathrm{H_2}$ spectra,[38] another case in which the dopant molecule should fit readily into a single substitutional vacancy.

In stark contrast, we find that spectra of many larger species, such as lower symmetry polyatomic molecules, and hydrogen- or van der Waals-bonded clusters of smaller dopant molecules, show no evidence of overall rotation. We believe end-over-end rotation is inhibited by strong anisotropic interactions within the lower symmetry multi-substitutional trapping sites required to accommodate such large species. Thus, these larger species likely exist in the ''librational'' limit, oscillating around certain equilibrium orientations instead of rotating as a unit.[23] Yet, despite such strong dopant–host interactions, many of these larger dopant systems exhibit even sharper vibrational absorptions than those observed for smaller dopants trapped in highly symmetrical single substitutional sites! A satisfactory analysis of the spectra of these larger librating systems must deal with the additional complication of simultaneously considering both inherent and trapping-site-induced spectral features.

Before attempting such analyses, we turn first to a simpler model system of a linear triatomic molecule such as $\mathrm{CO_2}$ in solid $p\mathrm{H_2}$. Our IR spectra of $\mathrm{CO_2}/p\mathrm{H_2}$ samples show complicated patterns of sharp lines which do not appear to match a rotational dynamics (*vide infra*), and so may be comparable in this respect to the larger dopants. However, the gas-phase vibrational transitions of $\mathrm{CO_2}$ are very well known; thus, any peculiar features in spectra of $\mathrm{CO_2}/p\mathrm{H_2}$ are immediately attributable to either dopant–dopant interactions or to interactions with the $p\mathrm{H_2}$ host. We think the $\mathrm{CO_2}/p\mathrm{H_2}$ system will prove to be an excellent arena for evaluating the various elements of the RTC models in the limit of strongly hindered rotation.

In what follows we describe briefly our experimental methods and present our preliminary high-resolution IR absorption data for the $\mathrm{CO_2}/p\mathrm{H_2}$ system. We will show that the strongest absorption features are due to isolated $\mathrm{CO_2}$ molecules and not to $(\mathrm{CO_2})_n$ clusters. We discuss these monomer spectra in terms of candidate trapping site structures, and the corresponding rotational vs librational dynamics of the trapped molecules. We will give a list of hypotheses about the possible origins of the numerous weaker absorption features but will attempt no quantitative application of crystal-field or RTC models at this time. We end this manuscript with a summary, and list some of our immediate plans for future experimental and theoretical work to test the proposed hypotheses.

2. EXPERIMENTAL

Our experimental apparatus and sample preparation techniques have been described in detail before.[16,17,21] Doped $p\mathrm{H_2}$ solids are prepared by rapid vapor deposition of pre-cooled $p\mathrm{H_2}$ gas and room temperature $\mathrm{CO_2}$ gas onto a $\mathrm{BaF_2}$ substrate cooled to $T\approx 2$ K in a liquid helium (lHe) bath cryostat. We operate the ortho/para hydrogen converter at 15 K, yielding a flow of pre-cooled $p\mathrm{H_2}$ containing $\approx 0.01\%$ residual orthohydrogen ($o\mathrm{H_2}$) impurities.[17] The $p\mathrm{H_2}$ flow impinges upon the substrate at a 45° angle; during a deposition the pressure of uncondensed $p\mathrm{H_2}$ gas remains below $\sim 10^{-4}$ Torr. The $\mathrm{CO_2}$ dopant is metered into the deposition cryostat from a separate gas handling manifold; the dopant inlet is situated at an angle of 45° from the substrate surface normal, at 90° to the $p\mathrm{H_2}$ source. Individual sample preparation details are given below in the figure captions.

We record IR absorption spectra of our $\mathrm{CO_2}/p\mathrm{H_2}$ samples across the 800 to 7800 $\mathrm{cm^{-1}}$ range at a resolution of 0.008 $\mathrm{cm^{-1}}$; the main optical axis is parallel to the substrate normal. The Fourier transform IR spectrometer (Bruker IFS120HR) is equipped with a glowbar source, a KBr beamsplitter, and a liquid nitrogen cooled HgCdTe detector. To accommodate the IR diagnostic, the entire optical path is enclosed within a 0.5 $\mathrm{m^3}$ polycarbonate box purged with a constant flow of dry $\mathrm{N_2}$ gas.

3. RESULTS

Figure 1 shows the $\upsilon_3\ ^{12}\mathrm{C}^{16}\mathrm{O_2}$ region of absorption spectra from three different as-deposited $p\mathrm{H_2}$ solids containing $\mathrm{CO_2}$ concentrations ranging from ~ 0.01 ppm up to 1.2 ppm. The concentrations are estimated as described previously[21] using a value of 550 km/mol for the υ_3 $\mathrm{CO_2}$ integrated absorption coefficient.[39] The peaks labeled α, β, and γ dominate all three spectra, but show minor sample-to-sample variations in relative intensities. Not shown are the $\upsilon_3\ ^{13}\mathrm{C}^{16}\mathrm{O_2}$ and $\upsilon_3\ ^{16}\mathrm{O}^{12}\mathrm{C}^{18}\mathrm{O}$ regions of the spectrum depicted in trace (1c), in which similar features, also matrix-shifted by ≈ -5 $\mathrm{cm^{-1}}$ from the gas-phase vibrational band origins,[40,41] appear for each natural abundance isotopomer. The observed peak positions and linewidths are summarized in Table I.

Figure 2 shows the effects of repeated temperature cycling on the $\upsilon_3\ ^{12}\mathrm{C}^{16}\mathrm{O_2}$ band of the 1.2 ppm $\mathrm{CO_2}/p\mathrm{H_2}$ sample depicted in trace (1c). The most pronounced change observed during the initial warming from $T=2.4$ to 4.8 K is the strong irreversible decrease in the intensity of the γ peak at 2344.64 $\mathrm{cm^{-1}}$; the same behavior is observed for the other $\mathrm{CO_2}$ isotopomers, as well. We also note the simultaneous growth of the α' peak at 2343.91 $\mathrm{cm^{-1}}$, the weakening and sharpening of the α line, the strengthening and broadening of the β peak, and the appearance of a ≈ 0.5 $\mathrm{cm^{-1}}$ broad absorption lump near 2344.6 $\mathrm{cm^{-1}}$. Trace (2c) shows that upon re-cooling to $T=2.4$ K the α and α' peaks weaken, a new α'' line appears at 2343.98 $\mathrm{cm^{-1}}$ together with other weaker

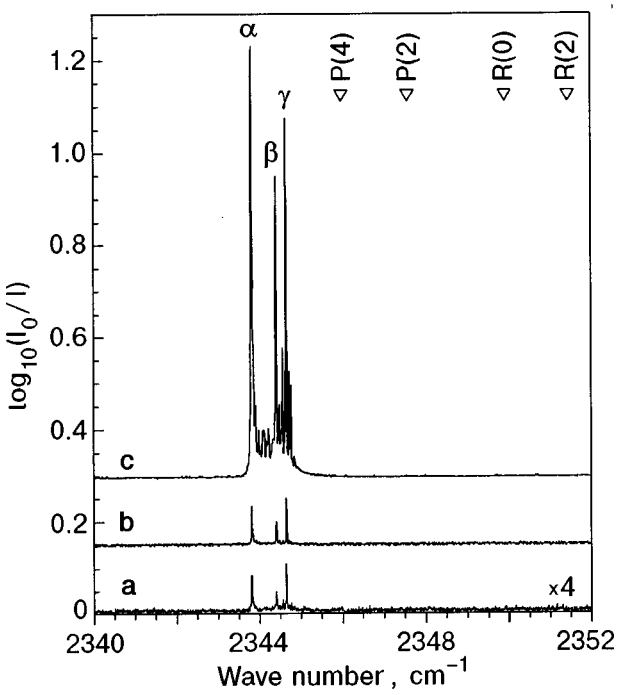

FIG. 1. IR absorption spectra of three as-deposited pH_2 solids at $T=2.4$ K containing different concentrations of natural isotopic abundance CO_2. Trace (1a) is for a 13 ppm CO/pH_2 sample containing ~0.01 ppm CO_2 as an unintentional impurity; sample thickness is 2.7 mm. Trace (1b) is for an 8 ppm HCl/pH_2 sample containing ≈0.04 ppm CO_2 as an unintentional impurity; sample thickness is 3.0 mm. Trace (1c) is for a 1.2 ppm CO_2/pH_2 sample that is 1.4 mm thick. The inverted triangles at the top of the figure indicate the positions of several gas phase ro-vibrational lines for the v_3 mode of $^{12}C^{16}O_2$ (Ref. 40). Trace (1a) has been rescaled by a multiplicative factor of 4; all the traces have been displaced vertically for ease of presentation.

features in the 2343.6 to 2343.9 cm^{-1} region, the β feature strengthens and broadens further, and the 2344.6 cm^{-1} lump broadens and/or diminishes. Repeating the temperature cycle, traces (2d) and (2e), shows the largely reversible nature of these changes. As reported in Table I, the broadening of the v_3 $^{12}C^{16}O_2$ β feature upon annealing is largely due to the appearance of a shoulder on the red side of the main peak; the v_3 $^{16}O^{12}C^{18}O$ β feature actually splits completely into two sharp, well-resolved peaks separated by ≈0.02 cm^{-1}.

Figure 3 shows the 2345 to 2350 cm^{-1} region of the same spectra as depicted in Fig. 2. Several sharp new peaks appear upon temperature cycling, most notably those near 2345.25, 2345.37, 2346.67, and 2347.25 cm^{-1}.

4. DISCUSSION

4.1. Isolation of CO_2 molecules

We assign the α, β, and γ features to isolated CO_2 molecules as opposed to $(CO_2)_n$ clusters due to: (1) the extreme dilutions of the samples, (2) the lack of any systematic concentration dependence, and (3) the absence (for as-deposited CO_2/pH_2 solids) of any other absorption features outside a narrow ≈1 cm^{-1} window. Assessing the validity of this last point requires a brief review of the literature on $(CO_2)_n$ clusters.

The gas-phase vibrational band origin for the localized asymmetric stretch mode of ''slipped parallel'' CO_2 dimers is observed[42] to be shifted by +1.63 cm^{-1} relative to the monomer v_3 $^{12}C^{16}O_2$ band origin at 2349.14 cm^{-1}; theoretical calculations[43–45] predict shifts of between 0 and +2 cm^{-1}, depending on the dimer geometry. The cyclic C_{3h} symmetry CO_2 trimer band origin is shifted by +2.58 cm^{-1} (Ref. 46) and the noncyclic C_2 symmetry CO_2 trimer shows two bands with origins shifted by −5.85 cm^{-1} and +3.58 cm^{-1} (Ref. 47), all shifts again referenced to the gas-phase monomer v_3 band origin. Larger gas-phase $(CO_2)_n$ clusters[48] and ultrafine particles[49] show broad absorptions across the 2340 to 2380 cm^{-1} range. The absorption maximum in pure, crystalline, natural isotopic abundance solid CO_2 occurs at 2344.8 cm^{-1}, but solid samples prepared by different methods can show absorptions anywhere between 2330 and 2380 cm^{-1} (Refs. 50–53).

Matrix isolation studies involving general $X–CO_2$ complexes are far too numerous to list here exhaustively.[54–56] The IR absorption spectrum of a 1 ppm CO_2/N_2 solid carefully prepared from the melt shows a single sharp line with a width of ≈0.007 cm^{-1} at $T=11$ K, which is assigned to librating CO_2 molecules isolated in single-substitutional sites.[57] All other previously reported v_3 region spectra of solely CO_2 doped rare gas,[58–62] deuterium,[63,64] and pH_2 (Ref. 65) matrices show multiple absorption features spanning a 5 to 10 cm^{-1} range. These features are preparation-, concentration-, and annealing-dependent, and are assigned to CO_2 molecules in multiple trapping sites, and/or to aggregated $(CO_2)_n$ species. Most directly relevant to this discussion are the spectra of $(CO_2)_n$ clusters in solid pH_2, which show a complicated pattern of peaks throughout the 2345 to 2350 cm^{-1} region.[65]

Finally, the absence of additional features in traces (1a) and (1b), for which the CO_2 is actually an unintentional impurity in samples containing ~10 ppm of other dopants, further supports the argument for negligible dopant aggregation under the present sample preparation conditions. Not shown are spectra from other experiments at higher HCl concentrations which *do* show absorption features in the 2346 to 2346 cm^{-1} region attributable to $(HCl)_m(CO_2)_n$ complexes.[66] These 2 to 5 cm^{-1} blue shifts from the matrix isolated monomer absorptions are in line with the +2 cm^{-1} shift reported in previous $HCl/CO_2/Ar$ studies.[67,68] Thus, clustering during deposition to form $(CO_2)_n$ should be even less important for the more dilute 1.2 ppm CO_2 sample depicted in trace (1c).

We thus conclude with confidence that the α, β, and γ features are due to isolated CO_2 molecules. The appearance of *all* detectable absorption features in as-deposited samples within a narrow ≈1 cm^{-1} region, especially traces (1c) and (3a), further suggests that even these weaker features may also be due to isolated CO_2 molecules. The new weak features which appear only upon annealing, especially those with significant shifts from the band center, may be due to $(CO_2)_n$ clusters. We will discuss these possibilities further in the following sections.

4.2. CO_2 molecule trapping site(s)

We attribute the appearance of (at least) three separate absorption peaks for monomeric CO_2 to trapping of CO_2

TABLE I. Peak positions (cm^{-1}) and widths (FWHM, rounded to nearest 0.005 cm^{-1}), and assignments for the main IR absorptions in CO_2/pH_2. The labels α, β, and γ refer to the three largest peaks observed in as-deposited samples; the labels α' and α'' refer to two additional strong features that appear between α and β upon temperature cycling. The ''as-deposited'' spectra are taken at $T=2.4$ K, the ''annealing'' spectra at $T=4.8$ K, and the ''annealed'' spectra upon re-cooling to $T=2.4$ K. The gas-phase vibrational band origins, υ_0, are estimated from data in Ref. 40.

Label	Peak positions (widths)			Assignment
	as-deposited	annealing	annealed	
α	2278.296 (0.040)	2278.300 (0.015)	2278.299 (0.010)	ν_3 $^{13}C^{16}O_2$
α′		n.o.		ν_0 = 2283.48
α″			2278.454w (0.025)	
β	2278.861 (0.030)	2278.872 (0.030)	2278.867 (0.025)	
γ	2279.099 (0.015)			
α	2326.835 (0.035)	2326.842 (0.015)	2326.842 (0.015)	ν_3 $^{16}O^{12}C^{18}O$
α′		n.o.		ν_0 = 2332.11
α″			n.o.	
β	2327.41w	2327.42w	2327.399 (0.010) 2327.422 (0.010)	
γ	2327.656 (0.020)			
α	2343.813 (0.040)	2343.818 (0.020)	2343.814 (0.015)	ν_3 $^{12}C^{16}O_2$
α′		2343.912 (0.015)		ν_0 = 2349.14
α″			2343.979 (0.020)	
β	2344.395 (0.025)	2344.404 (0.030)	2344.397 (0.040)*	
γ	2344.639 (0.020)			

w-weak, signal/noise ~1; n.o.—not observed, signal/noise <1;*—shoulder at 2344.372 cm^{-1}.

molecules in multiple trapping sites. Each distinct trapping site by definition corresponds to a different time-averaged structure of dopant and host molecules and so, in principle, can generate a distinct pattern of gas-to-matrix spectral shifts for the dopant vibrational transitions. For purposes of this discussion, we can ascribe the formation of multiple trapping sites during the highly nonequilibrium sample deposition process to (1) imperfections in the underlying host crystal structure, and/or (2) mismatches in the ''sizes'' of host and guest molecules.

As mentioned in the Introduction, the microscopic structure of our rapid vapor deposited pH_2 solids is far from that of the perfect, single hcp crystals that can be produced by slowly freezing liquid pH_2 (Ref. 69). The hcp (...*ABABAB*...) and fcc (...*ABCABCABC*...) structures are only two of the infinite number of densest close-packed structures that can be produced by stacking of close-packed (''basal'') planes. Patterns with longer repeat units (polytypism), non-periodic structures such as twin and stacking faults, and even random stacked close-packed structures are also possible.[70]

Fortunately, the combination of IR and Raman spectroscopies of pure solid pH_2 reveals the symmetries of the sites occupied by the pH_2 molecules.[71–74] We have not detected any vacancy defects in as-deposited undoped pH_2 solids, and we have further shown that these samples are not amorphous; rather, they appear to the densest close-packed solids made up of separate hcp and fcc regions.[16,22,74] The introduction of up to ~1000 ppm concentrations of dopants like CH_4 and CO, which are nearly the same ''size'' as a pH_2 molecule in the van der Waals sense, does not significantly affect the pH_2 structure. Thus, trapping of such dopants in single-substitutional vacancies results in the formation of two distinct classes of trapping sites: of D_{3h} symmetry in hcp regions, and O_h symmetry in fcc regions. The experimental CH_4/pH_2 and CO_2/pH_2 spectra are all consistent with this relatively simple picture.[22,38]

However, if our spectroscopic diagnostics are only sensitive to interactions with nearest neighbor pH_2 molecules, then we would necessarily detect *only two* pH_2 environments for *any* arbitrary stacking pattern of basal planes, i.e., sites in layers ($\underline{B}$) embedded in regions of local hcp stacking ($XA\underline{B}AX$, ''hcp-like''), or local fcc stacking ($XA\underline{B}CX$, ''fcc-like''). Dopants substituted into hcp-like sites would experience external fields of very nearly D_{3h} symmetry, while those in fcc-like sites would exist in nearly octahedral environments. Depending on the particulars of the dopant–pH_2 interactions, the distinction between, for example, ''hcp-like'' and ''true hcp'' may be undetectable in a given spectroscopic experiment.

In the case of CO_2 as the dopant, the situation is further complicated by the larger size of CO_2 relative to the pH_2 host. Figure 4 shows this size discrepancy in a semi-

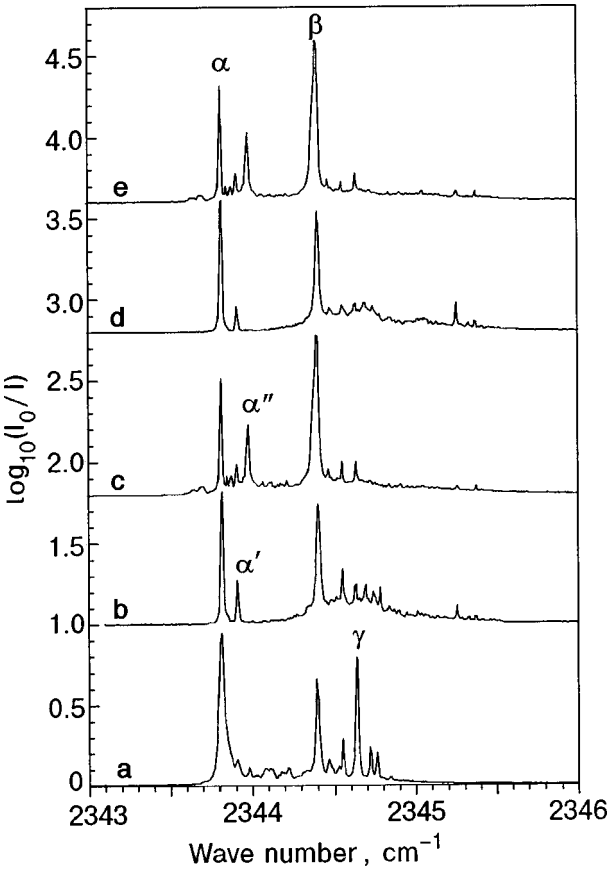

FIG. 2. Annealing behavior of the 1.2 ppm CO_2/pH_2 sample described in Fig. 1. Trace (2a) is an expanded view of the as-deposited spectrum presented above in trace (1c). The temperature sequence is: (2a) $T=2.4$ K, (2b) $T=4.8$ K, (2c) $T=2.4$ K, (2d) $T=4.8$ K, and (2e) $T=2.4$ K. The labels α' and α'' denote two new features that grow in during annealing.

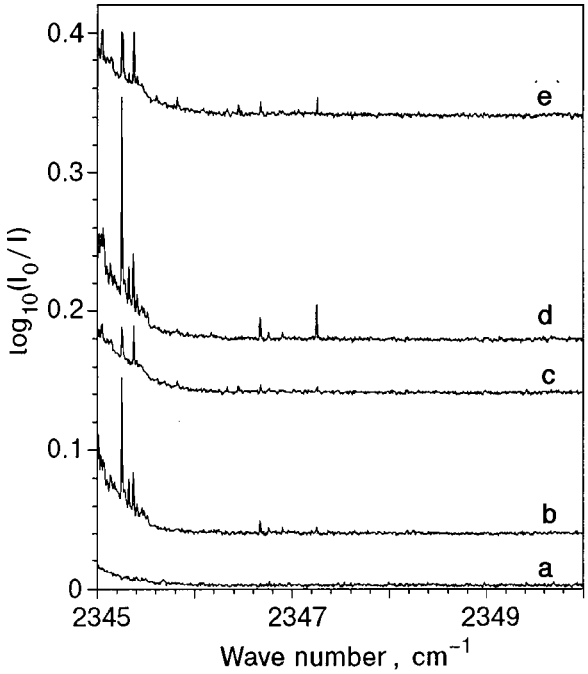

FIG. 3. Continuation of the spectra presented in Fig. 2.

quantitative manner, with the CO_2 molecule depicted in single-, double-, and triple-substitutional vacancies in basal planes of spherical pH_2 molecules. Overlap between molecular outlines indicates repulsive interactions, whereas intervening space indicates attractive interactions.

The pH_2 molecules are drawn as circles with diameters representing the 3.8 Å nearest-neighbor separation in solid pH_2 at lHe temperatures.[69] We use the nearest-neighbor separation, instead of the minimum separation for the pH_2-pH_2 interaction potential, to include the effects of quantum zero-point motion on the structure of solid pH_2, which would be absent in a simple potential energy minimization. We were unable to find an angle-dependent CO_2-pH_2 interaction potential in the literature, so we resorted to a recently calculated CO_2–He potential instead.[75] Since the minima of the (spherically averaged) He–He, H_2–H_2, and He–H_2 potentials occur at separations of: 2.94 Å,[76] 3.4 Å,[69] and 3.4 Å,[77] respectively, we expect only minor differences between the length scales of the CO_2-pH_2 and CO_2–He potentials. Subtracting the 1.9 Å effective radius of the pH_2 molecules from the angle-dependent minimum of the CO_2–He potential produces the outline of the CO_2 molecule. The ''dip'' in towards the central C atom indicates the presence of an attractive well, and correctly reflects the experimentally determined T-shaped global minimum CO_2–He geometry.[78]

Judging from the drawings in Fig. 4, we consider it unlikely, but not impossible, for a CO_2 molecule to occupy a single-substitutional vacancy in solid pH_2. A relaxed trapping site structure would require considerable distortion of the surrounding pH_2 molecules away from their original lattice positions, leading to numerous smaller repulsive pH_2-pH_2 interactions. On the other hand, the double-substitutional site readily accommodates a CO_2 molecule, and the triple-substitutional site appears perhaps overly spacious.

We can most easily explain our observation of three main peaks in the spectra of as-deposited CO_2/pH_2 solids by trapping of CO_2 molecules in three distinct double-substitutional vacancies. In each case the CO_2 molecules should exist as strongly hindered librators and not as rotors. By comparison with the recent CO_2/N_2 experiments,[57] we would expect a single sharp line as the main signature for each trapping site. There is only one type of double-substitutional site in an fcc solid, while there are two different ways of removing two adjacent host molecules in an hcp solid. These are designated ''in-plane'' (ip) if both host molecules are removed from the same basal plane, and ''out-of-plane'' (oop) otherwise.[79]

Based on their annealing behaviors, we assign the three major lines to CO_2 molecules trapped in double-substitutional sites as follows: the α line to the oop-hcp site,

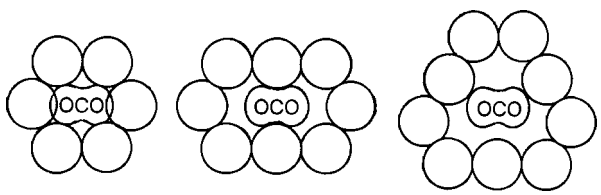

FIG. 4. Hypothetical trapping sites for CO_2 molecules in solid pH_2 based on single-, double-, and triple-substitutional vacancies in close-packed planes of pH_2 molecules.

the β line to the ip-hcp site, and the γ line to the fcc site. The virtual disappearance of the γ line upon annealing matches our previous experience with irreversible loss of fcc regions during annealing. We attribute the α line decrease and β line increase upon annealing to the improved alignment of the hcp crystallite *c*-axis directions with the substrate surface normal. Since our IR beam propagates parallel to this same direction, CO_2 molecules oriented perpendicular to the surface normal will exhibit better alignment of their v_3 mode transition dipoles with the electric field of the IR beam.

We exclude trapping of CO_2 molecules in triple-substitutional sites because such molecules should exist as slightly hindered rotors. Since the rotational constant of CO_2 is only ≈ 0.4 cm^{-1}, several rotational levels would be populated at the temperatures employed in these experiments. We see no evidence in the spectra for the evenly spaced absorption lines expected for rotational transitions from such levels. We note that our results do not absolutely exclude the possibility of trapping of CO_2 molecules in single-substitutional sites. In analogy to the argument made previously for the double-substitutional sites, one can conceive of two types of relaxed single-substitutional sites in hcp pH_2 which differ in the orientation of the trapped CO_2 molecule with respect to the hcp *c* axis.

One final point of comparison is the absorption linewidths expected for the single vs double-substitutional trapping sites. In the first case, both ends of the CO_2 molecule would experience strong repulsive interactions with the nearest-neighbor pH_2 molecules, suggesting the likelihood of strong coupling between the CO_2 v_3 asymmetrical stretching mode and the pH_2 solid. For the double-substitutional site, especially if the center of mass of the CO_2 molecule is strongly localized near the center of the trapping site, the ends of the CO_2 molecule should experience much weaker attractive interactions with those pH_2 nearest neighbors aligned with the molecular axis. In this case, we would expect very weak coupling of the v_3 mode with the pH_2 solid, and correspondingly narrow absorption lines.

4.3. Weak absorption features

We turn finally to the origins of the numerous weaker absorption features in the CO_2/pH_2 spectra. Ultimately, successful quantitative modeling of these features should yield the best insights into the CO_2 trapping site structures and librational dynamics, as well as the more general lessons we hope will help us interpret the spectra of larger non-rotating dopant systems. At present, however, we can only offer our qualitative speculations in the form of a list of hypotheses to be examined in the future.

The same multiple trapping site argument used above to explain the α, β, and γ peaks can be extended to include some or all of the peaks observed in the 2343.5 to 2345 cm^{-1} region in as-deposited CO_2/pH_2 samples. In place of double-substitutional sites in hcp and fcc regions we substitute the concepts of hcp-like and fcc-like trapping sites discussed above. In contrast to the CH_4/pH_2 case, for which we found no such distinction, for CO_2/pH_2 subtle differences in final relaxed trapping site structures due to non-nearest-neighbor interactions might induce the $\sim$10% differences in gas-to-matrix shifts required to account for these minor peaks. The irreversible changes observed upon annealing would thus correspond to the disappearance of some of these metastable trapping site structures. The logical extreme of this model, in which each and every line corresponds to the absorption of CO_2 molecules in a particular trapping site, raises the interesting notion of inhomogeneities as discrete, countable entities; challenging the traditional ''continuous'' depiction of inhomogeneous broadening.

The extreme dilution of our samples weighs against attributing the weak features in the 2343.5 to 2345 cm^{-1} region to long-range interactions between CO_2 molecules. Vibrational shifts due to resonant interactions between CO_2 molecules die off with increasing separation as R^{-3} (Ref. 46); their absolute magnitudes fall below ~ 0.1 cm^{-1} for separations greater than ≈ 20 Å. At a concentration of 1 ppm in solid pH_2, the number density of CO_2 molecules is only 2.6×10^{16} cm^{-3}; for a random distribution the mean separation between closest CO_2 molecules is ≈ 200 Å. Furthermore, denoting the distribution of separations between closest CO_2 molecules as $f(R)dR$, then from the peak value near $R = 200$ Å, $f(R)$ tends towards zero as R^2 for decreasing separations. Thus, very few of the CO_2 molecules will be close enough to communicate in this manner. An intriguing mechanism in which dopants interact via the strain fields they induce in the surrounding host lattice has been proposed to explain sharp features in IR absorption spectra of SF_6/Ar matrices.[80] In fact, the spectra reported in that study bear a passing resemblance to our CO_2/pH_2 spectra. However, we find it difficult to accept that such a mechanism could operate over the $\sim$100 matrix host diameters intervening between CO_2 dopants in our 1 ppm samples.

The models proposed so far in this section cannot explain the observed *reversible* temperature-dependent changes to the spectra. Several of the weaker features appear to originate from thermally populated initial states. On the other hand, the α'' line appears to originate from a very easily thermally depopulated initial state; we estimate that the height of the α'' peak decreases $\approx$50-fold upon warming from $T = 2.4$ to 4.8 K. Since the lowest-lying vibrational state of a gas-phase CO_2 molecule is the v_2 bending mode at 667 cm^{-1}, these thermally populated states must involve interactions with the pH_2 solid, although we can as yet offer no specifics as to the libration–translation dynamics involved.

Another possibility is the aggregation of oH_2 impurities around the CO_2 molecules. Assuming complete equilibration in our ortho/para converter[17] at $T = 15$ K, the residual oH_2 concentration is $\approx$100 ppm. Actually, assuming natural isotopic abundance, the pH_2 solids should also contain $\approx$300 ppm HD molecules, but HD molecules are immobilized in the solid at *l*He temperatures. On the other hand, the $J = 1$ ''ortho'' excitations are mobile by a process known as ''quantum diffusion,'' i.e., the conversion of adjacent oH_2–pH_2 pairs into pH_2–oH_2 pairs.[69,73,81,82] Any $J = 1$ excitation that diffuses into the vicinity of a trapped CO_2 molecule would localize to form an oH_2–CO_2 pair bound together via the electric quadrupole–quadrupole (EQQ) interaction. Based on previously published HD/oH_2/pH_2 and $D_2/oH_2/pH_2$ spectra,[4,5] this same EQQ interaction should be capable of producing complex features over a ~ 1 cm^{-1} region of the CO_2 spectrum. In this picture, the revers-

ible temperature-dependent spectral changes could be attributed to absorptions involving different ''orientational'' states of the $o\mathrm{H}_2$ molecules, rather than the libration–translation dynamics of the CO_2 molecules.

Given the present data, we can only note in passing that the weak features in the 2345 to 2348 cm^{-1} region (Fig. 3), which grow in upon annealing, show blue shifts relative to the α and β peaks, consistent with clustering of a small fraction of the CO_2 molecules to form CO_2 dimers and trimers.

5. CONCLUSIONS AND FUTURE DIRECTIONS

We have reported high-resolution IR absorption spectra of CO_2 molecules isolated in rapid vapor deposited $p\mathrm{H}_2$ solids. The absence of a regularly spaced progression of lines is taken as evidence that the CO_2 molecules cannot rotate, and instead exist as strongly hindered librators. The three main absorption features are assigned to CO_2 molecules trapped in double-substitutional sites in hcp and fcc regions of the as-deposited solids. Numerous weaker spectral features remain unexplained. Reversible temperature-dependent intensities demonstrate that some of these weaker transitions originate from low-lying thermally populated states. Some of the 2 to 5 cm^{-1} blue-shifted weak features observed upon annealing of the samples may be due to small $(\mathrm{CO}_2)_n$ clusters.

We are preparing to perform a new series of experiments on $\mathrm{CO}_2/p\mathrm{H}_2$ samples, including the use of isotopically substituted CO_2 molecules. Breaking the inversion symmetry of the CO_2 molecule by trapping the $^{16}\mathrm{O}^{12}\mathrm{C}^{18}\mathrm{O}$ isotopomer will alter the nature of the allowed librational states. Trapping gradually increasing concentrations of CO_2 molecules should permit the identification of spectral features due to dimers and larger clusters. Manipulating the residual $o\mathrm{H}_2$ concentration by varying the ortho/para converter temperature should clarify the importance of $o\mathrm{H}_2$–CO_2 clustering.

We expect that quantum simulation techniques will be very valuable in elucidating the trapping site structures and librational dynamics of the $\mathrm{CO}_2/p\mathrm{H}_2$ system, as demonstrated previously for O_2 doped hydrogen solids.[83–86]

We thank the authors of Refs. 57 and 65 for advance copies of their manuscripts. We thank the referee for pointing out a serious error in our original discussion of the temperature dependence of the α'' peak.

*E-mail: mario_fajardo@ple.af.mil

[1] M. Okumura, M. C. Chan, and T. Oka, Phys. Rev. Lett. **62**, 32 (1989).
[2] T. Oka, Annu. Rev. Phys. Chem. **44**, 299 (1993).
[3] T. Oka, Fiz. Nizk. Temp. **22**, 134 (1996) [Low Temp. Phys. **22**, 96 (1996)].
[4] D. P. Weliky, K. E. Kerr, T. J. Byers, Y. Zhang, T. Momose, and T. Oka, J. Chem. Phys. **105**, 4461 (1996).
[5] Y. Zhang, T. J. Byers, M. C. Chan, T. Momose, K. E. Kerr, D. P. Weliky, and T. Oka, Phys. Rev. B **58**, 218 (1998).
[6] T. Momose, J. Chem. Phys. **107**, 7695 (1997).
[7] T. Momose, M. Miki, T. Wakabayashi, T. Shida, M. C. Chan, S. S. Lee, and T. Oka, J. Chem. Phys. **107**, 7707 (1997).
[8] T. Momose, H. Katsuki, H. Hoshina, N. Sogoshi, T. Wakabayashi, and T. Shida, J. Chem. Phys. **107**, 7717 (1997).
[9] T. Momose and T. Shida, Bull. Chem. Soc. Jpn. **71**, 1 (1998).
[10] H. Hoshina, T. Wakabayashi, T. Momose, and T. Shida, J. Chem. Phys. **110**, 5728 (1999).
[11] R. Steinhoff, K. V. S. R. Apparao, D. W. Ferguson, K. N. Rao, B. P. Winnewisser, and M. Winnewisser, Appl. Opt. **32**, 6577 (1993).
[12] R. Steinhoff, K. V. S. R. Apparao, D. W. Ferguson, K. N. Rao, B. P. Winnewisser, and M. Winnewisser, Can. J. Phys. **72**, 1122 (1994).
[13] M. Mengel, B. P. Winnewisser, and M. Winnewisser, Phys. Rev. B **55**, 10420 (1997).
[14] M. Mengel, B. P. Winnewisser, and M. Winnewisser, J. Mol. Spectrosc. **188**, 221 (1998).
[15] *Proceedings of the High Energy Density Matter (HEDM) Contractors' Conference, held 17–20 May 1998 in Monterey, CA*, M. R. Berman (Ed.), U.S. Air Force Office of Scientific Research, Arlington, VA (1999).
[16] M. E. Fajardo and S. Tam, J. Chem. Phys. **108**, 4237 (1998).
[17] S. Tam and M. E. Fajardo, Rev. Sci. Instrum. **70**, 1926 (1999).
[18] P. C. Souers, Hydrogen Properties for Fusion Energy, Univ. of California Press, Berkeley (1986).
[19] M. E. Fajardo, J. Chem. Phys. **98**, 110 (1993).
[20] M. E. Fajardo, S. Tam, T. L. Thompson, and M. E. Cordonnier, Chem. Phys. **189**, 351 (1994).
[21] S. Tam, M. Macler, and M. E. Fajardo, J. Chem. Phys. **106**, 8955 (1997).
[22] S. Tam, M. E. Fajardo, H. Katsuki, H. Hoshina, T. Wakabayashi, and T. Momose, J. Chem. Phys. **108**, 4237 (1998).
[23] L. Pauning, Phys. Rev. **36**, 430 (1930).
[24] A. F. Devonshire, Proc. R. Soc. London, Ser. A **A153**, 601 (1936).
[25] W. H. Flygare, J. Chem. Phys. **39**, 2263 (1963).
[26] H. F. King and D. F. Hornig, J. Chem. Phys. **44**, 4520 (1966).
[27] R. E. Miller and J. C. Decius, J. Chem. Phys. **59**, 4871 (1973).
[28] H. Friedmann and S. Kimel, J. Chem. Phys. **43**, 3925 (1965).
[29] M. T. Bowers, G. I. Kerley, and W. H. Flygare, J. Chem. Phys. **45**, 3399 (1966).
[30] H. Friedmann and S. Kimel, J. Chem. Phys. **47**, 3589 (1967).
[31] H. Friedmann, A. Shalom, and S. Kimel, J. Chem. Phys. **50**, 2496 (1969).
[32] P. D. Mannheim, Phys. Rev. B **5**, 745 (1972).
[33] P. D. Mannheim, J. Chem. Phys. **56**, 1006 (1972).
[34] J. Manz, J. Am. Chem. Soc. **102**, 1801 (1980).
[35] M. Allavena, H. Chakroun, and D. White, J. Chem. Phys. **77**, 1757 (1982).
[36] H. Kono and S. H. Lin, J. Chem. Phys. **78**, 2607 (1983).
[37] I. L. Garzon and E. Blaisten-Barojas, J. Chem. Phys. **83**, 4311 (1985).
[38] M. E. Fajardo, S. Tam, and T. Momose (unpublished).
[39] *Molecular Spectroscopy: Modern Research Volume III*, edited by K. N. Rao (Academic Press, New York, 1985).
[40] G. Guelachvili and K. N. Rao, *Handbook of Infrared Standards* (Academic Press, New York, 1985).
[41] G. Guelachvili *et al.*, Spectrochim. Acta, Part A **52**, 717 (1996).
[42] M. A. Walsh, T. H. England, T. R. Dyke, and B. J. Howard, Chem. Phys. Lett. **142**, 265 (1987).
[43] R. Eggenberger, S. Gerber, and H. Huber, Mol. Phys. **72**, 433 (1991).
[44] Z. Slanina, S. J. Kim, and K. Fox, Vib. Spectrosc. **4**, 251 (1993).
[45] L. M. Nxumalo, T. A. Ford, and A. J. Cox, J. Mol. Struct. **307**, 153 (1994).
[46] M. J. Weida, J. M. Sperhac, and D. J. Nesbitt, J. Chem. Phys. **103**, 7685 (1995).
[47] M. J. Weida and D. J. Nesbitt, J. Chem. Phys. **105**, 10210 (1996).
[48] J. A. Barnes and T. E. Gough, J. Chem. Phys. **86**, 6012 (1987).
[49] G. E. Ewing and D. T. Sheng, J. Phys. Chem. **92**, 4063 (1988).
[50] W. E. Osberg and D. F. Hornig, J. Chem. Phys. **20**, 1345 (1952).
[51] B. E. Wood and J. A. Roux, J. Opt. Soc. Am. **72**, 720 (1982).
[52] M. Falk, J. Chem. Phys. **86**, 560 (1987).
[53] M. A. Ovchinnikov and C. A. Wight, J. Chem. Phys. **99**, 3374 (1993).
[54] *Vibrational Spectroscopy of Trapped Species*, edited by H. E. Hallam (Wiley, London, 1973).
[55] D. W. Ball, Z. H. Kafafi, L. Fredin, R. H. Hauge, and J. L. Margrave, *A Bibliography of Matrix Isolation Spectroscopy: 1954–1985*, Rice Univ. Press, Houston, TX (1988).
[56] D. W. Ochsner, D. W. Ball, and Z. H. Kafafi, *A Bibliography of Matrix Isolation Spectroscopy: 1985–1997* (U.S. Naval Research Laboratory, Washington, DC, 1998).
[57] M. Vetter, A. P. Brodyanski, and H. J. Jodl, J. Phys. Chem. **104**, 3698 (2000).
[58] L. Fredin, B. Nelander, and G. Ribbegard, J. Mol. Spectrosc. **53**, 410 (1974).
[59] R. Guasti, V. Schettino, and N. Brigot, Chem. Phys. **34**, 391 (1978).
[60] L. M. Nxumalo and T. A. Ford, J. Mol. Spectrosc. **327**, 145 (1994).
[61] Y. Ogawara, A. Bruneau, and T. Kimura, Anal. Chem. **66**, 4354 (1994).
[62] E. Knozinger and P. Beichert, J. Phys. Chem. **99**, 4906 (1995).
[63] M. J. Irvine and A. D. E. Pullin, Aust. J. Chem. **35**, 1961 (1982).
[64] M. J. Irvine and A. D. E. Pullin, Spectrochim. Acta A **43**, 611 (1987).

[65] M. Fushitani, T. Shida, T. Momose, and M. Rasanen, J. Phys. Chem. A **104**, 3635 (2000).
[66] M. E. Fajardo and S. Tam (unpublished).
[67] L. Andrews, R. T. Arlinghaus, and G. L. Johnson, J. Chem. Phys. **78**, 6353 (1983).
[68] N. Fourati, B. Silvi, and J. P. Perchard, J. Chem. Phys. **81**, 4737 (1984).
[69] I. F. Silvera, Rev. Mod. Phys. **52**, 393 (1980).
[70] C. Kittel, *Introduction to Solid State Physics 6th Edition* (Wiley, New York, 1986).
[71] J. Van Kranendonk and H. P. Gush, Phys. Lett. **1**, 22 (1962).
[72] J. Van Kranendonk and G. Karl, Rev. Mod. Phys. **40**, 531 (1968).
[73] J. Van Kranendonk, *Solid Hydrogen: Theory of the Properties of Solid* H_2, *HD*, and D_2 (Plenum Press, New York, 1983).
[74] G. W. Collins, W. G. Unites, E. R. Mapoles, and T. P. Bernat, Phys. Rev. B **53**, 102 (1996).
[75] G. Yan, M. Yang, D. Xie, J. Chem. Phys. **109**, 10284 (1998).
[76] J. B. Anderson, C. A. Traynor, and B. M. Boghosian, J. Chem. Phys. **99**, 345 (1993).
[77] W. R. Rodwell and G. Scoles, J. Phys. Chem. **86**, 1053 (1982).
[78] M. J. Weida, J. M. Sperhac, D. J. Nesbitt, and J. M. Hutson, J. Chem. Phys. **101**, 8351 (1994).
[79] A. B. Harris, A. J. Berlinsky, and W. N. Hardy, Can. J. Phys. **55**, 1180 (1977).
[80] D. Hallamasek, E. Babka, and E. Knozinger, J. Mol. Struct. **408/409**, 125 (1997).
[81] L. I. Amstutz, J. R. Thompson, and H. Meyer, Phys. Rev. Lett. **21**, 1175 (1968).
[82] R. Oyarzun and J. Van Kranendonk, Phys. Rev. Lett. **26**, 646 (1971).
[83] A. V. Danilychev, V. E. Bondybey, V. A. Apkarian, S. Tanaka, H. Kajihara, and S. Koda, J. Chem. Phys. **103**, 4292 (1995).
[84] M. Sterling, Z. Li, and V. A. Apkarian, J. Chem. Phys. **103**, 5679 (1995).
[85] Z. Li, V. A. Apkarian, and L. B. Harding, J. Chem. Phys. **106**, 942 (1997).
[86] Z. Li and V. A. Apkarian, J. Chem. Phys. **107**, 1544 (1997).

This article was published in English in the original Russian journal. Reproduced here with stylistic changes by the Translation Consultant.

Rovibrational transitions and nuclear spin conversion of methane in parahydrogen crystals

M. Miki and T. Momose*

Division of Chemistry, Graduate School of Science, Kyoto University and Japan Science and Technology Corporation (JST), Kyoto 606-8502, Japan

(Submitted February 7, 2000; revised May 25, 2000)
Fiz. Nizk. Temp. **26**, 899–908 (September–October 2000)

Solid parahydrogen is an excellent matrix for matrix-isolation spectroscopy because of its high spectral resolution. Here we describe the rovibrational structure and nuclear spin conversion of CH_4 embedded in parahydrogen crystals studied by infrared absorption spectroscopy. The vibration–rotation absorptions of CH_4 exhibit time-dependent intensity changes at 4.8 K. These changes are interpreted to be a result of the $I=1\rightarrow I=2$ nuclear spin conversion that accompanies the $J=1\rightarrow J=0$ rotational relaxation. The half-lifetime of the upper $J=1$ rotational state is unchanged by the addition of up to 2% orthohydrogen molecules but decreases with more than 10% orthohydrogen molecules. The increase of the decay rate at higher orthohydrogen concentration indicates that the magnetic field gradient across CH_4 due to the orthohydrogen molecules mixes the nuclear spin states, which accelerates the conversion. © *2000 American Institute of Physics.* [S1063-777X(00)00609-5]

1. INTRODUCTION

Matrix isolation spectroscopy at cryogenic temperatures has grown to be a methodology for a variety of applications in the field of molecular spectroscopy. Its application to the study of unstable molecules has piloted gas-phase spectroscopy.[1] Not only unstable but also stable molecules in cryogenic matrices have been the subject of studies for understanding physics and chemistry in the condensed phase.[2]

In the early works by Lewis in the 1940s, organic molecular solids were used as the isolation matrices.[3] Rare gas matrices, which were introduced by Pimentel and his co-workers,[4] have been widely used in recent studies because of their chemically inert property and weak perturbations. The interaction from the environment, however, is not small due to the proximity of surrounding atoms and molecules, which makes the spectral linewidths of matrix-isolated species broader than those in the gas phase. The typical linewidth of vibrational transitions in rare gas matrices is on the order of 0.1–1 cm^{-1}. The spectra in the condensed phase must contain much important information, such as intermolecular interactions and hindered motion of molecules under perturbation of the surrounding electrostatic potentials. Unfortunately, the broadening of the spectra wipes out most of the fine spectral structures containing such information.

Recently, it was found that the spectra of molecules in parahydrogen crystals are surprisingly sharp, as was initially noted by Oka and his co-workers.[5–7] They studied parahydrogen crystals using high-resolution infrared and Raman spectroscopy and showed that not only the parahydrogen itself but also isotopic impurities such as orthohydrogen and deuterated hydrogen in parahydrogen crystals exhibit sharp absorption features.[8,9] The sharpest transition so far observed is the absorption of deuterated hydrogen, whose width is only 4 MHz (full width at half maximum, FWHM).[8] The width is almost two orders of magnitude narrower than that of Doppler-limited gas phase spectra.

The sharp linewidth indicates that parahydrogen crystals are a promising medium for high-resolution matrix isolation spectroscopy.[7,10] Following the work of the group in Chicago, the authors' group in Kyoto[11] and Fajardo's group at Edwards Air Force Base[12,13] have independently initiated high-resolution spectroscopic studies of atoms and molecules embedded in parahydrogen crystals. We showed that most of the spectral widths of molecules in parahydrogen crystals are sharper than 0.01 cm^{-1} at low temperatures.[14] The spectral resolution of 0.01 cm^{-1} is high enough to discuss intermolecular interactions and molecular motions in the condensed phase in great detail.[11]

In a series of papers we have extensively studied rotation–vibration transitions of methane molecules embedded in parahydrogen crystals by high-resolution infrared absorption spectroscopy.[14–19] The analysis of observed spectra reveals that the rotational energy levels of the methane is fully quantized, having the rotational quantum number J as a good quantum number. Here, we again discuss methane molecules in parahydrogen crystals, but we focus on the nuclear spin conversion of methane.

In the case of CH_4, the four equivalent protons can be coupled into three nuclear spin states, $I=0$, 1, and 2. The Pauli principle requires that only certain nuclear spin wave functions couple with any particular electron–vibration–rotation wave-functions.[20,21] As a result, the $J=0$ rotational state is associated with the $I=2$ nuclear spin quintet state and the $J=1$ state is the $I=1$ triplet state, while the $J=2$ state is coupled with both the $I=1$ triplet state and the $I=0$ singlet state. Even if the temperature is lowered sufficiently, the equilibrium distribution cannot be achieved because conversion among the different nuclear spin states is forbidden.[22] Only weak nuclear spin–nuclear spin magnetic interaction and spin–rotation interaction may cause the conversion among different nuclear spin states in the gas phase.[23–25] In condensed phases, evidence for the triplet (I

$=1) \rightarrow$quintet ($I=2$) transition in solid methane has been observed by proton magnetic resonance spectroscopy.[26–34] The transition of methane in solid argon and krypton has been observed by infrared spectroscopy.[35,36] A conversion time of about 100 min has been reported in these condensed phases, which is still a slow process compared with other relaxations.

In a previous paper[16] we briefly reported the fact that the $J=1$ rotational level is populated in spite of the null Boltzmann factor at the observed temperature, and that the population of the $J=1$ rotational level decreases with time, which can be attributed to a relaxation of rotational energy accompanying a nuclear spin conversion. The present article presents additional data and arguments to support the view that the existence of impurity orthohydrogen in parahydrogen crystal increases the conversion rate.

In Sec. 2 we briefly describe the properties of parahydrogen crystals to demonstrate the usefulness of parahydrogen matrices for isolation spectroscopy. Experimental details are given in Sec. 3. In Sec. 4, infrared absorption spectra of CH_4 embedded in parahydrogen crystals and their analyses are briefly overviewed. Analysis and discussion on the nuclear spin conversion are given in Sec. 5.

2. PARAHYDROGEN MATRIX

There are two kinds of hydrogen molecules existing in nature: *para-* and *orthohydrogen*. The parahydrogen molecule possesses a nuclear spin angular momentum of $I=0$, while for orthohydrogen $I=1$. Because the total wave function of H_2 has to be antisymmetric with respect to the permutation of hydrogen atoms, parahydrogen in its ground electronic state is associated with the rotational states of even quantum numbers, while orthohydrogen is associated with odd numbers. Since the interconversion between $I=0$ and $I=1$ nuclear spin states is very slow in the absence of an external magnetic field, the parahydrogen and orthohydrogen can be considered to be different molecules under normal conditions. Since the rotational constants of hydrogen molecules is as large as 60 cm^{-1} (Ref. 37), the para- and orthohydrogen occupy rotational quantum numbers of $J=0$ and $J=1$, respectively, at liquid He temperatures. Herein, the terms *para-* and *orthohydrogen* are used to signify hydrogen molecules with $J=0$ and $J=1$, respectively.

Since parahydrogen, with the rotational quantum number $J=0$, has no permanent electric moments of any order, we consider the molecule to be spherical, like rare gas atoms. Due to the spherical nature of parahydrogen, the crystal of parahydrogen provides a homogeneous environment for a guest molecule. On the other hand, orthohydrogen, with the rotational quantum number $J=1$, has a permanent quadrupole moment.[38] Thus the interaction influenced by orthohydrogen is stronger than that by parahydrogen. From the spectroscopic point of view, the existence of orthohydrogen in the crystal causes additional broadening due to the quadrupolar interaction.[8] Therefore, it is desired that the concentration of orthohydrogen be as low as possible. The concentration of orthohydrogen can be reduced to less than 0.05% by using an ortho–para converter[11,13] operated at 13.8 K.

The crystal structure of pure parahydrogen is a complete hexagonal close-packed (hcp), as has been proved spectroscopically.[6] The lattice constant of solid hydrogen (3.78 Å) is considerably larger than that of Ne (3.16 Å). The large lattice constant of hydrogen results from large zero-point lattice vibration due to the small mass of H_2. The large lattice constant of parahydrogen provides more free space for a guest molecule as compared with other matrices.

The importance of parahydrogen as the matrix for infrared spectroscopy was first proposed by Oka *et al.*[7,10] and has been proved by the authors' group[11,16] and Fajardo's group.[12,13] Independently, Miyazaki *et al.* found that the parahydrogen matrix is useful for ESR spectroscopy because parahydrogen does not have any magnetic moments which cause a broadening of ESR linewidths.[39]

Visible and UV spectroscopy of atoms in solid hydrogen has been conducted by Fajardo *et al.* They have studied the reactive dynamics of dopants in solid hydrogen with the ultimate aim of finding high-performance rocket propellants.[40]

Infrared studies of rovibrational transitions of molecules isolated in parahydrogen crystals have been developed by the authors' group and Fajardo's group, independently. Techniques for making parahydrogen crystals in two groups are different. In Kyoto, we made the crystals in an enclosed cell, as is described in the next section.[11,16] In the Edwards Air Force Base research, Fajardo developed a technique to grow transparent crystals on a cold surface in an open vacuum. Due to the relatively high vapor pressure of H_2 even at liquid He temperatures,[41] the standard deposition technique which is usually employed for isolation spectroscopy of rare gas matrices can not be applied straightforwardly. Fajardo found a condition for growing completely transparent crystals of millimeter thickness by controlling the deposition rate and the temperature of the substrate.[13] On the other hand, our enclosed cell technique allows us to grow crystals at a higher temperature, which maintains the equilibrium between gas and solid phases without encountering the problem of vaporization of samples.

The two methods have their own advantages and disadvantages. The advantage of growing the crystal in an enclosed cell is that the crystal structure surrounding the guest molecules becomes completely hcp.[16] Therefore the fine structure of the observed spectra in an enclosed cell can be treated by a quantitative analysis of the molecular interaction and molecular motions in the condensed phase based on first principles. Crystals grown by Fajardo's deposition technique are found to be a mixture of hcp and fcc structures.[19] The different environment surrounding embedded molecules causes extra transitions, which makes the quantitative analysis of the spectra more difficult. On the other hand, one can dope any molecules in solid hydrogen by the deposition technique, while a very limited number of molecules can be isolated by our enclosed cell technique.

3. EXPERIMENTS

Parahydrogen crystals were grown in a cylindrical copper cell with both ends enclosed by BaF_2 windows with indium gaskets. Pure parahydrogen gas containing less than 0.05% orthohydrogen was obtained by passing high purity ($>$99.9995%) normal hydrogen gas through an ortho–para converter at 14 K. A detail of the converter is given in a previous review article.[11] About 10 ppm of methane was

mixed with the converted hydrogen gas at room temperature. Concentrations of orthohydrogen higher than 0.05% were controlled by adding normal hydrogen to the converted parahydrogen gas. Then, the mixed gas was continuously introduced into the copper cell installed under the cold surface of a standard Dewar-type liquid He cryostat. The temperature of the cell was kept at 8 K during the crystal growth, which takes about 2 hours. The typical flow rate of the gas was 100 cm^3/min. The crystal, which was completely transparent, was grown from the copper wall toward the inside. The crystal thus grown is a completely hexagonal close-packed structure, as is proved by the stimulated Raman gain spectroscopy of the $Q_1(0)$ transition[6] and infrared absorption of methane in the crystal.[16,19] The c axis of the crystal is along the direction of crystal growth.

Infrared absorption spectra were observed by a Fourier transform infrared (FTIR) spectrometer (Nicolet Magna 750) with a resolution of 0.25 cm^{-1}. A globar source, KBr beam splitter, and a liquid-N_2-cooled HgCdTe (MCT) detector were used for recordings. All the measurements were done at 4.8 K.

In an experiment to determine the concentration dependence of orthohydrogen impurity on the conversion rate, orthohydrogen molecules were added to the premixed gas in concentrations of 0.05, 0.2, 2, 10, 20, 30, and 75% while maintaining the concentration of CH_4. The conversion rate was followed by observing the relative intensities of the FTIR absorption of the lines arising from different nuclear spin states. Several spectra were recorded for each sample intermittently at reasonably separated times. One recording took about 10 minutes. During the interval of the recordings, the globar source was turned off in order to avoid conversion due to photoexcitation by the globar light.

4. OBSERVED SPECTRA AND ROVIBRATIONAL ENERGY LEVELS OF METHANE

Since the intermolecular distance of solid hydrogen of 3.78 Å is significantly larger than the van der Waals diameter of methane at about 3.24 Å, methane molecules can rotate almost freely in para-hydrogen crystals.[42] In previous papers, we have shown that the rotational quantum number J of the methane is still a good quantum number in parahydrogen crystals and that the effective rotational constant is only 10% smaller than that in free space.[15,16,18]

Figure 1 shows an FTIR spectrum of the ν_3 band of methane in a parahydrogen crystal. The orthohydrogen concentration is 0.05%. The large splitting, of about 9 cm^{-1}, is assigned to the rotational branches of methane; the transitions at around 3008 cm^{-1} are assigned to $P(1)$, those at around 3017 cm^{-1} to $Q(1)$, those at around 3025 cm^{-1} to $R(0)$, and those at higher than 3031 cm^{-1} to $R(1)$. The small splittings of 0.5 cm^{-1} appearing in each rotational branch are due to the M quantum number of methane, which is the projection of the rotational quantum number J along the crystal axis. The splitting of the M-sublevels is caused by the crystal field of solid parahydrogen.

All the transitions appearing in Fig. 1 can be quantitatively interpreted by assuming that methane occupies a substitutional site of the hcp crystal structure of solid hydrogen, and the methane, having T_d symmetry, rotates freely under

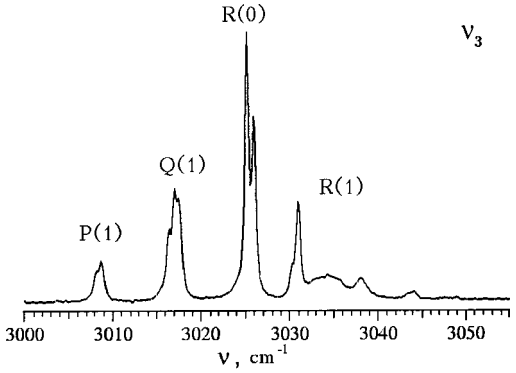

FIG. 1. Infrared absorption spectrum of the ν_3 transition of CH_4 embedded in a parahydrogen crystal. The orthohydrogen concentration is 0.05%. The spectral resolution is 0.25 cm^{-1}.

the crystal field of D_{3h} symmetry. In this case, the first anisotropic crystal field potential is found to be

$$\begin{aligned} V(\Omega) &= \varepsilon_{3c}\frac{1}{2}[D^{(3)}_{2,3}(\Omega) - D^{(3)}_{-2,3}(\Omega) \\ &\quad + D^{(3)}_{2,-3}(\Omega) - D^{(3)}_{-2,-3}(\Omega)] \\ &= \varepsilon_{3c}\frac{\sqrt{6}}{4}[-2\cos 2\chi \cos\theta \cos 3\varphi \\ &\quad + \sin 2\chi(1+\cos^2\theta)\sin 3\varphi]\sin\theta \end{aligned} \tag{1}$$

where $\Omega \equiv (\chi, \theta, \varphi)$ is the Euler angle of methane relative to the crystal axis, and $D^{(l)}_{m,n}(\Omega)$ is Wigner's rotation matrix.[43] The definition of the Euler angles and of Wigner's rotation matrix is the same as employed by Hougen.[44] The symbol ε_{3c} is a crystal-field parameter to be determined by analysis of the observed spectra. Equation (1) can be easily derived with the use of the extended group theory.[15,45]

The interaction potential $V(\Omega)$ in Eq. (1) causes the splittings of degenerate M-sublevels of the spherical rotor in the free space. The rotational energy levels in the ground vibrational state can be calculated as the eigenvalues of the matrix of Hamiltonian $H = B''J^2 + V(\Omega)$ where J is the rotational angular momentum operator, and B'' is the rotational constant of the ground state. The rotational levels in the triply degenerate excited vibrational states can be obtained by taking into account the Coriolis interaction in addition to the rotational Hamiltonian. In a previous paper, we have determined molecular constants of methane and the crystal field parameter, ε_{3c}, by the least-squares fitting of the observed transition wave numbers with the use of the crystal-field potential given in Eq. (1).[16] Refer to our previous papers for a complete analysis.[15,16]

It should be noted that all the observed absorption lines can be assigned to the rotational branches, and thus the so-called rotationless transition[46,47] is absent in our spectrum. Rotationless transition have been observed in the case of water isolated in rare gas matrices.[46,47] Recently, it was observed that H_2O in solid parahydrogen also exhibits a rotationless transition.[48] The presence of rotationless transitions were interpreted as indicating that the molecules are firmly trapped in interstitial sites of the lattice. The absence of the rotationless transition in the case of methane in parahydro-

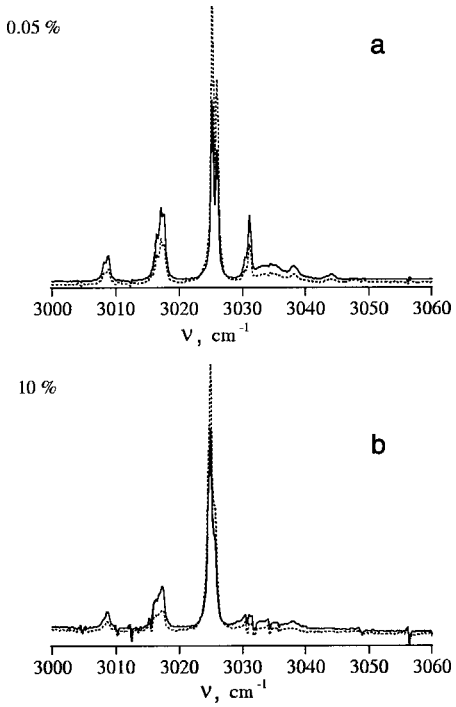

FIG. 2. Temporal behavior of the ν_3 transition of CH_4 in para-hydrogen crystals with orthohydrogen concentration of 0.05% (a) and 10% (b). The solid line is the spectrum observed just after crystal growth. The dotted line is the spectrum observed 2 hours after crystal growth. The sharp spikes are due to the absorption of moisture in the air.

gen crystals confirms that methane occupies a substitutional site of the crystal, but not any interstitial sites.

Figure 2 represents a time-dependent change of spectral structure for the ν_3 transition (spectra of crystals with the ortho concentration of 0.05% and 10%, respectively). The solid line is the spectrum observed immediately after the growth of the crystal, while the dotted line is the spectrum observed 2 hours after crystal growth. It is clearly seen that all the absorptions except those at around 3025 cm^{-1} become weak after a few hours, while the absorptions around 3025 cm^{-1} become strong.

In Table I the observed integrated intensities of the $R(0)$ and $Q(1)$ transitions at various times are given for the crystals with orthohydrogen concentrations of 0.05, 0.2, 2.0, 10, 20, 30, and 75%, respectively. Note that the time when we finished making the crystal was taken as the origin of time ($t=0$) given in the second column. It is observed that the integrated intensity of the $R(0)$ transition increases with time, while that of the $Q(1)$ transition decreases. The time-dependent absorption changes are due to the nuclear spin conversion of methane. In the next section we discuss the conversion in detail.

TABLE I. Time-dependent absorption intensities of CH_4 in parahydrogen crystals.

ortho concentration, %	Time, min[a]	$I[R(0)]$[b]	$I[Q(1)]$[b]	Sum[c]	$c(t)$[d]
0.05	50	0.104	0.041	0.223	0.467
	85	0.113	0.038	0.223	0.506
	175	0.137	0.031	0.227	0.604
	205	0.140	0.030	0.227	0.617
	270	0.152	0.027	0.230	0.660
	340	0.161	0.024	0.231	0.698
0.2	32	0.044	0.020	0.104	0.429
	92	0.046	0.015	0.088	0.521
	152	0.052	0.014	0.091	0.568
2.0	50	0.122	0.048	0.261	0.467
	100	0.138	0.042	0.260	0.531
	160	0.151	0.036	0.255	0.591
	220	0.161	0.033	0.257	0.627
	270	0.171	0.030	0.258	0.663
10	60	0.146	0.046	0.279	0.523
	115	0.172	0.040	0.288	0.597
	160	0.184	0.034	0.283	0.651
	220	0.199	0.029	0.283	0.703
	280	0.209	0.023	0.276	0.758
	340	0.205	0.022	0.269	0.763
20	14	0.143	0.038	0.253	0.565
	74	0.179	0.027	0.257	0.696
	134	0.191	0.020	0.249	0.767
	194	0.198	0.018	0.250	0.791
30	15	0.598	0.147	1.024	0.584
	75	0.751	0.092	1.018	0.738
	135	0.795	0.074	1.010	0.787
	195	0.809	0.067	1.003	0.806
	255	0.813	0.065	1.002	0.812
75	6	0.439	0.052	0.590	0.744
	36	0.472	0.045	0.603	0.783
	66	0.476	0.043	0.601	0.792
	96	0.475	0.042	0.597	0.796

[a] The time when we finished making the crystals was taken as the origin of time ($t=0$).
[b] Integrated intensity of all M-sublevels of each transition.
[c] The value of $I[R(0)]+2.9I[Q(1)]$, which is supposed to be a constant irrespective of time after the crystal growth (see text). The absolute value of the sum varies depending on the concentration of CH_4 in crystals.
[d] The mole fraction of $J=0$ methane, defined in Eq. (2).

5. NUCLEAR SPIN CONVERSION

It is convenient to review the salient features of the nuclear spin modification of the methane molecule. The Pauli principle requires the total wave-function of molecules to be antisymmetric with respect to the permutation of any identical nuclei. It follows the fact that only certain nuclear spin wave function couples with any particular electron–vibration–rotation wave functions. The symmetry of the rotational wave function of a CH_4 molecule is connected to the symmetry of the nuclear spin wave function by the requirement that the total wave function be antisymmetric with re-

spect to the interchange of any two protons. It was fully discussed by Wilson[20] that the requirement is met if both rotation and spin wave functions belong to the same representation in the pure rotational tetrahedral (T) point group. The two $I=0$ states

$$12^{-1/2}[2|\alpha\alpha\beta\beta\rangle+2|\beta\beta\alpha\alpha\rangle-|\alpha\beta\alpha\beta\rangle-|\beta\alpha\alpha\beta\rangle-|\alpha\beta\beta\alpha\rangle-1\beta\alpha\beta\alpha\rangle],$$

$$4^{-1/2}[|\alpha\beta\alpha\beta\rangle+|\beta\alpha\beta\alpha\rangle-|\alpha\beta\beta\alpha\rangle-|\beta\alpha\alpha\beta\rangle]$$

belong to the irreducible representation E, the nine $I=1$ states

$$4^{-1/2}[|\alpha\alpha\alpha\beta\rangle-|\alpha\alpha\beta\alpha\rangle+|\alpha\beta\alpha\alpha\rangle-|\beta\alpha\alpha\alpha\rangle],$$

$$2^{-1/2}[|\alpha\beta\alpha\beta\rangle-|\beta\alpha\beta\alpha\rangle],$$

$$4^{-1/2}[|\beta\beta\beta\alpha\rangle-|\beta\beta\alpha\beta\rangle+|\beta\alpha\beta\beta\rangle-|\alpha\beta\beta\beta\rangle],$$

$$4^{-1/2}[|\alpha\alpha\alpha\beta\rangle-|\alpha\alpha\beta\alpha\rangle-|\alpha\beta\alpha\alpha\rangle+|\beta\alpha\alpha\alpha\rangle],$$

$$2^{-1/2}[|\alpha\beta\beta\alpha\rangle-|\beta\alpha\alpha\beta\rangle],$$

$$4^{-1/2}[|\beta\beta\beta\alpha\rangle-|\beta\beta\alpha\beta\rangle-|\beta\alpha\beta\beta\rangle+|\alpha\beta\beta\beta\rangle],$$

$$4^{-1/2}[|\alpha\alpha\alpha\beta\rangle+|\alpha\alpha\beta\alpha\rangle-|\alpha\beta\alpha\alpha\rangle-|\beta\alpha\alpha\alpha\rangle],$$

$$2^{-1/2}[|\alpha\alpha\beta\beta\rangle-|\beta\beta\alpha\alpha\rangle],$$

$$4^{-1/2}[|\beta\beta\beta\alpha\rangle+|\beta\beta\alpha\beta\rangle-|\beta\alpha\beta\beta\rangle-|\alpha\beta\beta\beta\rangle]$$

belong to the irreducible representation F, and the five $I=2$ states

$$|\alpha\alpha\alpha\alpha\rangle,$$

$$4^{-1/2}[|\alpha\alpha\alpha\beta\rangle+|\alpha\alpha\beta\alpha\rangle+|\alpha\beta\alpha\alpha\rangle+|\beta\alpha\alpha\alpha\rangle],$$

$$6^{-1/2}[|\alpha\alpha\beta\beta\rangle+|\beta\beta\alpha\alpha\rangle+|\alpha\beta\alpha\beta\rangle+|\beta\alpha\beta\alpha\rangle+|\beta\alpha\alpha\beta\rangle+|\alpha\beta\beta\alpha],$$

$$4^{-1/2}[|\beta\beta\beta\alpha\rangle+|\beta\beta\alpha\beta\rangle+|\beta\alpha\beta\beta\rangle+|\alpha\beta\beta\beta\rangle],$$

$$|\beta\beta\beta\beta\rangle$$

belong to the irreducible representation A. Therefore, the $J=0$ rotational state having the A representation in T is combined with $I=2\,(A)$ spin states, the $J=1$ rotational states having the F representation are combined with $I=1\,(F)$ spin states, and the $J=2$ rotational states having the E and F representations are combined with $I=0\,(E)$ and $I=1\,(F)$ spin states, respectively.

The same coupling between rotation and nuclear spin wave functions is required also for a CH_4 molecule in a crystal, since the symmetry of space does not affect on the symmetry of the permutation of nuclei within a molecule. In Table II, the representation of the rotational wave function and the coupled nuclear spin state are listed for $J=0$, 1, and 2 levels of the ground vibrational state. The first, second, and third columns show the total rotational angular momentum J, the representation of the rotational wave function in the extended group G,[15] and the total nuclear spin angular momentum I, respectively. The $J=0$ rotational state is combined with $I=2$ spin states, the $J=1$ rotational states are combined with $I=1$ spin states, and the $J=2$ rotational states are combined with either $I=0$ or $I=1$ spin states. The fourth column shows the statistical weight of each level.[20]

TABLE II. Energies and Boltzmann distribution of the vibrational ground state of CH_4 in parahydrogen crystals.

J	$\Gamma^{a}_{\rm rot}$	I	Statistical weight	Term value[b], cm^{-1}	Equilibrium distribution at 5 K	
					without NSC[c]	after NSC[d]
2	$E\overline{E}$	0	4	36.448	0.0	0.0
2	$E\overline{F_2}$	1	6	31.426	0.0	0.0
2	$A_1\overline{E}$	0	2	29.527	0.01	0.0
2	$E\overline{F_2}$	1	6	28.828	0.0	0.0
2	$A_1\overline{F_2}$	1	3	27.789	0.0	0.0
2	$E\overline{E}$	0	4	23.501	0.12	0.0
1	$A_2\overline{F_1}$	1	3	9.485	0.16	0.03
1	$E\overline{F_2}$	1	6	8.815	0.40	0.08
0	$A_1\overline{A_1}$	2	5	0.000	0.31	0.89

[a] Representation of the rotational wave function in the extended group $G={}'D'_{3h}\otimes\overline{{}'G'_{24}}$ (See Ref. 15).
[b] Calculated with the molecular parameters obtained in Ref. 15.
[c] Population of each rotational level at 4.8 K if the nuclear spin conversion is completely forbidden. The ratio of the A, F, and E nuclear spin states is assumed to be 5:9:2 at room temperature.[22]
[d] Population of each rotational level at 4.8 K without the nuclear spin modification.

The fifth column of Table II shows the energies of the ground vibrational state of CH_4 in parahydrogen crystals, calculated using the previously determined parameters $B=4.793\,cm^{-1}$ and $\varepsilon_{3c}=-25.8\,cm^{-1}$. Together with the statistical weight in the fourth column, the population of each state at any temperature can be calculated. The equilibrium distribution at 4.8 K with and without the nuclear spin conversion is given in the sixth and seventh columns of Table II. Without the nuclear spin modification, the equilibrium Boltzmann distribution of the ground rotational levels at 4.8 K has to be 0.89, 0.08, and 0.03 for the $J=0$ level, $J=1$, $M=1$ level, and $J=1$, $M=0$ level, respectively. However, as is seen in Fig. 1, the spectral intensity of $P(1)$, $Q(1)$, and $R(1)$, all of which are transitions from the $J=1$ levels, are apparently stronger than the intensity predicted from the equilibrium distribution given in the seventh column in Table II. This indicates that there is an appreciable population of the $J=1$ levels just after the crystal growth, contrary to the 4.8 K Boltzmann distribution. The non-Boltzmann distribution is due to the nuclear spin modification.

It should be noted that no absorption from the $J=2$ rotational states was observed at any time, as is seen in Fig. 2, although the lowest rotational state coupled with the $I=0$ nuclear spin state is the $J=2$ state. There has to be an appreciable population in the $J=2$ levels just after the cooling

of the temperature of CH_4, as is seen in Table II,[22] but we have never observed transitions from the $J=2$ levels. The absence of the $J=2$ population may be explained by fast relaxation from the $J=2$ levels to $J=1$. The $J=2$ rotational state is coupled not only with the $I=0$ nuclear spin state but also with the $I=1$ nuclear spin states. Due to the proximity between the $I=0$ and $I=1$ in the $J=2$ level, the nuclear spin–rotation interaction could yield mixing between the $I=0$ and $I=1$ nuclear spin states, which results in the fast relaxation from the $J=2$ to $J=1$ rotational states. The relaxation might be too fast to observe on our experimental time scale. In the following, we consider only the conversion from the $J=1$ levels to $J=0$.

In order to discuss the nuclear spin conversion process quantitatively, we define the mole fraction of the $J=0$ state as

$$c(t)=[J=0]_t/([J=0]_t+[J=1]_t) \tag{2}$$

where $[J=0]_t$ represents the concentration of $J=0$ molecules at time t. The mole fraction is related to the integrated absorption intensities as

$$c(t)=I[R(0)]_t/(I[R(0)]_t+AI[Q(1)]_t) \tag{3}$$

where $I[R(0)]_t$ and $I[Q(1)]_t$ are the integrated intensities of the $R(0)$ and $Q(1)$ transitions, respectively, and A is a constant which is equal to the ratio of the transition probabilities of $R(0)$ and $Q(1)$. Although we do not know the transition probability exactly, we can estimate it by the fact that the sum of $[J=0]_t+[J=1]_t$, which is proportional to $I[R(0)]_t+AI[Q(1)]_t$, should be constant at all times. We found that the value of $A=2.9$ gives approximately constant values of $I[R(0)]_t+AI[Q(1)]_t$ as is seen in the fifth column of Table I. We therefore assume here that the $R(0)$ transition is 2.9 times stronger than the $Q(1)$ transition for the ν_3 mode of CH_4 in parahydrogen crystals. With the assumption of $A=2.9$, the mole fraction at any given time is obtained as shown in the last column of Table I.

The change of the mole fraction with time is plotted in Fig. 3 for different orthohydrogen concentrations. If we treat the time-dependent change of the methane absorption spectra with first-order kinetics, the time dependence of the mole fraction $c(t)$ may be written as

$$c(t)=[c(0)-c(\infty)]\exp(-kt)+c(\infty), \tag{4}$$

where k is the sum of the $J=1\rightarrow J=0$ rate and the $J=1\leftarrow J=0$ rate. In Fig. 3 the best-fit functions of the form of Eq. (4) are also drawn for each concentration. Here the value of $c(\infty)=0.89$, given in Table II as the equilibrium distribution, was assumed for the samples with low orthohydrogen concentration ($\leqslant$10%). For higher orthohydrogen concentration ($\geqslant$10%), we treated the $c(\infty)$ as a parameter of the fitting.[49] The conversion rate k defined in Eq. (4) obtained from the least-squares fitting method are plotted in Fig. 4 as a function of the orthohydrogen concentration.

The first-order kinetics in Eq. (4) gives acceptable agreement with all the experimental time dependence, as is seen in Fig. 3. This indicates that the simple first-order kinetics is appropriate for the nuclear spin conversion of methane in parahydrogen crystals.

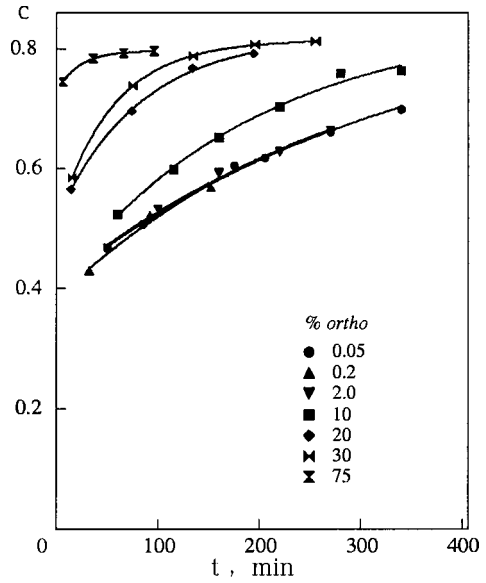

FIG. 3. The time-dependent behavior of $J=0$ methane molecules at various orthohydrogen concentrations. The solid lines are the theoretical curves of Eq. (4).

It is seen in Figs. 3 and 4 that the conversion rate is unchanged by the addition of up to 2% orthohydrogen but increases with more than 10% orthohydrogen. The fact that the conversion rate increases with increasing orthohydrogen concentration indicates that the nuclear spin conversion is enhanced in the presence of orthohydrogen molecules. Since the orthohydrogen has a magnetic moment,[38] the magnetic field from the orthohydrogen enforces the forbidden spin relaxation from $I=1$ to $I=2$.

In order to obtain a qualitative picture of the effect of orthohydrogen concentration on the spin conversion rate, it is necessary to know the number and distances of orthohydrogen molecules from a methane molecule. Here we approximate the number of orthohydrogen molecules on the assumption of a homogeneous distribution of orthohydrogen and methane molecules in the crystal. If we assume that the crys-

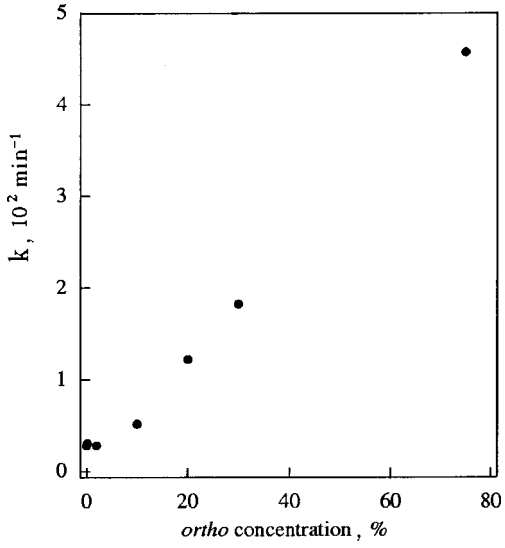

FIG. 4. Dependence of the conversion rate upon orthohydrogen concentration. To obtain the conversion rate, the first-order kinetics of Eq. (4) was assumed.

tal is a hexagonal close-packed structure whose nearest-neighbor distance is 3.783 Å, it is roughly obtained that the average distances between methane and orthohydrogen molecules are 9.8 Å, 7.2 Å, and 6.2 Å for concentrations of 1, 2, and 5%, respectively. On the other hand, one orthohydrogen molecule always exists next to methane in the case of 8%, and two or more orthohydrogen molecules exist next to methane for more than 16%.

The fact that the conversion rate is unchanged below 2% indicates that the magnetic field of orthohydrogen is only effective when the orthohydrogen is next to methane. The basic interaction which causes nuclear spin conversion is the intermolecular magnetic dipole–dipole interaction between protons, which has been discussed by Wigner for the case of gas phase H_2 spin conversion,[50] by Motizuki and Nagamiya for H_2 spin conversion in solid hydrogen[51], and by Nijman and Berlinsky for CH_4 conversion in solid methane.[52] The distance dependence of the conversion rate in the condensed phase caused by the intermolecular magnetic dipole–dipole interaction has been found to be R^{-8} or higher.[51,52] Therefore, it is reasonable to consider that the conversion by orthohydrogen is applicable only for nearest neighbors in our case. Consequently, we can conclude that the increase of the conversion rate of above 10% orthohydrogen is caused by the magnetic dipole–dipole interaction between methane and the nearest-neighbor orthohydrogen molecule(s), while the conversion at lower concentrations is caused by other mechanisms.

The mechanisms of the conversion at lower orthohydrogen concentrations are not yet clear. One possibility is the conversion caused by a strong paramagnetic impurity of O_2 molecules. Evidently, trace O_2 could not be eliminated in our sample. We guess that the concentration of O_2 molecules in our crystal is 10^{-8} or less. In order to clarify the role of O_2 impurity, the oxygen concentration dependence of the conversion rate has to be observed. However, we would like to note that the observed conversion rate of $3\times10^{-3}\,\mathrm{min}^{-1}$ at low orthohydrogen concentration is one-half of the conversion rate of CH_4 in solid Ar matrix which is $6\times10^{-3}\,\mathrm{min}^{-1}$ (Ref. 36). The observed $6\times10^{-3}\,\mathrm{min}^{-1}$ rate has been interpreted as due to the spin–spin interaction within the molecule.[36] Therefore, we believe that the conversion rate of $3\times10^{-3}\,\mathrm{min}^{-1}$ in solid parahydrogen is likely to be caused by mechanisms other than an impurity of O_2 molecules.

The data presented in this article are still preliminary. Further experiments are indispensable for a quantitative discussion on the mechanisms of the nuclear spin conversion of CH_4. Since the rotational energy levels of methane in parahydrogen crystals are completely determined, we will be able to discuss not only the basic mechanisms of the conversion, but also more finer details such as rotational M-sublevel dependence of the conversion. Since the parahydrogen crystal has been characterized much better than any other crystal, the observed nuclear spin conversion may play a priming role for a deeper understanding of the nuclear spin conversion processes in the condensed phase.

The research herein was supported in part by the Grants-in-Aid for Scientific Research of the Ministry of Education, Science, Culture, and Sports of Japan.

*Email: momose@kuchem.kyoto-u.ac.jp

[1] M. E. Jacox, J. Phys. Chem. Ref. Data **27**, 115 (1998).
[2] V. E. Bondybey and V. A. Apkarian, Chem. Phys. **189**, 137 (1994).
[3] G. N. Lewis, D. Lipkin, and T. T. Magel, J. Am. Ceram. Soc. **63**, 3005 (1941).
[4] E. Whittle, D. A. Dows, and G. C. Pimentel, J. Chem. Phys. **22**, 1943 (1954).
[5] M. Okumura, M.-C. Chan, and T. Oka, Phys. Rev. Lett. **62**, 32 (1989).
[6] T. Momose, D. P. Weliky, and T. Oka, J. Mol. Spectrosc. **153**, 760 (1992).
[7] T. Oka, Annu. Rev. Phys. Chem. **44**, 299 (1993).
[8] D. P. Weliky, K. E. Kerr, T. J. Byers, Y. Zhang, T. Momose, and T. Oka, J. Chem. Phys. **105**, 4461 (1996).
[9] Y. Zhang, T. J. Byers, M.-C. Chan, T. Momose, K. E. Kerr, D. P. Weliky, and T. Oka, Phys. Rev. B **68**, 218 (1998).
[10] M.-C. Chan, *Ph.D. Thesis*, The University of Chicago (1991).
[11] T. Momose and T. Shida, Bull. Chem. Soc. Jpn. **71**, 1 (1998).
[12] M. E. Fajardo and S. Tam, J. Chem. Phys. **108**, 4237 (1998).
[13] S. Tam and M. E. Fajardo, Rev. Sci. Instrum. **70**, 1926 (1999).
[14] H. Katsuki and T. Momose, Phys. Rev. Lett. **84**, 3286 (2000).
[15] T. Momose, J. Chem. Phys. **107**, 7695 (1997).
[16] T. Momose, M. Miki, T. Wakabayashi, T. Shida, M.-C. Chan, S. S. Lee, and T. Oka, J. Chem. Phys. **107**, 7707 (1997).
[17] T. Momose, H. Katsuki, H. Hoshina, N. Sogoshi, T. Wakabayashi, and T. Shida, J. Chem. Phys. **107**, 7717 (1997).
[18] H. Hoshina, T. Wakabayashi, T. Momose, and T. Shida, J. Chem. Phys. **110**, 5728 (1999).
[19] S. Tam and M. E. Fajardo, H. Katsuki, H. Hoshina, T. Wakabayashi, and T. Memose, J. Chem. Phys. **111**, 4191 (1999).
[20] E. B. Wilson Jr., J. Chem. Phys. **3**, 276 (1935).
[21] A. W. Maue, Ann. Phys. (Leipzig) **20**, 555 (1937).
[22] M. Hepp, G. Winnewisser, and K. M. T. Yamada, J. Mol. Spectrosc. **164**, 311 (1994).
[23] R. F. Curl Jr., J. V. V. Kasper, and K. S. Pitzer, J. Chem. Phys. **46**, 3220 (1966).
[24] P.-N. Yi, I. Ozier, and C. H. Anderson, Phys. Rev. **165**, 92 (1968).
[25] I. Ozier, P.-N. Yi, A. Khosla, and N. F. Ramsay, Phys. Rev. Lett. **24**, 642 (1970).
[26] R. P. Wolf and W. M. Whitney, *Low Temperature Physics*, J. G. Daunt *et al.* (Eds.) (Plenum Press, Inc., New York, 1965).
[27] H. P. Hopkins Jr., P. L. Donoho, and K. S. Pitzer, J. Chem. Phys. **47**, 864 (1967).
[28] K. P. Wong, J. D. Noble, M. Bloom, and S. Alexander, J. Magn. Reson. **1**, 55 (1969).
[29] P. van Hecke and L. van Gerven, Physica (Amsterdam) **68**, 359 (1973).
[30] G. J. Vogt and K. S. Pitzer, J. Chem. Thermodyn. **8**, 1011 (1976).
[31] J. E. Piott and W. D. McCormick, Can. J. Phys. **54**, 1784 (1976); *ibid.* **54**, 1799 (1976).
[32] K. J. Lushington and J. A. Morrison, Can. J. Phys. **55**, 1580 (1977).
[33] J. Higinbotham, B. M. Wood, and R. F. Code, Phys. Lett. A **66**, 237 (1978).
[34] S. Buchman, D. Candela, W. T. Vetterling, and R. V. Pound, Phys. Rev. B **26**, 1459 (1982).
[35] F. H. Frayer and G. E. Ewing, J. Chem. Phys. **46**, 1994 (1967).
[36] F. H. Frayer and G. E. Ewing, J. Chem. Phys. **48**, 781 (1968).
[37] G. Herzberg, *Molecular Spectra and Molecular Structure, Vol. I, Spectra of Diatomic Molecules*, Krieger Publishing Co., Malabar, Florida (1989).
[38] J. van Kranendonk, *Solid Hydrogen. Theory of the Properties of Solid* H_2, HD, and D_2 (Plenum Press, Inc., New York, 1983).
[39] T. Miyazaki, K. Yamamoto, and J. Arai, Chem. Phys. Lett. **219**, 405 (1994).
[40] M. E. Fajardo, S. Tam, T. L. Thompson, and M. E. Cordonnier, Chem. Phys. **189**, 351 (1994).
[41] P. C. Souers, *Hydrogen Properties for Fusion Energy*, University of California Press, Berkeley (1986).
[42] L. Pauling, Phys. Rev. **36**, 430 (1930).
[43] E. P. Wigner, *Group Theory*, Academic Press, New York (1959).
[44] J. T. Hougen, *International Review of Science Physical Chemistry*, Vol. 3, Ser. 2, Spectroscopy, p. 75, D. A. Ramsay (Ed.), Butterworths, London (1976).
[45] R. E. Miller and J. C. Decius, J. Chem. Phys. **59**, 4871 (1973).
[46] R. L. Redington and D. E. Milligan, J. Chem. Phys. **37**, 2162 (1962).
[47] R. L. Redington and D. E. Milligan, J. Chem. Phys. **39**, 1276 (1963).

[48] T. Momose and T. Oka (in preparation).
[49] Since the interaction between orthohydrogen and methane is much stronger than that between parahydrogen and methane, molecular parameters of methane with orthohydrogen next to it could be different from those of methane surrounded by only parahydrogen molecules. Therefore, the equilibrium value $c(\infty)$ is not necessarily be equal to 0.89 for higher orthohydrogen concentration. The $c(\infty)$ values determined by the least-squares fitting were 0.85 (10%), 0.82 (20%), 0.81 (30%), and 0.80 (75%).
[50] E. Wigner, Z. Phys. Chem. Abt. B **23**, 28 (1933).
[51] K. Motizuki and T. Nagamiya, J. Phys. Soc. Jpn. **11**, 93 (1956).
[52] A. J. Nijman and A. J. Berlinsky, Can. J. Phys. **58**, 1049 (1980).

This article was published in English in the original Russian journal. Reproduced here with stylistic changes by the Translation Consultant.

Atomic oxygen in solid deuterium

A. V. Danilychev and V. A. Apkarian*

Department of Chemistry, University of California, Irvine, California 92697-2025

H. Kajihara, S. Tanaka, and S. Koda

Department of Chemical System Engineering, Faculty of Engineering, the University of Tokyo, Hongo 7-3-1, Bunkyo-ku, Tokyo 113, Japan

(Submitted June 8, 2000)
Fiz. Nizk. Temp. **26**, 909–917 (September–October 2000)

Atomic oxygen is photogenerated in solid D_2 by 193 nm irradiation of samples initially doped with molecular oxygen. The atoms are detected by laser-induced fluorescence at the $O(^1S \rightarrow {}^1D)$ transition, which occurs at 559 nm, with a fluorescence lifetime of 230 μs. The absorption leading to this emission is indirect, attributed to $O_2(X):O(^3P)$ pairs. Complementary studies are carried in solid D_2 co-doped with Xe and O_2, in which, in addition to ionic XeO centers, the atomic $O(^1S \rightarrow {}^1D)$ transition with a radiative lifetime of 50 μs is observed. The photogeneration of the atomic centers and the stability of the atomic and molecular emissions are sensitive to sample preparation and thermal and irradiation histories. In annealed solids at temperatures below 6.5 K the atomic emission does not bleach, implying that the vertically prepared $O(^1D)$ atoms undergo intersystem crossing to form $O(^3P)$ rather than react with D_2. The barrier to insertion on the $O(^1D)+D_2$ potential energy surface in solid D_2 is explained as a many-body polarization effect. The recombination of $O(^3P)$ atoms can be initiated thermally and can be monitored by their thermoluminescence at the molecular $O_2(A' \rightarrow X)$ transition. The thermal onset of recombination varies between 5.5 K and 9 K, depending on the sample preparation method. In all cases, the thermally induced recombination is catastrophic, accompanied by thermal runaway, pressure burst, and material loss. This is interpreted as an indication that the process is initiated by self-diffusion of the host, consistent with the notion that atomic O centers stabilize the host lattice. © *2000 American Institute of Physics.* [S1063-777X(00)00709-X]

1. INTRODUCTION

Oxygen-doped solid hydrogen and its isotopes provide an opportunity for the study of photophysics and -chemistry in quantum hosts. In addition to fundamental motivations, solid hydrogen doped with atomic oxygen is a prototype of a mono-propellant, which, with optimized dopant concentration, could have a significantly enhanced specific impulse over the standard liquid oxygen/hydrogen mix presently used as rocket fuel.[1] The present study was motivated by the absence of the rudimentary data required to assess the possibility of this concept.[2] Our experimental studies show the stability of atomic oxygen with respect to diffusion, and, more significantly, we uncover the non-reactivity of both ground-state and electronically excited atomic oxygen with the D_2 host. Reports of these findings have appeared as conference proceedings[3] and in a thesis.[4] Here, we collect some of the more important observations, which have served as the basis for theoretical analyses that have already been published.[5,6]

The experimental plan is based on our prior studies of atomic and molecular oxygen in rare gas solids.[7–9] The *in situ* photogeneration of atomic oxygen, by ArF laser irradiation of O_2-doped solid hydrogen at 193 nm, is the proposed starting point. Note that, although this radiation provides an energy 1.3 eV in excess of the dissociation limit of the molecule, the strong cage effect in rare gas solids prevents dissociation of the molecule, and the recombinant emission over the various electronic states that correlate with $O(^3P)+O(^3P)$ is observed.[10,11] Due to the light mass and week forces in the hydrogen quantum solid, we would expect significantly reduced stopping power of the host. Whether O_2 will undergo facile photodissociation under 193 nm irradiation in solid hydrogen is the first question of interest. Quite clearly, in addition to the different kinematics of quantum versus classical solids, now reactive channels for the formation of OH and H_2O are open to the photodissociation of O_2. The laser induced fluorescence (LIF) probes used in our experiments give no evidence as to the presence of these reactive channels; we only detect molecular and atomic oxygen, and in both cases only a fraction of the population is detected. We have previously reported on the spectroscopy of molecular O_2 isolated in solid hydrogen and deuterium.[12] We rely on the orbitally forbidden $A'(^3\Delta_u)-X(^3\Sigma_g^-)$ transition, known as the Herzberg III band,[13] as the laser-induced fluorescence probe of the isolated molecules. This transition gains its intensity by matrix-induced mixing between $O_2(A')$ and the nearby repulsive $O_2(^3\Pi)$ state. Based on the symmetry requirements for the mixing, we have argued that only molecules isolated in fcc sites and oriented along the [111] axis of the unit cell are observable. Only a fraction of the molecules are observable in solid D_2, and none are detectable in solid H_2, although the presence of the isolated molecules could be verified there by thermal cycling of solids

over-coated with a film of Xe. It was inferred that in solid H_2 the guest O_2 molecules are exclusively isolated in hcp sites. This consideration is the main reason for carrying out the present studies in solid D_2, in which metastable fcc sites can be produced via thermal cycling. In rare gas solids both atomic and molecular oxygen can be monitored through fluorescence induced by laser irradiation at 193 nm. The same applies in solid D_2, although, as will be argued, this non-resonant probe is also limited to detection of special sites. Nevertheless, the availability of a method of monitoring O atoms, via its $O(^1S \rightarrow {}^1D)$ emission, allows verification of its photogeneration and permits drawing direct conclusions with regard to chemical stability and thermally induced recombination. As will be discussed, we find the concept of an atomic impurity diffusing through the solid lattice to be misguided. The more surprising result is the absence of chemistry on the $O(^1D) + H_2$ potential energy surface, which in gas phase binary collisions would lead to formation of OH+H (Ref. 14), but in the presence of a third body should form H_2O. According to the most refined potential energy surfaces the gas phase reaction is barrier-free.[15] To ensure that the solid state observations of non-reactivity were not a peculiarity of the special sites probed, we carry out measurements in solid D_2 co-doped with O_2 and Xe, in which Xe acts as a sensitive detector of atomic oxygen in its various electronic states.[16] These studies more definitively confirm the chemical stability of $O(^1D)$ in solid D_2. This unexpected result could not be rationalized in molecular dynamics calculations using refined, non-additive, but covalent pair potentials.[6] However, the more recent theoretical treatment, using the diatomics-in-molecules approach, which takes into account the ionicity of interactions, succeeds in providing a rationale for the many-body origin of the reaction barrier.[17] Here we provide the experimental data that has inspired these theoretical developments.

2. EXPERIMENTAL

We prepare the doped films by spray-deposition of premixed gaseous samples on an oxygen-free copper substrate, mounted on the cryotip of a He flow-cryostat (see schematic in Fig. 1). The cryostat is contained in an all-stainless-steel, ultrahigh-vacuum shroud fitted with metal-sealed MgF_2 and sapphire windows. A silicon diode of ± 0.05 K accuracy (Lakeshore Cryotronics) mounted on the back of the copper substrate, is used for temperature measurements. The shroud is evacuated with a turbomolecular pump to a base pressure below 10^{-8} Torr at room temperature. The samples are deposited at temperatures ranging from 3.8 K to 5.5 K, with film growth rates ranging from 1.6 μm/min to 3.6 μm/min. The sample thickness is measured during deposition by monitoring interference fringes from a reflected He: Ne laser. Typical film thicknesses vary from 50 to 100 μm. The films are transparent to the eye.

Emission from the sample is recorded using either an optical multichannel analyzer (Princeton Applied Research OMA3) equipped with a 0.25-m polychromator, or using a photomultiplier (Hamamatsu R-666) after dispersing the radiation through a 0.75-m monochromator (Spex). A digitizing/averaging scope (Tektronics 2430) is used to record transients, which are then transferred to a personal computer for further data analysis. The same computer is also interfaced to the temperature sensor/controller and the time delay generator used to synchronize the lasers.

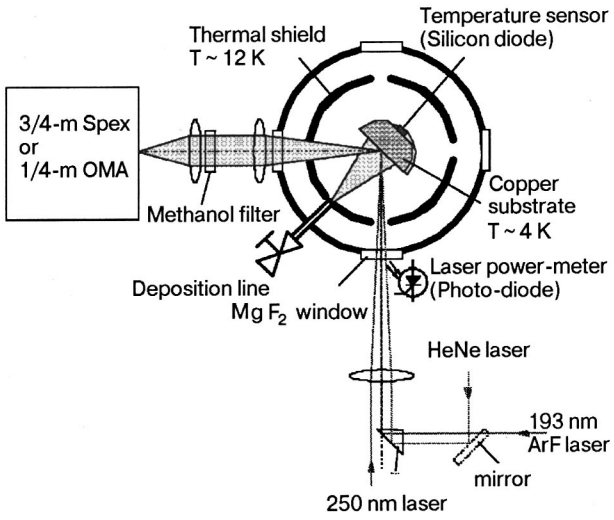

FIG. 1. Experimental setup. The He flow cryostat is adapted for simultaneous monitoring of fluorescence induced by the 193 nm laser and the doubled dye laser from the same interrogation volume. The temperature of the cryotip is monitored with a Si diode, the output of which is read out by the computer, along with the fluorescence and thermoluminescence data. The He:Ne laser is used to monitor thickness of the growing film; otherwise the films are invisible to the eye.

As excitation source, the doubled output of an excimer-pumped dye laser and/or the direct output of an ArF laser operating at 193 nm is used. In many of the experiments the two lasers are synchronized to correlate resonantly induced fluorescence from the molecules with the 193-nm-induced chemistry and fluorescence of atomic and molecular oxygen.

3. RESULTS

3.1. O_2-doped solid D_2

The majority of experiments were performed in oxygen-doped solid deuterium samples with a gas mix composition of 1:500. Excitation of O_2/D_2 samples at 193 nm leads to emission on both molecular $O_2(A'^3\Delta_u \rightarrow X^3\Sigma_g)$ and atomic $O(^1S \rightarrow {}^1D)$ transitions, as shown in Fig. 2a. The fluorescence lifetime of the molecular emission is 5.4 μs, while that of the atomic emission at 559 nm is 230 μs (measured at 4 K). In addition to this LIF scheme, the photogeneration of O atoms can be verified through their thermoluminescence (TL). The thermally driven recombination of atoms, $O(^3P) + O(^3P)$, produces the same $A' \rightarrow X$ spectrum, as shown in Fig. 2b. The same emission spectrum is obtained through resonant $A' \leftarrow X$ excitation of the molecule, as previously described in some detail.[12] Note that the fluorescence yield of the resonant excitation depends on structural changes of the solid, since it probes only a sub-ensemble of molecules in fcc sites. Also, the 193-nm-induced molecular emission is contingent upon cage-induced recombination of the atoms and is therefore not a direct probe of the molecular concentration. Further, the excitation resonance responsible for the 193-nm-induced atomic emission is not clear. We can establish that the atomic emission arises from a broad structureless absorption. This is illustrated in Fig. 3 and contrasted

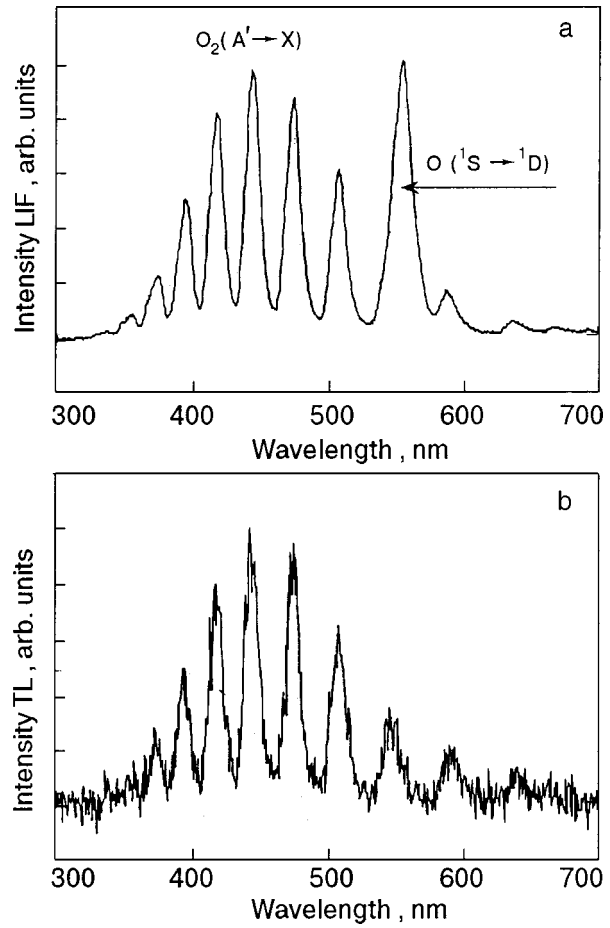

FIG. 2. Laser induced fluorescence (a) and thermoluminescence (b) from O_2 doped D_2 solids irradiated at 193 nm. The atomic $O(^1S \rightarrow {}^1D)$ emission, at 559 nm, appears in the laser induced fluorescence spectrum in (a).

with the sharp molecular resonances in the same spectral range. A search for direct access of the emitting atomic state, via the forbidden $^1S \leftarrow {}^3P$ transition near 297 nm, failed. Thus, the 193 nm probe of the O atoms is also indirect and, as will be shown below, not a quantitative probe of the atom concentration in the solid.

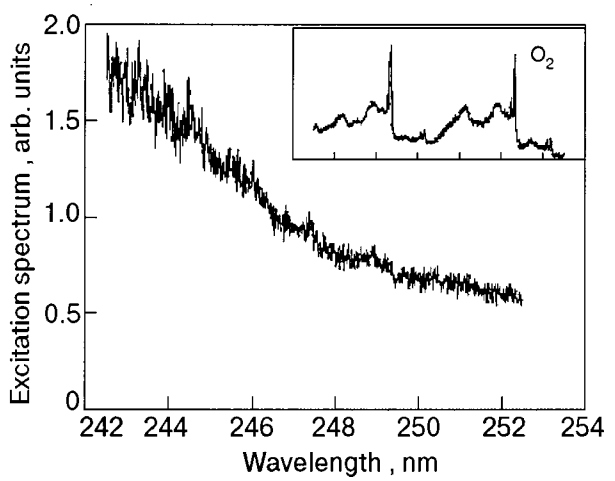

FIG. 3. Excitation profile of the atomic $O(^1S \rightarrow {}^1D)$ emission. In the inset, the excitation spectrum for the molecular $O_2(A' \rightarrow X)$ emission is shown.

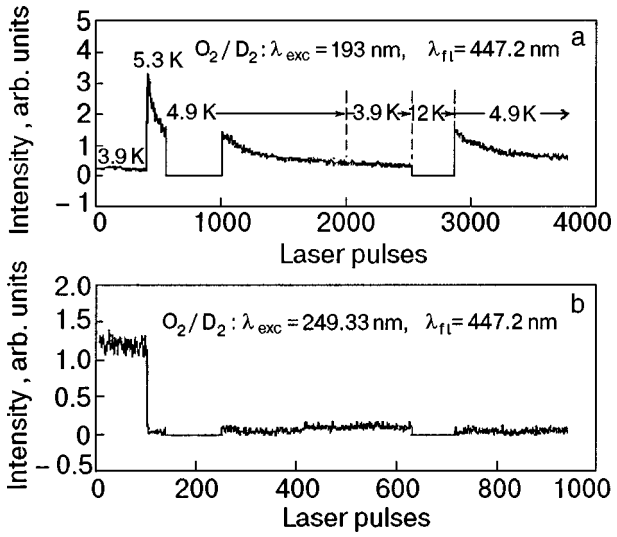

FIG. 4. Thermal and irradiation histories of molecular laser induced fluorescence in a quench-condensed solid. The sample, 0.2% O_2 in solid D_2, was deposited at 3.8 K. The temperature is varied during irradiation, and its history is indicated in (a). The flat regions centered at 200 and 700 pulses of the 249 nm laser correspond to periods where the laser beams were blocked off.

To correlate the thermal and irradiation histories of the atomic and molecular fluorescence, we simultaneously monitor LIF from the 193 nm laser and the doubled dye laser. The latter is tuned to the molecular $A'(v'=8) \leftarrow X(v''=0)$ resonance at 249.33 nm, the lasers are delayed by 1 ms relative to each other, and the fluorescence is gate-detected to distinguish the various contributions. Figures 4 and 5 illustrate typical histories in ''quench''-condensed samples, prepared by slow deposition at 3.8 K, the lowest temperature of the cryostat. The data illustrate that:

a) In the freshly deposited samples, at 3.9 K, 193 nm irradiation does not cause a measurable change in either the resonantly induced O_2 emission (Fig. 4), or in the 193 nm induced atomic and molecular emissions (Fig. 5).

b) Upon warming the sample to 5.5 K with continued irradiation, a sudden, tenfold growth in the 193-nm-induced molecular and atomic emissions are observed. This is accompanied by a sudden 90% loss of the resonantly induced molecular emission. This sudden transition suggests gross structural change in the lattice. With continued irradiation, the 193-nm-induced emission decays in time, while the resonantly induced emission does not recover. Clearly, the O_2 molecules probed by the two different lasers belong to two different ensembles. The 193-nm-induced the emission intensity remains constant decay is verified to be laser aided, by noting that when the irradiation is interrupted. The level to which the emission decays is temperature dependent. When the temperature is lowered to 4 K, the emissions subside to pre-warmup level.

c) The resonantly induced molecular emission does not respond when the warm-up cycle is repeated (Fig. 4). The 193-nm-induced molecular emission repeats its behavior (Fig. 5b), and the atomic emission does not fully regenerate in subsequent cycles (Fig. 5a).

d) Note the thermal runaway at 5.3 K, as evidenced by the temperature spikes in Fig. 5c. They repeat at the same

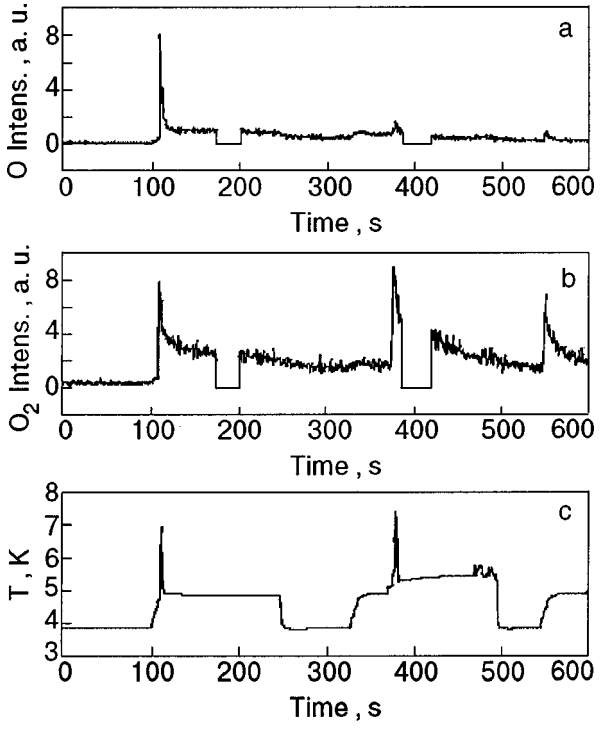

FIG. 5. Thermal and irradiation histories of 193-nm-induced atomic (a) and molecular (b) fluorescence in the quench-condensed solid (0.2% O_2 in solid D_2). The thermal runaway spike is associated with gross change in the morphology due to phase transition of islands in the solid (c).

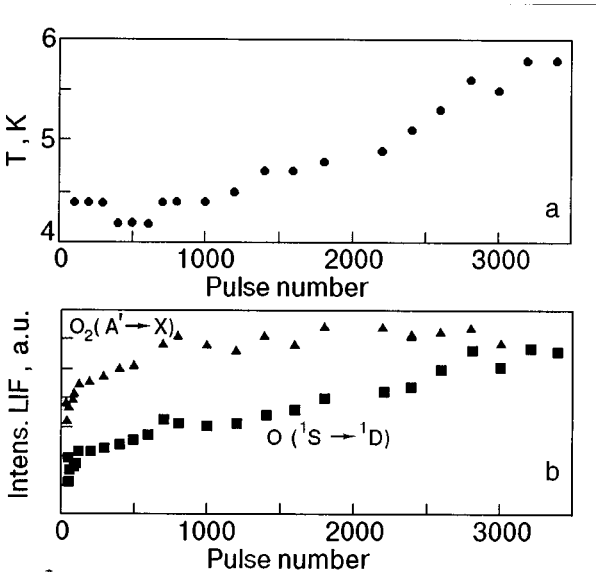

FIG. 6. Thermal (a) and irradiation (b) history of an O_2:D_2 sample deposited at 5 K and annealed at 9 K prior to irradiation. The data points are the 193-nm-induced fluorescence from O and O_2 as a function of the number of laser pulses.

temperature and are clearly independent of the atom content of the solid. This behavior is consistent with the known reversible, hysteretic phase transition of quench-condensed solid deuterium.[18] The initial 90% drop in the resonantly induced molecular fluorescence can therefore be understood as due to an fcc-to-hcp phase transition in crystallites. The transition evidently generates sites in which the 193-nm-induced O_2 fluorescence is observed.

A substantively different behavior is observed in samples deposited at higher temperature, between 4.5 K and 5.5 K. An example is shown in Fig. 6 for a sample deposited at 5 K, annealed at 9 K, then slowly cooled to 4.4 K to start the radiation process. A correlated growth of both atomic and molecular fluorescence is observed upon 193 nm irradiation at 4.4 K. As the temperature is increased to 6 K with continued irradiation, both atomic and molecular emissions grow. As long as the temperature is held constant, these emissions remain stable at this level.

In principle, glow curves obtained by a programmed temperature ramp should enable the characterization of diffusion and recombination kinetics of atoms. This method has previously been implemented successfully for atomic oxygen in rare gas solids.[8] We have failed to obtain any meaningful glow curves in solid D_2. The recombination occurs suddenly, leading to a flash that lasts only ~ 10 μs. The flash is always accompanied by a temperature and pressure surge, similar to the laser-induced fluorescence spikes shown in Fig. 5. The temperature at which the catastrophic recombination occurs depends on the gross sample morphology, determined mainly by sample deposition conditions. In samples prepared by slow deposition at 3.8 K, the recombination occurs between 5.5 K and 7.5 K. In samples deposited at somewhat higher temperatures, 4.5 K–55 K, and at a deposition rate of ~ 3 μm/min, the recombination occurs at a temperature between 7 K and 9 K. In samples which are pre-annealed at 9 K, then cooled to 4 K and irradiated, the TL is observed at temperatures as high as 11 K.

3.2. N_2O-doped solid N_2 and neat solid O_2

Extensive 193 nm irradiation of N_2O doped solid N_2(M/R=1:1000) and neat solid O_2 did not produce any detectable emission from atomic O. Given the fact that N_2O dissociates readily in solid N_2 (Ref. 19), the absence of 193-nm-induced O atom emission supports the notion that the atomic LIF observed in solid D_2 arises from special centers. The absence of 193-nm-induced atomic emission in solid O_2 establishes that the observed emission in solid D_2 is not from clusters of O_2.

3.3. Solid D_2 co-doped with O_2 and Xe

To avoid the uncertainty of LIF detection of O atoms in solid D_2, we carried out a set of studies in ternary solids prepared at a mole ratio of $1{:}5{:}500O_2{:}Xe{:}D_2$. After depositing the samples at 5 K, the O_2 excitation spectra were investigated with the doubled dye laser. The excitation and emission spectra of O_2 are identical to those obtained in the absence of Xe, indicating that only isolated molecules are interrogated in both cases. This is consistent with the fact that the $A' \rightarrow X$ emission is quenched by Xe. Excitation at 193 nm immediately produced a bright emission from XeO centers, as illustrated in Fig. 7. The molecular fluorescence induced at 193 nm, which was the dominant feature in the O_2/D_2 samples (see Fig. 2) is practically absent in the spectrum of Fig. 7. The spectrum now consists entirely of atomic emissions. In the time-integrated spectrum, the $O(^1S \rightarrow {}^1D)$ emission can clearly be identified. While the peak is virtually unshifted at 559 nm, the effect of Xe is to reduce the radiative lifetime to 50 μs (230 μs in D_2). Thus, it may be more

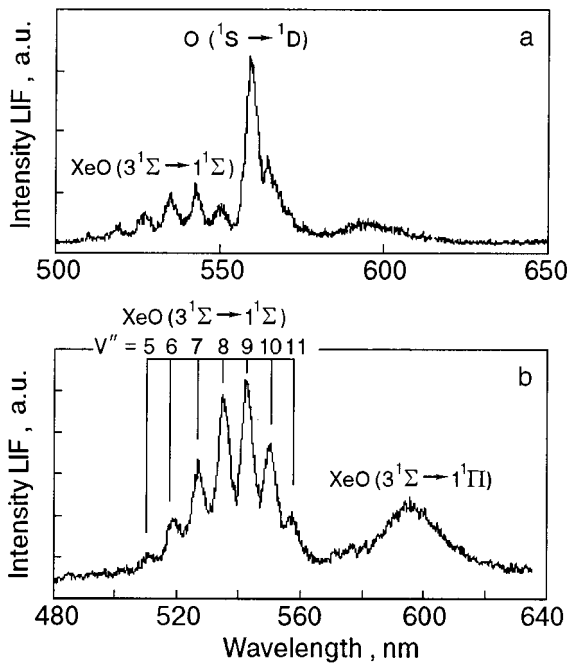

FIG. 7. Fluorescence spectrum obtained with 193 nm irradiation of solid D_2 co-doped with O_2 and Xe(O_2:Xe:D_2=1:5:500). The spectrum (a) is obtained with time integration, the spectrum (b) is obtained with a 100 ns gate. All features in the spectrum (b) have the same lifetime of (130 ± 5) ns, while the atomic oxygen emission (a) has a lifetime of 50 μs.

appropriate to assign this transition to $XeO(2^1\Sigma \rightarrow 1^1\Sigma)$ (Ref. 20). In addition, a vibrational progression centered at 530 nm and a broad band at 590 nm are observed. Both of these emissions have lifetimes of (130 ± 5) ns. Accordingly, they can be separated from the atomic emission by gated detection, as shown in Fig. 7b. With the help of the Xe–O potential energy curves illustrated in Fig. 8, the nature of these emissions can be identified with some confidence.[21] Given that the vibrational progression and the band at 590 nm have the same lifetime, they are likely to originate from the same upper state. Given their short radiative lifetime, they can be confidently assigned to the $Xe^+O^- \rightarrow XeO$ charge transfer transitions. Given that only the $XeO(1^1\Sigma)$ state, which correlates with $O(^1D)+Xe(^1S_0)$, is deep enough to sustain the vibrational progression, the transition can safely be assigned to $Xe^+O^-(3^1\Sigma) \rightarrow XeO(1^1\Sigma)$. This would then suggest that the broad emission at 590 nm is due to $Xe^+O^-(3^1\Sigma) \rightarrow XeO(^1\Pi)$. In both cases the terminal state of the transition correlates with $O(^1D)+Xe(^1S_0)$. The vibrational progression seen here is quite similar to that observed for XeO in solid Ar,[22] and the numbering is simply taken from there.

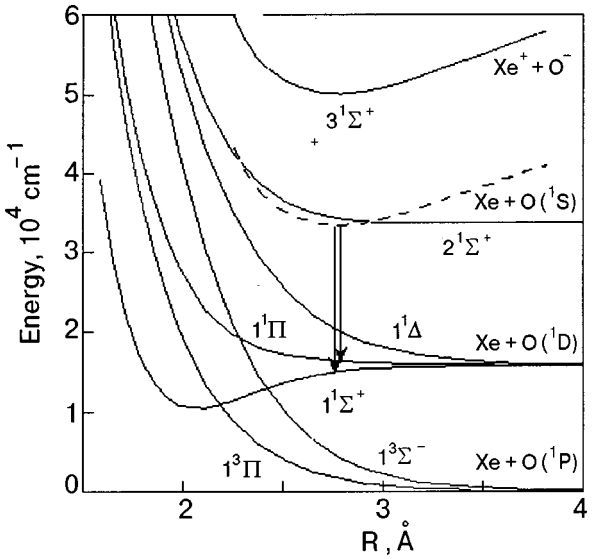

FIG. 8. The gas phase XeO potentials and the required placement of the upper emitting state (dashed line) in the fluorescence spectrum of Fig. 7. Note that a double minimum is implied to arise from the mixing between $3^1\Sigma$ and $2^1\Sigma$ potentials.

We monitored the 193-nm-induced fluorescence of the atomic centers as the samples were warmed up. The emission stays nearly constant up to 12 K, and permanently decays as D_2 starts to evaporate. These samples do not show significant TL, presumably because $O_2(A')$ is quenched by Xe. All recombination must occur at Xe sites as the D_2 evaporates.

4. DISCUSSION

4.1. The non-reactivity of O(^1D)

The interpretation of the experiments in O_2/Xe/D_2 is the most direct with regard to the chemical stability of atomic oxygen in its various electronic states in solid D_2. The observation of the molecular resonant excitation immediately after deposition establishes the presence of isolated molecules. Subsequent irradiation at 193 nm generates the O and XeO emissions without a trace of the molecular spectrum. We may conclude that O_2 can be photodissociated in solid D_2 by 193 nm irradiation. Despite the excess energy of 1.3 eV, the impulsively generated $O(^3P)$ atoms survive in the D_2 host. The absence of any 193-nm-induced recombinant molecular fluorescence is a good indication that the cage is ineffective in solid D_2.

The O atoms scavenged by Xe are interrogated via the XeO charge transfer transitions, which can be assigned with some confidence. They invariably terminate on the $O(^1D)$ + Xe potential energy surface. We can be sure that the O: Xe pair is surrounded by D_2, since in Xe clusters the XeO emissions occur at 740 and 370 nm.[7] The fact that the XeO transitions do not bleach with extended irradiation, establishes that the photogenerated $O(^1D)$ atoms do not react with the host.

It would seem that the proximity of Xe atoms is sufficient to generate a barrier toward the $O(^1D)++D_2$ reaction. This barrier cannot be due to the binding between $O(^1D)$ and Xe, since, at least in the 559 nm transition, which is redshifted from the gas phase value of 557.7 nm, the transition must terminate on the flat part of the interaction potential. The perturbation that may be ascribed to Xe is the change in transition dipole of the atomic $^1S \rightarrow {}^1D$ emission, evidenced by the shortening of the radiative lifetime to 50 μs. The origin of this perturbation is well understood to be due to the ionicity of the $XeO(2^1\Sigma)$, which is derived by mixing with the $Xe^+O^-(3^1\Sigma)$ charge transfer state. Indeed, to rationalize the observed emission spectra of the charge transfer states, we must conclude that due to solvation in the polarizable medium, the $Xe^+O^-(3^1\Sigma)$ and $XeO(2^1\Sigma)$ potentials are strongly mixed. The situation is quite similar to that of XeO

in solid Ar (which has polarizability similar to that of H_2), for which we had suggested the creation of a double minimum due to the crossing of the solvated $Xe^+O^-(3^1\Sigma)$ and $XeO(2^1\Sigma)$ potentials.[7] This is shown schematically in Fig. 8. Note that the double minimum can arise by mixing between the charge transfer and covalent state, rather than the creation of an actual crossing which would require the lowering of the $Xe^+O^-(3^1\Sigma)$ state by $\sim$1.5 eV.[21] The fact that the radiative lifetime of the transition is 130 ns is sufficient to identify the nature of the transition as that of charge transfer, and therefore the upper state as Xe^+O^-. Why would this prevent chemistry on the terminal $O(^1D)+D_2$ surface? We surmise that the partial charge in $Xe^{\delta+}O^{\delta-}$ prevents the formation of the O–H bond, which can only proceed by developing positive charge on the targeted hydrogen molecule. In effect, the partial charge transfer on the $Xe+O(^1D)$ can be thought to create a polarization barrier. This is the essence of the theoretical analysis of O-doped solid H_2 which we consider next.[17]

Consider the $O(^1S\rightarrow{}^1D)$ transition in D_2 in the absence of Xe. Independent of the excitation channel, since this emission does not bleach, we have to conclude that atomic oxygen in all of its electronic states, and in particular in its ^1D state, does not react with the host. This, at first, seems at odds with the well-established fact that the $O(^1D)+H_2$ surface does not contain a reaction barrier. The diatomics in molecules (DIM) calculations of Kunz, in which $O(H_2)_n$ is considered with the explicit inclusion of the ionic manifold of states for the cluster, show the many-body nature of the barrier.[17] The picture is as follows: The $O(^1D)-H_2$ interaction gains its binding character due to its ionicity. When in the middle of an octahedral array of H_2 molecules, the central O atom can mix with the charge transfer states of all neighbors. The insertion coordinate, however, requires the localization of charge on one hydrogen molecule to reach the ionicity of the O–H bond in its H–O–H transition state. The barrier arises as the energy of localization of the excited state charge density, from the 12 nearest neighbors to one molecule. The charge distribution in the excited state is mirrored by the polarization on the ^1D surface. In effect, the polarization barrier centers the O atom in the cubic site and prevents the reaction. In the absence of the many, there is no barrier. To our knowledge, this is the most direct demonstration of a many-body-potential control of chemical dynamics.

4.2. Nonresonant excitation mechanism: $O_2(X):O(^3P)$ centers

Although 193-nm-excitation is used to follow both O and O_2 in solid D_2, the mechanism of this excitation is indirect, preventing quantitative determinations of impurity concentrations and photodissociation yields. The excitation spectrum in Fig. 3 indicates that the atoms are accessed through a broad band that cannot be ascribed to the isolated atom but rather to an M–O adduct, similar to the charge transfer states of Xe–O. Similarly, the observation that the 193-nm-induced molecular emission grows with irradiation time, as seen in Fig. 6, clearly indicates that we are not simply interrogating the molecular concentration. The close correlation of the thermal and irradiation histories of 193-nm-induced O and O_2 emissions suggests a common origin. The most consistent assignment that can be offered is that the absorption is due $O_2(X):O(^3P)$ pairs, distinct from ozone. Since both O and O_2 are present in the sample, O_3 can be formed. However, the excitation wavelengths used, 193 nm-255 nm, do not have the requisite energy to produce $O(^1S)$ from the ground state of ozone, and cannot therefore explain the LIF signal over the $O(^1S\rightarrow{}^1D)$ transition. The main dissociation channel of ozone in this excitation range is the production of $O(^1D)$.[19] As in the case of N_2O and O_3 isolated in rare gas solids, we expect that ozone would undergo facile photodissociation in solid D_2. Even though the magnitude is difficult to obtain with confidence, *ab initio* calculations invariably show an angle dependent potential barrier to formation of O_3 from $O_2(X):O(^3P)$.[23,24] A continuous excitation spectrum, starting near 250 nm, can then be ascribed to absorption over the dense manifold of intermolecular O_2-O potentials, from which branching to $O_2+O(^1S)$ and to $O_2(A')+O$ is to be expected.

The above consideration complicates the interpretation of the 193-nm-driven photodissociation yields of O_2 in solid D_2. The samples containing Xe indicate facile dissociation, accompanied by migration of O atoms to reach the Xe sites. In the absence of Xe we cannot establish photodissociation probabilities or, equivalently, the caging efficiency of the host, since the observed atomic and molecular densities can entirely be attributed to special centers. Indeed, in samples where LIF from the atomic centers is nearly absent, a strong thermoluminescence is observed upon warm-up, indicating that only a fraction of the O atoms are spectroscopically detected. Nevertheless, it is clear that chemistry, namely formation of H_2O, is not a significant channel in the dissociative excitation of O_2.

4.3. Thermally induced recombination

The thermally induced recombination of oxygen atoms in solid D_2 differs fundamentally from what is observed in the classical rare gas solids. There, it is always possible to ramp up the temperature at a rate at which the glow curve can be measured, to extract the diffusion kinetics of impurities in the solid. This is not possible in the solid hydrogens. Instead of a glow curve, we obtain a sudden flash, accompanied by an uncontrollable thermal runaway and pressure surge. In effect, the host diffuses around the impurities. The theoretical analysis of O-doped solid hydrogens gives a useful perspective.[6] Due to the deeper guest–host potential, hydrogen molecules are significantly more localized near the impurity site. In fact, a linear increase in the density of the solid is predicted as a function of concentration of O atoms. In effect, the O atoms are coated with a layer of hydrogen, which is less mobile than the bulk. It would therefore be difficult to imagine the coated impurity diffusing while the host retains its integrity as a solid. The experimental observation is rationalized as the fusion of O centers in a solid undergoing gross structural change due to self-diffusion of the host, with the recombination energy of the guests serving as positive feedback for the thermal runaway.

5. CONCLUSIONS

Atomic oxygen can be photogenerated *in situ* in solid D_2 by photodissociation of molecular oxygen. The atomic centers in such a solid are stable, both chemically and physically. The non-reactivity of $O(^1D)$ with the host is particularly striking, and rationalized to result from a polarization barrier of strictly many-body origin.[17] In pre-annealed samples, the atomically doped solids have been shown to be stable up to $T=11$ K. Indeed, in earlier simulations it had been argued that atomic oxygen stabilizes the host lattice and increases its density.[6] This is indirectly verified in the present, study by recognizing that O atoms recombine only after the host loses its integrity as a solid. Thus this exploratory study seems to resolve some of the more rudimentary issues with regard to the consideration of oxygen-doped solid hydrogen as a propellant. In this regard, the experiments do not provide a reliable estimate of the concentration of atomic centers or the achievable doping levels, considerations crucial to assess specific impulse.

The spectroscopy, photodynamics, and photophysics of impurities in solid hydrogens raise many fascinating questions. A more quantitative study of the very system we have described, for example by combining IR and visible methods, would be quite useful. The present studies remain qualitative with regard to several important questions. With regard to the caging ability of the solid, based on the O_2:Xe:D_2 experiments, we believe it to be small. Based on the thermal and irradiation histories of fluorescence we have postulated the presence of $O_2(X)$:$O(^3P)$ pairs that do not form ozone. Infrared studies could nicely resolve this issue. More generally, solid hydrogen could be used as an ideal nonperturbing medium of weak forces to investigate intermolecular potential energy surfaces.[25] Finally, in the present study the effects of ortho- and parahydrogen have been completely neglected. They need not be invoked to explain any of the observations, and it is believed that due to the paramagnetic nature of the impurities, at the concentrations of impurities used, the solid host is entirely in the ground spin state.

This research was supported through grants from the US AFOSR, S04611-90-K-0035 and F49620-95-1-0213. We thank the Ministry of Education of Japan for support to H.K. and S.T. during their stays in Irvine. The discussions with P. Kuntz, which resulted in his DIM treatment of $O(^1D)$ in H_2, have been quite fruitful. We thank M. Petterson for his critical comments and discussions, and N.T.A. for help with graphics.

*E-mail: aapkaria@uci.edu

[1] P. G. Carrick, *Specific Impulse Calculations of High Energy Density Solid Cryogenic Propellants 1: Atoms in Solid* H_2, report PL-TR-93-3014, of the Propulsion Directorate of the Phillips Laboratory, USAF, (1993).
[2] The same general motivation had earlier resulted in the Broida report *Formation and Trapping of Free Radicals*, edited by A. M. Bass and H. P. Broida (Academic Press, 1960).
[3] V. A. Apkarian, in *Proceedings of the High Energy Density Matter (HEDM) Conferences of the USAF, Woods Hole 1995*; *ibid.*, Z. Li and V. A. Apkarian, Boulder (1996); *ibid.*, V. A. Apkarian, Washington DC (1997).
[4] A. V. Danilychev, *Ph.D. Thesis*, UC Irvine (1994).
[5] M. Sterling, Z. Li, and V. A. Apkarian, J. Chem. Phys. **103**, 5679 (1995); Z. Li and V. A. Apkarian, J. Chem. Phys. **107**, 1544 (1997).
[6] Z. Li, V. A. Apkarian, and L. B. Harding, J. Chem. Phys. **106**, 942 (1997).
[7] W. G. Lawrence and V. A. Apkarian, J. Chem. Phys. **97**, 2229 (1992).
[8] A. V. Danilychev and V. A. Apkarian, J. Chem. Phys. **99**, 8617 (1993).
[9] A. V. Danilychev and V. A. Apkarian, J. Chem. Phys. **100**, 5556 (1994).
[10] A. C. Becker, U. Schurath, H. Dubost, and J. P. Galaup, Chem. Phys. **125**, 321 (1988).
[11] S. Koda and H. Kajihara, Bull. Chem. Soc. Jpn. **70**, 1225 (1997); H. Kajihara, T. Okamura, and S. Koda, Chem. Phys. Lett. **256**, 126 (1996); H. Kajihara, T. Okamura, F. Okada, and S. Koda, Laser Chem. **15**, 83 (1995).
[12] A. V. Danilychev, V. E. Bondybey, V. A. Apkarian, S. Tanaka, H. Kajihara, and S. Koda, J. Chem. Phys. **103**, 4292 (1995).
[13] G. Herzberg, Can. J. Phys. **31**, 657 (1953).
[14] For a most recent study, see: M. Alagia, N. Balucani, L. Cartechini, P. Casavecchia, E. H. vanKleef, G. G. Volpi, P. J. Kuntz, and J. J. Sloan, J. Chem. Phys. **108**, 6698 (1998).
[15] G. C. Schatz, A. Papaioannou, L. A. Pederson, L. B. Harding, T. Hollebeek, T. S. Ho, and H. Rabitz, J. Chem. Phys. **107**, 2340 (1997).
[16] L. R. Leclair and J. W. Mcconkey, J. Chem. Phys. **99**, 4566 (1993).
[17] P. J. Kuntz, Chem. Phys. **240**, 19 (1999).
[18] H. Meyer, Physica B **197**, 360 (1994).
[19] A. V. Benderskii and C. A. Wight, Chem. Phys. **189**, 307 (1994).
[20] T. H. Dunning and P. J. Hay, J. Chem. Phys. **66**, 3767 (1977).
[21] For a recent study of the XeO potentials, see: M. Yamanishi, K. Hirao, and K. Yamashita, J. Chem. Phys. **108**, 1514 (1998).
[22] J. Goodman, J. C. Tully, V. E. Bondybey, and L. E. Brus, J. Chem. Phys. **66**, 4802 (1977).
[23] A. Banichevich, S. D. Peyerimhoff, and F. Grein, Chem. Phys. Lett. **173**, 1 (1990).
[24] G. J. Atchity and K. Rudenberg, Theor. Chem. Acc. **96**, 176 (1997).
[25] Simon Tam and Mario E. Fajardo, Fiz. Nizk. Temp. **26**, 889 (2000) [Low Temp. Phys. **26**, 661 (2000)].

This article was published in English in the original Russian journal. Reproduced here with stylistic changes by the Translation Consultant.

Structure characteristics of methane-doped solid normal hydrogen

N. N. Galtsov, A. I. Prokhvatilov, and M. A. Strzhemechny*

B. Verkin Institute for Low Temperature Physics and Engineering, National Academy of Sciences of Ukraine, 47 Lenin Ave., 61164 Kharkov, Ukraine
(Submitted February 7, 2000)
Fiz. Nizk. Temp. **26**, 918–922 (September–October 2000)

Structure studies of the quantum crystal of solid normal hydrogen doped with methane and deuteromethane are carried out by powder x-ray diffraction within the temperature range 5 to 12 K. The concentration of the dopants in the gas mixtures used for sample preparation by quench condensing is varied from 0.5% to 5%. It is established that the equilibrium solubility of both methanes is substantially below the lower fraction indicated. The abnormally high apparent extra volumes per impurity may be ascribed to van der Waals complexes formed around isolated dopant particles. © *2000 American Institute of Physics.* [S1063-777X(00)00809-4]

INTRODUCTION

Recently, solid hydrogen with the lowest possible concentration of the orthomodification has been suggested[1] as a promising material for matrix isolation. Optical spectra of molecules embedded in solid hydrogen allow investigation of rather intimate quantum-crystal effects in the dynamics of these matrix-isolated molecules. There is also another interesting aspect, namely, the possibility of looking into some properties of the hydrogen matrix itself, in particular, into the response of the nearest-neighbor environment to the introduction of a single molecular impurity. Additional interest in these solid-state issues comes from the fact that solid hydrogen is a quantum crystal, and all the solid-state renormalizations should take account of this circumstance. The recent work of Momose and co-workers[2–4] on the infrared spectra of the methanes CH_4 and CD_4, matrix isolated in parahydrogen, provides a good basis for a detailed study of the above effects. In particular, they fitted their spectra within the rigid lattice approach and extracted the values of the crystal field parameters and the renormalized rotational constants. For complete understanding of the effects observed, a few issues still need theoretical consideration and comparison with the relevant experiment. First, quantum-crystal renormalization of the parameters (and, possibly, of the form) of the noncentral interaction potential of the methane molecule with its matrix environment. Second, calculation of the displacements of nearest neighbors within Nosanow's[5] or more advanced[6,7] approaches. These displacements are important for the evaluation of the crystal field parameters, also to be renormalized in a quasistatic approximation for a soft lattice, which constitutes the third issue. Such evaluations, known for classical systems,[8] require reconsideration for the case of quantum crystals. Finally, one more problem is the evaluation of the dynamic renormalization of the rotational constant of a single matrix-isolated methane molecule. For the classical case such a procedure is known.[9] The difficulty of this program is aggravated by the fact that good energy surfaces for the interaction between CH_4 and H_2 are at present unavailable.

It is obvious that, however precise, the optical data give information on the rotational spectrum of the matrix-isolated molecule but do not tell directly about the actual geometry of the relaxed lattice around the impurity, which can be inferred from the known or assumed potentials. In this respect, structure studies, in which some independent conclusions about the response of the surrounding lattice can be drawn directly, may be treated as complementary to optical measurements. This was our main motivation of the work reported here.

An additional motivation of this structure study was to see whether the methane molecule in solid hydrogen exhibits the effect of abnormal excess volume, which is well observable, for example, in the $Ne–H_2$ system[10,11] and cannot be observed in some other dilute hydrogen-based solid mixtures.[12] The strong effect of even weak doping with neon was attributed to the formation of van der Waals complexes $Ne(H_2)_n$. From optical and x-ray studies at high pressures and room temperature[13] it follows that the n-H_2–CH_4 system exhibits numerous stoichiometric compositions in the solid. We thought that some related effects might be felt at low temperatures in molar volumes as a function of the impurity concentration.

EXPERIMENTAL

Experiments were carried out on a DRON-3M powder x-ray diffractometer equipped with a liquid helium cryostat. The diffractometer control and the data collection and processing were automated. The samples were prepared by quench condensing gas mixtures of known composition on a flat copper substrate at a temperature close to 5 K. Normally, we obtained polycrystalline samples about 0.1 mm thick with grain sizes $10^{-4}-10^{-5}$ mm. Condensation of every batch resulted in a heating of the substrate by 3 to 4 K. The purity of the gases used for sample preparation were: normal hydrogen 99.999%, methane and deuteromethane 99.99%. The error in the impurity concentration measured by means of the $P-V-T$ method did not exceed 5% of the rated impurity fraction. The concentration ranges studied are 0.5% to 5% for CH_4 and 1% to 5% for CD_4. The temperature ranges are from 5 K to the melting points of the hydrogen matrices.

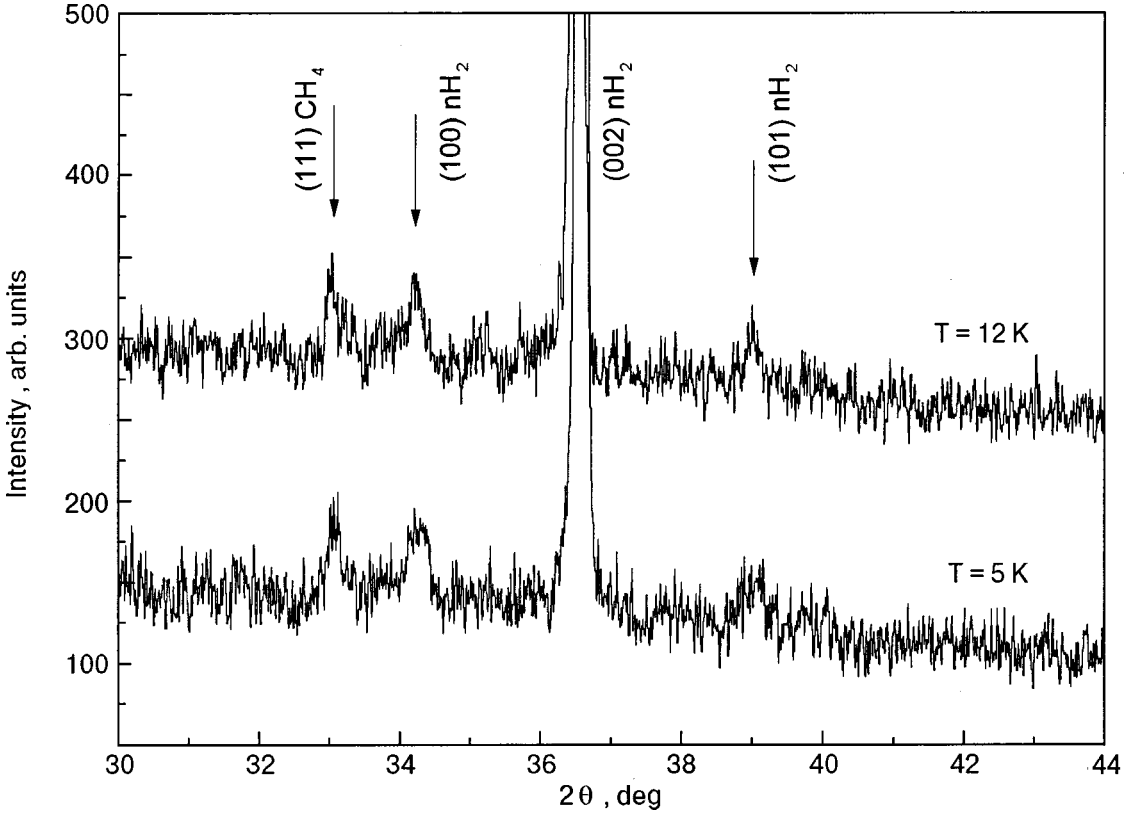

FIG. 1. X-ray powder diffraction patterns from n-H_2+0.5%CH_4 solid mixtures at the temperatures indicated. The most intense methane line (cubic 111) is well discernible. The arrows indicate Bragg reflections. Traces are shifted vertically to avoid overcrowding. The intensity counts are in arbitrary units but which are the same for all traces.

Temperature stabilization and measurement were performed to within ±0.05 K. The lattice parameters were determined to within ±0.02%.

RESULTS AND DISCUSSION

Typical diffraction patterns for the region of smaller diffraction angles, where the most intense reflections from the solid mixtures n-H_2+0.5%CH_4 and n-H_2+1%CD_4 were observed, are reproduced in Figs. 1 and 2. Both plots include patterns from as-prepared samples at 5 K and from the same samples warmed up to and kept for 30 minutes at 12 K. Figure 2 also shows a diffraction pattern taken after a cooldown to 5 K following the above annealing. The patterns from both systems exhibit a very strong (002) texture with the hexagonal close-packed layers of n-H_2 being predominantly parallel to the substrate plane. The presence of methane impurities serves as a factor that stabilizes the texture obtained during quenching. The texture did not undergo noticeable changes when the crystals were warmed up to premelting temperatures and subsequently cooled down (see Fig. 2). Similar textures were observed previously when pure n-H_2 or p-H_2 samples were also quench condensed on cold substrates at liquid helium temperature.[14,15] But unlike doped crystals, warming up polycrystalline pure hydrogen samples to a few tenths of a kelvin below T_m usually resulted in an enhanced texture, viz., presumably due to recrystallization, the crystals exhibited single-crystal features: the reflection (002) grew in intensity by orders of magnitude, and the other lines disappeared. Subsequent cooldown did not change the patterns obtained at higher temperatures.

Even for methane and deuteromethane fractions about 1% and lower, the diffraction patterns display the brightest (111) line of the respective fcc lattices of both CH_4 and CD_4 (see Figs. 1 and 2); this line grew in intensity as the dopant fraction was increased.

Heating of the samples entailed a noticeable shift of all visible reflections to smaller diffraction angles, which is caused by thermal expansion. When subsequently cooled down back to 5 K the positions of the lines were restored (see Fig. 2) completely, as inferred from the calculated lattice parameters before and after warmup. It should be also added that the linewidths did not change after thermocycling. Such behavior implies that the methane molecules have not been redistributed during the procedure.

Owing to the considerable molar volume difference between the n-H_2 matrix (22.83 cm^3/mol)[14] and CH_4 (30.27 cm^3/mol)[16] or CD_4 (29.37 cm^3/mol),[17] formation of the solid mixtures should be accompanied by substantial lattice distortions around the impurities, which in turn must entail broader and weaker diffraction lines. In our experiments the reflections belonging to the matrix are narrow (0.2° to 0.4°), comparable with those in pure normal hydrogen. This finding, together with the fact that we see reflections from a methane-rich phase, gives us grounds to conclude that the equilibrium solubility of the methanes in solid hydrogen is extremely low.

The molar volumes of the normal hydrogen matrix doped with the light and heavy methane isotopes are plotted in Figs. 3a and 3b. One can see that within the entire concentration range studied, starting with fractions as low as

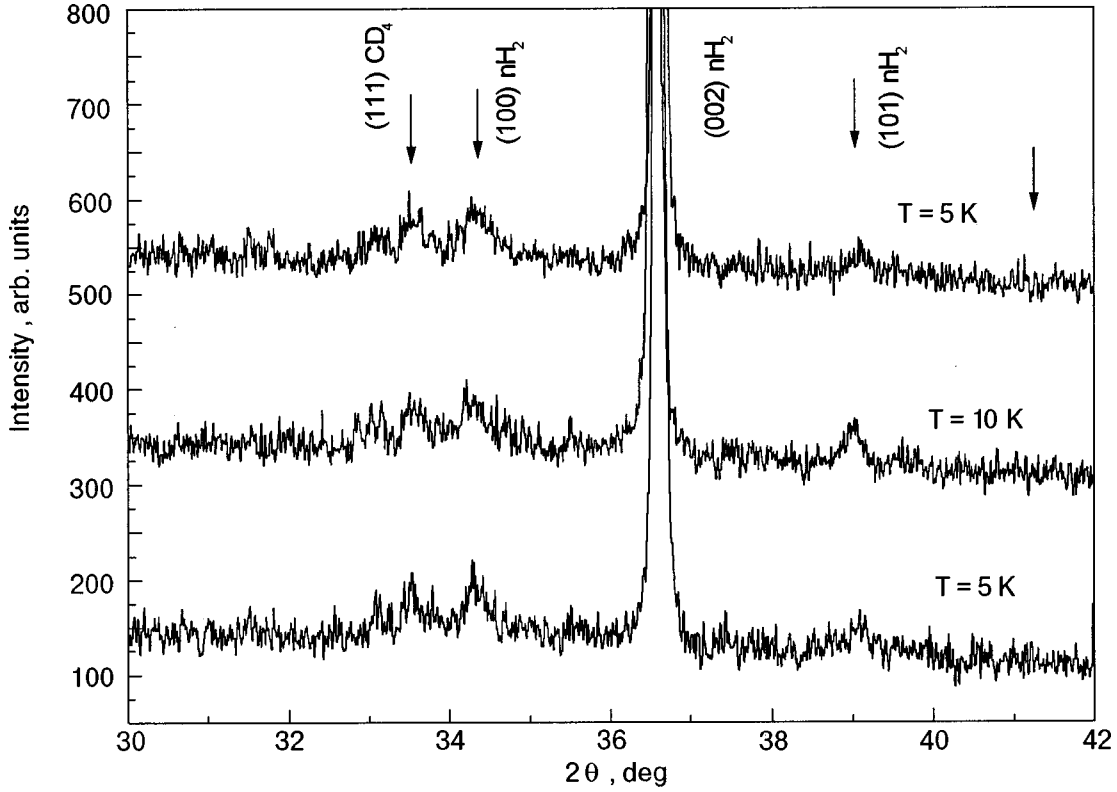

FIG. 2. X-ray powder diffraction patterns from n-H_2+1%CD_4 solid mixtures at the temperatures indicated. The pattern with the thick downward arrow is for the same sample cooled down to 5 K after a warmup to 12 K. Other notations are as in Fig. 1.

0.5% of CH_4 and 1% of CD_4, the molar volume of the matrix is virtually concentration independent. A similar independence holds for higher temperatures, 1 or 2 K below the melting point of n-H_2. This result is in line with the conclusion formulated above that the equilibrium solubility of methane molecules in hydrogen is very low, at a level of few tens of ppm.

Notwithstanding the low solubility, the effect of this molecular impurity on the lattice parameters of the matrix is abnormally strong, just as in the case of neon. Introduction of a small amount of methane results in an increase of the molar volume of the matrix by 1.3%. If these solid solutions were ideal, the dissolution of 1% methane would have increased the volume of the matrix by 0.3% (for deuteromethane the figure is 0.28%). If we assume that half of the dopant is in dispersed form, we would obtain for the reduced extra volume per impurity, $[V(x)-V_0]/(xV_0)$, a very large value of around 5.2 ± 1.8. We think that the effect observed in the normal hydrogen matrix might be, at least in part, due to van der Waals complexes formed around the methane impurities, as has been assumed for the presumably similar effect in neon-doped normal hydrogen.[8]

We note that the introduction of methane molecules into the hydrogen lattice entails an effect on the measured molar volume of the matrix, which is comparable to that due to thermal expansion over the entire range of existence of the solid phase ($\Delta V/V=1.4\%$)[16] or due to conversion ($\Delta V/V=1.04\%$).[17] This must lead to noticeable changes in the thermodynamic and structural characteristics of hydrogen–methane alloys. As to the latter, we found that the admixture

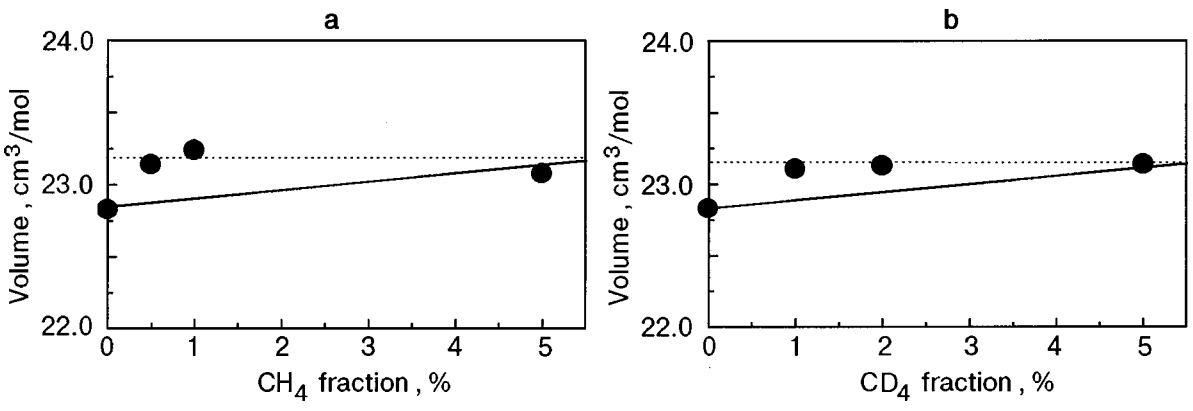

FIG. 3. The molar volumes of n-H_2–CH_4 (a) and n-H_2–CD_4 (b) alloys versus the methane concentration as calculated form the patterns at 5 K. The impurity concentrations correspond to their content in the gas mixtures from which the polycrystal samples were prepared.

of methane leads not only to larger molar volumes but tends to change the c/a ratio closer to its ideal value of 1.633. At 5 K the lattice parameters of the 1% CH_4 in H_2 mixture are: $a=3.791$ Å; $c=6.176$ Å; $c/a=1.630$; $V=23.12\ \mathrm{cm}^3/\mathrm{mol}$. These values are close to those found for parahydrogen.[15] Deuteromethane produces a similar effect.

In conclusion, powder x-ray studies of the lattice parameters of solid normal hydrogen doped with CH_4 and CD_4 at fractions down to 0.5% have shown that the equilibrium solubility of both methanes is very low. An abnormally strong effect of methane impurities on the molar volume of the normal hydrogen matrix has been documented. The effect is tentatively ascribed to a specific quantum-crystal response of the lattice to the formation of van der Waals complexes around the methane impurities.

*E-mail: strzhemechny@ilt.kharkov.ua

[1] T. Momose and T. Shida, Bull. Chem. Soc. Jpn. **71**, 1 (1998).
[2] T. Momose, J. Chem. Phys. **107**, 7695 (1997).
[3] T. Momose, M. Miki, T. Wakabayashi, and T. Shida, J. Chem. Phys. **107**, 7707 (1997).
[4] H. Hoshina, T. Wakabayashi, T. Momose, and T. Shida, J. Chem. Phys. **110**, 5728 (1997).
[5] L. H. Nosanow, Phys. Rev. **146**, 120 (1966).
[6] H. Horner, Z. Phys. **242**, 432 (1971).
[7] T. R. Koehler, Phys. Rev. **165**, 942 (1968).
[8] S. E. Kalnoi, M. A. Strzhemechny, V. V. Sumarokov, and Yu. A. Freiman, Fiz. Nizk. Temp. **13**, 809 (1987) [Sov. J. Low Temp. Phys. **13**, 462 (1987)].
[9] T. N. Antsygina and V. A. Slusarev, Teor. Mat. Fiz. **77**, 234 (1980).
[10] A. S. Barylnik, A. I. Prokhvatilov, M. A. Strzhemechny, and G. N. Shcherbakov, Fiz. Nizk. Temp. **19**, 625 (1993) [Low Temp. Phys. **19**, 447 (1993)].
[11] A. S. Barylnik, A. I. Prokhvatilov, and G. N. Shcherbakov, Fiz. Nizk. Temp. **21**, 787 (1995) [Low Temp. Phys. **21**, 607 (1995)].
[12] G. N. Shcherbakov, A. I. Prokhvatilov, M. A. Strzhemechny, and A. S. Barylnik, *Abstracts, Cryocrystals-2 International Conference, September 1997*, Vroclaw (1997).
[13] M. S. Somayazulu, L. W. Finger, R. J. Hemley, and H. K. Mao, Science **271**, 1400 (1996).
[14] I. N. Krupskii, A. I. Prokhvatilov, and G. N. Shcherbakov, Fiz. Nizk. Temp. **9**, 858 (1983) [Sov. J. Low Temp. Phys. **9**, 446 (1983)].
[15] I. N. Krupskii, A. I. Prokhvatilov, and G. N. Shcherbakov, Fiz. Nizk. Temp. **9**, 83 (1983) [Sov. J. Low Temp. Phys. **9**, 42 (1983)].
[16] A. I. Prokhvatilov and A. P. Isakina, Fiz. Nizk. Temp. **9**, 419 (1983) [Sov. J. Low Temp. Phys. **9**, 213 (1983)].
[17] A. I. Prokhvatilov and A. P. Isakina, Phys. Status Solidi A **78**, 147 (1983).

This article was published in English in the original Russian journal. Reproduced here with stylistic changes by the Translation Consultant.

Formation and characterization of neutral krypton and xenon hydrides in low-temperature matrices

J. Lundell, L. Khriachtchev, M. Pettersson, and M. Räsänen*

Laboratory of Physical Chemistry, University of Helsinki, P.O. Box 55 (A. I. Virtasen aukio 1), FIN-00014 University of Helsinki, Finland
(Submitted March 9, 2000)
Fiz. Nizk. Temp. **26**, 923–936 (September–October 2000)

A family of rare-gas-containing hydrides HXY (where X=Kr or Xe, and Y is an electronegative fragment) is described. These molecules are experimentally prepared in low-temperature matrices by photodissociation of a hydrogen-containing HY precursor and thermal mobilization of the photodetached hydrogen atoms. The neutral HXY molecules are formed in a concerted reaction H+Y→HXY. Experimental evidence for the formation of these species is essentially based on strong infrared absorption bands that appear after annealing of the photolyzed matrices and are assigned to the H-X stretch of the HXY molecules. Computationally, the formation of these HXY molecules decreases the H-X distance by a factor of $\geqslant 2$ from its van der Waals value, which emphasizes their true chemical bonding, possessing both covalent and ionic contributions. The estimated dissociation energies vary from 0.4 to 1.4 eV and hold promise for forthcoming observation of these molecules in the gas phase. The experiments with the HXY molecules widen our knowledge on solid-state photolysis dynamics of hydrogen-containing species. In particular, the photolysis of small HY hydrides in solid Xe seems to be a quite local process, and the accompanying losses of H atoms play a minor role.
 [S1063-777X(00)00909-9]

INTRODUCTION

The rare gas atoms have generally been regarded as inert due to their stable electronic structure lacking chemical bond formation capabilities. However, back in 1933 Pauling suggested, based on consideration of the ionic radii of different elements, that xenon and krypton were capable of neutral chemical compounds especially with fluorine.[1] It took three decades before Bartlett was able to make the first rare gas compound.[2] This molecule constituted an ionic $Xe^+[PtF_6]^-$ crystal, which was later shown[3] to consist most probably of a mixture of $XeF^+PtF_6^-$ and $XeF^+PtF_{11}^-$. Simultaneously with Bartlett's discovery, Hoppe and coworkers[4] were able to isolate XeF_2, and slightly thereafter Claassen *et al.*[5] prepared XeF_4. These pioneering findings stimulated enthusiastic research on rare-gas-containing molecules, and several xenon compounds, in which Xe was bound to fluorine or oxygen, were reported and reviewed extensively later on.[6–16] The theory of Xe binding has been authoritatively discussed by Coulson.[17]

Neutral-xenon chemistry has been enriched constantly, and several xenon-containing species of similar ionic nature to those of Bartlett's first report have been characterized. The first Xe–N bond was found in $FXeN(SO_2F)_2$ by LeBlond and DesMarteau,[18] and many similar but more complex compounds have been characterized since then.[19–26] Neutral $FXeCF_3$ and $Xe(CF_3)_2$ have been discussed in the literature,[27–29] but neither of them has been spectroscopically characterized. A stable Xe–C bonded molecule, fluorophenylxenon (II) fluoroborate ($[C_6H_5Xe][B(C_6H_5)_3F]$) was reported in 1989,[30] and a number of organoxenonium compounds have been prepared.[31,32] The latest molecule to join the family of organic Xe compounds is $C_6H_5XeF_2^+BF_4^-$, reported in early 2000 by Frohn and coworkers.[33] The chemistry of fluorine-containing rare gas compounds has been recently thoroughly reviewed by Holloway and Hope.[34] The chemistry of krypton is much more sparse than that of Xe. The first Kr bonds were found in fluorine-containing compounds KrF_2 (Refs. 35–37) and KrF_4 (Ref. 38) in analogy to xenon. In addition, krypton is known to bind with nitrogen and oxygen, and these studies have been pioneered by the Schrobilgen group.[39–42] Besides the neutral Xe- and Kr-containing compounds, a large number of ionic rare gas species have been predicted and found, and the reader is encouraged to look, for example, in Refs. 43–47.

The first characterization of KrF_2 and KrF_4 especially took advantage of the low-temperature matrix-isolation technique, which was originally developed to study unstable molecules and reaction intermediates.[48–50] The substance to be studied is deposited in large dilution with inert gases on a cold surface or generated photochemically *in situ* from a precursor molecule already deposited. The solid rare gas environment is regarded as inert towards chemical bond formation and the cage effect is employed to isolate the chemical system under study. Further examples of rare-gas-containing molecules are, for example, $XeCl_2$ (Ref. 51), XeClF (Refs. 37, 52), and $FXeBF_2$ (Ref. 53).

Evidently the formation of such molecules makes the inertness of the solid rare gases questionable, and, indeed, recent reviews of photochemical processes in low-temperature matrices underline the interaction between molecular species with the environment upon irradiation.[54,55] These interactions and their consequences on dynamics and chemistry will be discussed in this review, and we will describe the solid-state synthesis of several HKrY and HXeY

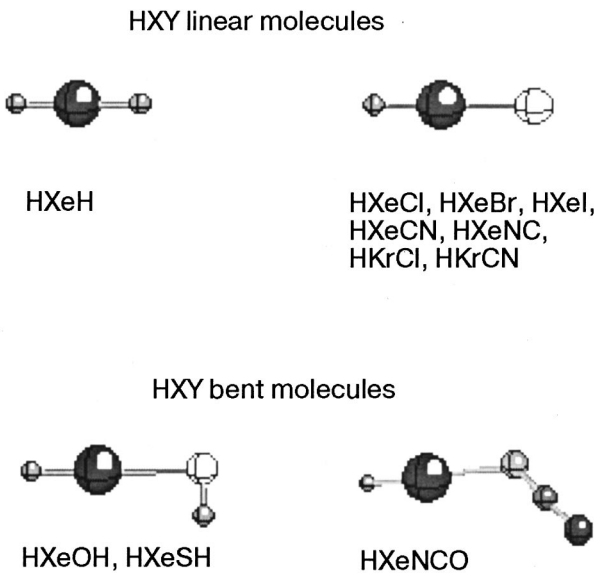

FIG. 1. The known neutral HKrY and HXeY molecules.

(Y=an electronegative fragment) rare-gas-containing molecules in low-temperature matrices. It should be emphasized that these molecules are not van der Waals complexes but truly chemically bound species with very characteristic vibrational spectra. The HKrY and HXeY molecules are prepared from a suitable hydrogen-containing precursor (HY), which is photodecomposed, producing a hydrogen atom and an electronegative fragment (Y). After preparation of the neutral photoproducts, hydrogen atoms are mobilized thermally. The neutral HKrY and HXeY molecules are then formed in a concerted reaction H+Kr/Xe+Y→→HXeY/HKrY. Quantum chemical calculations are combined with the experimental results to aid the interpretation and understanding of the structure, spectral characteristics, energetics, and bonding of these new molecules. The formation of the HKrY and HXeY molecules involves motion of hydrogen atoms, and the extent of photo and thermally activated chemical processes highlights the basic concept of fragment mobilization in the solid rare gas lattice. Studies of the formation of HXY molecules at various precursor concentrations and at different extents of photodissociation indicate strongly that the primary photolysis of HY molecules is a very local event. We shall show that the analysis involving the novel compounds can shed light on the solid-state dynamics regarding particularly the mobility of H atoms. This review is essentially based on experimental and computational research on the reactivity of rare gases carried mainly out at the Laboratory of Physical Chemistry, University of Helsinki during 1995–1999,[56–69] and all the experimentally observed molecules included in this review are shown in Fig. 1.

COMPUTER EXPERIMENTS ON HXeY AND HKrY MOLECULES

All the HXY (X=Xe or Kr) molecules have been prepared in solid rare gases and there does not exist experimental data on their geometries and charge distributions. From the computational point of view the rare-gas-containing molecules are challenging. The large number of electrons quite rapidly prohibit the use of extensive quantum chemical methods by increasing the computational task beyond the current computer capabilities. As a useful approach, effective core potentials (ECPs) are used, which reduces the number of electrons taken into account in the calculations. Many possible ECPs are available and usually 8 or 18 electrons are included in the valence shell, and the core is substituted by an effective potential resembling the behavior of the inner electrons. This approach has been taken in all the studies of HXeY and HKrY molecules discussed below, and computational data of the experimentally observed HXeY and HKrY molecules are collected in Table I.

Calculated structures and energetics. The first computational studies of HXeY and HKrY molecules employed second-order perturbation theory and small basis sets (MP2/LANL1DZ).[53,54] These calculations are very economic and fast, and for the equilibrium structures they are surprisingly adequate. Up to now our experience of these calculations on the HXeY and HKrY molecules shows that they are able to predict the existence of the molecule. This fact is evidenced, for example, by halogen-containing HKrY molecules. The calculations predict that HKrCl should exist but that HKrBr and HKrI are not stable. Indeed, this corresponds to experimental observations: only HKrCl has been isolated in low-temperature matrices,[56] but not HKrBr or HKrI despite extensive attempts. These low-level MP2/LANL1DZ calculations give reasonable bond distances and vibrational frequencies. On the other hand, they predict the HXY molecules to be higher in energy than the neutral atomic dissociation limit. For higher-level calculations this is reversed, as was pointed out by Runeberg and coworkers based on their high-level *ab initio* calculations on HXeH.[70,71] This work is the best and most extensive computation on HXeH, and the authors studied its structural and vibrational properties as well as the energetics by various computational methods from the perturbation theory (MPn) to the state-of-the-art coupled cluster (CCSD(T)) and multireference configuration interaction (MR-CI) calculations. The study showed that increasing the level of correlation requires also a larger and flexible basis set to achieve chemically reliable results for HXeH. For this molecule, practical methods like MP2 with a standard basis set including multiple polarization and diffuse functions predict a Xe-H bond distance of ca. 1.86 Å. The most extensive CCSD(T) calculations by Runeberg *et al.*[70,71] estimate the Xe–H bond in HXeH to be around 1.95 Å. It must be noted here that this value is much shorter than the Xe–H van der Waals minimum being 3.8 Å.[72]

For all known Xe-containing hydrides the MP2 calculations estimate a Xe–H bond between 1.66 and 1.86 Å, the longest Xe–H bond being found for HXeH. It can be noted that the calculated parameters follow a general trend. The H–Xe bond length decreases with increasing partial positive charge on the xenon. The positive charge residing on xenon is largest (+0.88) for the HXeNC molecule, corresponding to the shortest Xe–H bond length (1.659 Å). For deeper bound HXeY molecules the contribution of $(HXe)^+$ increases, and the HX bond length approaches the value of the XeH^+ cation, for which computations at the same level predict a bond distance of 1.596 Å. The reason for this is the

TABLE I. Computational properties of different HXeY and HKrY compounds at the MP2 level.[a)]

Compound	r(X–H)	r(X–Y)	r(X–Z)	q(H)	q(X)	q(Y)	q(Z)	Dipole moment, D	EA (Y), eV [e)]
	Å								
HXeH	1.861			−0.344	0.688			0.0	0.754
HXeSH [b)]	1.774	2.729	1.334	−0.226	0.671	−0.435	−0.009	4.5	2.314
HXeI	1.747	3.095		−0.178	0.645	−0.467		6.4	3.059
HXeOH [c)]	1.718	2.208	0.962	−0.237	0.818	−0.814	0.232	4.1	1.828
HXeCN	1.707	2.392	1.178	−0.203	0.847	−0.401	−0.242	7.4	3.821
HXeBr	1.694	2.837		−0.156	0.802	−0.647		7.3	3.364
HXeCl	1.685	2.663		−0.165	0.816	−0.651		7.2	3.613
HXeNCO [d)]	1.675	2.326	N–C 1.215	−0.169	0.863	−0.566	C 0.263	7.8	
			C–O 1.193				O −0.391		
HXeNC	1.659	2.342	1.187	−0.161	0.880	−0.424	−0.295	9.3	3.821
HKrCN	1.466	2.349	1.177	−0.206	0.886	−0.488	−0.193	9.2	3.821
HKrCl	1.435	2.666		−0.178	0.887	−0.709		9.4	3.613

[a)]For Xe and Kr 18-VE ECP and for I 17-VE ECP were used, while all other atoms are described by $6-311++G(2d,2p)$ basis set.
[b)]The calculated Xe–S–H angle is 91°.
[c)]The calculated angles are H–Xe–O 177° and Xe–O–H 109°.
[d)]The calculated angles H–Xe–N, Xe–N–C and N–C–O are 178°, 125°, and 178°, respectively.
[e)]Electron affinity, from *Handbook of Chemistry and Physics*, CRC Press, Boca Raton, 72nd ed. (1991).

larger ionic contribution $(HXe)^+Y^-$ in the molecule, and this is discussed in more details below. Similarly for the Kr compounds the increasing charge separation approaches KrH^+ for which the calculated bond distance is 1.382 Å. It is also worth noting that all these molecules have very large dipole moments due to the extensive charge separation.

The HXY molecules observed experimentally up to now are shown in Fig. 1. HXeH is the smallest and simplest of the family of rare gas hydrides, but HKrH does not exist either computationally or experimentally. One of the hydrogens in these species can be substituted with an electronegative fragment to form a linear HXY molecule, where Y is a halogen or a pseudohalogen like CN. A second group of rare-gas-containing hydrides is obtained from bent hydrogen containing precursors, and the rare gas atom is inserted into the H-Y bond. Such molecules characterized so far are: HXeOH, HXeSH, and HXeNCO. The HXeSH molecule is the first example of a Xe–S bond[60] with a Xe–S–H angle of around 91°, which is very similar to the angle of H_2S. Moreover, the calculated S–H bond distance of 1.334 Å is very close to the experimental S–H bond in H_2S, being 1.336 Å.[73] Similarly, the HXeOH and HXeNCO molecules follow closely the structure of their precursors, i.e., water and HNCO. It appears that the rare gas atom inserted into a covalent H–Y bond has a negligible effect on the rest of the molecule. This observation opens up interesting possibilities that can be first tested by computational methods. The success with Xe insertion into the O–H bond of water prompted us also to test this idea on larger systems. Computations on formic acid indicate that the HCOOXeH molecule is stable, and the HCOO group is only slightly perturbed from its structure in the HCOOH monomer.[74] This idea can be extended to other carboxylic acids and amino acids, which all behave similarly to formic acid. The largest molecule tested was aspartic acid ($HOOCCH_2CHNH_2COOH$), where the most prominent insertion of Xe into the side chain of the molecule was noted. This result suggests that in principle Xe can bind metastably to amino acids, which are building blocks for proteins. In this respect it is important to note that it has been suggested that anesthetic substances bind directly to proteins, but yet no definitive evidence of the location of the binding sites exists.[75] Since Xe is known to have an anesthetic effect, the insertion of Xe into a covalent O–H bond might have an impact on understanding its anesthetic mechanism.

It should be noted that computationally the HXeY and HKrY molecules are practically linear with respect to the H–Xe–Y bond. For HXeOH the deviation from linearity is about 3°, and for the carboxylic and amino acids deviations up to 5° have been reported.[74] For the nitrogen bound Xe compound HXeNCO a few degrees tilt in the H–Xe–N bond is found.[68] For $FXeOSO_2F$ also the F–Xe–O angle was previously reported to be 177.5° (Ref. 76), bearing some similarity to the H–Xe–O and H–Xe–N groups in the HXeY molecules. In principle, a simple explanation for this can be found from the three-center four-electron model applied for FXeF[17] and HXeH.[70,71] The highest occupied (σ_g) orbital is

centered around the terminal H and F atoms in HXeH and FXeF, respectively. This molecular orbital is nonbonding and is occupied by two electrons. In HXeH, the lowest orbital (σ_g) is formed from the $5p$ orbital of xenon and the s orbitals of the hydrogens. This molecular orbital possesses two additional electrons and is responsible for the covalent bonding. A similar simple linear model should be valid also for other HXY molecules if the other s orbitals are replaced by the proper orbital of the Y fragment. The tilt in the linear bond indicates small external perturbations in the bonding induced by the rest of the molecule.

A model of bonding. Even though the equilibrium structure of the HXeY and HKrY molecules are qualitatively reproduced also with the modest computational approaches compared to the state-of-the-art approaches, the energetics of the rare-gas-containing molecules is more challenging. The origin of the bonding can be understood on the basis of a model in which both neutral (HXY) and ionic (HX^+Y^-) bonds contribute. The idea of the ion pair was originally applied on HXe^+Cl^- by Last and George based on semiempirical DIIS calculations.[77] It is informative to discuss the main factors affecting the stability of the HXY molecules. In principle the HXY molecules have a strongly ionic nature for the equilibrium structure, which is evident from the partial charges in Table I. This equilibrium structure corresponds to an ion pair dissociation limit $HX^+ + Y^-$. However, when the HXY molecule is stretched along the molecular axis the ionic adiabatic potential surface is crossed by a repulsive surface corresponding to the neutral fragments H+X+Y. The dissociation limit of the HXY molecules corresponds to the neutral fragments due to the avoided crossing between the neutral and ionic potential surfaces. Therefore the ionization potential (IP) of X, electron affinity (EA) of Y, and the dissociation energy (D_e) of XH^+ determine the energetics between the neutral and ionic limits. A low ionization potential of X and a large electron affinity of Y are favorable to the formation of HXY. The D_e values of XeH^+ and KrH^+ are about 4.05 and 4.8 eV, respectively.[78–81] The closer the ionic surface lies to the neutral surface, the larger is the expected interaction between the two surfaces and the further from the HXY minimum is the avoided crossing. Altogether, there is a rather subtle balance between the different factors affecting the energetics of HXY compounds, and their properties depend strongly on Y. One factor is the electron affinity of the Y fragment (shown in Table I) and also the effective size of Y. A small Y^- could be thought intuitively to stabilize HXY more than a larger one because it can approach closer to the HX^+ fragment, hence producing a larger Coulombic stabilization. This consideration indicates that the lighter rare gases, especially argon, could form similar HArY molecules. However, the ionization potential of Ar is larger (15.759 eV) than that of Kr and Xe, and ArH^+ is less stable (3.87 eV) than KrH^+ and XeH^+ (Ref. 82). Nevertheless, based on the simple arguments discussed above argon could combine with an extremely electronegative fragment to form a new HArY molecule. Indeed, computationally both HArCl and HArF have been characterized.[56] CCSD(T)/6-31G(d,p) calculations predict HArF to be the more strongly bound of these two molecules, with a binding energy of 0.2 eV.[56]

In terms of resonance structures, HXY should be described as a resonance hybrid between several possible structures, the most important being HX^+Y^-. The other important structures are neutral H–X–Y and ionic H^-X^+Y. The ionic structures tend to stabilize the compound and the neutral structure destabilizes it. Recently the bonding nature of HXY molecules has been studied by topological analysis of the Electron Localization Function (ELF), in which three different resonance structures were considered: H^+XY^-, HX^+Y^-, and HX^-Y^+ (Ref. 83). For HXeCl and HKrCl the second structure has the largest weight, about 60%. For the first structure the approximate weight is about 20%, and the remaining 20% resides on the structure with the positive charge localized on the halogen. It was therefore concluded that the positive charge is mainly localized on the rare gas atom, and that the H–X bond is mostly covalent in nature. It was concluded about the interaction between the rare gas atom and the halogen that this binding is mostly of a so called unshared-electron type, i.e., the interaction is mainly ionic but with a nonnegligible fraction of a covalent character. This conclusion is in agreement with the simple model derived above, where both neutral and ionic potential surfaces contribute to the HXY molecule.

The H–X bond distance reflects directly the fraction of the ionic contribution in the molecule. The computationally strongest HXY molecule among the experimentally observed ones is HXeCN, which has a dissociation energy of 1.43 eV[59] with respect to the dissociation limit H+Xe+CN. CISD (configuration interaction with single and double excitations) calculations on HXeCl estimate the binding energy to be 0.9 eV, and the first excited state was found to include a minimum in accordance with the curve crossing. The first excited state was calculated to be bound by 2.0 eV and lie almost 5 eV above the ground state for the $X\,^1\Sigma^+$ equilibrium structure.[84] In general, computationally the ground-state HXY molecules are bound by 0.4–1.4 eV.

Vibrational properties. The agreement of the calculated and experimental vibrational frequencies reflect the adequacy of the potential energy surface for the given theoretical approach. As noted above, the equilibrium structures are reasonably well reproduced already at modest computational levels, and therefore the vibrational frequencies are also qualitatively correct. However, the HXY molecules are relatively weakly bound, and the potential energy surface near the dissociation limit cannot be described accurately without extensive basis sets and electron correlation. For HXeH the MP2 calculation gives the following frequencies: symmetric stretch at 1559 cm^{-1}, antisymmetric stretch at 1385 cm^{-1}, and bending at 876 cm^{-1}. Increasing the electron correlation to CCSD(T) decreases both the symmetric and the antisymmetric stretches to 1279 and 1216 cm^{-1}, respectively.[70,71] Also, the CCSD(T) calculations predict the bending mode at 773 cm^{-1}. Recently we studied the effect of anharmonicity for HXeH at the MP2 level, and found that both the antisymmetric stretch and the bending modes are much more harmonic than the symmetric stretch.[85] These results are collected in Table II and compared with the harmonic MP2 and CCSD(T) results. The symmetric stretch, which corresponds to the lowest energy path for dissociation of the molecules, is predicted to decrease by about 100 cm^{-1} from its harmonic value.

TABLE II. Comparison of calculated and measured vibrational frequencies of some HXeY compounds. The numbers in the parentheses are the IR intensities[a] (in km·mol^{-1}).

Compound	ν (Xe–H)	2ν (Xe–H)	δ (H–Xe–Y)	2δ (H–Xe–Y)	ν (Xe–Y)
HXeH					
MP2 harm.	1385 (2503)		876 (69)		1559 (0)
CCSD(T) harm.	1279		773	1666 (0)	1216
MP2 anharm.	1337 (4594)	2648 (0)	839 (69)		1469 (0)
Experiment	1166, 1181		701		840 [b]
HXeCl					
MP2 harm.	1740 (2058)		595 (4)	1143 (0)	267 (46)
MP2 anharm.	1642 (1288)	3194 (20)	577 (2)		260 (2)
Experiment	1648				
HXeBr					
MP2 harm.	1679 (4102)		526 (1)		182 (29)
MP2 anharm.	1544 (1445)	2967 (15)	506 (2)	997 (33)	180 (48)
Experiment	1504	2869	489	965	
HXeI					
MP2 harm.	1514 (5423)		500 (1)		143 (18)
MP2 anharm.	1359 (2429)	2585 (51)	477 (1)	937 (44)	142 (38)
Experiment	1193	2190	450	886, 896	129 [c]
HXeOH					
MP2 harm.	1823 (1456)		653 (7) [d]		437 (126) [e]
CCSD(T) harm.	1678		629 [d]		419 [e]
MP2 anharm.	1713 (1043)	3342 (12)	627 (5) [d]	1242 (4)	425 (269) [e]
Experiment	1578				

[a]Calculated using dipole moments obtained from SCF wavefunctions.
[b]Calculated from the $\nu_1+\nu_3$ combination band observed at 2003 cm^{-1}.
[c]Calculated from the $\nu_1+\nu_3$ combination band observed at 1322 cm^{-1}.
[d]HXeO out-of-plane bend.
[e]Xe–OH stretch.

The anharmonic vibrational calculations are based on the *ab initio* calculated points on the potential energy surface, which allows us to estimate the wave numbers of the combinations and overtones. For example, an experimentally observed band at 2003 cm^{-1} belongs to HXeH, but no conclusive assignments for this mode could be given. The anharmonic MP2 calculations predict the combination band of the symmetric and antisymmetric stretchings to have significant intensity, and we can assign the 2003 cm^{-1} band accordingly. This gives us an indirect measure of the IR-inactive symmetric stretch, which should be about 840 cm^{-1}. The derived wave number is much lower than predicted by any computational methods using the harmonic approach to calculate the vibrational frequencies.

The X–H stretching motion is an essential part of the vibrational calculation of the HXY molecules. For more strongly bound HXY molecules the MP2 vibrational calculations become better, but HXeH (as well as HXeSH) represents a borderline case and requires more-sophisticated computational approaches. In the course of our work, we have found that even the moderate MP2 calculations give reasonable qualitative results not only for the structures, charge separation, and vibrational frequencies but also for the high intensities of the X–H stretching absorptions. The calculated intensities for the Xe–H stretch in various molecules are shown also in Table II. For the strongly bound molecules like HXeCl and HXeBr, the MP2 calculations are good enough to reproduce the correct molecular properties and PES characteristics. Even though the computational vibrational frequencies are generally overestimated, the systematic trend among the present HXY molecules is correctly predicted. When a HXY molecule is strongly bound, the Xe–H bond distance is shorter, and this is reflected as a blue shift of the X–H stretching vibration. This is in accord with the experimental Xe–H wave numbers, which shift to higher values from the most weakly bound HXeSH to the most strongly bound HXeNC, as shown in Fig. 2, where the experimentally observed Xe–H stretching wave numbers are plotted against the calculated harmonic values. For comparison, the XeH^+ vibrational frequency in the gas phase has been reported at 2270 cm^{-1} (Ref. 78).

EXPERIMENTAL RESULTS

Formation of HKrY *and* HXeY *molecules*. The starting point for solid-state synthesis of the HXY molecules is to choose a hydrogen-containing precursor like H_2O, H_2S, hydrogen halides, HNCO, etc. The precursor molecule (HY) is

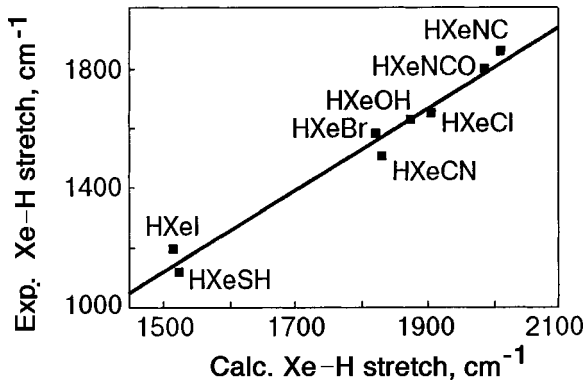

FIG. 2. Comparison of calculated (MP2) and experimental Xe–H stretching values for HXY molecules.

diluted with excess of krypton or xenon, and the mixture is trapped on a cold surface of an IR-transparent window. It is important that the precursor be as monomeric as possible, since precursor aggregation complicates the photochemistry, as has been shown, for example, in the case of hydrogen halides.[86] In order to promote the isolated precursor to a dissociative state, various light sources can be used. For hydrogen halides simple UV lamps are suitable, since the dissociation energies of these molecules are around 4 eV.[87] Additionally in the preparation of HXY molecules, excimer lasers (248, 193, and 157 nm) and tunable (down to 225 nm) radiation of an optical parametric oscillator have been used. The main objective of the photodecomposition process is to separate the H and Y fragment of the HY precursor. The extent of the mobility of the fragments during the primary photolysis, especially of the hot H atoms, will be addressed below.

Upon photolysis, neutral fragments H and Y are localized in a rare gas matrix. For example, in the cases of HI and HBr the presence of I and Br atoms is clearly evidenced by their spin–orbit ($^2P_{1/2} \leftarrow {}^2P_{3/2}$) absorptions at around 7600 and 3600 cm^{-1}, respectively.[61] Both the H atoms and Y fragments are stable below the mobilization temperature of hydrogen atoms (30–50 K). In very dilute matrices (M/A ratio$>$1000), it is possible to convert a major part of the precursor to H atoms and neutral Y fragments. In more concentrated matrices, other processes like clusterization and photoinduced reactions of hydrogen atoms produce more complicated products as well as hydrogen molecules.[61,88] The second step in the solid-state synthesis of HXY molecules is annealing of the photolyzed matrix to the point where the H atoms start to diffuse. Several separate experiments have shown that the diffusion occurs at around 30 and 40 K in solid Kr and Xe.[59,88–93] The diffusing H atoms eventually find a rare gas atom which has a fragment Y as a near neighbor, and the three fragments H, Y, and X react forming the HXY molecule. Reaction of two hydrogen atoms with a Xe atom between them produce HXeH. In the case of krypton, this last reaction has not been observed to occur, and also computationally the HKrH molecule is unstable. Most importantly, in solid Xe the HXeY and HXeH molecules seem to be the major trapping sites for H atoms and Y fragments in solid rare gases after mobilization of hydrogen atoms.[65]

A valuable observation was made concerning the formation of the HXeNCO molecule in HNCO photolysis in solid Xe.[68] The rare gas molecule was observed to form not only in the annealing but also directly in the photolysis of HNCO. The kinetics of HXeNCO was followed during 193 nm photolysis, and the HXeNCO molecule rises rapidly, reaches a maximum, and decreases eventually completely due to its own photodecomposition. The experiment was performed photolyzing HNCO using different wavelengths (225, 240, 250, 266 nm), but the formation of HXeNCO was observed to occur only under 193 nm irradiation. The maximum concentration of HXeNCO produced during photolysis was estimated to be about 0.4% from the initial concentration of the precursor HNCO. There are different alternatives for the mechanism of formation of HXeNCO: HXeNCO can be formed directly from HNCO/Xe in a photoisomerization process, or it can be formed from a hydrogen atom loosing its kinetic energy in the immediate vicinity of the NCO fragment. Nevertheless, once formed, the subsequent photodecomposition of HXeNCO provides much more kinetic energy to the H atom than the direct dissociation of the HNCO precursor at the same irradiation wavelength. Finally, it should be noted that HXeNCO can be decomposed by 405 nm irradiation, and it produces HNCO and H+NCO with a branching ratio of 70%/30%[68].

In general, the HXY molecules are easily detected by IR spectroscopy due to the extremely intensive X–H stretching absorptions,[56–60,62–64,68] and the position of the stretching band is very characteristic for each Y. In addition to the Xe–H absorption bands, other bands like combinations, overtones, and fundamental bands characteristic of the Y residue in the HXY molecules have been observed, and they are collected in Tables II and III, including the frequencies for the deuterated species also. A striking example of the sensitivity of the υ(Xe–H) absorption on the properties of the Y fragment is found by comparing the two isomers of HXeCN. For the lowest-energy isomer HXeCN the υ(Xe–H) absorption is at 1624 cm^{-1} and it shifts by +227 cm^{-1} to 1851 cm^{-1} for the higher energy species HXeNC.[59] In fact, this also measures the anisotropy of the CN fragment.

Several vibrational overtones and combinations have been reported for the HXY molecules (see Table II). For HXeI and HXeBr both the bending and the Xe–H stretching overtones show measurable intensities arising from anharmonic effects. The most striking effect is the enhanced intensity of the bending overtones compared with the fundamental bands for HXeBr and HXeI. For HXeCl, the bending overtone is predicted by anharmonic MP2 calculations to be of low intensity, and indeed, this vibration has not been observed experimentally. For the Xe–H stretching vibrations of HXeBr and HXeI, the first overtones are computationally rather weak compared with the fundamental modes, but they are still intensive enough to be observed experimentally.

The overtones of HXeI have played an important role in resolving the mechanism of formation of the HXY molecules.[58] The υ(Xe–H) frequency of HXeI is at 1193 cm^{-1}, 2υ(Xe–H) is at 2190 cm^{-1} and around energies 3υ(Xe–H) close shown to 3000 cm^{-1} the molecule decomposes.[58] This is shown schematically in Fig. 3. The HXeI infrared photodissociation experiment yields an ab-

TABLE III. The observed IR absorptions (in cm^{-1}) of different HXeY and HKrY compounds.

Compound	ν [X–H(D)]	δ [H–X–Y]	ν [X–Y]	ν [Y]
HXeCl	1648			
DXeCl	1198			
HXeBr	1504	489		
DXeBr	1100			
HXeI	1193	450	129[a]	
DXeI	893			
HXeCN	1624			
DXeCN	1178			
HXeNC	1851			2044 (νCN)
DXeNC	1339			
HXeNCO	1788			2148 (ν_{as}NCO)
DXeNCO	1299			2145 (ν_{as}NCO)
HXeOH	1578			
HXeOD	1572			
DXeOH	1149			
DXeOD	1141			
HXeSH(D)	1119			
DXeSH(D)	833			
HXeH	1166, 1181 (ν_{as})	701		
	840 (ν_{sym})[b]			
HXeD	1093 (νXe–H)	621		
	753 (νXe–D)			
DXeD	846, 856	514		
HKrCl	1476	544		
DKrCl	1106			
HKrCN	1497	618		
DKrCN	1109			

[a]Calculated from the difference between the $\nu_1+\nu_3$ combination band (1322 cm^{-1}) and the antisymmetric stretch (ν_3, 1193 cm^{-1}).
[b]Calculated from the difference between the $\nu_1+\nu_3$ combination band (2003 cm^{-1}) and the antisymmetric stretch (ν_3, 1166 cm^{-1}).

sorption profile for the $3v$(Xe–H) transition with an onset at 2950 cm^{-1}, which could be considered as an approximate value for the D_0 dissociation energy of HXeI. After the IR decomposition the molecular form can be restored by annealing at temperatures considerably below those needed for the global mobilization of H atoms in solid xenon. Therefore, the $3v$(Xe–H) excitation of HXeI produces atoms in close contact with each other, and HXeI can be recovered by slight warming or even at the lowest temperatures by tunneling, as

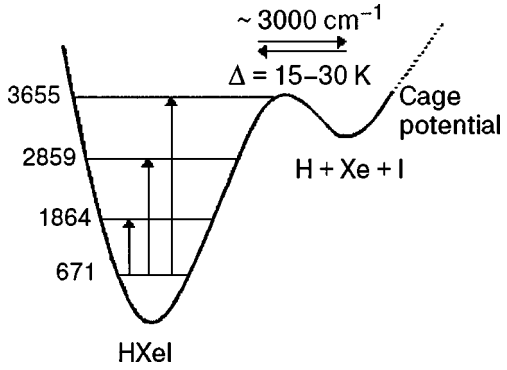

FIG. 3. Photodissociation upon IR irradiation and recombination upon annealing of HXeI.

pictured in Fig. 3. The increase of the spin–orbit absorption of iodine atoms at around 7600 cm^{-1} is correlated with the infrared-induced decrease of HXeI and vice versa.[58] The low energy of the infrared photons, which is insufficient to produce ionic centers in the matrix, indicates that the HXY molecules correlate with the neutral atom asymptote. Additional evidence for formation of HXY from neutral atoms is available from Feldman and coworkers.[91,92] These authors combined infrared and ESR-spectroscopic methods to study electron-irradiated xenon matrices containing various hydrocarbons, and they found that the decrease of hydrogen atoms correlated with the growth of HXeH. Adding electron scavengers which enhance ion formation decreased the yield of HXeH.[91,92]

We can also estimate the anharmonicity of the v(Xe–H) stretch from the experiments, and the derived anharmonicity constant ($\omega_e x_e$) is about 100 cm^{-1} in solid Xe.[94] This value has been used to calculate the energy levels of v(Xe–H) in HXeI, and they are marked accordingly in Fig. 3. The experimentally derived barrier height for the recombination of the neutral fragments to form HXeI is around 700 cm^{-1} (Ref. 58).

As mentioned above, one of the most weakly bound molecules HXeI dissociates already at $3v$(Xe–H) excitation. Besides this, the electronically excited states lead to decomposition of the HXY molecules. All HXY molecules decompose with visible or UV light, and the decomposition onsets vary from near IR to 350 nm. HXeH was found to be the most photostable member of this family, and it is rather long-lived under 400 nm irradiation. The electronic states involved in the photodecomposition of the HXY molecules are not known yet, but there exists a trend in the VIS-UV-stability of these molecules. For example, the onset of photodecomposition of the halogenated xenon hydrides is the following: HXeI dissociates at wavelengths below ~700 nm, HXeBr below ~450 nm, and the most stable of this series, HXeCl, requires wavelengths below ~350 nm.

Production of H *atoms in the photolysis of small hydrides in solid* Xe. The experimental preparation of the HXY hydrides is closely connected with the dynamics of H atoms in rare-gas solids, both during photolysis and annealing. A general description of these processes can be found in a recent review by Apkarian and Schwentner,[54] and we discuss below only some aspects of solid-state photolysis related to the present consideration. A number of experiments with

HXeY compounds allow us to estimate the absolute amount of H atoms generated under UV photolysis of an HY precursor in solid Xe. This consideration especially concerns light-induced travel distances of ''hot'' H atoms after photolysis and their losses via the two most evident reactions: $H+H\rightarrow H_2$ and $H+HY\rightarrow H_2+Y$. This approach allows us to distinguish the local and global primary photolysis events.

The UV photolysis of HI, HCN, and HNCO in Xe was studied, and the concentrations of I atoms, CN, or NCO radicals were measured by IR absorption spectroscopy.[58,59,68] It was found that annealing of the photolyzed matrices at 40–50 K decreases the concentration of I atoms, CN, or NCO radicals typically by about 40%, and this decrease was attributed to the formation of HXeI, HXeCN, and HXeNCO molecules. Furthermore, HXeH molecules were formed in annealing, consuming some part of the photogenerated H atoms. The results clearly indicate that the amount of H atoms after photolysis is comparable with the amount of the other dissociated part (I, CN, or NCO) and also with the amount of the photolyzed precursors. It follows that loss channels due to extensive mobility of H atoms do not play a major role during photolysis of HY precursors in monomeric matrices.

Ternary HI/CO/Xe matrix mixtures were prepared in order to estimate the lower limit of the H atom concentration produced in photolysis by monitoring the decrease of CO during annealing due to the reaction $H+CO\rightarrow HCO$.[69] A HI/CO/Xe=1/2/2000 matrix was extensively photolyzed at 310 nm. Upon annealing, the amount of HCO formed corresponded to ~15% of photolyzed HI, and HXeI and HXeH were formed with an efficiency similar to the case of CO-free matrices. During the photolysis, HCO appeared but its amount remained an order of magnitude smaller than the amount measured after annealing. Thus the proportion of H atoms consumed to HCO during the photolysis is about 1% despite the twice-higher CO concentration compared to that of HI. This observation indicates a low probability for the distant reaction of the hot H atom with CO or/and a short-distance travel of the H atoms. It is plausible that a similar inefficiency is also applicable to losses via the reactions $H+H\rightarrow H_2$ and $H+HY\rightarrow H_2+Y$.

Thus it can be concluded that losses of hot H atoms due to extensive light-induced travel in a low-temperature Xe lattice are quite minor. Moreover, the losses of H atoms during annealing seem to be essentially due to the formation of Xe-containing molecules. On the other hand, additional losses are evidenced by the gradual decrease of HXeI in multiple cycles of annealing and selective light-induced decomposition of HXeI,[69] and formation of H_2 molecules is the most probable process. In this respect, the diffusion-limited reactions of H atoms with HXeH and HXeY molecules should be taken into account.

As mentioned earlier, the losses of H atoms during UV photolysis should be connected with its light-induced travel distance. The experiments with rare-gas-containing molecules at various precursor concentrations support only very limited light-induced travel distances under UV photolysis in solid Xe. In this respect, the efficient generation of HXeI in low-temperature annealing (~30 K) of photolyzed HI/Xe matrices is an important observation.[69] The increase of HXeI during annealing is presented in Fig. 4. Two stages of annealing producing HXeI, around 28 and 40 K, be approximately distinguished and they should be qualitatively connected with local and global mobility of H atoms. Indeed, it is well established that the global mobility of H atoms in solid Xe starts at temperatures above 38 K.[92,93] On the basis of the efficient low-temperature formation of HXeI, we have suggested a quite local distribution of H atoms in the primary photolysis of HI in solid Xe.[69] In this model, the locally trapped H atoms can form HXeI via reacting with the parent I atom in the low-temperature annealing, similarly to the process discussed above for the IR decomposition of HXeI. Furthermore, the local distribution of H atoms generated in photolysis agrees with the absence of major losses of H atoms during primary photolysis. This conclusion of minor losses of H atoms *during photolysis* should be distinguished from the diffusion-controlled processes *during annealing* when H atoms move globally and may quite efficiently form H_2 molecules, as mentioned earlier.

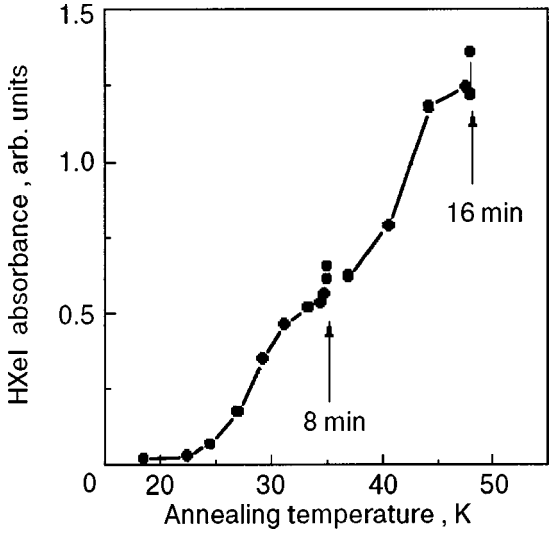

FIG. 4. The formation of HXeI molecules in annealing. The HI/Xe (1/2000) matrix was photolyzed at 310 nm. The annealing was performed with the 2 K/min rate. At temperatures 35 and 48 K the warming up was stopped for about 8 and 16 min in order to check the saturation of the reaction.

The experimental model of local photolysis agrees completely with the molecular dynamics simulations of 273 nm photolysis of HI in solid Xe.[95,96] These computations indicate that the photolysis of HI is a rather local process and the obtained trajectories lead to trapping of the H atom in the nearest interstitial sites. Eloranta *et al.*employed another approach in simulating the distribution of H atoms under photolysis in different rare-gas matrices.[97] In their study, an H atom was placed into a substitutional site of a perfect fcc lattice and provided with 2.5 eV of kinetic energy, and most of the resulting trapping position in solid Xe corresponded to the nearest interstitial site.

Experiments with HXeI molecules suggest the existence of hidden secondary processes during photolysis.[69] The proportion of HXeI forming in low-temperature annealing (<38 K) becomes smaller for longer irradiation times. Most importantly, this proportion decreases further with irradiation time even after *complete* decomposition of HI, approaching zero for very long irradiation. The HXeH/HXeI ratio measured

after annealing at 48 K increases with irradiation time, and it is influenced by the irradiation time after the complete decomposition of HI as well: it increases in prolonged photolysis. On the basis of these observations, it was concluded that H atoms could be driven from the parent cage not only in the preliminary decomposition of HI but also in some secondary processes involving other species. The first hidden process was suggested to be neutralization of Xe_2H^+, which provides kinetic energy for the H atom when the Xe atoms relax quickly from the perturbed (bound) configuration to their lattice positions. The mobile electrons providing the neutralization are photodetached from the Y^- fragments. The other proposed hidden process involves the HXeI potential surface: if an escaping H atom forms the HXeI intermediate, it can gain more kinetic energy in photodecomposition of the HXeI molecules. In consonance with the latter hypothesis, HXeNCO was found to form directly in photolysis of HNCO in solid Xe, as described earlier.[68] In the case of HI, no detectable amount of HXeI is observed in the photolysis of HI, most probably because of a very effective photodissociation of HXeI. Up to now, the computer simulations of the photolysis of HI in solid Xe do not include the molecular HXeI potential, and this neglect might be a severe oversimplification of the system, suggesting the need for a theoretical reinvestigation of the process.

Some controversial conclusions on the dynamics of small hydrides in rare gas solids can be found in literature. LaBrake *et al.* suggested a migration distance of ~10 nm for H atoms upon 193 nm photolysis of HBr in a Xe matrix, extensive losses of H atoms via the $H+HBr \rightarrow H_2+Br$ reaction, and a very small amount of H atoms generated in the photolysis.[88] The conclusions derived in Ref. 88 are based on the deviation of the LIF (laser-induced fluorescence) kinetics of photodissociative fragments from the simplest one-exponential form. Some support for such extensive losses was obtained by Eloranta *et al.*, who reported extremely low amounts of H atoms in UV photolysis of HBr and HCl in a Xe matrix based on the very weak EPR signals from H atoms.[97] In a more recent paper of their laboratory,[98] the possibility was suggested that the signal from H atoms trapped only in lattice substitutional sites was measured in Ref. 97.

The origin for the disagreement between the LIF and IR absorption estimates of the photoproduct concentrations in rare gas matrices can be explained by taking into account the evolution of matrix optical properties during photolysis. The problem with quantitative analysis of photolysis kinetics by using LIF measurements was explicitly demonstrated experimentally. For instance, in the 193 nm photolysis of HCN/Kr matrices, the 775 nm emission of CN clearly saturates faster than its IR absorption does (Fig. 5), and this saturation was explained by self-limitation of the photolysis.[63] Other related examples can be found elsewhere.[67] The observed disproportion evidently breaks the assumption of proportionality between the LIF signal and the product concentration used in Ref. 88, casting strong doubts about the numerical estimates of H-atom travel distance and losses during HBr photolysis in Xe.

In order to describe LIF kinetics properly, a number of factors should be considered, being extremely difficult to do

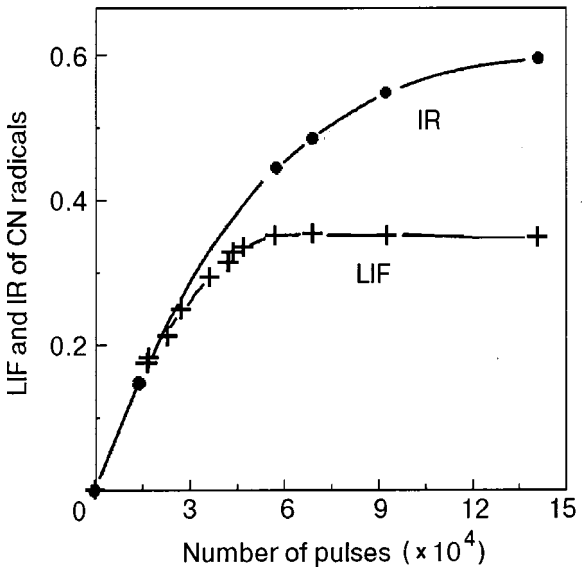

FIG. 5. The LIF and IR absorption kinetics of CN during 193 nm photolysis of a HCN/Kr matrix at 7.5 K. The last data point corresponds to decomposition of 65% of HCN.

in practice. First, rare gas solids often cannot be regarded as optically thin, and the depletion of the excitation field during its penetration into the matrix layer plays an important role in quantitative kinetic studies.[63,67,99–101] If a sample contains a sufficient number of precursor molecules, photogenerated new species can essentially absorb the photolysis radiation and hence decrease strongly the photolysis efficiency for deeper matrix layers. Hence the *in situ*-detected LIF signal of the photogenerated species saturates faster than their averaged concentration does.[63] This effect was also qualitatively discussed by Gödderz *et al.*[102]

The second factor strongly influencing LIF kinetics is introduced by photogenerated species that are capable strongly of absorbing the detected emission. This process can strongly alter the detected LIF spectra from different matrix depths, thereby introducing an additional error between the LIF and true kinetics. One example of rising absorbers is provided by a charge-transfer mechanism known for species like oxygen, iodine, etc. in rare gas solids.[99,100,103] The extraordinary disappearance of one emission band in the NO progression generated in the 193 nm photolysis of HNCO/Xe matrices was explained by considering charge-transfer absorption.[67]

Finally, Rayleigh scattering enhances the two above-mentioned mechanisms because it increases the path length of radiation in the sample and limits penetration of the radiation into the deeper matrix layers even if the matrix absorption is rather weak. Even alone, Rayleigh scattering destroys the ideal one-exponential photolysis kinetics for concentration due to spatial redistribution of the radiation intensity.[63]

Intrinsic properties. Until recently, the HXY molecules have been prepared in solid rare gases, mainly Kr and Xe. Since the molecules are strongly polar, there arises the question of their intrinsic stability and of the stabilization effect of the polarizable hosts. To address this question of intrinsic stability, photolysis of HBr and HCl in Xe-doped neon matrices was performed.[104] Quite surprisingly, even at very high dilution, mobilization of H atoms in Ne at ~9–10 K resulted

in new absorptions at wave numbers similar to the υ(Xe–H) of HXeBr and HXeCl in pure Xe matrices. These absorptions showed proper deuteration shifts for HXeBr and HXeCl, and the species responsible could be photodecomposed similarly to HXeBr and HXeCl in Xe. Based on these facts the forming molecules were identified as HXeBr and HXeCl in a Ne surrounding. This result shows experimentally the intrinsic stability of the HXY species, supporting the computational results, and suggest their existence in the gas phase as well. The υ(Xe–H) wave numbers of HXeCl and HXeBr in solid Ne are shifted about 50 cm^{-1} downwards from the values reported in Xe.[56] This shift can be considered to measure the stabilization effect of the solid Xe environment.

CONCLUSIONS

The solid-state photochemical production of several Kr and Xe hydrides has been described, and the IR spectra of these molecules has been given. For aiding the experimental interpretation, extensive *ab initio* calculations have been performed. Computationally, the formation of these hydrides decreases the Rg–H distance, for example, by more than a factor of two from its van der Waals value.

These HKrY and HXeY molecules possess both covalent and ionic contributions to the bonding, and their dipole moments are quite large. The extensive charge-transfer nature of these molecules is evidenced also by the strong Rg-H stretching vibrations both computationally and experimentally. These hydrides are produced in low-temperature matrices by photodissociation of a hydrogen-containing precursor and thermal mobilization of the photodetached hydrogen atom. The estimated dissociation energies vary from 0.4 to 1.4 eV and warrant observation of these molecules in the gas phase as well.

The photolysis of small hydrides in solid Xe seems to be a quite local process, and losses of H atoms play a minor role. The controversial estimates of the light-induced travel distances can originate from an improper treatment of LIF data. The effects of matrix optics become more important for shorter photolysis/LIF wavelengths due to Rayleigh scattering, and in particular they might be deeply problematic in vacuum UV experiments. As a qualitative conclusion of practical importance for matrix-isolation studies, matrix optics should be taken into account while extracting numerical dissociation parameters from LIF kinetics. In fact, FTIR measurements provide more-reliable data for such a quantitative analysis.

*E-mail: Markku.Rasanen@helsinki.fi

[1] L. Pauling, J. Am. Chem. Soc. **55**, 1895 (1933).
[2] N. Bartlett, Proc. Chem. Soc. **218**, (1962).
[3] F. O. Sladky, P. A. Bulliner, and N. Bartlett, J. Chem. Soc. A **2179**, (1969).
[4] R. Hoppe, W. Dähne, H. Mattauch, and K. H. Rödder, Angew. Chem. **74**, 903 (1962).
[5] H. H. Classen, H. Selig, and J. G. Malm, J. Am. Chem. Soc. **84**, 3593 (1962).
[6] J. R. Morten and W. E. Falconer, J. Chem. Phys. **39**, 427 (1963).
[7] E. Tommila, Suomen Kemistilehti A **36**, 209 (1963).
[8] J. G. Malm, H. Selig, J. Jortner, and S. A. Rice, Chem. Rev. **65**, 199 (1965).
[9] F. O. Sladky, P. A. Bulliner, N. Bartlett, B. G. DeBoer, and A. Zankin, Chem. Commun. (London), 1048 (1968).
[10] V. M. McRae, R. D. Peacock, and D. R. Russell, Chem. Commun. (London), 62 (1969).
[11] J. H. Holloway and J. G. Knowles, J. Chem. Soc. A, 756 (1969).
[12] N. Bartlett, M. Gennis, D. D. Gibler, B. K. Morrell, and A. Zalkin, Inorg. Chem. **12**, 1717 (1973).
[13] D. E. McKee, C. J. Adams, and N. Bartlett, Inorg. Chem. **12**, 1722 (1973).
[14] N. Bartlett and F. O. Sladky, *Comprehensive Inorganic Chemistry*, Vol. 3 (Pergamon Press, New York, 1973), p. 213.
[15] K. Seppelt and D. Lentz, Prog. Inorg. Chem. **29**, 167 (1982).
[16] J. H. Holloway, J. Fluorine Chem. **33**, 149 (1986).
[17] C. A. Coulson, J. Chem. Soc., 1442 (1964).
[18] R. D. LeBlond and D. D. DesMarteau, J. Chem. Soc. Chem. Commun., 555 (1974).
[19] D. D. DesMarteau, J. Am. Chem. Soc. **100**, 6270 (1978).
[20] D. D. DesMarteau, R. D. LeBlond, S. F. Hossain, and D. Nothe, J. Am. Chem. Soc. **103**, 7734 (1981).
[21] A. A. A. Emara and G. J. Schrobilgen, J. Chem. Soc. Chem. Commun., 1644 (1987).
[22] A. A. A. Emara and G. J. Schrobilgen, J. Chem. Soc. Chem. Commun., 257 (1988).
[23] G. J. Schrobilgen, J. Chem. Soc. Chem. Commun., 1506 (1988).
[24] J. Foropopoulos Jr. and D. D. DesMarteau, J. Am. Chem. Soc. **104**, 4260 (1982).
[25] J. F. Sawyer, G. J. Schrobilgen, and S. J. Sutherland, Inorg. Chem. **21**, 4064 (1982).
[26] G. A. Schumacher and G. J. Schrobilgen, Inorg. Chem. **22**, 2178 (1983).
[27] R. Faggiani, D. K. Kennepohl, C. J. L. Lock, and G. J. Schrobilgen, Inorg. Chem. **25**, 563 (1986).
[28] M. Wechsberg, P. A. Bulliner, F. O. Sladky, R. Mews, and N. Bartlett, Inorg. Chem. **11**, 3063 (1972).
[29] L. J. Turbini, R. E. Aikman, and R. J. Lagow, J. Am. Chem. Soc. **101**, 5833 (1979).
[30] D. Naumann and W. Tyrra, J. Chem. Soc. Chem. Commun., 47 (1989).
[31] V. V. Zhdankin, P. J. Stang, and N. S. Zefirov, J. Chem. Soc. Chem. Commun., 578 (1992).
[32] D. Naumann, W. Tyrra, R. Gnann, D. Pfolk, T. Gilles, and K. F. Tebbe, Z. Anorg. Allg. Chem. **623**, 1821 (1997).
[33] H. J. Frohn, N. LeBlond, K. Lutar, and B. Zemva, Angew. Chem. Int. Ed. Engl. **39**, 391 (2000).
[34] J. H. Holloway and E. G. Hope, in *Advances in Inorganic Chemistry*, Vol. 46 (Academic Press, London, 1999), p. 51.
[35] J. J. Turner and G. C. Pimentel, Science **140**, 975 (1963).
[36] D. R. MacKenzie, Science **141**, 1171 (1963).
[37] W. F. Howard and L. Andrews, J. Am. Chem. Soc. **96**, 7864 (1974).
[38] A. V. Grosse, A. D. Kirschenbaum, A. G. Streng, and L. V. Streng, Science **139**, 1047 (1963).
[39] G. J. Schrobilgen, J. Chem. Soc. Chem. Commun., 863 (1988).
[40] J. C. P. Sanders and G. J. Schrobilgen, J. Chem. Soc. Chem. Commun., 1576 (1989).
[41] R. J. Gillespie and G. J. Schrobilgen, Inorg. Chem. **15**, 22 (1976).
[42] G. J. Schrobilgen, J. Chem. Soc. Chem. Commun., 1506 (1988).
[43] G. Frenking and D. Cremer, in *Structure and Bonding, Noble Gas and High Temperature Chemistry*, edited by M. J. Clarke *et al.* (Springer, Berlin, 1990), p. 17.
[44] G. J. Schrobilgen, in *Synthetic Fluorine Chemistry*, edited by G. A. Olah, R. D. Chambers, and G. K. Surya Prakash (John Wiley and Sons, New York, 1992).
[45] I. Last and T. F. George, in *Clsuter Ions*, C. Y. Ng, T. Baer, and I. Powis (Eds.), John Wiley and Sons, New York (1993) and References therein.
[46] M. Beyer, E. V. Savchenko, G. Niedner-Schatteburg, and V. E. Bondybey, J. Chem. Phys. **110**, 11910 (1999).
[47] P. Pyykkö, Eur. J. Chem. (2000) (in press).
[48] E. Whittle, D. A. Dows, and G. C. Pimentel, J. Chem. Phys. **22**, 1943 (1954).
[49] I. Norman and G. O. Porter, Nature (London) **174**, 508 (1954).
[50] H. Broida and J. R. Pellam, Phys. Rev. **95**, 845 (1954).
[51] L. Y. Nelson and G. C. Pimentel, Inorg. Chem. **6**, 1758 (1967).
[52] V. E. Bondybey, Doctoral Thesis, Univ. of California (1971).
[53] C. T. Goetschel and K. R. Loos, J. Am. Chem. Soc. **94**, 3018 (1972).
[54] V. A. Apkarian and N. Schwentner, Chem. Rev. **99**, 1481 (1999).
[55] V. E. Bondybey, M. Räsänen, and A. Lammers, Annu. Rev. Genet. C **95**, 331 (1999).
[56] M. Pettersson, J. Lundell, and M. Räsänen, J. Chem. Phys. **102**, 6423 (1995).

[57] M. Pettersson, J. Lundell, and M. Räsänen, J. Chem. Phys. **103**, 205 (1995).
[58] M. Pettersson, J. Nieminen, L. Khriachtchev, and M. Räsänen, J. Chem. Phys. **107**, 8423 (1997).
[59] M. Pettersson, J. Lundell, L. Khriachtchev, and M. Räsänen, J. Chem. Phys. **109**, 618 (1998).
[60] M. Pettersson, J. Lundell, L. Khriachtchev, E. Isoniemi, and M. Räsänen, J. Am. Chem. Soc., 7979 (1998).
[61] M. Pettersson and J. Nieminen, Chem. Phys. Lett. **283**, 1 (1997).
[62] M. Pettersson, Doctoral Thesis, University of Helsinki (1998).
[63] L. Khriachtchev, M. Pettersson, and M. Räsänen, Chem. Phys. Lett. **288**, 727 (1998).
[64] M. Pettersson, L. Khriachtchev, J. Lundell, and M. Räsänen, J. Am. Chem. Soc. **121**, 11904 (1999).
[65] M. Pettersson, J. Lundell, and M. Räsänen, Eur. J. Inorg. Chem., 729 (1999).
[66] L. Khriachtchev, M. Pettersson, S. Pehkonen, E. Isoniemi, and M. Räsänen, J. Chem. Phys. **111**, 1650 (1999).
[67] L. Khriachtchev, M. Pettersson, S. Jolkkonen, and M. Räsänen, Chem. Phys. Lett. **316**, 115 (2000).
[68] M. Pettersson, L. Khriachtchev, J. Lundell, S. Jolkkonen, and M. Räsänen, J. Phys. Chem. A **104**, 3579 (2000).
[69] M. Pettersson, L. Khriachtchev, J.-R. Roozeman, and M. Räsänen, Chem. Phys. Lett. **323**, 506 (2000).
[70] N. Runeberg, M. Seth, and P. Pyykkö, Chem. Phys. Lett. **246**, 239 (1995).
[71] N. Runeberg, Doctoral Thesis, University of Helsinki (1996).
[72] R. W. Bickes Jr., B. Lantzsch, J. P. Toennies, and K. Walaschewski, Faraday Discuss. Chem. Soc. **55**, 167 (1973).
[73] W. C. Lane, T. H. Edwards, J. R. Gillis, E. S. Bonomo, and F. J. Murcray, J. Mol. Spectrosc. **95**, 365 (1982).
[74] J. Lundell, M. Pettersson, and M. Räsänen, Computers and Chemistry **24**, 325 (2000).
[75] N. Franks and W. R. Lieb, Nature (London) **367**, 607 (1994).
[76] N. Bartlett, M. Wechsberg, G. R. Jones, and R. D. Burbank, Inorg. Chem. **11**, 1124 (1972).
[77] I. Last and T. F. George, J. Chem. Phys. **89**, 3071 (1988).
[78] J. W. C. Johns, J. Mol. Spectrosc. **106**, 124 (1984).
[79] H. E. Warner, W. T. Connor, and R. C. Woods, J. Chem. Phys. **81**, 5413 (1984).
[80] R. Klein and P. Rosmus, Z. Naturforsch. Teil A **39**, 349 (1984).
[81] K. A. Peterson, R. H. Petrmichl, R. L. McClain, and R. C. Woods, J. Chem. Phys. **95**, 2352 (1991).
[82] S. A. Rogers, C. R. Brazier, and P. F. Bernath, J. Chem. Phys. **87**, 159 (1987).
[83] S. Berski, B. Silvi, J. Lundell, S. Noury, and Z. Latajka, in *Progress in Theoretical Chemistry and Physics*, C. Minot *et al*. (Eds.), Kluwer, Amsterdam (2000) (in press).
[84] M. Johansson, M. Hotokka, M. Pettersson, and M. Räsänen, Chem. Phys. **244**, 25 (1999).
[85] J. Lundell, G. M. Chaban, and R. B. Gerber, J. Phys. Chem. B **404**, (2000) (in press).
[86] M. Lorenz, D. Kraus, M. Räsänen, and V. E. Bondybey, J. Chem. Phys. **112**, 3803 (2000).
[87] H. Okabe, *Photochemistry of Small Molecules* (Wiley, New York, 1978).
[88] D. LaBrake, E. T. Ryan, and E. Weitz, J. Chem. Phys. **102**, 4112 (1995).
[89] H. Muto, K. Nunome, and M. Iwasaki, J. Phys. Chem. **84**, 3402 (1980).
[90] D. LaBrake and E. Weitz, Chem. Phys. Lett. **211**, 430 (1993).
[91] V. I. Feldman and F. F. Sukhov, Chem. Phys. Lett. **255**, 425 (1996).
[92] V. I. Feldman, F. F. Sukhov, and A. Yu. Orlov, Chem. Phys. Lett. **280**, 507 (1997).
[93] J. Eberlein and M. Creutzburg, J. Chem. Phys. **106**, 2188 (1997).
[94] J. Lundell, M. Pettersson, L. Khriachtchev, M. Räsänen, G. M. Chaban, and R. B. Gerber, Chem. Phys. Lett. **322**, 389 (2000).
[95] R. Alimi, R. B. Gerber, and V. A. Apkarian, J. Chem. Phys. **89**, 174 (1988).
[96] R. Alimi and R. B. Gerber, Chem. Phys. Lett. **173**, 393 (1990).
[97] J. Eloranta, K. Vaskonen, and H. Kunttu, J. Chem. Phys. **110**, 7917 (1999).
[98] T. Kiljunen, J. Eloranta, and H. Kunttu, J. Chem. Phys. **110**, 11814 (1999).
[99] M. E. Fajardo and V. A. Apkarian, J. Chem. Phys. **85**, 5660 (1986).
[100] M. E. Fajardo and V. A. Apkarian, J. Chem. Phys. **89**, 4102 (1988).
[101] J. R. Sheats, J. J. Diamond, and J. M. Smith, J. Phys. Chem. **92**, 4922 (1988).
[102] K. H. Godderz, N. Schwentner, and M. Chergui, J. Chem. Phys. **105**, 451 (1996).
[103] W. G. Lawrence and V. A. Apkarian, J. Chem. Phys. **97**, 2229 (1992).
[104] M. Lorenz, M. Räsänen, and V. E. Bondybey, J. Phys. Chem. A **104**, 3770 (2000).

This article was published in English in the original Russian journal. Reproduced here with stylistic changes by the Translation Consultant.

EXAFS studies of the trapping site structure for molecules isolated in cryogenic matrices

P. Roubin and S. Varin

P2IM, Université de Provence, Centre Saint-Jérôme, 13 397 Marseille cedex 20, France

C. Crépin

LPPM, Bât 213, Centre Universitaire Paris-Sud, 91 898 Orsay cedex, France

B. Gauthier-Roy

LPMA, Université P. et M. Curie, 4 Place Jussieu, 75 252 Paris cedex 05, France

A.-M. Flank, P. Lagarde, and F. Ténégal

Lure, Bât 209D, Centre Universitaire Paris-Sud, 91 898 Orsay cedex, France
(Submitted May 11, 2000)
Fiz. Nizk. Temp. **26**, 937–946 (September–October 2000)

We present here results concerning the first attempt of determining the trapping site structure of molecules isolated in inert matrices at low temperature by the EXAFS (Extended X-ray Absorption Fine Structure) method. The experiments have been performed at the *K* edge of argon, silicon, sulfur, and chlorine for pure solid argon, and for SiH_4, OCS, and HCl isolated in different cryogenic matrices. The EXAFS technique is sensitive to the local environment around the absorbing atom, and the spectral features induced by the matrix material (Ar, Xe, N_2, and CH_4) are clearly evidenced here. The data allow a characterization of the double substitutional site for OCS in argon and xenon, while no structure can be determined for the accommodation of SiH_4 in argon. A discussion of the best choice for the guest/host system to obtain a good EXAFS signal is included.
[S1063-777X(00)01009-4]

1. INTRODUCTION

Isolating molecules in cryogenic and inert matrices usually leads to simplified spectra because of the absence of a rotational structure, but these spectra often show fingerprints due to the weak interaction existing with the solvent. The question then arising is about the nature of the trapping cage. Generally, using spectroscopic methods is not straightforward for obtaining a direct comparison between a calculated structure and the experimental observations. Other techniques as x rays or neutron diffraction are more suitable to get structural information directly, but these methods are sensitive to the long-range order in the matrix rather than to the local environment around the molecular impurity.[1–3]

X-ray absorption is another way to obtain structural information about the environment: as a matter of fact, the x-ray absorption spectra are deeply modified when going from the gas phase to the condensed phase and are sensitive to the nearest neighbors surrounding the absorbing atom. The low-frequency part of the spectrum is called XANES (X-ray Absorption Near-Edge Structure) and contains information about the electronic structure, while the high-frequency part of the spectrum is called EXAFS (Extended X-ray Absorption Fine Structure) and gives directly the distances between the absorbing atom and its neighbors. We will present in part 2 an introduction to the basics concerning the way to obtain the structural information by this latter method.

Previous EXAFS experiments concerning species isolated in matrices have focused on the study of the species structure itself. In some of these studies,[4,5] a distance related to the matrix cage has also been measured. The only work fully devoted to cryogenic inert matrix structure concerns different rare gas and nitrogen matrices.[6] The authors performed EXAFS measurements on solid xenon, krypton, argon and on mixed rare gas matrices, at the *K* edge of Ar (3203 eV) and Kr (14 330 eV) and at the L_3 edge of Xe (4782 eV). They were able to compare the miscibility of xenon and krypton in argon, neon, and nitrogen matrices, and they measured a Kr-Ar distance of 3.82 Å for diluted Kr in Ar, intermediate between the pure argon and the pure krypton ones, and close to the free ArKr molecule value.

The experiments presented in this paper are the first attempt of characterizing the environment of a molecule trapped in a cryogenic medium by the EXAFS technique. We will review here the results obtained for molecules (OCS, SiH_4 and HCl) in rare gas, nitrogen and methane matrices, excited at the *K* edge of an atom belonging to the molecule (S, Si and Cl). Up to now, we have obtained both qualitative and quantitative results, and we will point out the main criteria to be considered in order to get the most advantage out of this kind of experiments.

2. INTRODUCTION TO THE BASICS OF X-RAY ABSORPTION IN THE CONDENSED PHASE

Figure 1a shows the x-ray absorption spectrum of argon in the gas phase[7] (μ_0) and in the solid phase (μ). This last

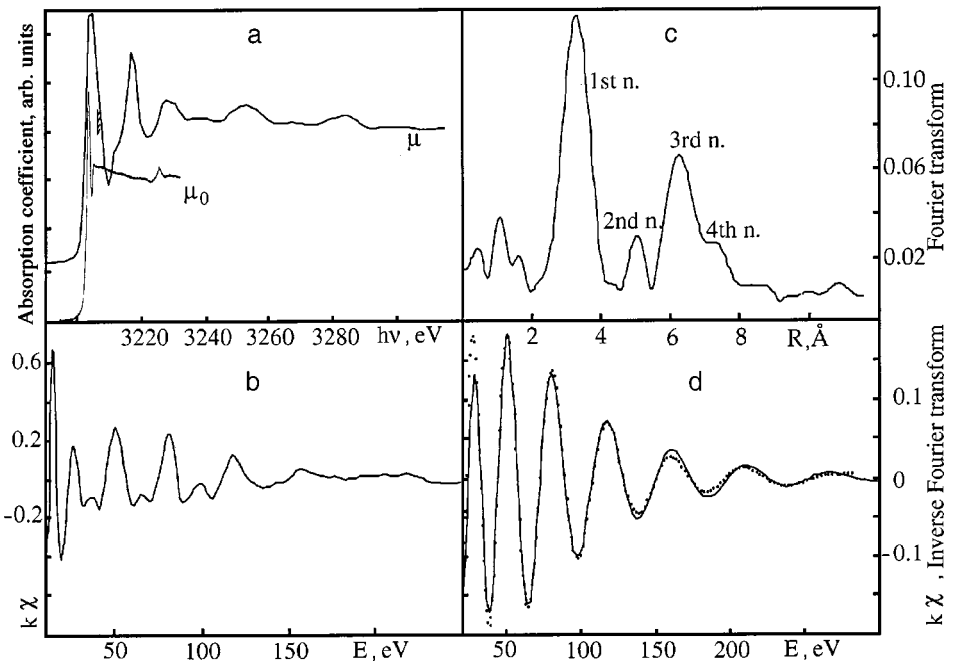

FIG. 1. X-ray absorption at the *K* edge of solid argon. (a) Solid argon (μ); gas phase[7] (μ_0); the hatched lines indicate the ionization limit; (b) EXAFS oscillations ($k\chi$) as a function of the photoelectron kinetic energy; (c) Fourier transform of the EXAFS oscillations; (d) inverse Fourier transform of the first-neighbor peak: the dots correspond to the experimental data and the continuous line corresponds to a fit with the electronic parameters given by the FEFF code.

spectrum has been obtained by us and is in good agreement with previously published results.[8] It is recorded as a function of the photon energy $h\nu$ for the excitation of an electron belonging to the *K* shell ($n=1$) of the argon atom at energy $E_0 \approx 3202$ eV.

The first intense line of the gas phase spectrum is due to the absorption towards the $4p$ Rydberg state ($1s \rightarrow 4p$ dipole-allowed transition), the weaker structure at about 2 eV from the first line is due to the next $1s \rightarrow 5p$ transition.[7,9] Above the ionization limit (indicated by the hatched lines), the absorption cross section decreases monotonically. Note that the peak at 3225 eV is due to multielectronic effects.[7,10] On the contrary, for the solid phase, the spectrum contains additional oscillations, which are due to the structure of the nearest neighbor of the absorbing atom. This oscillatory structure is characteristic of solids, liquids, or molecular gases, and its theory was originally proposed by Krönig in 1931.[11] It was only worked out in detail after 1974 with the works of Stern *et al.*,[12] Lee and Pendry,[13] and Ashley and Doniach.[14] At the same time, it became a very fruitful and powerful experimental tool with the development of synchrotron radiation. We will present here the main ideas for the understanding of these experiments (for more details, see, for example, Refs. 15 and 16).

For a photon energy well above the absorption edge the ejected electron possesses a kinetic energy *E* which is approximately equal to $h\nu - E_0$. This energy is large compared with its interaction energy with the surrounding atoms, and the photoelectron can be modeled by a free outgoing wave. This wave is scattered by the neighboring potentials and, as a result, the final state is the superposition of the outgoing and scattered waves (Fig. 2). Single scattering—i.e., scattering by only one atom—is a first-order process and is generally the most important. The absorption cross section is proportional to the square of the usual dipolar matrix element $M_{if} = |\langle \psi_i | H | \psi_f \rangle|$, where ψ_i is the initial-state wave function, corresponding to the electron in the atomic core of the central atom, and ψ_f is the final-state wave function, corresponding to the propagating photoelectron. The matrix element is nonzero only in the region where the core state is nonzero—that is, on the absorbing atom. It is thus only necessary to determine the final wave function at the center of the absorbing atom. The optical path length contributing to the phase shift between the outgoing and the backscattered waves is then $2kR$, *R* being the distance between the central atom and its scattering neighbor and *k* the photoelectron wave vector. *k* is given in a first rough approximation by the following formula: $\hbar^2 k^2 / 2m = h\nu - E_0$, where *m* is the mass of the electron. The waves will add or subtract depending on the photoelectron energy, and this will give rise to the EXAFS oscillations. The EXAFS spectrum is defined by $\chi = (\mu - \mu_0)/\mu_0$ and is obtained here after fitting the atomic ab-

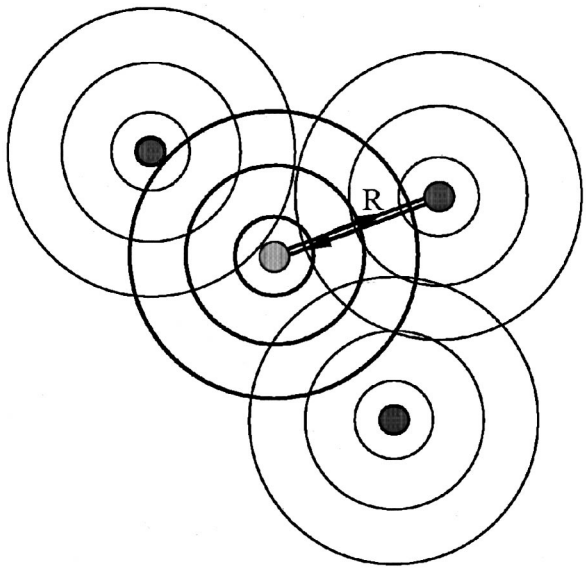

FIG. 2. Schematic of the EXAFS interferences: the bold circles represent the electronic direct outgoing wave (wave number *k*) coming from the absorbing atom which interferes with the different scattered waves coming from its neighbors. The corresponding optical phase shift is $2kR$.

sorption μ_0 by a polynomial function of degree 3 and normalizing the data by the Lengeler–Eisenberger method.[17] The qualitative picture given above can be directly translated into an expression for χ, and the formula obtained is

$$\chi = \sum_i \frac{F_i(k)}{kR_i^2} \sin(2kR_i + \phi_i) \times \exp(-2R_i/\lambda)\exp(-2k^2\sigma_i^2),$$

where i designates the different neighbors of the central atom at distance R_i; F_i is the backscattering amplitude due to atom i, and ϕ_i contains the different phase shifts undergone by the electronic wave during first, its passage through the central atom (δ_1), second, to its back-scattering (φ_i), and finally to its passage through the central atom, so that $\phi_i = 2\delta_1 + \varphi_i$; λ designates the electronic mean free path (a few Å), and the term $\exp(-2R_i/\lambda)$ phenomenologically takes into account the decoherence of the outgoing and the scattered waves due to both the core and the photoelectron lifetimes. It represents the probability that the electron travels to the backscattering atom and returns without scattering or the core hole being filled. λ contributes to the weakness of the far neighbor contribution in the EXAFS signal and is a function of k. Oscillations are also damped as a function of k by the thermal disorder: noncorrelated movements of the central and the scattering atoms lead to a spreading of the instantaneous values of R_i, which can be modeled, for a low disorder and for a Gaussian distribution of the distances, by a factor of $\exp(-2k^2\sigma_i^2)$, analogous to the Debye–Waller factor in diffraction experiments. σ_i^2 is the relative mean-square variation of the interatomic distance R_i and can be approximated by the Debye model.[18] The introduction of a larger factor than that expected by thermal fluctuations may be necessary in order to fit the experimental damping, and this reveals the existence of some additional static disorder.

The experimental spectrum χ is often weighted by k in order to give more importance to its high-frequency part, and Fig. 1b shows the EXAFS spectrum $k\chi$ corresponding to the absorption of solid argon plotted in Fig. 1a. In the following, we will plot $(k\chi)$ as a function of E and, when necessary, the spectra will be offset for clarity. Figure 1c shows the Fourier transform corresponding to the EXAFS data of Fig. 1b. A Kaiser window going from 2.1 to 8.7 $Å^{-1}$ (17 to 290 eV) has been used to calculate this Fourier transform. The different peaks emerging in Fig. 1c at 3.3, 5.0, 6.2, and 7.2 Å correspond to the first, second, third, and fourth shells of the argon atom's nearest neighbors and are very similar to previous results.[8] Remember that it is necessary to take into account the phase shift ϕ_i in order to get the actual distances in the crystal.

According to the EXAFS formula, knowledge of electronic parameters such as F_i, ϕ_i, and λ allows one to obtain structural parameters such as R_i, σ_i^2, and the number of neighbors. One way to obtain these electronic parameters is to calculate them by the FEFF code.[19] This code gives the contributions of both the single- and multiple-scattering processes by investigating all the different scattering paths. It then calculates their corresponding effective amplitude (F_{eff}, from which FEFF takes its name) and effective phase shift (ϕ_{eff}), so that the total EXAFS spectrum can be readily obtained by adding all their contributions with the simple formula mentioned above. In the case of molecular species isolated in matrices, we are mainly interested in the intermolecular scattering, but we have to remember that this contribution will add with the intramolecular one. We always took into account in the simulated EXAFS spectra all the single- and multiple-scattering paths whose length were less than 8 Å and contributing more than 2.5%. In the simulations concerning isolated molecules in argon or xenon, we used the Debye–Waller factor given by the FEFF program for a temperature of 15 K, with a Debye temperature of 92 K for argon and 64 K for xenon. All the simulations presented in this paper were done with the FEFF6 version of the code.

Figure 1d shows the fit of the inverse Fourier transform of the first-neighbor peak of Fig. 1c with the amplitude and phase shift calculated by the FEFF program. A σ^2 factor of 0.024 $Å^2$ and a distance of 3.75(1) Å are obtained for this fit. This last value is in good agreement with previous determinations[6,8] and gives an indication of the validity of the phase shift as determined by the FEFF code. Let us recall here that the nearest neighbor distance in argon (respectively, xenon) is 3.76 (4.34) Å at 20 K.

3. EXPERIMENTAL

When studying isolated molecules, the signal was recorded in a fluorescence mode, while for pure argon it was in a transmission mode. The first method allows a selective detection of the signal due to the absorbing molecule and is thus more efficient for dilute samples. The gas mixture was deposited onto an Al foil stuck with silver paste on the cold finger of a He-cooled cryostat. The mixture was prepared outside the vacuum cell and introduced through a tube opening at about 2 cm in front of the cold sample holder at a rate of about 20 μmol/min, so that the deposition conditions were similar to the usual ones. The concentration was 1:100 and the temperature was about 15 K during all the experiments. The thickness of the film was a few microns, as can be estimated by the observation of visible interference fringes during the deposition. The basic pressure in the cell was 10^{-8} Torr, and the pressure was increased to 10^{-5} Torr during the deposition.

The photoabsorption measurements were carried out at the Laboratoire pour l'Utilisation du Rayonnement Electromagnetique (LURE-Orsay) on the SA32 beamline equipped with a double-crystal [InSb (111)] monochromator, which allows an energy resolution ranging from about 0.7 eV for a photon energy of 1800 eV to about 1.4 eV at 3500 eV. The SuperACO storage ring was operating at 800 MeV, with a typical current of 200 mA. The incident beam was monitored by measuring the total electron drain current of a polyurethane foil covered by 80 nm of Ti, located downstream the monochromator. The focused spot on the sample was about 500 μm horizontally and 300 μm vertically. The energy calibration was performed by taking the K edge of a sample of ZnS at 2472 eV. The absorption spectra at the K edge of silicon (1839 eV), sulfur (2472 eV), chlorine (2833 eV), and argon (3206 eV) were collected in the fluorescence mode as a function of the incident photon energy with a 1 eV step. We recorded several scans for each sample, so that the total collecting time for one point ranged from 10 to 20 s. The

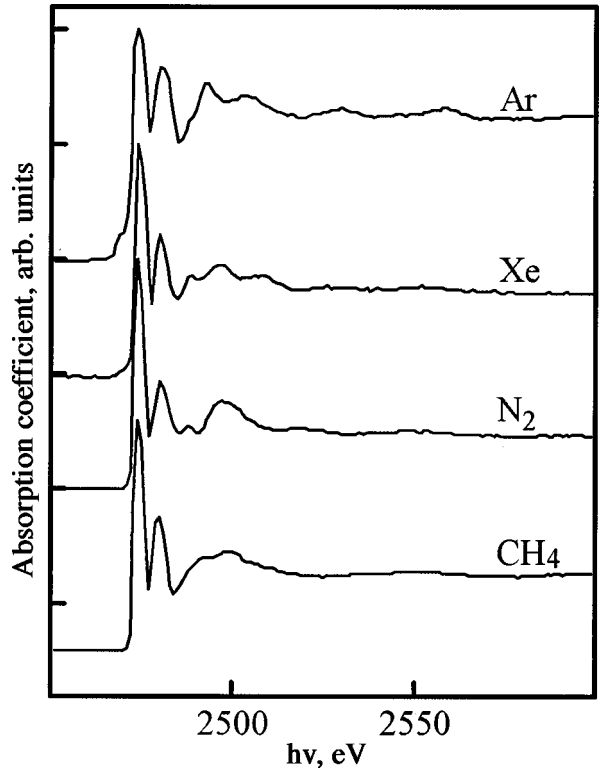

FIG. 3. X-ray absorption spectra at the *K* edge of *S* for OCS isolated in argon, xenon, nitrogen, and methane matrices. The fluorescence signals have been normalized to unity at the maximum of the first line.

fluorescence yield was measured at 90° from the incident x-ray beam by a seven-element Ge detector (Eurisys-Mesures) for the $K_{\alpha_1}/K_{\alpha_2}$ lines, with an energy resolution better than 150 eV. In the case of pure solid argon, the setup was different and the direct absorption spectrum through argon deposited onto a thin Al foil was recorded with a silicon diode detector.

4. RESULTS AND DISCUSSION

4.1. Probing the host material: OCS isolated in argon, xenon, nitrogen, and methane matrices

Figure 3 shows the absorption coefficient μ displayed as a function of the photon energy from 2450 to 2600 eV at the *K* edge of the sulfur atom in the case of argon, xenon, nitrogen, and methane matrices. The pre-edge contribution has been subtracted for each spectrum after its fit by a linear regression, except for xenon. For this last case the signal was much weaker than for the other cases, because the absorption of the fluorescent photons by the matrix itself reduces their escape depth. Such a low-level signal frequently induces a perturbed profile for the data: in order to correct it on this figure, we have subtracted a fit of all the data above the edge by a polynomial function of degree two.

The corresponding EXAFS spectra ($k\chi = k(\mu - \mu_0/\mu_0)$) are displayed in Fig. 4 as a function of the photoelectron's kinetic energy. Oscillations are clearly visible up to 300 eV above the absorption edge.

A close look at Fig. 4 shows some similarity on the high-energy part of the oscillations (from 80 to 350 eV) especially for the Xe, N_2, and CH_4 matrices. The following

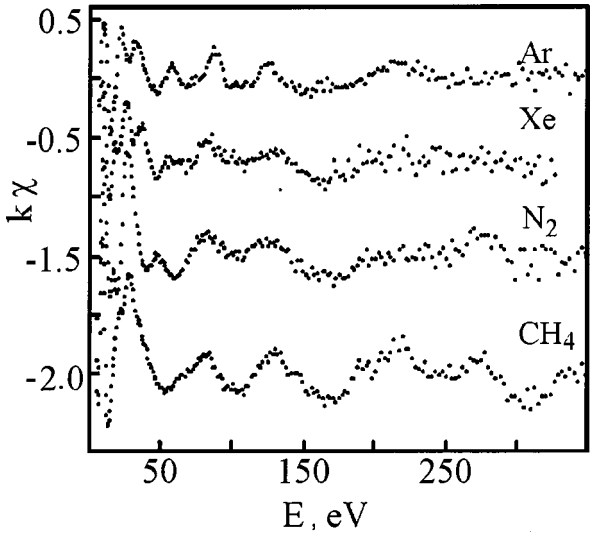

FIG. 4. EXAFS oscillations $k\chi$ of the spectra of Fig. 3 as a function of the photoelectron energy. The spectra have been shifted for the sake of clarity, but the scale is exact for their amplitudes.

questions are then arising: do these spectra actually contain information about the OCS environment? Don't they only reveal the structure of OCS itself? Moreover, the concentration of 1:100 is indeed high enough for clustering to occur, and the spectra may also only reflect the structure of some aggregates. As a matter of fact, infrared measurements performed on OCS isolated in nitrogen, in argon or in xenon[20,21] reveal that clustering and/or multiple trapping sites were prevalent under all but the most dilute conditions (1/50000), and so we will examine now in detail whether there is evidence for a signature of isolation in our spectra.

The same data are given on an expanded scale (10–100 eV) in Fig. 5 in order to focus on the low-energy part of the spectra. Significant differences are observed on the oscillations, reflecting differences in the environment of the absorbing sulfur atom. This proves that, whatever the exact rate of clustering in the matrix, a signal corresponding to the iso-

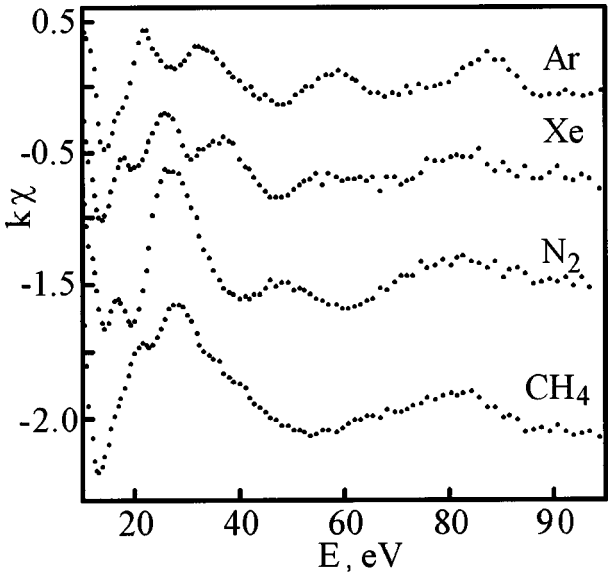

FIG. 5. The same as Fig. 4 on an expanded scale.

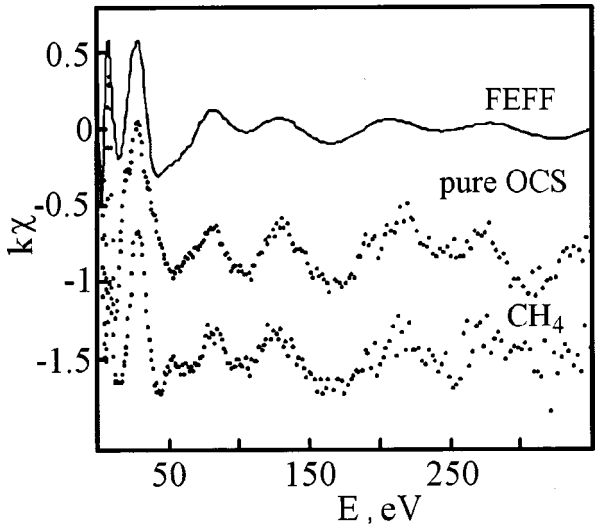

FIG. 6. The same as Fig. 4 for OCS isolated in methane and pure OCS, and FEFF simulations of the OCS molecular single scattering signal.

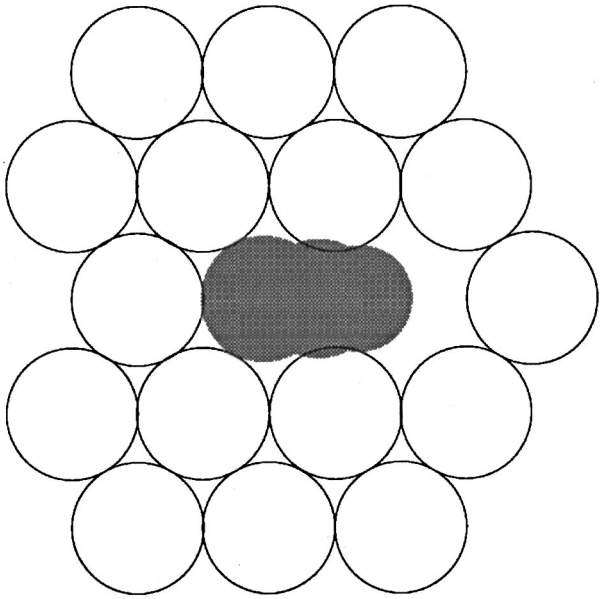

FIG. 7. Scheme of the two-hole trapping site for OCS in an argon matrix.

lated molecule and, thus, information about the molecular cage structure is unambiguously present in these measurements.

In order to clear up this point, we have recorded the EXAFS spectrum of pure OCS deposited under the same conditions. It is represented in Fig. 6 and is compared with the data for OCS isolated in methane. We recognize once more the same high-energy oscillations, and the question of clustering rises again. We have also done an FEFF simulation of solid OCS based on the $R3m(C_{3v}^5)$ crystal structure determined by neutron diffraction.[22] We have extracted from the calculation the EXAFS contribution of the excited OCS molecule by selecting only the intramolecular single diffusion paths, and this result is added in Fig. 6. It is clear that the resulting periods of the oscillations fit those of the experimental spectra, and we can conclude that the high-energy structures appearing for OCS isolated in Xe, N_2, and CH_4 are mainly due to intramolecular S-C and S-O scattering.

Let us explain now why the matrix signature is mainly present only in the first part of the spectra. A general reason is the damping induced by the thermal excitation of atomic movements: as a matter of fact, intramolecular bonds are stiffer than intermolecular bonds, and the σ^2 factor is much lower for a pair of atoms both belonging to the molecule than for a sulfur–argon pair. In the case of CH_4 and N_2, a second reason is the well-known poor scattering efficiency of the low-Z atoms. In addition, the backscattering amplitudes decrease as the photoelectron kinetic energy increases, and the more rapidly the lighter the element. For example, the maximum of the backscattering amplitude is found for a kinetic energy of about 20 eV in the case of N, while it is about 90 eV in the case of Ar. These reasons explain why we do not measure a significant contribution coming from the N or C neighbors for an energy larger than 50 eV.

The IR spectrum and the trapping site for OCS isolated in argon and xenon have been modeled by Winn.[23] The molecule is found to accommodate a two-hole site, as represented schematically in Fig. 7. In the case of argon, the sulfur atom is roughly at the center of one of the two holes, and the neighboring argon atoms occupy different well-defined positions, with S-Ar distances spreading around a mean value of 3.74 Å. In the case of xenon, in addition to this site, a second site, in which the oxygen atom is at the center of one of the two holes, has been found to be unstable. Figure 8 compares the EXAFS signals of OCS isolated in argon or in xenon with FEFF simulations performed with the geometry deduced from Ref. 23 and corresponding to Fig. 7—the sulfur atom being about at the center of a substitutional hole. Concerning the xenon matrix, the FEFF results corresponding to the unstable site are not represented here, for the sake of clarity, but they clearly do not agree with the experimental signal. On the contrary, Fig. 8 shows that the oscillations corresponding to the calculated stable site agree well with the three first main structures observed between 20 and 100

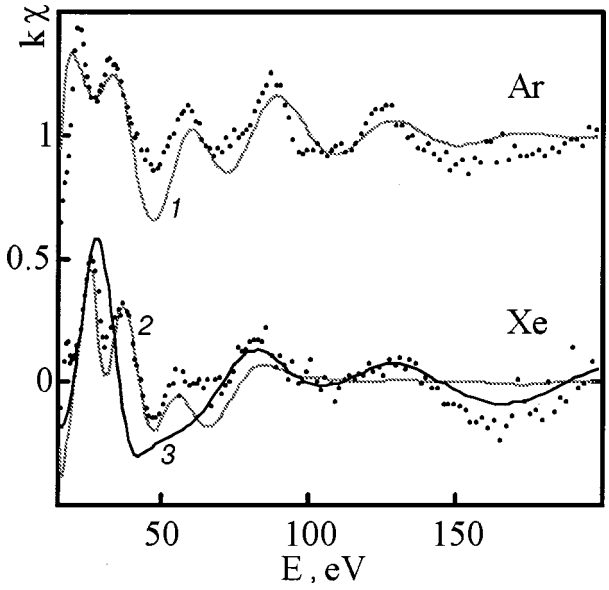

FIG. 8. EXAFS oscillations (dots) and FEFF simulations of the two-hole site of Ref. 23 for OCS isolated in argon (*1*) and in xenon (*2*). In the latter case, the additional line *3* is the FEFF simulation of molecular OCS as in Fig. 6.

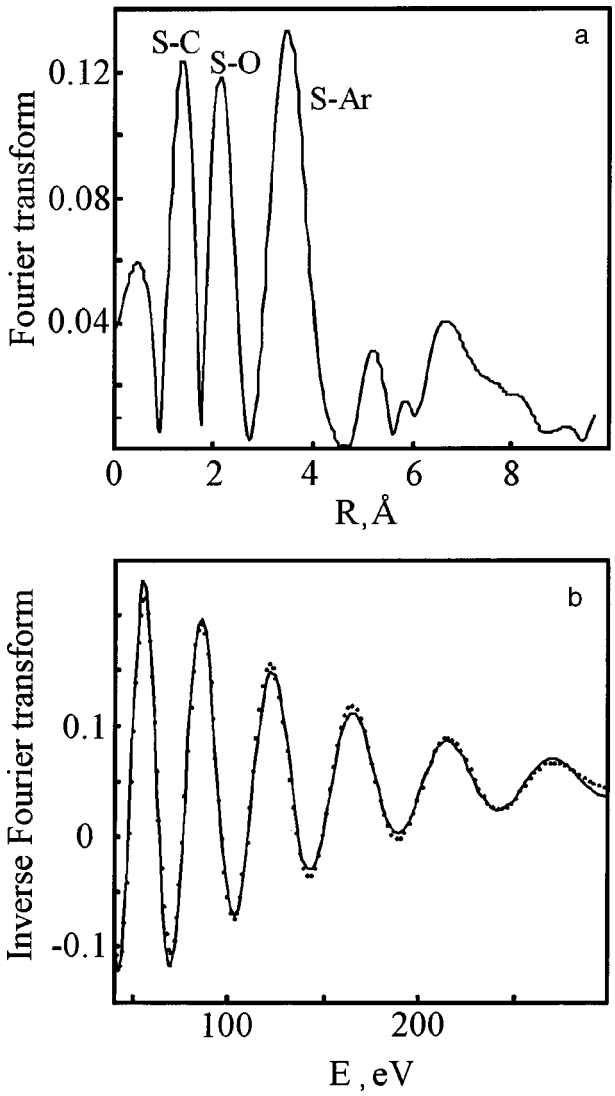

FIG. 9. OCS isolated in argon.[24] (a) Fourier transform of the EXAFS oscillations represented in Fig. 4; (b) inverse Fourier transform: the dots correspond to the experimental data, and the continuous line corresponds to a fit with the electronic parameters given by the FEFF code.

eV. The line 3 corresponds to the EXAFS simulations of the OCS molecule alone as for Fig. 6, and it fits well the oscillations between 100 and 250 eV. This shows that the S–Xe contribution is only visible up to 100 eV—as a matter of fact, the backscattering amplitude rapidly decreases above 90 eV—and confirms that the following part of the spectrum is dominated by the pure OCS contribution. In the case of argon, it seems, clear that the main oscillating period obtained in the calculations is larger than the experimental one, and this reveals that the measured mean S–Ar distance is larger than the calculated one. On the other hand, we can observe that the sulfur–rare gas contribution is more dominant for argon than for xenon, and thus the OCS/Ar system appears the best candidate for a quantitative analysis of the signal.

This has been done in a previous paper[24] and the results are summarized now. The Fourier transform of the EXAFS spectrum obtained for OCS in argon (Fig. 9a) shows three peaks corresponding to S–C, S–O, and S–Ar distances, so that the structure of the first shell of argon atoms surrounding OCS can be analyzed by fitting the oscillations given by the inverse Fourier transform of the peak corresponding to the S–Ar distance (Fig. 9b). We found that our results were consistent with a shell of 11 argon atoms at a mean distance of 3.78(1) Å, larger than the pure Ar–Ar distance found with the same FEFF data (3.75(1) Å). A static disorder around this position has been measured by an additional Debye–Waller factor of $\sigma^2 = 0.006\,\text{Å}^2$, which corresponds to a root-mean-square displacement of about 0.08 Å. This disorder is moderate and this is in good agreement with the measured relaxation of the argon positions in order to accommodate the molecule. These parameters for the cage are also in agreement with the two-hole site picture represented in Fig. 7, and they differ only slightly from the perfect cage structure calculated by Winn:[23] they correspond to a structure which is less organized (a unique mean S–Ar distance instead of a set of well-defined positions) and to a larger mean S–Ar distance (3.78 Å instead of 3.74 Å). We must remark that the concentration of our sample (1/100) is high enough so that our matrix crystal is probably disturbed by the OCS dopant, and it is thus not surprising to obtain a structure that differs from the perfect one.

4.2. Probing the distortion induced by the guest molecule: OCS, HCl, and SiH_4 isolated in an argon matrix

The absorption spectra of SiH_4 and HCl isolated in an argon matrix at the *K* edge of the silicon and the chlorine atom, respectively, have been recorded and are reported in Fig. 10a. For comparison, the spectrum of OCS in argon at the sulfur *K* edge, already presented in the preceding section, is reproduced in the same figure, as well as the spectrum of pure argon recorded at the argon *K* edge. This last spectrum can be thought of here as Ar in Ar. A shift of the photon energy corresponding to the *K* electron binding energy E_0 is applied for each spectrum in order to be able to compare them, so that the abscissa is $h\nu - E_0$ and roughly corresponds to the photoelectron kinetic energy. The oscillations are observed above the absorption edge in the cases of OCS, HCl, and Ar, while they are much more rapidly damped in the case of SiH_4. Moreover, when existing, they undoubtedly show a similarity, especially in the 40–150 eV region (Fig. 10b), which proves that they are the signature of a similar argon environment. The peak existing for HCl only, at about the origin of the energy scale of Fig. 10a, corresponds to the transition towards the molecular antibonding σ^* state.[25] The following peak can be readily compared for HCl in argon and for pure argon: it corresponds to the $1s \rightarrow 4p$ Rydberg transition,[8,25] which is expected to be very similar in both cases because of similar electronic structures.

The EXAFS signals $(k\chi)$ for pure argon and for HCl isolated in argon are superimposed in Fig. 11, and no significant difference is observed between the two spectra. This confirms that a single substitutional site readily accepts HCl without perturbation of the crystalline structure. The size of the molecule is actually close to the size of the argon atom, and, moreover, it is well-known that the molecule undergoes almost free rotation in the cage, indicating a negligible hindering[26,27] by the neighboring atoms. The beating between different oscillations that is observed in the spectra (see Fig. 11) is due to the addition of the contributions of the different shells of argon surrounding the excited atom and of multiple scattering. A detailed analysis of the different path

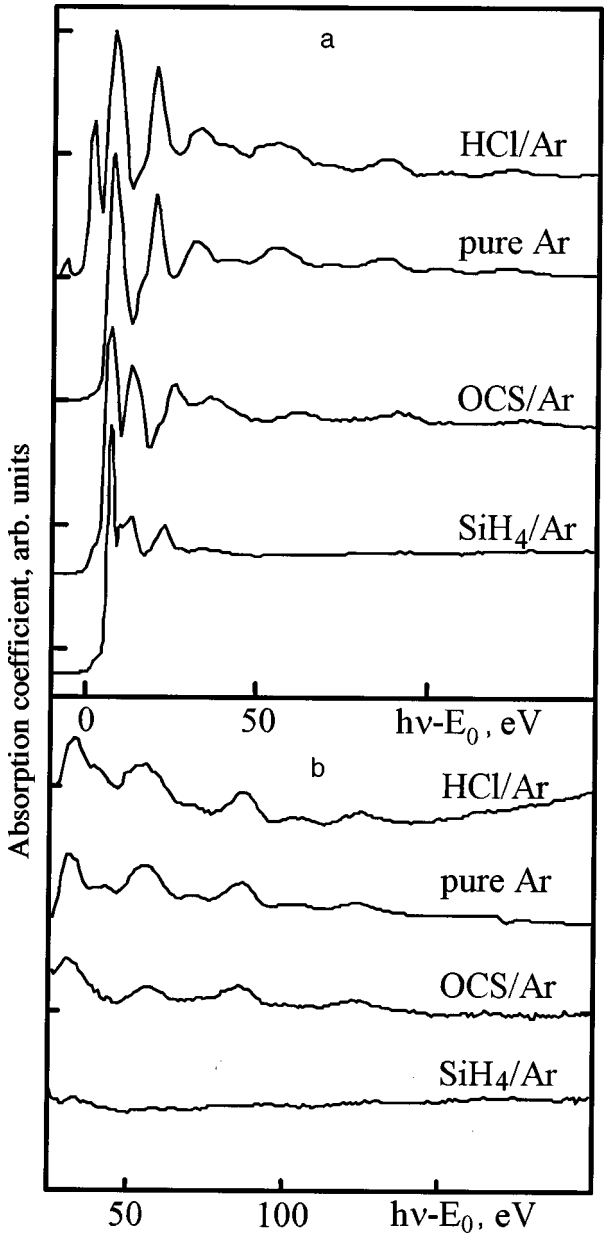

FIG. 10. X-ray absorption spectra as a function of the shifted photon energy $(h\nu - E_0)$, E_0 being the K edge energy of Cl for HCl, S for OCS, and Si for SiH_4 (fluorescence mode) and the K edge of Ar for pure argon (transmission mode). In the case of HCl, the spectrum has been corrected to eliminate an important unwanted structure at 45 eV due to a glitch: (a) spectra from -10 to 150 eV; (b) the same spectra in an extended range.

contributions given by the FEFF code shows that the main oscillating structure corresponds to the sine function built with the first nearest neighbors at a distance of 3.75 Å, while the secondary maxima appearing at $E = 67$ and 100 eV are due to a constructive addition of the third and fourth shell sine functions and of the double-scattering contributions, especially those coming from two Ar scattering atoms aligned with the central atom. This latter signal indeed involves a forward scattering and is enhanced because of its high amplitude (focusing effect).

On the contrary, silane, whose tetrahedral symmetry is well-suited for a cubic crystal, does not give rise to long-range oscillations. Infrared spectroscopy[28,29] reveals two peaks for the Si–H stretching band of silane isolated in argon, indicating two sites for its accommodation. The mean low-frequency peak arises over a very broad and structured band due either to rotation or to multiple configurations of the site. Silane is approximately a sphere whose diameter is 5 Å and is probably too large to fit into a one-atom vacancy of an argon crystal. It will neither easily occupy a two-atom one (Fig. 7), which can accommodate only a prolate molecule of reduced size. We have also considered the case of the four-atom vacancy of tetrahedral symmetry, as has been done for some metallic atoms.[30] In Fig. 12 the FEFF results obtained for silane in a one-atom vacancy and for silane in a four-atom vacancy are compared with the experimental data. There is clearly no agreement between the oscillating structures of the simulations and the experimental results, and we cannot draw a conclusion as to the validity of either of the two sites. Nevertheless, the experimental spectrum may also

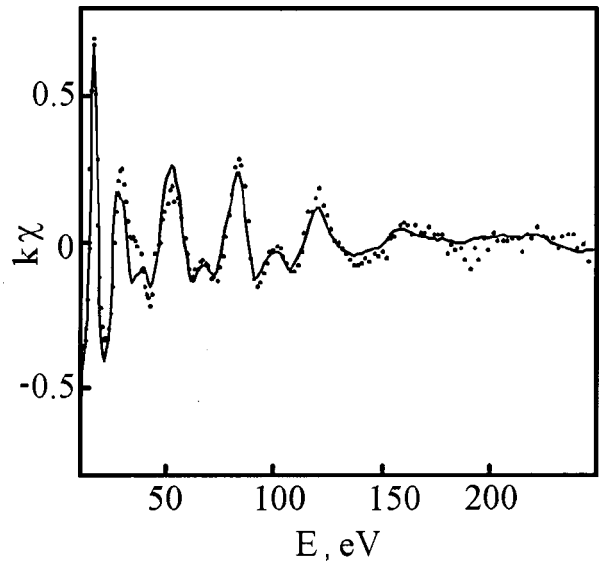

FIG. 11. EXAFS spectra $(k\chi)$ as a function of the photoelectron energy of pure argon (continuous line) and of HCl (dots) isolated in argon.

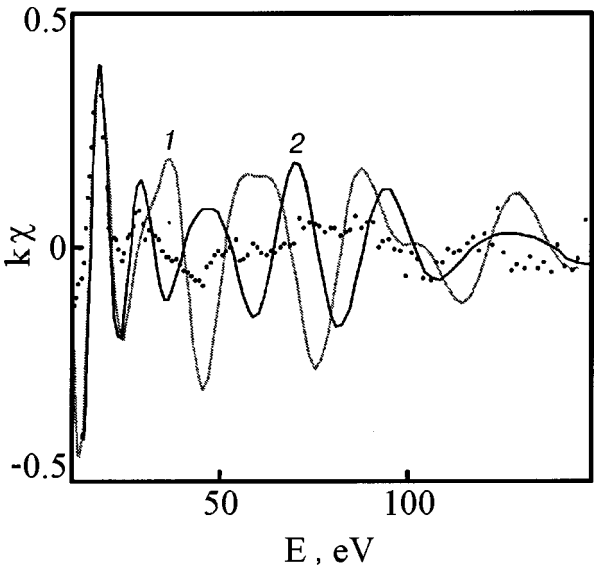

FIG. 12. EXAFS spectrum $(k\chi)$ of silane isolated in argon (dots) and FEFF simulations of silane in a one-hole site (line *1*) and in a four-hole site (line 2).

result from the addition of two signals, as suggested by the infrared results. Unfortunately, the EXAFS oscillations extend in too short a range to give any valuable information by the usual Fourier transform operation. We can only conclude that the mean environment of silane does not present enough simplicity to give rise to long-range EXAFS oscillations.

5. CONCLUSION

We have presented here the results of EXAFS experiments performed at the *K* edge of Si, S, and Cl for SiH_4, OCS, and HCl isolated in argon and for OCS isolated in argon, xenon, nitrogen, and methane. The signature of the different matrix environments of OCS is clearly evidenced in the low-frequency part of the spectra, and, on the other hand, the signature of molecular OCS is dominant in the high-frequency part, except in the case of the argon matrix. As a matter of fact, to obtain a signal containing a non-negligible intermolecular contribution, the host atom must not only have a good scattering efficiency in order to get a large amplitude for the oscillations (and thus, not a low-*Z* atom) but must also weakly absorb the x-ray radiation in order to get a good signal-to-noise ratio in the fluorescence detection mode (and thus, not a high-*Z* atom).

For this reason, we have been able to do a complete analysis of the EXAFS oscillations only in the case of OCS in argon. We have measured an S-Ar of 3.78 Å, and we have shown that this slight relaxation of the argon cage is enough to accommodate the molecule without perturbing the long-range order of the matrix. These results are consistent with the usual two-hole site picture invoked for such a linear molecule and are not far from a previous modeling[23] valid only for a perfect matrix. For OCS in xenon, the results are entirely consistent with the same modeling and confirm the calculated location of OCS inside the two vacancies. The case of silane in argon is totally different, and only a highly damped signal has been measured, so that, in agreement with previous infrared results, we can rule out the hypothesis of a single well-defined cage around the molecule and even the hypothesis of a disordered one-hole or four-hole site.

In conclusion, we think that probing the matrix environment of a dilute sample with the EXAFS technique in this soft x-ray region is not a simple task because of the poor signal-to-noise ratio and the problem of absorption by the matrix itself. Nevertheless, consistent results have been obtained here, and this proves that the technique can really give important information about the site structure and, even if a quantitative analysis is not always possible, that it can provide valuable information about the ordering around the molecule.

[1] C. S. Barret and L. Meyer, J. Chem. Phys. **41**, 1078 (1964).
[2] Y. Sonnenblick and Z. H. Kalman, J. Cryst. Growth **58**, 143 (1982).
[3] W. Langel, W. Schuller, E. Knözinger, and H.-W. Fleger, J. Chem. Phys. **89**, 1741 (1988); A. Becker, W. Langel, S. Maass, and E. Knözinger, J. Phys. Chem. **97**, 5525 (1993).
[4] N. A. Young and M. D. Spicer, J. Mol. Struct. **222**, 77 (1990); I. R. Beattie, P. J. Jones, and N. A. Young, J. Am. Chem. Soc. **114**, 6146 (1992); N. A. Young, J. Chem. Soc. Dalton Trans. **249**, (1996).
[5] P. A. Montano and G. K. Shenoy, Solid State Commun. **35**, 53 (1980); P. A. Montano, W. Schulze, B. Tesche, G. K. Shenoy, and T. I. Morrison, Phys. Rev. B **30**, 672 (1984).
[6] W. Malzfeldt, W. Niemann, P. Rabe, and R. N. Schwentner, in *Exafs and near Edge Structure*, A. Bianconi, I. Incoccia, and S. Stipcich (eds.), Springer-Verlag, Berlin (1983); W. Malzfeldt, W. Niemann, P. Rabe, and R. Haensel, in Exafs and near Edge Structure III, K. O. Hogson, B. Hedman, and J. E. Penner-Hahn (eds.), Springer-Verlag, Berlin (1984).
[7] R. D. Deslattes, R. E. LaVilla, P. L. Cowan, and A. Henins, Phys. Rev. A **27**, 923 (1983); R. D. Deslattes, Aust. J. Phys. **39**, 845 (1986).
[8] E. Rühl, C. Heinzel, A. P. Hitchcock, H. Schmelz, C. Reynaud, H. Baumgärtel, W. Drube, and R. Frahm, J. Chem. Phys. **98**, 6820 (1993).
[9] M. Breinig, M. H. Chen, G. E. Ice, F. Parente, and B. Crasemann, Phys. Rev. A **22**, 520 (1980).
[10] M. Deutsch, N. Maskil, and W. Drube, Phys. Rev. A **46**, 3963 (1992).
[11] De L. Kronig, Z. Phys. **70**, 317 (1931).
[12] D. E. Sayers, F. W. Lytle, and E. A. Stern, Phys. Rev. Lett. **27**, 204 (1971); E. A. Stern and D. E. Sayers, Phys. Rev. Lett. **30**, 174 (1973); E. A. Stern, Phys. Rev. B **10**, 3027 (1974); E. A. Stern, D. E. Sayers, and F. W. Lytle, Phys. Rev. B **11**, 4836 (1975).
[13] P. A. Lee and J. B. Pendry, Phys. Rev. B **11**, 2795 (1975).
[14] C. A. Ashley and S. Doniach, Phys. Rev. B **11**, 1279 (1975).
[15] P. A. Lee, P. H. Citrin, P. Eisenberger, and B. M. Kincaid, Rev. Mod. Phys. **53**, 769 (1981).
[16] *X-ray Absorption, Principles, Applications, Techniques of EXAFS, SEXAFS and XANES*, edited by D. C. Koningsberger and R. Prins (John Wiley and Sons, New York, 1987).
[17] B. Lengeler and P. Eisenberger, Phys. Rev. B **21**, 4507 (1980).
[18] G. Beni and P. M. Platzmann, Phys. Rev. B **14**, 1514 (1976).
[19] J. J. Rehr, J. Mustre de Leon, S. I. Zabinsky, and R. C. Albers, J. Am. Chem. Soc. **113**, 5135 (1991); J. Mustre de Leon, J. J. Rehr, S. I. Zabinsky, and R. C. Albers, Phys. Rev. B **44**, 4146 (1991).
[20] F. D. Verderame and E. R. Nixon, J. Chem. Phys. **44**, 43 (1966).
[21] V. I. Lang and J. S. Winn, J. Chem. Phys. **94**, 5270 (1991).
[22] J. S. W. Overell, G. S. Pawley, and B. M. Powell, Acta Crystallogr., Sect. B: Struct. Crystallogr. Cryst. Chem. **38**, 1121 (1982).
[23] J. S. Winn, J. Chem. Phys. **94**, 5275 (1991).
[24] P. Roubin, S. Varin, C. Crepin, B. Gauthier-Roy, A.-M. Flank, R. Delaunay, M. Pompa, and B. Tremblay, J. Chem. Phys. **109**, 7945 (1998).
[25] S. Bodeur, J.-L. Marechal, C. Reynaud, D. Bazin, and I. Nenner, Z. Phys. D: At., Mol. Clusters **17**, 291 (1990).
[26] D. Maillard, A. Schriver, and J.-P. Perchard, J. Chem. Phys. **71**, 505 (1979).
[27] M. Allavena, H. Chakrouna, and D. White, J. Chem. Phys. **77**, 1757 (1982).
[28] R. E. Wilde, T. K. K. Srinivasan, R. W. Harral, and S. G. Sankar, J. Chem. Phys. **55**, 5681 (1971).
[29] N. Legay-Sommaire and F. Legay, J. Phys. Chem. **102**, 8759 (1998).
[30] M. E. Fajardo, J. Chem. Phys. **98**, 119 (1993); J. A. Boatz and M. E. Fajardo, J. Chem. Phys. **101**, 3472 (1994).

This article was published in English in the original Russian journal. Reproduced here with stylistic changes by the Translation Consultant.

Physical aspects of matrix isolation technique: FTIR studies on CO and CO_2 in O_2 and N_2 matrices

M. Minenko, M. Vetter, A. P. Brodyanski, and H. J. Jodl*

Fachbereich Physik, Universität Kaiserslautern, Erwin Schrödinger Str., 67663 Kaiserslautern, Germany
(Submitted April 26, 2000; revised June 20, 2000)
Fiz. Nizk. Temp. **26**, 947–962 (September–October 2000)

The matrix isolation technique is traditionally used to investigate the properties of the matrix-isolated species themselves or to solve some special questions of the theory of defects in solids. We showed here that the optical spectroscopy of real matrix-isolated molecules can be successfully used to investigate the host crystal qualities, too. We demonstrated the capacity of modern FTIR spectroscopy to study the properties of cryocrystals such as phase transitions, solubility boundaries, orientational order parameter, etc., by monitoring the behavior of the IR-active molecules, which are present in matrices under investigation as a natural contamination (40 ppb). Due to the excellent optical quality of our crystal samples, we were able to determine a part of the binary phase diagram CO–O_2 (at CO concentrations less than 1 ppm) as well as to investigate the kinetics of phase transitions. Furthermore, we successfully used the spectroscopy of the matrix-isolated molecules to proof that the α-β phase transition of the matrix crystal (O_2) is of first order.
[S1063-777X(00)01109-9]

1. INTRODUCTION

The matrix isolation (MI) technique is used in general to investigate properties of the isolated molecules (or small groups of them) such as their shape, their spectrum, the relaxation of molecular excitations, etc., as well as their chemical and physical behavior. Recently[1] we have shown that the matrix isolation technique can also be used successfully to render some fundamentally important information on the properties of the host crystal, where these molecules were dissolved (CO or CO_2 in a N_2 matrix). The principal prerequisite to employ the MI technique for this special purpose is to work with a *real* MI case to avoid any segregation processes or cluster formation and to neglect any interaction between dissolved impurities. The basic physical idea of our approach is relatively simple: the spectroscopic characteristics of the internal vibrations of a well-isolated molecule (frequency, bandwidth) are unambiguously determined only by the properties of this molecule itself and the crystal field of the host crystal in which this molecule is embedded. Changes in the crystal-field-varying external conditions (such as temperature, pressure) cause corresponding changes in spectroscopic characteristics of the MI molecule. Therefore, by monitoring the behavior of this MI molecule carefully, we can probe the host crystal qualities such as phase transitions, intermolecular distance, order parameter, dynamics, and relaxation processes, etc. Moreover, starting from a *real* MI case it is possible to investigate the low-concentration part of the phase diagram of binary systems correctly. Our previous results[1] change traditional opinions about the MI case, such as the solubility limit in cryocrystals; we have shown that the thermodynamic equilibrium solubility limit for CO_2 molecules in solid nitrogen is lying at molar concentrations of about $10^{-7}-10^{-6}$.

FTIR spectroscopy is a substantially more sensitive tool in comparison with Raman scattering to investigate small impurity concentrations. Therefore, it is meaningful to employ IR-active MI molecules to probe indirectly of host crystal qualities of spectroscopically inactive matrices (rare gas solids, etc.). In Fig. 1, we present the internal vibration spectrum of CO molecules matrix isolated in solid oxygen. Our oxygen gas used (purity 99.998%) contains these CO molecules as a residual contamination. Analyzing the integrated intensity of this peak in combination with known absorption coefficient of CO, we determined the CO concentration in the solid oxygen to be 4×10^{-8}.

Our aim is to study the *real* matrix isolated case and to probe solid-state aspects of the matrix. We have chosen CO_2 and CO molecules matrix isolated in solid nitrogen and oxygen as an example. Our paper is structured as follows: in Sec. 2, we briefly describe our experimental procedure (method, crystal growth, determination of impurity concentration, etc.). Experimental results are presented together with the discussion in Sec. 3. We will analyze first the phase transitions in the host crystals. Second, we will interpret the behavior of mode frequency to gain information on the host crystal qualities; third, we will study the low-concentration part of the phase diagrams (CO_2 in nitrogen and oxygen, and CO in oxygen); fourth, we will discuss mode relaxation processes of impurities in these selected cryocrystals.

2. EXPERIMENTAL PROCEDURE

We investigated CO_2 and CO molecules dissolved in condensed phases of nitrogen and oxygen at equilibrium vapor pressure by FTIR spectroscopy in the temperature range from 10 to 90 K. The spectra of the impurity fundamentals were recorded in the mid-infrared spectral region by a Fourier spectrometer (Bruker IFS 120 HR). Two sets of light sources and beam splitters were used: a glowbar source and a

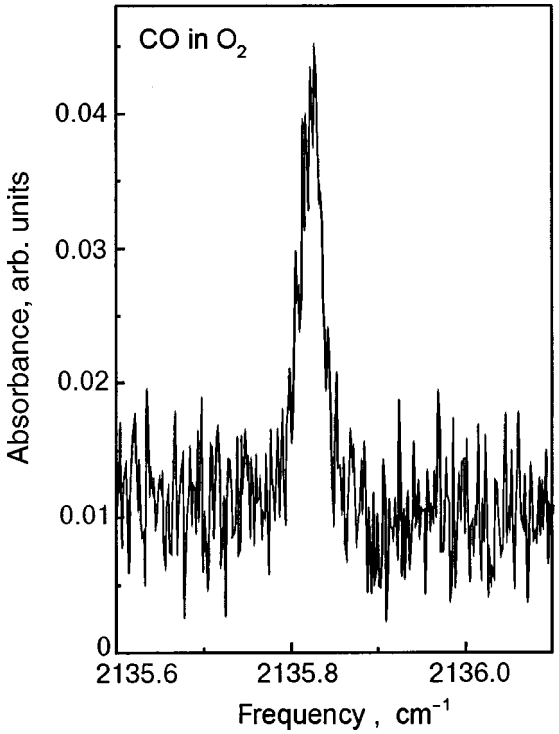

FIG. 1. Mid-IR spectrum of the internal vibration of the CO molecules matrix isolated in α-oxygen ($T=11$ K, spectral resolution 0.003 cm^{-1}). The CO molecules are present in our oxygen (99.998%) as a residual contamination (CO/O_2 ratio $\sim 4\times 10^{-8}$).

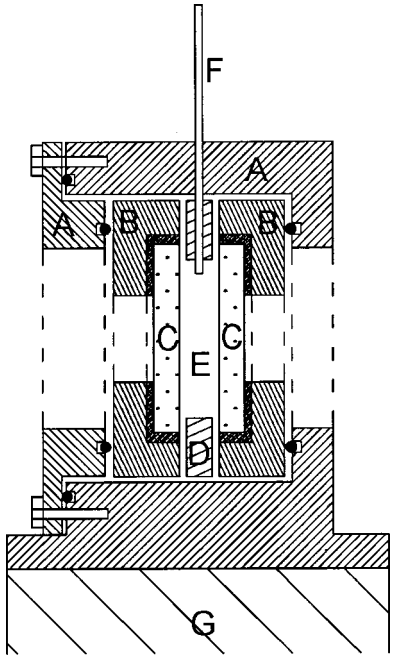

FIG. 2. The sample cell specially designed for IR-spectroscopic investigations of cryocrystals and their mixtures at zero pressure.

KBr beam splitter (spectral range 800–5000 cm^{-1}) as well as a tungsten lamp and a CaF_2 beam splitter (spectral range 1900–11000 cm^{-1}). The diameter of the diaphragm was 1 and 0.8 mm, respectively. Liquid-N_2-cooled InSb and MCT detectors were used. The frequency resolution was varied from 0.003 to 3 cm^{-1}, depending on the bandwidth of the investigated spectral lines. A cutoff filter for the spectral region 2000–3000 cm^{-1} was used to improve the signal/noise ratio.

To investigate cryocrystals in the whole spectral region (from far infrared to ultraviolet) on the *same* sample without changing the window material, a special sample cell with diamond windows (accessible spectral range 10–43000 cm^{-1}) was designed (Fig. 2). This cell consists of a brass corpus *A* and two copper discs *B* with polycrystalline diamond windows *C* (⌀3 mm). The diamond windows are glued onto the copper discs. The copper discs are separated by a brass ring *D* (inner diameter of 10 mm) as a spacer to vary the sample thickness. The inner area *E* between the two copper discs serves as the sample chamber. Copper was selected as a material for sample chamber to exclude considerable thermal gradient across our sample. The thickness of the samples was 1.2 mm in the present studies. The indium rings were used to seal the sample chamber (shown by dark dots in Fig. 2). A steel capillary tube *F* connects the sample chamber with the gas system.

The sample cell was mounted on a cold finger of a closed-cycle He cryostat (position *G* in Fig. 2). The sample temperature was measured by a calibrated Si diode with a temperature resolution of 0.005 K in the temperature region below 25 K and 0.05 K at higher temperatures. The accuracy of the temperature, stabilized by a computer, was better than ± 0.01 K at $T \leqslant 25$ K and ± 0.03 K at higher temperatures. To obtain information on the real absolute sample temperature the Si diode was calibrated by comparing a registered sample temperature to known fixed thermodynamic temperature points (solid-solid phase transitions, melting and boiling points of 5 substances: H_2, Ne, CH_4, O_2, N_2). This procedure allows us to reach an absolute accuracy of determination of the sample temperature of about 0.1 K in the whole temperature range from 10 to 120 K.

To ensure good thermal contact with copper discs (position *B* in Fig. 2) a sample gas was condensed to liquid at overpressure of about one bar. This overpressure was maintained until a crystal was completely grown. The samples were slowly grown from the liquid to obtain perfect crystals with good optical quality. This crystal quality was immediately controlled by eye (microscope) during growth as well as by a determination of the bandwidth of the MI molecule fundamental at low temperature. The grown crystals were completely transparent to visible light and had very small residual inhomogeneous broadening (about 0.01 cm^{-1}). We could not detect any traces of the IR-inactive N_2 or O_2 vibron (host crystal); consequently, our crystals are perfect. To overcome the difficulties connected with the big volume jump at the γ-β phase transition in solid oxygen (about 5.4%[2]) and to obtain high quality crystals of low-temperature O_2 phases, a special procedure worked out in Ref. 3 was used and slightly modified for our demands. γ-O_2 crystal of perfect quality was slowly (0.05 K/h) cooled through the γ-β phase transition. At a temperature slightly lower than the γ-β transition point ($\Delta T = 0.02-0.03$ K) a perfect crystal of β-oxygen was grown at constant temperature (temperature fluctuations were smaller than ± 0.02 K). The changes in our samples during whole growth procedure were continuously monitored spectroscopically. During the recrystallization of the β phase, we observed an increase of the optical transpar-

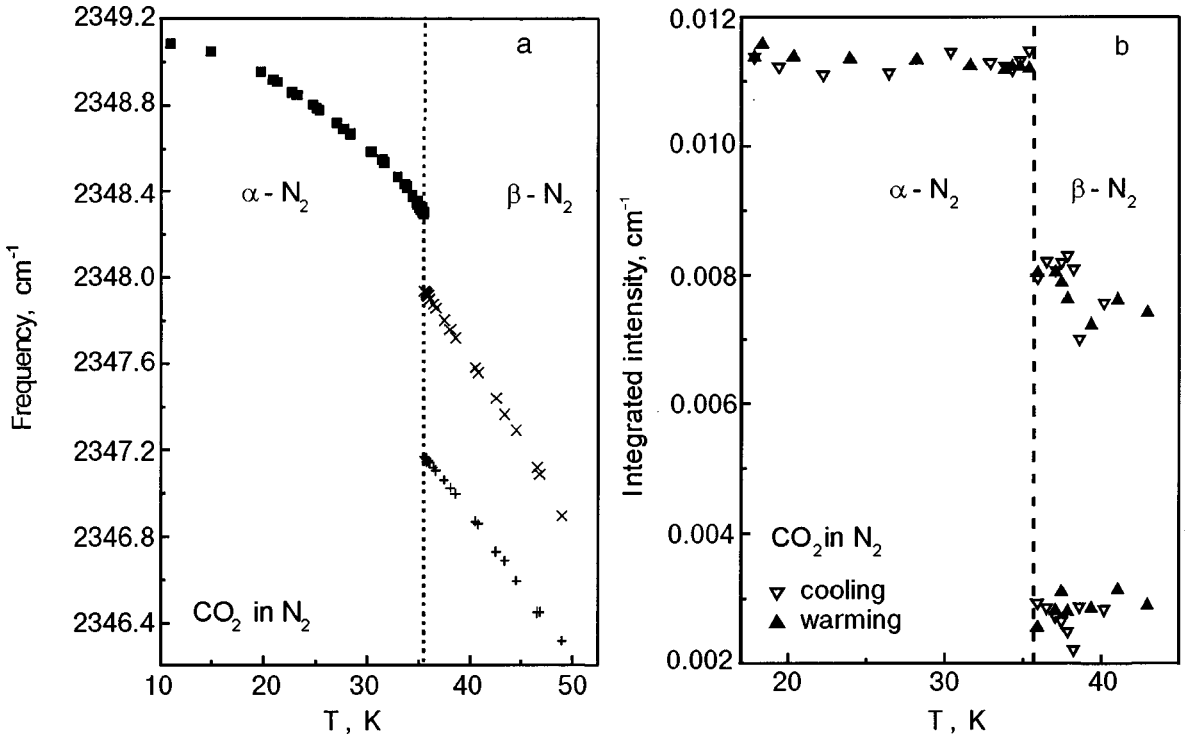

FIG. 3. Temperature dependences of the spectroscopic characteristics of the v_3-fundamental of CO_2 matrix isolated in solid nitrogen: frequency (a) and integrated intensity (b). The CO_2 molecules were present in our nitrogen gas (99.999%) as a residual contamination ($CO_2/N_2 = 1.35\times10^{-7}$).

ency of our samples. If the transparency did not improve further more, the crystal of β-oxygen was slowly (0.1 K/min) cooled down. Near phase transitions, the samples were cooled (or warmed) at a much slower rate (0.005 K/min). Two series of experiments with different admixture/matrix (A/M) ratio were carried out for both matrix materials (N_2 or O_2). In the first series (A), we monitored the behavior of the IR-active molecules, which were present in our sample gases (O_2, 99.998% and N_2, 99.999%) as residual contaminations: CO_2 in nitrogen (135 ppb) as well as CO (about 40 ppb) and CO_2 (about 1 ppm) in oxygen. In the second series (B), we investigated nitrogen enriched in CO_2 (75 ppm) and oxygen enriched in CO (about 0.9 ppm).

The methods used to determine the impurity concentration in solid nitrogen were described in Ref. 1. In the case of the oxygen samples, we determined the A/M ratio via known absorption coefficients[1,4] as well as via partial pressure.

3. RESULTS AND DISCUSSION

3.1. Investigation of phase transitions

a) **N_2 matrix**. To test our approach—to probe host crystal quality—we first studied the well-investigated α-β phase transition in solid nitrogen. This phase transition is a first-order phase transition accompanied by a volume jump (about 0.8%) at the equilibrium vapor pressure.[5] The low-temperature α-phase of solid N_2 has $Pa3$ cubic structure and possesses long-range orientational order. The hexagonal β-phase (space group $P6_3/mmm$) is an orientationally disordered phase.

To probe indirectly the α-β phase transition of the matrix (N_2), we monitored the behavior of the CO and CO_2 fundamentals as a function of temperature. Although both substances react sensitively to this phase transition (see Ref. 1), the most obvious changes are observed in the spectroscopic characteristics of the v_3-CO_2 fundamental (Fig. 3). These changes were completely reproducible under cooling and warming. One v_3-CO_2 band in the α phase is split into two bands in the β phase exactly at the phase transition point (Fig. 3a). The clear jump is observed in the temperature-dependent bandwidth of the MI molecules at this temperature, too. These observations, gained by the spectroscopy of MI molecules, are confirmed by monitoring the two-vibron band of α-N_2, which disappears in the β phase (see Fig. 6 Ref. 1). The integrated intensity of the v_3-CO_2 fundamental is proportional to the total number of MICO_2 molecules. The intensity of the one v_3-CO_2 band in the α phase is equal to the total intensity of two v_3-CO_2 bands in β-N_2 (Fig. 3b). Since the number of MI molecules is constant at this transition, the MI CO_2 molecules must be distributed between two different sites in β-N_2, in accordance with the two possible orientational positions in the hcp structure of β-N_2 (Ref. 1).

The detailed analysis of the α-β phase transition[1] showed that the spectroscopic behavior of the CO_2 fundamental mirrors all characteristics of a first-order phase transition: a frequency jump; a thermal hysteresis of all of the spectroscopic characteristics; the coexistence of the α and β phases.

b) **O_2 matrix**. For 30 years it has remained unclear in the literature if the α-β phase transition in solid oxygen is of first or second order. We applied the matrix isolation technique to clarify this question.

O_2 molecules possess nonzero electronic spin in the ground electronic state. Therefore, solid oxygen combines properties of a cryocrystal and of a magnetic material. Solid oxygen exists in three phases at ambient pressure: γ-O_2 (T

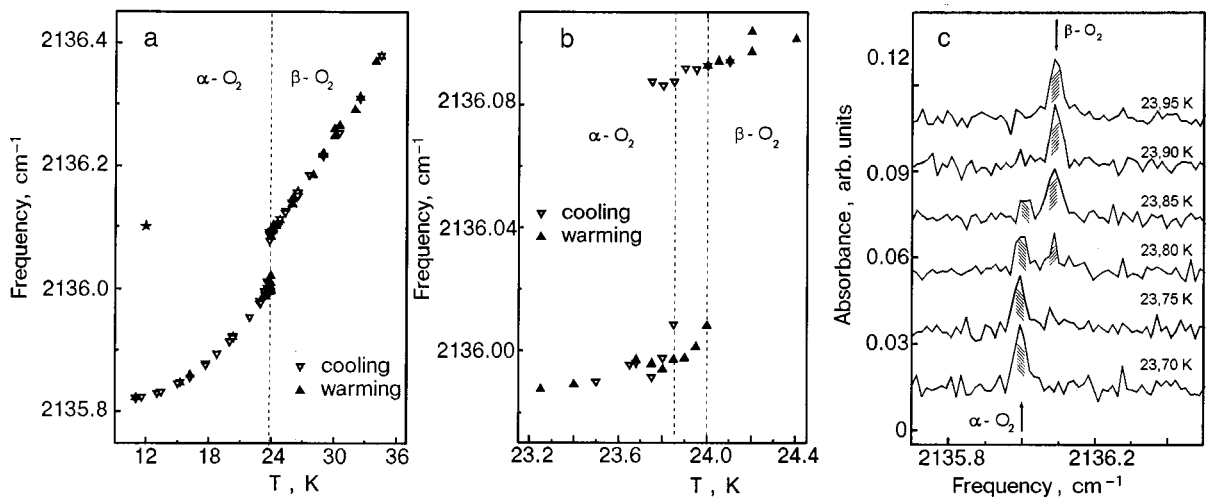

FIG. 4. Temperature behavior of the internal vibration of the CO molecules matrix isolated in solid oxygen ($CO/O_2 \sim 4\times10^{-8}$); temperature dependence of the CO fundamental frequency (star is the data of Ref. 19) (a); thermal hysteresis of the α-β phase transition in solid oxygen (b); the coexistence region of the α and β phases during cooling, from monitoring of the CO fundamental band in both phases (c). The resolution was 0.003 to 0.037 cm^{-1}, and the error in absolute frequencies is smaller than the symbols.

$=54.36-43.8\,K$), β-O_2 ($T=43.8-23.87\,K$) and α-O_2 ($T \leqslant 23.87\,K$). The low temperature α phase is an antiferromagnet,[6] whereas the β and γ phases possess no long-range magnetic order.[7] β-O_2 has the rhombohedral lattice of space group $R\bar{3}m$, whereas the structure of the α-O_2 belongs to the space group $C2/m$.[6,8] The crystal structures of the α and β phases are actually very similar, and both structures consist of closed-packed layers (basal planes). The distance between nearest molecules in the basal plane (3.2–3.4 Å) is substantially smaller than the distance between nearest neighbors from different layers ($\geqslant$4.2 Å).[2]

The properties of solid oxygen near its phase transitions have been extensively investigated by different experimental techniques: by x-ray and neutron diffraction,[2,12,14] heat capacity measurements,[10,13] IR and Raman spectroscopy,[9,22] thermal conductivity,[31] etc. However, the available experimental and theoretical data on the order of the α-β phase transition are both of a contradictory nature. On the experimental side the α-β phase transition is considered to be of second order according to the temperature dependence of the magnon frequency observed in Ref. 9 and to a λ-like anomaly of the heat capacity observed in Ref. 10. The parallel and perpendicular magnetic susceptibilities do not coincide at the α-β phase transition point.[11] Thermal hysteresis was observed by elastic neutron diffraction[12] and heat capacity measurements.[13] Consequently, this α-β phase transition is considered to be first order on the basis of the experimental results of Refs. 11–13. X-ray studies[14] demonstrate that both phases coexist within 1 K near the α-β phase transition; however, those authors did not detect any hysteresis.

In theoretical literature[15–17,32] there is also no consensus on the physical origin and classification of the α-β phase transition: a pure crystallographic transition, magnetically driven, and/or magnetoelastically driven. Different theoretical models to describe this phase transition have been exploited to characterize the order of this phase transition. For example, the authors of Ref. 15 described the α-β phase transition as a second-order transition, while according to Refs. 17 and 25 the α-β phase transition is of first order.

To obtain unambiguous experimental information on the order of the α-β phase transition we carefully monitored the behavior of the spectroscopic characteristics of the internal vibration of CO molecules MI in solid oxygen. In the literature, we found one spectroscopic study on CO dissolved in solid oxygen (resolution 0.25–0.30 cm^{-1}).[18] CO molecules were produced by UV photolysis of O_2: H_2CO and O_2:$H_2C_2O_2$(2000:1) solid mixtures at $T=12\,K$.

Figure 4a shows the temperature dependence of the CO fundamental in the α and β phases of solid oxygen, reproducible in cooling and warming. At temperatures higher than 34 K, the CO peak becomes very broad (bandwidth about 0.1 cm^{-1} at 34 K) and therefore cannot be observed at such small CO concentrations. A jump in frequency is clearly visible at the α-β phase transition. This change in the environmental shift of the vibration frequency of the MI molecules ($\omega_{crystal}-\omega_{gas}$) is determined by changes (i) in the intermolecular distances of the host crystal and by changes (ii) in the host crystal orientational order parameter.[1,19]

Figure 4b presents the temperature dependence in fine steps (0.05 K) of the CO fundamental frequency in the vicinity of the α-β phase transition for one of our samples. The temperature at which the new band shows up as proof of the new phase lies at 23.85 and 24 K on cooling and warming, respectively. The concrete temperature values varied from one sample to the other, but these fluctuations were not more than 0.1 K. Our temperature range for hysteresis is a bit smaller than the thermal hysteresis observed in Ref. 13.

Figure 4c shows our spectra near the $\beta\rightarrow\alpha$ phase transition. The coexistence region of the α and β phases is clearly visible at 23.85 and 23.80 K. This coexistence of the α and β phases was observed in every sample (5 series) as well as during both cooling and warming.

The jump in the CO fundamental frequency ($0.09\pm0.01\,cm^{-1}$) at the α-β phase transition is comparable with the temperature-caused changes in frequency in the temperature range of α-O_2 ($0.17\ cm^{-1}$). Since the intermolecular interaction between O_2 molecules in the basal plane is substantially stronger than the interlayer interaction,[20] the jump

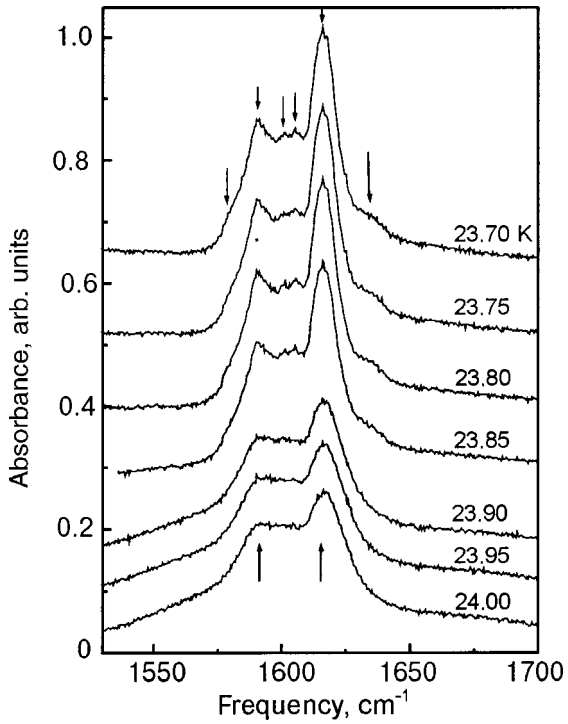

FIG. 5. Spectra of the oxygen vibron side band in the vicinity of the α-β phase transition. The arrows indicate the maxima in the side bands.

in the CO frequency is mainly determined by changes in the basal plane. Our own analysis of the structural data of others[2] showed that no discontinuity is observed in the area of the basal plane of a unit cell (representing the β phase by the monoclinic axes) at the α-β phase transition. Therefore, the frequency shift of 0.09 cm^{-1} obtained by us reflects the monoclinic distortion of the basal plane of solid oxygen, which appears/disappears at the point of the α-β phase transition and, consequently, can serve as a quantitative measure of this distortion.

Thus we have obtained strong experimental evidence (frequency jump, thermal hysteresis, coexistence of the α and β phases) that the α-β phase transition in solid O_2 is a *first-order* phase transition.

This result gained by analysis of the spectroscopic data of MI molecules, i.e., indirectly, was confirmed by the careful investigation of the behavior of the oxygen vibron side band, i.e., directly. Figure 5 demonstrates the temperature evolution of the side-band spectrum in the vicinity of the α-β phase transition during warming of the sample. The β-O_2 side band contains only two maxima (at 1591 and 1617 cm^{-1}) without any additional fine structure (spectrum at $T=24$ K). These maxima had been observed previously[21] and assigned to an IR absorption of a combination of oxygen vibron [$v_0=1552$ cm^{-1} (Ref. 22)] with a libron (39 cm^{-1}) and a lattice phonon (65 cm^{-1}), respectively. Both features exist in the side band of α-oxygen, too (spectrum at $T=23.70$ K). However, the maximum at higher frequency is substantially enhanced in comparison to the one in the β-O_2 side band; the additional contribution originates from the second libron branch ($\approx$70 cm^{-1}), which exists in α-oxygen only. The α-O_2 side band also possesses an additional fine structure (at frequencies about 1601 and 1606 cm^{-1}) between the two main maxima and two small maxima (at 1580 and 1636 cm^{-1}). The maxima of the fine structure correspond to a combination of the oxygen vibron with lattice phonons at the Brillouin zone boundary—frequencies of 49 and 54 cm^{-1} relative to the vibron frequency. The features at 1580 and 1636 cm^{-1} relate to a high frequency magnon (frequency about 28 cm^{-1}) and a lattice phonon (frequency about 84 cm^{-1}), respectively. Each of these six values in the phonon sideband spectra for α-O_2 agrees quite well with experimental[9,22] and theoretical[23] data. As can be seen, no observable changes in the spectra occur in the temperature range from 23.7 to 23.85 K. By a temperature of 23.9 K all the extra features of the α-O_2 side band have already vanished and only the typical side band of β-O_2 is present. A subsequent increase to 24 K causes no further changes in the spectra. Therefore, the first-order phase transition occurs between 23.85 and 23.90 K during warming of the sample. A similar behavior shows up between 23.80 and 23.75 K during cooling of this sample. In other words, thermal hysteresis takes place in the spectroscopic characteristics of solid oxygen at the α-β phase transition, too. It is important to note that these temperature points (23.85 K$\rightarrow$23.90 K and 23.80 K$\rightarrow$23.75 K) coincide exactly with the values determined by monitoring the behavior of the CO molecules in the same sample.

This eminent behavior—such as discontinuity and hysteresis—at the α-β phase transition is not only observed at the vibron side band and at the internal vibration of CO matrix isolated in solid oxygen, but is also clearly confirmed by us at other elementary excitations of O_2, such as excitons, exciton–vibrons, and two-vibron bound states. A two-phase coexistence temperature region was observed too.[1)]

All these spectroscopic results allow us to draw two conclusions: first, the α-β phase transition in solid oxygen is of the first order; second, the changes in the host crystal lattice at a phase transition can be successfully probed by spectroscopy on the guest molecules.

3.2. Indirect estimation of volume changes in the host crystal

In general, the temperature dependence of one mode frequency must somehow contain the temperature dependence of the crystal volume. Therefore, we will try to exploit this in the MI case and deduce information on matrix volume.

An environmental frequency shift of the internal vibration of a MI molecule ($\omega_{\text{crystal}}-\omega_{\text{gas}}$) is determined by the interaction between the embedded molecule and the molecules of the host crystal, averaged over relative translational and orientational motions of the impurity and the matrix molecules.[19] The general formulas for the environmental frequency shift of the linear molecules are given in Ref. 1. In our case of CO in solid oxygen and nitrogen (two atomic linear molecules matrix isolated in the orientationally ordered phases), these expressions can be written in the self-consistent approximation in the following form:

$$\Delta\omega\equiv\omega_{\text{crystal}}-\omega_{\text{gas}}=\frac{B_e}{\omega_e}\left\{\sum_j A(R_j)+\eta_{\text{imp}}\left[\sum_j U_1(R_j)+\sum_j U_0(R_j)\eta_j\right]\right\}=KW(R,T). \quad (1)$$

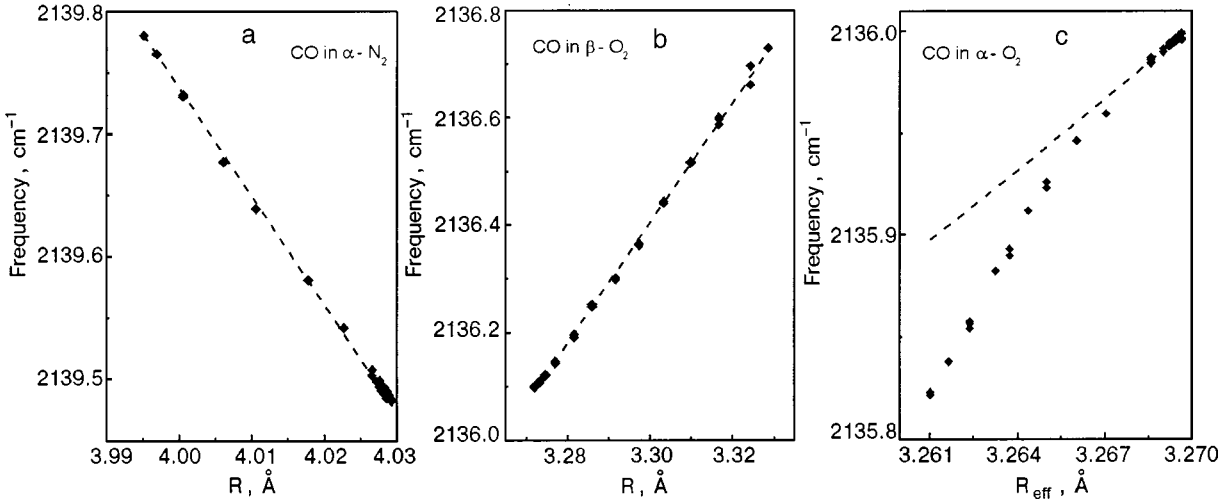

FIG. 6. Internal vibrational frequency ω of the CO molecules matrix isolated in orientationally ordered phases of solid nitrogen and oxygen versus the nearest-neighbor separation R: CO in α-nitrogen ($CO/N_2 = 5\times10^{-7}$) (a); CO in β- and α-oxygen (b) and (c), respectively ($CO/O_2 \sim 4\times10^{-8}$ as well as 4×10^{-7}). The experimental and theoretical values according to Eq. (1) are shown by diamonds and dashed lines.

Here B_e and ω_e are the rotational and harmonic vibrational constants of the MI molecule, respectively; η_{imp} and η_j are the orientational order parameter of the MI and host crystal molecules, respectively; R_j is the intermolecular distance between the MI molecule and the jth matrix particle; $A(R)$, $U_1(R)$, and $U_0(R)$ are combinations of the first and second derivatives of the potential energy of the MI molecule in a matrix with respect to the impurity interatomic distance, which are evaluated at the equilibrium interatomic distance; $K = B_e/\omega_e$; W is the normalized matrix shift.

The three force constants presented in (1) have different origins: $A(R)$ is determined by the isotropic part of the intermolecular interaction between the MI and host crystal molecules, whereas $U_1(R)$ and $U_0(R)$ are formed by the noncentral part. The force constants A, U_1, and U_0 in Eq. (1) are functions of the distance R between the MI molecule and host-crystal molecules. Of course, the host-crystal molecules are deformed by the impurity around them. The deformation field around an impurity causes some changes in the force constant quantities in comparison to the undeformed crystal. However, the temperature-caused changes in the deformation field (e.g., an excess volume caused by one impurity) are mainly determined by the thermal expansion of the host crystal.[24] Therefore we expect that the temperature behavior of the mode frequency of our MI molecule is governed mainly by the thermal expansion of the host crystal lattice, too.

We confirmed these general considerations by spectroscopic data for CO molecules MI in α-nitrogen and β-oxygen (Fig. 6a and 6b) (as well as for CO_2 in solid nitrogen)[1] as follows. Taking in account that the temperature-caused changes in the intermolecular distance of the host crystal are relatively small (about 1%) at the equilibrium vapor pressure, we can expand the normalized matrix shift W in equation (1) into a Taylor series:

$$W(R(T)) = W(R)|_{R_0} + (\partial W/\partial R)|_{R_0}[R(T) - R_0] + \text{higher orders}, \quad (2)$$

where R is the distance between nearest neighbors in the α-nitrogen and β-oxygen. Combining Eq. (2) and Eq. (1), we obtain a simple expression to model the experimentally determined mode frequency behavior $\Delta\omega(T)$ in the phases where this behavior is governed by one crystal lattice parameter. The $W(R_0)$ and $\partial W/\partial R_0$ values obtained by modeling the experimental data are presented in Table I. The nearest-neighbor distance R at 0 K and 24 K was chosen as R_0 for the α-N_2 and β-O_2, respectively.

The agreement achieved between experiment and model is excellent (Fig. 6a and 6b). Consequently, it means that spectroscopic data on MI molecules can be successfully used to deduce and estimate the molar volume changes in a host crystal if this is not known!

We drew this conclusion from spectroscopic measurements at equilibrium vapor pressure. Nevertheless, we expect that the same situation takes place also qualitatively at high pressure, i.e., the temperature behavior of the mode frequency of MI molecules during any isobaric route mainly reflects the thermal expansion of the matrix material. The corresponding experiments are planned to prove our assumption directly. Now we would like to discuss this mode frequency behavior of MI molecules in more detail. Comparing Figs. 6a and 6b, this behavior of the mode frequency of CO molecules MI in solid nitrogen is quite different from the behavior in solid oxygen. This qualitatively different behavior comes from the difference in the nature of the stability of the α-nitrogen and oxygen phases as well as from the differ-

TABLE I. Normalized matrix shift of CO fundamental frequency in different matrices.*

Host crystal	$W(R_0)$, cm^{-1}	$\partial W/\partial R_0$, cm$^{-1}\cdot$Å^{-1}
α-nitrogen	−3911 ± 11	−9942 ± 412
α- and β-oxygen	−8066 ± 44	−12560 ± 81

*For details, see Eq. (2).

ence in the intermolecular potential between the MI molecules and host crystal particles. The α-N_2 structure is stabilized by the *central* part of the intermolecular potential together with the quadrupole component of the noncentral interaction,[5] whereas the *noncentral* part of the repulsive interaction is responsible for the stability of the orientationally ordered phases of solid oxygen.[20] Therefore, the matrix shift of the fundamentals of impurity molecules is governed by the sum of an isotropic and a quadrupole–quadrupole interaction in case of α-nitrogen and by the noncentral part of the repulsive interaction in the case of α- and β-O_2.

Unexpected behavior of the CO fundamental was observed in α-oxygen. We tried to model the experimental frequency $\omega(T)$ or $\omega(R)$ similarly to the situation in β-O_2. Because of the monoclinic distortion in α-oxygen, two independent variables must be used in that case. We chose the effective distance between neighbors R_{eff} ($R_{\text{eff}}=\sqrt{3^{-1/2}S}$, S is the area of the basal plane of a unit cell) and the relative distortion in the b direction δ ($\delta=b-R_{\text{eff}}$; b is the unit cell parameter). This selected geometry allows us to preserve the similarity of α and β phases: R_{eff} like S, shows no discontinuity at the α-β phase transition, and δ is zero in β-O_2 by definition. Then, we can paraphrase (2) in a form that is applicable to the special case of α-O_2:

$$W_{\alpha-O_2}(R(T),\delta(T))=W(R_0)+(\partial W/\partial R_0)\times[R_{\text{eff}}(T)-R_0]+(\partial W/\partial\delta)|_0\,\delta(T). \tag{3}$$

As values for $W(R_0)$ and $\partial W/\partial R_0$ in the case of the α phase we kept the corresponding values obtained earlier for the β phase. The value $(\partial W/\partial\delta)|_0$ was obtained by modeling the experimental dependence at temperatures near the α-β phase transition and is equal to (486 ± 2) cm^{-1} Å^{-1}. This value is substantially smaller than the $\partial W/\partial R_0$ value (see Table 1). It means that the changes in frequency of the CO fundamental in α-oxygen are mainly determined by the changes in the area S of the unit cell basal plane. This result of our modeling is shown by a dashed line in Fig. 6c. A relatively small but distinct discrepancy is seen between the modeled $\omega(R)$ and experimental $\omega(T)$ values. This difference between experiment and theory (about 0.07 cm^{-1}) exceeds considerably the experimental inaccuracy (±0.005 cm^{-1}). We associate this deviation (Fig. 6c) with an increase in the magnetic order as the temperature decreases. Due to the strong dependence of the exchange interaction J_{ij} on the mutual orientation Ω_{ij} of interacting i and j molecules[23] ($J_{ij}=f(R_{ij},\Omega_{ij})$), an influence of the magnetic order on the orientational order parameter[26] must be considered here too, i.e., an increase in the magnetic order causes a mutual increase in the orientational order parameter. Therefore, the difference between the modeled $\omega(R)$, (broken line) and experimental $\omega(T)$ (symbols in Fig. 6c) values reflects the temperature-caused changes in the orientational order parameter, resulting from changes in the magnetic order of the α-oxygen, which were not taken into account in Eq. (3).

3.3. Determination of part of the binary phase diagram

a) *Solubility limit of* CO_2 *in oxygen and nitrogen*. In liquid oxygen, we observed the ν_3-fundamental of the CO_2 molecules matrix isolated in liquid oxygen at 2342 cm^{-1} (Fig. 7). In our IR spectra of liquid oxygen we could not observe and identify any other impurity absorptions. This ν_3-CO_2 band is present in the spectra of both series of our samples (*A* and *B*), with no substantial differences in frequency, bandwidth, and integrated intensity. Therefore we believe that our oxygen gas contains CO_2 molecules as a residual contamination without external leakage of the vacuum system. We did not find any information in the literature about CO_2 molecules in condensed phases of oxygen.

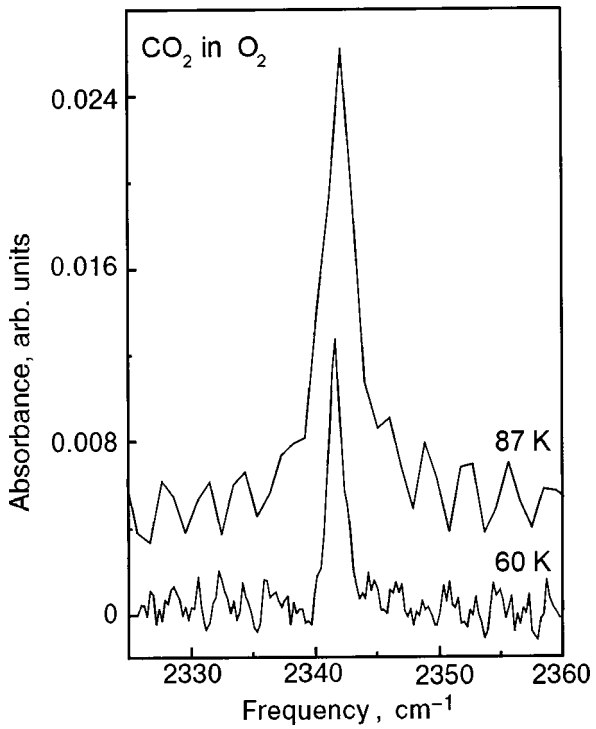

FIG. 7. Spectra of the ν_3-fundamental of the CO_2 molecules matrix isolated in liquid oxygen at two different temperatures. The CO_2 molecules are present in our oxygen (99.998%) as a residual contamination.

The temperature dependence of the mode frequency and the bandwidth is presented in Figs. 8a and 8b, respectively. The spectral resolution was 0.3–3 cm^{-1} in these measurements. Both temperature dependences were quite reproducible on cooling and warming. The profile of the ν_3-CO_2 fundamental is rather well described by a Lorentzian function. The temperature dependence of the integrated intensity was very surprising to us (Fig. 8c). This behavior was reproducible but not identical on cooling and warming. On cooling, the intensity increases slightly from 87 to 82 K, remains almost constant to 72 K, and decreases rapidly to 60 K. A very weak trace is visible at 57 K and disappears completely near the melting point; no traces of this band are observable in the solid state. This band of the MI CO_2 reappears during warming at 75 K. As the temperature increases, the integrated intensity of this band increases, too.

To estimate the amount of CO_2 molecules in liquid oxygen we compared the integrated intensity of the ν_3-CO_2 band in liquid oxygen with our data on the intensity of this band in α-nitrogen (see Fig. 3b). In the latter case, the CO_2 concentration (135 ppb) was independently determined by mass spectroscopy. This comparison shows that the concentration

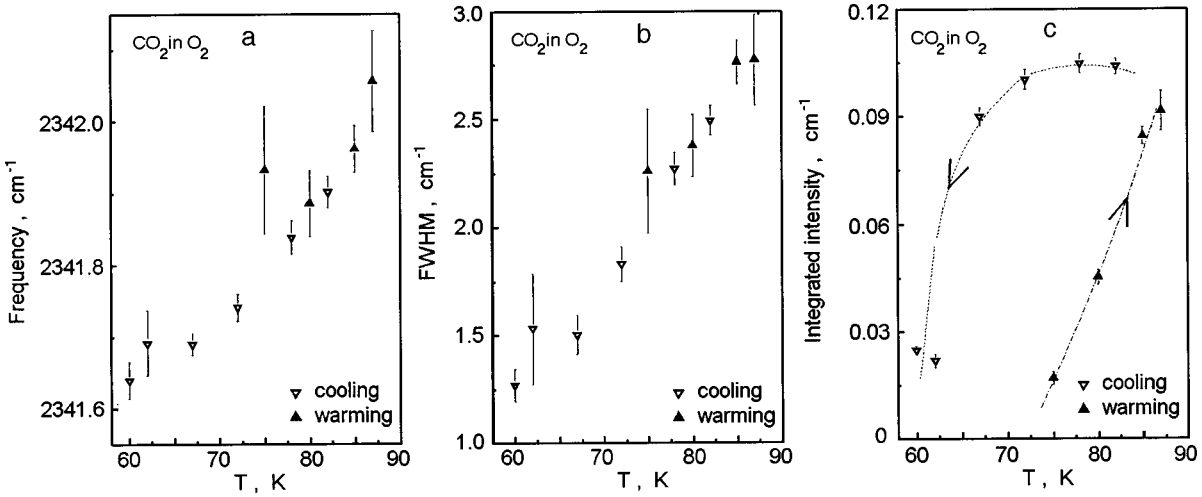

FIG. 8. Temperature dependences of the frequency (a), bandwidth (b), and integrated intensity (c) of the ν_3-internal vibrations of the CO_2 molecules matrix isolated in liquid oxygen (the lines in Fig. 8c emphasis a sequence in time). Bars show experimental inaccuracy.

of the CO_2 in liquid oxygen is varied from about 1.4 ppm at 82 K to about 0.19 ppm at 60 K.

We interpret this specific result as a direct determination of the thermodynamic solubility limit of CO_2 in oxygen. The solubility of the CO_2 in liquid oxygen decreases as the temperature decreases and becomes practically zero in solid oxygen: the CO_2 molecules evaporate out of the sample. During warming of the sample, CO_2 molecules are again dissolved in the sample. The different behavior at opposite temperature routes can originate from differences in kinetics during evaporation and dissolution.

A similar low solubility is also observed for CO_2 in solid nitrogen.[1] In nitrogen samples doped with 75 ppm CO_2 (series *B*), we observed spectroscopically crystalline clusters of about 200 CO_2 molecules in solid N_2. Besides this band due to clusters, an additional band was observed, which we assigned to the v_3-mode of CO_2 molecules matrix isolated in N_2. Due to Ref. 1, we believe that the solubility limit of CO_2 in solid nitrogen lies at about 1 ppm (or less).

b) *Influence of small amounts of* CO *on phase transitions in solid oxygen*. No information on the O_2–CO phase diagram exists up to now.[27] To investigate part of the O_2–CO phase diagram at small concentrations of CO we premixed 0.9 ppm CO gas with O_2 gas (series *B* of our samples), condensed this gas mixture at 87 K, and grew the crystal samples as described in Sec. 2. Only monomers of CO were observed in these samples. The integrated intensity of the CO band is $0.008 \pm 0.001\ \mathrm{cm}^{-1}$. Using the absolute absorption coefficient for gaseous CO,[4] we estimate the actual concentration of the CO in solid oxygen ($3-4\times10^{-7}$). The temperature evolution of the CO fundamental band near the α-β phase transition during cooling is shown in Fig. 9a. One can clearly recognize that the intensity of the CO band in β-O_2 is decreasing, whereas the intensity in α-O_2 is increasing as the temperature decreases. Therefore we can associate these changes in the spectra (Fig. 9a) to changes in the phase composition of the sample during the α-β phase transition. This transition is extended for 0.6 K (23.90–23.30 K in Fig. 9a) in this series of our samples in comparison to 0.15 K in samples of series *A* (Fig. 4c). In general, two external factors control a phase transformation rate at first order phase transition: (i) degree of overcooling (or overheating), i.e., the difference between the actual temperature and temperature of the transition point (23.90 K in the case shown in Fig. 9a), and (ii) exposure time at concrete temperature point in the two-phase temperature region. To determine which factor mainly rules the kinetics of the α-β phase transition in solid oxygen, some spectra were specially recorded during this phase transition at constant temperature as a function of time up to hours. About 3% of the new phase was created during 11 h at the constant temperature only, as displayed in Fig. 9b. The following decrease in temperature of 0.05 K creates about 40% of the new phase (the time of recording of the spectrum is about 3 h) (see Fig. 9a). Therefore, time-depending kinetics does not play a significant role at the α-β phase transition in solid oxygen, unlike the α-β phase transition in solid nitrogen (see Fig. 7c of Ref. 1).

To investigate the influence of CO on the α-β phase transition in more detail, we monitored the behavior of the CO fundamental near this transition in both opposite temperature routes (during cooling and warming) and determined the integrated intensity of the CO bands in both coexisting phases. The ratio of the integrated intensity of the CO band in the α phase (at the $\beta \rightarrow \alpha$ phase transition) and in the β phase (at $\alpha \rightarrow \beta$ phase transition) to the total intensity of two coexisting bands corresponds to the relative portion $C_{\mathrm{imp}} (0 \leqslant C_{\mathrm{imp}} \leqslant 1)$ of CO molecules dissolved in this phase (Fig. 10a). It is obvious that the transition on warming ($T_{\alpha\rightarrow\beta}$) begins at a lower temperature than the transition on cooling ($T_{\beta\rightarrow\alpha}$), i.e., the α-β transition in solid oxygen has been split into two transitions in these samples!

According to our considerations, there are two reasons for this feature ($T_{\alpha\rightarrow\beta} < T_{\beta\rightarrow\alpha}$). First, this temperature behavior results from some peculiarities of the α-β phase transition (magnetic + structural transitions, intermediate phase, etc.) and due to relatively high intensity of the CO band in these samples, this special oxygen feature could be observed. Second, it is a usual splitting of phase transitions in binary systems (O_2–CO in our case). To differentiate between these two possibilities we probed the β-γ phase transition by monitoring the oxygen vibron side band, whose shape is qualitatively different in these two phases (see Fig. 10b).

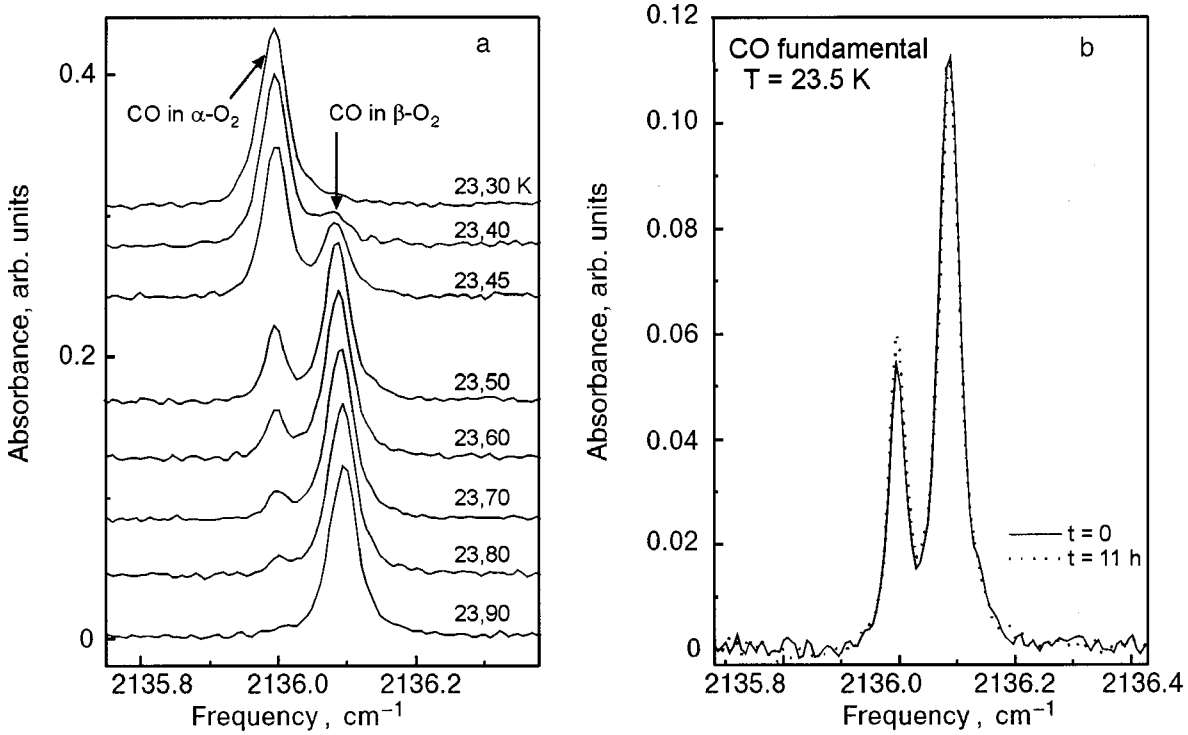

FIG. 9. Spectra of the CO band in the coexistence region of the α and β phases of solid oxygen ($CO/O_2 \sim 4\times10^{-7}$) during cooling: temperature evolution (a); spectra recorded at 23.5 K just after a temperature decrease (solid line) and 11 h later (dashed line) (b). The resolution is 0.015 cm^{-1}.

Temperature steps of 0.05 K were used. A shift of about 0.2 K towards higher temperatures is clearly observed for our samples enriched in CO (see Table II).

It means that CO molecules indeed influence the phase transitions in solid oxygen even at such low-concentrations (about 4×10^{-7}).

The second remarkable feature in Fig. 10a is the different temperature behavior of the integrated intensity of CO bands during $\beta\rightarrow\alpha$ and $\alpha\rightarrow\beta$ phase transitions. In general, the phase transformation in the two-phase region is accompanied by two processes: first, a change in the volume ratio of the co-existing phases, and second, a change in the concentration of the impurity in these phases. Both processes influence the temperature dependence of the C_{imp} values. Therefore, the difference in kinetics of $\beta\rightarrow\alpha$ and $\alpha\rightarrow\beta$ phase transitions, observed by monitoring the intensity of the CO bands, could result, in principle, from the thermodynamic equilibrium redistribution of the CO molecules between two coexisting phases. To verify this explanation of the results observed, we calculated the relative amount of the

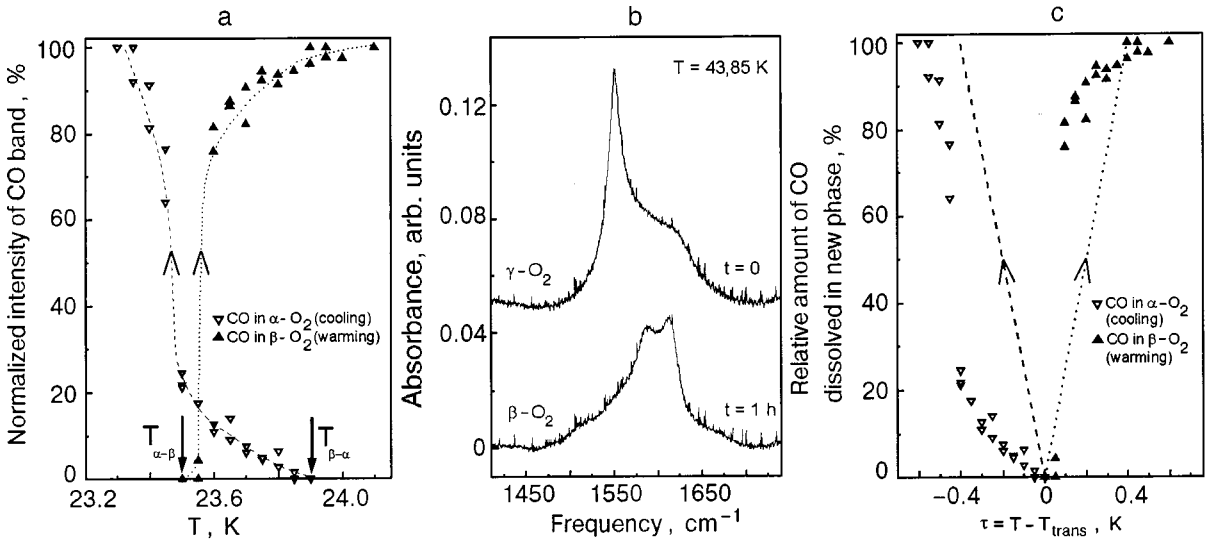

FIG. 10. Influence of CO molecules (concentration$\sim4\times10^{-7}$) on phase transitions in solid oxygen: the ratio of the integrated intensity of the CO band in the α phase during cooling ($\triangledown$) and in the β phase during warming ($\blacktriangle$) to the total intensity of two coexisting phases (a); the vibron side bands recorded during $\gamma\rightarrow\beta$ phase transition just after a temperature decreased (γ phase) and 1 hour later (β phase) (b); the same experimental values as in Fig. 10a in comparison with the portion of CO molecules dissolved in the new phase, calculated by Eq. (4) using the Gibbs phase rule (dashed lines—on cooling, dotted line—on warming) as a function of a suitable relative temperature $\tau = T - T_{trans}$ (c).

TABLE II. The β-γ phase transition points obtained monitoring the vibron side bands.

Samples	Temperature of the phase transition, K	
	$\gamma \rightarrow \beta$ (on cooling)	$\beta \rightarrow \gamma$ (on warming)
A (O_2, 99.998%)	43.65	43.90
B (O_2 + 0.9 ppm CO)	43.85	44.00

impurity dissolved in a new phase (C_{imp}) in the two-phase temperature region using the Gibbs phase rule. Due to very small concentrations of the second component, we presumed that both phase boundaries are linear functions of the total impurity concentration. As a result, we obtained the following simple equation for the temperature dependence of the C_{imp} values:

$$C_{\text{imp}} = |\tau| / (T^{c}_{\text{trans}} - T^{w}_{\text{trans}}), \quad \tau = T - T_{\text{trans}}. \tag{4}$$

Here T^{c}_{trans} and T^{w}_{trans} are the transition points on cooling and warming, respectively ($T_{\beta\rightarrow\alpha}$ and $T_{\alpha\rightarrow\beta}$ in our case); T_{trans} is the transition point on the thermal route that is considered; $T_{\alpha\rightarrow\beta} \leqslant T \leqslant T_{\beta\rightarrow\alpha}$; $0 \leqslant C_{\text{imp}} \leqslant 1$.

According to the thermodynamic calculations [Eq. (4)], the temperature-caused changes in C_{imp} must be identical during cooling and warming. However, this is not the case (Fig. 10c). On decreasing temperature, the experimental C_{imp} values increase noticeably more slowly than the calculated ones at $\tau \geqslant -0.4$ K. At $\tau = -0.45$ K ($T = 23.45$ K), the relative portion of CO molecules dissolved in the phase increases practically by a jump and shows behavior similar to the theory for lowering temperature. At the $\alpha \rightarrow \beta$ phase transition (warming), the portion of new β phase grows very quickly at $\tau = 0.1$ K ($T = 23.6$ K) and changes very slowly at higher temperatures. All these changes were *completely* reproducible during every temperature cycle. In our opinion, two different physical mechanisms are responsible for these peculiarities of the kinetics of the α-β phase transition. First, the nucleation and growth of the new phase inside the β and α phases create different deformation fields, and therefore the elastic strains accompanying the $\alpha \rightarrow \beta$ transition are different on opposite temperature routes. Second, the nonmagnetic β phase is nucleated on the CO impurities; therefore, CO molecules accelerate the $\alpha \rightarrow \beta$ phase transition.

The O_2-rich part of O_2-CO phase diagram reconstructed from our results is shown in Fig. 11. We expect peritectoid and eutectoid points for the β-γ and α-β phase transitions, respectively, at higher concentrations of CO. Remarkably, our diagram starts at concentration as low as $\sim 10^{-7}$, whereas usual $T-x\%$ diagrams start at % only (see the phase diagram in the inset of Fig. 11).

3.4. Bandwidth of the CO fundamental in solid nitrogen and oxygen

For possible theoretical studies, we display the temperature dependences of CO mode in O_2 in Table III. Figure 12 shows the temperature dependence of the CO fundamental bandwidth in solid nitrogen and solid oxygen for comparison. The temperature dependence of FWHM of the fundamental band of the CO molecules matrix isolated in solid oxygen does not show any noticeable changes at the α-β phase transition. To model the measured profile of absorption bands of MI CO molecules a Voigt function was used. Then this Voigt profile was deconvoluted into a Gaussian and a Lorentzian component, as shown in Fig. 12.

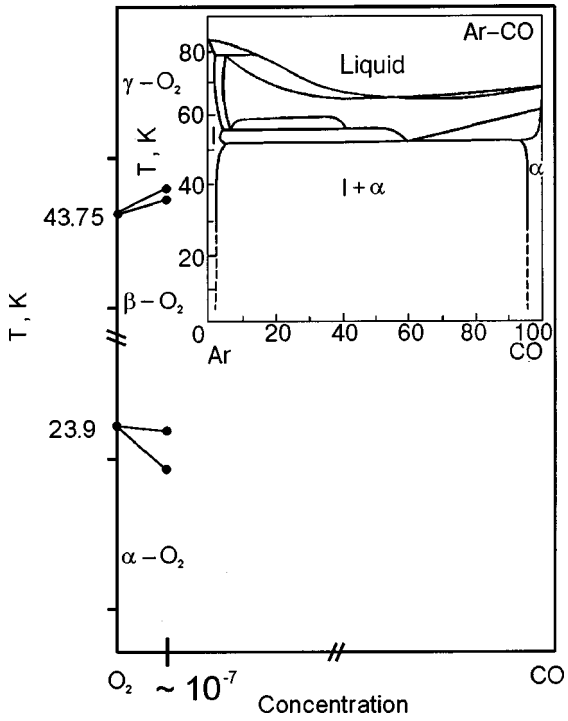

FIG. 11. Oxygen-rich part of the O_2–CO phase diagram. The Ar–CO diagram[27] is used for illustration purposes.

a) **Gaussian bandwidth**. In general,[1] the Gaussian bandwidth is a superposition of an inhomogeneous broadening and a quasistatic broadening. The former results from some host crystal imperfections and has practically no temperature dependence. The latter originates from instantaneous fluctuations of the environmental frequency shift of the impurity internal vibration because of orientational and translational motions of both dissolved and host crystal molecules. That is why the quasistatic broadening possesses a temperature dependence. Both components of the Gaussian bandwidth contribute to the residual ($T \rightarrow 0$ K) Gaussian broadening; however, only the inhomogeneous broadening can serve as a measure to characterize crystal structure perfection.

The Gaussian component of the CO fundamental bandwidth in solid nitrogen is characterized by small values at low temperatures (Fig. 12a). According to our modeling[1] the inhomogeneous broadening is zero in that case, and the residual Gaussian broadening ($T \rightarrow 0$ K) is determined by the zero-point oscillations of the CO and N_2 molecules.

The Gaussian bandwidth of the CO fundamental in solid oxygen is much larger in comparison to the case of solid N_2 and has no clear temperature dependence at low temperatures. Therefore the residual Gaussian broadening of the CO band ($T \rightarrow 0$ K) is mainly determined by imperfections of the oxygen crystal.

The Gaussian component of the fundamental bandwidth of CO in N_2 and in O_2 is characterized by a pronounced temperature dependence at temperatures higher than 20 and

TABLE III. Frequencies of the CO fundamental in orientationally ordered phases of solid oxygen (experimental inaccuracy ± 0.005 cm^{-1}).

Temperature, K	ω_{0-1}, cm^{-1}
α-oxygen	
11	2135.822
13	2135.838
15	2135.855
17	2135.882
18	2135.891
19	2135.912
20	2135.924
21	2135.946
22	2135.959
23	2135.986
23.5	2135.999
β-oxygen	
24	2136.099
24.5	2136.108
25	2136.121
26	2136.144
28	2136.193
30	2136.249
32	2136.299
34	2136.363
36	2136.442
38	2136.517
40	2136.594
42	2136.672

30 K (Fig. 12), due to quasistatic broadening. Near phase transitions, fluctuations of the orientational order become very large and therefore cause a strong increase in the Gaussian bandwidth (e.g., about 5 K below $T_{\alpha\beta}$ in solid nitrogen).

b) **Lorentzian bandwidth**. The Lorentzian bandwidth broadening of the impurity fundamental is determined by depopulation and dephasing processes and can be modeled by the following formula at not too high temperatures:

$$\Delta_L = B_{\text{depop}}(1+n_{\text{depop}}) + B_{\text{deph}} n_{\text{deph}}(1+n_{\text{deph}}). \quad (5)$$

Here B_{depop}, n_{depop} and B_{deph}, n_{deph} are the squares of the effective anharmonic coupling coefficients and the occupation numbers of corresponding phonons (ω_{depop} and ω_{deph}) for the depopulation and dephasing processes, respectively.[28]

The dephasing process in Eq. (5) may contain two physically different kinds of lowest-order quartic processes: a dephasing by host crystal lattice phonons,[28] and a dephasing by localized (or quasi-localized) modes induced by an impurity.[29] Let us now, model the experimental temperature dependence of the Lorentzian bandwidth by Eq. (5). First step: in the case of CO molecules matrix isolated in both crystals, only one depopulation decay channel exists at low temperatures, i.e., energy transfer to the isotope ^{13}CO. That is why we chose the difference between the frequencies of ^{12}CO and ^{13}CO isotopes (47.2 cm^{-1}) as the frequency ω_{depop} of lattice phonons involved in the depopulation processes. Because ω_{depop} is about 50 cm^{-1} and the concentration of the ^{13}CO isotope is very low, the contribution of depopulation processes to the Lorentzian bandwidth is expected to be very small. Second step: we varied three other parameters (B_{depop}, B_{deph}, and ω_{deph}) in Eq. (5). The result of our modeling is shown in Figs. 12a and 12b by dashed lines. The frequencies of the phonons involved and the values of the anharmonic coefficients obtained by modeling are presented in Table IV. In the case of α-nitrogen the frequency ω_{deph} (31 cm^{-1}) of a mode suited for a dephasing process matches very well with the frequency of one of the maxima of the phonon density of states (DOS) of the host crystal.[5] This means that the coupling of the CO internal vibrations with the α-N_2 lattice phonons is responsible for the broadening of the CO fundamental by dephasing processes. The vibronic dephasing of the CO molecules matrix isolated in solid oxygen is governed by a mode with frequency $\omega_{\text{deph}} = 77$ cm^{-1} (Table IV). This frequency is close to the high-frequency boundary of the phonon density of states of solid oxygen (83 cm^{-1}) and does not match with its maxima (40 and 70 cm^{-1}).[30] We think that this mode at $\omega_{\text{deph}} = 77$ cm^{-1} corresponds to a localized mode generated by perturbations due to the embedding of the CO molecules in the oxygen crystal. This analysis shows that the CO molecules fit into the nitrogen crystal, whereas the CO molecules cause significant perturbations in the oxygen crystal.

Our modeling of the Lorentzian broadening of the CO fundamental gives reasonable results only up to 32 K for both matrices. The pure dephasing mechanism results from the anharmonic interaction between the MI and host crystal molecules. Because we considered only the lowest-order quartic processes in Eq. (5), the observed discrepancy between the experimental values and fitted values shows that higher terms of the dephasing processes must be taken into account at higher temperatures.

4. CONCLUSION

Our aim was twofold: first, to realize the *real* matrix isolated case (impurity/matrix ratio $\sim 10^{-7} - 10^{-8}$); second, to probe the matrix material by analyzing the data on the matrix isolated molecules. This was achieved for CO and CO_2 isolated in solid nitrogen and oxygen by FTIR spectroscopy. We investigated several impurity concentrations. We were able to grow optically perfect crystals (inhomogeneous bandwidth), and cooling and heating of the sample over a wide range proved the reproducibility of the measurements.

From our spectroscopic data we are able to draw conclusions about the matrix isolated particle and its coupling to the matrix: from the mid-IR spectra we determined the frequency, bandwidth, integrated intensity, and band shape of the molecular vibration (CO and CO_2) as a function of temperature, concentration, and matrix (O_2 and N_2). For ex-

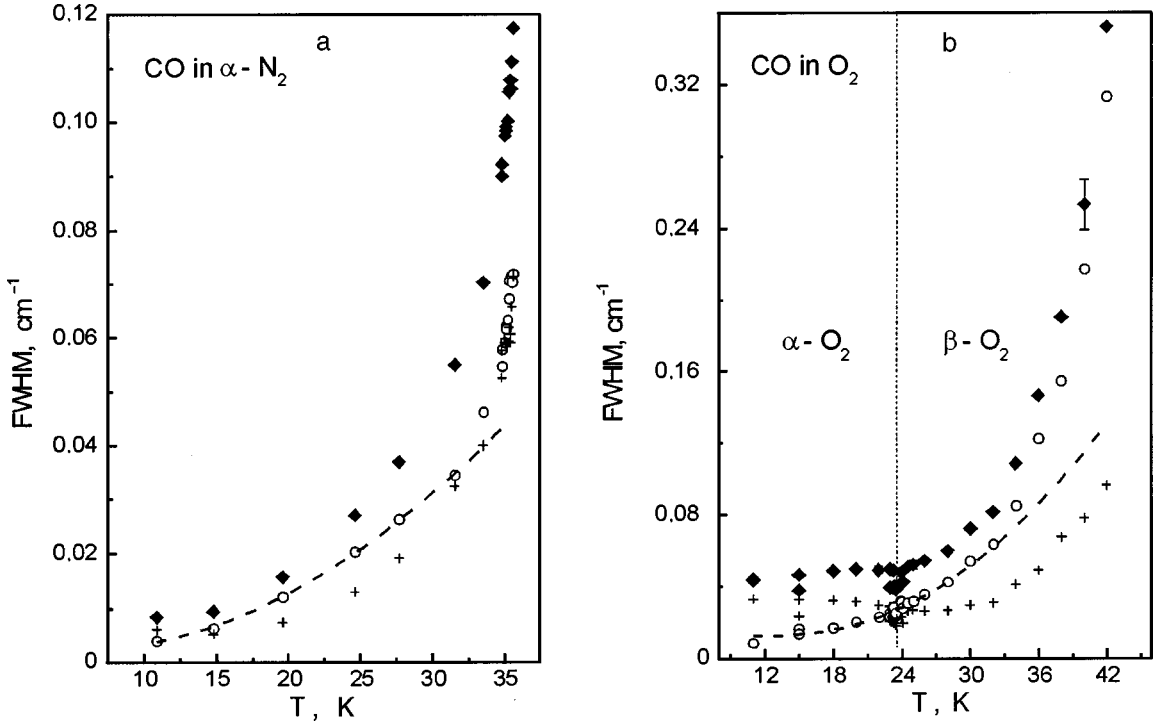

FIG. 12. Temperature dependence of the CO fundamental bandwidth in the orientationally ordered phases of solid nitrogen (a) and oxygen (b) (experimental values, ◆): the spectral profile of this band was first deconvoluted into a Lorentzian (○) and a Gaussian (+) band. The dashed line shows our fit of the bandwidth by a pure Lorentzian band shape.

ample: the measured band shape (Voigt profile) was modeled by a Gaussian and Lorentzian component. The Gaussian part of the bandwidth contains two terms: the inhomogeneous term mirrors the crystal quality ($\Gamma(T\rightarrow 0)<0.01\,\mathrm{cm}^{-1}$), and the quasistatic term is related to the orientational and translational relative motions between the impurity and matrix molecules. Near phase transitions, this quasistatic contribution to the Gaussian bandwidth increases enormously, and we characterize this anomalous behavior as a precursor to the phase transition. The Lorentzian part of the bandwidth is mainly governed by dephasing processes via lattice phonons (including localized modes) and is hardly affected by depopulation processes via isotopes of impurity molecules.

From our spectroscopic data of matrix-isolated molecules, we are able to draw conclusions indirectly about the matrix itself. We are able to classify the order of phase transitions of the matrix material via fingerprints in spectra (jump in frequency, hysteresis, coexistence of phases, etc.). This method was confirmed by direct observation of phonon side bands and a two-vibron band of the matrix, which show a distinctive behavior at phase transitions. From the temperature dependence of the environmental frequency shift ($\omega_{\mathrm{crystal}}-\omega_{\mathrm{gas}}$) of impurity vibrations, we could unambiguously draw conclusions about the thermal expansion of the matrix material, which sometimes is not known. Commonly, the matrix-isolated case is realized by 1‰ or 1%, whereas we studied an impurity/matrix ratio of about $10^{-7}-10^{-8}$. Therefore, we could make correct statements about the influence of the amount of impurities on the phase transition of the matrix and clearly determine solubility limits (CO_2 in N_2 or O_2 about 1 ppm).

TABLE IV. Parameters of the relaxation processes determining Lorentzian broadening of the CO bandwidth in α-nitrogen and orientationally ordered phases of solid oxygen.

Matrix	ω_{depop}	B_{depop}	ω_{deph}	B_{deph}
	cm^{-1}			
α-nitrogen	47.2	0.003	31	0.08
Oxygen	47.2	0.013	77	1.5

This work was supported by Deutsche Forschungsgemeinschaft (Grant No. Jo 86/11-1) and H. J. J. acknowledges support by NATO (Grant No. 950285). We appreciate the help of S. Medvedev during the last stages of the experiments. The authors are grateful to both referees for critical remarks.

*E-mail: jodl@physik.uni.kl.de

[1)]The coexistence of α and β phases near the α-β phase transition could be caused, in principle, by small temperature gradients in our samples. One may consider several origins for such gradient: 1) heating of our sample by light irradiation; since the illumination of our sample as well as its absorption is different in different regions (mid-IR to visible spectral region), and since the two-phase region in our spectra is always present, this is no explanation; 2) a permanent temperature gradient throughout the sample due to the cold finger and cell geometry. Since we varied the diaphragms of illumination (from 0.8 to 1.5 mm) and also since the spectra were not affected, this cannot be the case. In addition, we studied 5 samples and 11 heating/cooling cycles and reproduced all our results. Therefore, we are convinced to that we are monitoring the true phase coexistence region in our spectra.

[1] M. Vetter, M. Jordan, A. P. Brodyanski, and H. J. Jodl, J. Phys. Chem. A **104**, 3698 (2000).
[2] I. N. Krupskii, A. I. Prokhvatilov, Yu. A. Freiman, and A. I. Erenburg, Fiz. Nizk. Temp. **5**, 271 (1979) [Sov. J. Low Temp. Phys. **5**, 130 (1979)].
[3] A. F. Prikhotko, Yu. G. Pikus, and L. I. Shanskii, Opt. Spectrosc. **54**, 277 (1983).
[4] P. Varasani and S. Sarangi, J. Quant. Spectrosc. Radiat. Transf. **15**, 473 (1975); B. Schurin and R. E. Ellis, J. Chem. Phys. **45**, 2528 (1966); C. L. Korb, R. H. Hunt, and E. K. Plyler, J. Chem. Phys. **48**, 4252 (1968).
[5] *Physics of Cryocrystals*, edited by V. G. Manzhelii, and Yu. A. Freiman (AIP, Woodbury, New York, 1997).
[6] R. A. Alikhanov, JETP Lett. **5**, 430 (1967); R. J. Meier and R. B. Helmholdt, Phys. Rev. B **29**, 1387 (1984).
[7] M. F. Collins, Proc. Phys. Soc. **89**, 415 (1966); D. E. Cox, E. J. Samuelssen, and K. H. Beckurts, Phys. Rev. B **7**, 3102 (1973); F. Leoni and F. Sacchetti, Phys. Rev. B **7**, 3112 (1973).
[8] C. S. Barret, L. Meyer, and J. Wasserman, J. Chem. Phys. **47**, 592 (1967).
[9] T. G. Blocker, M. A. Kinch, and F. G. West, Phys. Rev. Lett. **22**, 853 (1969).
[10] C. H. Fagerstroem and A. C. Hollis-Hallet, J. Low Temp. Phys. **1**, 3 (1969).
[11] C. Uyeda, K. Sugiyama, and M. Date, J. Phys. Soc. Jpn. **54**, 1107 (1985).
[12] P. W. Stephens and C. F. Majkrzak, Phys. Rev. B **33**, 1 (1986).
[13] L. Lipinski, A. Szmirka-Grzebyk, and H. Manuszkiewicz, Cryogenics **36**, 921 (1996); J. Low Temp. Phys. **111**, 399 (1998).
[14] A. S. Baryl'nik and A. I. Prokhvatilov, Fiz. Nizk. Temp. **20**, 912 (1994) [Low Temp. Phys. **20**, 716 (1994)].
[15] V. A. Slyusarev, Yu. A. Freiman, and R. P. Yankelevich, JETP Lett. **30**, 270 (1979); Sov. J. Low Temp. Phys. **6**, 105 (1980); *ibid.* **7**, 265 (1981).
[16] Yu. B. Gaididei and V. M. Loktev, Sov. J. Low Temp. Phys. **7**, 643 (1981).
[17] B. Kuchta, T. Luty, and R. J. Meier, J. Phys. C: Solid State Phys. **20**, 585 (1987).
[18] M. Diem, Tai-Ly Tso, and E. K. C. Lee, Chem. Phys. **73**, 283 (1982).
[19] A. D. Buckingham, Faraday Soc. Trans. **56**, 26 (1960).
[20] A. P. Brodyanskii and Yu. A. Freiman, Fiz. Nizk. Temp. **11**, 426 (1985) [Sov. J. Low Temp. Phys. **11**, 231 (1985)].
[21] H. W. Lowen, K. D. Bier, and H. J. Jodl, J. Chem. Phys. **93**, 8565 (1990).
[22] K. D. Bier and H. J. Jodl, J. Chem. Phys. **81**, 1192 (1984).
[23] A. P. J. Jansen and A. van der Avoird, J. Chem. Phys. **86**, 3583 (1987).
[24] L. D. Yantsevich, Ph.D. Thesis, Institute for Low Temperature Physics and Engineering, Kharkov, (1987); A. P. Brodyanskii and M. A. Strzhemechny, Fiz. Nizk. Temp. **16**, 367 (1990) [Sov. J. Low Temp. Phys. **16**, 203 (1990)]; M. A. Strzhemechny, A. I. Prokhvatilov, and L. D. Yantsevich, Physica B **198**, 267 (1994).
[25] A. J. R. da Silva and L. M. Falicov, Phys. Rev. B **52**, 2325 (1995).
[26] A. P. Brodyanskii and Yu. A. Freiman, Fiz. Nizk. Temp. **11**, 994 (1985) [Sov. J. Low Temp. Phys. **11**, 548 (1985)].
[27] V. G. Manzhelii, A. I. Prokhvatilov, I. Ya. Minchina, and L. D. Yantsevich, *Handbook of Binary Solutions of Cryocrystals*, Begel House, New York (1996).
[28] P. Foggi and V. Schettino, Riv. Nuovo Cimento **15**, 1 (1992).
[29] D. J. Diestler and A. H. Zewail, J. Chem. Phys. **71**, 3103 (1979); **71**, 3113 (1979); D. Robert and L. Galatry, *ibid.* **64**, 2721 (1976).
[30] R. D. Etters, K. Kobashi, and J. Belak, Phys. Rev. B **32**, 4097 (1985).
[31] A. Jezowski, P. Stachowiak, V. V. Sumarokov, J. Mucha, and Yu. A. Freiman, Phys. Rev. Lett. **71**, 97 (1993).
[32] J. M. Dundon, Phys. Lett. A **61**, 58 (1977); E. Domany and E. K. Riedel, Phys. Rev. Lett. **40**, 561 (1978).

This article was published in English in the original Russian journal. Reproduced here with stylistic changes by the Translation Consultant.

FTIR studies of annealing processes and irradiation effects at 266 nm in ozone–amorphous ice mixtures

H. Chaabouni, L. Schriver-Mazzuoli, and A. Schriver*

Laboratoire de Physique Moléculaire et Applications, Unité propre du CNRS, Université Pierre et Marie Curie, Tour 13, case 76, 4 place Jussieu 75252 Paris Cedex 05, France
(Submitted 14 March 2000)
Fiz. Nizk. Temp. **26**, 963–971 (September–October 2000)

Fourier transform infrared (FTIR) spectroscopy is used to study the vibrational spectrum of ozone trapped in amorphous ice (a situation observed on icy satellites in the solar system). Evaporation of ozone from ice is investigated from 30 to 150 K under a static pressure of 10^{-7} Torr. Condensed and chemisorbed ozone on the surface of micropores is released at a temperature between 40 and 80 K, and ozone in water lattice evaporates starting from 120 K. The release of ozone probes the gradual transformation of water ice. The photochemistry of ozone in excess ice is also investigated using 266 nm laser irradiation. At low temperature, condensation of H_2O/O_3 mixtures leads to ozone trapped in pores and cavities, and H_2O_2 is produced through the hydrogen-bonded complex between ozone and free OH bonds. At higher temperature, when a solid solution of ozone in water is observed, H_2O_2 is formed by the reaction of the excited oxygen atom $O(^1D)$ with the nearest water molecules. Kinetic studies suggest that recombination of the dioxygen molecule with ground-state atomic oxygen $O(^3P)$ is a minor channel. [S1063-777X(00)01209-3]

1. INTRODUCTION

Due to the importance of ozone in the atmosphere, infrared spectra of isotopic and natural ozone have been widely studied in the gas phase and in various matrices.[1] Recently, from observations by the Hubble Space Telescope, oxygen and ozone have been recently identified on Ganymede (a satellite of Jupiter)[2–5] and on Rhea and Dione (two Saturnian satellites).[6] All these satellites have surfaces rich in water ice. Oxygen, which resides in a condensed state at the surface of Ganymede in spite of the temperature range (80 to 140 K, depending on the latitude), is produced from the decomposition of water molecules in the surface ice by plasma bombardment. Thanks to defect-trapping bubble production by the ion fluxes,[7] surface adsorption, and clathrate formation, a large fraction of oxygen can stay in small ice voids. Dissociation of oxygen by UV photons or incident ions produces ozone, which in turn dissociates. Competition between active production and destruction of ozone leads to an O_2-O_3 equilibrium. On Ganymede the density ratio of $[O_3]/[O_2]$ was estimated[4] to be 10^{-4} to 10^{-3}, a value in agreement with the Chapmann equations[8] including quenching of $O(^1D)$ by O_2 and O_3. Although there is a general understanding of the processes involved, a quantitative understanding has not been achieved. In the present work we describe the IR spectra of ozone-water mixtures at low temperature, and then we examine the capacity of amorphous water ice for trapping O_3 at temperatures between 15 and 150 K. Finally, photodissociation of ozone in ice at 266 nm is reported. Ten years ago, as a part of their studies on photochemistry of solid ozone, Sedlacek and Wight mentioned briefly that irradiation of ozone in excess ice produced hydrogen peroxide, HOOH.[9] We confirm this observation and show that there are two origins for H_2O_2 formation: first a low-temperature one due to an ozone monolayer chemisorbed at the surface of the pores, and another one at higher temperature due to ozone which has diffused in the water ice lattice.

2. EXPERIMENTAL

The helium gas used was supplied by Air Liquide (N55). Water vapor was taken from distilled water (Prolabo for chromatography) which was first subjected to several degassing cycles under vacuum. Ozone was prepared from oxygen (Air Liquide N50) contained in a glass vacuum finger excited by a Tesla-coil discharge with trapping of ozone at liquid nitrogen temperature. Residual oxygen was removed by a freeze–pump–thaw cycle with liquid nitrogen. Water–ozone gas mixtures were deposited onto a gold-plated mirror with helium as carrier gas. Above 15 K, helium does not condense. Several H_2O/O_3/He mixtures with different ratios of O_3 and H_2O were prepared. The total pressures of ozone and water were typically 12 Torr, and the pressure of helium was 150 Torr. Cooling was provided by an Air Product Displex 202A rotating closed-cycle refrigerator with KBr optical windows for performing IR measurements and one quartz window for UV photolysis. The static pressure was 10^{-7} Torr. The temperature of the metal substrate was controlled by a silicon diode (Scientific Instruments 9600-1). The gas mixture was deposited via a capillary with a rate of 6 μmol·h^{-1}. The deposition nozzle parameters were 1 mm inner diameter and a distance of 20 mm from the gold substrate. The thickness of the layers was typically less than 500 Å. The spectra were recorded with a FTIR Bruker IFS 113 v spectrometer in the reflection mode (angle of incidence 5° from the normal to the surface). The nominal resolution was 0.5 and 2 cm^{-1}. Ozone photodissociation was carried out at 266 nm using the fourth harmonic of a Nd–YAG laser (YG 781C-20 from Quantel) which operates at 20 Hz with a 4-ns

pulse duration. The initial power was adjusted to 10–25 mJ per pulse. The light intensity was spatially homogenized with a divergent lens placed in front of the cryostat UV window. The fluence inside the cryostat was estimated from the power measured with a PSV 3102 Gentic S/N 61592 detector with a cross section of 1.76 cm^2 that was placed after the lens and a CaF_2 window simulating the entrance window of the cryostat.

3. SPECTROSCOPY

3.1. Water ice

At low pressure and temperature, water ice exists in metastable states which are not in thermodynamic equilibrium. All structural transitions are time-dependent and irreversible.[10] Water vapor deposition below 30 K results in the formation of high-density amorphous ice (1.1 $g\cdot cm^{-3}$), generally labeled as I_{ah}, which has a great degree of polymorphism depending primarily upon the deposition conditions. Between 30 and 70 K, I_{ah} transforms gradually into another, more ordered amorphous ice, labeled low-density ice, I_{al}(0.94 $g\cdot cm^{-3}$) which exists till about 130 K. At the glass transition temperature 127–133 K, I_{al} transforms into a third amorphous phase, called the ''restrained phase'' (I_{ar}), which has the character of a strong liquid and which coexists with cubic ice I_c from 130 to 220 K. The transition of both I_c and I_{ar} in hexagonal ice is only observed under confinement pressure at 195–223 K. Crystalline ice is converted to amorphous ice by ion irradiation[11,12] and short-wavelength UV irradiation.[13]

Amorphous ice is microporous, with a wide pore size distribution (from 10 to 30 Å). Apparent surface areas have been calculated from gas adsorption isotherms. According to deposition temperature and hence to the morphology of the amorphous ice, the surface areas can vary from about 40 to about 200 $m^2\cdot g^{-1}$ (Refs. 14–16). Thus the density which is measured from the compact bulk depends on the number and the distribution of voids and can reach values of less than 0.75 $g\cdot cm^{-2}$ (Ref. 17).

Numerous studies have been devoted to the IR spectra of ice because the coupled υ_{OH} band, the band most studied up to now, reflects the structure of ice, and its shape and the frequency of its maximum can therefore be used to distinguish the different forms of ice between 10 and 160 K. A thorough description of the absorptions of water under our experimental conditions has been recently reported.[18] Spectral effects on the υ_{OH} stretching band related to structural differences are discussed in light of previous works. Figure 1 compares typical spectra of ice films deposited at different temperatures. High-density amorphous ice (I_{ah})($T<30$ K) has a strong polymorphism, and according to the deposition rates the broad band around 3380 cm^{-1} is often accompanied by secondary maxima as illustrated in Fig. 1 (traces a, b, c). Narrow bands observed at about 3690 and 3671 cm^{-1} are assigned to free OH bonds (dangling bands) of water clusters. The more ordered low-density amorphous phase (I_{al}) is characterized by a band at about 3250 cm^{-1} (whatever the deposition type) with a shoulder at 3380 cm^{-1}, corresponding to a small amount of high-density amorphous ice which persists over extended periods of time and above 130 K. In our configuration, no dangling OH band at 3699 cm^{-1}, characterizing triple coordinated water molecules at the surface, were observed, perhaps because of orientation effects or to their weakness. When I_{al} is obtained by annealing of a I_{ah} film we observe an increase in intensity of the broad coupled υ_{OH} band due to formation of OH...O bonds. Spectra of water ice deposited directly at 150–160 K or obtained by annealing of amorphous ice above 130 K are characterized by a partially resolved doublet at about 3200 and 3130 cm^{-1}.

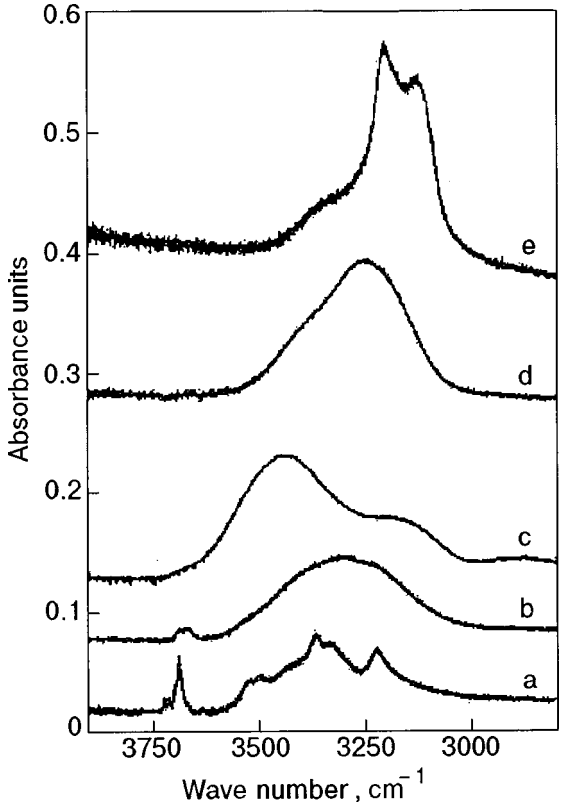

FIG. 1. Typical infrared spectra in the υ_{OH} region of water ice films deposited: at 11 K with different deposition rates, $\mu mol\cdot h^{-1}$: 0.06 (a), 2 (b), 6 (c); at 70 K (d); at 150 K (e).

3.2. Solid ozone

As previously reported,[19] solid ozone has two solid phases, an amorphous phase which is obtained below 11 K and a crystalline phase which is obtained above 50 K. Over the temperature range 11–50 K, condensation of ozone results in a mixture of disordered and ordered phases. The amorphous phase is stable until 50 K and the crystalline phase sublimes from 61 K with an activation energy of (23 $\pm$2) $kJ\cdot mol^{-1}$.

Representative spectra of ozone deposited at different temperatures are shown in Fig. 2 in the υ_3 region of ozone. As can be seen, the υ_3 band, the most intense in the gas phase or in matrices, shifts from 1037 cm^{-1} to 1026.2 cm^{-1} and narrows, with a full width at half maximum (FWHM) from 9.1 cm^{-1} to 1.4 cm^{-1}, when going from the amorphous to the crystalline phase. The two satellites features measured at 1054.4 and 1048.0 cm^{-1} in the spectrum of crystalline ozone have been assigned to clusters of ozone formed in the gas phase. Characteristics of other bands (fundamentals and combinations) are given in Ref. 19.

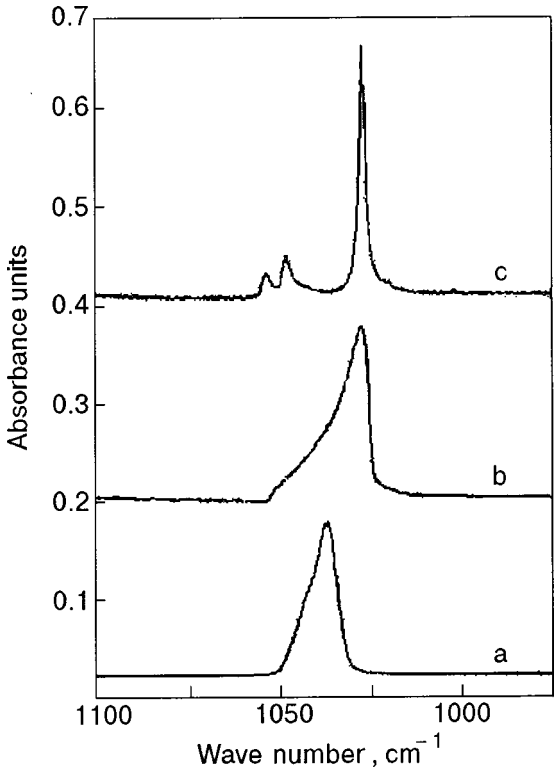

FIG. 2. FTIR spectra in the υ_3 region of condensed films of ozone deposited on Au substrates at different temperatures *T*, K: 11 (a); 30 (b); 55 (c).

3.3. Water/ozone mixtures

In order to examine the effect of water ice on the spectrum of ozone, several mixtures with different H_2O/O_3 ratios (from 0.25 to 10) were deposited at 30 K with helium as the carrier gas. Higher ratios could not be accurately studied due to the weakness of ozone in thin ice films. Figure 3 compares the spectra of some films with different compositions. In the υ_3 region of ozone, the spectrum of the sample rich in ozone (trace a) is nearly similar to the spectrum of pure ozone deposited at 30 K (see Fig. 2, trace b). With increasing water concentration, the υ_3 ozone band broadens, becomes more symmetrical, and shifts weakly towards high frequency. However, small changes were observed in the profile of the band from one sample to another with similar composition, indicating that ozone in ice is in different states depending on the condensation process, as discussed below. In the less ozone-rich film (trace d of Fig. 3) the υ_3 absorption appeared as a nearly symmetrical band with a maximum at 1035.6 cm^{-1} and a FWHM of 10.2 cm^{-1}. In the υ_{OH} region of water, a new band located between 3647 cm^{-1} and 3640 cm^{-1}, depending on the composition, appeared due to the interaction of ozone with water molecules having a free OH bond. Such a band (hereafter labeled D_{ga}) was also observed when ozone was deposited on the surface of a thin water film, and it was assigned to a monolayer of ozone hydrogen bonded to water molecules in the bulk pores of amorphous ice.[19] In the mixture rich in ozone this band appeared as a shoulder on the dangling bands at 3683 and 3666 cm^{-1} characterizing free OH groups of water clusters.

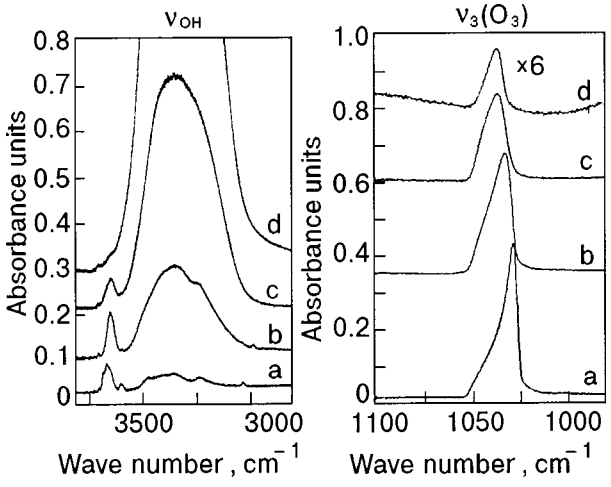

FIG. 3. Infrared spectra in water υ_{OH} and ozone υ_3 regions of H_2O/O_3 mixtures deposited at 30 K. Initial ratio: 0.25 (a); 1 (b); 5 (c); 10 (d).

In spite of premixing of the water and ozone gases, experiments showed that condensation of ozone/water mixtures at low temperature has varying efficiency and leads to several uncontrolled metastable states of ozone. As a matter of fact, the ratio between integrated intensities of the υ_{OH} coupled band and of the υ_3 ozone band was not accurately correlated to the initial ratio of H_2O/O_3 pressures. In the same manner, the ratio between integrated intensities of the perturbed OH band at 3640.5 cm^{-1}(D_{ga}) and of the υ_3 ozone band varied from 0.7 to 3 for films having the same initial composition. Amorphous ice is a disordered material containing pores, cracks, voids, and capillarities, into which ozone can penetrate. According to the composition, codeposition of H_2O/O_3 samples on cold substrates at 30 K can generate separate ozone layers on the amorphous ice surface, ozone large clusters trapped in the ice, a monolayer of ozone molecules hydrogen-bonded to water in the pores, condensed ozone in the pores or cracks, and, probably, only a very small amount of ozone in substitutional sites of the ice lattice.

4. TEMPERATURE EFFECTS

Two sets of experiments were carried out. In the first set, after deposition at 30 K the mixed films were annealed at 160 K at a rate of 5 K· min^{-1}, and successive spectra were recorded after each temperature increase. In the second set, mixed films were deposited directly at 70 K.

4.1. Mixtures deposited at 30 K

4.1.1. Mixtures rich in ozone

Figure 4 shows the evolution with temperature of a spectrum of a initial mixture rich in ozone (H_2O/O_3=0.25). Between 30 and 50 K, the intensity of the υ_3 band of ozone and of the associated dangling band D_{ga} at 3647.5 cm^{-1} remained unchanged, while the υ_{OH} band of water increased in intensity, indicating that I_{ah} begins to transform into I_{al}, with the loss of the 3683 and 3666 cm^{-1} features assigned at free OH in clusters. Only the frequency of the D_{ga} absorption shifted from 3647.5 cm^{-1} to 3642.4 cm^{-1}. In the 50–55 K temperature range, amorphous ozone (multilayers and ozone in interaction with water) disappeared, as monitored by the disappearance of the high frequency of the υ_3 band and the decrease in intensity of the D_{ga} feature, which was now located at 3640.5 cm^{-1}. From 55 to 60 K the spectra

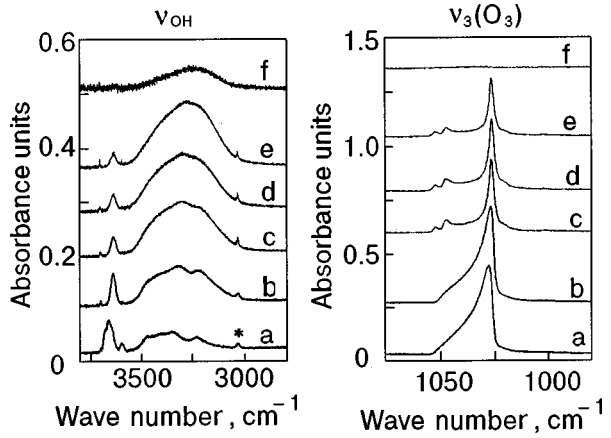

FIG. 4. Annealing effects on the υ_{OH} band of water and on the υ_3 band of ozone after deposition at 30 K of a H_2O/O_3 mixture rich in ozone (H_2O/O_3=0.25): after deposition at 30 K (a); after successive annealing at different temperatures *T*, K: 50 (b); 55 (c); 60 (d); 65 (e); 70 (f). All spectra are recorded at the annealing temperature. (* is $3\upsilon_3$ band of ozone).

remained unchanged. Above 60 K, crystalline ozone (multilayers and ozone in interaction with water) began to evaporate and disappeared totally at 70 K. Water ice also disappeared nearly totally at 70 K along with the ozone.

The overall behavior of water between 30–60 K, similar to that of a pure water film, suggests that water molecules trapped in the ozone matrix probably diffuse in the ozone as the temperature increases, forming islands of water molecules which stay inside the ozone and sublimate when the ozone desorbs.

4.1.2. Mixtures rich in water

As expected, a great difference was found between films rich in ozone, which sublimate at 70 K, and films rich in water, which evolve nearly in the same manner for initial ratios H_2O/O_3 ranging from 2 to 10. Figure 5 shows typical spectra of an H_2O/O_3 film (initial ratio 3) deposited at 30 K and gradually annealed at 150 K, and Fig. 6 presents the evolution of the integrated intensities of the υ_3 ozone band and of the D_{ga} band as a function of temperature as well as

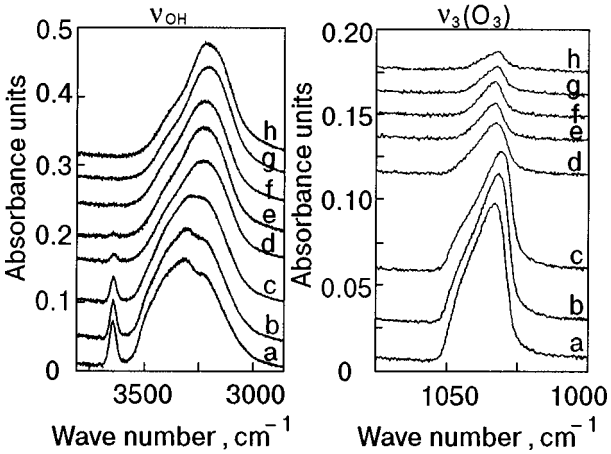

FIG. 5. Spectral changes with temperature in the υ_{OH} region of water and in the υ_3 region of ozone after deposition at 30 K of a H_2O/O_3 mixture rich in water (H_2O/O_3=3): after deposition at 30 K (a); after annealing at different temperatures *T*, K: 50 (b); 60 (c); 70 (d); 80 (e); 120 (f); 140 (g); 150 (h).

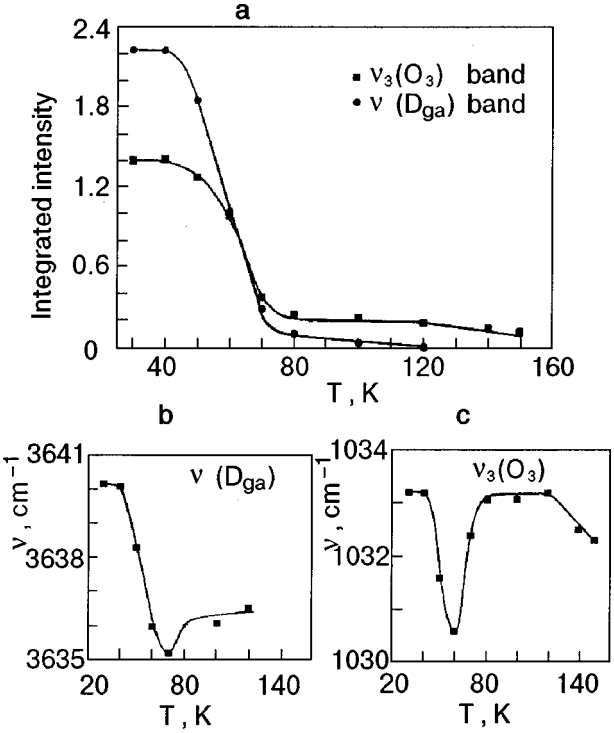

FIG. 6. Integrated band intensities as a function of temperature for the associated ozone dangling band and ozone υ_3 band of the experiment presented in Fig. 5(a). Temperature dependence of frequencies of the associated OH band (3640 cm^{-1}) (b) and the υ_3 ozone band (1033 cm^{-1}) (c) of the experiment presented in Fig. 5.

the evolution of the frequencies of the υ_3 ozone band and the associated OH band (D_{ga}) with temperature. Two distinct ranges of ozone release are observed. The first part starts at 50 K and stops at 80 K. The second part starts at 120 K and is totally exhausted when the sample is kept at 150 K. The same trend was observed in other experiments, except that in some, but not all, of the more water-rich samples ozone remained at 160 K, suggesting that the formation of a local hydrate clathrate could occur by rearrangement in the solid state, depending on the mixture composition as well as condensation and annealing processes. Indeed, ozone release, which is in competition with ozone diffusion in the bulk of water at temperatures higher than 60 K,[19] results from changes in the ice morphology. Between 50 to 80 K the release of ozone condensed in the pores parallels the structural transformation of high-density amorphous ice into low-density amorphous ice, as monitored by the evolution of the υ_{OH} band shape. Between 50 to 60 K few changes are observed, and the intensity of the υ_3 ozone band weakly diminishes. Between 60 to 70 K the transformation is achieved, and a strong decrease of the υ_3 ozone band is observed. Upon warming, the pores collapse and the part of the ozone trapped in the pores is released. From 120 to 150 K low-density amorphous ice transforms into crystalline ice, and the rearrangement of water molecules opens some of the blocked channels and results in the loss of diffused ozone in substitutional water sites. These results are similar to previous findings for the release of CH_4, Ar, N_2, Ne, H_2,[20,21] and CO[21–24] from water ice.

As is seen from Fig. 6, the profile and the frequency of the υ_3 ozone absorption change with the temperature. In the

30–60 K temperature range, the initial band at 1033.2 cm^{-1}(FWHM=17 cm^{-1}) shifts gradually to 1030.6 cm^{-1}. Above 80 K, a narrower, nearly symmetric band (FWHM=10.2 cm^{-1}) clearly emerges and shifts from 1033.1 to 1032.3 cm^{-1} between 120 and 150 K. In fact, the υ_3 ozone band is a composite of several overlapping bands which probe the annealing-produced changes in the surrounding water solid and the diffusion of ozone in water ice. The OH dangling bond in interaction with ozone is also very sensitive to the structural change of ice with temperature, but warming of the ice substrate affects this band differently than the υ_3 ozone band. From 40 to 80 K, it diminishes monotonically and shifts from 3640.1 to 3636.1 cm^{-1}. This band probes the collapse of the pores, which begins at 40 K without the release of ozone at this temperature; ozone begins to sublimate from 50 K. Traces of this band are observed between 80 to 120 K but not above 120 K, indicating that the crystalline ice is nonporous.

4.2. Mixtures rich in water deposited at 70 K

Direct deposition of mixtures above 80 K showed that ozone was not trapped in water ice. Deposition at 70 K, a temperature at which solid ozone sublimes, led to a solid solution of ozone in water. Ozone appeared as a very weak band at a frequency in agreement with that observed previously between 80–120 K and with a comparable intensity for the same initial composition. When the temperature was increased from 140 to 160 K, ozone was slowly released, but a part remained in the bulk until evaporation of the water. This behavior might be an indication of the formation of local clathrates, as suggested previously, but it could also be due to ozone locked in deep voids without the possibility of release.

Overall, the experiments described above show that ozone that is produced on icy satellites of the solar system by photodissociation of oxygen can be kept inside water ice at temperatures higher than 120 K.

5. IRRADIATION EFFECTS

Irradiation with the 266 nm laser line (photon flux=5 $\times 10^{16}$ photons·$cm^{-2}\cdot s^{-1}$) was carried out at 17 K, first on H_2O/O_3 mixtures rich in water, deposited at 17 K, and then on a mixture annealed at 130 K and cooled to 17 K. In mixtures deposited at 17 K, ozone is mainly trapped in pores and voids as probed by the strong D_{ga} band at 3636 cm^{-1}, while in the preannealed mixture ozone resides mainly in the water lattice.

At an incident wavelength of 266 nm ozone produces atoms O(^1D) and O(^3P) with primary quantum yields of 0.83 and 0.17, respectively.[25]

5.1. Mixtures deposited at 17 K

Figure 7 compares in the 3750–700 cm^{-1} region a typical spectrum recorded after deposition at 17 K with a spectrum recorded at 17 K after 80 min of irradiation corresponding to the total disappearance of ozone. After irradiation, two weak, broad bands at 2858 cm^{-1} and 1425 cm^{-1} (FWHM =79 cm^{-1} and 102 cm^{-1}, respectively), with a weak feature at 1256 cm^{-1} appeared. These two new bands can be unambiguously assigned to hydrogen peroxide according to published data.[26] They are quite comparable in frequency and width to bands observed in the spectrum of amorphous hydrogen peroxide deposited at 83 K, as shown in Fig. 1 of Ref. 26. They correspond to the ($2\upsilon_2$,$\upsilon_2+\upsilon_6$,$2\upsilon_6$) and υ_2 modes of H_2O_2, respectively. The weak band at 1256 cm^{-1} can be assigned to the υ_6 mode.

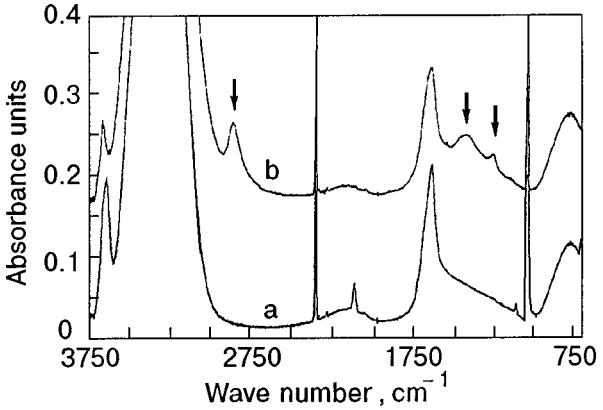

FIG. 7. 3750-700 cm^{-1} region in the spectrum of a H_2O/O_3 mixture (H_2O/O_3=4): after deposition at 17 K (a); after irradiation at 17 K for 80 min with a 266 nm laser line (photon flux=$5\cdot10^{16}$ photons·$cm^{-2}\cdot s^{-1}$)(b). New bands which appear after irradiation are indicated by arrows.

Figure 8 shows the key regions of spectra recorded after different irradiation times. After 100 seconds, the D_{ga} band disappears totally, the 2858 cm^{-1} absorption of H_2O_2 nearly reaches its maximum in intensity, and the υ_3 ozone band is reduced to 17% of its initial intensity. Upon subsequent photolysis the ozone that remains in the lattice disappears totally after 80 min of irradiation, with only a weak increase in intensity of the 2858 cm^{-1} absorption. These results are an indication that in this experiment the formation of hydrogen peroxide is mainly due to photodissociation of ozone chemisorbed on the water surface of micropores. In the –O–H:O_3 complex, H_2O_2 is formed by the transfer of an oxygen atom from ozone to H_2O. Such behavior is in agreement with previous studies in matrices. In an argon matrix, irradiation of the isolated one-to-one complex H_2O:O_3 also led to the formation of H_2O_2 (Ref. 27).

Kinetic studies of the disappearance of ozone and appearance of H_2O_2 were carried out. The decrease in the concentration of ozone was tracked by the decrease of the integrated intensity A of the D_{ga} absorption at 3636 cm^{-1} and of

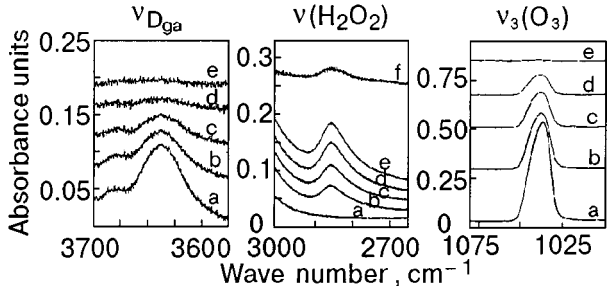

FIG. 8. Comparison of the spectra in the 3700-3575 cm^{-1}, 3000-2650 cm^{-1} and 1080–1000 cm^{-1} regions of a H_2O/O_3 mixture (H_2O/O_3=4): after deposition at 17 K (a); after irradiation at 17 K with a 266 nm laser line (photon flux=$5\cdot10^{16}$ photons·$cm^{-2}\cdot s^{-1}$) for 20 s (b), 40 s (c), 100 s (d), 80 min (e). Difference spectrum between (e) and (d) is (f).

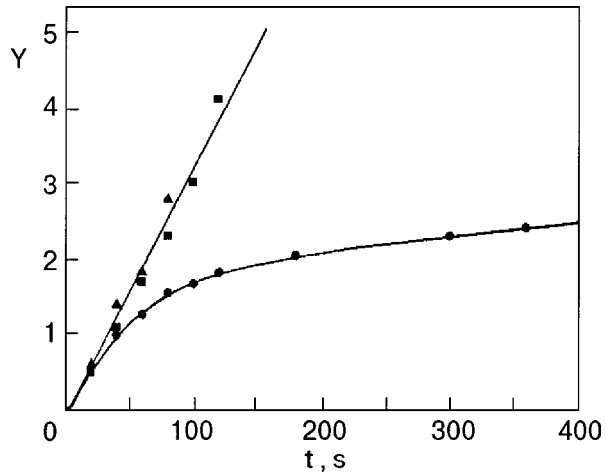

FIG. 9. Plots of $\ln(A^0_{O_3}/A^t_{O_3})$ (●), $\ln(A^0_{D_{gs}}/A^t_{D_{gs}})$ (▲), and $-\ln(1-A^t_{H_2O_2}/A^\infty_{H_2O_2})$ (■), denoted as Y, versus the operating time of the laser at 266 nm (photon flux$=5\cdot10^{16}$ photons$\cdot$cm$^{-2}\cdot$s^{-1}) for a H_2O/O_3 mixture ($H_2O/O_3=4$) deposited and irradiated at 17 K.

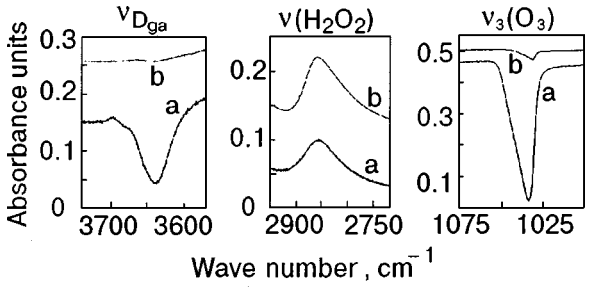

FIG. 10. Comparison of the key region of the difference vibrational spectra between spectra recorded before irradiation and after irradiation at 17 K of a H_2O/O_3 mixture deposited at 17 K (a) and of a H_2O/O_3 mixture annealed at 130 K and then cooled at 17 K (b).

the υ_3 ozone absorption. The increase of the concentration of hydrogen peroxide was monitored by the increase of the integrated intensity A of the 2858 cm^{-1} absorption peak, which reached an asymptotic limit A^∞ at long times. Plots of $\ln(A^0_{O_3}/A^t_{O_3})$, $\ln(A^0_{D_{ga}}/A^t_{D_{ga}})$, and $-\ln[(A^\infty_{H_2O_2}-A^t_{H_2O_2})/A^\infty_{H_2O_2}]$ versus irradiation times for a typical experiment (photon flux$=5\times10^{16}$ photons$\cdot$cm$^{-2}\cdot$s^{-1}) are shown in Fig. 9. The kinetics of H_2O_2 and of the –O–H:O_3 complex conforms to a first-order process with an apparent rate constant of $(3.5\pm0.5)\times10^{-2}$ s^{-1} (photon flux$=5\times10^{16}$ photons$\cdot$cm$^{-2}\cdot$s^{-1},) whereas the ozone kinetics does not conform to a first-order process. Two distinct phases are observed. The first phase shows the same linear dependence versus time as observed for H_2O_2 and –O–H:O_3 curves, whereas the second phase, at longer times, is characterized by a smaller plot with an apparent rate constant of 6×10^{-4} s^{-1}. Such kinetic curves have also been found for photodissociation of solid ozone[9] and ozone trapped in argon matrices[28] and have not been accurately explained. In fact, as recently demonstrated by Kriachtchev *et al.*,[29] during photolysis in the condensed phase the medium becomes more absorbing and leads to decrease of the laser intensity with depth. Thus the photolysis is more efficient near the surface as compared with deeper in the bulk, where it slows down with time. As a matter of fact, the kinetic rates at the same photon flux on a thicker water ice film were lowered.

5.2. Annealed mixture

A H_2O/O_3 mixture (initial ratio 4) was deposited at 40 K and slowly annealed at 130 K till the disappearance of the associated OH band (D_{ga}); this process was accompanied by the formation of partially cubic ice. Then the sample was cooled to 17 K and irradiation was carried out at 266 nm with the same photon flux used previously. Growth of the 2858 cm^{-1} band was observed, indicating that H_2O_2 in this experiment is produced by reaction of the O(^1D) atom with the nearest H_2O molecules. Two unexpected observations were made. First, the υ_2 band of hydrogen peroxide at 1425 cm^{-1} did not appear. Secondly, the ratio of integrated intensities between the 2858 cm^{-1} band, which appeared at the end of irradiation, and the ozone band at 1031.5 cm^{-1}, which disappeared totally after 10 min, was very different from that observed after irradiation of unannealed mixtures, as illustrated in Fig. 10. It was found to be 25, a value forty times larger than the ratio found previously. The following explanations can be suggested for these observations.

Absence of the υ_2 band of hydrogen peroxide can be due to our configuration using infrared reflection with an angle of incidence of 5°. Indeed, with this near-normal incidence on the surface, due to the metal surface selection rules, only the transverse optical mode, with a transition dipole moment parallel to the surface, can be excited. Thus in ordered ice the H_2O_2 molecule produced by the reaction of atomic oxygen with a water molecule could have an orientation preventing the observation of the 1425 cm^{-1} band.

In the first set of experiments (unannealed mixtures deposited at 17 K) the υ_3 ozone band corresponds not only to complexed ozone but also to pure condensed ozone on the surface or in the pores. Only the hydrogen-bonded complex between ozone and water produces hydrogen peroxide, and hence the ratio between the intensities of the 2858 cm^{-1} and the 1033 cm^{-1} absorption lines can be weaker than that observed after irradiation of isolated ozone trapped in the ice lattice. This explanation is in agreement with the temperature effects described in Sec. 4.1.2, which showed that a very small amount of ozone resides in the lattice. The great difference between the initial ozone that produced the same amount of H_2O_2 by irradiation in the two experiments (Fig. 10) indicates that deposition of a H_2O/O_3 mixture at 17 K leads mainly to ozone multilayers in pores and voids. However, a difference in the IR absorption coefficients between ozone on the ice surface and ozone inside the water lattice cannot be ruled ont.

Kinetic studies of the appearance of H_2O_2 and of the disappearance of ozone were carried out. The same shape of the kinetic curves was observed for H_2O_2 and O_3. The curves were similar to that previously observed for ozone (see Fig. 9) with a rate, at short times, of the same order of magnitude $(4.0\pm0.5)\times10^{-2}$ s^{-1} for a photon flux of 5×10^{16} photons$\cdot$cm$^{-2}\cdot$s^{-1}. Recall that the photokinetic rate constant $k(\lambda)$ depends on the photodissociation cross section $\sigma(\lambda)$ in cm^2/molecule (base e) of ozone at 266 nm, the quantum yield $\varphi(\lambda)$, and the photon flux $F(\lambda)$ in photons$\cdot$cm$^{-2}\cdot$s^{-1}:

$$k(\lambda)=\sigma(\lambda)\varphi(\lambda)F(\lambda).$$

Thus at short times the photodissociation of ozone forming an $O(^1D)$ atom appears with the same apparent quantum yield for ozone in the $-O-H:O_3$ complex, pure condensed ozone (as verified in a subsequent experiment where amorphous pure ozone was irradiated under the same experimental conditions), and ozone in the lattice. Unfortunately, in the absence of knowledge of the photoabsorption cross sections of ozone at 266 nm in water ice and in the condensed state, it is not possible to calculate it. Indeed, as was shown by Vaida *et al.* in the visible[30] and also qualitatively in this laboratory,[31–33] the absolute photoabsorption cross sections of species in condensed matter can be strongly modified with respect to their values in the gas phase.

Some information on the photolytic process can be obtained from the value of the rate constant found in our experiments. The kinetic rate of about $3.5\times10^{-2}\,s^{-1}$ at short times is comparable to the kinetic rate found for the photodissociation of ozone in nitrogen[31] at a comparable photon flux and hence very different from the kinetic rate found for the photodissociation of ozone in argon matrices ($9\times10^{-4}\,s^{-1}$).[28] In the argon matrix but not in nitrogen matrix, the major pathway of ozone photodissociation is the reformation of ozone in the cage from photofragments O and O_2, and the weak decrease of ozone is due to the exit of oxygen atom from the cage. A different situation is observed in water ice. As in the nitrogen matrix, photodissociation of ozone in ice is followed by the reaction of excited atomic oxygen with host molecules. Thus the possibility that the photogenerated $O(^1D)$ atoms may be quickly quenched to $O(^3P)$ atoms by collisions with the water molecule and then recombine with molecular oxygen appears as a slight probability. Unfortunately, the ratio between the IR absorption coefficients of the 2858 cm^{-1} absorption (H_2O_2) and the 1033 cm^{-1} band (O_3) is unknown, and the efficiency (probably very high) of the reaction between the mobile $O(^1D)$ atom and a nearest water molecule of the ice lattice cannot be accurately estimated.

Although much work remains in extending and quantifying our irradiation experiments, the results obtained in this pioneering work may be of interest in planetology. In particular, the formation of hydrogen peroxide by both the photodissociation of an $-O-H:O_3$ complex and the reaction of an $O(^1D)$ atom with host water molecules has been demonstrated. Hydrogen peroxide has not been identified on Ganymede and other icy satellites of the solar system because it has no spectral absorption in the visible. The presence of H_2O_2 has to be taken into account for evaluating quantitatively the amount of O_3 produced from O_2 in ice. Furthermore, dissociation of H_2O_2 into OH radicals can lead to subsequent reactions. Future experiments are planned in this laboratory. In particular, the determination of the UV photoabsorption cross sections of ozone in ice and its formation through the photodissociation of oxygen trapped in amorphous water ice and amorphous ice containing sulphur dioxide will be studied.

This work was supported in part by Program National de Chimie Atmosphérique and Program National de Planétologie.

*E-mail: schriver@ccr.jussieu.fr

[1] L. Schriver-Mazzuoli, A. Shriver, C. Lugez, A. Perrin, C. Camy-Peyret, and J. M. Flaud, J. Mol. Spectrosc. **176**, 85 (1996).
[2] J. R. Spencer, J. Geophys. Res. **100**, 19049 (1995).
[3] W. M. Calvin, R. E. Johnson, and J. R. Spencer, Geophys. Res. Lett. **23**, 673 (1996).
[4] K. S. Noll, R. E. Johnson, A. L. Lane, D. L. Domingue, and H. A. Weaver, Science **273**, 341 (1996).
[5] R. E. Johnson and W. A. Jesser, Astrophys. J. **480**, L79 (1997).
[6] K. S. Noll, T. L. Roush, D. P. Cruikshank, R. E. Johnson, and Y. J. Pendleton, Nature (London) **388**, 45 (1997).
[7] J. Gittus, *Irradiation Effects in Crystalline Solids* (Applied Science, London, 1978).
[8] J. W. Chamberlain and D. A. Hunten, *Theory of Planetary Atmospheres* (Academic, New York, 1987).
[9] A. J. Sedlacek and C. A. Wight, J. Phys. Chem. **93**, 509 (1989).
[10] P. Jenniskens and D. F. Blake, Astrophys. J. **473**, 1113 (1996).
[11] G. A. Baratta, G. Leto, F. Spinella, G. Strazzulla, and G. Foti, Astron. Astrophys. **252**, 421 (1991).
[12] R. L. Hudson and M. H. More, J. Phys. Chem. **96**, 6500 (1992).
[13] A. Kouchi and T. Kuroda, Nature (London) **344**, 134 (1990).
[14] E. Mayer and R. Pletzer, Nature (London) **319**, 298 (1986).
[15] J. A. Ghormley, J. Chem. Phys. **48**, 503 (1968).
[16] B. Schmitt, J. Ocampo, and J. Klinger, J. Phys. (Paris) **48**, 519 (1987).
[17] B. S. Berland, D. E. Brown, M. A. Tolbert, and S. M. George, *International Symposium Physics and Chemistry of Ices, Lebanon, New Hampshire, USA*, August 26–30 (1996).
[18] L. Schriver-Mazzuoli and A. Schriver, J. Mol. Struct. (submitted).
[19] H. Chaabouni, L. Schriver-Mazzuoli, and A. Schriver, J. Phys. Chem. (submitted).
[20] D. Laufer, E. Kochavi, and A. Bar-Nun, Phys. Rev. B **36**, 9219 (1987).
[21] A. Bar-Nun, G. Herman, D. Laufer, and M. L. Rappaport, Icarus **63**, 317 (1985).
[22] A. Kouchi, J. Cryst. Growth **99**, 1220 (1990).
[23] A. Givan, A. Loewenschuss, and C. J. Nielsen, Vib. Spectrosc. **12**, 1 (1996).
[24] S. A. Sandford and L. J. Allamendola, Icarus **76**, 201 (1988).
[25] H. A. Michelsen, R. J. Salawitgh, P. O. Wennberg, and J. G. Anderson, Geophys. Res. Lett. **21**, 2227 (1994).
[26] J. A. Lannon, F. D. Verderame, and R. W. Anderson Jr., J. Chem. Phys. **54**, 2112 (1971).
[27] L. Schriver-Mazzuoli, C. Barreau, and A. Schriver, Chem. Phys. **140**, 429 (1990).
[28] M. Bahou, L. Schriver-Mazzuoli, and A. Schriver, J. Chem. Phys. **110**, 8636 (1999).
[29] L. Kriachtchev, M. Petterson, and M. Rasanen, Chem. Phys. Lett. **299**, 727 (1998).
[30] V. Vaida, D. J. Donaldson, S. J. Strickler, S. L. Stephens, and J. W. Birks, J. Phys. Chem. **93**, 506 (1989).
[31] M. Bahou, L. Schriver-Mazzuoli, C. Camy-Peyret, and A. Schriver, J. Chem. Phys. **108**, 6884 (1998).
[32] A. Hallou, L. Schriver-Mazzuoli, A. Schriver, and P. Chaquin, Chem. Phys. **237**, 251 (1998).
[33] M. Bahou, L. Schriver-Mazzuoli, A. Schriver, and P. Chaquin, Chem. Phys. **216**, 105 (1997).

This article was published in English in the original Russian journal. Reproduced here with stylistic changes by the Translation Consultant.

Experimental analysis of $^{13}CO_2$ infrared stimulated emissions in solid argon

H. Chabbi, P. R. Dahoo,[1)] H. Dubost,[2)] B. Gauthier-Roy, A.-M. Vasserot, and L. Abouaf-Marguin

*Laboratoire de Physique Moléculaire et Applications du CNRS, associé ǵ l'Université Pierre et Marie Curie, Tour 13, boite 76, 4 place Jussieu, 75252 Paris Cedex 05, France**

(Submitted March 10, 2000)
Fiz. Nizk. Temp. **26**, 972–980 (September–October 2000)

Vibrational stimulated emissions of CO_2 trapped in low temperature argon matrices have been found experimentally not only in the 16 μm region (v_2 manifold) but also at 10 μm ($v_3 - v_1$ transition) in the double trapping site of concentrated samples. A detailed experimental description of these emissions is reported, including spectral analysis, time-resolved studies, laser energy dependence, and concentration and temperature effects. The characteristics of the emissions are discussed, giving some insight into the nonradiative intramolecular V–V transfers from the laser excited level $v_3 = 1$ towards the v_2 manifold, and inside this manifold. © *2000 American Institute of Physics*. [S1063-777X(00)01309-8]

INTRODUCTION

Recently[1–3] we have shown that low-temperature matrices offer favorable conditions for the observation of vibrational stimulated emission. Excitation by an infrared laser pulse leads to large population inversions among the vibrational levels of the guest molecules, so that the matrix becomes an amplifying medium at the corresponding frequencies. Spontaneously emitted photons are then amplified on their passage through the sample, a phenomenon usually called amplified spontaneous emission (ASE).[4,5] When it originates from a vibrational transition, the process is also referred to as IRSE (infrared stimulated emission) or VSE (vibrational stimulated emission). This phenomenon only happens if the population of excited molecules exceeds a threshold, which discriminates between stimulated and spontaneous processes. When compared to spontaneous emission, a VSE signal appears amplified and shortened by a factor which can reach several orders of magnitude, depending on numerous factors such as the linewidth and line strength of the transition, density of excited molecules, thickness of the sample, and temperature. The amplified pulse should be followed by the spontaneous fluorescence of the molecules, whose population inversion has decreased to under threshold. This has been observed, for example, in the case of CO trapped in a mercury doped nitrogen matrix.[6] The stimulated peak is about 150 times larger than the maximum of the remaining long fluorescence, and it is only observed in a narrow temperature interval (17–22 K). In most experiments,[1–3] on the contrary, we detect a giant pulse without any longer spontaneous signal, this fluorescence being obviously too weak for the sensitivity of our detection. Among the three triatomic molecules recently studied, O_3[1], CO_2[2], and N_2O[3], CO_2 provides the richest system due to the rather long time scale of the 16 μm emissions. Moreover, these emissions arise from different vibrational levels in the v_2 manifold.

The aim of the present paper is to complete the preliminary results[2] by a thorough experimental study involving spectroscopic details, time analysis, and concentration and temperature effects. Besides, a new result has been obtained: we have found stimulated emission also in the 10 μm region.

EXPERIMENTAL SETUP

Details about the apparatus and experimental procedures can be found in Refs. 1 and 7. We briefly recall here the main features. Solid argon samples are obtained by deposition of a gaseous mixture onto a gold plated copper mirror held at 18 K in a liquid helium cryostat. The sample thickness is known from the amount of gaseous mixture used during the deposition. A calibration of the thickness versus this amount is recorded during growth of the sample using a He–Ne laser. The sample is then cooled to 5 K. Carbon and platinum resistors measure the temperature, which can be varied between 5 and 30 K. The concentration of the CO_2/Ar mixture is chosen in the range 1/200–1/10000. The infrared excitation pulse is obtained by frequency difference between a dye laser (pumped by a frequency doubled YAG laser) and the YAG residual. The system, purchased from Quantel (France), generates pulses of 200 μJ maximum energy, 5 ns time width, and 0.8 cm^{-1} spectral width. The repetition rate is 20 Hz. The laser, focused on an area of 2×10^{-2} cm^2, impinges normally on the sample mirror. The detection angle, usually 45°, can be varied by $\pm$8SD. Signals are detected using an MCT detector (Belov Technology) and accumulated in a digital oscilloscope (Tektronix TDS 540). A high-pass filter ($\lambda_c = 8$ μm) is used to get rid of the scattered laser light. Absorption spectra of the sample are recorded using a Bruker IFS 113V FTIR spectrometer with a maximum resolution of 0.03 cm^{-1}. Emissions are spectrally analyzed by means of filters, or through a Perkin-Elmer monochromator equipped with a 16 μm blazed grating (60 lines/mm). The effective resolution is a few cm^{-1}.

EXPERIMENTAL RESULTS

1. Spectral analysis

1a). Absorption spectroscopy

It is now well known from experimental work[8] and from calculations[9] that argon matrices offer two different trapping

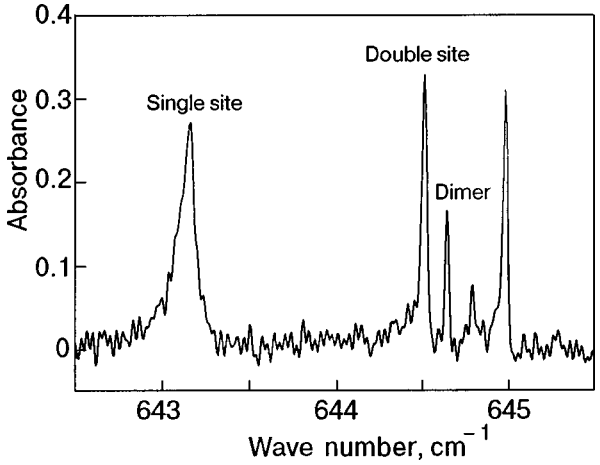

FIG. 1. FTIR absorption spectrum of $^{13}CO_2$ in solid argon at 16 μm (CO_2/Ar=1/2300, $T=5$ K, thickness$\approx$13 μm, resolution=0.03 cm^{-1}).

sites to the CO_2 molecule. The more stable one is unambiguously assigned to a single substitutional site, where the molecular axis coincides with the C_4 symmetry axis of the site. The other site is ''unstable,'' which means that the absorption by molecules in this site decreases irreversibly upon annealing. It is described as a more or less distorted double substitutional site, where the molecule is placed asymmetrically, which results in the lifting of the v_2 mode degeneracy. For a quantitative study of stimulated effects, we need linewidth values for CO_2 under our experimental conditions, namely after deposition at 18 K, a temperature chosen a little lower than usual in order to favor the double site, so that the same detection conditions can be used for the two sites. Then at 5 K we recorded, with our best resolution, the absorption spectra of unannealed samples similar to those studied in emission experiments. The v_2 region is displayed in Fig. 1: the low-frequency line (FWHM=92×10^{-3} cm^{-1}) belongs to the single site. The high-frequency doublet (FWHM=38×10^{-3} and 30×10^{-3} cm^{-1}) is assigned to the double site. Two very narrow extra lines, which do not decrease upon annealing, cannot be confused with the double-site monomer absorption, and we tentatively assign them to a dimer. These assignments rest upon irreversible annealing effects: heating the sample up to 32 K, during a few minutes, results in an increase of the two small lines at 644.6 and 644.8 cm^{-1} (dimer ?), whereas the 643.2 isolated line decreases by 5% (monomer, stable site) and the 644.5–645.0 cm^{-1} doublet decreases by 23% (monomer, unstable site). The measured linewidths are consistent with those obtained[10] with a resolution of 0.010 cm^{-1} for $^{12}CO_2$ in argon deposited at 20 K (FWHM=75×10^{-3}, 29×10^{-3}, and 25×10^{-3} cm^{-1}, respectively, at 5 K). In the v_3 region, which will be used for excitation, we measure linewidths of 0.36 and 0.12 cm^{-1}, respectively, for the single and double sites.

1b) Absorption of the exciting laser by the v_3 mode

Specific experiments have been performed to get the number of photons absorbed from the laser, tuned through the v_3 region: the laser is presently incident at $i=45°$ and the transmitted energy is collected after reflection on the sample mirror, so that the absorption length is equal to the thickness

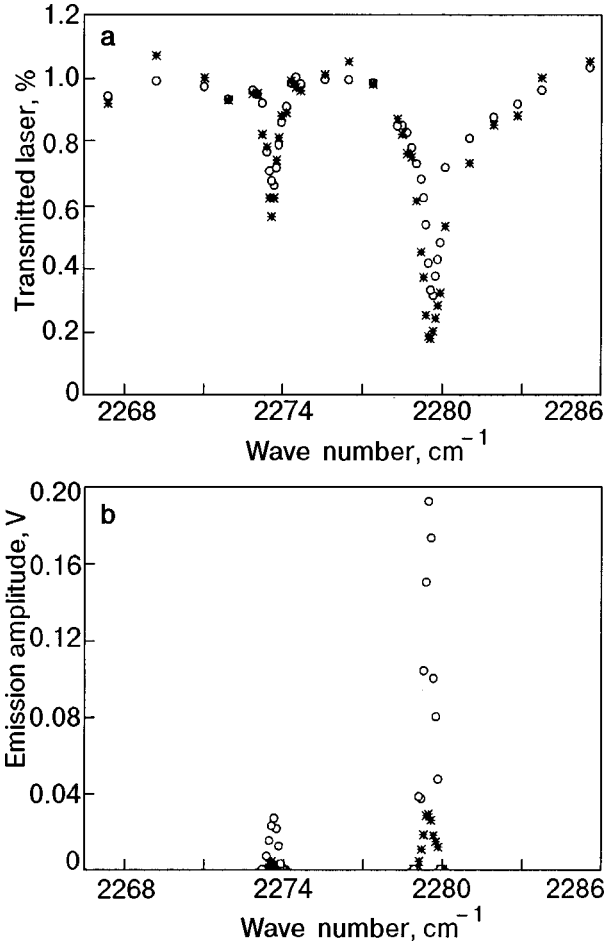

FIG. 2. Spectral analysis of the excitation for laser energies 50 (*) and 77 μJ/pulse (○) (CO_2/Ar=1/2000, $T=5$ K, thickness$\approx$90 μm). Transmission spectrum of the laser, at incidence 45° (a): excitation spectrum of the 16 μm emission, detected at incidence 0° (b).

of the sample multiplied by $2\sqrt{2}$. As the v_3 transition of CO_2 is very intensive, saturation of the absorption may occur, especially for dilute samples, which can be checked by comparing the ''laser transmission spectrum'' recorded point by point, for different laser energies. We emphasize that by this procedure the laser width and the molecular linewidth are automatically taken into account. Moreover, an additional detector is placed at $i=0°$ in order to monitor the emission, thus providing the corresponding excitation spectrum. This has been done at the concentration of 1/2000 for different sample thicknesses. Figure 2 displays the results for a 90 μm thick sample and clearly shows saturation effects, which means that, at least in the first layers, at high energy, the percentage of excited molecules approaches 50%. This had been predicted in Ref. 2 and is now quantitatively established. Doubling the thickness decreases the saturation effect appearing on the spectrum, which only gives a mean value of the excited population, as the excitation is not homogeneous all over the sample. The perfect correlation between the emission and the absorption is clearly established for the two sites.

Besides, this experiment allows an additional observation concerning the absence of directionality of the emission. As a matter of fact, the detector, without a lens and remaining at a constant distance from the sample, sees a constant

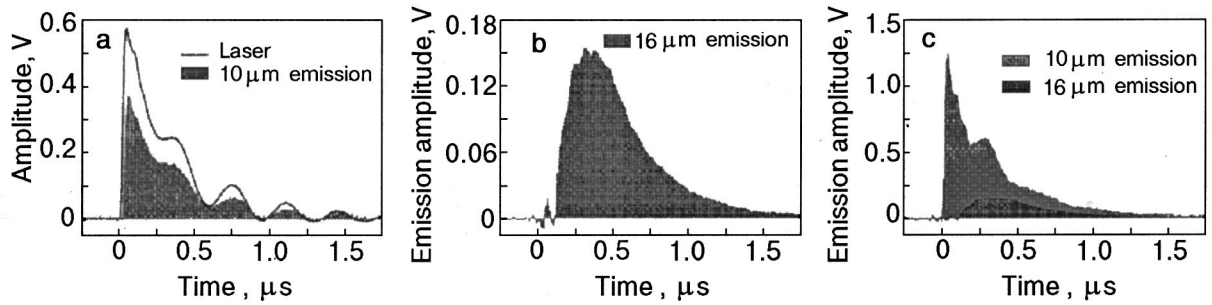

FIG. 3. Discrimination between 10 μm and 16 μm emissions by means of filters (CO_2/Ar=1/525, $T=5$ K, thickness$\approx$40 μm). Detection through a BaF_2 plate (a); detection through a $\lambda_c=13$ μm high-pass filter (b); detection without filter (c). In each case, except to record the laser, a $\lambda_c=8$ μm high-pass filter eliminates the scattered laser light.

signal (largest deviation=16%) when the direction of observation is moved between 0 and $\pm 10°$. Going back to the usual geometry, with the laser beam coming in normally to the mirror, and moving the detection to $45\pm 8°$, also gives an equal signal within the same precision. As the absorption length is now reduced by a factor of $\sqrt{2}$, there is a little, if any, increase of the emission efficiency when the observation angle is increased.

1c) Emissions in the 10 and 16 μm regions

In the N_2O case[3] the v_3-v_1 transition, originating from the laser-excited $v_3=1$ level, is the only transition observed, i.e., amplified by stimulated emission. It was not observed for CO_2/Ar samples of similar concentration (1/2000) and similar thickness (90 to 260 μm). It was searched for, and found, at higher concentrations (1/500 and 1/200) but coming only from molecules in the double site. With the 60 lines/mm grating, we cannot observe 10 μm radiation through the monochromator. We then characterize the 10 μm emission by CaF_2 or BaF_2 plates absorbing at 16 μm. A 5 mm thick CaF_2 plate decreases the emission by a factor of 1/3. The emission is highly unstable, which makes its detection tricky. Only single shots are meaningful. Even when optimization is achieved, and for large laser shots, the emission intensity is random. Figure 3a displays a particularly strong single-shot signal detected through a BaF_2 window. Replacing the BaF_2 by a high-pass filter ($\lambda_c=13$ μm) allows the detection of the 16 μm emission described previously, in Ref. 2, which is shown in Fig. 3b. Figure 3c displays the total signal, only through an 8 μm high pass filter to eliminate the scattered laser light. The trace presented in Fig. 3b is shown in heavy shading in Fig. 3c to recall its contribution to the total signal. Using the BaF_2 plate, we checked the lack of directionality of the 10 μm emission, and found that it is not polarized, just as was found for the 16 μm emission. The 16 μm emission, analyzed through the Perkin-Elmer monochromator, exhibits three lines for each site, shifted by 1 cm^{-1} in wave number from one site to the other. The measured wave numbers (626, 613, and 595 cm^{-1}) allow their unambiguous assignment to combination bands inside the v_2 manifold, as is shown in Fig. 4. The lines at 626 and 595 cm^{-1} are identified with the $11^10(2)\rightarrow 10^00(2)$ and $11^10(2)\rightarrow 02^20(1)$ transitions, whereas the 613 cm^{-1} emission comes from the $10^00(2)\rightarrow 01^10(1)$ transition. The fundamental v_2 transition at 644 cm^{-1} has been searched for without success.

2. Time analysis

2a) 10 μm emission

Short-time measurements are limited by the characteristics of the detection. The apparent half-width of the 5 ns laser pulse, reaching about 400 ns, is shown in Fig. 3a, where the laser is recorded in the absence of absorption and without any filter. The 10 μm emission appears with a delay too small to be measured. Both decays, identical, reflect the time constant of the system.

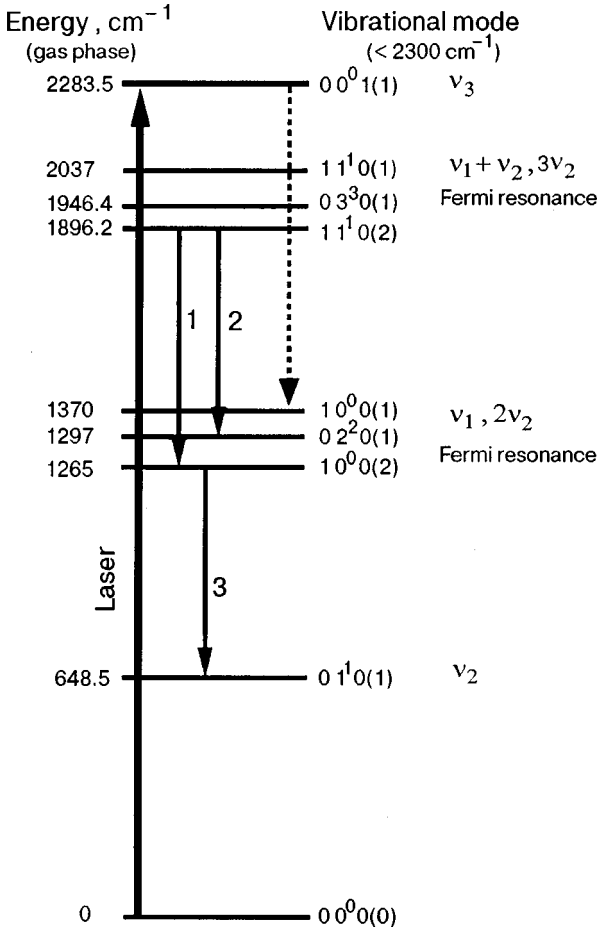

FIG. 4. Vibrational energy levels of $^{13}CO_2$ up to 2300 cm^{-1}. 1, 2, 3: 16 μm emissions (——) and 10 μm emission (— — —).

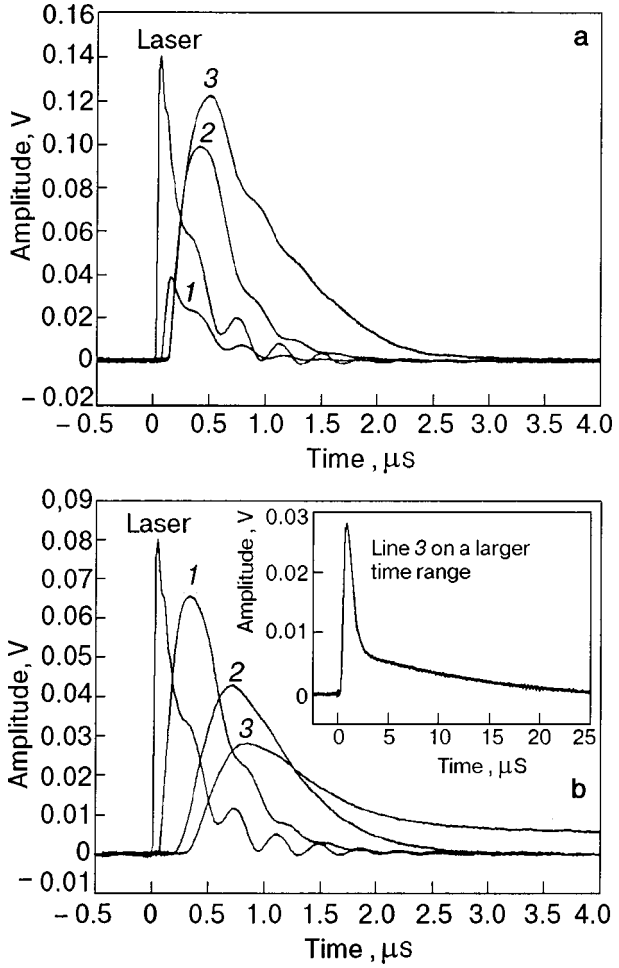

FIG. 5. Time and frequency resolved 16 μm emissions (CO_2/Ar= 1/2000, T= 5 K, thickness≈360 μm); single site (a) and double site (b).

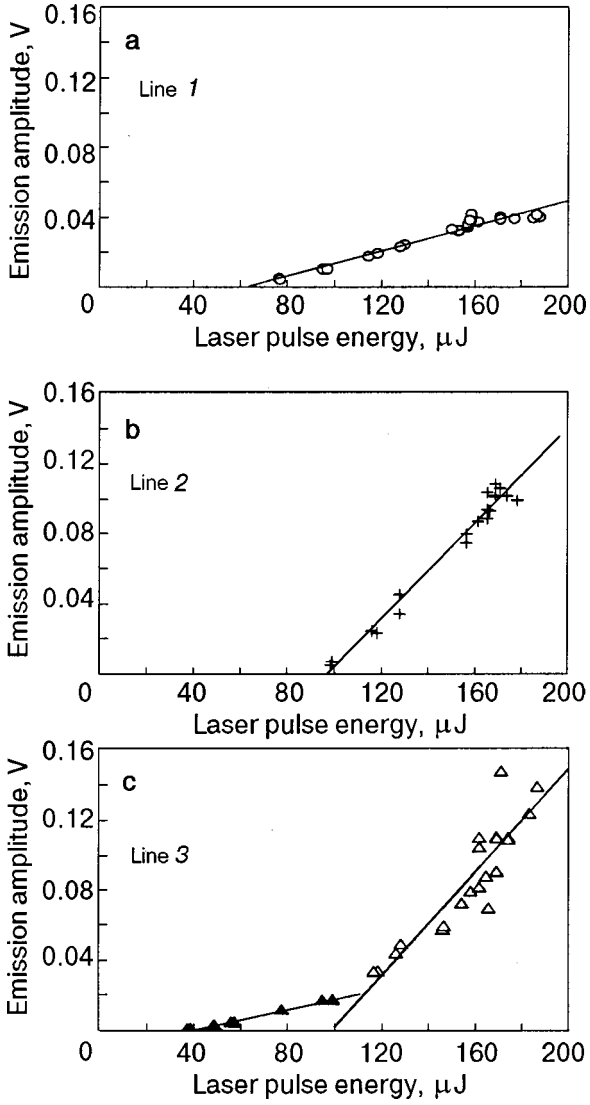

FIG. 6. Dependence of the emission amplitude on the laser pulse energy (T= 5 K, sample thickness≈360 μm, single site), 16 μm emissions, CO_2/Ar= 1/2000, line *1* (○); line *2* (+); line *3*, short and long components (△ and ▲, respectively).

2b) 16 μm emissions

One the contrary, a measurable delay is found for the onset of the 16 μm emissions. Their time shape is clearly different from the laser one, as detected through the monochromator in the fourth order of the grating (Fig. 5). This time analysis of the dispersed emission reveals that the three lines of the two sites have different time behaviors. The onset and the signal maximum are reached faster in the single site than in the double one. Moreover, for a given site, the three lines exhibit a different time delay, and they have been numbered according to this delay. Last but not least, the 613 cm^{-1} emission (line *3*) of the double site shows a peculiar, rather intricate, time behavior. An intense peak, on a short time scale similar to that for the other two lines, is followed by a much weaker and longer component, covering a few tens of microseconds.

3. Threshold measurements

The dependence of the emission amplitude on laser energy is shown for each transition in Fig. 6 (single site) and 7 (double site). These data correspond to 360 μm thick samples at concentrations of 1/2000 and 1/500 for the 16 and 10 μm emissions, respectively. Below a sharp energy threshold, depending on the transition, no signal is usually detected. Above the threshold the dependence seems approximately linear in the range studied, as was observed in the O_3 (Ref. 1) and N_2O (Ref. 3) cases. The existence of such a threshold gives direct evidence of the stimulated character of the process, in addition to the large amplification and shortening effects relative to spontaneous fluorescence.

The $2v_2^0 - v_2^1$ transition at 613 cm^{-1} (line 3) behaves peculiarly in the two sites. In the double site, the short component exhibits a sharp threshold at 115 μJ, whereas the longer one, with a much weaker amplitude, shows a slower decrease. Finally, it disappears into noise, and it is impossible to measure a precise threshold different from zero. The stimulated or spontaneous character of this component is then not established. For the single site, Fig. 5 does not show two distinct time components for this transition. However, at high laser energy, the delay of this emission is smaller and its width (FWHM) is broader, as if a short component of similar amplitude was added at the beginning of the signal. This observation may be used to discuss the two regimes appearing in Fig. 6c. A high threshold of 100 μJ is assigned

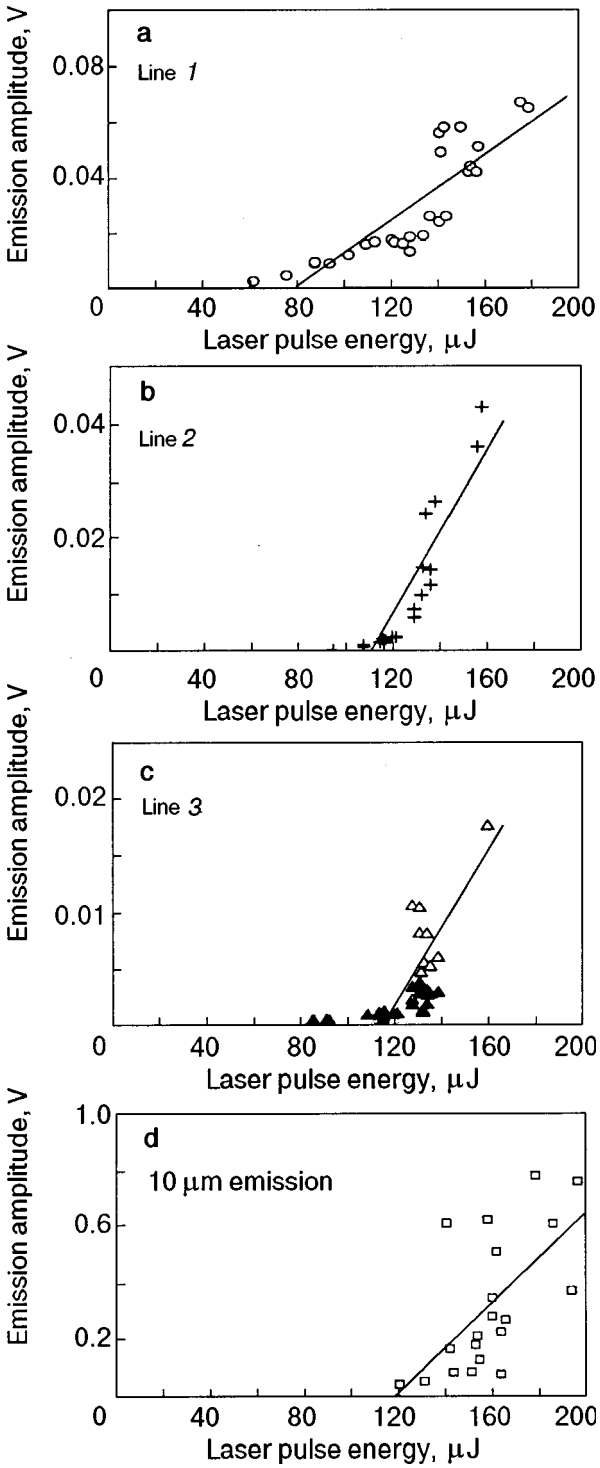

FIG. 7. Dependence of the emission amplitude on the laser pulse energy ($T=5$ K, sample thickness$\approx 360\ \mu$m, double site), 16 μm emissions, $CO_2/Ar=1/2000$: line *1* (○), line *2* (+), line *3*, short and long components (△ and ▲, respectively); 10 μm emission, $CO_2/Ar=1/520$ (□).

to the additional short part, the global threshold being lower, at 40 μJ.

The threshold value measured for each component is an essential parameter for any quantitative discussion, provided that the laser absorption is known. To sum up, the present results are the following: threshold values of 65, 97, 100 (and 40) μJ are found for lines *1*, *2*, and *3*, respectively, in the single site, which absorbs about 86% of the laser energy. The corresponding values for the double site (Fig. 7) are 80, 110, and 115 μJ, with an absorption around 50%. Figure 7d yields a threshold of 120 μJ for the 10μm emission from a sample of similar thickness, but with a concentration increased by a factor of 4, resulting in an evaluated absorption of the order of 94%.

4. Concentration and temperature effects

The most important concentration effect is the appearance of the 10 μm emission of the double site for concentrations higher than 1/1000. On the contrary, in this case, the 16 μm emission is weaker than for the concentrations of 1/1000 and 1/2000. In this range the 16 μm signals are maximum, if one compares samples of approximately equal optical density, i.e., keeping constant the product of the concentration by the thickness. Of course, a concentration decrease from 1/2000 to 1/10000 also decreases the signals, since we cannot grow samples thick enough to keep the optical density constant. We focus our attention on the concentration dependence of the long component of line *3* in the double site, because it could be assigned to spontaneous emission from its time behavior and its threshold uncertainty. We unsuccessfully tried exponential fits of its decay. However, a time constant extracted from its last part shows an unusual concentration dependence, as it clearly decreases with increasing dilution.

Another way to characterize the time behavior of this component is to decrease the laser energy below the threshold of the short component. We thus observe an onset, a maximum and a decay, and an approximate value of the time during which the signal remains higher than the noise. Once again, this time clearly decreases with increasing dilution.

Temperature effects can be studied up to 30 K only for the single site, since the density of double sites decreases irreversibly upon annealing. For the single site, increasing the temperature from 5 to 17 K results in an increase of line *1* by about 35%, including a very little increase in duration, measured by its full width at half maximum (FWHM). Between 17 and 21 K this line remains approximately constant. It disappears at 28 K. On the contrary, lines *2* and *3* keep on decreasing from 5 to 21 K. Their amplitude and width decrease together, and they disappear at 22 K (line *3*) and 23 K (line *2*). At 5 K, after this temperature cycling, the emissions of the three lines are increased by about 40% (line *1*) and more than 60% (lines *2* and *3*). This effect may be explained by a narrowing of the lines due to annealing.

For the double site, the temperature dependence studied up to $T=21$ K is approximately similar. Lines *2* and *3* decrease and disappear at 20 and 19 K, respectively, whereas line *1* is nearly constant. Moreover, such a mild temperature cycling also produces an overall increase of the emissions at $T=5$ K, very likely related to a line narrowing.

DISCUSSION

1. Inversion population threshold for ASE

ASE is considered to start as soon as one spontaneous photon produces a stimulated photon on its passage through the sample. Defining a mean path length $\langle \mathbf{l} \rangle$ as the mean distance from any point to the boundaries of the excited volume, this condition can be written as

$$\sigma_{ul}\Delta N_{ul}\langle \mathbf{l}\rangle \geqslant 1, \tag{1}$$

where $\sigma_{ul}[\mathrm{cm}^2]$ is the cross section for stimulated emission from upper level u to lower level l, and $\Delta N_{ul}[\mathrm{cm}^{-3}]$ is the population inversion between these two levels. Equivalently, one can define a loss coefficient $\alpha_L = 1/\langle \mathbf{l}\rangle$ and write

$$\sigma_{ul}\Delta N_{ul} - \alpha_L \geqslant 0. \tag{2}$$

The threshold condition for the population inversion ΔN_{ul}^T is then

$$\sigma_{ul}\Delta N_{ul}^T = \alpha_L \tag{3}$$

with

$$\sigma_{ul} = \frac{8\pi^3}{3hc}\frac{v_{lu}}{\gamma_{lu}}|R_{lu}|^2\frac{1}{n}\left(\frac{n^2+2}{3}\right)^2; \tag{4}$$

σ_{ul} mainly depends on molecular parameters, such as the squared transition moment $|R_{lu}|^2$, the wavenumber v_{lu}, and the linewidth γ_{lu} of the transition. It is also related to the nature of the matrix by its refractive index n, but does not depend on the geometry of the sample. On the contrary, α_L is essentially related to the thickness of the sample and the diameter of the laser-excited spot. Consequently, we can compare threshold population inversions ΔN_{ul}^T for different transitions provided that the matrix and the geometry of the sample are not changed. This can be performed at a semiquantitative level, taking the following gas phase values[11–13] for $|R_{lu}|^2$: 1.77×10^{-3}, 0.67×10^{-3}, 50.6×10^{-3}, 20.3×10^{-3}, and 21.9×10^{-3} Debye^2 for the transitions $v_3 - v_1$, $v_3 - 2v_2$, $3v_2^1 - 2v_2^0$, $3v_2^1 - 2v_2^2$, and $2v_2^0 - v_2^1$, respectively. The $|R_{lu}|^2$ values of the 10 μm transitions are one or two orders of magnitude smaller than the 16 μm ones, which explains why detection of 10 μm emission requires higher concentrations, although the emitting level is directly laser excited.

For the linewidths γ_{lu}, which cannot be measured at the solid argon temperature for combination or hot bands, we tentatively use the values measured in the present study for the corresponding fundamentals. The measured thresholds displayed in Fig. 6 for the emissions of the double site can be analyzed within this approximation. First, considering the 10 μm emission, we can safely assign it to the $v_3 - v_1$ transition on the basis of the $|R_{lu}|^2$ values, which makes the $v_3 - 2v_2$ threshold higher by a factor of 2.6. A calculated value of $64\times10^{-19}\,\mathrm{cm}^2$ is found for the cross section σ_{ul} of the $v_3 - v_1$ emission. Using the threshold energy, and the estimated absorption of 94%, we get the inversion population threshold $\Delta N_{ul}^T \cong 0.37\times10^{19}\,\mathrm{cm}^{-3}$. We then obtain $\alpha_L \cong 24\,\mathrm{cm}^{-1}$ for the loss coefficient. This value is somewhat too high for a 360 μm thick sample, when compared to the value of 26 cm^{-1} determined using the 10 μm emission of N_2O (Ref. 3) in a 180 μm thick sample. Taking into account how $\langle \mathbf{l}\rangle$ depends on the thickness, if one neglects light scattering, we would have predicted $\alpha_L \cong 18\,\mathrm{cm}^{-1}$. Nevertheless the order of magnitude is correct. More interesting is the comparison with the other emissions in similar samples. The value $\alpha_L = 24\,\mathrm{cm}^{-1}$ allows a prediction of ΔN_{ul}^T equal to 9.5×10^{16}, 25×10^{16}, and $23\times10^{16}\,\mathrm{cm}^{-3}$ for lines *1*, *2*, and *3*, respectively. Let us compare these values with the experimental threshold values of the $v_3 = 1$ level population, 110×10^{16}, 180×10^{16}, and $180\times10^{16}\,\mathrm{cm}^{-3}$, respectively. This shows that only about 10% of the molecules have relaxed from the $v_3 = 1$ level towards the $3v_2$ one, when ASE starts in the v_2 manifold. Using the delay of line *1* (~70 ns) we get an order of magnitude value $k = 3\times10^7\,\mathrm{s}^{-1}$ for this intramolecular V-V transfer rate in the double site.

2. Low directionality of the emissions

In the experimental Section, we established that the emissions exhibit low directionality. This observation is in contradiction with the high directionality predicted for ASE in the gas phase,[4,5] where the length of the amplifying medium is a crucial parameter. In the present experiment, the excited part of the sample is a disk about 200 μm thick and 1.5 mm in diameter, so that the preferential emission direction should be in the plane of the disk. However, in the matrix case, light scattering by the polycrystalline material, for both excitation and emission, provides random propagation directions as well as random optical path lengths. The low directionality of the emission, which is proven here, can then be understood.

3. Time behavior of the emissions and relaxation scheme

The 10 μm emission reproduces almost exactly the laser pulse, within the response time of the detection. This is not surprising, since this emission comes from the level $v_3 = 1$ directly excited by the laser and was observed also in the N_2O case. This does not provide any information on the lifetime of this level, since ASE itself decreases the population below threshold.

For the 16 μm emissions, it is surprising that two signals (lines *1* and *2*) exhibit such different time behaviors even though they come from a common level ($3v_2^1$), which is populated via intramolecular V-V transfer from the $v_3 = 1$ level. One easily understands that the threshold for ASE is reached faster for the transition with the higher transition moment (line *1*). But we have to explain why the onset of line *2* coincides with the decay of line *1*, although the emitting population is the same for the two lines. Moreover, in the double site, line *1* is the more intense, while in the single site the reverse is true. Let us consider the level scheme displayed in Fig. 4. ASE operating on line 1 tends to equalize instantaneously the populations of the upper and lower levels, resulting in saturation of the gain. If the relaxation of the lower level is not fast, both populations increase as the transfer $v_3 \rightarrow 3v_2^1$ goes on. Such a process has been described by Apkarian[14] using a kinetic model for a two-level system. The emitted signal exhibits oscillations on a very short time scale, corresponding to a step-by-step increase of the lower level population. When the $3v_2^1$ population reaches the threshold for ASE on line *2*, the dominant process changes. Indeed, a well known ''energy gap law''[15] for multiphonon vibrational relaxation in matrices states that the nonradiative rates decrease exponentially with the number of phonons to be created for energy conservation. One can then safely assume that the lower level of line *2*($2v_2^2$) relaxes faster than that of line *1*($2v_2^0$) because of the small energy difference

between these two levels as compared to the gap of 613 cm^{-1} between $2v_2^0$ and v_2^1. Consequently, the gain of the amplifying medium on line *2* does not saturate, since there is no equilibration of the populations. Moreover, ASE on line *2* contributes to the population of the lower level of line *1*, which qualitatively explains why, when line *2* is on, line *1* is off. The relative intensities of lines *1* and *2*, going from one site to the other, is probably explained by differences between the nonradiative rates populating $3v_2^1$. In the double site, where the molecule has a wider space, it is probably less coupled to the phonon bath, so that all rates are smaller. This is consistent with the longer delay before the onset of the three lines. This effect may be different for the different nonradiative transfer rates. A clue confirming this interpretation is provided by the temperature effect. When the matrix is heated, the V–V nonradiative transfer rates generally increase. Saturation of the gain on line *1* is decreased by the faster relaxation of the lower level $2v_2^0$. Line *1* is then favored. Moreover the nonradiative relaxation of level $3v_2^1$ is also faster. The two channels (radiative and nonradiative) that depopulate $3v_2^1$ are then increasing. This explains the decrease of line *2*, until finally its threshold cannot be overcome. The delay observed for the onset of line *3* reflects the time necessary for the different transfers (radiative and nonradiative) to provide the threshold population inversion of line *3*. A quantitative rationalization of the time evolution of the emissions would imply a complete kinetic model, inspired by that of Apkarian[12] but taking into account the whole v_2 manifold instead of a two-level system, and including the nonradiative V–V transfers between all the involved levels. This model may allow an estimation of the transfer rates.

4. Concentration behavior of line 3 in the double site: stimulated or spontaneous emission?

When recording spontaneous emission, one has a direct access to the lifetime of the emitting level. In matrices, due to possible intermolecualr V–V transfers towards impurities or dimers, occurring at high concentration, it is generally observed[16] that the lifetimes increase with increasing dilution, up to a limit where the molecules can be considered as perfectly isolated in the lattice. One then gets the intrinsic lifetime of the level, as governed by the interaction of the molecule with the lattice. The concentration dependence observed for line *3* and mentioned above does not fit in with such a scheme. This unusual dependence proves that the signal does not yield the $2v_2^0$ lifetime. There must remain some stimulated effect, even under threshold, spoiling the lifetime measurements. Indeed, a single-shot record of this long component, around the threshold, exhibits random bursts of stimulated emission (Fig. 8), which closely resembles the spiking often encountered in solid-state lasers.[17]

Nevertheless, the duration of line *3* emission proves that the $2v_2^0$ level remains populated after 20 μs (Fig. 5b), which sets a higher limit ($\sim 10^5\ s^{-1}$) for the intramolecular vibrational relaxation rates inside the v_2 manifold. The kinetic model suggested in the preceding discussion should be able to shed more light on this question. It is presently in progress at L. P. M. A.

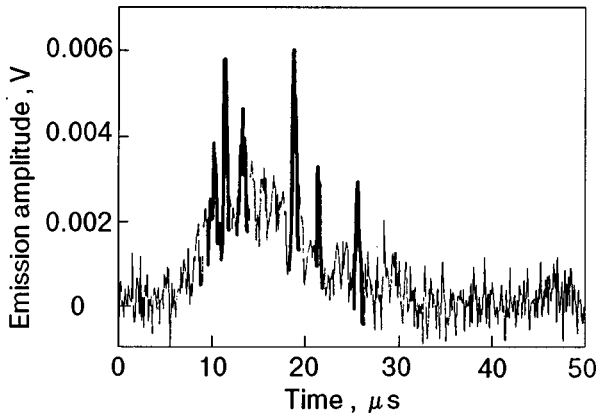

FIG. 8. Single-shot record of line *3*, just below the threshold of its short component ($T=5$ K, $CO_2/Ar=1/2000$, sample thickness≈ 260 μm, double site).

CONCLUSION

Vibrational emissions of $^{13}CO_2$ trapped in argon matrices have been studied in the 10 μm and 16 μm regions. They all behave like stimulated emission, even in the case of the long component of the $2v_2^0-v_2^1$ transition, which lasts over some tens of microseconds. An order of magnitude value of $3\times 10^7\ s^{-1}$ can be set for the nonradiative V–V transfer rate from the excited v_3 level to the $3v_2^1$ level. Other intramolecular V–V transfer inside the v_2 manifold have been discussed qualitatively. A quantitative estimate of these rates might be extracted from a kinetic model including spontaneous and stimulated emission and nonradiative transfers. Simulations based on this model are presently in progress.

[1)]Present address: Laboratoire de Magnétisme et d'Optique de Versailles, Bâtiment Fermat, 45 avenue des Etats-Unis, 78035 Versailles, France.
[2)]Present address: Laboratoire de Photophysique Moléculaire du CNRS, Bâtiment 213, Université de Paris-Sud, 91405 Orsay Cedex, France
*E-mail: la@ccr.jussieu.fr

[1] D. Jasmin, P. Brosset, R. Dahoo, B. Gauthier-Roy, and L. Abouaf-Marguin, J. Chem. Phys. **108**, 2302 (1998).
[2] H. Chabbi, P. R. Dahoo, B. Gauthier-Roy, A.-M. Vasserot, L. Abouaf-Marguin, M. Broquier, H. Dubost, R. Kolos, A. Tramer, J.-M. Berset, and J.-M. Ortega, Chem. Phys. Lett. **285**, 252 (1998).
[3] H. Chabbi, P. R. Dahoo, B. Gauthier-Roy, A.-M. Vasserot, and L. Abouaf-Marguin, J. Phys. Chem. A (in press).
[4] L. Allen and G. I. Peters, J. Phys. A **4**, 238 (1971).
[5] Y. Ogi and K. Tsukiyama, Chem. Phys. Lett. **296**, 384 (1998).
[6] C. Crepin, F. Legay, N. Legay-Sommaire, and A. Tramer, Opt. Commun. **58**, 100 (1986).
[7] D. Jasmin, P. Brosset, P. R. Dahoo, V. Raducu, B. Gauthier-Roy, and L. Abouaf-Marguin, J. Chem. Phys. **101**, 7337 (1994).
[8] R. Guasti, V. Schettino, and N. Brigot, Chem. Phys. **34**, 391 (1978).
[9] P. R. Dahoo, I. Berrodier, V. Raducu, J.-L. Teffo, H. Chabbi, A. Lakhlifi, and L. Abouaf-Marguin, Eur. Phys. J. D **5**, 71 (1999).
[10] N. Legay-Sommaire and F. Legay, Private communication, L. P. P. M., Orsay, France (1999).
[11] J.-Y. Mandin, V. Dana, M. Badaoui, G. Guelachvili, M. Morillon-Chapey, Q. Kou, R. B. Wattson, and L. S. Rothman, J. Mol. Spectrosc. **155**, 393 (1992).
[12] J. W. C. Johns and J. Wander Auwera, J. Mol. Spectrosc. **140**, 71 (1990).
[13] L. S. Rothman, R. L. Hawkins, R. B. Wattson, and P. R. Gamache, JQSRT **48**, 537 (1992).
[14] V. A. Apkarian, Chem. Phys. Lett. **110**, 168 (1984).

[15] V. E. Bondybey, in *Chemistry and Physics of Matrix-Isolated Species*, edited by L. Andrews and M. Moskovits (North Holland, Amsterdam, 1989).
[16] H. Dubost and F. Legay, in *Chemistry and Physics of Matrix-Isolated Species*, edited by L. Andrews and M. Moskovits (North Holland, Amsterdam, 1989).
[17] W. Koechner, *Solid-state Laser Engineering*, 4th edition, Springer-Verlag, Berlin (1996).

This article was published in English in the original Russian journal. Reproduced here with stylistic changes by the Translation Consultant.

Infrared and EPR spectroscopic study of open-shell reactive intermediates: F+NH_3 in solid argon

E. Ya. Misochko, I. U. Goldschleger,* and A. V. Akimov

Institute of Problems of Chemical Physics of the Russian Academy of Sciences, 142432 Chernogolovka, Moscow District, Russia

C. A. Wight

Department of Chemistry, University of Utah, Salt Lake City, Utah 84112, USA
(Submitted February 1, 2000)
Fiz. Nizk. Temp. **26**, 981–991 (September–October 2000)

Mobile F atoms react with NH_3 molecules in an argon matrix at temperatures $T=7-35$ K. The open-shell NH_2–HF complex was observed by EPR and infrared spectroscopies as the main product of this reaction. The hyperfine constants of the NH_2–HF complex $a_N=1.20$ mT, $a_H=2.40$ mT, and $a_F=0.70$ mT were determined from the EPR spectra of samples using NH_3, $^{15}NH_3$ and ND_3 isotopomers. Prominent features of the infrared spectrum of NH_2–HF are a strongly red-shifted HF stretching mode ($\Delta\upsilon\approx-720\,cm^{-1}$ relative to that for isolated HF) and strong absorptions at 791 and 798 cm^{-1} attributed to HF librational modes in the complex. Quantum chemistry calculations reveal that the hydrogen-bonded NH_2–HF complex has a planar C_{2v} structure and a binding energy of 51 kJ/mol. Calculated hyperfine constants and vibrational frequencies of the complex are in good agreement with those observed in the EPR and IR experiments. [S1063-777X(00)01409-2]

1. INTRODUCTION

The dynamics of atom–molecule reactions are important in many areas of chemistry, including atmospheric chemistry, combustion/flame suppression, and chemical lasers. Long-lived intermediate complexes play a special role in such reactions because they can allow extensive energy redistribution and randomize the final scattering angles of the products. It is therefore essential to gain a detailed knowledge of reaction intermediates, especially in the region of a transition state, in order to develop a comprehensive description of any elementary chemical reaction. This type of investigation constitutes one of the most active fields of modern chemical research. Various time-resolved techniques are being used to access this part of potential energy surface of elementary gas phase reactions (see, for example, Refs. 1–3). However, low-temperature spectroscopy of matrix-isolated species continues to play a prominent role due to its universality and reliability in the interpretation of experimental data. For the last 20 years, a variety of methods have been developed for stabilizing intermediates in cryogenic inert matrixes, such as freezing of reaction products from the gas discharge, photolysis and radiolysis of complexes, and laser ablation (see, for example Refs. 4–6).

Recently we have used a combination of FTIR and EPR techniques in rare gas matrices to study free radicals and radical–molecule complexes formed by reaction of fluorine atoms with small polyatomic molecules. This methodology takes advantage of the widely used matrix isolation technique for immobilizing molecular species as well as the high mobility of fluorine atoms in rare gas solids, as observed by Apkarian *et al.*[7,8] The quantum yield for photodissociation of F_2 in solid argon is nearly unity if the initial kinetic energy of photogenerated ''hot'' F atoms is more then 0.5 eV. The ''hot'' F atoms formed by UV photolysis are believed to migrate over distances approaching 3 nm.[9–11] Once thermalized, the F atoms are essentially immobile in the matrix at temperatures less than 18 K. However, at 20–26 K, F atoms are able to diffuse approximately 10 nm on a time scale of 10^2-10^4 s because the barrier to thermal diffusion in solid argon is only 4.5–5.8 kJ/mol.[8] The ability to control the mobility of F atoms through changes in temperature provides a unique opportunity to carry out solid-state chemical reaction of F atoms with isolated molecules in an argon matrix. Because the crystalline environment prevents reaction products from flying apart and promotes fast relaxation of excess energy released in the reaction, the stabilization and spectroscopic observation of open-shell intermediate species that are not observable in gas phase studies can be realized.

Based on these unique peculiarities of F atoms, we have determined the spectral characteristics of open-shell intermediates formed in reactions of mobile F atoms with ethene,[12] methane,[13,14] hydrogen,[15] carbon monoxide,[10,16] oxygen,[16] nitric oxide,[17] and ozone.[18] We have shown that the combination of two complementary spectroscopic techniques, EPR and FTIR, allows one to obtain:

a) direct evidence of a radical intermediate (by EPR spectroscopy);

b) the complete set of hyperfine (hf) constants of stabilized intermediates;[14,17]

c) reliable assignments of the infrared bands of the intermediate from comparison of kinetics of radical formation obtained in EPR measurement with kinetics of growth of new bands in FTIR measurements;[12,17]

d) branching ratios for reaction channels that yield closed-shell and radical products;[12,16]

e) molecular structure of intermediate species in the lattice from comparisons of measured and calculated hf constants and vibration frequencies.[15,16]

Particular attention has been given to H-atom abstraction reactions:

$$F+RH \rightarrow HF+R. \quad (1)$$

We have observed the open-shell complexes CH_3-HF and H-HF as intermediate products in reactions of diffusing F atoms with CH_4 and H_2 molecules trapped in a matrix.[13–15] EPR spectroscopy is especially useful in these studies because the hf interaction of the unpaired electron with magnetic nuclei in the complex is very sensitive to the distance between the radical R and the HF molecule and to their mutual orientation.

In the present study, we have used this approach to study the reaction of F atoms with NH_3 molecules isolated in an argon matrix. Usually, gas phase reactions of type (1) give rise to extensive HF internal excitation and population inversions,[19] which are required for laser action. However, attempts to obtain an inverted HF state distribution in

$$F+NH_3 \rightarrow HF+NH_2, \quad \Delta H_0 \approx -130 \text{ kJ/mol} \quad (2)$$

were unsuccessful, despite its high exothermicity.[20,21] It was assumed that the failure was due to formation of a long-lived FNH_3 species during the reaction. The existence of such an intermediate complex causes randomization of the exoergicity among its internal modes. *Ab initio* calculations performed by Goddard *et al.*[22] predicted that the NH_2–HF formed in the exit channel of reaction (2) should be bound by ~50 kJ/mol (~33 kJ/mol when corrected for zero-point energy effects). In our preliminary EPR study[23,24] we observed the intermediate complex NH_2–HF for the first time. In the present paper we report a detailed EPR, FTIR, and computational study of this reaction intermediate to obtain the total set the hf constants and vibrational frequencies. The results show that the structure of the complex and the binding energy are close to the predictions of Goddard *et al.*,[22] and that the complex suffers only a minor distortion in the argon lattice relative to its gas phase equilibrium geometry.

2. EXPERIMENTAL

The experimental technique used was described in detail elsewhere.[14] Briefly, solid argon films doped with reactant molecules were formed by vapor deposition of Ar-NH_3 and Ar-F_2 gas mixtures through separate inlets onto a substrate at 15 K (sapphire for EPR experiments; CsI for the infrared study). The sample composition was typically Ar:NH_3:F_2 =1000:1:1. Infrared spectra were recorded with a Mattson Model RS/1000 FTIR spectrometer (spectral region from 500 to 4000 cm^{-1} and spectral resolution 0.5 cm^{-1}).

In the EPR experiments (performed in Russia), argon (99.9995%) and fluorine (99.9%) were used without purification. Ammonia $^{14}NH_3$ (and $^{15}NH_3$) was used after drying over NaOH. Deuterated ammonia, ND_3, was prepared by repeated exchange of NH_3 with D_2O followed by distillation and drying over NaOD. The deuterium isotopic purity was estimated at 90%. In FTIR experiments (performed in the United States), argon (Spectra gases, 99.999%), fluorine (Spectra gases, 10% in argon), NH_3 (Matheson), and ND_3 (Cambridge Isotope Laboratories, Inc., 99% D) were used without further purification.

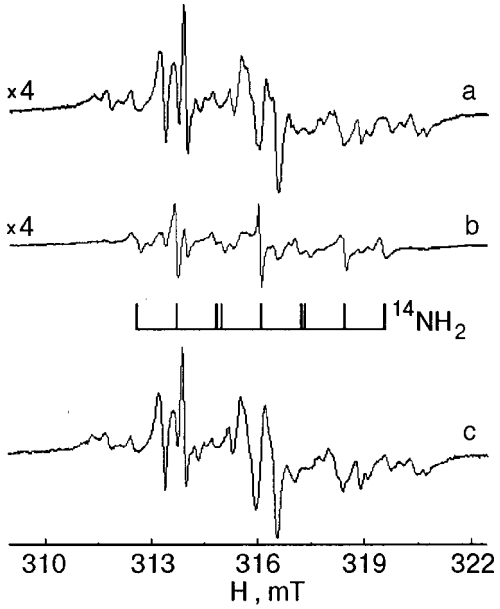

FIG. 1. EPR spectra of the Ar:NH_3:F_2=1000:1:1 sample after exhaustive photolysis at 15 K (a); after subsequent cooling to 7.7 K (b); after annealing of the photolyzed sample for 30 min at 25 K and subsequent lowering the temperature to 15 K (c). Intensities of the spectra are corrected in accordance with the Curie law.

Fluorine atoms were generated by UV photolysis of F_2 molecules using 337 nm laser light in the EPR experiments, and 355 nm laser light in the infrared experiments. The average laser power did not exceed 20 mW/cm^2 in either type of experiment. To distinguish the chemical reactions involving photogenerated ''hot'' F atoms from those of diffusing thermal atoms, photolysis of F_2 molecules was performed at 15 K and the samples were subsequently annealed in a separate step.

The EPR spectra of freshly prepared samples exhibit no lines due to paramagnetic species. Very weak infrared bands of CO_2 (661.9 and 2340.5 cm^{-1}) were found in the IR spectra of deposited samples. A sharp absorption assigned to FO_2 (1490 cm^{-1}) appears in the spectra of photolyzed samples at 20–25 K. Oxygen is a common impurity in fluorine gas and is difficult to remove by fractional distillation.

3. RESULTS AND DISCUSSION

3.1. EPR spectra of dilute mixtures Ar:NH_3:F_2=1000:1:1 photolyzed at 15 K

A complex anisotropic spectrum consisting of two series of lines (shown in Fig. 1a) is produced by 337 nm laser photolysis at 15 K. In the initial stage, the intensity of the EPR lines is proportional to the photolysis period, but approaches a limiting value under exhaustive photolysis due to depletion of the F_2 concentration. Temperature-induced changes of line shapes and intensities are reversible in the range 7.7–18 K, which shows that the concentration of radicals does not change after completion of photolysis. Lowering the temperature causes a broadening of most of the anisotropic lines, whereas lines in the other series are

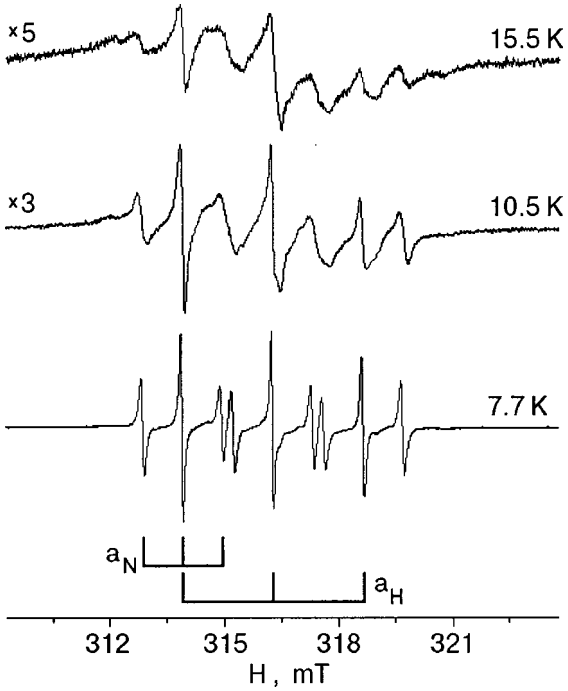

FIG. 2. EPR spectra of NH_2 radical generated by UV photolysis of NH_3 molecules in solid argon at different temperatures.

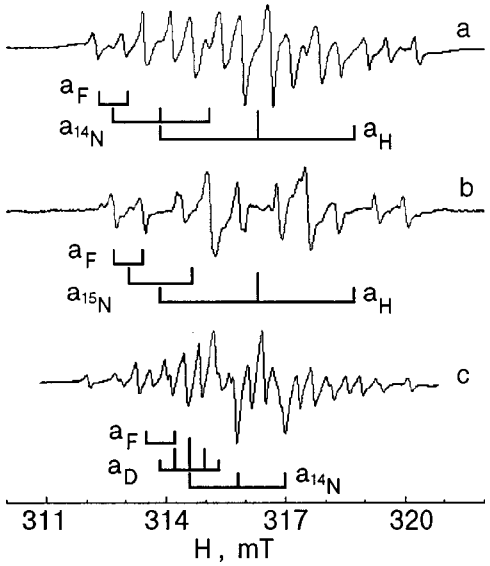

FIG. 3. EPR spectra of the samples after photolysis at 15 K and subsequent annealing at 25 K: Ar:$^{14}NH_3$:F_2 (a); Ar:$^{15}NH_3$:F_2 (b); Ar:$^{14}ND_3$:F_2 (c). All spectra were recorded at 35 K. (The $^{14}ND_3$ used in experiments contains ~10% $^{14}NH_3$; therefore, the weak outer lines in this spectrum correspond to $^{14}NH_2$–HF).

narrowed. Only 9 narrow lines remain in the spectrum at 7.7 K, as shown in Fig. 1b. Thus, the spectra correspond to the superposition of spectra of at least two products. The EPR spectrum of the radical whose lines are narrowed upon cooling consists of 9 lines: a 1:1:1 triplet of triplets with hf splittings of 1.05 and 2.40 mT, and $g=2.0058$. Recall that usually only absolute values of hf constants are determined in EPR experiments. The hf constants and g factor are all in good agreement with the data of Cochran *et al.*[25] obtained for the radical NH_2 in solid argon at 4.2 K ($a_H=2.38$ mT, $a_N=1.04$ mT and $g=2.0049$).

To elucidate the unusual temperature behavior of EPR lines of NH_2 radical in temperature region 7.7–15 K, a series of additional experiments was carried out. The samples Ar:NH_3=1000:1 were irradiated by a deuterium lamp at 7.7 K to generate stabilized NH_2 radicals. EPR spectra of NH_2 radical at different temperatures are shown in Fig. 2. The spectrum detected at 7.7 K corresponds to the spectrum of NH_2 radical shown in Fig. 1b. There are three prominent features of the spectrum of stabilized NH_2. The first and well-known peculiarity is that two equivalent hydrogens of NH_2 yield the triplet pattern 1:1:1, instead of the expected 1:2:1 at 7.7 K.[25] The second is that different linewidths are observed for components corresponding to different nuclear projections of the N atom. The third feature of this spectrum is the unusual temperature broadening of the EPR lines observed in this study.

Because the same spectral lines of NH_2 in Ar:NH_3 mixtures are observed following photolysis of Ar:NH_3:F_2 samples, we may conclude that NH_2 is one of the photolysis products formed in reaction (2) of photogenerated ''hot'' F atom with NH_3 molecule. However, the NH_2 concentration did not exceed 15% of the total concentration of radicals.

3.2. EPR spectra of products forming upon annealing of the samples Ar:NH_3:F_2 photolyzed at 15 K

To initiate reaction of diffusing thermal F atoms, we annealed the photolyzed samples at temperatures $T>20$ K. The post-annealing EPR spectrum (measured at 15 K) is shown in Fig. 1c. Comparison of the spectra before (Fig. 1a) and after annealing shows that concentration of NH_2 radicals does not change, but the intensity of lines of the other radical increase approximately fourfold due to reaction of F atoms that diffuse through the argon matrix. The EPR lines of this radical become narrow and isotropic at temperatures above 30 K, as shown in Fig. 3a. The spectrum consists of narrow lines (~0.1 mT) formed from a 1:1:1 triplet splitting with $a_1=1.20$ mT, a 1:2:1 triplet with $a_2=2.40$ mT, and a doublet $a_3=0.70$ mT. Because $a_2\approx 2\times a_1$, four of the lines are unresolved due to accidental overlapping. Thus, only 14 lines are observed in the spectrum, instead of the usual 18 lines associated with a triplet of triplets of doublets. Two of the triplet splittings, a_1 and a_2, are similar to those of the NH_2 radical, and this allows us to ascribe the doublet splitting a_3 to the magnetic interaction with one of the magnetic nuclei of the HF molecule bound to the complex NH_2–HF. In order to distinguish the hf constants on H, F, and N nuclei, we have performed a series of similar experiments with isotopically substituted ammonia.

EPR spectra obtained after photolysis and annealing of matrices containing Ar:$^{15}NH_3$:F_2 and Ar:ND_3:F_2 are shown in Figs. 3b and 3c, respectively. Referring to Fig. 3b, the use of $^{15}NH_3$ leads to replacement of the triplet ($a_N(^{14}N)=1.20$ mT) by a doublet ($a_N(^{15}N)=1.55$ mT), while two other splittings, a_2 and a_3, remain the same. In the samples containing ND_3, the triplet ($a_H=2.40$ mT) is replaced by a quintet ($a_D=0.37$ mT). These results permit a definitive assignment of the hf constants a_1 and a_2 to the NH_2 group. The last doublet splitting a_3 (which was unchanged by isotopic substitution) is ascribed to the ^{19}F atom, because it is

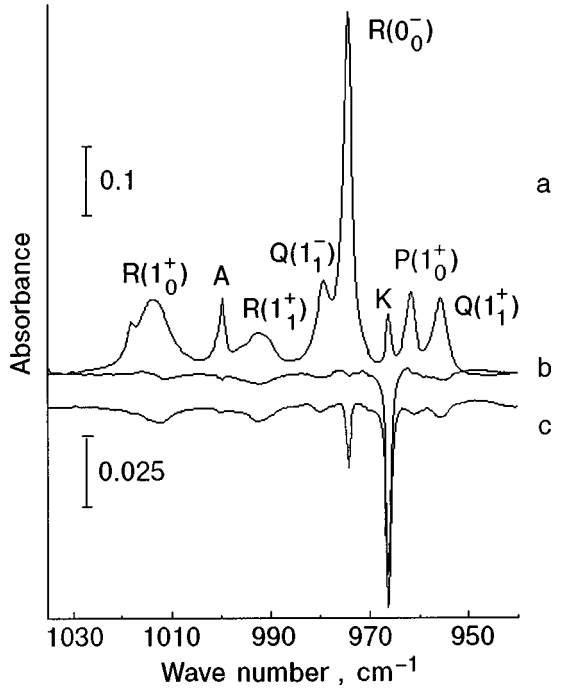

FIG. 4. Infrared spectra of the υ_2 region of NH_3 in $Ar:NH_3:F_2=1000:1:1$ sample at 15 K [trace (a)]. Traces (b) and (c) are difference spectra showing changes of band intensities after 20 min and 300 min photolysis 355 nm at power 10 mW/cm^2, respectively.

the only other atom in the system having a nuclear spin $I=1/2$. Because NH_2F is a closed-shell molecule, we can attribute the EPR spectrum to the radical–molecule complex NH_2–HF, presuming that the hf constant of the H atom of the HF molecule a_H is less than spectral resolution 0.05 mT.

Therefore, the main product in the reactions of photogenerated ''hot'' and thermally diffusing F atoms with isolated ammonia is the open-shell complex NH_2–HF:

$$F+NH_3 \longrightarrow NH_2-HF. \tag{3}$$

3.3. Infrared absorption spectra of dilute mixtures $Ar:NH_3:F_2=1000:1:1$ photolyzed at 15 K

NH_3 molecules trapped in rare gas matrices at low temperatures have been the subject of numerous experimental studies.[26–28] It has been shown that the υ_2 bending vibrational mode for NH_3 in an argon matrix exhibits several well-resolved bands, which can be assigned to transitions involving rotation and inversion of the NH_3 molecule. The assignment of these bands given by Abouaf-Margulin *et al.*[27] is shown in Fig. 4a for the sample $Ar:NH_3:F_2=1000:1:1$. The band at 1000 cm^{-1}, labeled *A* in Fig. 4a, is due to dimers of NH_3 (Ref. 27). The broad band at 966 cm^{-1}, labeled *K* in Fig. 4a, was assigned earlier by Andrews and Lascola[29] to the reactant complex $[F_2–NH_3]$. These authors ascribed a new weak absorption at 781 cm^{-1} to the perturbed F_2 vibrational mode in this complex. Our experimental evidence supports their assignment of these bands: both of them (966 and 781 cm^{-1}) appear in samples containing F_2 and NH_3 molecules only, and their intensities are proportional to the concentration of F_2 molecules in $Ar:NH_3:F_2$ samples.

The kinetics of UV photolysis of the $Ar:NH_3:F_2$ samples exhibit two characteristic times. The infrared bands of the

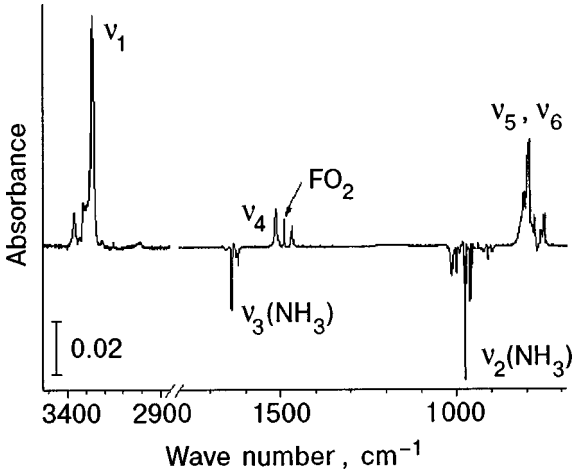

FIG. 5. Difference spectrum of photolyzed sample $Ar:NH_3:F_2=1000:1:1$ before and after annealing at 25 K. The spectra were recorded at 15 K.

complex $[F_2–NH_3]$ are totally destroyed in the initial stage of photolysis: $\tau_1 \approx 10$ min for a photolysis laser intensity of 10 mW/cm^2. Prolonged photolysis leads to a reduction of the IR bands of isolated NH_3 molecules as shown in Figs. 4b and 4c. Only about 1–2% of the NH_3 is consumed after exhaustive photolysis, and the time scale for this process is $\tau_2 \approx 200$ min under the same conditions as above.

Photolysis reveals two new series of bands. The first series grows in the initial stage at the same rate as the disappearance of the $[F_2–NH_3]$ complexes. These product bands were observed by Andrews and Lascola previously[29] and were attributed to the closed-shell product complex NH_2F–HF:

$$[F_2-NH_3] \xrightarrow{h\nu} NH_2F-HF. \tag{4}$$

The second series of new bands appears at 3267, 1512, 1465, and 797 (791) cm^{-1} under prolonged photolysis ($\tau_2 \approx 200$ min). Also, weak, sharp absorptions in the 3800–3900 cm^{-1} region appear due to formation of isolated HF molecules.[30] Their intensities are 10–20 times less intense

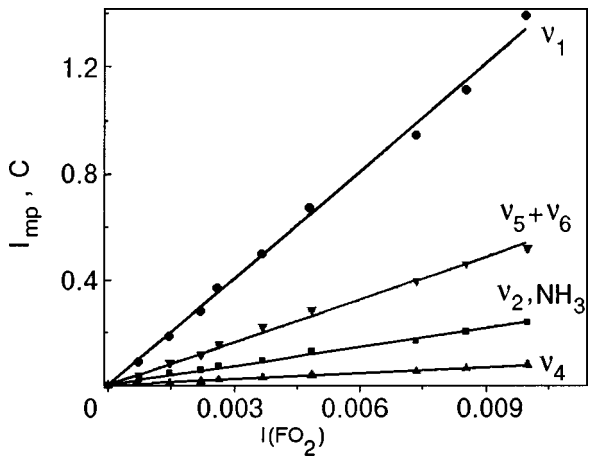

FIG. 6. Growth of the intensities I_{mp} of the major product bands and consumption C of the NH_3 band versus intensity I of the FO_2 (1490 cm^{-1}) band during annealing of the photolyzed sample $Ar:NH_3:F_2$.

than the band at 3267 cm^{-1}. Growth of this second series of bands occurs at the same rate as consumption of isolated NH_3.

Using the difference in photochemical reaction rates, we can distinguish photoinitiated reactions in complexes from reactions of translationally ''hot'' F atoms formed from photolysis of isolated F_2 molecules. The photodissociation quantum yield of F_2 in solid argon at 355 nm is $\Phi_0 \approx 0.3-0.5$.[7] The photodissociation rate $k_d = \sigma/\Phi_0$ (where $\sigma = 10^{-20}\,cm^2$ is the absorption cross section of F_2, and I is the light intensity) is very close to the observed ''slow'' photochemical reaction rate $(\tau_2)^{-1}$. Therefore, we may conclude that consumption of isolated NH_3 and the corresponding formation of new products (the second series of bands plus HF) result from the reaction of translationally ''hot'' F atoms with isolated NH_3 molecules.

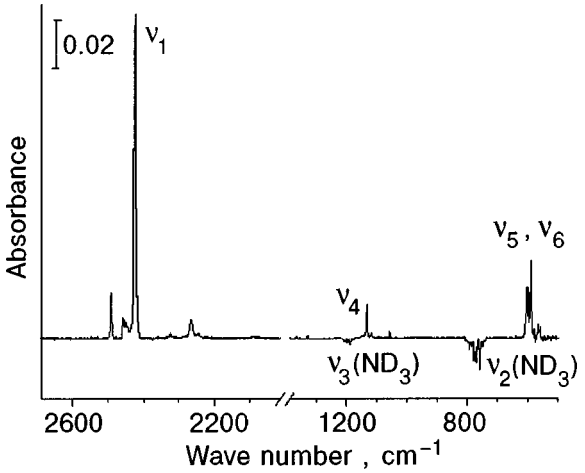

FIG. 7. Difference spectrum of a photolyzed sample Ar:ND_3:F_2=1000:1:1 before and after annealing at 25 K. The spectra were recorded at 15 K.

3.4. Annealing of the Ar:NH_3:F_2 samples photolyzed at 15 K

Annealing of photolyzed samples was carried out by step-by-step procedure. After completion of photolysis at 15 K, the sample was annealed for 3–5 min at 25 K. Then the temperature was lowered back to 15 K, and the IR spectrum was recorded. This cycle of photolysis (annealing) was repeated 10–12 times until the reaction was complete. The final IR spectrum is shown in Fig. 5. Annealing is accompanied by the consumption of isolated NH_3 molecules and the growth of the same series of intense bands at 3267, 1512, 1465, and 797(791) cm^{-1} that appeared upon prolonged photolysis. In addition, a sharp band at 1490 cm^{-1} due to FO_2 radical appeared also. This radical is formed by addition reaction of diffusing F atoms with impurity O_2 molecules, as was shown in our previous study:[16]

$$F + O_2 \longrightarrow FO_2. \tag{5}$$

Although the presence of a minor O_2 impurity might be viewed as a nuisance, we have used reaction (5) as an internal standard for characterizing the reaction rate of diffusing F atoms during the annealing cycles. Figure 6 shows the intensities of the major product bands and the decrease of the NH_3 band relative to the FO_2 band upon annealing of the sample. The linear dependences of changes in the band intensities provide convincing evidence that this series corresponds to a primary reaction product of diffusing thermal F atoms with isolated NH_3 molecules. Note that the reaction of thermal F atoms consumes ~10% of the NH_3 molecules, about 5 times greater than the yield during exhaustive UV photolysis at 15 K.

As we have concluded in the EPR study, the main reaction product of photogenerated ''hot'' and thermal F atoms with isolated ammonia is the open-shell complex, NH_2–HF. To assign the observed IR bands, we have performed similar experiments with ND_3.

The infrared spectrum of a photolyzed and annealing sample Ar:ND_3:F_2 is shown in Fig. 7. It illustrates the consumption of isolated ND_3 molecules (series of bands in the υ_2 and υ_3 regions of ND_3 at 760 and 1200 cm^{-1}) and the

TABLE I. Vibrational frequencies of the complex NH_2–HF (ND_2-DF).

Assignment	Wave number, cm^{-1}			
	NH_2–HF		ND_2–DF	
	expt.	calc.[a]	expt.	calc.
$\nu_1(a_1)$ HF str.	3267 (17.5)	3486	2423 (17.5)	2531
$\nu_2(b_2)$ NH_2 str. asym	3211 tentatively	3497 (0.4)		2575 (0.5)
$\nu_3(a_1)$ NH str. sym		3401 (0.4)		2458 (0.1)
$\nu_4(a_1)$ NH_2 bend	1512 (1.0)	1527 (1.0)	1132 (1.0)	1127 (1.0)
$2\nu_5$ or $2\nu_6$	1465 (0.4)		1056 (0.05)	
$\nu_5(b_2)$ HF libration (in-plane)	797 (3.1)	860 (6.3)	601 (3.2)	622 (4.5)
$\nu_6(b_1)$ HF libration (out-of plane)	791 (3.4)	817 (8.5)	587 (3.5)	596 (6.8)
$\nu_7(b_1)$		280		212
$\nu_8(a_1)$ hydrogen-bond stretch		257		244
$\nu_9(b_2)$		221		164

[a]Relative integrated intensities of bands are given in parentheses.

growth of a series of new bands at 2423, 1132, 1056, and 601(587) cm^{-1}. Growth of these products bands and diminution of ND_3 bands are linear with increasing intensity of the FO_2 band at 1490 cm^{-1}, similar to the result with NH_3. It is apparent that the number of new product bands and their pattern of intensities correlate closely with the NH_3 results, as shown in Table I. This permits a straightforward determination of the isotopic shifts. For example, the isotopic shift for the strongest band at 3267 cm^{-1}, $\Delta\upsilon = 844\,cm^{-1}$, is close to that calculated for a pure HF vibration $\Delta\upsilon = 898\,cm^{-1}$. Since the infrared band of HF molecule isolated in argon lies at $\upsilon > 3900\,cm^{-1}$, the position of its absorption below 3700 cm^{-1} is characteristic of an HF molecule that is strongly hydrogen-bonded with another molecule.[31] Thus, we definitively assign this band to the HF molecule in the complex. The band at 1512 cm^{-1} lies very close to the υ_2 bending vibration of NH_2 in solid argon, 1523 cm^{-1} (Ref. 32). Its observed isotopic shift $\Delta\upsilon = 385\,cm^{-1}$ is in good agreement with calculated $\Delta\upsilon = 440\,cm^{-1}$, and, hence, we attribute this band to the υ_2 bending of the NH_2 group of the NH_2–HF complex.

The combined results of the EPR and infrared experiments provides clear and convincing evidence that the primary reaction product of F atoms with isolated NH_3 molecules in solid argon is the open-shell complex, NH_2–HF. A detailed description of the infrared bands is given below, based on the observed data and vibrational analysis for calculated structure of the NH_2–HF complex.

3.5. Calculated structure and vibrational analysis of the NH_2–HF complex

We carried out quantum chemical calculations in order to clarify the structure of the NH_2–HF complex, and to establish its spectroscopic characteristics (hyperfine constants and fundamental vibrations). All of computations were performed using the Gaussian 98 suite of codes.[33] A density functional method B3LYP with AUG-cc-pVTZ basis set was used for geometry optimization and calculation of the spectroscopic characteristics.

The NH_2–HF complex has a planar equilibrium structure with C_{2v} symmetry. The optimized geometry is similar to that calculated earlier by Goddard *et al.*[22] The binding energy of the complex is equal to 51 kJ/mol (34 kJ/mol when corrected for zero-point energy effects). The geometry and both experimental and calculated isotropic hf constants of the complex are given in the scheme

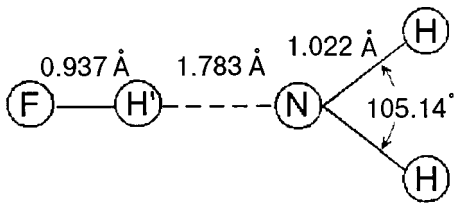

a(calc), mT	−0.70	0.02	1.15	−2.30
a(exp), mT	0.70	<0.05	1.20	2.40

(6)

The calculated hf constants a_N, a_H, and a_F are in good agreement with those obtained in experiment. The calculated hf constant at the proton of the HF molecule a_H is less than 0.05 mT and, as was noted above, could not be resolved under our experimental conditions.

The calculated frequencies and relative intensities of IR bands for NH_2–HF and ND_2–DF complexes are listed in Table I. If the HF molecule is bound to the radical–molecule complex, its two rotational degrees of freedom become two HF librational modes in the complex (υ_5,υ_6), whereas the HF fundamental (υ_1) remains in the complex. These fundamentals give rise to very strong infrared absorptions that are predicted by the calculations and observed in the experiments for both NH_3 and ND_3 isotopomers. The three translational degrees of freedom become a hydrogen-bond stretching mode (υ_8) and two bending modes of the complex (υ_7,υ_9); these fundamentals occur at low frequencies and give rise to much weaker absorptions.

A relatively weak band at 1465 cm^{-1} of NH_2–HF could be ascribed to one of the overtones $2\upsilon_5$ or $2\upsilon_6$, or possibly to both of them because the shape of this band shows a superposition of two unresolved bands split by 2–3 cm^{-1}. In the deuterated complex this band lies at 1056 cm^{-1}, and its relative intensity is about 10 times less than for the normal proteated complex, providing support for the assignment as an overtone.

In general, the agreement with the calculated and observed frequencies and isotopic shifts is excellent. The single exception is a ~200 cm^{-1} difference between the observed and calculated frequency of the HF stretch vibration in the complex. This is likely due to anharmonicity of the intramolecular and intermolecular potentials.[34,35] The calculations predict weak intensities for the NH stretching vibrational modes of the complex. In the IR spectrum, a weak broad band at 3007 cm^{-1} in Ar:NH_3:F_2 (2265 cm^{-1} in Ar:ND_3:F_2) is observed (see Figs. 5 and 7). We tentatively assign this band to the NH asymmetric stretch, although a reasonable alternative assignment could be to the HF stretch in the complex located in a perturbed lattice site.

In our previous paper[24] we calculated the charge distribution in the complex NH_2–HF. In line with this distribution, we have concluded that the contribution of electrostatic intermolecular interaction to the binding energy of the complex is 12-15 kJ/mol, i.e., ~25% of the total binding energy. On this basis, we conclude that the NH_2–HF complex has significant covalent bonding character, and the nature of the intermolecular bond should be similar to that in the hydrogen-bonded NH_3–HF complex.[36] It was shown earlier that displacement of the fundamentals of a hydrogen-bonded complex below their isolated value and the appearance strong infrared absorptions originating from librational modes in the complex are indicative of a strong intermolecular hydrogen bond.[37] Although various hydrogen-bonded molecular complexes M–HF have been studied by spectroscopic methods,[38,39] to our knowledge there are no systematic data on the thermodynamics of the hydrogen-bonded molecular complexes M–HF. Thus we can compare our data with those for the well-studied strong hydrogen-bonded complex NH_3–HF only. The energy of the hydrogen bond, 64 kJ/mol, has been calculated by several quantum chemistry methods.[36] Infrared absorptions of this complex were detected at 3041(υ_1) and 916 cm^{-1} (2-fold degenerate υ_5) in

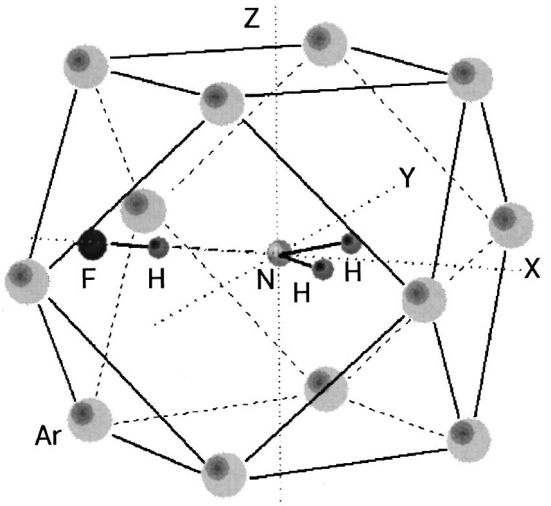

FIG. 8. Arrangement of the complex NH_2–HF in argon lattice. Twelve nearest-neighbor argon atoms are shown.

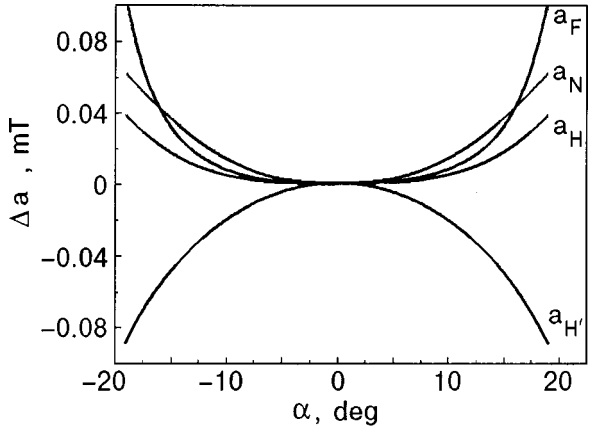

FIG. 9. Differences between the calculated isotropic hyperfine constants of NH_2–HF and those for the equilibrium geometry as a function of the out-of-plane bending angle α.

an argon matrix by Andrews.[31] Comparison of these bands with those obtained for NH_2–HF shows that the binding energy of the NH_2–HF complex should be comparable to that of NH_3–HF. Hence the calculated binding energy of NH_2–HF complex, 51 kJ/mol, is quite reasonable.

3.6. Arrangement NH_2–HF complex in an argon lattice

Starting from the calculated structure, we performed a geometry optimization of the NH_2–HF complex in an argon lattice. A detailed description of energy minimization procedure for NH_2–HF located in a substitutional site of an argon cluster containing 365 atoms was given earlier in a previous paper.[23,24] In the first step, we have used the ''hard'' collinear complex obtained in computations (Scheme *6*). In those calculations, the complex retained its collinear structure and sizes. The resulting arrangement of the complex in Ar cluster is shown in Fig. 8. The position of the nitrogen atom of the NH_2 group is close to the center of the substitutional site (0,0,0). At the other end of the complex, the fluorine atom of the HF molecule occupies the nearest octahedral interstitial site $O_h(-a/2,0,0)$, where $a=0.54$ nm is the parameter of Ar lattice. Obviously, any external forces directed along the C_2 axis of the complex should induce an out-of-plane deformation and should lower the symmetry of the complex from C_{2v} to C_s. To investigate this possibility, we performed additional calculations that included two floppy coordinates of the complex: the distance between N and H′ atoms, $R_{NH'}$, and the out-of-plane angle α:

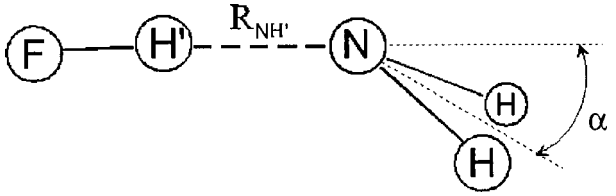

(7)

The corresponding force constants $k_R=24$ N/m and $k_\alpha=5.3$ N/m were obtained from quantum chemistry calculations. Optimization of this ''floppy'' complex in the lattice results in a slight distortion of its geometry: $\Delta R_{NH'}=0.001$ nm, and $\alpha\leqslant 4°$. Such minor deformations of the complex are probably due to the near coincidence between the N-F distance and one-half the lattice period, $a/2$. The good fit of this molecule extends to the perpendicular axes as well, as shown in Fig. 8. The two nearest argon atoms along the x axis, located at $(a,0,0)$ and $(-a,0,0)$, shift only $+0.002$ and -0.0016 nm from their initial (undistorted) positions, respectively.

The calculated hf constants are sensitive to the out-of-plane bending angle α, particularly if α is greater than 10° (Fig. 9). Based on the excellent agreement of the measured hf constants with those calculated for the C_{2v} structure, we may conclude complex suffers at most a minor distortion in the argon lattice relative to its gas phase equilibrium geometry. This conclusion is further supported by the fact that the observed HF librational modes in the complex, υ_5 and υ_6, are nearly degenerate, like the doubly degenerate bending mode in a linear triatomic molecule.

3.7. Rotation of NH_2 in an argon lattice

As shown in the previous sections, two types of radical products are observed: NH_2–HF complexes, and isolated NH_2 free radicals. The EPR spectrum of the complex is anisotropic at 15 K, and thermal averaging of the anisotropic magnetic interactions in the complex occurs only at temperatures above 30 K, as shown in Fig. 3. Because the complex has a large size along its C_2 axis, it is difficult to imagine that the averaging of the anisotropic interactions occurs by reorientation of this axis in the lattice. Our calculations show that the barrier to this type of rearrangement is high, ~4–12 kJ/mol. It is more likely that the averaging of anisotropy occurs via intramolecular bending vibrations in the complex and large amplitude libration of the NH_2 group in the lattice.

Figures 1 and 2 illustrate that the EPR spectrum of the isolated NH_2 radical exhibits the aforementioned unusual 1:1:1 triplet splitting of the protons. In contrast, the expected 1:2:1 triplet splitting for two equivalent protons of NH_2 group is observed in the EPR spectrum of the NH_2–HF com-

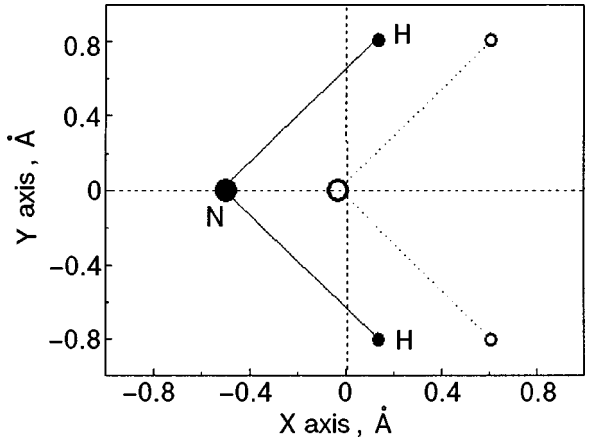

FIG. 10. Arrangement of the NH_2 radical in an argon lattice. The directions of the axes coincide with those of the lattice shown in Fig. 8.

plex. McConnel[40] attributed the 1:1:1 triplet pattern of NH_2 to free rotation in the argon lattice at 4.2 K. The Pauli principle requires that the overall symmetry of the wave function is antisymmetric with respect to permutation of the two protons. The electronic wave function is antisymmetric with respect to rotation about the C_2 axis. Therefore, rotational states having even J quantum numbers (2, 2, 4, etc.) are uniquely associated with the symmetric proton nuclear spin state ($I_H=1$). Conversely, odd-J states are associated with the antisymmetric $I_H=0$ proton nuclear spin state. Given the small rotational moment for rotation about the C_2 axis, most of the NH_2 radicals are in the $J=0$ rotational level at argon matrix temperatures, and we should expect to observe the three components of the EPR hyperfine structure with equal intensities.

However, Jen[41] pointed out that this mechanism cannot explain the different linewidths of components of the EPR spectrum having different nuclear projections of the N atom. This means that the anisotropy of the magnetic interactions is not completely averaged due to hindered (noncoherent) rotation. The apparent contradiction can be resolved if the stabilized NH_2 has one rotational degree of freedom around the C_2 axis only, whereas rotations around other axes of the radical are strongly hindered in a lattice. Figure 10 shows the calculated arrangement of the NH_2 radical in a substitution site of the argon lattice. The NH_2–HF complex, in contrast, exhibits a normal 1:2:1 hyperfine splitting due to the proton nuclear spins. The important distinction is that whereas rotation about the C_2 axis is essentially unrestricted for NH_2 (calculated barrier of $E_b=420$ J/mol), the corresponding motion in the NH_2–HF complex is strongly hindered (calculated barrier $E_b=2100$ J/mol). Perturbation of rotational motion in the solid phase was first studied by Pauling[42] and Devonshire,[43] who calculated energy levels for a linear molecule in a field with O_h symmetry. They showed that the lowest energy level of a strongly hindered rotor is a doublet that has both symmetric and antisymmetric components, as shown in Scheme (8):

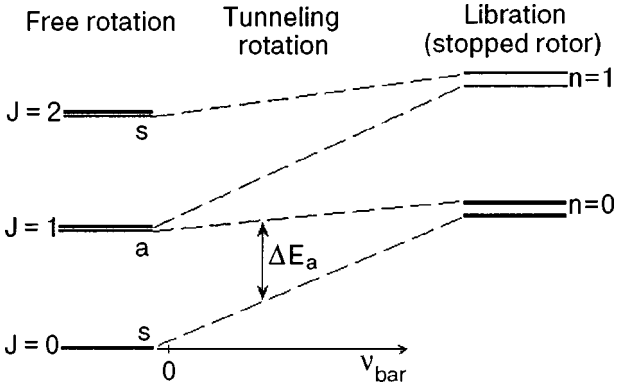

(8)

In this case, both proton nuclear spin states are represented equally, resulting in the familiar 1:2:1 hyperfine splitting pattern in the EPR spectrum.

4. CONCLUSIONS

In the present research we have demonstrated that the combined use of infrared and EPR spectroscopic techniques to study radical intermediates formed in solid-state chemical reaction of mobile F atoms enabled us to observe and make reliable assignments for the hyperfine constants and vibrational frequencies. It was shown that the geometry of the stabilized intermediate can be determined by comparison of the measured spectroscopic data with those from quantum chemistry calculations. The main results of this study are as follows:

1. The radical-molecule complex NH_2–HF is observed as an intermediate product in the reactions of mobile F atoms with NH_3 molecules trapped in solid argon.

2. The EPR spectrum of NH_2–HF is characterized by three hyperfine splittings: the 1:1:1 triplet with $a_N=1.20$ mT, the 1:2:1 triplet with $a_H=2.40$ mT, and the doublet splitting $a_F=0.7$ mT. The hf constant at the H atom of the HF molecule is less than 0.05 mT.

3. A strong red shift of the HF band relative to isolated HF, $\Delta\nu\approx 720\ \mathrm{cm}^{-1}$, is observed in the infrared spectrum of the NH_2–HF complex. The next prominent feature is a strong doublet band at $\sim 800\ \mathrm{cm}^{-1}$ that corresponds to the two in-plane and out-of-plane HF librational modes of the complex, ν_5 and ν_6. These features of the IR spectrum of the complex are indicative of the relatively strong intermolecular hydrogen bond in the complex.

4. Density functional calculations revealed that the NH_2–HF complex has a planar C_{2v} structure and a binding energy of 51 kJ/mol (34 kJ/mol when corrected for zero-point energy effects). The calculated hf constants of the complex are in good agreement with those observed in EPR experiments. The calculated vibrational frequencies for NH_2 bending and HF librational modes in the complex, ν_5 and ν_6, correspond well to those obtained in FTIR measurements. The $\sim 200\ \mathrm{cm}^{-1}$ difference between the observed and calculated frequency of the HF stretching vibration in the complex is due to anharmonicity of the intramolecular and intermolecular potentials.

5. If the C_2 axis of the NH_2–HF complex coincides with the C_4 axis of the host fcc argon crystal, then the interaction with lattice atoms induces only minor distortions to the equi-

librium structure relative to that in the gas phase. However, the interactions between the complex and host argon atoms hinder rotation of the NH_2 group about its C_2 axis, whereas this motion is essentially unrestricted in isolated NH_2.

We thank the Russian Foundation for Basic Research (Grant 98-03-33175) and the U.S. National Science Foundation (Grant CHE-9970032) for supporting this research.

*E-mail: ilya@icp.ac.ru

[1] Y. T. Lee, Ber. Bunsenges. Phys. Chem. **74**, 135 (1974).
[2] A. H. Zewail, Science **242**, 1645 (1988).
[3] K. Liu, J. C. Polany, and S. Yang, J. Chem. Phys. **98**, 5431 (1993).
[4] M. E. Jacox, in *Chemistry and Physics of Matrix Isolated Species* (Elsevier, 1989).
[5] L. Andrews, J. Phys. Chem. **88**, 2940 (1984).
[6] L. B. Knight Jr., in *Chemistry and Physics of Matrix Isolated Species* (Elsevier, 1989).
[7] H. Kunntu, J. Feld, R. Alimi, A. Becker, and V. A. Apkarian, J. Chem. Phys. **92**, 4856 (1990).
[8] J. Feld, H. Kunntu, and V. A. Apkarian, J. Chem. Phys. **93**, 1009 (1990).
[9] R. Alimi, R. B. Gerber, and V. A. Apkarian, J. Chem. Phys. **92**, 3551 (1990).
[10] E. Ya. Misochko, A. V. Akimov, and C. A. Wight, Chem. Phys. Lett. **293**, 547 (1998).
[11] V. A. Apkarian and N. Schwentner, Chem. Rev. **99**, 1481 (1999).
[12] E. Ya. Misochko, A. V. Benderskii, and C. A. Wight, J. Phys. Chem. **100**, 4496 (1996).
[13] E. Ya. Misochko, A. V. Benderskii, A. U. Goldschleger, V. A. Akimov, and A. F. Shestakov, J. Am. Chem. Soc. **117**, 11997 (1995).
[14] E. Ya. Misochko, A. V. Benderskii, A. U. Goldschleger, V. A. Akimov, A. V. Benderskii, and C. A. Wight, J. Chem. Phys. **106**, 3146 (1997).
[15] A. U. Goldschleger, E. Ya. Misochko, V. A. Akimov, I. U. Goldschleger, and V. A. Benderskii, Chem. Phys. Lett. **267**, 288 (1997).
[16] E. Ya. Misochko, A. V. Akimov, and C. A. Wight, Chem. Phys. Lett. **274**, 23 (1997).
[17] E. Ya. Misochko, V. A. Akimov, I. U. Goldschleger, A. I. Boldyrev, and C. A. Wight, J. Am. Chem. Soc. **121**, 405 (1999).
[18] E. Ya. Misochko, A. V. Akimov, and C. A. Wight, J. Phys. Chem. A **103**, 7972 (1999).
[19] B. E. Holmes and D. W. Sester, in *Physical Chemistry of Fast Reactions 2* (Plenum Press, New York, 1979).
[20] D. J. Donaldson, J. J. Sloan, and J. D. Goddard, J. Chem. Phys. **82**, 4524 (1985).
[21] S. Wategaonkar and D. W. Sester, J. Chem. Phys. **86**, 4477 (1987).
[22] D. Goddard, D. J. Donaldson, and J. J. Sloan, Chem. Phys. **114**, 321 (1987).
[23] I. U. Goldschleger, A. V. Akimov, and E. Ya. Misochko, Mendeleev Commun. **4**, 132 (1999).
[24] I. U. Goldschleger, A. V. Akimov, and E. Ya. Misochko, J. Mol. Struct. (in press).
[25] E. L. Cochran, F. J. Adrian, and V. A. Bowers, J. Chem. Phys. **51**, 2759 (1969).
[26] G. C. Pimentel, M. O. Bulanin, and M. Van Thiel, J. Chem. Phys. **36**, 500 (1962).
[27] L. Abouaf-Margulin, M. E. Jacox, and D. E. Milligan, J. Mol. Spectrosc. **67**, 34 (1977).
[28] B. Guathier-Roy, P. Boissel, L. Abouaf-Margulin, J. Pourcin, and P. Verlaque, J. Mol. Spectrosc. **115**, 147 (1986).
[29] L. Andrews and R. Lascola, J. Am. Chem. Soc. **109**, 6243 (1987).
[30] M. T. Bowers, G. I. Kerley, and W. H. Flygare, J. Chem. Phys. **45**, 3399 (1966).
[31] L. Andrews, J. Phys. Chem. **88**, 2940 (1984).
[32] D. E. Milligan and M. E. Jacox, J. Chem. Phys. **43**, 4487 (1965).
[33] M. J. Frisch, G. W. Trucks, H. B. Schlegel, G. E. Scuseria, M. A. Robb, J. R. Cheeseman, V. G. Zakrzewski, J. A. Montgomery, Jr., R. E. Stratmann, J. C. Burant, S. Daprich, J. M. Millam, A. D. Daniels, K. N. Kudin, M. C. Strain, O. Farkas, J. Tomasi, V. Barone, M. Cossi, R. Cammi, B. Mennucci, C. Pomelli, C. Adamo, S. Clifford, J. Ochterski, G. A. Petersson, P. Y. Ayala, Q. Cui, K. Morokuma, D. K. Malick, A. D. Rabuck, K. Raghavachari, J. B. Foresman, J. Cioslowski, J. V. Ortiz, B. B. Stefanov, G. Liu, A. Liashenko, P. Piskorz, I. Komaromi, R. Gomperts, R. L. Martin, D. J. Fox, T. Keith, M. A. Al-Laham, C. Y. Peng, A. Nanayakkara, C. Gonzalez, M. Challacombe, P. M. W. Gill, B. Johnson, W. Chen, M. W. Wong, J. L. Andres, C. Gonzalez, M. Head-Gordon, E. S. Replogle, and J. A. Pople, Gaussian 98, Revision A3, Gaussian, Inc., Pittsburgh, PA (1998).
[34] G. Herzberg, *Spectra of Diatomic Molecules* (Van Nostrand Reinhold, New York, 1950).
[35] B. Silvi, R. Wieczorek, Z. Latajka, M. E. Alikhani, A. Dkhissi, and Y. Bouteiller, J. Chem. Phys. **111**, 6671 (1999).
[36] Y. Zhang, C.-Y. Zhao, and X. Z. You, J. Phys. Chem. A **101**, 2879 (1997).
[37] G. C. Pimentel and A. L. McCellar, *The Hydrogen Bond*, edited by W. H. Freeman (San Francisco, 1960).
[38] A. C. Legon, Chem. Soc. Rev. **22**, 153 (1993).
[39] K. R. Leopold, G. T. Fraser, S. E. Novick, and W. Kleperer, Chem. Rev. **94**, 1807 (1994).
[40] H. M. McConnel, J. Chem. Phys. **29**, 1422 (1958).
[41] C. K. Jen, *Electron spin resonance of trapped radicals, Formation and Trapping of Free Radicals*, edited by A. M. Bass and H. P. Broida (Academic Press, New York, 1960).
[42] L. Pauling, Phys. Rev. **36**, 430 (1930).
[43] A. F. Devonshire, Proc. R. Soc. London, Ser. A **153**, 601 (1936).

This article was published in English in the original Russian journal. Reproduced here with stylistic changes by the Translation Consultant.

Reactions of laser-ablated aluminum atoms with nitrogen during condensation at 10 K. Infrared spectra and density functional calculations for Al_xN_y molecular species

L. Andrews,* M. Zhou,[1)] G. V. Chertihin, and W. D. Bare

Chemistry Department, P.O. Box 400319, University of Virginia, Charlottesville, VA 22904-4319, USA

Y. Hannachi

Laboratorie de Physico-Chimie Moleculaire (CNRS UMR 3805), Universite Bordeaux I, 351, Cours de la Liberation, F-33405 Talence, Cedex France

(Submitted February 11, 2000)
Fiz. Nizk. Temp. **26**, 992–1000 (September–October 2000)

Laser-ablated aluminum atoms react with dinitrogen on condensation at 10 K to form N_3 radicals and the subject molecules, which are identified by nitrogen isotopic substitution, further reactions on annealing, and comparison with isotopic frequencies computed by density functional theory. The major AlN_3 product is identified from three fundamentals and a statistically mixed nitrogen isotopic octet pattern. The aluminum-rich Al_2N and Al_3N species are major products produced on annealing to allow diffusion and further reaction of trapped species. This work provides the first experimental evidence for molecular Al_xN_y species that may be involved in ceramic film growth. © *2000 American Institute of Physics*. [S1063-777X(00)01509-7]

INTRODUCTION

The importance of aluminum nitride as a semiconductor and ceramic material[1] has led to numerous investigations of the solid material[2] and its formation by chemical vapor deposition (CVD) from reactions of aluminum alkyls.[3,4] The only molecular aluminum nitride investigated. AlN, has been observed by emission[5] and investigated by post-Hartree–Fock *ab initio* calculations.[6,7] In order to prepare Al_xN_y species of relevance to the CVD process, laser-ablated Al atoms have been reacted with ammonia.[8] Such compounds have been modeled by electronic structure calculations.[9]

A recent investigation of laser-ablated Ga atoms reacting with nitrogen revealed a series of Ga_xN_y species that increase stepwise on annealing to allow diffusion and reaction to form Ga_3N and GaN_3 in a manner that might approximate gallium nitride film growth.[10] The stability of similar Al_3N and AlN_3 molecules has been verified by recent electronic structure calculations.[11] However, investigations of the B/N_2 reaction revealed NBNN as the most abundant product.[12,13] Here follows a combined matrix infrared spectroscopic and density functional theoretical study of novel Al_xN_y molecular species.

EXPERIMENTAL AND COMPUTATIONAL METHODS

The technique for laser ablation and infrared matrix investigation has been described previously.[12,14,15] The aluminum target (Aesar, 99.998%) was mounted on a rotating rod. The 1064 nm Nd:YAG laser beam (Spectra Physics, DCR-11) was focused on the metal target. Laser energies ranging from 20–60 mJ/pulse were used in the experiments. Ablated aluminum atoms were codeposited with pure nitrogen onto a 10 K CsI window at a rate of 2–4 mmol/h for 30 min to 2 h. Nitrogen (Matheson) and isotopic $^{15}N_2$ (Isotec), $^{14}N_2+^{15}N_2$, and $^{14}N_2+^{14}N^{15}N+^{15}N_2$ (Isotec) mixtures were employed. Infared spectra were record with 0.5 cm^{-1} resolution and 0.1 cm^{-1} accuracy on a Nicolet 750 instrument. Matrix samples were annealed to different temperatures, and selected samples were subjected to broadband photolysis by a medium pressure mercury arc lamp (Philips, 175W) with the globe removed (240–580 nm).

Density functional theory (DFT) calculations were done for potential product molecules expected here using the Gaussian 94 program.[16] Most calculations employed the hybrid B3LYP functional, but comparisons were done with the BP86 functional as well.[17,18] The 6-311+G* basis set was used for both Al and N atoms,[19] and the cc-pVDZ set was employed in several computations.[20] The geometries were fully optimized and the frequencies were calculated from analytic second derivatives.

RESULTS

Infrared spectra and density functional calculations of aluminum–nitrogen reaction products will be presented in turn.

Infrared spectra. Matrix isolation infrared experiments were done on a 10 K salt window with laser-ablated aluminum and pure nitrogen. Representative infrared spectra are illustrated in Figs. 1, 2, and 3 for Al in pure nitrogen for three regions, and the product absorptions are listed in Table I. The strong N_3 radical[12,21] absorption at 1657.7 cm^{-1} (not shown) is 13 times stronger than the N_3^- band at 2003.3 cm^{-1}. As a measure of limited oxide contamination, the NO band at 1874.7 cm^{-1} is very weak (absorbance $A=0.001$, not shown), and trace Al_2O is detected at 988.7 cm^{-1} ($A=0.005$).[22] The major aluminum product absorbs at 2150.9/2144.0 cm^{-1}, 1391.9/1386.0 cm^{-1}, and 509.7 cm^{-1} (not shown) with $A=0.036$, 0.006, and 0.004, respectively. Another product has bands at 1501.6 and 956.7 cm^{-1}, another at

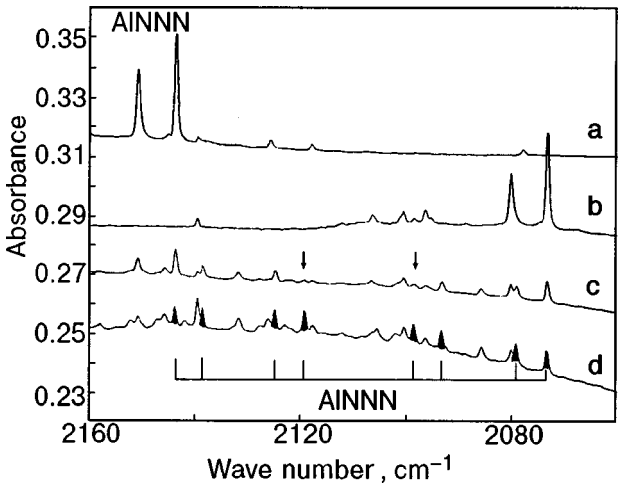

FIG. 1. Infrared spectra in the 2160–2060 cm^{-1} region for pure nitrogen isotopic samples codeposited with laser-ablated Al atoms after annealing to 25 K. (a) $^{14}N_2$, (b) $^{15}N_2$, (c) 50% $^{14}N_2$+50% $^{15}N_2$, and (d) 25% $^{14}N_2$+50% $^{14}N^{15}N$+25% $^{15}N_2$ (major site octet indicated).

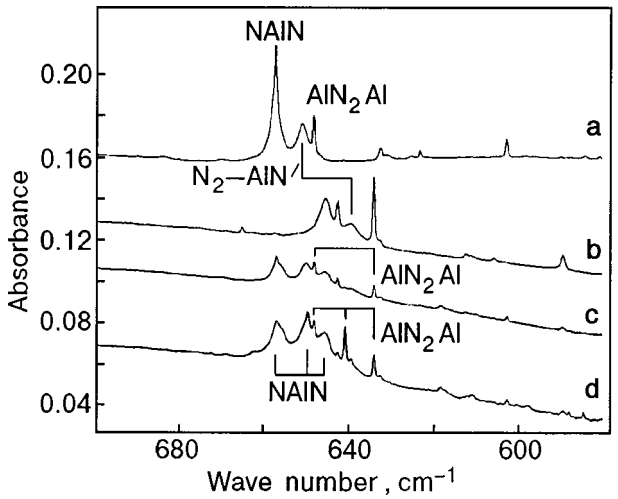

FIG. 3. Infrared spectra in the 700–580 cm^{-1} region for the same pure nitrogen isotopic samples as in Fig. 1.

777.9/770.3 cm^{-1}, and different products absorb at 656.9 and 650.7 cm^{-1}. Finally, an experiment with the lowest laser energy used here markedly reduced the 956.7 and 779.9/770.3 cm^{-1} bands relative to other products.

Similar experiments were done with $^{15}N_2$, and the shifted bands are reported in Table I. Analogous investigations with $^{14}N_2$+$^{15}N_2$ and $^{14}N_2$+$^{14}N^{15}N$+$^{15}N_2$ mixed isotopic samples gave important diagnostic multiplets. Isotopic spectra are compared in Figs. 1–3 and the multiplet absorptions are listed in Table I.

Calculations. Langhoff *et al.* have performed CASSCF and MRCI calculations on the $^3\Pi$ ground state of AlN and found 744 cm^{-1} and 1.816 Å and 746 cm^{-1} and 1.813 Å for the harmonic frequency and bond length, respectively.[7] Our B3LYP/6-311+G* calculation gave 730 cm^{-1} and 1.805 Å for the AlN ground state, which are in very good agreement and serve to ''calibrate'' the calculations reported here. The B3LYP/cc-pVDZ calculation gave 717 cm^{-1} and 1.821 Å for AlN.

Three isomers were considered for Al_2N, including a triangle, AlAlN, and AlNAl. The $^2\Sigma_u^+$ AlNAl species was the most stable (the C_{2v} form is 54.5 kcal/mol higher and the

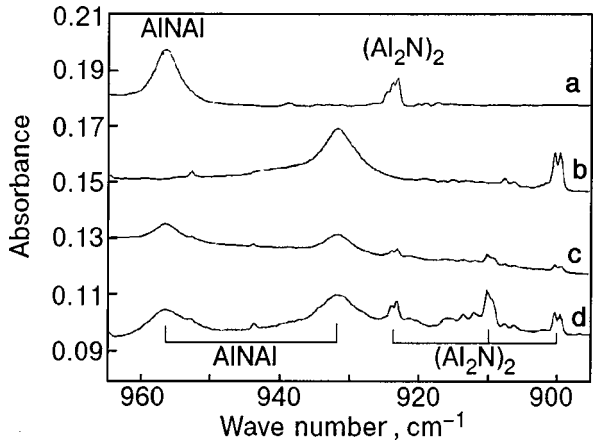

FIG. 2. Infrared spectra in the 965–895 cm^{-1} region for the same pure nitrogen isotopic samples as in Fig. 1.

$C_{\infty v}$ structure 76.6 kcal/mol higher at the B3LYP/cc-pVDZ level). Table II shows that the cc-pVDZ set gave slightly longer (0.017 Å) bonds and a 47 cm^{-1} lower antisymmetric stretching frequency than the 6-311G* set for Al_2N. The Al_2N molecule has a high computed Al-N-Al frequency, near that for Al-O-Al.

Following our work with boron, where NBNN was the major product species,[12,13] we calculated NAlNN and found ($^1A'$) NAlNN to be 73.0 kcal/mol *above* ($^1\Sigma^+$) AlNNN aluminum azide, presumably owing to weaker Al-N bonds. Our results for AlNNN (Table II) are in accord with recent MP2 calculations.[11] Similar B3LYP calculations were done with NBNN and BNNN for comparison, and the boron azide is 34.0 kcal/mol higher. The BNNN stretching frequencies are 2324 cm^{-1} (742 km/mol), 1519 (536) and 979 (128). Also, following our observation of NBN,[12] the aluminum analog was calculated to have a $^4\Pi_u$ ground state.

After finding Al_2N to be a stable radical, the saturated Al_3N molecule was computed to be very stable. The Al-N bond lengths and highest frequencies (B3LYP) suggest that the molecule is essentially trigonal planar, in agreement with higher level calculations.[11]

Six structures of formula Al_4N_2 that might result from the dimerization of Al_2N radicals were calculated at the B3LYP/cc-pVDZ level, and the results are summarized in Table III. The two lowest-energy structures are shown in Fig. 4. The global minimum has a plane of symmetry, and a strong infrared absorbing frequency calculated at 1153 cm^{-1}. The C_{2v} bridged structure is 28.5 kcal/mol higher and has lower frequencies. The linear species is 39.1 kcal/mol higher, but it has a strong fundamental calculated at 1132 cm^{-1}. The coplanar (C_{2v}) version of the global minimum is 95.1 kcal/mol higher and is not listed.

Figure 4 illustrates the geometries of important AF_xN_y species.

DISCUSSION

The new product absorptions will be identified from isotopic shifts, splitting patterns, and density functional isotopic frequency calculations.

TABLE I. Infrared absorptions (cm^{-1}) for laser-ablated Al atom reactions with pure N_2 during condensation at 10 K.

$^{14}N_2$	$^{15}N_2$	$^{14}N_2 + {}^{14}N^{15}N + {}^{15}N_2$	$^{14}N_2/{}^{15}N_2$	Identification
2327.6	2250.3	2327.6, 2289.6, 2250.3	1.03435	N_2
2178.4	2106.5		1.03413	$(N_2–AlNNN)$
2172.3	2100.6		1.03413	$(N_2–AlNNN)$
2167.9	2096.4	weak intermediate bands	1.03411	$(N_2–AlNNN)$
2150.9	2080.1		1.03404	AlNNN site
2144.0	2073.2	2144.0, 2138.7, 2125.1, 2119.4, 2098.8, 2093.4, 2079.5, 2073.4	1.03415	AlNNN
2077.8	2009.6		1.03394	$X–N_3^-$
2003.3	1837.5	2003.2, 1992.7, 1981.7, 1959.4, 1948.7, 1937.4	1.03396	N_3^-
1874.7	1841.8		1.01786	NO
1657.7	1603.5	1657.7, 1649.3, 1640.0, 1621.5, 1613.0, 1603.5	1.03380	N_3
1501.6	1474.9	1501.6, 1474.9	1.01810	AlNAl
1391.9	1345.4		1.03456	AlNNN site
1386.0	1340.2	weak intermediate bands	1.03417	AlNNN
1132.8	1106.0		1.02423	Al_xN_y
1126.8	1100.4		1.02399	Al_xN_y
1061.9	1040.7		1.02037	Al_xN_y
1054.3	1033.4		1.02022	Al_xN_y
956.7	931.7	956.7, 931.7	1.02683	AlNAl
923.2	899.4	923.2, 909.2, 899.4	1.02646	$(Al_2N)_2$
777.9	758.6	777.9, 758.6	1.02544	Al_3N
770.3	751.2	770.3, 751.2	1.02540	Al_3N
680.0	664.9	680.0, 773.0, 664.9	1.02271	$Al_xN_y–(N_2)_x$
656.9	645.4	656.9, 649.5, 645.4	1.01782	NAlN
650.7	636.5	650.7, 636.5	1.02231	$N_2–AlN$
648.2	634.0	648.2, 640.8, 634.0	1.02240	Al_2N_2
632.7	612.3	632.7, 618.2, 612.3	1.03332	Al_xN_y
623.6	605.8	624, 610, 606	1.02872	Al_xN_y
602.6	589.4	602.6, 589.4	1.02240	Al_xN_y
509.7	501.5		1.01635	AlNNN
486.7	472.5	486.7, 472.5	1.03005	Al_xN_y

AlN. The first product to be considered is AlN; the gas phase fundamental is 746.8 cm^{-1} and theoretical calculations sustain this assignment.[5–7] Although the 670–760 cm^{-1} region contains no significant absorption, a 650.7 cm^{-1} band grows slightly on annealing and almost disappears on photolysis. This band shows a 14/15 isotopic frequency ratio of 1.02231, which is just below the harmonic Al-N diatomic ratio of 1.02264. Furthermore, the 650.7 cm^{-1} band exhibits a doublet in mixed isotopic spectra providing evidence for a single N atom vibration. The gas phase-to-nitrogen-matrix shift is excessive for an isolated molecule, so we believe a better assignment for the 650.7 cm^{-1} band is to a perturbed AlN molecule. We note that AlN is a $^3\Pi$ state and that both NAlNN and AlN_3 are singlet states. Although AlNNN (see

TABLE II. Calculated (B3LYP/6-311+G*) geometry, frequencies (cm^{-1}) and intensities (km/mol) for the AlN, Al_2N, Al_3N, NAlN, NAlNN, AlNNN and Al_2N_2 molecules.

Molecule	Geometry	Frequencies (Intensities)
AlN ($^3\Pi$)	Al–N: 1.805 Å	730.1 (12) 713.9 (12)[a]
Al_2N ($^2\Sigma_u^+$)	Al–N: 1.731 Å Linear	131.8 (35), 524.9 (0), 1051.4 (97) 128.3 (33), 524.9 (0), 1023.3 (92)[a]
Al_2N ($^2\Sigma_u^+$)	Al–N: 1.748 Å Linear	77.7 (2×15), 509.2 (0), 1004.3 (72)[b] 75.6, 509.2, 977.4[a,b]
Al_2N^- ($^1\Sigma_g^+$)	Al–N: 1.746 Å Linear	119.0 (2×2), 518.7 (0), 1129.8 (685) 115.8 (1×2), 518.7 (0), 1099.5 (643)[a]
Al_3N ($^1A_1$) C_{2v}	Al_1N: 1.8495 Å $Al_{2,3}N$: 1.850 Å $\angle Al_2–N–Al_3$: 120.1°	153.8 (3), 154.3 (3), 217.0 (0), 427.5 (0), 751.5 (328), 751.9 (329) 153.2 (3), 153.8 (3), 210.8 (0), 427.5 (0), 732.4 (312), 732.8 (314)[a]
Al_3N ($^1A_1'$)D_{3h}	Al–N: 1.863 Å	141.1 (3×2), 200.6 (0.1), 414.3 (0), 731.9 (309×2)[c]
NAlN ($^4\Pi_u$)	Al–N: 1.804 Å Linear	122.2 (43), 146.2 (86), 643.2 (0), 725.7 (582) 120.2 (41), 143.8 (83), 621.5 (0), 713.8 (563)[a]
NAlNN ($^1A'$)	N–Al: 1.746 Å Al–N: 2.021 Å N–N: 1.106 Å N–Al–N: 87.1° Al–N–N: 177.7°	89.8 (47), 230.6 (4), 259.0 (17), 326.4 (12), 840.1 (21), 229.6 (381)
AlNNN ($^1\Sigma^+$)	Al–N: 1.826 Å N–N: 1.206 Å N–N: 1.138 Å	94.4 (2), 497.4 (167), 625.4 (17), 626.4 (18), 1466.0 (320), 2271.2 (1018), 91.6 (2), 490.8 (162), 604.2 (16), 605.2 (17), 1416.9 (301), 2194.4 (950)[a]
N_3^- ($^1\Sigma_g^+$)	1.1832 Å	628.2 (7×2), 1351.8 (0), 2078.5 (1241)
AlN_2Al ($^3\Sigma_g^-$)	Al–N: 1.860 Å N–N: 1.204 Å	82.2 (2), 257.7 (0), 369.2 (0), 634.3 (579), 1739.4 (0)
AlN_2Al ($^3\Sigma_g^-$)	Al–N: 1.888 Å N–N: 1.204 Å	78.4 (1×2), 224.9 (0×2), 355.9 (0), 612.0 (509), 1757.1 (0)[b] 76.7 [π_u], 217.5 [π_g], 355.9 [π_g], 598.5 [σ_u], 1697.8 [σ_g][a,b]
$(AlN)_2$ (^1A_g)	Al–N: 2.041 Å N–N: 1.267 Å	160.4 (0.2), 195.3 (21), 337.0 (0), 554.2 (0), 571.5 (509), 1445.9 (0) 156.9 (0.2), 191.0 (20), 337.0 (0), 536.5 (0), 558.9 (487), 1396.8 (0)[a]
$(AlN)_2$ (^1A_g)	Al–N: 2.074 Å N–N: 1.263 Å	156 (0), 193 (18), 331 (0), 553 (0), 564 (463), 1453 (0)[b]

[a] Frequencies for ^{15}N substitution,
[b] cc-pVDZ basis set,
[c] BP86 functional; (2×2) is to denote doubly degenerate mode of intensity 2, etc.

below) increases on annealing, there is no evidence for the higher energy NAlNN isomer. Perhaps the perturbation is at the metal center, i.e., NN–AlN.

The AlN molecule is prepared here by direct reaction (1) between the atoms, which is

$$Al+N \rightarrow AlN \quad (\Delta E = -60 \text{ kcal/mol}), \tag{1}$$

calculated (B3LYP without ZPE) to be exothermic. The presence of N atoms in these experiments is confirmed by observation of the N_3 radical.[12,21]

AlN_3. The major aluminum product in solid nitrogen absorbs at 2150.9/2144.0 cm^{-1}, 1391.9/1386.0 cm^{-1}, and 509.7 cm^{-1}. These bands increase 10% on 25 K annealing, almost disappear on 240–580 nm photolysis, recover in part on subsequent 30 K annealing, and increase more on 35 K annealing. The observed intensities are 0.0379/0.0074/0.0061 a.u. after 25 K annealing. The diagnostic mixed isotopic pattern for the strong higher frequency band is a sextet with $^{14}N_2+^{15}N_2$ and an octet with $^{14}N_2+^{14}N^{15}N+^{15}N_2$ (Fig.

TABLE III. Calculated (B3LYP/cc-pVDZ) relative energies (kcal/mol) geometries, frequencies (cm^{-1}), and intensities (km/mol) for Al_4N_2 molecules.

Symmetry	Energy	Lengths, angles	Frequencies (Intensities)[a]
C_s	0.0	$Al_{1,2}$–N_1: 1.879 Å N_1–Al_3 : 1.810 Å Al_3–N_2 : 1.693 Å N_2–Al_4: 1.791 Å $Al_{1,2}$–N_1–Al_3 : 116.9° N–Al–N: 179.3° Al_3–N_2–Al_4: 164.3°	a': 245 (17), 355 (2), 532 (116), 814 (127), 1153 (504) a'': 723 (334) 239, 353, 528, 794, 1126[b] 704[b]
C_{2v} , $^1A_1$	28.5	Al_1–N_1: 2.065 Å Al_3–N_2 : 1.846 Å N_1–N_2 : 1.439 Å N_1–Al_1–N_2 : 40.8° N_1–N_2–Al_3 : 165.6° Al_1–N_1N_2–Al_2: 125.1°	a_1: 311 (41), 387 (3), 1067 (8) a_2: 212 (0), b_1: 506 (267) 308, 386, 1033[b] 200, 495, 205, 648[b]
$D_{\infty h}$, $^1\Sigma_g^+$	39.1	Al_1–Al_2 : 2.554 Å Al_1–N_1 : 1.690 Å N_1–Al_3 : 1.810 Å	σ_g : 545 (0), 1154 (0) σ_u : 499 (126), 1132 (803) 544, 1126, 499, 1103[b]
C_s , $^3A'$	44.7	$Al_{1,2}$–N_1: 1.887 Å N_1–Al_3 : 1.794 Å Al_3–N_2 : 1.700 Å N_2–Al_4 : 1.787 Å Al_2–N_1–Al_3 : 136.2° Al_1–N_1–Al_3 : 135.6° Al_3–N_2–Al_4 : 144.1°	a': 223 (30), 372 (45), 543 (45) 595 (17), 230 (883), 1086 (220) a'': 243 (38) 186, 222, 369, 531, 580, 860, 1061, 238[b]
D_2 , $^3B_2$	78.6	Al–N: 1.925 Å N–N: 1.369 Å Al_1–NN–Al_3 : 69.7°	a_1 : 338 (0), 962 (0) b_1 : 217 (0), 493 (10) b_2 : 217 (17), 525 (59) b_3 : 287 (239), 603 (222) 338, 930, 211, 482[b] 210, 514, 286, 588[b]

[a]All real frequencies; only those above 200 cm^{-1} listed;
[b]$^{15}N^{15}N$ substituted frequencies.

1, arrows mark positions of Al-15-14-15 and Al-14-15-14 isotopic bands unique to the statistically mixed isotopic experiment). These sextet and octet patterns are much clearer for the GaNNN species, where annealing increases one matrix site and removes the other;[10] nevertheless, these multiplets identify the vibration of three inequivalent nitrogen atoms.

Since this band is in the azide stretching region, AlN_3 was investigated by DFT and found to be a stable $^1\Sigma^+$ molecule (Table II). The three strong stretching fundamentals are calculated at 2271.2, 1466.0, and 497.4 cm^{-1} with 6/2/1 relative intensities. Scale factors of 0.947 and 0.949 are required to fit the upper two N-N stretching modes and 1.025 to fit the lower Al-N stretching mode. The same calculation predicted the strong N_3^- mode at 2078.5 cm^{-1}, which requires a 0.964 scale factor and is appropriate for the B3LYP functional.[23] The relative intensities are also modeled reasonably well by the B3LYP functional, except that the intensity of the weaker symmetric N-N-N stretching mode is overestimated relative to the stronger antisymmetric N-N-N stretching mode. The calculated and observed 14/15 isotopic ratios match and verify the normal mode assignments. Similar agreement between experiment and theory was found for GaN_3 (Ref. 10). The gas phase observation of CaN_3 and SrN_3, our matrix formation of the MN_3 (M=Al, Ga, In, Tl) molecules, and the synthesis of $Al(N_3)_3$ show that these azides are physically stable molecules.[10,24,25]

Two mechanisms for the formation of AlN_3 come to mind: the reaction of Al with an N_3 radical, and the AlN reaction with N_2—the strongly exothermic (B3LYP) reactions (2a) and (2b):

$$Al+N_3 \rightarrow AlN_3 \quad (\Delta E = -94 \text{ kcal/mol}), \tag{2a}$$

$$AlN+N_2 \rightarrow AlN_3 \quad (\Delta E = -49 \text{ kcal/mol}). \tag{2b}$$

Mixed $^{14}N_2+^{15}N_2$ isotopic spectra can in principle distinguish between these two reactions, but complications from two matrix-site absorptions reduce the accuracy of band in-

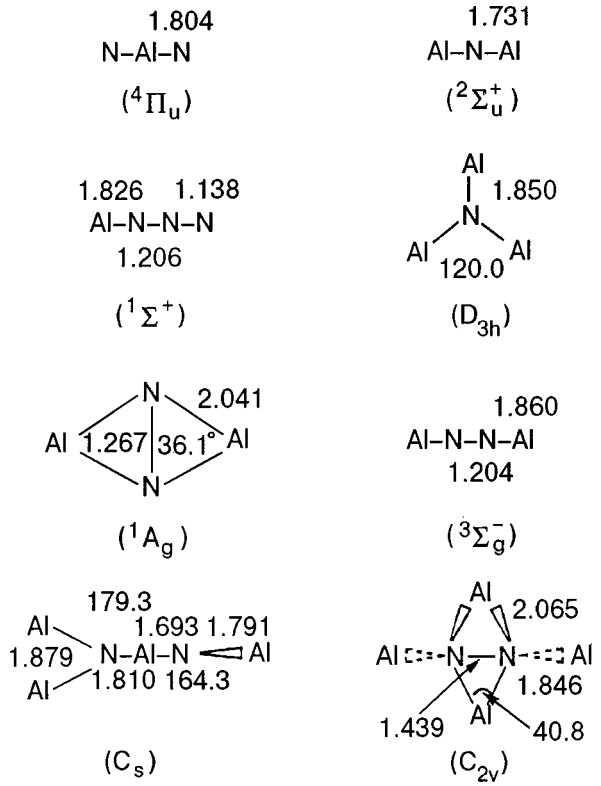

FIG. 4. Optimized geometries of Al_xN_y products computed by B3LYP/6-311+G*. Bond lengths in Å and angles in degrees. Al_4N_2 structures calculated with cc-pVDZ basis set.

tensity measurements. However, for GaN_3, the mixed isotopic spectra were clearly resolved for the major site absorption, and it was suggested that about 80% of the GaN_3 product is formed from the N_3 radical reaction.[10]

NAlN. The strong 656.9 cm^{-1} band also increased on annealing and decreased markedly on photolysis. This band showed a small $^{14}N_2/^{15}N_2$ ratio (1.01782) and an approximate 1:2:1 triplet pattern with $^{14}N_2+^{14}N^{15}N+^{15}N_2$, which is characteristic of *two equivalent* N atoms (Fig. 3). In fact the 14/15 isotopic ratio for the harmonic antisymmetric vibration of a linear N-Al-N unit is 1.01673. Our B3LYP calculations find a stable linear NAlN molecule ($^4\Pi_u$ state) with σ_u frequency at 725.7 cm^{-1}, in very good agreement with the matrix observation. The slightly higher observed 14/15 ratio might suggest a slight bending of the molecule in the matrix. The scale factor 0.905 required to fit the calculated and observed bands is lower than other comparisons reported here; this suggests that higher-level calculations might provide a better description of the $^4\Pi_u$ state of NAlN.

The NAlN molecule is formed by the reaction of N with the metal center in AlN, reaction (3), which is exothermic. However, NAlN is higher energy than Al+N_2 by 120 kcal/mol,

$$N+AlN\rightarrow NAlN(^4\Pi_u) \quad (\Delta E=-44 \text{ kcal/mol}) \qquad (3)$$

(B3LYP), but NAlN clearly is kinetically stable. Even Al-N_2 is a van der Waals molecule (bound by 4 kcal/mol as estimated by B3LYP).

The analogous NGaN molecule was observed at 586.4, 584.1 cm^{-1} (^{69}Ga, ^{71}Ga), where resolved isotopic splitting confirmed the vibration of a single gallium atom.[10]

AlNAl. The 956.7 cm^{-1} band increases slightly on annealing but almost *doubles* on photolysis. The mixed isotopic spectra reveal a doublet absorption (Fig. 2) for the vibration of *a single* nitrogen atom and a large (1.02683) nitrogen 14/15 isotopic ratio. In fact the 14/15 isotopic ratio for the harmonic antisymmetric vibration of a linear Al-N-Al unit is 1.02750. Our B3LYP calculation finds the most stable Al_2N species to be linear AlNAl ($^2\Sigma_u^+$), with a calculated σ_u mode at 1051.4 cm^{-1}, in very good agreement with the matrix spectrum. The scale factor 0.910 again suggests that higher-level calculations might produce a better fit, and indeed the cc-pVDZ basis set (Table II) produces a 1004.3 cm^{-1} σ_u frequency, in better agreement with the observed value (0.953 scale factor). The 956.7 cm^{-1} band is assigned to AlNAl in solid nitrogen.

The sharp 1501.6 cm^{-1} band tracks with the 956.7 cm^{-1} band on annealing and photolysis, and it too shows the doublet mixed isotopic spectrum for the vibration of *a single* nitrogen atom. Its appearance in the NO region and 14/15 isotopic ratio invited consideration of such a species, but AlNO and AlON absorb elsewhere.[26] The differences $1501.6-956.7=544.9\,cm^{-1}$ and $1474.9-931.7=543.2\,cm^{-1}$ for the ^{15}N counterpart provide a mode that shows *very little* ^{15}N shift and is near the 524.9 cm^{-1} calculated value for the σ_g mode of AlNAl. A slight amount of bending of the molecule would decrease the 14/15 ratio of the σ_u mode and increase the 14/15 ratio of the σ_g mode. Although the 1501.6 cm^{-1} band absorbance (0.008) is larger relative to the 956.7 cm^{-1} band (0.014) than normally found for a combination band and a fundamental, linear molecules often have relatively strong combination bands, and the 1501.6 cm^{-1} band is assigned to the $\sigma_u+\sigma_g$ combination band for AlNAl.

Similar experiments with laser-ablated Al atoms and 4% N_2 in argon reveal weak 981.3, 974.8 cm^{-1} bands with the same isotopic behavior that can be assigned to AlNAl in solid argon.[27] This suggests a matrix shift for the pure nitrogen environment, and the argon matrix bands clearly fit the DFT frequency calculations better.

The sequential reactions of Al atoms with AlN are exothermic, based on our B3LYP calculations:

$$AlN+Al\rightarrow AlNAl \quad (\Delta E=-114 \text{ kcal/mol}), \qquad (4)$$

$$AlNAl+Al\rightarrow Al_3N \quad (\Delta E=-86 \text{ kcal/mol}). \qquad (5)$$

Al_3N. Two sharp bands at 777.9, 770.3 cm^{-1} also increased slightly on annealing but markedly on photolysis, more on subsequent annealing, and remained strong after 35 K annealing, in contrast to AlNAl, which almost disappeared. Only the same pure isotopic bands were observed in mixed isotopic experiments, so again *a single* nitrogen atom is involved. These bands exhibited virtually the same isotopic 14/15 ratio, 1.02542 ± 0.00002, which is slightly smaller than the above 956.7/931.7 ratio for AlNAl. Hence, the 777.9, 770.3 cm^{-1} bands are also due to an antisymmetric Al-N-Al stretching mode, with a slightly smaller included angle, and the product may involve further Al reaction with AlNAl.

Our B3LYP and BP86 and recent higher-level calculations[11] show that Al_3N is stable, and the strong e' mode predicted at 751.7 cm^{-1} with 14/15 ratio 1.02606 is

extremely close to the observed value. The 777.9, 770.3 cm^{-1} bands are assigned to the e' mode of Al_3N split by interaction with the nitrogen matrix.

The major product in argon matrix experiments[27] at 773.1 cm^{-1} increases and remains on annealing to 40 K. The sharp doublet with mixed isotopic precursor and the 1.02547 isotopic frequency ratio show that this is the same Al_3N species observed in the nitrogen matrix. Finally, the observation of a single band for the e' mode of Al_3N in solid argon shows that the splitting in the nitrogen matrix is environmental and suggests that the split mode in the B3LYP calculation is due to symmetry breaking inherent in the calculation.[28] The D_{3h} symmetry of the molecule maintained with the pure density functional BP86 (Table II) is also expected in the gas phase.

Al_3N. The anomalously low electron affinity recently measured for Al_3N is characteristic of a closed-shell molecule,[29] which is calculated to be very stable;[30] these observations are in accord with the matrix infrared spectrum and behavior reported here for Al_3N.

Al_2N_2. The most stable Al_2N_2 isomer is the $(^1A_1')$ rhombic ring,[11] and this characteristic $(AlN)_2$ structure exhibits diatomic isotopic ratios. However, the linear AlNNAl molecule is only 1.8 kcal/mol higher at the B3LYP level with both basis sets, and the σ_u mode also exhibits the diatomic isotopic ratio. The sharp 648.2 cm^{-1} band meets these requirements: a 1.02240 isotopic ratio and a triplet with $^{14}N_2+^{14}N^{15}N+^{15}N_2$ for *two equivalent* nitrogen atoms. The b_{1u} mode of the singlet rhombus is predicted at 571.5 cm^{-1}, whereas the σ_u mode of triplet AlNNAl is 634.3 cm^{-1} (Table II). Clearly, the latter fits the 648.2 cm^{-1} band more closely, and it is assigned accordingly.

Note, however, that a strong 648.2, 634.0 cm^{-1} doublet is observed with $^{14}N_2+^{15}N_2$, indicating that *a single dinitrogen* molecule is reacting to form AlNNAl. Although Al-N_2 is only a van der Waals molecule, another Al atom will react to give the stable AlNNAl product,

$$Al+N_2+Al\rightarrow AlNNAl \quad (\Delta E=-42 \text{ kcal/mol}). \qquad (6)$$

Reaction (6) is 42 kcal/mol exothermic.

$(Al_2N)_2$. Both nitrogen and argon matrix experiments[27] contain a weak band near 924 cm^{-1} that grows on annealing and remains at the end of annealing cycles. These bands form 1:2:1 triplets in *both* mixed isotopic experiments, so *two equivalent* nitrogen atoms from *different* nitrogen molecules are required. The 14/15 ratios 1.0264 also denote an antisymmetric Al-N-Al vibration of a nearly linear Al-N-Al subunit. The annealing behavior suggests a high Al/N species. The 924 cm^{-1} band is tentatively assigned to an Al_2N dimer. Unfortunately, none of the Al_4N_2 calculations (Table IV) fit particularly well, but this is a difficult system to calculate.

Higher Al_xN_y absorptions. The nitrogen matrix experiments contain bands at 1132.8, 1126.8, 1061.9, and 1054.3 cm^{-1}, which increase on annealing and show 14/15 isotopic ratios near the diatomic AlN value. Unfortunately, no mixed isotopic data can be obtained from this congested spectral region. The 1132.8, 1126.8 cm^{-1} bands are destroyed by photolysis, while the 1061.9, 1054.3 cm^{-1} bands increase and remain on final annealing. Clearly, these bands are due to higher Al_xN_y clusters. In this regard a linear AlNAlAlNAl chain has a very strong stretching mode predicted at 1132 cm^{-1}, which suggests that Al_xN_y chains absorb in this region.

CONCLUSIONS

Laser-ablated aluminum atoms react with dinitrogen on condensation at 10 K to form N_3 radicals and AlN_2, Al_2N, Al_2N_2, AlN_3 and Al_3N molecules, which are identified by nitrogen isotopic substitution, further reactions on annealing, and comparison with isotopic frequencies computed by density functional theory. The major AlN_3 product is identified from three fundamentals and a statistically mixed nitrogen isotopic octet pattern. The aluminum-rich Al_2N and Al_3N species are major products produced on annealing to allow diffusion and further reaction of trapped species. This work provides the first experimental evidence for molecular Al_xN_y species that may be involved in ceramic film growth.

We gratefully acknowledge partial research support from the N.S.F., P.R.F., and C.N.R.S.

*E-mail: lsa@virginia.edu
[1)]Permanent address: Laser Chemistry Institute, Fudan University, Shanghai, P. R. China

[1] T. J. Morz Jr., Ceram. Bull. **70**, 849 (1991).
[2] See, for example: K. Miwa and A. Fukumoto, Phys. Rev. B **48**, 789 (1993); E. Ruiz, S. Alvarez, and P. Alemarz, Phys. Rev. B **94**, 7115 (1994); A. K. Knudsen, Bull. Am. Ceram. Soc. **74**, 97 (1995); R. Y. Krupitskaya and G. W. Auner, J. Appl. Phys. **84**, 2861 (1998); G. T. Kiehne, G. K. L. Wong, and J. B. Ketterson, J. Appl. Phys. **84**, 5922 (1998).
[3] *Chemistry of Aluminum, Gallium, Indium and Thallium*, edited by A. J. Downs (Chapman and Hall, New York, 1993).
[4] A. Y. Timoshkin, H. F. Bettinger, and H. F. Schaefer III, J. Am. Chem. Soc. **119**, 5668 (1997).
[5] J. D. Simmons and J. K. McDonald, J. Mol. Spectrosc. **41**, 584 (1972).
[6] M. Pelissier and J. P. Malrieu, J. Mol. Spectrosc. **77**, 322 (1979).
[7] S. R. Langhoff, C. W. Bauschlicher, Jr., and L. G. M. Petterson, J. Chem. Phys. **89**, 7354 (1988).
[8] D. V. Lanzisera and L. Andrews, J. Phys. Chem. A **101**, 5082 (1997).
[9] R. D. Davy and K. L. Jaffrey, J. Phys. Chem. **98**, 8930 (1994).
[10] M. F. Zhou and L. Andrews, J. Phys. Chem. A **104**, 1648 (2000).
[11] B. H. Boo and Z. Liu, J. Phys. Chem. A **103**, 1250 (1999).
[12] P. Hassanzadeh and L. Andrews, J. Phys. Chem. **96**, 9177 (1992).
[13] L. Andrews, P. Hassanzadeh, T. R. Burkholder, and J. M. L. Martin, J. Chem. Phys. **98**, 922 (1993).
[14] T. R. Burkholder and L. Andrews, J. Chem. Phys. **95**, 8697 (1991).
[15] L. Andrews, T. R. Burkholder, and J. T. Yustein, J. Phys. Chem. **96**, 10182 (1992).
[16] M. J. Frisch, G. W. Trucks, H. B. Schlegel, P. M. W. Gill, B. G. Johnson, M. A. Robb, J. R. Cheeseman, T. Keith, G. A. Petersson, J. A. Montgomery, K. Raghavachari, M. A. Al-Laham, V. G. Zakrzewski, J. V. Ortiz, J. B. Foresman, J. Cioslowski, B. B. Stefanov, A. Nanayakkara, M. Challacombe, C. Y. Peng, P. Y. Ayala, W. Chen, M. W. Wong, J. L. Andres, E. S. Replogle, R. Gomperts, R. L. Martin, D. J. Fox, J. S. Binkley, D. J. Defrees, J. Baker, J. P. Stewart, M. Head-Gordon, C. Gonzalez, and J. A. Pople, Gaussian 94, Revision B.1, Gaussian, Inc., Pittsburgh, PA (1995).
[17] C. Lee, E. Yang, and R. G. Parr, Phys. Rev. B **37**, 785 (1988).
[18] J. P. Perdew, Phys. Rev. B **33**, 8822 (1986); A. D. Becke, J. Chem. Phys. **98**, 5648 (1993).
[19] A. D. Mclean and G. S. Chandler, J. Chem. Phys. **72**, 5639 (1980); R. Krishnan, J. S. Binkley, P. Seeger, and J. A. Pople, J. Chem. Phys. **72**, 650 (1980).
[20] D. E. Woon and T. H. Dunning Jr., J. Chem. Phys. **98**, 1358 (1993).

[21] T. Tian, J. C. Facelli, and J. Michl, J. Phys. Chem. **95**, 8554 (1991).
[22] S. M. Sonchik, L. Andrews, and K. D. Carlson, J. Phys. Chem. **87**, 2004 (1983).
[23] I. Bytheway and M. W. Wong, Chem. Phys. Lett. **282**, 219 (1998).
[24] C. R. Brazier and P. F. Bernath, J. Chem. Phys. **88**, 2112 (1988).
[25] C. J. Linnen, D. E. Macks, and R. D. Coombe, J. Phys. Chem. B **101**, 1602 (1997).
[26] L. Andrews, M. F. Zhou, and W. D. Bare, J. Phys. Chem. **102**, 5019 (1998).
[27] L. Andrews, M. F. Zhou, G. V. Chertihin, W. D. Bare, and Y. Hannachi, J. Phys. Chem. A **104**, 1656 (2000).
[28] C. D. Sherill, M. S. Lee, and M. Head-Gordon, Chem. Phys. Lett. **302**, 425 (1999).
[29] S. K. Nayak, B. K. Rao, P. Jena, X. Li, and L.-S. Wang, Chem. Phys. Lett. **301**, 379 (1999).
[30] S. K. Nayak, S. N. Khanna, and P. Jena, Phys. Rev. B **57**, 3787 (1998).

This article was published in English in the original Russian journal. Reproduced here with stylistic changes by the Translation Consultant.

Optical spectra of CuO_2 and matrix effect upon its structure

N. Caspary

Infineon Technologies, D-81739 München, Germany

E. V. Savchenko*

B. Verkin Institute for Low Temperature Physics and Engineering, National Academy of Sciences of Ukraine, 47 Lenin Ave., Kharkov 61164, Ukraine

A. Thoma and A. Lammers

Teradyne GmbH, D-81673 München, Germany

V. E. Bondybey**

Institut für Physikalische und Theoretische Chemie der TU München, 85747 Garching, Germany

(Submitted June 22, 2000)
Fiz. Nizk. Temp. **26**, 1001–1010 (September–October 2000)

Optical absorption and laser-induced fluorescence (LIF) spectra of CuO_2 in solid matrices are investigated, and previous visible studies are extended into the infrared. Several new electronic states are observed and their vibrational frequencies determined. The matrix data are compared with the results of recent gas phase CuO_2^- photodetachment studies, and with *ab initio* calculations. We also discuss the unusually large matrix effects and medium-induced electronic and vibrational frequency shifts observed for CuO_2. © *2000 American Institute of Physics.* [S1063-777X(00)01609-1]

1. INTRODUCTION

Copper oxides, and CuO_2 in particular, are interesting species which have been studied quite extensively. One of the first laser-induced fluorescence studies in rare gas matrices in fact involved the CuO_2 molecule.[1] A strong visible absorption, and an intense fluorescent progression observed when matrices containing copper were irradiated by the 488 nm line of an argon ion laser, were actually originally attributed to the diatomic CuO. The same spectrum was later reexamined by several other investigators, and the unusually large vibrational frequency shift observed in comparison with the known CuO gas phase value remained a mystery for more than a decade.[2,3] In 1982 Tevault showed conclusively with the help of isotopic substitution that the emitter actually contains two oxygen atoms.[4] A subsequent reexamination of the fluorescence using a tunable pulsed dye laser then revealed that the molecule is in all probability linear and centrosymmetric, with the observed progression involving the totally symmetric Cu-O stretching vibration.[5] In the same neon matrix study the bending frequencies both in the ground state and in the excited electronic state could be also identified.

Numerous theoretical studies of copper oxides have suggested that at least two isomeric forms of the CuO_2 dioxide should exist: the covalent linear centrosymmetric species, and a $Cu–O_2$ complex. While the theoretical studies suggested a C_{2v}, T-shaped geometry for the latter isomer,[6,7] probably the global minimum on the CuO_2 potential surface, the experimental evidence seems to favor two nonequivalent oxygen atoms and a C_s symmetry for the complex. Theoretical investigations of the inserted, covalent form yielded a linear compound with a $D_{\infty h}$ symmetry,[8,9] and the recent CASSCF study of Mochizuki *et al.* also predicted the existence of numerous low-lying excited electronic doublet states.[10,11]

The existence of two CuO_2 isomers was confirmed experimentally in the gas phase by a recent photodetachment study of Wu *et al.*[12,13] These authors detected the bent complex species with a detachment energy of about 1.5 eV, while the linear CuO_2 has a much higher electron affinity of around 3.45 eV. In agreement with the theoretical prediction, they also detected several low-lying excited electronic states, with at least three of them located within less than 1 eV above the ground state. Most recently, Chertihin *et al.*[9] have reexamined copper oxides in solid argon and observed a closely spaced doublet infrared absorption at 823.0 and 818.8 cm^{-1}. This they assigned to the asymmetric stretching vibration of the symmetric CuO_2 isomer, based on its behavior and on the appearance of a triplet of such doublets with relative intensity ratios of 1:2:1 in experiments employing an oxygen sample enriched to 50% with ^{18}O.

Over many years we have frequently observed spectra of the symmetric CuO_2 species while using a laser vaporization technique developed in our laboratory. The oxide was also always produced whenever copper electrodes were used in our pulsed discharge technique. The copper atom apparently is not spontaneously inserted into a ground-state oxygen molecule, but the oxide forms efficiently by the reaction of translationally or electronically excited copper atoms produced by the laser vaporization or the cathode sputtering processes. During these studies we made a variety of new observations, and several new and puzzling effects emerged. These results are reviewed, interpreted, and summarized in this manuscript.

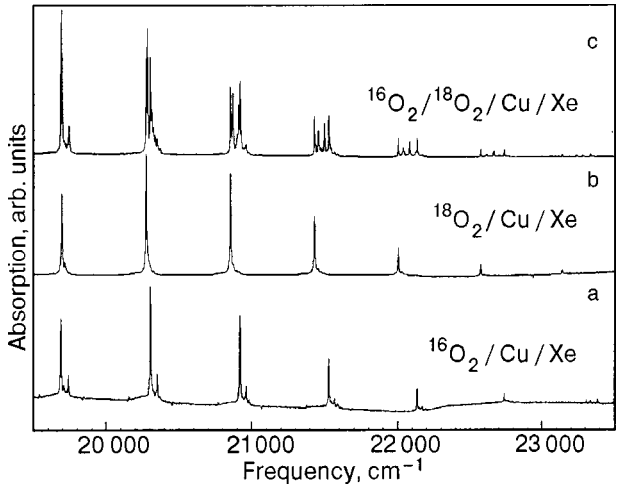

FIG. 1. Absorption spectra of different CuO_2 isotopomers in a xenon matrix. The upper trace contains $^{16}OCu^{16}O$, $^{16}OCu^{18}O$ and $^{18}OCu^{18}O$ in a ratio of approximately 1:1.5:1. The matrices of the two lower spectra were generated from the pure isotopic gases and therefore contain only $^{16}OCu^{16}O$ (a) and $^{18}OCu^{18}O$ (b), respectively. The side bands in trace (a) can be seen as site effects.

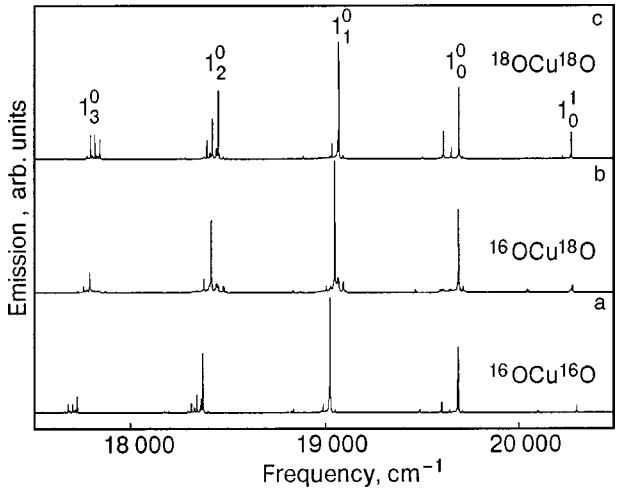

FIG. 2. Comparison of the laser-induced fluorescence spectra for three different isotopomers of copper oxide in a xenon matrix: $^{16}OCu^{16}O$ (a), $^{16}OCu^{18}O$ (b), and $^{18}OCu^{18}O$ (c). For each species the 1_0^2 state was excited. The assignments of the weak transitions is shown in Fig. 3.

2. EXPERIMENTAL

2.1. Fluorescence of CuO_2 and its ground-state structure

We examined the spectra in a number of different matrices, neon, argon, krypton and xenon, as well as in solid N_2. The spectra exhibit interesting medium effects, which will be discussed later, and their interpretation is complicated by the presence of multiple sites. In solid xenon the spectra are least obscured by such multiple ''site effects,'' and we will therefore focus our initial discussion on this matrix.

Typical CuO_2 absorption spectra in solid xenon obtained using $^{16}O_2$ and $^{18}O_2$, respectively, are shown in Figs. 1a and 1b. Each spectrum reveals a strong progression involving the upper-state symmetric stretching frequency v_1, but even in xenon one can detect numerous much weaker bands mainly due to minor sites. Excitation of the individual vibronic bands produces the well-known intense fluorescence spectrum of the CuO_2 oxide. This is shown for the two isotopic molecules in Figs. 2a and 2c. While the observed bands can easily be fitted to obtain spectroscopic constants for either of the two isotopic species individually, if one attempts a global analysis including the data for both isotopes, a very poor fit with large systematic errors results. All the computed bands of $Cu^{16}O_2$ come out 2.5 cm^{-1} too high, and those of $Cu^{18}O_2$ come out too low by a comparable amount, clearly on account of a zero-point energy problem and the failure to include the other vibrational modes of CuO_2 in the fitting process.

The zero-point energy difference contains information about the nontotally symmetric CuO_2 vibrations, and in particular about v_3. The asymmetric stretching vibration v_3, which is spectrally forbidden in an allowed electronic transition of the linear centrosymmetric CuO_2, should become weakly allowed and be in principle observable if the symmetry is lowered by asymmetric isotopic substitution. We have therefore carried out experiments with an equilibrated mixture of both oxygen isotopes and have obtained emission spectra for the third asymmetric species $^{16}OCu^{18}O$, as shown in Fig. 2b. As exemplified in the expanded section shown in Fig. 3, the spectrum indeed revealed additional emission bands which had no counterparts in the spectra of the pure, symmetric isotopic molecules. These bands, exemplified in Fig. 3 by the (0,0,0–0,0,1) transition, clearly involve the asymmetric stretching frequency v_3. Unlike the main v_1 progressions, the bands involving v_3 exhibit distinct ^{63}Cu–^{65}Cu isotopic splitting, yielding values of 816.75 cm^{-1} and 812.6 cm^{-1} for the v_3'' ground state vibration of the two copper isotopic species of $^{16}OCu^{18}O$ in solid xenon. From this a frequency of 830.8 cm^{-1} can be computed for $^{63}Cu^{16}O_2$, which is consistent with the infrared absorption measurements of Chertihin *et al.* in argon matrices[9] and provides additional support for their assignment of the 823.0 cm^{-1} frequency they observed to the linear $D_{\infty h}CuO_2$.

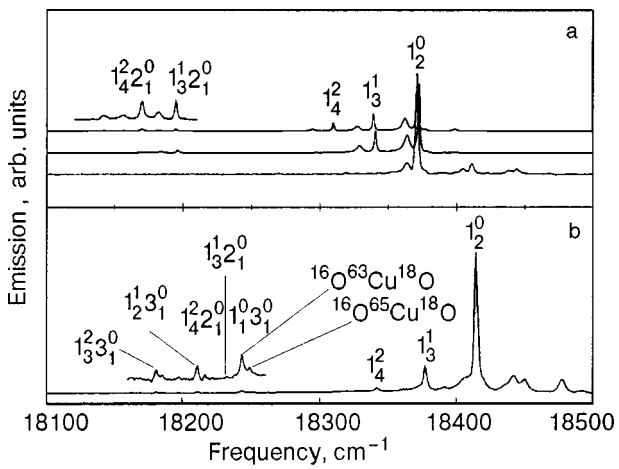

FIG. 3. Assignment of the weak bands in the emission spectrum. Figure a shows some parts of the emission spectra of $^{16}OCu^{16}O$. The matrix was excited for the upper trace in the 1_0^2, for the middle trace in the 1_0^1, and for the lower trace in the 0_0^0 transition. Figure b shows the same spectrum for $^{16}OCu^{18}O$, excited in the 1_0^2 state.

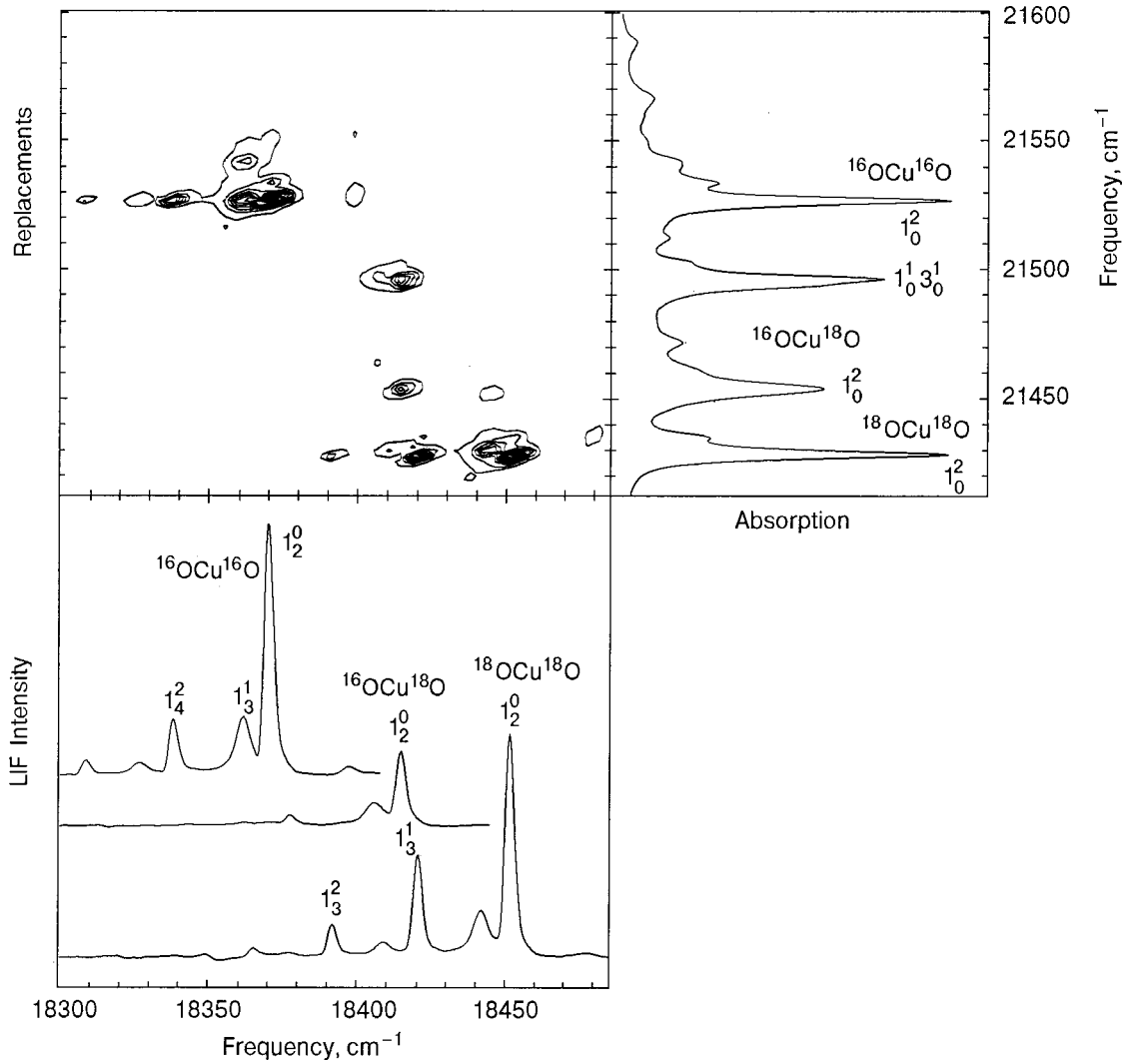

FIG. 4. Part of a 3D spectrum of the different isotopomers of OCuO in solid xenon. The absorption spectrum is plotted along the abscissa, and the three LIF spectra are plotted on the ordinate. The LIF spectra can be seen as a cut through the 3D spectrum parallel to the ordinate axis.

2.2. Vibrational structure of the excited *E* state

A further problem emerges if one now tries to analyze and assign the absorption spectrum of the mixed isotopic molecule. An absorption spectrum observed in an experiment with a 1:1 mixture of $^{16}O_2$ and $^{18}O_2$ is shown in Fig. 1c. Unlike the fluorescence spectrum, where one easily identifies groups of three approximately equidistant isotopic bands with an intensity ratio of 1:2:1, as one might expect for a molecule with two equivalent oxygen atoms, in absorption there seem to be groups of four bands of nearly equal intensities. Two of them, according to the excitation spectra in the case of pure isotopic samples, are undoubtedly due to the symmetric species $Cu^{16}O_2$ and $Cu^{18}O_2$, respectively, but the remaining two absorption bands appear only when both isotopes are present, and are clearly due to the isotopically mixed molecules.

The question thus arises whether there are two distinct $^{16}OCu^{18}O$ molecules, that is, whether the two oxygen atoms are not equivalent, or if the splitting is homogeneous, with two absorption bands appearing for each vibronic level of the mixed isotopic molecule. This question can be unambiguously answered by examining the emission spectra, and even more clearly with the help of a three-dimensional equal-intensity plot of the type shown in Fig. 4. An examination of such plots is very useful to distinguish intrinsic spectral features from inhomogeneous ''site effect.'' In the present case, they show that excitation of either of the two distinct absorptions appearing in the isotopically mixed samples produces the same, unshifted emission spectrum, that is, that the splitting is homogeneous and both new absorption bands belong to the same molecular species.

A further clue is obtained if one uses the zero-point energy difference discussed above to estimate the upper-state asymmetric stretching frequency υ_3'. When a joint fit of the $Cu^{16}O_2$, $Cu^{16}O^{18}O$, and $Cu^{18}O_2$ isotopic data, including the ground state υ_3'' bands discussed in the previous paragraphs, is carried out, with the other vibrational modes of CuO_2 included in the fitting process with the upper-state asymmetric stretch as an adjustable parameter, the systematic errors mentioned above disappear, and one obtains a nearly perfect fit of the data (RMS error <0.15 cm^{-1}). The unknown upper state υ_3' of the mixed $Cu^{16}O^{18}O$ converges to a value of around 610 cm^{-1}, very close to the expected symmetric stretching frequency. The measured values of υ_1' are 617.13 and 582.08 cm^{-1} in $Cu^{16}O_2$ and $Cu^{18}O_2$, respectively, suggesting that the υ_1' and υ_3' modes of the dioxide may have

very similar frequencies and that the asymmetric isotopic substitution in $^{16}O^{63}Cu^{18}O$ may result in a strong mixing of the two stretching frequencies.

2.3. Normal mode analysis and vibrational mode mixing in CuO_2

This idea of mixing the nearly isoenergetic (0,0,1) and (1,0,0) upper state levels, which may interact when the symmetry is broken by the asymmetric isotopic substitution, can be tested by normal coordinate analysis,[14] which we carried out for both the ground and excited electronic states of CuO_2 using all the available isotopic data. With the values of 661.2, 641.04, and 623.86 cm^{-1} measured for υ_1, the symmetric stretching vibration of the three oxygen isotopic species, and the 816.76 and 812.6 cm^{-1} υ_3 frequencies observed for the asymmetric $^{16}O^{63}Cu^{18}O$ and $^{16}O^{65}Cu^{18}O$ molecules in the ground states, one computes a Cu–O stretching force constant of $k_r = 4.219$ mdyn/Å, with a very small interaction force constant $k_{rr} = -0.095$ mdyn/Å. These are somewhat lower than for similar transition metal dioxides like TiO_2 ($k_r = 6.9$ mdyn/Å, $k_{rr} = 1.86$ mdyn/Å) or CrO_2 ($k_r = 6.65$ mdyn/Å, $k_{rr} = 1.21$ mdyn/Å) but are still indicative of rather strong, multiple metal-oxygen bonds. Inspection of the normal coordinates indicates that even for the mixed isotopic molecule, $^{16}OCu^{18}O$, the 641.04 cm^{-1} frequency is to a very good approximation a symmetric stretching vibration, involving very little motion of the central copper atom. This normal-mode analysis predicts values of $\upsilon_3 \approx 830$ and 799 cm^{-1} for the unobserved asymmetric stretches of the isotopically pure, symmetric $Cu^{16}O_2$ and $Cu^{18}O_2$ molecules, respectively. One also computes for the symmetrical $Cu^{17}O_2$ molecule vibrational frequencies almost identical to those observed for the asymmetrical $^{16}OCu^{18}O$ oxide with the same overall mass.

A similar analysis carried out for the excited electronic state data reveals quite a different situation. Assigning the observed 617.13, 582.08, and 592.42 cm^{-1} frequencies to the υ_1 symmetric stretching mode of the three isotopomers, and the fourth, 625.2 cm^{-1}, vibration to υ_3 of $^{16}OCu^{18}O$, one obtains a considerably smaller value for the Cu–O stretching force constant, $k_r = 3.035$ mdyn/Å, with a much larger, positive stretch-stretch interaction force constant $k_{rr} = 0.56$ mdyn/Å. The calculation predicts for the unobserved asymmetric υ_3 modes of $Cu^{16}O_2$ and $Cu^{18}O_2$ values of 628.9 and 605.3 cm^{-1}, indicating that in both isotopic molecules the upper-state υ_1 and υ_3 vibrational frequencies are very close, differing by only about 11.6 and 23.2 cm^{-1}, respectively. The asymmetric isotopic substitution results, however, in a strong interaction, with the two levels ''repelling'' each other. As a result, the splitting of its vibrational frequencies, $\upsilon_1 = 591.6\ cm^{-1}$ and $\upsilon_3 = 625.2\ cm^{-1}$, increases from the expected value of about 17.4 cm^{-1}–the average of the splitting in the pure isotopic molecules–to 33.6 cm^{-1}. These computed frequencies differ substantially from those obtained for the symmetric $Cu^{17}O_2$ molecule, for which the interaction is absent. Here the splitting of the computed vibrations $\upsilon_1 = 616.7\ cm^{-1}$ and $\upsilon_3 = 598.75\ cm^{-1}$ is only 17.9 cm^{-1}, almost exactly intermediate between the $Cu^{16}O_2$ and $Cu^{18}O_2$ values. Analysis of the normal modes of $^{16}OCu^{18}O$ reveals that they resemble more closely a ^{16}O–Cu and Cu–^{18}O vibration, respectively, rather than a symmetric and asymmetric stretch, and both vibrations involve appreciable motion of the central copper atom. A further consequence of the level mixing is that both the bands observed in the spectrum, nominally (1,0,0) and (0,0,1) in $(\upsilon_1', \upsilon_2', \upsilon_3')$ notation, exhibit a ^{65}Cu–^{63}Cu isotopic splitting. Such strong interactions and breakdown of the selection rules would not be surprising in symmetric hydrides (e.g. HCCD), where the difference of masses is a factor of two, but is fairly uncommon where heavier atoms are involved.

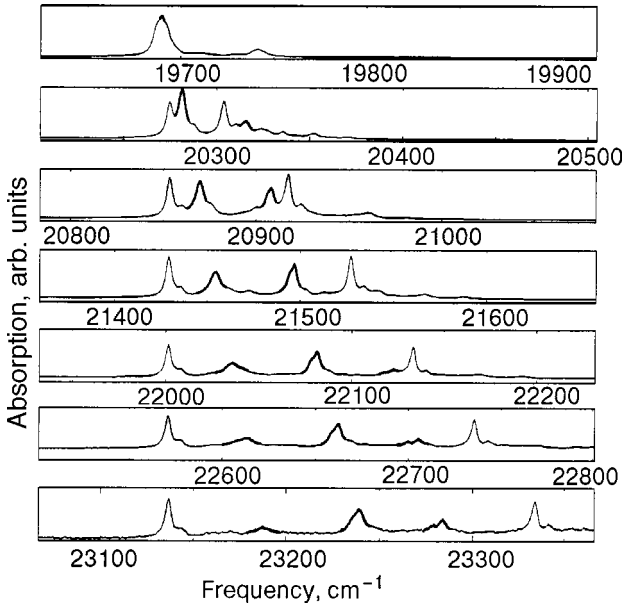

FIG. 5. Absorption spectrum of OCuO, generated from the isotopic mixtures of ^{16}O, $^{16}O^{18}O$ and ^{18}O. The absorption of $^{16}OCu^{18}O$ lies between that of $^{16}OCu^{16}O$ and $^{18}OCu^{18}O$ and is emphasized by using a heavier line.

This interaction due to the reduced symmetry of $^{16}OCu^{18}O$ is not restricted to the (1,0,0) and (0,0,1) levels of the excited CuO_2 state but propagates also to higher levels of vibrational excitation. Thus the (2,0,0) level can– and does–mix with the (1,0,1) and (0,0,2) levels, yielding a group of three absorptions. Similarly, (3,0,0), (2,0,1), (1,0,2), and (0,0,3) can interact, and the intensity in the mixed molecule is distributed between more and more levels as one proceeds to higher and higher levels of excitation, even though for high values of υ_1' not all of the interacting levels can be identified. The appearance of such interacting multiplets can clearly be observed in the absorption spectrum in Fig. 5. The situation is quite similar to the appearance of ''Fermi polyads'' in the spectra of many linear molecules exhibiting Fermi resonances, most commonly between the symmetric stretch and the even overtones of the bending vibration.

2.4. Vibrational relaxation and hot fluorescence

Vibrational relaxation in polyatomic molecules is usually fast, and very often only the emission from the vibrationless level of excited electronic states is observed. Unlike the previous studies of CuO_2 in lighter rare gas matrices, where mainly relaxed emission was detected, in the xenon matrix the vibrational relaxation is apparently considerably slower, and a rather intense unrelaxed ''hot'' fluorescence from upper-state levels up to $\upsilon_1 = 6$ is quite strong and easily

observable. At first sight one might perhaps expect stronger guest–host interactions and, consequently, faster relaxation in the more polarizable solid xenon, but, somewhat surprisingly, exactly the opposite trend is frequently observed. One difference is that in the less polarizable neon the guest–host interactions tend to be repulsive, while in the looser sites of the larger, more polarizable, heavier rare gases, and in particular in solid xenon, attractive interactions usually prevail. The molecular vibration against the steep repulsive potential in solid neon or argon may result in a stronger coupling between the molecular vibration and the phonon modes of the lattice. Also, classically one might expect a more efficient energy transfer from the light atoms such as oxygen to lattice atoms with a mass comparable to neon, than to the much heavier xenon.

We have examined spectra with an excitation of up to $v_1'=6$ of the upper state, and a typical spectrum is shown in Fig. 3. It contains sequences of bands corresponding to emission from all the $(v_1',0,0)$ levels up to $v_1'=6$, with the ground state vibrational progressions extending to $v_1''\approx 10$. Similar to the relaxed emission, also the hot fluorescence of the asymmetric $^{16}OCu^{18}O$ molecule contains, besides the strong v_1'' progressions, numerous weaker bands missing in the symmetric isotopic species $Cu^{16}O_2$ and $Cu^{18}O_2$. These are transitions of the type $1_n^m 3_1^0$, that is, involving one quantum of v_3''. They all show a distinct splitting into two components due to the naturally occurring isotopes ^{63}Cu and ^{65}Cu (abundances 69% and 31%).

It is perhaps useful to note that although intense unrelaxed fluorescence from upper-state levels involving v_1' excitation is observed, there is no evidence for emission from levels involving the other modes, v_2' or v_3'. This may be not extremely surprising. The v_2' mode has a much lower frequency than v_1', and based on the energy gap law, one would expect an efficient vibrational relaxation. On the other hand, as discussed in the previous Section, the v_3' mode has a higher vibrational frequency than v_1' but lies very close above it. The levels involving the upper state v_3' of the type (v_1,v_2,v_3) will relax efficiently into the nearby levels (v_1+1,v_2,v_3-1) just a few wave numbers below them.

2.5. The ground state bending vibration

Upon close examination the emission spectra of the symmetric species $Cu^{16}O_2$ and $Cu^{18}O_2$ reveal not only the main v_1'' progressions but also numerous very weak bands, as shown in Fig. 3a, which are, however, of a different nature than those observed for the asymmetric $^{16}OCu^{18}O$ molecule, and clearly cannot be attributed to the v_3'' vibration. These bands are all shifted approximately 160 cm^{-1} from the main v_1'' progression bands, and can be reasonably assigned to transitions of the type $1_n^m 2_1^0$, that is, to bands involving one quantum of the ground state bending vibration v_2''. Two interesting observations can be made, however. In the first place, these bands are only observed for $m\geqslant 1$, that is, for hot emission originating from levels involving at least one quantum of v_1'. In the second place, the value of v_2'' implied, ≈ 160 cm^{-1}, is considerably smaller than the 193 cm^{-1} previously measured in solid neon.

The absence of the bands involving the bending from the vibrationally relaxed spectrum is quite conspicuous—the corresponding bands originating from the vibrationless (0,0,0) level must be at least an order of magnitude weaker than the bands from vibrationally excited $(v_1',0,0)$ levels. Strictly speaking, bands involving one quantum of v_2'' are symmetry-forbidden and should not appear at all in the spectrum of a linear, centrosymmetric CuO_2. One possible explanation would be that the bending potential changes with stretching mode excitation. One could then invoke a small barrier to the linearity of CuO_2, whose height increases with v_1' excitation. The molecule in the vibrationless level would then still be linear, but the hot fluorescence would follow the bent molecule selection rules, with the molecule deviating slightly from linearity in levels with v_1' excitation. The ground-state v_2'' frequency also exhibits a large anharmonic interaction constant $x_{12}''=-6.9\,cm^{-1}$. Its medium shift in comparison with neon is rather large, but not unprecedented, and will be discussed in a Section dealing with matrix effects.

2.6. The upper state bending vibration and Renner-Teller splitting

Fluorescence excitation spectra typically provide a better signal-to-noise ratio and more details than absorption spectra. If one examines the region between the bands of the main $v_1'CuO_2$ progression in more detail, numerous weaker bands are again detected. Thus in the *F–X* excitation spectrum of $Cu^{16}O_2$ one detects a very weak band about 120 cm^{-1} above the vibrationless $(v_1'=0)$ level, then a rather broad doublet at 166 and 185 cm^{-1}, a sharp weak band at 230.1 cm^{-1}, and finally a moderately strong band at 342.8 cm^{-1}. These bands do not form easily recognizable regular progressions, but almost identical patterns are detected above the $v_1'=1,2$ and higher levels of the main v_1' progression. Furthermore, in the excitation spectrum of the isotopic $Cu^{18}O_2$ molecule a very similar structure is detected, only the intervals are slightly reduced, in fact almost exactly by the ratio which would be expected for the bending v_2 frequency of CuO_2.

The simplest explanation would be to attribute this complex pattern to a relatively large Renner–Teller splitting of the v_2' vibration in the excited doublet state, perhaps into components near 115 and 170 cm^{-1}, with the bands near 230 and 340 cm^{-1} being the corresponding overtones. One problem with this interpretation is that it would require the excited state to be an orbitally degenerate $^2\Pi$ or possibly a $^2\Delta$ state, while theory seems to predict a $^2\Sigma$ state closest to the excited *E*-state energy. Nor does this interpretation explain the differences in the shapes of the different bands, and it gives no clue as to why the two higher energy bands are sharp, while the band near 170 cm^{-1} appears as a doublet and is broadened. A gas phase study of the CuO_2 spectra would clearly be very desirable, and necessary to answer this question unambiguously and determine the symmetry of the *E* state.

2.7. Lower-lying electronic states of CuO_2

Shirk and Bass noted already in their early experiment that a new progression of bands in solid argon seems to begin at 16595 cm^{-1}, and a similar observation was made in

a later solid neon LIF study. There was some controversy as to whether this further transition involves emission from the excited E state into some lower-lying electronic state, or if the E state relaxes nonradiatively into a lower state located at 16595 cm^{-1}, which then fluoresces into the ground state. In our present work we observe not only this progression whose origin is shifted to 15799.6 cm^{-1} is solid xenon, but also an additional one with an even lower energy originating at 13003.5 cm^{-1}. As noted previously, in the xenon matrix vibrational relaxation is slow, and an extensive vibrationally unrelaxed emission from levels with $v'>0$ is detected. The observed hot fluorescence answers the above controversy unambiguously: depending on which vibrational level of the F state is excited, all three transitions exhibit the same vibrationally unrelaxed band structure, demonstrating that all the spectra involve emission directly from the excited CuO_2 E-state levels into the electronic ground state (X) and into two other, low-lying electronic states. These states, which we denote A and B, are located in solid xenon at 3387.3 and 6683.4 cm^{-1} above the X-state, respectively.

Using an infrared germanium detector and extending the spectra to even lower energies, an additional band system near 9500 cm^{-1} is detected. The new spectrum seems to involve at least two progressions of bands, with the strongest being located near 8420 cm^{-1}. In solid xenon the bands are rather broad, but even in this case, when higher vibrational levels of the E state are excited, one observes what appears to be vibrationally unrelaxed emission, suggesting again that emission probably originates from the E state and ends in two further low-lying states, D and C, at energies near 11270 and 11060 cm^{-1}, respectively. These infrared emissions sharpen appreciably in the solid. Specifically for the ''*b* site'' investigated most extensively in the previous neon matrix study they are shifted to 11110.5 and 11309.5 cm^{-1}, respectively.

2.8. Electronic structure of CuO_2

The electronic structure of the molecule is surely rather complex, and it is not well understood. Mochizuki *et al.*[11] in their theoretical investigation of the linear form of CuO_2 find some thirty electronic states within the range of energies studied in this work, that is, below 25000 cm^{-1}. In agreement with previous suggestions they conclude that the molecule has an $X\,^2\Pi_g$ ground state, and based on population analysis find that, as could be expected, the bonding is considerably more covalent than in CuF_2, which can be well represented by the ionic structure $F^-Cu^{2+}F^-$. The authors assign the strong visible matrix absorption, referred to as the E state in this work, to the fully allowed transition into the second state of $^2\Sigma_u^+$ symmetry, calculated to lie at 20079 cm^{-1}.

The xenon matrix data provide extensive new information about the CuO_2 properties and electronic structure. In addition to the extensively studied E state, which, in solid xenon, occurs at 19686.9 cm^{-1}, the emission spectra provide evidence for at least four other, lower-lying electronic states, located in the xenon matrix at 3387.3, 6683.4, 11060, and 11270 cm^{-1}. The theoretical study mentioned above predicts the lowest excited electronic states to lie at 6304 cm^{-1} ($^2\Pi_u$), 7592 cm^{-1} ($^2\Sigma_g^-$), and 8365 cm^{-1} ($^2\Delta_g$), and the authors suggested that ''the emission band around 3850 cm^{-1},'' is due to the $^2\Pi_u \leftrightarrow X\,^2\Pi_g$ transition. This, however, is due to their misunderstanding of the previous experimental data; there is no observed 3850 cm^{-1} emission band in neon—the existence of a state at 3850 cm^{-1} (the analog of the 3387.3 cm^{-1} band in xenon) was inferred from an observed visible emission originating in the E state ($2\,^2\Sigma_u^+$ based on the Mochizuki *et al.*[11] assignment). If the E state emitting in the matrix is indeed $2\,^2\Sigma_u^+$, then all the lower states observed should be of *gerade* symmetry, an $E(2)\,^2\Sigma_u^+ \leftrightarrow {}^2\Pi_u$ emission would naturally be parity-forbidden. Perhaps the 7592 cm^{-1} $^2\Sigma_g^-$ state might be an alternative assignment for the 3387.3 cm^{-1} xenon matrix state. It may also be noted that one often finds $\Pi \leftrightarrow \Pi$ transitions to be more intense than $\Pi \leftrightarrow \Sigma(\Delta\Lambda = \pm 1)$, and one of the states of $^2\Pi_u$ symmetry might be an alternative candidate for the E state, since the observed complex bending frequency structure observed in our work would be easier to explain with a $\Lambda > 0$ upper state. In view of the expected large density of low-energy states, confident specific assignments without gas phase rotational analysis are quite difficult.

The CuO_2 molecule was recently investigated in the gas phase by means of CuO_2^- photodetachment spectroscopy by Wu *et al.*[12] Their work, in addition to establishing an electron affinity of 3.47 eV for the dioxide, also indentified several low-lying electronic states near 2580, 5080, and 6430, 9680, and 13630 cm^{-1}. Except for the 6530 cm^{-1} state, the differences between the photoelectron work and the xenon matrix data seem to lie well outside the combined stated error limits of the two works. It is at this point not obvious if different electronic states are involved, if the actual errors are larger than estimated, or if the differences can be explained by the matrix medium effects to be discussed below.

2.9. Molecular constants of CuO_2 in xenon

The efficient formation of the oxide and its high transition moment resulted in high quality spectra, so that overall more than 300 vibronic bands for six different isotopic species of CuO_2 in xenon matrix were measured. Part of this data is summarized in Table 1. The observed bands involve, however, mainly the totally symmetric v_1 vibration. The data for the other vibrational modes are naturally more fragmentary.

Table 2 shows the spectroscopic constants obtained by a global fit of the observed transitions, using the appropriate isotopic relationships for the data of the isotopic molecules. The v_1 potential in both the E and X states is well approximated by a Morse potential. Without including terms higher than quadratic, the observed v_1 levels extending up to $v''=10$ and $v'=6$ are reproduced with an error of <0.2 cm^{-1}. In the table we give the vibrational frequencies v_i directly measured in the experiment, rather than the ω_i constants of the polynominal Dunham-type expansion. The latter have the disadvantage of depending on the intermode coupling and change whenever an additional anharmonic constant is included. Besides the fundamental frequencies, also a number of the anharmonic x_{ii} constants could be established. It is interesting to note the uncommonly large values of the intermode coupling constants x''_{12} and x''_{13}.

TABLE I. Summary of the OCuO vibronic bands (in cm^{-1}) in different matrices. The parameters were chosen according to the zero-point energy of $^{16}OCu^{16}O$.

Matrix	Site	Electronic state											
		X			*A*		*B*	*C*	*D*		*E*		
		ω_1^0	ω_2^0	ω_3^0	ω_1^0	ω_2^0	ω_1^0	ω_1^0	ω_1^0	ω_2^0	ω_1^0	ω_2^0	ω_3^0
Neon	*f*	655.8											
	a	655.5									608.3		
	*b*1	661.5									614.5		
	*b*2	654.7			590 [5]						607.7		
	c	660.3									612.3		
	d	659.7	193.4					640.8	636.8	234	611.5	135.6	
Argon [15]	*c*	651.6									608.1		
	b	670.4		823.0 [9]							627.5		
	a	668.5									625.9		
Xenon	*a*	664.2	161.5	830.3	597.8	113	569.7				618.9	118	628
	b	662.7									615.6		
N_2		663.8			826.7 [9]						614.1		

2.10. Medium effects

Since CuO_2 has now been examined in all rare gases and also in solid nitrogen, it is of interest to comment on the medium-induced shifts and changes in its molecular constants and properties, which are, as previously noted, unusually large. The molecule occurs in all matrices in several different sites, but if the most populous site in each matrix is considered, the T_e value of the *E* state shifts from 20700 cm^{-1} in solid neon to 20486.5, 20064, and 19686.9 cm^{-1} in solid argon, krypton, and xenon. Such a shift of more than 1000 cm^{-1} or 5% is considerably larger than typically observed. Even more remarkable are the large shifts between different sites in the same matrix. Thus the T_e values in six different sites in neon span an energy range of 163 cm^{-1}, while three sites in argon are spread over 223 cm^{-1}. One usually observes large matrix shifts for molecular ions, or highly polar compounds. Naturally, linear centrosymmetric CuO_2 has no dipole, but the compound is very likely to be quite ionic, with highly polar Cu–O bonds, which might explain the large effects.

Interestingly, the lower states for which data are available, *A*, *C*, and *D*, seem to exhibit much smaller shifts of more typical magnitudes. For example, comparing the most-studied sites in neon and xenon, the *D*–*X* transition shifts from 11309.5 to 11268.5 cm^{-1}, a shift of 41 cm^{-1}, while the *E*–*X* transition at less than twice the overall energy exhibits a shift of more than 1000 cm^{-1}. In general, one usually observes particularly minor shifts between two or more states which arise from the same, or a very similar electronic configuration.

Besides large electronic shifts, CuO_2 also experiences unusually large shifts in the excited *E*-state vibrational frequencies. Thus in neon the v_1' frequency ranges from 607.7 to 614.5 cm^{-1}. In argon the reddest ''*c*'' site has a v_1' value of 608.1 cm^{-1}, well within the neon range, while in two ''bluer'' sites it shifts drastically to 627.5 and 625.9 cm^{-1}, a change of more than 3%. In solid krypton and xenon the v_1 then gradually returns back to lower frequencies. A possible interpretation would be that there are two types of sites, one appearing only in neon and argon, and another yielding strongly blue-shifted vibrational frequencies. The latter site occurs in all the heavier rare gases, it is only in argon that

TABLE II. The vibratiional frequencies obtained by a fit not including terms higher than quadratic. The observed v_1 levels extending up to $v''=10$ and $v''=6$ are reproduced with an error of <0.2 cm^-. We used the frequencies v_i directly measuered in the experiment, rather than the ω_i constants of the polynomial Dunham-type expansion.

Isotope	Upper state			Ground state		
	ν_1	ν_3	ν_2	ν_1	ν_3	ν_2
$^{16}O^{63}Cu^{16}O$	617.1		138.1		661.2	190.0
	617.6	629.3	138.0	830.8	661.4	189.9
$^{18}O^{63}Cu^{18}O$	582.1		132.9		623.86	183.6
	582.4	605.7	132.9	799.7	623.98	183.4
$^{16}O^{63}Cu^{18}O$	592.4	625.5		816.9	641.1	
	592.0	625.7	135.5	816.8	641.0	186.4
$^{16}O^{65}Cu^{18}O$	591.5	623.9		812.6	641.0	
	591.0	623.2	134.8	812.6	640.9	185.4
$^{17}O^{63}Cu^{17}O$						
	599.3	616.9	135.4	814.5	641.8	186.2

both types of sites are present—perhaps double and triple substitution sites.

Also unusual is the behavior of the formally forbidden bending modes, which appear weakly in the matrix spectra and which, based on the limited data, undergo particularly large medium-induced frequency changes. The v_2'' seems to decrease from 196 cm^{-1} in solid neon to the $\approx$160 cm^{-1} value observed in xenon, an almost 20% shift. It is, however, a common experience that low-frequency bending modes are most likely to be affected by the condensed medium. An extreme example is the v_2'' frequency of C_3, which changes from 63 cm^{-1} in the gas phase to 84 cm^{-1} is solid argon, a more than 25% shift. Such changes are caused, on the one hand, by the resistance of the host matrix to bending of the guest, but are also due to partial charge transfer from the rare gas to the molecular orbitals of the guest, increasing (or decreasing) its rigidity. The ability of the matrix to donate electrons will naturally correlate with the polarizability and ionization potential of the matrix atoms, but it will also depend sensitively on the specific nature and geometry of the matrix site. Charge transfer interactions may be particularly significant for strongly polar or ionic compounds such as CuO_2, and this might explain the unusually large medium effects observed.

SUMMARY

We have investigated the optical absorption and laser-induced fluorescence spectra of CuO_2 in several solid matrices. We found several new electronic states and determined their vibrational frequencies. The matrix data are compared with the results of recent gas phase CuO_2^- photodetachment studies and with *ab initio* calculations. We found and discussed the unusually large matrix effects and medium-induced electronic and vibrational frequency shifts for this molecule.

*Partially supported by DFG and BMBF, Germany.
**E-mail: bondybey@ch.tum.de

[1] J. S. Shirk and A. M. Bass, J. Chem. Phys. **52**, 1894 (1970).
[2] M. J. Griffiths and R. F. Barrow, J. Chem. Soc., Faraday Trans. **273**, 943 (1977).
[3] H. M. Rojhantalab, L. Allamandola, and J. Nibler, Ber. Bunsenges. Phys. Chem. **82**, 107 (1978).
[4] D. E. Tevault, J. Chem. Phys. **76**, 2859 (1982).
[5] V. E. Bondybey and J. H. English, J. Phys. Chem. **88**, 2247 (1984).
[6] J. Hrusák, W. Koch, and H. Schwarz, J. Chem. Phys. **101**, 3898 (1994).
[7] H. P. C. W. Bauschlicher, S. R. Langhoff, and M. Sodupe, J. Phys. Chem. **97**, 856 (1993).
[8] T. K. Ha and M. T. Nguyen, J. Phys. Chem. **89**, 5569 (1985).
[9] G. V. Chertihin, L. Andrews, J. Charles, and W. Bauschlicher, J. Phys. Chem. A **101**, 4026 (1997).
[10] Y. Mochizuki, U. Nagashima, S. Yamamoto, and H. Kashiwagi, Chem. Phys. Lett. **164**, 224 (1989).
[11] Y. Mochizuki, K. Tanaka, and H. Kashiwagi, Chem. Phys. **151**, 11 (1991).
[12] H. Wu, S. R. Desai, and L.-S. Wang, J. Chem. Phys. **103**, 4363 (1995).
[13] H. Wu, S. R. Desai, and L.-S. Wang, J. Phys. Chem. A **101**, 2103 (1997).
[14] P. R. Stannard, M. L. Elert, and W. M. Gelbart, J. Chem. Phys. **74**, 6050 (1981).
[15] A. Lammers, *Fourier-Transform-Spektroskopie von* T1 *und* CuO_2 *in Edelgasmatrizen. Diplomarbeit*, Master's thesis, Institut für Physikalische und Theoretische Chemie der Technischen Universität München, 1994.

This article was published in English in the original Russian journal. Reproduced here with stylistic changes by the Translation Consultant.

Spectroscopy of yttrium dimers in argon matrices

L. Fang, X. Chen, X. Shen, Y. Liu, D. M. Lindsay, and J. R. Lombardi*

Department of Chemistry and Center for Analysis of Structures and Interfaces (CASI), The City College of New York (CCNY), New York, NY 10031, USA

(Submitted February 5, 2000)
Fiz. Nizk. Temp. **26**, 1011–1015 (September–October 2000)

The absorption and resonance Raman spectra of yttrium dimers (Y_2) in argon matrices are measured for the first time. The absorption spectrum (scattering depletion spectrum SDS) shows a weak, broad transition centered near 485 nm. Resonance Raman spectra obtained by exciting into this absorption band with several visible laser lines (465.5–496.5 nm) give a single, sharp progression with up to ten Stokes transitions. These data give $\omega_e = 184.4(4)\ \mathrm{cm}^{-1}$, with $\omega_e x_e = 0.30(3)\ \mathrm{cm}^{-1}$, leading to a spectroscopic dissociation energy of $D_e = 3.5(4)$ eV. Comparison of our results with several *ab initio* calculations adds confirmation to the assignment of the ground state of Y_2 to be the $^1\Sigma_g^+$ state.
[S1063-777X(00)01709-6]

INTRODUCTION

In the past two decades, research on transition-metal clusters has attracted the attention of a number of theoretical and experimental scientists.[1] It is clear that an understanding of the multiple-metal bonding often observed in the ground states of transition metal dimers depends on accurate determination of crucial structural parameters such as vibrational frequencies, force constants, dissociation energies, etc. Work has been carried out in this regard by this and other laboratories on several second row transition metal dimers (Zr_2,[2] Nb_2,[3] Mo_2,[4] Ru_2,[5] Rh_2,[6] Pd_2,[7] and Ag_2[8]). However, relatively little work has been carried out on the dimer of yttrium. In the present paper we report the first matrix isolation optical absorption and resonance Raman spectra of Y_2. Previous work on the atomic spectrum has been reported by Klotzbuecher and Reva.[9]

EXPERIMENT

The City College of New York metal cluster deposition source has been described in previous publications.[2,3,10] Briefly, an intense (typically 15 mA at 25 keV) argon ion beam from a CORDIS ion source sputters on a water cooled yttrium target (Alfa, 99.9%) maintained at 300 V. Secondary ions are extracted with a modified Colutron model 200-B lens system and then mass selected using a Wien filter (Colutron 600-B) in conjunction with an approximately 175 mm free drift distance and a 6.5 mm diameter aperture. The mass resolution is 6–7, enough to discriminate against possible oxide contaminants, as well as provide unambiguous filtering and metal clusters or atoms. After mass selection, the ion beam is bent by 10° using two electric plates to eliminate neutrals and then guided and focused to the deposition region by two einzel-like lenses.

Samples of Y_2 are obtained by mass selection after sputtering a metal target with high-energy Ar ions. This ensures discrimination against spectral interference from atoms and higher clusters of Y, as well as various oxides of Y. We observe a weak, broad optical transition near 485 nm. Exciting with Ar^+ laser radiation in this region enables us to

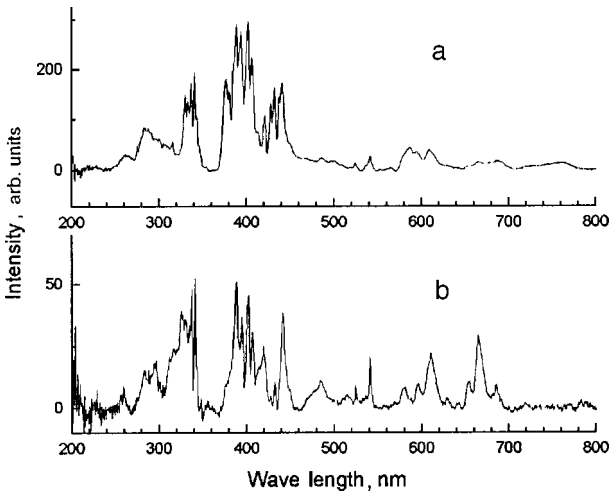

FIG. 1. Scattering depletion spectra of atom (a) and of yttrium dimer (b).

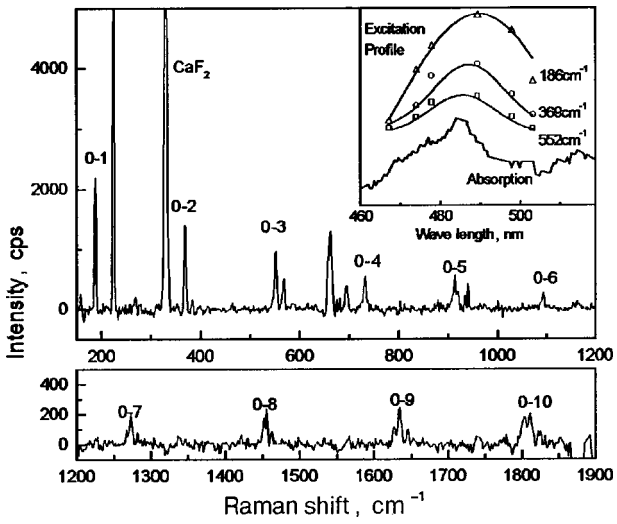

FIG. 2. Typical Raman spectra for Y_2 in argon matrix.

TABLE I. Raman frequency shifts for yttrium dimers in argon matrices.

v″	1	2	3	4	5	6	7	8	9	10
Raman shift, cm^{-1}	183.5	366.1	548.8	730.7	912.5	1093.3	1273.6	1454.3	1632.3	1810.1
Std. Dev.	0.6	0.4	0.7	0.7	0.7	0.7	0.4	0.6	1.0	1.3

obtain a sharp resonance Raman spectrum with a long progression of overtones.

Yttrium dimer ions were codeposited with Ar and electrons (generated from a heated tungsten filament) on a polished CaF_2 substrate (~14 K). Matrices were grown at ~5 μm/h with an Ar: metal dilution ratio of approximately 10^4:1. The deposition region was surrounded by a ''Faraday cage'' whose potential with respect to the sputtering target controls the kinetic energy (10 eV in this experiment) of deposited ions. Ion currents under ''soft landing'' conditions were approximately: Y^+ (250 nA),Y_2^+ (25 nA).

Under similar conditions, we deposited the yttrium atom in an argon matrix. By comparing the intensity of known atomic excitation features in a dimer deposition with those obtained from deposition of atom under similar conditions, the fragmentation ratio of dimers is estimated to be 10%.

Matrix samples were interrogated *in situ* using both absorption and Raman spectroscopy. As previous described,[2,3,10] for the absorption measurements, both deuterium and tungsten lamps were employed as excitation light sources, dispersed by a single 1/4m monochromator, reflected by a plane mirror (controlled by a stepping motor), which allows the light to be scanned across the 8 mm wide sample. The absorption measurements were made by collecting the light scattered at 90° to that incident, a technique termed scattering depletion spectroscopy (SDS).[3]

After obtaining absorption spectra, the Raman spectra were measured by exciting the sample with appropriate laser wavelength within the absorption region. In this experiment on Y_2, the visible output (457.9–514.5 nm) of an argon ion laser (Spectra Physics model 2045) was employed. The scattered light was collected at 90° and focused into a Triple mate Spectrometer (Spex 1877E, 0.6 m). The scattered light was detected with a liquid-nitrogen-cooled CCD system (Spectrum One+CCD30+DM3000R Software). The resolution of the detection system for the Y_2 experiment was set about 2 cm^{-1} (at 500 nm). The Raman shifts of Y_2 were calibrated using the CaF_2 (substrate at 16 K) line at 327 cm^{-1}.

SPECTRA AND ANALYSIS

Figure 1 shows the scattering depletion spectrum (SDS) of the atom (a), which is essentially the same as Klotzbuecher's result,[9] and of the dimer of yttrium (b).

Figure 2 shows a typical Raman spectrum (excited with 488 nm) for Y_2 in argon matrix (14 K, dimer content ~75 nA/h) and, as an inset, a portion of the absorption spectrum (SDS) of the same sample compared with several excitation profiles.

The SDS shows a broad, weak band centered at 485 nm, and closely parallels the excitation profile, which further confirms its assignment to the yttrium dimer.

Resonance Raman spectra of Y_2 were obtained at five different argon ion laser emissions in the visible region (465.5–496.5 nm). Up to ten Stokes transitions were observed, and the average value of these measurements give the Raman shifts, which are listed in Table I.

Analysis of these data by standard techniques[11] (linear fit of $\Delta G_{v+1/2}$ versus v gives $\omega_e = 184.4(4)\ cm^{-1}$, with $\omega_e x_e = 0.30(3)\ cm^{-1}$, leading to a spectroscopic dissociation energy of $D_e = 3.5(4)$ eV, and the force constant $k_e = 0.90(1)$ mdyn/Å. Attempts to obtain higher anharmonic corrections ($\omega_e y_e$) failed to improve the standard deviation, so it may be safely inferred that such corrections are negligible. Our observed vibrational frequency is essentially the same as that of Yang *et al.*[12] $\omega_e = 185(2)$, obtained by ZEKE spectroscopy.

Note that several of the observed Raman lines are accompanied by one or more weaker satellite lines. Since there are no isotopes that need to be considered, it is most likely that they are due to site effects in the Ar matrix. Similar effects have been observed in other dimer spectra.[3] We have used only the most intense line in each group for our analysis.

DISCUSSION

It is of interest to compare our measured value of the force constant k_e for Y_2 with those of other members of the second row transition metal dimers. These are given in Table II.

As can be seen the force constants increase almost linearly from left to right. The ground state atomic configurations are (Y) $5s^2 4d^1$,(Zr) $5s^2 4d^2$,(Nb) $5s^1 4d^4$, (Mo) $5s^1 4d^5$. However, in transition metals, bonding is usually more favorable if at least one atom has an s^1 configuration, requiring some promotion energy. Thus, considering a configuration $5s^1 4d^m$ ($m = 2-5$), the force constant is proportional to the number of d electrons involved in bonding. (A complementary, nearly linear decline in force constant was observed[5–7] in the series Ru_2, Rh_2, Pd_2, indicating a configuration $5s^1 4d^m$ [$(m = 7-9)$]. We can conclude that, at least for the early second-row transition metal dimers, each d electron available for bonding makes a nearly equal additional contribution to the bond order.

TABLE II. Ground state vibrational frequencies ω_e and force constants k_e for several second row transition metal dimers.

	Y_2 (this work)	Zr_2 (2)	Nb_2 (3)	Mo_2 (4)
ω_e, cm^{-1}	184.4	305.7	420.5	477.1
k_e, mdyne/Å	0.90	2.51	4.84	6.43

TABLE III. Theoretical and thermodynamic results for low state parameters of Y_2 and spectroscopic data (this work).

Reference	Method	Low state	r_e, Å	ω_e, cm^{-1}	D_e or D_0, eV	T_e, eV
D. G. Dai and K. Balasubramanian [15]	CASSCF + MRSDCI	$^5\Sigma_u^-$	3.03	172	2.56	0.0
		$^1\Sigma_g^+$	2.76	180	3.09	0.55
S. P. Walch and C. W. Bauschlicher, Jr. [14]	CI	$^5\Sigma_u^-$	3.03	171	2.44	0.00
	CI	$^1\Sigma_g^+$	2.74	206	2.93	0.87
	CASSCF	$^1\Sigma_g^+$	2.73	205	1.74	–
G. Verhaegan, S. Somoes, and J. Drowart [12]					1.62 ± 0.22	
This work	Isolated matrix			184.4 ± 0.4	3.5 ± 0.4	

Of several previous publications on Y_2, only one is experimental: Verhaegan, Somoes, and Drowart[13] determined the bonding energy using third-law analysis of the high-temperature Knudsen effusion mass spectrum. Their result was $D_0(Y_2)=1.62\pm0.22$ eV, in sharp disagreement with our spectroscopic value of 3.5 ± 0.4 eV. The third law technique suffers from the requirement that ω_e and r_e must be known, as well as the electronic partition function, and the results are often unreliable. However, the spectroscopic technique also has difficulties, in that a Morse potential is assumed to govern the nuclear motion. In transition metals this assumption is not always even close. This is caused by the fact that, where both $s-s$ and $d-d$ bonding is important, due to their disparate spatial extensions, d orbitals often have considerably different dissociation ranges than s orbitals. The best example of this is the case of Cr_2,[14] where serious deviations from a Morse potential are observed and the spectroscopic value is misleading. However, in Y_2 it is most likely that the bond order is small, perhaps near one. Thus only one electron pair is involved in dissociation, and the above effect of different s and d bonding will not be important. We also have observed regular behavior all the way up to the ninth harmonic ($n=10$). We feel, therefore, that our value for D_e is more likely to be correct.

The remaining work on Y_2 has been theoretical. Walch and Bauschlicher[15] have carried out a complete active-space multiconfiguration-self-consistent field (CAS-MCSCF) calculation both with and without the followed configuration interaction (CI). Their results indicate that the ground state is $^5\Sigma_u^-$ $(5s\sigma_g^2 5s\sigma_u^1 4d\sigma_g^1 4d\pi_{xu}^1 4d\pi_{yu}^1)$, which stems from the $5s^2 4d^1+5s^1 4d^2$ atomic configurations. A nearby, low-lying state ($T_c=0.87$ eV) is the $^1\Sigma_g^+$ $(5s\sigma_g^2 4d\pi_{xu}^2 4d\pi_{yu}^2)$ state arising from the $5s^1 4d^2+5s^1 4d^2$ configurations. In similar calculations in Sc_2 this latter state lies considerably higher than that in Y_2, which indicates larger contributions of d-electron bonding in the second row. Dai and Balasubramanian[16] have carried out similar complete active-space self-consistent field (CASSCF) calculations followed by multi-reference configuration interaction (MRSDCI) in which both single and double excitations are considered. Up to 2.6 million configurations are included in this calculation. Their results are quite similar to those of Walch and Bauschlicher (see Table III). Comparison of the SCF calculations both with and without the CI contributions show that increasing the CI lowers the relative energy of the higher state considerably (to $T_e=0.55$ eV). In conjunction with the lack of an observable ESR spectrum,[17] Dai and Balasubramanian conclude that the $^1\Sigma_g^+$ state is most likely the ground state. Our Raman results (see Table III) are consistent with this conclusion. The experimental value for ω_e of 184.4 cm^{-1} is quite close to that of 180 cm^{-1} in the CASSCF+MRSDCI calculation of Dai and Balasubramanian for the $^1\Sigma_g^+$ state. Similarly our $D_e=3.5(4)$ eV compares favorably with their value of 3.09 eV for the same state.

The theoretical results are listed and compared with this work in Table III.

Due to the rather large calculated differences in r_e for the $^5\Sigma_u^-$ and $^1\Sigma_g^+$ states, the determination of an accurate experimental value for r_e would be helpful to determine the

TABLE IV. Experiment data of the third row metal diatomic molecules.

Molecule	State	ω_e, cm^{-1}	r_e, Å	$k_e^{-1/3}$, (mdyn/Å)$^{-1/3}$	Reference
Mo_2	$X^1\Sigma_g^+$	477.1	1.938	0.537	[21]
Mo_2	$A^1\Sigma_u^+$	449	1.937	0.560	[21]
Ag_2	$X(O_g^+)^1\Sigma_g^+$	192.4	2.531	0.949	[1,22]
Ag_2	$A(O_u^+)^1\Sigma_u^+$	155.3	2.655	1.095	[1,22]
Sr_2	$B^1\Pi_u$	80.4	3.85	1.816	[23]

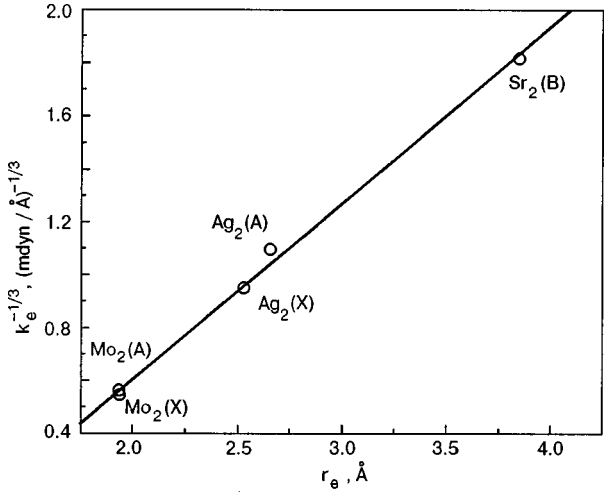

FIG. 3. Correlation between force constant k_e and parameter r_e.

nature of the ground state. Badger's[18] rule may be employed here on the fourth-row metal diatomic molecules following Weisshaar's results[19] on the third-row metal elements. Unfortunately, only a very few experimental data (listed in Table IV) have been reported until now, especially of the bond length r_e. The normal form of Badger's rule has the format: $k_e(r_e - d_{ij})^3 = C$, where d_{ij} is a constant that is different depending on the row number of the periodic table in which each atom resides and C may be taken as the same for all molecules ($C = 1.86\,\text{mdyn}\cdot\text{Å}^2$ if k_e is in mdyn/Å and r_e, d_{ij} in Å). However, it is found that allowing C to vary with periodic table row gives considerably better fits.[19,20] The C value in Ref. 19 varies from 0.53 (3,4) to 5.83 (H,3T), depending on the row of the periodic table.

In order to determine the constant d_{44} and C of the fourth-row metal diatomic molecules, a linear least squares fit was employed to five pairs of experimentally determined ω_e, r_e (see Table IV and Fig. 3), leading to $d_{44} = 1.09$ Å and $C = 3.41\,\text{mdyn}\cdot\text{Å}^2$ (the linear correlation coefficient is 0.998). Using our experimental result $\omega_e = 184.4\,\text{cm}^{-1}$, the bond length of Y_2 may be obtained as an interpolated point on this graph. It is found to be 2.65 Å, which is only slightly shorter than Dai's result ($r_e = 2.76$ Å) for the $^1\Sigma_g^+$ state. For the $^5\Sigma_u^-$ state his result is 3.03 Å. This lends additional support to the presumption that $^1\Sigma_g^+$ is very likely the ground state.

This work was supported by the National Science Foundation under Cooperative Agreement No. RII-9353488 and Grant No. CHE-9412804 and by the City University of New York PSC-BHE Faculty Research Award Program. We are also indebted to Dr. Werner E. Klotzbuecher for his helpful discussion of the atomic spectra.

*E-mail: lombardi@scisun.sci.ccny.cuny.edu

[1] M. D. Morse, Chem. Rev. **86**, 1049 (1986).
[2] Z. Hu, Q. Zhou, J. R. Lombardi, D. M. Lindsay, in *Spectroscopy of Mass-Selected Zirconium Dimers in Argon in Physics and Chemistry of Finite Systems: from Clusters to Crystals*, P. Jena, S. N. Kahana, and B. K. Rao (eds.), Kluwer Academic, Dordrecht (1992).
[3] Z. Hu, B. Shen, S. Deosaran, J. R. Lombardi, D. M. Lindsay, and W. Harbich, Proc. SPIE **1599**, 65 (1991).
[4] Y. M. Efremov, A. N. Samoilova, V. B. Kozhukhovsky, and L. B. Gurvich, J. Mol. Spectrosc. **73**, 430 (1978).
[5] H. Wang, Y. Liu, H. Haouri, R. Craig, J. R. Lombardi, and D. M. Lindsay, J. Chem. Phys. **106**, 6534 (1997).
[6] H. Wang, H. Haouri, R. Craig, Y. Liu, J. R. Lombardi, and D. M. Lindsay, J. Chem. Phys. **106**, 2101 (1997).
[7] J. Ho, K. M. Ervin, K. L. Polak, M. K. Gilles, and W. C. Lineberger, J. Chem. Phys. **95**, 4845 (1991).
[8] K. P. Huber and G. Herzberg, *Constants of Diatomic Molecules* (Van Norstrand, New York, 1979).
[9] E. W. Klotzbucher and I. D. Reva, in *XVII IUPAC Symp. on Photochemistry*, Barcelona, Spain, 19–24 July (1998).
[10] Z. Hu, B. Shen, S. Deosaran, J. R. Lombardi, D. M. Lindsay, and W. Harbich, J. Chem. Phys. **95**, 2206 (1991).
[11] G. Herzberg, *Molecular Spectra and Molecular Structure, I. Spectra of Diatomic Molecules* (D. Van Nostrand Company, Inc., New York, 1950).
[12] D. S. Yang, B. Simard, P. A. Hackett, A. Breces, and M. Z. Zgierski, Int. J. Mass Spectrom. Ion Phys. **159**, 65 (1996).
[13] G. Verhaegan, S. Somoes, and J. Drowart, J. Chem. Phys. **40**, 239 (1964).
[14] S. M. Casey and D. G. Leopold, J. Phys. Chem. **97**, 816 (1993).
[15] S. P. Walch and C. W. Bauschlicher Jr., in *Comparison of ab initio Quantum Chemistry with Experiment for Small Molecules*, edited by R. J. Barlett (D. Reidel, Dordrecht, 1985).
[16] D. G. Dai and K. Balasubramanian, J. Chem. Phys. **98**, 7098 (1993).
[17] L. B. Knight, Jr., R. W. Woodward, R. J. Van Zee, and W. Jr. Weltner, J. Chem. Phys. **79**, 5820 (1983).
[18] R. M. Badger, J. Chem. Phys. **2**, 128 (1934); *ibid.* **3**, 710 (1935).
[19] J. C. Weisshaar, J. Chem. Phys. **90**, 1429 (1989).
[20] D. R. Herschbach and V. W. Laurie, J. Chem. Phys. **35**, 458 (1961).
[21] J. B. Hopkins, P. R. R. Langridge-Smith, M. D. Morse, and R. E. Smalley, J. Chem. Phys. **78**, 1627 (1983).
[22] B. Simard and P. A. Hackett, Chem. Phys. Lett. **186**, 4 (1991).
[23] C. Bordas, M. Broyer, J. Chevaleyre, and Ph. Dugourd, Chem. Phys. Lett. **197**, 562 (1992).

This article was published in English in the original Russian journal. Reproduced here with stylistic changes by the Translation Consultant.

A synchrotron radiation study of high-lying excited states of matrix-isolated atomic magnesium

P. Kerins, B. Healy, and J. G. McCaffrey*

Department of Chemistry, National University of Ireland, Maynooth, Co. Kildare, Ireland
(Submitted February 12, 2000; revised June 21, 2000)
Fiz. Nizk. Temp. **26**, 1016–1022 (September–October 2000)

Previous steady-state and time-resolved luminescence spectroscopy of $3p^1P_1$ atomic magnesium, isolated in thin film samples of the solid rare gases, is extended to include the higher energy $4p^1P_1$ excitation. Well-resolved site splittings are recorded in Mg/Ar samples for excitation to the $4p^1P_1$ level. A small red shift in the absorption energy to the $4p^1P_1$ level for Mg/Ar contrasts with a small blue shift on absorption to the $3p^1P_1$ level. Direct emission from the $4p^1P_1$ level is not observed in any of the rare gas matrices; instead, intense emission from the low energy $3p^1P_1$ level is. Measurements of the emission decay curves in Mg/Ar have revealed slow rates in the steps feeding the $3p^1P_1$ level following $4p^1P_1$ excitation. The reason for the differential shifting of the $4p^1P_1$ and $3p^1P_1$ levels as well as the lack of direct $4p^1P_1$ emission is thought to be related to the strong binding interaction between Mg in the $4p^1P_1$ state and the rare gases. [S1063-777X(00)01809-0]

1. INTRODUCTION

In recent times, the luminescence spectroscopy of matrix-isolated metal atoms, i.e., neutral metal atoms isolated at high dilution in the solid rare gases (M/RG), has been used as a sensitive probe of guest–host interactions in solid-state spectroscopy. This has arisen because of *i*) the sensitivity of these ''ligand-free'' optical centers to their host environment, *ii*) the simple, face-centered cubic (fcc) packing structures of the solid rare gases, and *iii*) the increasing availability of accurate pair potentials for several metal atom/rare gas atom (M·RG) van der Waals diatomics. Recent theoretical work[1] from the Maynooth Group on the luminescence spectroscopy of atomic zinc isolated in the solid rare gases (Zn/RG) has indicated close agreement between spectral simulations based on the use of sums of Zn·RG pair potentials[2] and the experimentally[3] observed emission.

The spectral simulations are an extension of the theoretical methods developed by Beswick and co-workers[4] in simulations of the vibronic spectra of gas phase metal atom-rare gas cluster species. In the solid state simulations the potential energy surfaces of the Jahn–Teller active vibrational modes of atomic Zn isolated in the solid rare gases Ar, Kr, and Xe have been calculated for a $Zn{\cdot}RG_{18}$ cluster species. This cluster comprises the first and second spheres surrounding a guest metal atom occupying a substitutional site of an fcc lattice. Reliable calculations are possible because of the existence of detailed information on the lattice parameters of the fcc unit cells of the solid rare gases as well as accurate Zn·RG and RG·RG pair potentials. As well as indicating dominant localized interactions in the Zn/RG matrix systems, details of the microscopic motion of atomic zinc occurring during optical cycles in the solid rare gases were also obtained from simulations of the observed luminescence.

With the increasing availability of accurate diatomic interaction potentials, obtained from laser spectroscopy of metal atom-rare gas atom (M·RG) van der Waals complexes in supersonic expansions,[5] the range of systems, including open-shell systems, amenable to this detailed analysis is steadily growing. One of the most interesting examples in this regard is the recent observation made by Breckenridge and co-workers[6] on the doubly excited $Mg(3p_\pi 3p_\pi {}^3P_J)\cdot RG[{}^3\Sigma^-]$ valence states of the Mg·RG diatomics (RG=He, Ne, Ar and Kr) accessed from the singly excited $Mg(3s_\sigma 3p_\pi {}^3P_J)\cdot RG[{}^3\Pi]$ metastable state. Theoretical analysis of the very strong binding energy ($D_0 = 2850\,cm^{-1}$) and short bond length ($R_0 = 2.41$ Å) in the molecular $^3\Sigma^-$ state of Mg·Ar, arising from the doubly excited $(3p)^2$ atomic magnesium configuration, indicates the importance of the absence of occupied metal *s* orbitals in the interaction with the closed shell rare gas atom. Partial occupancy of the 3*s* orbital in the lower-energy 3*s*3*p* metal atom valence state is responsible for increased repulsive interaction with the rare gas atom, giving rise to a greatly reduced binding energy (160 cm^{-1}) and an increased bond length (3.66 Å) for the $Mg(3s_\sigma 3p_\pi {}^3P_J)\cdot Ar[{}^3\Pi]$ metastable state. Full occupancy of the 3*s* orbital in the $Mg(3s_\sigma 3s_\sigma {}^1S_0)\cdot Ar[{}^1\Sigma]$ ground electronic state results in the molecular parameters.[7] $D_0 = 65\,cm^{-1}$ and $R_0 = 4.5$ Å, typical of van der Waals complexes. Comparison of the larger binding energy and shorter bond length of the neutral Mg·Ar $(3p_\pi 3p_\pi {}^3P_J)[{}^3\Sigma^-]$ state with the analogous values ($D_0 = 1240\,cm^{-1}$ and $R_0 = 2.82$ Å) in the ground $Mg^+(3s_\sigma {}^2S)\cdot Ar[{}^2\Sigma^+]$ state of the $Mg^+\cdot Ar$ cation, reveals the repulsive role played by the occupied 3*s* orbital in the bonding. Significantly, these results indicate the dominance of the repulsive *s* orbital interaction over the strongly attractive, dipole-induced interaction expected in the molecular cation.

It should be revealing, on several levels, to record the luminescence spectroscopy of highly excited states for matrix-isolated Group 2 and 12 metal atoms and compare data with the pair-potentials methods used for the spectral

simulation of lower-energy metal atom transitions. The areas of interest in such a comparison are:

—Considering the strong binding energies in highly excited states, is the occurrence of many-body effects manifested?

—Due to these states being within a few thousand wave numbers of the ionization limit of the metal atom, does the onset of delocalized behavior, such as exciton absorption, occur?

—Is the localized approach taken in the present cluster-based simulations valid for these strongly bound states?

—Is metal atom migration possible in these excited states, considering that the energy minima of the highly excited states are at very short bond lengths?

The metastable atoms, generated in copious amounts with the laser ablation technique used in the gas phase for producing metal vapor, are absent in low-temperature matrices, irrespective of the method used to generate the metal vapor. Therefore the one-photon techniques used in the gas phase are not of use in matrix work on doubly excited states. Instead of looking at the doubly excited states, we have examined the one-photon spectroscopy of high-lying, singly excited atomic states. In the present contribution the matrix luminescence of the $3p^1P_1$ state of atomic magnesium is extended in that excitation spectra have been recorded in the vacuum UV spectral region to reach the $4p^1P_1$ energy level.

Notwithstanding the vacuum spectroscopic techniques required to reach highly excited levels, the reduced oscillator strength of atomic transitions from the ground state to these states is a more fundamental deterrent to such measurements. In the case of Mg, for example, the transition probability of the $4p-3s$ singlet transition at 202.58 nm is $A=0.84\times10^8\,s^{-1}$, almost an order of magnitude smaller than the A value[8] of $4.95\times10^8\,s^{-1}$ for the $3p-3s$ singlet transition at 285.21 nm.[9] The use of synchrotron radiation (SR), with output intensities optimized in the VUV spectral region, compensates the reduced transition probabilities and, as it is already produced under ultrahigh vacuum conditions, facilitates the measurement of high-lying excited states.

Studies of the absorption spectroscopy of matrix-isolated metal atoms are quite comprehensive and well documented. Conversely, luminescence studies of the excited states of metal atoms are not nearly as extensive, but detailed studies[10] have been carried out for the lighter elements of the Group 1, 2, 11, and 12 elements. The first study of matrix-isolated atomic magnesium was that of Schnepp,[11] in which optical absorption spectra were recorded at 4.2 K using argon, krypton, and xenon as host materials. Schatz *et al.*[12] measured the MCD spectra of magnesium isolated in argon, and more recently the luminescence of matrix-isolated magnesium was recorded by McCaffrey and Ozin[13] in argon and krypton at 12 K. The latter work agreed with the absorption data of Schnepp in that the excitation bands observed in the vicinity of 285 nm and assigned to the $3p^1P_1\rightarrow3s^1S_0$ singlet transition of atomic magnesium all exhibited three-fold splitting.

With the objective of extending the experimental data base on the luminescence spectroscopy of matrix-isolated metal atoms, the spectroscopy of metal atoms in highly excited states has been undertaken using SR as the excitation source. The paper is structured as follows. Transitions to and from the $3p^1P_1$ energy level for the cases of Mg/Ar, Mg/Kr, Mg/Xe, and Mg/CF_4 will be reviewed briefly before the new data on the $4p^1P_1$ energy levels is presented. Because of the large signal strengths of the transitions observed in Mg/Ar, much of the detailed presentation will involve this system. Key differences in the spectroscopy of the $3p^1P_1$ and $4p^1P_1$ states will be highlighted and discussed.

2. EXPERIMENTAL

Thin film Mg/RG samples were prepared by the cocondensation of magnesium vapor, with the rare gases onto an LiF window. The metal vapor was produced by electron bombardment of 0.5 mm thick Mg foil (Goodfellow, 99.99% purity) coiled into a 5 mm diameter molybdenum cruicible in an Omicron EFM3 UHV evaporator. Preferential isolation of atoms over metal clusters was achieved using very low metal fluxes (<1 nA), and the isolation condition of samples was monitored by recording absorption spectra. Cryogenic temperatures were achieved with a Cryovac continuous-flow liquid-helium cryostat. The sample temperature was measured with a silicon diode mounted on the sample holder and set using a Lakeshore Cryotronics model 330 temperature controller. Deposition temperatures of 5, 12, 18, and 25 K were used with the rare gases Ne, Ar, Kr, and Xe, respectively.

An MKS 221A Baratron capacitance manometer, sensitive in the pressure range 0–1000 mbar, was employed to monitor the amounts of rare gas admitted to the gas handling system and consumed during sample formation. The UHV sample chamber containing the liquid-helium cryostat was pumped continuously with a Pfeiffer/Balzers TPU 240 turbomolecular pump. Vacuum, monitored with an HPS Division/MKS Series 423 I-Mag cold cathode gauge, was typically in the mid 10^{-10} mbar range prior to cool-down, dropping to 10^{-11} mbar after cool-down. Gas flow rates, controlled by a Granville-Phillips series 203 variable leak valve, were generally in the range of 3.5 to 5 mmol/h for periods of between 20 to 30 minutes. This resulted in the formation of thin film samples whose thickness was in the 30–50 μm range. Rare gases of 99.999% purity were used as supplied by Linde Technische Gase.

Since the optical layout of the HIGITI apparatus located at HASYLAB/DESY in Hamburg has been presented in our earlier work,[3] only a brief description will be given here. Synchrotron radiation optimized in the VUV spectral region was used as the excitation source. Absorption spectra were recorded by monitoring the amount of UV radiation directly transmitted through the Mg/RG samples, using a Valvo XP2020Q photomultiplier tube to detect the visible emission of a sodium salicylate UV-to-visible converter. All spectra were recorded linear in wavelength, but for purposes of analysis and discussion are presented linear in photon energy, in wave number units (cm^{-1}).

Luminescence measurements were made in the VUV spectral region with a modified 1 m Wadsworth monochromator for excitation, and a 0.4 m Seya-Namioka monochromator for emission. A Hamamatsu MCP 1645U-09 microchannel plate was used for photon detection. Nanosecond lifetime measurements were made using the time correlated

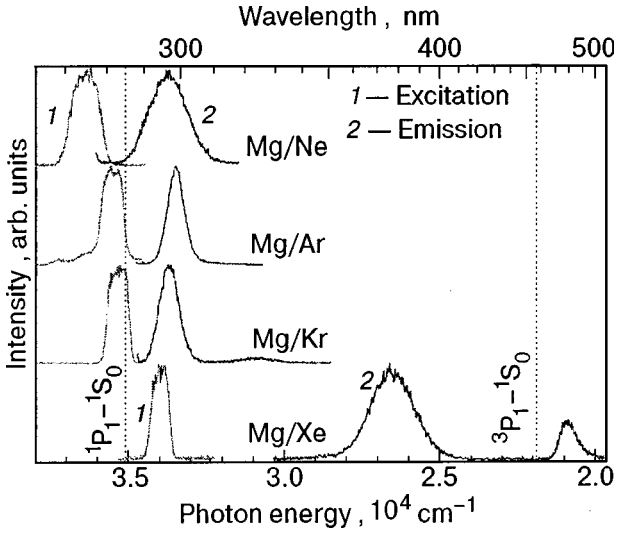

FIG. 1. A summary of the matrix luminescence spectroscopy recorded at 6 K for the $3p-3s$ transitions of atomic magnesium isolated in annealed samples of the solid rare gases Ne, Ar, Kr, and Xe. Excitation spectra are denoted as 1, while emission spectra are denoted as 2. The locations of the spin singlet $3p^1P_1 \leftarrow 3s^1S_0$ and triplet $3p^3P_1 \leftarrow 3s^1S_0$ transitions of atomic magnesium in the gas phase are given by the vertical dotted lines. Noteworthy in Mg/Ar is the presence of multiple features between 270 and 280 nm in the excitation spectra of annealed samples.

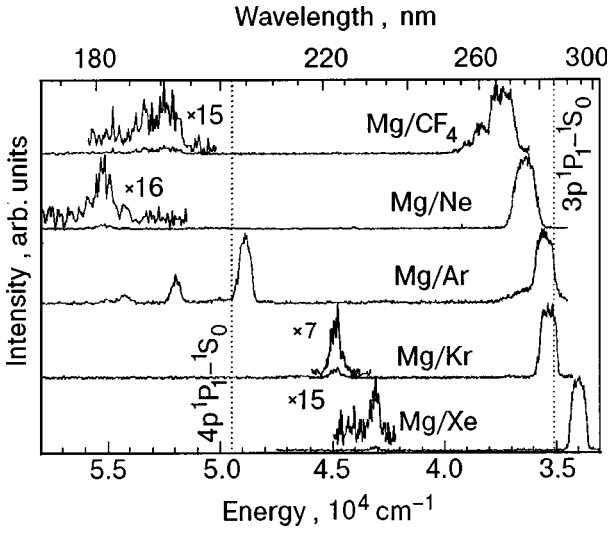

FIG. 2. A summary of the higher-energy $4p^1P_1$ bands and lower-energy $3p^1P_1$ excitation bands recorded by monitoring the $3p^1P_1 \rightarrow 3s^1S_0$ emission of atomic magnesium in the rare gases and CF_4. The excitation spectra have not been corrected for the wavelength-dependent output intensity of the synchrotron radiation source.

single photon counting (TCSPC) technique.[14] The synchrotron radiation[15] generated from the DORIS III storage ring at HASYLAB/DESY has a temporal profile of 120 ps (FWHM), and when provided in ''5 Bunch Mode,'' at a repetition rate of 5.208 MHz, decay times of up to 10 μs can be measured with TCSPC. Decay times were extracted by fitting trial functions, single, double or triple exponential functions, convoluted with the temporal profile of the SR excitation pulse, to the recorded decay profiles. The reconvolution and fitting was achieved using the ''ZFIT'' program[16] running on DEC Alpha 3000/500 AXP workstations in Maynooth and Hamburg. The fitting criterion was based on an optimization routine minimizing the sum of weighted residuals existing between the fit and the data set. The quality of a fit can be judged numerically by the χ^2 value obtained—in our fits the acceptable range was 0.98 to 1.1.

3. RESULTS

Luminescence from the $3p^1P_1$ level

Figure 1 presents a summary of the luminescence spectroscopy recorded at 6 K for the low-energy $3p^1P_1$ state of atomic magnesium isolated in the annealed solid rare gases. The spectra (1) shown in Fig. 1 are the excitation spectra recorded by monitoring the emission bands (2). Also shown in Fig. 1 are the locations of the singlet $3p^1P_1-3s^1S_0$ and triplet $3p^3P_1-3s^1S_0$ transitions of atomic magnesium in the gas phase.[9] Based on the spectral locations, the emission bands in the Ne, Ar, and Kr systems can be assigned to the singlet transition. Measurement of the radiative decay times of the emission bands at 370 and 470 nm in Mg/Xe has allowed assignment[17] of the latter band to the triplet $3p^3P_1-3s^1S_0$ transition and the former, to the singlet. Lifetime measurements of the emission present in the Mg/Ne,[18] Mg/Ar, and Mg/Kr systems[13] confirm the singlet assignments suggested by their spectral locations.

Luminescence from the $4p^1P_1$ level

When the excitation spectra of the singlet $3p^1P_1-3s^1S_0$ emission bands shown on the right in Fig. 1 were recorded into the vacuum-UV region, the results shown in Fig. 2 were obtained for the annealed Mg/RG systems and Mg/CF_4. The location of the singlet $4p^1P_1-3s^1S_0$ transition in the gas phase is also shown. It is evident in Fig. 2 that the most intense feature in the Mg/Ar system is observed in the vicinity of the gas phase $4p^1P_1$ transition. The Mg/Ar system exhibits three well-resolved peaks, a dominant band at 204.5 nm, another at 192.5 nm, and a weak one at 185 nm. Manifestation of multiple, non-resolved features are also present at 270 nm, on the blue wing of the lower $3p^1P_1$ band. Single peaks can be seen in Ne at about 182 nm, Kr at about 221 nm, and in Xe at 231 nm. The single short-wavelength peaks in the M/RG systems parallel the single bands present on the $3p^1P_1-3s^1S_0$ transition shown on right-hand side. Because of the spectral richness in the Mg/Ar system, annealing studies were undertaken to facilitate assignment. With the large emission intensity in this system, detailed kinetic measurements have also been made.

Mg/Ar on deposition

The complete excitation spectrum of the Mg/Ar 299 nm emission is presented in the lower portion of Fig. 3 as recorded for a freshly deposited sample. Five resolved excitation bands can be seen in the high-energy region. The positions of these bands are at 226.7, 214, 204.5, 192.5, and 185 nm. An ill-defined number of unresolved features are also present on the lower energy $3p^1P_1-3s^1S_0$ excitation spectrum between 270 and 290 nm. The emission spectrum shown on the right was produced with 282 nm excitation.

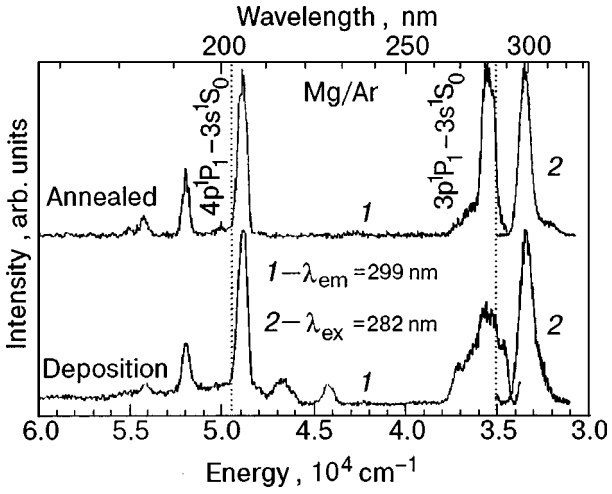

FIG. 3. Excitation bands recorded for magnesium atom emission at 299 nm in argon matrices before and after annealing. The emission bands shown on the right were produced with excitation at 282 nm. The gas phase positions of the singlet $4p^1P_1 \leftarrow 3s^1S_0$ and singlet $3p^1P_1 \leftarrow 3s^1S_0$ transitions are shown by the vertical lines.

The results of annealing studies, used to identify the origin of the resolved high-energy features, are now presented.

Mg/Ar annealed

The upper portion of Fig. 3 shows all the excitation bands of Mg/Ar recorded for the 299 nm emission after sample annealing to 32 K for 30 minutes. From a comparison of the two panels in Fig. 3, one can see that the bands at 226.7 nm and 214 nm in the spectrum of a freshly deposited sample are completely removed with annealing. Moreover, an underlying contribution to the baseline in the freshly deposited scan has been removed. This behavior is accompanied by the removal of the 290 nm red-wing features on the $3p^1P_1$ excitation band (2) in Fig. 3.

Emission bands produced from each of the excitation features (204.5, 192.5, and 185 nm) remaining after annealing all have a maximum intensity at 298 nm, but, as shown in Fig. 4, they have a varying intensity in the red wing. It should be pointed out that with high energy 204.5, 192.5, and 185 nm excitation, no emission was observed in the low 200 nm region which would correspond to direct $4p^1P_1 \rightarrow 3s^1S_0$ emission.

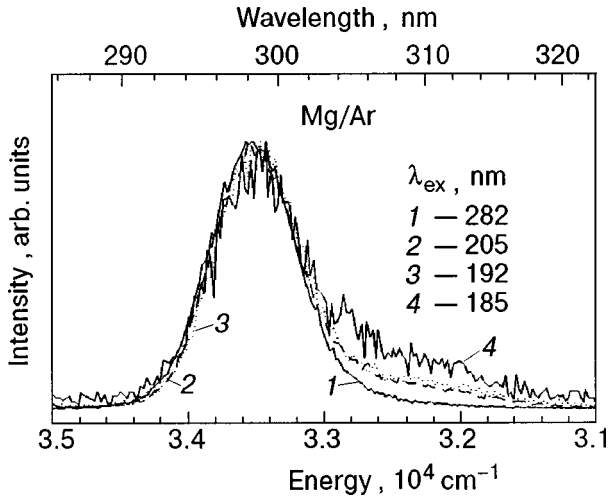

FIG. 4. The emission resulting from excitation of the major excitation features present in annealed Mg/Ar samples.

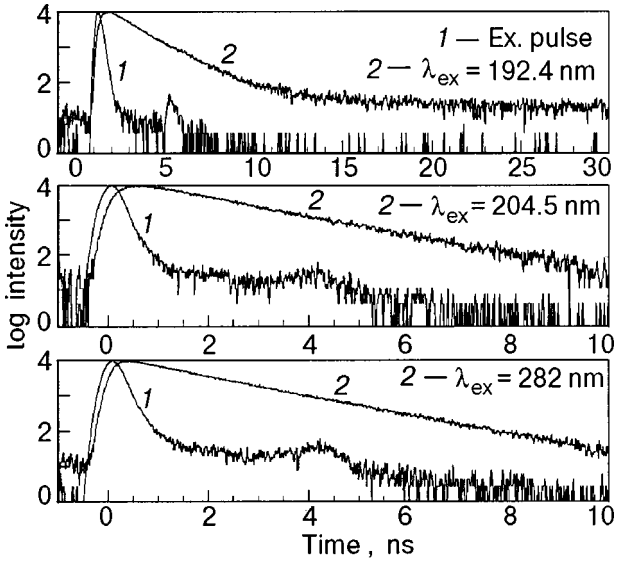

FIG. 5. Semi-log plots of the intensity decay profiles recorded for the 298 nm emission band produced with excitation of the three dominant excitation bands present in annealed Mg/Ar samples. The temporal profile of the synchrotron radiation excitation pulse is shown as (1), while (2), showing a gradual decrease in intensity, is the decay profile.

Figure 5 shows the decay profiles recorded for the 299 nm emission with the TCSPC technique by exciting at 282, 204.5, and 192.4 nm. The decay profiles for the 282 and 204.5 nm excitation are presented in a 10 ns time range, while the 192.4 nm excitation is shown in a 30 ns range. The simplest decay profile is exhibited by 282 nm excitation, i.e., from the direct $3p^1P_1 \leftarrow 3s^1S_0$ transition. As the excitation energy increases, the shape of the profiles changes under the influence of the associated rise times and long decay components. Table I lists the decay times and rise times extracted from fits to the emission decay curves. In agreement with earlier work,[13] the radiative decay time of the 299 nm emission produced with $3p^1P_1$ excitation at 282 nm is found to be 1.4 ns. This is represented by τ_1 in Table I and found to be present in the emission decay curves recorded for all three excitation wavelengths. The decay curve produced with excitation at 204.5 nm exhibits a rise time of 0.27 ns, which produces the delayed appearance of the profile shown in the middle panel of Fig. 5. Excitation at 192.4 nm results in the same rise time (0.22 ns) but with a long decay component of 20.8 ns in addition to the 1.4 ns radiative decay time. A summary of the decay kinetics is presented in Fig. 6.

TABLE I. Emission decay times measured at 6 K with the TCSPC technique by exciting into the high energy bands observed for magnesium in argon. The wavelengths listed are in units of nm, the decay times are in ns. Rise times are shown underlined. The percentage yields of all the observed components are also shown.

λ_{ex}	λ_{em}	τ_1	τ_2	τ_3	%(1)	%(2)	%(3)
282	299	1.46	–	–	100	–	–
204.5	299	1.46	<u>0.27</u>	–	89.3	10.7	–
192.4	299	1.43	20.8	<u>0.22</u>	86.2	4.6	9.17

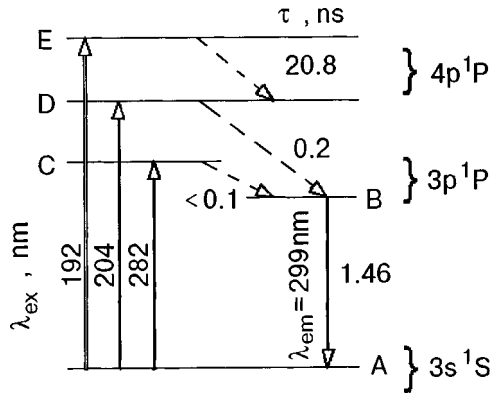

FIG. 6. A kinetic scheme of the relaxation process of the $4p^1P_1$ excited state leading to emission from the lower-energy $3p^1P_1$ level. Radiative transitions are shown by solid lines, nonradiative transitions connecting the excited state levels are represented by broken lines. The time constant of the nonradiative process connecting the absorbing (282 nm) and emitting level (299 nm) in the $3p^1P_1$ state is faster than the 0.1 ns temporal resolution of the measuring system. Level *E* is a resolved site splitting on the $4p^1P_1$ excited state.

4. DISCUSSION

Mg/Ar has three high-energy excitation bands in the vicinity of 200 nm, which have been shown in annealing studies (see Fig. 3) to be thermally stable. Examination of the term diagram for atomic magnesium reveals that for energies less than 50.000 cm^{-1} the states to be considered in the assignment of these bands are $4s^1S$ and ^3S, $3d^1D$ and ^3D, $4p^1P$ and ^3P. Of these states the spin triplets can be ruled out in absorption (excitation) transitions from the singlet $3s^1S$ ground state. Of the spin singlets the $4s^1S$ level at 43503 cm^{-1} (229.9 nm) and the $3d^1D$ level at 46403 cm^{-1} (215.5 nm) are parity-forbidden in transitions from the ground *S* state, leaving the $4p^1P$ level as the only one which can couple with a large oscillator strength ($A=0.84\times10^8\ s^{-1}$) to the ground state. The $4p^1P_1\leftarrow3s^1S_0$ transition of atomic magnesium, which occurs in the gas phase[6] at 202.6 nm is, because of its spectral proximity and its fully allowed nature, the obvious assignment, especially for the 204.5 nm band in Mg/Ar.

However, it has been observed in earlier matrix work on atomic calcium that the transition to the ^1D level, which is parity-forbidden in the gas phase, becomes partially allowed in the matrix. This effect has been observed in absorption[19] and excitation[20] work and is thought to arise from metal atom occupancy in low-symmetry sites. It has also been noted that the matrix shifts on the $3d^1D_2\leftarrow4s^1S_0$ transition are much smaller than on the corresponding $4p^1P_1\leftarrow4s^1S_0$ transition and, as expected, the absorption strengths of the former transition are about two orders of magnitude less than the fully allowed $^1P_1\leftarrow{}^1S_0$ transition. Given that the gas phase $3d^1D-3s^1S$ transition of atomic magnesium occurs at 46403 cm^{-1} (215.5 nm), a large blue shift of 2487 cm^{-1} would result for a $3d^1D_2$ assignment of the 204.5 nm (48900 cm^{-1}) band in argon matrices. It might be argued that this blue shift arises from a dominant Rydberg character in the $3d$ orbital. However, it is known that a blue shift of only 399 cm^{-1} occurs on the associated $3p^1P$ state of Mg in Ar whose *p* orbital would be expected[21] to have a more ''Rydberg-like'' character than the $3d$ orbital.

Given the strength of the three spectrally resolved high-energy excitation bands in the Mg/Ar system and their correspondence with features which are present but not resolved on the high-energy side of the $3p^1P_1$ excitation band (around 270 nm), the high-energy features are tentatively assigned as $4p^1P_1\leftarrow3s^1S_0$ excitations arising from multiple site occupancy of atomic magnesium in argon. Of the three excitation bands, the $4p^1P_1$ level assignment of the dominant band at 204.5 nm is the most definitive because of its close proximity to the gas phase line at 202.58 nm.[6] This matrix transition therefore exhibits a small red shift of -463 cm^{-1} from the gas phase $4p^1P_1\leftarrow3s^1S_0$ transition. In contrast, the 282 nm transition to the $3p^1P_1$ level is blue-shifted by $+399$ cm^{-1} from the corresponding gas phase value at 285.21 nm. This differential shifting of the excitation energies for the two transitions is quite revealing, since they share the same ground state. This suggests that slight repulsion dominates the $Mg(3p^1P_1)/Ar$ interaction, while a slight attraction dominates the $Mg(4p^1P_1)/Ar$ interaction.

Decay times of the emission produced with excitation of the three high energy bands are presented in Table I. From the common 1.4 ns decay time exhibited by all three emissions, and given that this is the radiative lifetime of the $3p^1P_1$ level, it can be stated that the terminating emitting level reached in relaxation from the $4p^1P_1$ level is the $3p^1P_1$ level. The mechanism of this electronic energy relaxation is not known, but assuming a strongly attractive $Mg(4p^1P_1)/Ar$ interaction, it probably involves a curve crossing of a deeply bound $Mg(4p^1P_1)\cdot Ar^1\Pi$ state by a repulsive $Mg(3p^1P_1)\cdot Ar^1\Sigma$ curve dissociating to the $3p^1P_1$ state. The efficiency of this process can be judged by the fact that the emission from the $4p^1P_1$ level is completely quenched. An assessment of the proposed relaxation mechanism awaits collection of spectroscopic data on the $Mg(4p^1P_1)\cdot Ar^1\Pi$ state of the 1:1 van der Waals complex. However, the analogous doubly excited $Mg(3p^{23}P_J)\cdot Ar^3\Sigma$ state has revealed very strong binding interactions, but matrix data has not yet been obtained on transitions reaching this state.

5. CONCLUSIONS

Excitation spectra have been recorded in the vicinity of the $4p^1P_1\leftarrow3s^1S_0$ transition of matrix-isolated atomic magnesium for the first time. The strong 204.5 nm peak of Mg/Ar closely matches the position of the $4p^1P_1\leftarrow3s^1S_0$ transition of atomic magnesium in the gas phase. Other weaker peaks at 192.5 and 185 nm in Mg/Ar probably arise from spectrally resolved transitions of magnesium atoms with multiple site occupancy. On the basis of this assignment, site splittings on transitions to the $4p^1P_1$ level are much better resolved than in the lower-energy $3p^1P_1\leftarrow3s^1S_0$ transition. The reason for the well-resolved site splittings is probably due to the stronger Mg–RG host interactions involved in the $4p^1P_1$ state than in the $3p^1P_1$ state. On the other hand, the reason for the particularly strong $4p^1P_1\leftarrow3s^1S_0$ transition in argon compared with the other rare gas matrices is not immediately evident.

Emission from the $4p^1P_1$ level is not observed in any of the Mg/RG systems following excitation of the $4p^1P_1$ level but indirect emission from the $3p^1P_1$ level is observed. The

most likely mechanism for the population cascade from the $4p^1P_1$ level to $3p^1P_1$ level is curve crossing of a strongly bound state correlating to the $4p^1P_1$ asymptote by a repulsive Σ-type curve dissociating to the $3p^1P_1$ state.

In the Mg/Ar system, the small red shift on the $4p^1P_1 \leftarrow 3s^1S_0$ absorption is in contrast to the small blue shift on the $3p^1P_1 \leftarrow 3s^1S_0$ transition. This is probably arising from the strongly attractive $Mg(4p^1P_1) \cdot Ar^1\Pi$ molecular state. Spectroscopic studies on this state have not been carried out yet, but existing work on the doubly excited $Mg(3p^{23}P_J) \cdot Ar^3\Sigma$ state have revealed very strong bound interactions.

We would like to acknowledge Dr. Peter Gürtler and Mr. Sven Petersen for their technical assistance during the course of this work. This research was funded in part by the European Union, TMR 1996-'98, ''Access to Large Scale Facilities'' Program and by the Irish Government Forbairt Basic Science research scheme, to whom B. H. and P. K. also gratefully acknowledge receipt of Ph.D studentships.

*E-mail: jmccaffrey@may.ie

[1] J. G. McCaffrey and P. N. Kerins, J. Chem. Phys. **106**, 7885 (1997).
[2] J. G. Kaup and W. H. Breckenridge, J. Phys. Chem. **99**, 13701 (1995).
[3] V. A. Bracken, P. Gürtler, and J. G. McCaffrey, J. Chem. Phys. **107**, 5290 (1997).
[4] J. Zuniga, A. Bastida, A. Requena, N. Halberstadt, and J. Beswick, J. Chem. Phys. **98**, 1007 (1993).
[5] W. H. Breckenridge, C. Jouvet, and B. Soep, ''Metal-atom/rare-gas van der Waals complexes,'' in *Advances in Metal and Semiconductor Clusters*, Vol. III, edited by M. A. Duncan (JAI Press, Greenwich, 1995).
[6] S. Massick and W. H. Breckenridge, J. Chem. Phys. **105**, 6154 (1996).
[7] R. R. Bennett, J. G. McCaffrey, I. Wallace, D. J. Funk, A. Kowalski, and W. H. Breckenridge, J. Chem. Phys. **90**, 2139 (1989).
[8] J. R. Fuhr and W. L. Wiese, *Atomic Transition Probabilities*, 10, *CRC Handbook of Chemistry and Physics*, edited by David R. Lide, 76th ed., 1995–1996.
[9] C. E. Moore, *Atomic Energy Levels*, Vol. 1 (National Bureau of Standards Circular number 467, U.S. Government, printing office, Washington D.C., 1957).
[10] C. Crepin-Gilbert and A. Tramer, Int. Rev. Phys. Chem. **18**, 485 (1999).
[11] O. Schnepp, J. Phys. Chem. Solids **17**, 188 (1961).
[12] L. Mowery, J. C. Miller, E. R. Krausz, P. N. Schatz, M. Jacobs, and L. Andrews, J. Chem. Phys. **70**, 3920 (1979).
[13] J. G. McCaffrey and G. A. Ozin, J. Chem. Phys. **101**, 10354 (1994).
[14] D. V. O'Connor and D. Phillips, *Time Correlated Single Photon Counting* (Academic Press, London, 1984).
[15] G. Zimmerer, Nucl. Instrum. Methods Phys. Res. A **308**, 178 (1991).
[16] ''ZFIT'' program *Nonlinear Least Squares Analysis of Fluorescence Decay Data* by M. Rehorek, H. Otto, W. Rettig, A. Klock, and modified by P. Gurtler and M. Joppien (last update, August 1995).
[17] J. G. McCaffrey, Ph.D. Thesis, Univ. of Toronto (1987).
[18] P. N. Kerins, M. Sc. Thesis, Nat. Univ. of Ireland, Maynooth, (1997).
[19] L. Andrews, W. W. Duley, and L. Brewer, J. Mol. Spectrosc. **70**, 41 (1978).
[20] V. E. Bondybey, J. Chem. Phys. **68**, 1308 (1977).
[21] This expectation is based on the larger quantum defect exhibited by the orbitals with smaller orbital quantum numbers, *l*.

This article was published in English in the original Russian journal. Reproduced here with stylistic changes by the Translation Consultant.

Thermal conductivity of solid krypton with methane admixture

V. V. Dudkin,* B. Ya. Gorodilov, A. I. Krivchikov, and V. G. Manzhelii

B. Verkin Institute for Low Temperature Physics and Engineering of the National Academy of Sciences of Ukraine, 47 Lenin Ave., 61164 Kharkov, Ukraine
(Submitted February 14, 2000)
Fiz. Nizk. Temp. **26**, 1023–1028 (September–October 2000)

The thermal conductivity of CH_4–Kr solid solutions is investigated at CH_4 concentrations 0.2–5.0% in the temperature range 1.8–40 K. It is found that the temperature dependence of the thermal conductivity has features typical of resonance phonon scattering. The analysis of the experimental results shows that the main contribution to the impurity-caused scattering of phonons is made by the scattering on rotational excitations of the nuclear spin T-species of CH_4 molecules. The phonon–rotation interaction parameter is estimated. © *2000 American Institute of Physics.* [S1063-777X(00)01909-5]

1. INTRODUCTION

The scattering of phonons by the rotational motion of molecules in solids is much less understood than the phonon-phonon scattering is. At the same time, there is experimental evidence that the phonon-rotation interaction in crystals can significantly influence both the absolute value and the temperature dependence of the thermal conductivity.[1–12] At low temperatures this effect can be predominant in systems with low-lying energy levels of the rotational motion of molecules.[9] Quantum molecular crystals (solid hydrogen and methane isotopes) and solutions of simple molecular substances in matrices of solidified rare gases belong to the above systems. To study the influence of molecular rotation upon the thermal conductivity of crystals, we chose solutions of methane in solid krypton.

Krypton and methane have close parameters of particle interaction and can therefore form a continuous solid solution over a wide range of concentrations.[13]

The energy levels of CH_4 rotation in the Kr matrix are arranged in such a way[14,15] that the phonon-rotation interaction can strongly influence the thermal conductivity at low temperatures. This is favorable for reliable separation of this interaction contribution to the thermal resistivity of the solutions.

The relative simplicity of the particles in the solution and the high symmetry of the host lattice, along with information available about the rotational spectra of the CH_4 molecules in the Kr matrix, make the description and interpretation of the thermal conductivity results comparatively easy.

Finally, the quantum character of the CH_4 rotation in the matrix attracts even more attention to this system. The methane molecule can exist in the form of three nuclear spin species–E, T, A, the total nuclear spins being 0, 1, and 2, respectively. Each species has its own systematics of rotational energy levels. The behavior of the impurity subsystem of the CH_4-Kr solution is dependent on the concentrations of the above species. The characteristic time of conversion of the nuclear spin species in the solution increases with decreasing temperature and reaches several hours at helium temperatures.[16] We should remember that the experimental results correspond to the equilibrium distribution of the species concentrations only when the time of the experiment exceeds the characteristic conversion times.

2. EXPERIMENTS

The thermal conductivity of solid krypton and Kr–CH_4 solutions (0.2, 0.5, 1.0 and 5.0% CH_4) were studied in the temperature range 1.8–40 K. The krypton used had the natural isotopic composition and a chemical purity of 99.94% (the impurities were 0.042% N_2, 0.012% Ar, and 0.005% O_2). The chemical purity of the methane was 99.99%. The Kr–CH_4 mixture was prepared in the gas phase at room temperature.

The crystals were grown from the liquid phase in a cylindrical stainless-steel container 38 mm long and 4.5 mm in inner diameter. The growth rate was 0.07 mm/min. The temperature gradient 0.18 K/mm was kept constant. The grown sample was cooled down to 30 K at a rate of 0.15 K/min, the gradient being the same.

The thermal conductivity was measured using the steady-state technique.[17] The total time taken to reach the steady state and to measure one value of the thermal conductivity varied with temperature from 2 h at 40 K to 20 min at the lowest temperature. The temperature dependence of the thermal conductivity $K(T)$ was taken at successively lower temperatures. As an example, Fig. 1a shows the time dependence of the average temperature $T(t)$ which was obtained while measuring the thermal conductivity of the sample with 1% CH_4. The dependences $T(t)$ let us know whether the concentrations of the nuclear spin CH_4 species come to equilibrium during measurement (see below). The temperature dependence of the thermal conductivity was also taken on the 1% CH_4 sample at rising T. The K values measured at the same T points under rising and falling temperatures varied within the random experimental error (3–5%). In the sample with 0.5% CH_4 the thermal conductivity observed at 5 K remained unaltered when the crystal was warmed to 13 K and then cooled rapidly (for 5 min).

The thermal conductivity data for pure Kr and for Kr with four CH_4 concentrations are shown in Fig. 2. In the high-temperature region ($T>20$ K) the results for pure Kr agree well with earlier data.[18,19] In the vicinity of the thermal

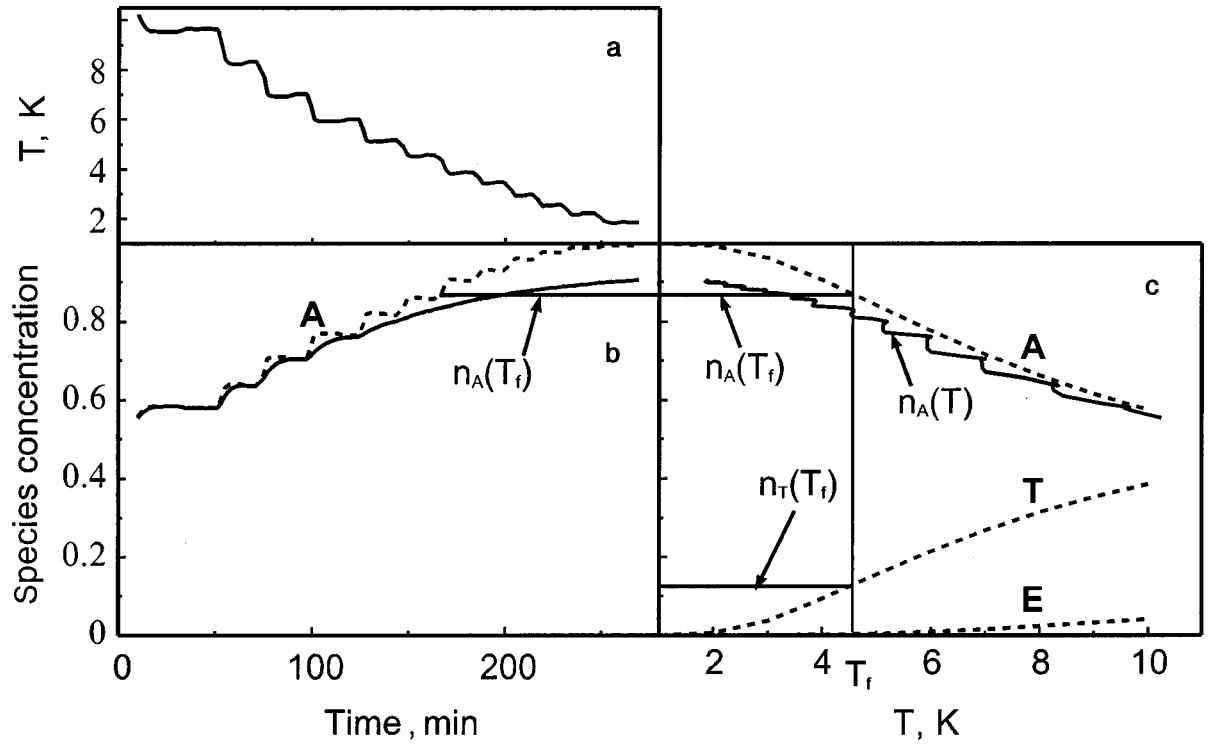

FIG. 1. Correlations between the temperature of the crystal and the CH_4 molecule distribution in nuclear spin species (illustrated for a Kr sample with 1%CH_4 admixture): dependence of the average temperature on time during measurement of thermal conductivity (a); time dependence of the equilibrium (dashed lines) and calculated (solid lines) concentrations of the species A in the impurity subsystem (b); equilibrium (dashed lines) and calculated (solid lines) concentrations of nuclear spin species as a function of temperature (c); $n_A(T_f)$ and $n_T(T_f)$ are the ''frozen'' concentrations of species A and T for $T=4.6$ K.

conductivity maximum the K value is about twice as high as in Ref. 19, which may be attributed to the better quality of our crystals. The thermal conductivity of solid Kr with CH_4 admixtures has not been studied before.

3. RESULTS AND DISCUSSION

It is seen in Fig. 2 that the CH_4 impurity strongly suppresses the thermal conductivity and alters the character of its temperature dependence. The latter feature is especially distinct in the solution with 5%CH_4. The $K(T)$ curve with a maximum at 5 K which is typically observed for pure Kr deforms into a curve with a dip near 8 K. This sort of dip is usually caused by the resonance scattering of phonons.

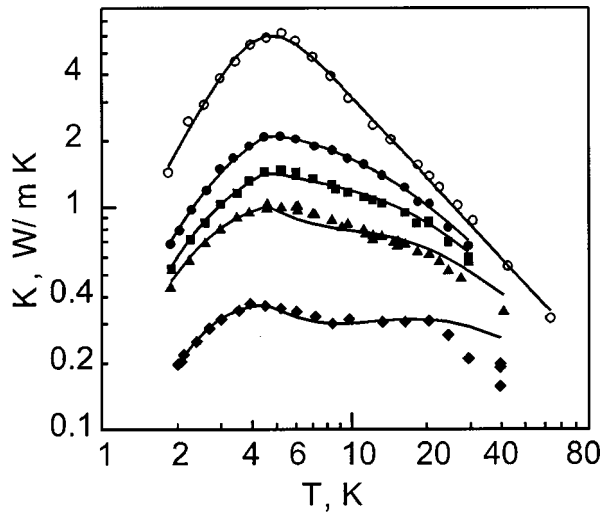

FIG. 2. Temperature dependence of the thermal conductivity of pure Kr (○) and Kr with CH_4 admixtures, %: 0.2 (●), 0.5 (■); 1.0 (▲), and 5.0 (◆); the solid lines are calculated curves.

The thermal conductivity measured on our crystals is described within the Debye model:

$$K=\frac{k_B}{2\pi^2 s}\left(\frac{k_B}{\hbar}\right)^3 T^3\int_0^{\Theta_D/T}\frac{\tau_{\rm tot}x^4e^x}{(e^x-1)^2}dx, \tag{1}$$

where s is the sound velocity; Θ_D is the Debye temperature, $x=\hbar\omega/k_BT$; and $\tau_{\rm tot}$ is the total phonon relaxation time for all resistive processes. The relaxation rate $\tau_{\rm tot}^{-1}$ of the Kr–CH_4 solution is a sum of the relaxation rates of pure Kr and CH_4-induced phonon scattering:

$$\tau_{\rm tot}^{-1}=\tau_{\rm Kr}^{-1}+\tau_{\rm CH_4}^{1}.$$

The phonon relaxation rate of Kr includes the terms describing phonon–phonon scattering (U processes) τ_U^{-1}, boundary scattering τ_B^{-1}, scattering on dislocations $\tau_{\rm dis}^{-1}$, and Rayleigh impurity scattering $\tau_{\rm imp}^{-1}$:

$$\tau_{\rm Kr}^{-1}=\tau_U^{-1}+\tau_B^{-1}+\tau_{\rm dis}^{-1}+\tau_{\rm imp}^{-1}. \tag{2}$$

The rates of the above mechanisms are described by the expressions:[20]

$$\tau_U^{-1}=A\omega^2T\exp(b/T), \tag{3}$$

$$\tau_B^{-1}=s/l, \tag{4}$$

$$\tau_{\rm dis}^{-1}=D\omega, \tag{5}$$

$$\tau_{\text{imp}}^{-1}=\sum_i \frac{\Gamma_i V}{4\pi s^3}\omega^4. \tag{6}$$

Here l is the characteristic mean free path determined by the grain sizes in the sample; $\Gamma=c(\Delta M/M)^2$, where c is the concentration of point defects, M is the mass of the host particles, and ΔM is the mass difference between the host and impurity particles.

The parameters of relaxation time in pure Kr obtained by fitting to the experimental results are as follows:

U processes: (A), $\text{s}\cdot\text{K}^{-1}$	4.41×10^{-16},
(b), K	15.77,
Boundary scattering (l), m	1.87×10^{-5},
Scattering on dislocations: (D)	2.09×10^{-4},
Impurity scattering: (Γ)	6.1×10^{-4}.

The isotopic scattering parameter Γ was not fitted but calculated from the concentrations and molecular weights of the impurities. The contribution of the N_2 and O_2 rotation to the thermal conductivity of pure Kr was not estimated because of a lack of information about the rotational spectra of N_2 and O_2 impurities in the Kr matrix. In fact, this contribution was effectively taken into account through selection of the other scattering parameters. The efficiency of this procedure is evident from the good agreement between the calculated curve and the experimental data for thermal conductivity of Kr (Fig. 2).

The CH_4 molecules contribute to the phonon scattering not only because their masses are different from those of the host atoms (Rayleigh scattering) but also because their rotational excitations come into interaction with phonons (phonon—rotation interaction). The expression for $\tau_{\text{CH}_4}^{-1}$ can therefore be written as a sum of the relaxation rates of these mechanisms:

$$\tau_{\text{CH}_4}^{-1}=\tau_{\text{Rayleigh}}^{-1}+\tau_{\text{rot}}^{-1}. \tag{7}$$

The analysis of phonon scattering by a rotating molecule is a sophisticated theoretical problem. The mechanism of phonon scattering by an impurity with two energy levels was consistently described by Klein.[3,21] The expression in Ref. 3 was used to interpret the dips in the temperature dependence of thermal conductivity of alkali halide crystals[3,4] and of solid argon with admixtures.[10] While describing the phonon scattering on CH_4 molecules, we should take into account the occupation of the rotational levels, which is dependent on temperature. We used Klein's expression[3] to write the relaxation rate of the phonon–rotation interaction as

$$\tau^{-1}=\frac{1}{3\pi\rho(\omega)}\sum_i d_i S\frac{\gamma_i^2(\omega/\omega_i)^4}{[1-(\omega/\omega_i)^2]^2+\gamma_i^2(\omega/\omega_i)^6}, \tag{8}$$

where $\rho(\omega)$ is the phonon density normalized to unity; S is the occupation of the ground state; $\omega_i=E_i/\hbar$ is the resonance frequency, and d_i is the degeneracy of the excited state with energy E_i.

The parameter γ_i describes the relation between broadening of the rotational energy levels induced by the crystal field and the energy difference of these levels. This is the basic parameter of the phonon–rotation interaction in Klein's model. In Refs. 3 and 4, γ was used as a fitting parameter different for each level. When the phonon–rotation interaction is absent, $\gamma=0$. For a weakly hindered rotation γ must be much smaller than unity.

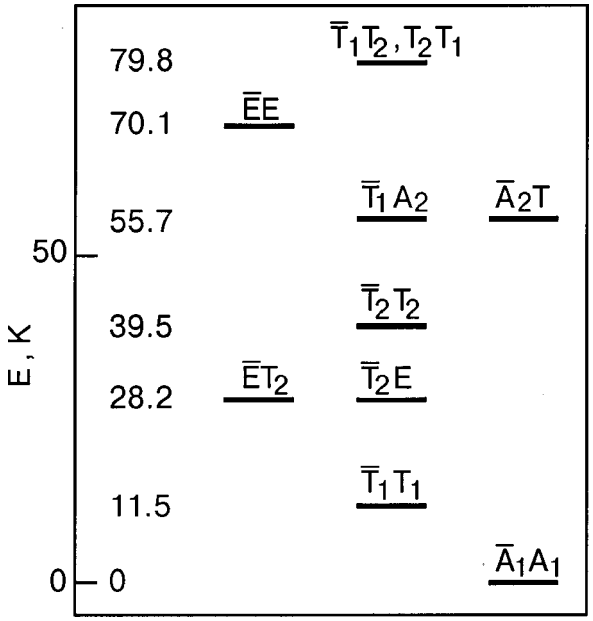

FIG. 3. Rotational spectrum of CH_4 molecule in the Kr matrix (crystal field symmetry O_h) for three nuclear spin species (according to Ref. 14).

The experimental information about the rotational energy spectrum of CH_4 in crystalline Kr concerns only the first three excited levels (inelastic neutron scattering data[22]). These data refer to the low-energy part of the spectrum and are not sufficient for calculating $\tau_{\text{CH}_4}^{-1}$ over the whole working interval of temperatures. The energies of the rotational levels of the CH_4 molecule in the crystal field of O_h symmetry were calculated as a function of the field strength.[14,15] We used the spectrum of Ref. 14 (Fig. 3) corresponding to the crystal field in which the energies of the low-lying excited levels are in good agreement with experimental values.

As was mentioned above, CH_4 molecules can exist in three species—E, T, A. They differ from each other by the total nuclear spin (0, 1, 2, respectively). Since the characteristic phonon scattering relaxation times are many orders of magnitude shorter than the conversion time, we can write τ_{rot}^{-1} as a sum of expression (8) for each spin species τ_α^{-1} (α=E,T,A):

$$\tau_{\text{rot}}^{-1}=c\sum_\alpha n_\alpha(T)\tau_\alpha^{-1}, \tag{9}$$

where c is the CH_4 concentration in the Kr matrix and n_α is the concentration of α species in the impurity subsystem.

The temperature dependence of the equilibrium species concentrations corresponds to the Boltzmann distribution. However, the equilibrium distribution may be disturbed significantly when the temperature changes during an experiment. According to Ref. 16, the characteristic time of CH_4 conversion in the Kr matrix increases with decreasing temperature and is 3.5 hours at 2 K.

The temperature dependences of the equilibrium E, T, A concentrations are shown in Fig. 1c. It is seen that species A predominates at low temperatures. In Fig. 1c the equilibrium

species-A concentrations $n_{A(eq)}$ are compared with the corresponding $n_{A(exp)}$ observed in our sample with 1%CH_4. The $n_{A(exp)}$ values were calculated from the thermal prehistory of the sample using the parameters of Ref. 16 for CH_4 conversion in the Kr matrix.

In our experiment the distribution of the molecules in spin states comes to equilibrium above 6 K. At lower temperatures the concentration is considerably different from its equilibrium value. The reason is that at these temperatures the characteristic conversion time is several times longer than the characteristic time of a thermal conductivity measurement (Fig. 1b and 1c).

To take into account the deviations of the spin species concentrations from the equilibrium value, we calculated the thermal conductivity within the following model: A characteristic temperature T_f (''freezing temperature'') was introduced. It was assumed that above T_f the spin species concentrations had the equilibrium values. Below T_f the concentration of a species is assumed to be constant and corresponding to the equilibrium distribution at $T=T_f$. The feasibility of the model is evident from Fig. 1c. The most suitable T_f is expected to be 4.3–5.0 K.

To bring the calculated and experimental temperature dependences of the thermal conductivity agreement, we used the fitting parameters γ (phonon–rotation interaction) and l (boundary scattering). The intensity of the Rayleigh scattering by a CH_4 molecule was calculated to be $\Gamma=0.655c$. The parameters of the other scattering mechanisms were the same as for pure krypton. The parameters obtained by fitting at $T_f=4.6$ K for different CH_4 concentrations are as follows:

CH_4 concentration (c), %	0.2	0.5	1	5
Boundary scattering parameter (l), 10^{-6}m	5.99	4.45	5.22	1.88
Phonon-rotation interaction parameter (γ)	0.029	0.027	0.029	0.023.

An increase in the impurity concentration usually leads to degradation of the crystal quality, which in turn is responsible for the decrease in the parameter l—the characteristic mean free path determined by the boundary scattering. We observed this on the sample with 5%CH_4.

The calculated curves are shown in Fig. 2 (solid lines). The model proposed provides a good quantitative description of the measured thermal conductivity and reproduces the features of its temperature dependence. The model permits us to compare the contributions of two mechanisms of phonon scattering on CH_4 molecules—Rayleigh scattering and the scattering induced by the phonon–rotation interaction. For example, at $T=8$ K the contributions of these mechanisms to the thermal resistivity are 0.2 and 2.5 $m\cdot K/W$, respectively; i.e., the rotational scattering predominates.

The contribution of the T species to the resonance phonon scattering is dominant below 20 K (see Figs. 2 and 3). The dip in the curve at 6–20 K is due to the resonance phonon scattering on low-energy rotational excitations of the T species. Below 6 K the behavior of the thermal conductivity is determined by the higher (nonequilibrium) concentration of the T species.

Figure 4 illustrates the agreement between the experimental and calculated temperature dependences of the thermal conductivity for the sample with 0.5%CH_4. The calculation was made assuming (*1*) an equilibrium distribution of the spin species in the whole measurement region; (*2*) $T_f=4.6$ K; (*3*) $T_f=10$ K. The agreement is good at $T_f=4.6$ K. The concentrations $n_A(T_f)$ and $n_T(T_f)$ of the A and T species at this temperature are shown in Fig. 1c. It is seen that below $T=4.6$ K the experimental curves deviate considerably from the equilibrium curves. Above 20 K the calculated curves run above the experimental ones. The discrepancy may be attributed to the fact that our simple calculation model does not include rotational levels whose energies exceed 70 K.

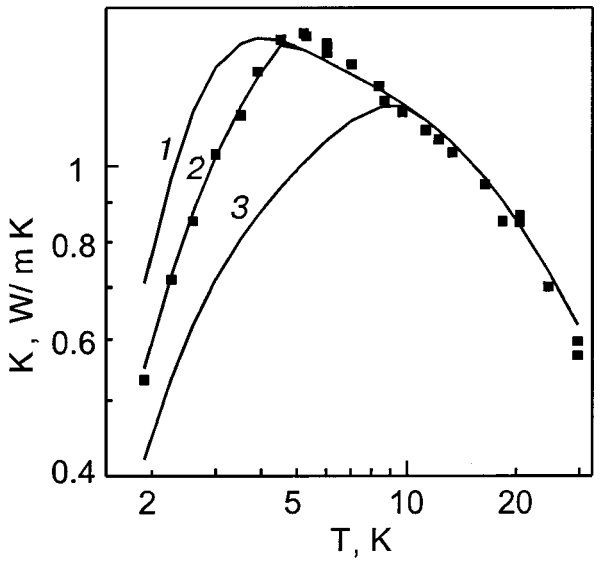

FIG. 4. Comparison of experimental data and calculated thermal conductivity curves for a Kr sample with 0.5%CH_4. The calculation was done for various values of the ''freezing'' temperature T (with index f): equilibrium distribution in the whole region of measurements, T (with index f)=0K (curve *1*); T (with index f)=4.6 K (curve *2*) and T (with index f)=10 K (curve *3*).

It should be noted that the model used did not take into account the role of CH_4 clusters in phonon scattering. We actually assume identical energy spectra and conversion rates for clusters and isolated molecules. This simplification might be most conspicuous in the low-temperature part of the curve taken on the sample with 5%CH_4. Nevertheless, the model describes the thermal conductivity of this sample quite well. In this context it would be interesting to study the low-temperature thermal conductivity of higher-concentration Kr–CH_4 solutions.

We are grateful to Prof. R. O. Pohl, Dr. V. A. Konstantinov, and O. V. Sklyar for helpful discussions.

*E-mail: dudkin@ilt.kharkov.ua

[1] C. T. Walker and R. O. Pohl, Phys. Rev. **131**, 1433 (1963).
[2] V. Narayanamurti, W. D. Seward, and R. O. Pohl, Phys. Rev. **148**, 481 (1966).
[3] R. L. Rosenbaum, C. K. Chau, and M. V. Klein, Phys. Rev. **186**, 852 (1969).
[4] D. P. Singh and G. S. Verma, Phys. Rev. B **4**, 4647 (1971).
[5] V. G. Manzhelii, V. B. Kokshenev, L. A. Koloskova, and I. N. Krupskii,

Fiz. Nizk. Temp. **1**, 624 (1975) [Sov. J. Low Temp. Phys. **1**, 624 (1975)].
[6] B. Ya. Gorodilov and V. B. Kokshenev, J. Low Temp. Phys. **81**, 45 (1990).
[7] B. Ya. Gorodilov, N. N. Zholonko, and P. Stachowiak, Fiz. Nizk. Temp. **19**, 339 (1993) [Sov. J. Low Temp. Phys. **19**, 240 (1993)].
[8] V. G. Manzhelii and V. A. Konstantinov, in *Die Kunst of phonons (Lectures from the Winter School of Theoretical Physics)*, edited by T. Paszkiewicz and K. Rapcewicz (Plenum Press, New York, 1994).
[9] *Physics of Cryocrystals*, edited by V. G. Manzhelii, Yu. A. Freiman, M. L. Klein, and A. A. Maradudin, (AIP Press, Woodbury, New York, 1996).
[10] P. Stachowiak, V. V. Sumarokov, and J. Mucha, Phys. Rev. B **58**, 2380 (1998).
[11] B. Ya. Gorodilov, V. V. Sumarokov, P. Stachowiak, and A. Jezowski, Phys. Rev. B **58**, 3089 (1998).
[12] V. A. Konstantinov, V. G. Manzhelii, V. P. Revyakin, and S. A. Smirnov, Physica B **262**, 421 (1999).
[13] V. G. Manzhelii, A. I. Prokhvatilov, I. Ya. Minchina, and L. D. Yantsevich, *Handbook of Binary Solutions of Cryocrystals* (Begell House Inc., New York/Wallingford (U.K.), 1996).
[14] K. Nishiyama and T. Yamamoto, J. Chem. Phys. **58**, 1001 (1973).
[15] T. Yamamoto, Y. Kataoka, and K. Okada, J. Chem. Phys. **66**, 2701 (1977).
[16] S. Grieger, H. Friedrich, B. Asmussen, K. Guckelsberger, D. Nettling, W. Press, and R. Scherm, Z. Phys. B: Condens. Matter **87**, 203 (1992).
[17] T. N. Antsygina, B. Ya. Gorodilov, N. N. Zholonko, A. I. Krivchikov, V. G. Manzhelii, and V. A. Slyusarev, Fiz. Nizk. Temp. **18**, 417 (1992) [Sov. J. Low Temp. Phys. **18**, 283 (1992)].
[18] I. N. Krupskii and V. G. Manzhelii, Sov. Phys. JETP **28**, 1097 (1969).
[19] P. Korpiun, J. Moser, F. J. Pieringer, and E. Luscher, in *Proceedings of the Second International Conference on Phonon Scattering in Solids, Nottingam (1975)*.
[20] R. Berman, *Thermal Conductivity in Solids* (Clarendon Press, Oxford, 1976).
[21] M. V. Klein, Phys. Rev. **186**, 839 (1969).
[22] B. Asmussen, M. Prager, W. Press, H. Blank, and C. J. Carlile, J. Chem. Phys. **97(2)**, 1332 (1992).

This article was published in English in the original Russian journal. Reproduced here with stylistic changes by the Translation Consultant.

Low-temperature anomalies in the magnetic and thermal properties of molecular cryocrystals doped with oxygen impurity

Yu. A. Freiman* and S. M. Tretyak

B. Verkin Institute for Low Temperature Physics and Engineering, National Academy of Sciences of Ukraine, 47 Lenin Ave., 61164 Kharkov, Ukraine

A. Jeżowski**

Trzebyatowski Institute for Low Temperatures and Structure Research, Polish Academy of Sciences, P.O. Box 937, 50-950 Wroclaw 2, Poland

(Submitted May 17, 2000)
Fiz. Nizk. Temp. **26**, 1029–1043 (September–October 2000)

The magnetic properties of oxygen pair clusters are investigated theoretically for different cluster geometries which can be realized by doping molecular cryomatrices with oxygen. Anomalous temperature and pressure behavior of the magnetic susceptibility, heat capacity, and entropy is predicted. It is proposed to use these anomalies for studying the parameters characterizing the oxygen clusters and the parameters of the host matrix: the effective spin-figure interaction constant D for the molecule in the matrix, the exchange parameter J, and the number of pair clusters N_p, which can deviate markedly from the purely random value $N_p = 6Nc^2$ (N is Avogadro's number, and c is the molar concentration of the impurity). The data on the magnetic susceptibility may be used to analyze the character of the positional and orientational short-range order in the solid solution. The value of D contains information about the orientational order parameter; the distance and angular dependence of the exchange interaction parameter are still subject to discussion in the literature. The temperature dependence of N_p contains information about diffusion and clusterization processes in the system. © *2000 American Institute of Physics.* [S1063-777X(00)02009-0]

1. INTRODUCTION

The study of the properties of cryocrystals doped with impurities is a well-known source of information about the impurity molecules isolated in the matrix. At the same time, rich information can be extracted from these studies on the matrix lattice dynamics and about the interaction of impurity molecules with the matrix and with each other.

Among of the most interesting in this respect are oxygen molecules, which are frequently employed as a probe of properties of atomic and molecular cryocrystals. As we know, O_2 in the electronic ground state has spin $S=1$ and is therefore paramagnetic. The triplet ground state of O_2, $^3\Sigma_g^-$, is split by the intermolecular spin-spin and spin-orbit interactions into a singlet with $M=0$ and a doublet with $M=\pm 1$. The splitting for the free particle (the so-called spin-figure constant) amounts to $D_0 = 5.71$ K.[1] Upon introduction of O_2 into a cryocrystal matrix, quasilocal levels appear in the low-energy part of the spectrum. As a result, such crystals display low-temperature anomalies in their thermal, optical, and magnetic properties.

One of the most studied is the N_2-O_2 system. Studies by Burford and Gracham,[2] Sumarokov *et al.*,[3] and Jeżowski *et al.*[4] were devoted to the specific heat and thermal expansion of solid nitrogen containing oxygen impurities. The anomalies found in those works correspond satisfactorily to the Schottky curve with a twofold degenerate upper level and splitting $D = 5.14$ K. The difference between D and D_0 results from the fact that the effective magnitude of the spin-figure constant for the embedded molecule in a crystal is renormalized by librational motion of the oxygen molecule.[5]

With increasing concentration of the impurity, an observable number of clusters of exchange-coupled molecules appears. Their appearance affects the position and magnitude of the impurity anomalies, since the magnetic spectrum of a cluster differs from that of a single molecule.[6,7]

Some further information on the impurity spectrum in N_2-O_2 solid solutions was obtained in EPR,[8,9] optical,[10,11] and thermal conductivity[12] studies.

There are several experimental studies of the magnetic susceptibility of cryocrystals doped with oxygen impurities,[13–15] but in the absence of a theory of the magnetic properties of such solid solutions, little information was extracted from these studies. At the same time, magnetic systems containing magnetically active molecules or molecular groups can exhibit unusual magnetic properties[16,17] as compared with ordinary magnets. In addition to solid oxygen and oxygen-containing solid solution of cryocrystals, some alkali hyperoxides are examples of such magnetic systems. The magnetic Hamiltonian in this case contains a new parameter, the angle θ between molecular axes. For matrix-embedded oxygen clusters this parameter is matrix-dependent. For example, in the case of a fluorine matrix, the angle θ is close to zero (the collinear cluster), for an α-nitrogen matrix, $\theta \simeq \arccos(1/3)$, and for a γ-nitrogen matrix, $\theta \simeq \pi/2$ (the orthogonal cluster).

Unlike the heat capacity studies, magnetic measurements can be performed in high-pressure conditions, which makes

it possible to use oxygen molecules as a probe for cryocrystals under high-pressure conditions.

In this paper we obtained exact analytical expressions for the contribution of a pair oxygen cluster to the magnetic susceptibility as a function of the parameters of the magnetic Hamiltonian—the intermolecular exchange interaction constant, the spin-figure constant, and the angle θ between the molecular axes. It will be shown that the magnetic susceptibility is very sensitive to changes in these parameters, and it is this sensitivity that makes the magnetic susceptibility an additional convenient characteristic for studying properties of both the host matrix and oxygen clusters. The most peculiar anomalies in the behavior of the magnetic heat capacity and magnetic entropy will be discussed in brief.

2. GENERAL EQUATIONS

The spin Hamiltonian of an exchange-coupled pair of oxygen molecules can be written as[3,7]

$$\mathcal{H}=\mathcal{H}_{sf}+\mathcal{H}_{\rm ex}; \tag{2.1}$$

$$\mathcal{H}_{sf}=D\left[(\mathbf{S}_1\cdot\mathbf{n}_1)^2+(\mathbf{S}_2\cdot\mathbf{n}_2)^2-\frac{2}{3}S(S+1)\right], \tag{2.2}$$

$$\mathcal{H}_{\rm ex}=J\mathbf{S}_1\cdot\mathbf{S}_2, \tag{2.3}$$

where D is the spin-figure constant, $\mathbf{S}_i$ are spin operators ($S=1$), $\mathbf{n}_i$ are the unit vectors of the molecular axes, and J is the exchange interaction constant.

In a magnetic field $\mathbf{H}=H\mathbf{j}$, where $\mathbf{j}$ is the unit vector along the magnetic field, the Hamiltonian (2.1) acquires an additional term, the Zeeman energy

$$\mathcal{H}_Z=-\mu_B g\mathbf{H}\cdot(\mathbf{S}_1+\mathbf{S}_2), \tag{2.4}$$

where μ_B is the Bohr magneton and g is the splitting factor.

An exact analytical expression for the zero-field magnetic susceptibility for the system described by the Hamiltonian (2.1) can be obtained by using perturbation theory, with Eq. (2.1) as the unperturbed Hamiltonian and the Zeeman interaction term (2.4) as the perturbation.[18] The total Hamiltonian for the system in the magnetic field is

$$\mathcal{H}_{\rm tot}=\mathcal{H}_{sf}+\mathcal{H}_{\rm ex}+\mathcal{H}_Z. \tag{2.5}$$

Let $E_i=E_i(H)$ be the set of eigenvalues of $\mathcal{H}_{\rm tot}$. Then the free energy $\mathcal{F}$, the magnetic moment M, and the magnetic susceptibility χ are given by the equations

$$\mathcal{F}=-T\ln\sum_i \mathrm{e}^{-\beta E_i(H)}; \tag{2.6}$$

$$M=\frac{\partial\mathcal{F}}{\partial H}=-\frac{1}{Z}\sum_i\frac{\partial E_i}{\partial H}\mathrm{e}^{-\beta E_i(H)} \tag{2.7}$$

$$\chi=\frac{\partial M}{\partial H}=-\frac{1}{Z}\sum_i\frac{\partial^2 E_i}{\partial H^2}\mathrm{e}^{-\beta E_i(H)} + \frac{\beta}{Z}\sum_i\left(\frac{\partial E_i}{\partial H}\right)^2\mathrm{e}^{-\beta E_i(H)}-\frac{\beta}{Z^2}\left[\sum_i\frac{\partial E_i}{\partial H}\mathrm{e}^{-\beta E_i(H)}\right]^2, \tag{2.8}$$

where $\beta=1/T, Z=\Sigma_i\exp(-E_i/T)$.

The energy corrections to the eigenvalues of the unperturbed Hamiltonian can be written in the form of a series in the magnetic field:

$$E_i(H)=E_i^{(0)}+\sum_{k=1}^{\infty}(\mu_B g)^k a_{ik}H^k. \tag{2.9}$$

Taking into account the relations

$$\frac{\partial E_i}{\partial H}=\sum_{k=1}^{\infty}(\mu_B g)^k a_{ik}kH^{k-1};$$

$$\frac{\partial^2 E_i}{\partial H^2}=\sum_{k=1}^{\infty}(\mu_B g)^k a_{ik}k(k-1)H^{k-2}, \tag{2.10}$$

we get the final expression for the zero-field magnetic susceptibility

$$\chi(T)_{H=0}=(\mu_B g)^2\left\{\frac{\langle a_{i1}^2\rangle}{T}-2\langle a_{i2}\rangle\right\}, \tag{2.11}$$

where

$$\langle a_{i1}^2\rangle=\frac{1}{Z}\sum_i a_{i1}^2\exp(-E_i/T);$$

$$\langle a_{i2}\rangle=\frac{1}{Z}\sum_i a_{i2}\exp(-E_i/T); \tag{2.12}$$

The last term in Eq. (2.8), which is the squared magnetic moment, vanishes in the limit of zero magnetic field (there is no spontaneous magnetization in the system under consideration), i.e., the following equality holds:

$$\sum_i a_{i1}e^{-\beta E_i^0}=0. \tag{2.13}$$

Thus the zero-field magnetic susceptibility is defined by the eigenvalues $E_i^{(0)}$ and by the coefficients a_{i1} and a_{i2} which determine first- and second-order corrections in the perturbation theory.

The eigenvalues $E_i^{(0)}$ determine the magnetic part of the impurity contribution to the heat capacity and entropy. The magnetic heat capacity is given by the expression

$$\frac{C_m}{k_B}=\frac{1}{T^2}\{\langle E^2\rangle-\langle E\rangle^2\}, \tag{2.14}$$

where

$$\langle E^2\rangle=\frac{1}{Z}\sum_i E_i^2\exp(-E_i/T);$$

$$\langle E\rangle=\frac{1}{Z}\sum_i E_i\exp(-E_i/T). \tag{2.15}$$

In a similar way, the magnetic entropy is given by the expression

$$\frac{S_m}{k_B}=\ln Z+\frac{\langle E\rangle}{T}. \tag{2.16}$$

Thus Eqs. (2.11), (2.14), and (2.16) give the contribution of the discrete set of magnetic energy levels to the magnetic susceptibility, magnetic heat capacity, and magnetic entropy, respectively.

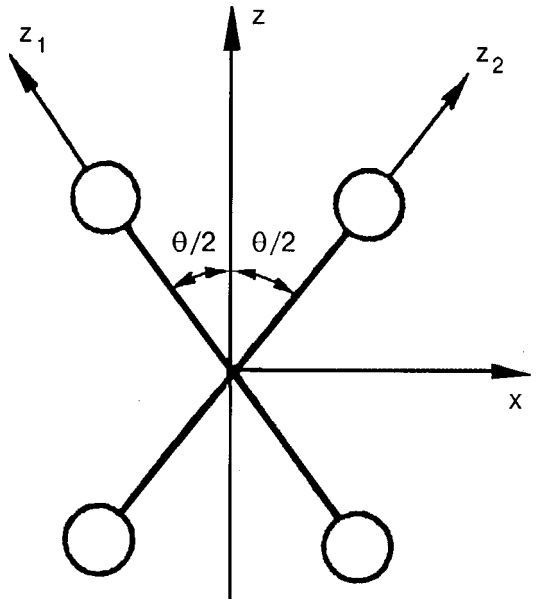

FIG. 1. Coordinate systems related to the molecular axes.

3. SPECTRUM OF EXCHANGE-COUPLED O_2-O_2 PAIR IN ZERO MAGNETIC FIELD

In order to calculate the coefficients a_{i1} and a_{i2} one needs to have a complete set of eigenvectors and eigenvalues of the unperturbed Hamiltonian (2.1).

The symmetry group of the Hamiltonian (2.1) is $\mathbf{D}_{2h}$ (Ref. 7) that is, the system under consideration has three mutially perpendicular twofold symmetry axes. Let us transform the coordinate system in such a way that allow us to use the symmetry considerations explicitly. First of all, we execute a parallel translation, making the centers of mass of the molecules coincide. This transformation does not change the symmetry of the Hamiltonian (2.1) and thus does not change the spectrum of the system. Then it is natural to choose the coordinate system *x,y,z* with the molecules lying in the *xz* plane and with the *z* axis directed along the bisector of the angle between the molecular axes.

Let us introduce two intrinsic coordinate systems (x_1,y_1,z_1) and (x_2,y_2,z_2) with the local *z* axis rotated with respect to the *z* axis by the angle $\pm\theta/2$ in the *xz* plane, so the local z_i axis is directed along the axis of the *i*th molecule (Fig. 1). The relation between the components of the spin operators in the fixed and rotated coordinate systems are:

$$
\begin{aligned}
&S_{1x}=S_{1x_1}\cos\frac{\theta}{2}+S_{1z_1}\sin\frac{\theta}{2};\\
&S_{1y}=S_{1y_1};\\
&S_{1z}=-S_{1x_1}\sin\frac{\theta}{2}+S_{1z_1}\cos\frac{\theta}{2};\\
&S_{2x}=S_{2x_2}\cos\frac{\theta}{2}-S_{2z_2}\sin\frac{\theta}{2};\\
&S_{2y}=S_{2y_2};\\
&S_{2x}=S_{2x_2}\sin\frac{\theta}{2}+S_{2z_2}\cos\frac{\theta}{2}.
\end{aligned}
\tag{3.1}
$$

Replacing the Cartesian spin components defined in the intrinsic coordinate systems by cyclic spin components according to the relations:

$$
\begin{aligned}
&S_{1x_1}=\frac{1}{\sqrt{2}}(S_1^-S_1^+);\quad S_{2x_2}\frac{1}{\sqrt{2}}(S_2^-S_2^+);\\
&S_{1y_1}=\frac{i}{\sqrt{2}}(S_1^-+S_1^+);\quad S_{2y_2}=\frac{i}{\sqrt{2}}(S_2^-+S_2^+);
\end{aligned}
\tag{3.2}
$$

we transform the Hamiltonian (2.1) into the form

$$
\begin{aligned}
\mathcal{H}=D\left[S_{1z_1}^2+S_{2z_2}^2-\frac{2}{3}S(S+1)\right]+J\Bigg\{&S_{1z_1}S_{2z_2}\cos\theta\\
&-(S_1^-S_2^++S_1^+S_2^-)\cos^2\frac{\theta}{2}-(S_1^-S_2^-+S_1^+S_2^+)\sin^2\frac{\theta}{2}\\
&+\frac{1}{\sqrt{2}}[(S_2^-S_2^+)S_{1z_1}-(S_1^-S_1^+)S_{2z_2}]\sin\theta\Bigg\}.
\end{aligned}
\tag{3.3}
$$

From the nine states $|S_{1z_1}\rangle|S_{2z_2}\rangle$ of the O_2-O_2 pair (S_{1z_1}, $S_{2z_2}=0,\pm1$) that realize the reproducible representation

$$
\Gamma=4A_{1g}+2B_{1g}+B_{2g}+2B_{3g},
\tag{3.4}
$$

we can form 9 orthonormal basis functions $\mathbf{\Phi}_i$ that transform according to the four irreducible representations of the group $\mathbf{D}_{2h}$ (see Appendix A).

Because of the symmetry, the matrix elements of the Hamiltonian (3.3) between states $\mathbf{\Phi}_i$ that transform according to different irreducible representations are zero. As a result, the Hamiltonian matrix in the basis of the function $\mathbf{\Phi}_i$ assumes the block-diagonal form

$$
\mathcal{H}=\begin{pmatrix}
\mathcal{H}_{B_{2g}} & 0 & 0 & 0\\
0 & \mathcal{H}_{B_{1g}} & 0 & 0\\
0 & 0 & \mathcal{H}_{B_{3g}} & 0\\
0 & 0 & 0 & \mathcal{H}_{A_{1g}}
\end{pmatrix},
\tag{3.5}
$$

where

$$
\begin{aligned}
&\mathcal{H}_{B_{2g}}=D+J;\\
&\mathcal{H}_{B_{1g}}=\begin{pmatrix} D-J\cos\theta & -J\sin\theta\\ -J\sin\theta & 2D+J\cos\theta\end{pmatrix};\\
&\mathcal{H}_{B_{3g}}=\begin{pmatrix} D+J\cos\theta & J\sin\theta\\ J\sin\theta & 2D-J\cos\theta\end{pmatrix};\\
&\mathcal{H}_{A_{1g}}=\begin{pmatrix}
0 & -J & J\cos\theta & 0\\
-J & 2D & J\cos\theta & 0\\
J\cos\theta & J\cos\theta & 2D & -\sqrt{2}J\sin\theta\\
0 & 0 & -\sqrt{2}J\sin\theta & D-J
\end{pmatrix}.
\end{aligned}
\tag{3.6}
$$

The constant term $(2/3)DS(S+1)$, which determines the reference level for the spectrum, was omitted in transforming the Hamiltonian (3.3) into the form Eq. (3.6).

For two interesting cases, $\theta=0$ (the collinear cluster) and $\theta=\pi/2$ (the orthogonal cluster), all the unperturbed eig-

envectors and eigenvalues can be found in an explicit analytical form, which in turn permits finding analytical expressions for the zero-field magnetic susceptibility. In the general case, analytical expressions can be found for the eigenvectors and eigenvalues corresponding to representations B_{1g}, B_{2g}, and B_{3g}, and the rest can be found by numerical diagonalization of the Hamiltonian $\mathcal{H}_{A_{1g}}$ [Eq. (3.6)]. The eigenvectors and eigenvalues are given in Appendix B.

The spectrum of an exchange-coupled pair of oxygen molecules as a function of the parameter J/D for different angles between the molecular axes is shown in Fig. 2. Figure 2a illustrates the sensitivity of the spectrum to the parameter θ. Figures 2b and 2c give the spectrum as a function of J/D for the collinear and orthogonal cluster, respectively. In the region $J/D \ll 1$ for all angles θ, the spectrum of the cluster is close to the spectrum of noninteracting molecules, and the effect of the exchange interaction is small. In the opposite limiting case $J/D \gg 1$ the behavior of the spectrum is also in fact universal for all angles. In the limit $J/D \to \infty$ the nine levels of the $({}^3\Sigma_g^-)$ $({}^3\Sigma_g^-)$ ground state of the pair split into a quintet of energy $+J$ (states with the total spin of the pair $S=2$), a triplet of energy $-J$ (total spin of the pair $S=1$), and a singlet of energy $-2J$ (total spin of the pair $S=0$). In the region $J/D \sim 1$ the spectrum of the cluster depends essentially on the angle between the molecular axes.

At low temperatures the thermal properties of the system (the heat capacity and the thermal expansion) are determined primarily by the gap between the ground state and the first excited state of the system ΔE. This value depends essentially on both J/D and θ. Near $\theta = \pi/2$ there is a certain range of θ where the two lowest levels as a function of J/D intersect. At $\theta = \pi/2$ the intersection takes place at $J/D = 3/4$ (Fig. 2c).

It is this sensitivity of the low-temperature thermal properties of the system to the position and to the value of the energy gap ΔE as a function of J/D and θ that was used in Refs. 3 and 7 to obtain information about the dependence of the exchange interaction of oxygen molecules on both the intermolecular separation and the intermolecular orientations.

As will be shown below, the zero-field magnetic susceptibility is strongly J/D- and θ-dependent; as a result, the low-temperature zero-field magnetic susceptibility can be used as a source of information on the peculiarities of the O_2-O_2 exchange interaction.

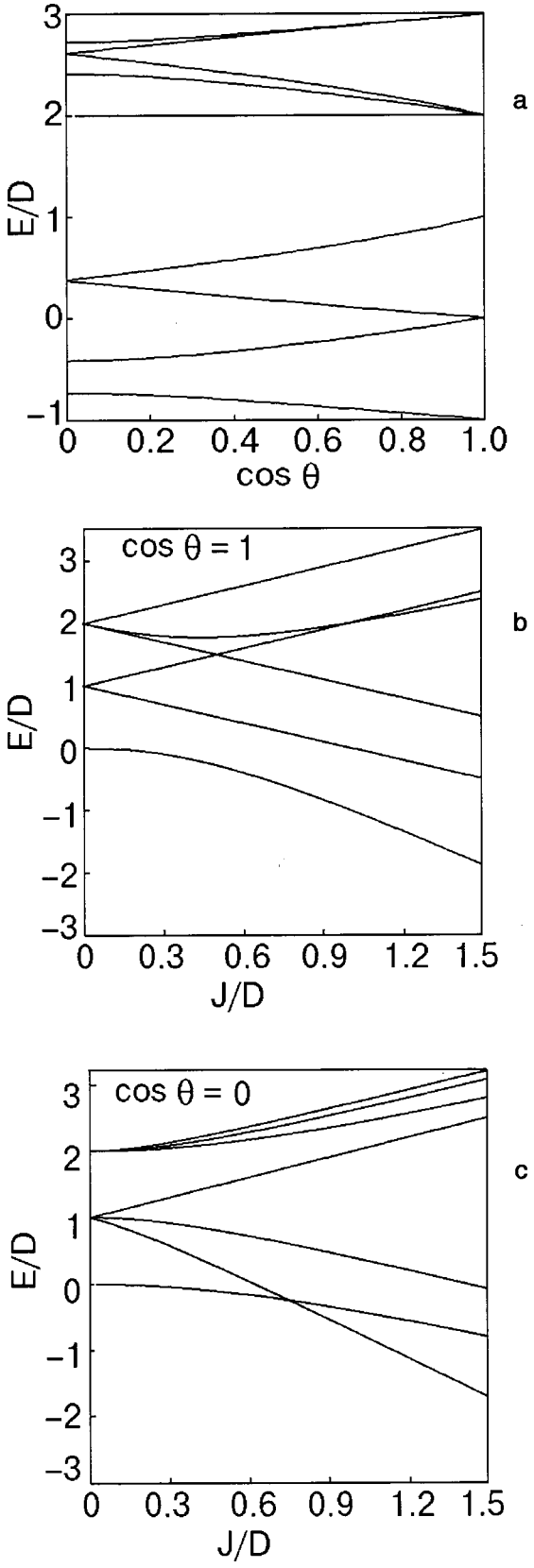

FIG. 2. Energy spectra of exchange-coupled pair oxygen clusters. Dependence of the energy spectrum on: the angle between the axes of the molecules ($J/D=1$) (a); J/D for the collinear cluster (b) and for the orthogonal cluster (c).

4. ZERO-FIELD MAGNETIC SUSCEPTIBILITY

4.1. Collinear O_2–O_2 cluster ($\theta=0$)

Transverse susceptibility ($\chi_{xx}=\chi_{yy}$). The spin spectrum of a collinear O_2–O_2 cluster consists in general of three doublet levels and three singlets. In the limit $J/D=0$, corresponding to a pair of noninteracting molecules, the nine levels of the system are split into the ground-state singlet and two quadruplets; in the opposite limit $J/D=\infty$ the spectrum consists of a singlet, a triplet, and a quintet (Fig. 2a). An additional degeneracy occurs at $J/D=1/2$ and $J/D=1$. All these particular cases should be considered separately.

It is easy to check that all the energy corrections of the first order are zero:

$$\Delta E_i^{(1)} = \langle \Psi_i | \mathcal{H}_Z | \Psi_i \rangle = 0. \tag{4.1}$$

The energy corrections of the second order can be found from the equation

$$\Delta E_i^{(2)}=\sum_{k\neq i}\frac{|\langle\Psi_i|\mathcal{H}_Z|\Psi_k\rangle|^2}{E_i^0-E_k^0} \tag{4.2}$$

in the case of nondegenerate levels; in the case of doublet levels the energy corrections can be found from the secular equation

$$\begin{vmatrix} \sum_{l\neq m}\frac{\mathcal{H}_Z^{ml}\mathcal{H}_Z^{lm}}{E_m^{(0)}-E_l^{(0)}}-\Delta E^{(2)} & \mathcal{H}_Z^{mn}+\sum_{l\neq m}\frac{\mathcal{H}_Z^{ml}\mathcal{H}_Z^{ln}}{E_m^{(0)}-E_l^{(0)}} \\ \mathcal{H}_Z^{nm}+\sum_{l\neq n}\frac{\mathcal{H}_Z^{nl}\mathcal{H}_Z^{lm}}{E_n^{(0)}-E_l^{(0)}} & \sum_{l\neq n}\frac{\mathcal{H}_Z^{nl}\mathcal{H}_Z^{ln}}{E_n^{(0)}-E_l^{(0)}}-\Delta E^{(2)} \end{vmatrix}=0, \tag{4.3}$$

where Ψ_i and $E_i^{(0)}$ are listed in Appendix B.

As follows from Eq. (4.1),

$$a_i^{(1)}=0, \quad i=1,2,...,9. \tag{4.4}$$

After finding the matrix elements with the help of Ψ_i given in Appendix B, we get from Eqs. (4.2) and (4.3) the set of coefficients $a_i^{(2)}$:

$$a_1^{(2)}=a_9^{(2)}=-\frac{1}{D}; \quad a_2^{(2)}=0;$$

$$a_3^{(2)}=a_5^{(2)}=a_6^{(2)}=\frac{1}{D};$$

$$a_7^{(2)}=\frac{2}{D}\frac{\left(J+\frac{1}{2}E_7^{(0)}\right)^2}{J^2+\frac{1}{2}(E_7^{(0)})^2}\left[\left(1-\frac{J}{D}+\frac{9}{4}\frac{J^2}{D^2}\right)^{1/2}-\frac{3}{2}\frac{J}{D}\right]^{-1};$$

$$a_8^{(2)}=-\frac{2}{D}\frac{\left(J+\frac{1}{2}E_8^{(0)}\right)^2}{J^2+\frac{1}{2}(E_8^{(0)})^2}\left[\left(1-\frac{J}{D}+\frac{9}{4}\frac{J^2}{D^2}\right)^{1/2}+\frac{3}{2}\frac{J}{D}\right]^{-1};$$

$$a_4^{(2)}=-\frac{1}{D}-(a_7^{(2)}+a_8^{(2)}). \tag{4.5}$$

A sum rule holds for the coefficients $a_i^{(2)}$:

$$\sum_i a_i^{(2)}=0. \tag{4.6}$$

Taking into account that all the $a_i^{(1)}$ coefficients equal zero [Eq. (4.4)], we find that the transverse zero-field magnetic susceptibility for a collinear cluster is described by the expression

$$\chi_\perp=-2(\mu_B g)^2\frac{\Sigma_i a_i^{(2)}e^{-\beta E_i^0}}{\Sigma_i e^{-\beta E_i^0}}. \tag{4.7}$$

Let us consider now the limiting cases $J/D\to 0$ and $J/D\to\infty$. Generally speaking, since the spectrum for each of these cases has a structure that differs from that considered above, each of them should be treated separately. In fact, the result may be obtained from the same Eq. (4.7) if we find the corresponding limits. Really, the only condition to be met is the condition of applicability of the perturbation theory, i.e., the separation between levels, which we consider as belonging to different zero-order energies, should be large compared with the perturbation energy. In the case $J/D\to 0$ the separation between the levels which tend to form quadruplets goes to zero as J, so the following inequality should hold:

$$J\gg\mu_B g H. \tag{4.8}$$

Thus, in passing to the limits $J/D\to 0$, $H\to 0$ in Eq. (4.7), we must take them in such a way that the inequality (4.8) is obeyed.

When $J/D\to 0$, $D\neq 0$ the limiting values of the $a_i^{(2)}$ and $E_i^{(0)}$ are as follows:

$$a_8^{(2)}=-\frac{2}{D}, \quad E_8^{(0)}=0; \quad a_1^{(2)}=a_9^{(2)}=-\frac{1}{D};$$

$$a_2^{(2)}=a_4^{(2)}=0; \quad E_1^{(0)}=E_2^{(0)}=E_4^{(0)}=E_9^{(0)}=D;$$

$$a_3^{(2)}=a_5^{(2)}=a_6^{(2)}=a_7^{(2)}=\frac{1}{D};$$

$$E_3^{(0)}=E_5^{(0)}=E_6^{(0)}=E_7^{(0)}=2D. \tag{4.9}$$

As a result, we get

$$\chi_\perp=4(\mu_B g)^2\frac{1}{D}\frac{1-e^{-\beta D}}{1+2e^{-\beta D}}, \tag{4.10}$$

which is twice the transverse susceptibility for a molecule described by the Hamiltonian $\mathcal{H}=DS_z^2$.

When $D\to 0$, $J\neq 0$,

$$a_7^{(2)}=-\frac{9}{D}, \quad E_7^{(0)}=J+\frac{2}{3}D;$$

$$a_8^{(2)}=0, \quad E_8(0)=-2J. \tag{4.11}$$

As a result, we get

$$\chi_\perp=2(\mu_B g)^2\frac{1}{T}e^{-\beta J}\frac{1+5e^{-2\beta J}}{1+3e^{-\beta J}+5e^{-\beta J}}, \tag{4.12}$$

which is the magnetic susceptibility of a Heisenberg antiferromagnet pair cluster.

In the low-temperature limit $\beta\Delta E\gg 1$, where ΔE is the gap between the ground and the first excited levels, taking into account only the two lowest levels, we get

$$\chi_\perp(T\to 0)=2(\mu_B g)^2|a_8^{(2)}|\times\left\{1+\left(\frac{1}{D|a_8^{(2)}|}-2\right)\exp\left(-\frac{\Delta E}{T}\right)\right\},$$

$$\Delta=\left(D^2-DJ+\frac{9}{4}J^2\right)^{1/2}-\frac{J}{2}, \tag{4.13}$$

where $a_8^{(2)}$ is defined by Eq. (4.5).

The zero-temperature limit

$$\chi_\perp(T=0)=4(\mu_B g)^2\frac{\left(J+\frac{1}{2}E_8^{(0)}\right)^2}{J^2+\frac{1}{2}(E_8^{(0)})^2}$$

$$\times\left[\left(D^2-DJ+\frac{9}{4}J^2\right)^{1/2}+\frac{3}{2}\frac{J}{D}\right]^{-1}, \quad (4.14)$$

where the ground state energy

$$E_8=+D-\frac{1}{2}J-\left(D^2-DJ+\frac{9}{4}J^2\right)^{1/2}. \quad (4.15)$$

In the limiting case of small and large J/D we get

$$\chi_\perp(T=0)=(\mu_B g)^2\frac{4}{D}\begin{cases}\left(1-2\dfrac{J}{D}\right), & \dfrac{J}{D}\ll 1\\ \dfrac{4}{81}\left(\dfrac{D}{J}\right)^3, & \dfrac{J}{D}\gg 1\end{cases}. \quad (4.16)$$

Thus, at small J/D, the zero-temperature transverse susceptibility decreases linearly with rising J/D, but at large J this quantity is practically suppressed.

In the high-temperature limit $\beta\Delta E\gg 1$, expanding Eq. (4.7) in powers of inverse temperature, we get corrections to Curie law:

$$\chi_\perp=\frac{4}{3}(\mu_B g)^2\frac{1}{T}\left\{\left(\frac{1}{6}D-\frac{2}{3}J\right)\frac{1}{T}-\left(\frac{1}{18}D^2+\frac{2}{9}DJ+\frac{1}{6}J^2\right)\frac{1}{T^2}+\ldots\right\}. \quad (4.17)$$

The expression in curly brackets gives the corrections to the Curie law.

Longitudinal susceptibility. As in the case of the transverse susceptibility, the coefficients $a_i^{(1)}$ and $a_i^{(2)}$ can be found from the first- and second-order energy corrections. As a result, we arrive at the following sets of coefficients $a_i^{(1)}$ and $a_i^{(2)}$:

$$a_1^{(1)}=a_2^{(1)}=1,\quad a_3^{(1)}=2;\quad a_4^{(1)}=a_9^{(1)}=-1;$$
$$a_6^{(1)}=-2;\quad a_5^{(1)}=a_7^{(1)}=a_8^{(1)}=0. \quad (4.18)$$

All the coefficients $a_i^{(2)}$ vanish in this case:

$$a_i^{(2)}=0,\quad i=1,\ldots,9. \quad (4.19)$$

Substituting the coefficients $a_i^{(1)}$ from Eq. (4.18) into Eq. (2.11) and taking into account Eq. (4.19), we arrive at the following expression for the longitudinal susceptibility:

$$\chi_\parallel=\chi_{zz}=\frac{2(\mu_B g)^2}{T}\frac{e^{-\beta(D-J)}+e^{-\beta(D+J)}+4e^{-\mu(2D+J)}}{\Sigma_i e^{-\beta E_i}}. \quad (4.20)$$

Considering that in this case the perturbation operator Eq. (2.4) commutes with the spin-figure interaction Hamiltonian $\mathcal{H}_{sf}$, the result [Eq. (4.20)] can be readily obtained by employing the fluctuation-dissipation relation[19]

$$\chi_{zz}=\frac{(\mu_B g)^2}{T}\frac{\mathrm{Sp}(S_{1z}^2+S_{2z}^2)e^{-\beta\mathcal{H}}}{\mathrm{Sp}e^{-\beta\mathcal{H}}}. \quad (4.21)$$

At low temperatures the longitudinal susceptibility exponentially goes to zero:

$$\chi_{zz}=2\frac{(\mu_B g)^2}{T}\exp\left[-\frac{1}{T}\left(D^2-DJ+\frac{9}{4}J^2\right)^{1/2}-\frac{J}{2}\right]. \quad (4.22)$$

The high-temperature expansion has the form

$$\chi_{zz}=\frac{4}{3}(\mu_B g)^2\frac{1}{T}\left\{1-\left(\frac{1}{3}D+\frac{2}{3}J\right)\frac{1}{T}+\left(-\frac{1}{18}D^2+\frac{4}{9}DJ-\frac{1}{6}J^2\right)\frac{1}{T^2}\ldots\right\}. \quad (4.23)$$

At $J=0$ Eq. (4.20) reduces to

$$\chi_{zz}=4(\mu_B g)^2\frac{1}{T}\frac{e^{-\beta D}}{1+2e^{-\beta D}}, \quad (4.24)$$

which is the longitudinal susceptibility for two noninteracting molecules.

At $D=0$, Eq. (4.20) reduces to Eq. (4.12), the magnetic susceptibility of a Heisenberg antiferromagnetic cluster.

Average susceptibility. The average or powder susceptibility is given by the expression

$$\overline{\chi}=\frac{1}{3}\chi_\parallel+\frac{2}{3}\chi_\perp. \quad (4.25)$$

In the general case $\overline{\chi}$ is given by Eqs. (4.4), (4.5), (4.7), and (4.20).

The low-temperature asymptotic expression for $\overline{\chi}$ is

$$\overline{\chi}(T\to 0)=\frac{2}{3}(\mu_B g)^2\left\{2|a_8^{(2)}|+\left[\frac{1}{T}+2|a_8^{(2)}|\left(\frac{1}{D|a_8^{(2)}|}-2\right)\right]\exp\left(-\frac{\Delta}{T}\right)\right\}, \quad (4.26)$$

where $a_8^{(2)}$ is defined by Eq. (4.5) and Δ, the gap between the ground and the first excited levels, is given by Eq. (4.13).

At zero temperature in the limiting case of small and large J/D we get

$$\overline{\chi}(T=0)=\frac{8}{3}(\mu_B g)^2\frac{1}{D}\begin{cases}\left(1-2\dfrac{J}{D}\right), & \dfrac{J}{D}\ll 1\\ \dfrac{4}{81}\left(\dfrac{D}{J}\right)^3, & \dfrac{J}{D}\gg 1\end{cases}. \quad (4.27)$$

The high-temperature asymptotic expression for $\overline{\chi}$ is given by Eqs. (4.17) and (4.23):

$$\overline{\chi}=\frac{4}{3}(\mu_B g)^2\frac{1}{T}\left\{1-\frac{J}{T}-\frac{1}{18}\frac{D^2+3J^2}{T^2}+\ldots\right\}. \quad (4.28)$$

As one can see, the factor that determines the deviation of the average susceptibility from the Curie law at high temperatures contains no terms linear in the spin-figure constant D, at any rate in terms up to T^{-2}.

4.2. Orthogonal O_2-O_2 cluster ($\theta=\pi/2$)

The eigenfunctions and eigenvalues of the unperturbed Hamiltonian (3.5) can readily be found in analytical form in this case (see Appendix B). In order of decreasing energy, the sequence of terms is as follows:

$$E_8\geqslant E_3=E_5\geqslant E_6>E_1>E_2=E_4\geqslant E_7,E_0. \quad (4.29)$$

There are two doublets; for the others, the equality sign, where indicated, is realized in the limiting cases $D=0$ and

$J=0$. The only crossing occurs between the E_7 and E_9 levels at $J/D=3/4$ (Fig. 2c). At $J/D>3/4$ the ground level is the E_9 term, and otherwise it is the E_7 term.

Calculation of the $\chi_{xx}=\chi_{zz}$ components. In the general case ($\theta\neq 0$), classification of the components into transverse and longitudinal loses meaning, but in the case $\theta=\pi/2$ the equality $\chi_{xx}=\chi_{zz}$ holds from symmetry considerations, so these components can be considered as an analog of the transverse component, while χ_{yy} is an analog of the longitudinal component.

Let us consider first the general case of J/D; the special case $J/D=3/4$ will be considered below. We will proceed in the same manner as in the previous Section. As a result, we get the following sets of coefficients $a_i^{(1)}$ and $a_i^{(2)}$:

$$a_i^{(1)}=0, \quad i=1,2,...,9;$$

$$a_1^{(2)}=-(a_2^{(2)}+a_3^{(2)}); \quad a_{2\ 3}^{(2)}=-\frac{1}{2}\frac{(m_3^2-l_3^2)^2}{J\pm\left(\frac{1}{4}D^2+J^2\right)^{1/2}-\frac{D}{2}};$$

$$a_4^{(2)}=\frac{(l_4l_6-m_4m_6)^2}{\frac{D}{2}-\left(\frac{1}{4}D^2+J^2\right)^{1/2}-(D^2+J^2)^{1/2}}+\frac{(l_4l_7-m_4m_7)^2}{\frac{D}{2}-\left(\frac{1}{4}D^2+J^2\right)^{1/2}+(D^2+J^2)^{1/2}}+(l_4+m_4)^2\times\left\{\frac{(l_8-m_8/\sqrt{2})^2}{\frac{J}{2}-\left(\frac{1}{4}D^2+J^2\right)^{1/2}-\left(\frac{1}{4}D^2+\frac{1}{2}DJ+\frac{9}{4}J^2\right)^{1/2}}+\frac{(l_9-m_9/\sqrt{2})^2}{\frac{J}{2}-\left(\frac{1}{4}D^2+J^2\right)^{1/2}+\left(\frac{1}{4}D^2+\frac{1}{2}DJ+\frac{9}{4}J^2\right)^{1/2}}\right\};$$

$$a_5^{(2)}=\frac{(l_5l_6-m_5m_6)^2}{\frac{D}{2}+\left(\frac{1}{4}D^2+J^2\right)^{1/2}-(D^2+J^2)^{1/2}}+\frac{(l_5l_7-m_5m_7)^2}{\frac{D}{2}+\left(\frac{1}{4}D^2+J^2\right)^{1/2}+(D^2+J^2)^{1/2}}+(l_5+m_5)^2\times\left\{\frac{(l_8-m_8/\sqrt{2})^2}{\frac{J}{2}+\left(\frac{1}{4}D^2+J^2\right)^{1/2}-\left(\frac{1}{4}D^2+\frac{1}{2}DJ+\frac{9}{4}J^2\right)^{1/2}}+\frac{(l_9-m_9/\sqrt{2})^2}{\frac{J}{2}+\left(\frac{1}{4}D^2+J^2\right)^{1/2}+\left(\frac{1}{4}D^2+\frac{1}{2}DJ+\frac{9}{4}J^2\right)^{1/2}}\right\};$$

$$a_6^{(2)}=-\left\{\frac{(l_4l_6-m_4m_6)^2}{\frac{D}{2}-\left(\frac{1}{4}D^2+J^2\right)^{1/2}-(D^2+J^2)^{1/2}}+\frac{(l_5l_6-m_5m_6)^2}{\frac{D}{2}+\left(\frac{1}{4}D^2+J^2\right)^{1/2}-(D^2+J^2)^{1/2}}\right\};$$

$$a_7^{(2)}=-\left\{\frac{(l_4l_7-m_4m_7)^2}{\frac{D}{2}-\left(\frac{1}{4}D^2+J^2\right)^{1/2}+(D^2+J^2)^{1/2}}+\frac{(l_5l_7-m_5m_7)^2}{\frac{D}{2}+\left(\frac{1}{4}D^2+J^2\right)^{1/2}+(D^2+J^2)^{1/2}}\right\};$$

$$a_{8\ 9}^{(2)}=-\left(l_{8\ 9}-\frac{1}{\sqrt{2}}m_{8\ 9}\right)^2\times\left\{\frac{(l_4+m_4)^2}{\frac{J}{2}-\left(\frac{1}{4}D^2+J^2\right)^{1/2}\mp\left(\frac{1}{4}D^2+\frac{1}{2}DJ+\frac{9}{4}J^2\right)^{1/2}}+\frac{(l_5+m_5)^2}{\frac{J}{2}+\left(\frac{1}{4}D^2+J^2\right)^{1/2}\mp\left(\frac{1}{4}D^2+\frac{1}{2}DJ+\frac{9}{4}J^2\right)^{1/2}}\right\}. \tag{4.30}$$

The magnetic susceptibility $\chi_{xx}=\chi_{zz}$ is defined by Eq. (2.11) with the coefficients $a_i^{(1)}$ and $a_i^{(2)}$ from Eq. (4.30).

Since at $J/D=3/4$ a change of the ground state occurs, the zero-temperature susceptibility is defined either by $a_7^{(2)}$ or $a_9^{(2)}$:

$$\chi_{xx}(T=0)=2(\mu_B g)^2\begin{cases}|a_7^{(2)}|, & \frac{J}{D}<\frac{3}{4}\\ |a_9^{(2)}|, & \frac{J}{D}>\frac{3}{4}\end{cases}. \tag{4.31}$$

In the limit of large and small J/D we obtain

$$\chi_{xx}(T=0)=(\mu_B g)^2\frac{2}{D}\begin{cases}1+\frac{3}{8}\frac{J^2}{D^2}, & \frac{J}{D}\ll 1\\ \frac{4}{81}\left(\frac{D}{J}\right)^3, & \frac{J}{D}\gg 1\end{cases}. \tag{4.32}$$

It is interesting to note that the result Eq. (4.32) for the orthogonal cluster is one-half of that for the collinear cluster [Eq. (4.16)], a fact which can be explained on purely geometrical considerations.

In the case $J/D=3/4$ the ground state is degenerate, and the coefficients a_7 and a_9 can be determined from the secular equation. As a result, no $a_i^{(1)}$ coefficients appear for this degenerate case. The coefficients $a_7^{(2)}$ and $a_9^{(2)}$ take the form:

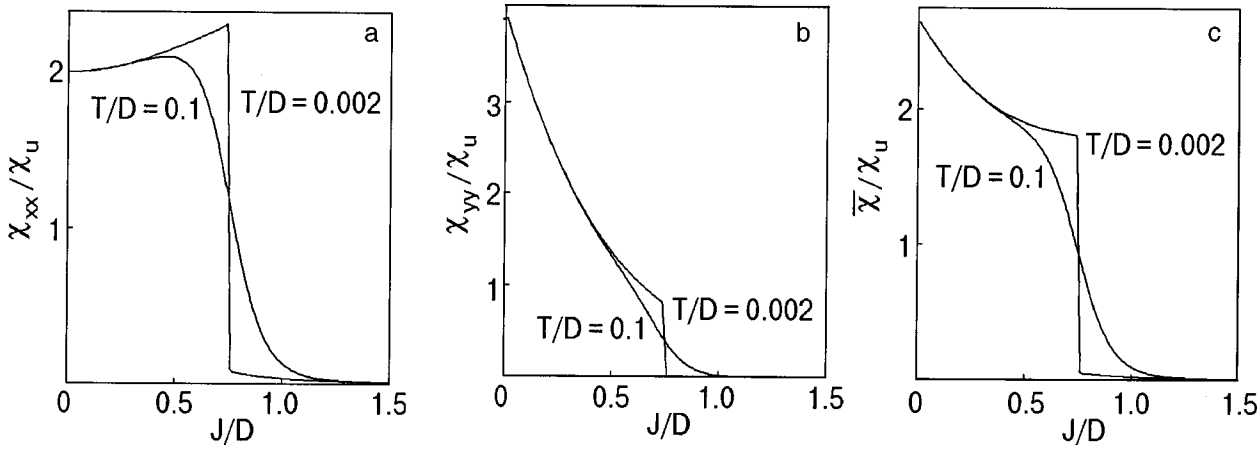

FIG. 3. Low-temperature magnetic susceptibility versus J/D: χ_{xx}/χ_u (a); χ_{yy}/χ_u (b); $\overline{\chi}/\chi_u$ (c), where $\chi_u=(g\mu_B)^2/D$.

$$a_{7\ 9}^{(2)}=\frac{1}{2}(a_{7(0)}^{(2)}+a_{9(0)}^{(2)})\pm\frac{1}{2}\Bigg\{(a_{7(0)}^{(2)}-a_{9(0)}^{(2)})^2+4\left(l_9-\frac{m_9}{\sqrt{2}}\right)^2\left[\frac{(l_4+m_4)(l_4l_7-m_4m_7)}{\frac{D}{2}-\left(\frac{1}{4}D^2+J^2\right)^{1/2}+(D^2+J^2)^{1/2}}+\frac{(l_5+m_5)(l_5l_7-m_5m_7)}{\frac{D}{2}-\left(\frac{1}{4}D^2+J^2\right)^{1/2}+(D^2+J^2)^{1/2}}\right]\Bigg\}, \tag{4.33}$$

where $a_{7(0)}^{(2)}, a_{9(0)}^{(2)}$ are the coefficients for the nondegenerate case.

The zero-temperature susceptibility at the level-crossing point is

$$\chi_{xx}(T=0)=(\mu_B g)^2|a_{7(0)}^{(2)}+a_{9(0)}^{(2)}|. \tag{4.34}$$

As a result, the zero-temperature magnetic susceptibility given by Eqs. (4.31) and (4.34) is a nonmonotonic discontinuous function of J/D at $J/D=3/4$. The jumps in the χ_{xx} versus J/D curve smears out with temperature. This peculiar behavior is displayed in Fig. 3a.

χ_{yy} component of the magnetic susceptibility. Having found the second-order energy corrections to the nondegenerate levels from Eq. (4.2) and that to the degenerate levels from Eq. (4.3), we arrive at the following sets of coefficients $a_i^{(1)}$ and $a_i^{(2)}$:

$$a_1^{(1)}=a_6^{(1)}=a_7^{(1)}=a_8^{(1)}=a_9^{(1)}=0;$$

$$a_{2\ 4}^{(1)}=\pm(l_2m_4-l_4m_2); \quad a_{3\ 5}^{(1)}=\pm(l_3m_5-l_5m_3); \tag{4.35}$$

$$a_1^{(2)}=-(a_6^{(2)}+a_7^{(2)}); \quad a_8^{(2)}=a_9^{(2)}=0;$$

$$a_3^{(2)}=a_5^{(2)}=-a_2^{(2)}=-a_4^{(2)};$$

$$a_2^{(2)}=a_4^{(2)}=-\frac{1}{4}\frac{(l_3m_4-l_4m_3)^2+(l_2m_5-l_5m_2)^2}{\sqrt{D^2/4+J^2}};$$

$$a_6^{(2)}=2\frac{(l_6-m_6)^2}{-J+\sqrt{D^2+J^2}};$$

$$a_7^{(2)}=-2\frac{(l_7-m_7)^2}{J+\sqrt{D^2+J^2}}. \tag{4.36}$$

In this case the coefficients a_7 and a_9 are unaffected by the crossing of the E_7 and E_9 levels, and Eq. (4.36) is universal for all J/D.

The zero-temperature susceptibility is

$$\chi_{yy}(T=0)=2(\mu_B g)^2\begin{cases}|a_7^{(2)}|, & \frac{J}{D}<\frac{3}{4}\\ \frac{1}{2}|a_7^{(2)}|, & \frac{J}{D}=\frac{3}{4}\\ 0, & \frac{J}{D}>\frac{3}{4}\end{cases}. \tag{4.37}$$

The function Eq. (4.37) exhibits a jump at $J/D=3/4$. In the limit of small J/D

$$\chi_{yy}(T=0)=4(\mu_B g)^2\frac{1}{D}\left(1-2\frac{J}{D}\right). \tag{4.38}$$

For $J/D>3/4$ the function $\chi_{yy}(T=0)$ is identically zero. The low-temperature behavior of χ_{yy} as a function of J/D is shown in Fig. 3b. As can be seen, the jump in χ_{yy} at the crossing of the two lowest spin levels is smaller than the jump in χ_{xx}. The jump smears out with temperature.

Average susceptibility. The zero-temperature average susceptibility for the orthogonal cluster is given by

$$\overline{\chi}(T=0)=\frac{2}{3}(\mu_B g)^2\begin{cases}2|a_7^{(2)xx}|+|a_7^{(2)yy}|, & \frac{J}{D}<\frac{3}{4}\\ |a_7^{(2)xx}|+|a_9^{(2)yy}|+\frac{1}{2}|a_7^{(2)yy}|, & \frac{J}{D}=\frac{3}{4}\\ 2|a_9^{(2)xx}|, & \frac{J}{D}>\frac{3}{4}\end{cases}. \tag{4.39}$$

In the limits small and large J/D we have

$$\overline{\chi}(T=0)=\frac{8}{3}(\mu_B g)^2\frac{1}{D}\begin{cases}1-\dfrac{1}{D}, & \dfrac{J}{D}\ll 1\\ \dfrac{1}{81}\left(\dfrac{D}{J}\right)^3, & \dfrac{J}{D}\gg 1\end{cases}. \tag{4.40}$$

The low-temperature behavior of the average susceptibility for the orthogonal cluster as a function of J/D is displayed in Fig. 3c for two temperatures. As one can see, the jump at the crossing of the two lowest spin levels smears out with temperature.

Comparing Eq. (4.40) with the equation for the collinear cluster [Eq. (4.27)] we arrive an equation which displays the sensitivity of the low-temperature susceptibility of pair clusters to the angle between the molecular axes:

$$\left(\frac{\overline{\chi}_{\theta=0}}{\overline{\chi}_{\theta=\pi/2}}\right)_{T=0}=\begin{cases}1-\dfrac{J}{D}, & \dfrac{J}{D}\ll 1\\ 4, & \dfrac{J}{D}\gg 1\end{cases}. \tag{4.41}$$

5. RESULTS AND DISCUSSION

The magnetic susceptibility for an arbitrary angle between the molecular axes is given by Eq. (2.11) with the help of the coefficients a_i from Appendix C. Figure 4 gives a comparison of $\overline{\chi}$ versus T/D curves for three cluster geometries for different values of J/D. As can be seen, except at very small J/D, the low-temperature magnetic susceptibility is very sensitive to the cluster geometry. At zero temperature the angle dependence of the average susceptibility can be given in analytical form:[20]

$$\overline{\chi}(\theta)=\frac{8}{3D}(\mu_B g)^2\begin{cases}1-\dfrac{J}{D}(1+\cos^2\theta), & \dfrac{J}{D}\ll 1\\ \dfrac{1}{81}\left(\dfrac{D}{J}\right)^3(1+3\cos^2\theta), & \dfrac{J}{D}\gg 1\end{cases}. \tag{4.42}$$

Anomalies in the behavior of the magnetic heat capacities and magnetic entropy for the orthogonal cluster are shown in Figs. 5 and 6. A double-maximum Schottky-type anomaly in the magnetic heat capacity and a peak in the magnetic entropy are a consequence of the crossing of the lowest spin levels of the system with a change in J/D. In an experiment different values of the parameter J/D can be obtained by changing the pressure applied to the system. The same behavior of the magnetic entropy was observed experimentally in $PrNi_5$ in Ref. 21. In this case the level crossing takes place in a strong applied magnetic field.

As follows from Fig. 2, similar anomalies are characteristic for clusters with arbitrary θ, since there is a minimum in the ΔE versus J/D curve, where ΔE is the gap between the two lowest spin levels. But in the absence of the crossing the anomalies are not so pronounced, and the Schottky anomaly in the heat capacity has only one peak.[3,7]

6. CONCLUSION

The magnetic properties of oxygen pair clusters have been investigated theoretically for different cluster geometries which can be realized by doping molecular cryomatrices with oxygen. Anomalous temperature and pressure behavior of the magnetic susceptibility, heat capacity, and entropy is predicted. It is proposed to use these anomalies for studying the parameters characterizing the oxygen clusters and the parameters of the host matrix: the effective spin-figure interaction constant for the molecule in the matrix, the exchange parameter, and the number of impurity clusters in the solid solution. As a result, the data on the magnetic susceptibility may be used to extract information about the positional and orientational short-range order in the solid solution and about diffusion and clusterization processes in the system.

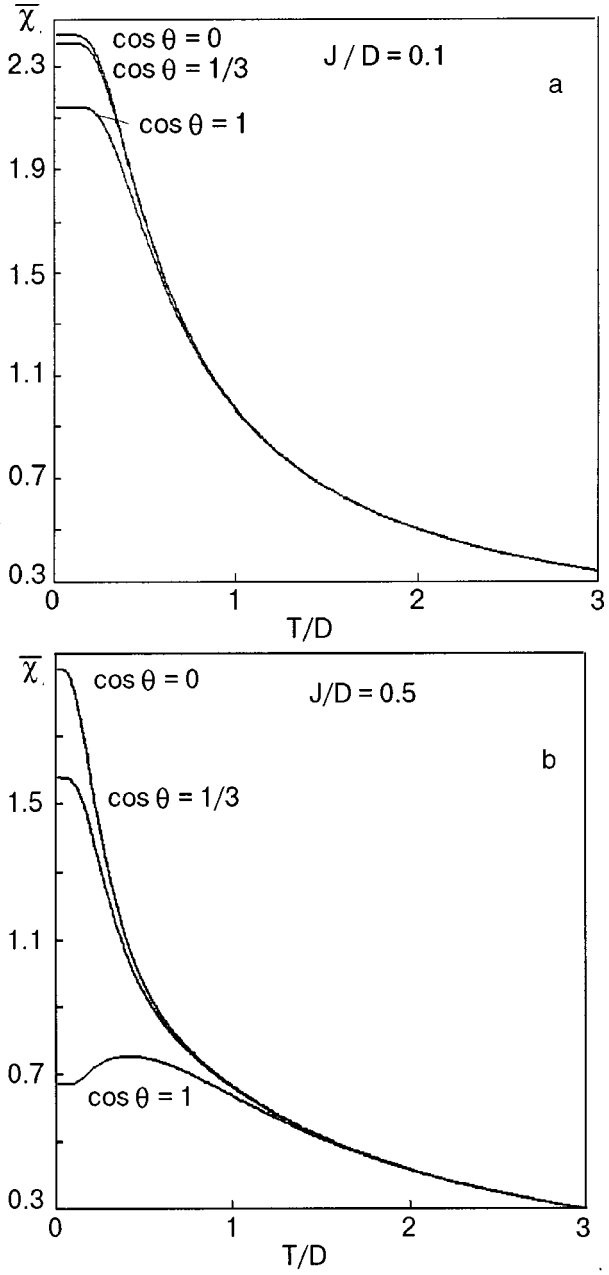

FIG. 4. Temperature dependence of the magnetic susceptibility of pair clusters of different geometry: $J/D=0.1$ (a); $J/D=0.5$ (b).

APPENDIX A

The orthonormal basis functions are

$$\Phi_1(B_{2g})=\frac{1}{\sqrt{2}}(\varphi_0\psi_- + \varphi_-\psi_0);$$

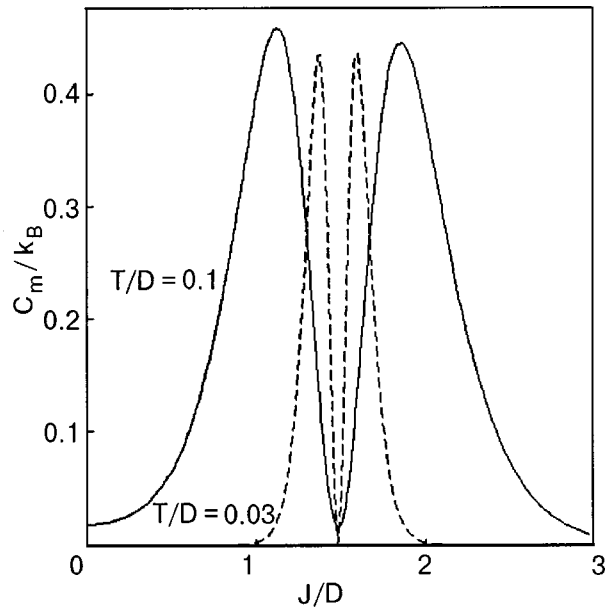

FIG. 5. Magnetic heat capacity.

$$\Phi_2(B_{1g})=\frac{1}{\sqrt{2}}(\varphi_0\psi_+-\varphi_+\psi_0);$$

$$\Phi_3(B_{1g})=\frac{1}{\sqrt{2}}(\varphi_+\psi_-+\varphi_-\psi_+);$$

$$\Phi_4(B_{3g})=\frac{1}{\sqrt{2}}(\varphi_0\psi_++\varphi_+\psi_0);$$

$$\Phi_5(B_{3g})=\frac{1}{\sqrt{2}}(\varphi_-\psi_+-\varphi_+\psi_-);$$

$$\Phi_6(A_{1g})=\varphi_0\psi_0;\quad \Phi_7(A_{1g})=\varphi_-\psi_-;$$

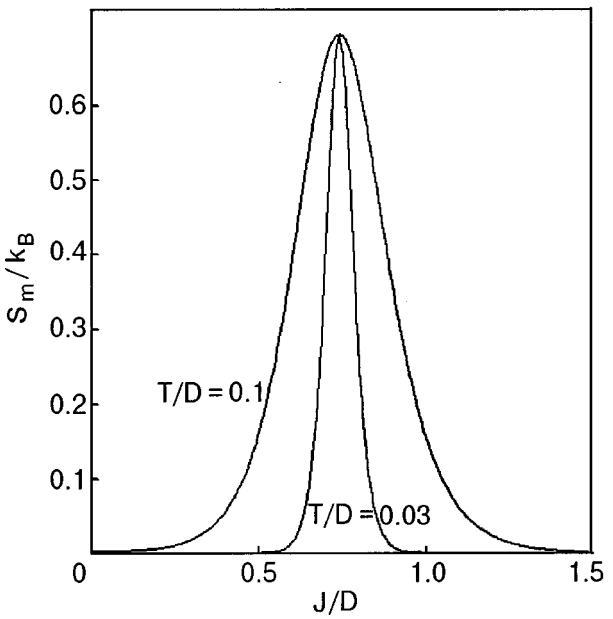

FIG. 6. Magnetic entropy.

$$\Phi_8(A_{1g})=\varphi_+\psi_+;\quad \Phi_9(A_{1g})=\frac{1}{\sqrt{2}}(\varphi_0\psi_--\varphi_-\psi_0), \tag{A1}$$

where $\varphi_0=|0\rangle$, $\varphi_\pm=(1/\sqrt{2})(|1\rangle\pm|-1\rangle)$, and $|0\rangle$, $|\pm1\rangle$ are eigenvectors of S_{1z_1}; in the same way $\psi_0=|0\rangle$, $\psi_\pm=(1/\sqrt{2})(|1\rangle\pm|-1\rangle)$ are formed from eigenvectors of S_{2z_2}.

APPENDIX B

The unperturbed eigenvectors and eigenvalues are

$$\Psi(B_{2g})=\Phi_1;\quad E_1=D+J;$$

$$\Psi^2_3(B_{1g})=l^2_3\Phi_2+m^2_3\Phi_3;$$

$$E^2_3=\frac{3}{2}D\mp\left(\frac{1}{4}D^2+DJ\cos\theta+J^2\right)^{1/2};$$

$$l^2_3=\frac{J}{D}\sin\theta\left\{\frac{J^2}{D^2}\sin^2\theta+\left(1-\frac{J}{D}\cos\theta-\frac{E^2_3}{D}\right)^2\right\}^{-1/2};$$

$$m^2_3=\pm(1-l^2_2)^{1/2};\quad \Psi^4_5(B_{3g})=l^4_5\Phi_4+m^4_5\Phi_5;$$

$$E^4_5=\frac{3}{2}D\mp\left(\frac{1}{4}D^2-DJ\cos\theta+J^2\right)^{1/2};$$

$$l^4_5=\frac{J}{D}\sin\theta\left\{\frac{J^2}{D^2}\sin^2\theta+\left(1+\frac{J}{D}\cos\theta-\frac{E^4_5}{D}\right)^2\right\}^{-1/2};$$

$$m^4_5=\pm\left(1-l^4_5\right)^{1/2}.$$

The remaining four eigenvectors and eigenvalues

$$\Psi_i(A_{1g})=\sum_6^9 c_{ik}(J/D,\cos\theta)\Phi_k;$$

$$E_i=E_i(J/D,\cos\theta),\quad i=6,7,8,9$$

belonging to the A_{1g} representation can be found in the general case only numerically as the result of a diagonalization of $\mathcal{H}_{A_{1g}}$ [Eq. (3.6)].

Explicit equations for the eigenfunctions and eigenvalues belonging to the fourfold representation A_{1g} for the two limiting cases of the collinear and orthogonal clusters are given below.

Collinear cluster ($\cos\theta=1$)

$$\Psi_6(A_{1g})=\frac{1}{\sqrt{2}}(\Phi_7+\Phi_8);\quad E^0_6=2D+J;$$

$$\Psi^7_8(A_{1g})=\left(\frac{J^2}{D^2}+\frac{(E^0_7)^2_8}{2D^2}\right)^{-1/2}\left\{\frac{J}{D}\Phi_6-\frac{E^0_7}{2D}(\Phi_7-\Phi_8)\right\};$$

$$E^7_8=D-\frac{J}{2}\pm\left(D^2-DJ+\frac{9}{4}J^2\right)^{1/2};$$

$$\Psi_9(A_{1g})=\Phi_9;\quad E^0_9=D-J.$$

Orthogonal cluster ($\cos\theta=0$)

$$\Psi_{7}^{6}(A_{1g})=l_{7}^{6}\Phi_6+m_{7}^{6}\Phi_7;\quad E_6=D\pm\sqrt{D^2+J^2};$$

$$l_{7}^{6}=\frac{J}{D}\left\{\left(\frac{J}{D}\right)^2+\left[\left(1+\left(\frac{J}{D}\right)^2\right)^{1/2}\pm 1\right]^2\right\}^{-1/2};$$

$$m_{7}^{6}=\mp\sqrt{1-l_{7}^{2}};\quad \Psi_{9}^{8}(A_{1g})=l_{9}^{8}\Phi_8+m_{9}^{8}\Phi_9;$$

$$E_{9}^{8}=\frac{3}{2}D-\frac{1}{2}J\pm\left(\frac{1}{4}D^2+\frac{1}{2}DJ+\frac{9}{4}J^2\right)^{1/2};$$

$$l_{9}^{8}=\frac{J}{D}\left\{\frac{J^2}{D^2}+\frac{1}{2}\left[\frac{1+J/D}{2}\mp\left(\frac{1}{4}+\frac{J}{2D}+\frac{9J^2}{4D^2}\right)^{1/2}\right]^2\right\}^{-1/2};$$

$$m_{9}^{8}=\mp(1-l_{9}^{2}{}_{8})^{1/2}.$$

APPENDIX C

Coefficients $a_i^{(2)}$ for the general case

In the general case all coefficients $a_i^{(1)}$ are zero, except for special cases of J/D when there is an additional (accidental) degeneracy in the spectrum. The coefficients $a_i^{(2)}$ are different for different components of the susceptibility. The sets of $a_i^{(2)}$ coefficients for χ_{xx}, χ_{yy}, and χ_{zz}, respectively, are as follows.

χ_{xx}:

$$a_1^{(2)}=-(a_2^{(2)}+a_3^{(2)});\quad a_{3}^{2(2)}=\frac{\left(l_{3}^{2}\sin\frac{\theta}{2}-m_{3}^{2}\cos\frac{\theta}{2}\right)^2}{E_1-E_{3}^{2}};$$

$$a_{5}^{4(2)}=\sum_{i=6}^{9}\frac{1}{E_{5}^{4}-E_i}\left\{\left(\sqrt{2}c_{i6}\cos\frac{\theta}{2}+\sqrt{2}c_{i8}\cos\frac{\theta}{2}-c_{i9}\sin\frac{\theta}{2}\right)l_{5}^{4}\right.$$
$$\left.+\left(-\sqrt{2}c_{i7}\sin\frac{\theta}{2}+\sqrt{2}c_{i8}\sin\frac{\theta}{2}-c_{i9}\cos\frac{\theta}{2}\right)m_{5}^{4}\right\}^2;$$

$$a_k=\sum_{i=6,7}\frac{1}{E_k-E_i}\left\{\left(\sqrt{2}c_{k6}\cos\frac{\theta}{2}+\sqrt{2}c_{k8}\frac{\theta}{2}-c_{k9}\sin\frac{\theta}{2}\right)l_i\right.$$
$$\left.+\left(-\sqrt{2}c_{k7}\sin\frac{\theta}{2}+\sqrt{2}c_{k8}\sin\frac{\theta}{2}-c_{k9}\cos\frac{\theta}{2}\right)m_i\right\}^2;$$

$k=6,...,9$.

Here c_{ik} are components of the eigenvectors belonging to the eigenvalues of Eq. (3.6). χ_{yy}:

$$a_1^{(2)}=-(a_6^{(2)}+a_7^{(2)}+a_8^{(2)}+a_9^{(2)});$$

$$a_{3}^{2(2)}=\sum_{i=4,5}\frac{(l_i m_3^2-m_i l_3^2)^2}{E_i-E_{3}^{2}};\quad a_{5}^{4(2)}=\sum_{i=2,3}\frac{(l_i m_{5}^{4}-m_i l_{5}^{4})^2}{E_i-E_{5}^{4}};$$

$$a_k=2\frac{(c_{k6}-c_{k7})^2}{E_k-E_1}(k=6,...,9).$$

χ_{zz}:

$$a_1^{(2)}=-(a_4^{(2)}+a_5^{(2)});$$

$$a_{3}^{2(2)}=\sum_{i=6}^{9}\frac{1}{E_{3}^{2}-E_i}\left\{\left(\sqrt{2}c_{i6}\sin\frac{\theta}{2}-\sqrt{2}c_{i8}\sin\frac{\theta}{2}+c_{i9}\cos\frac{\theta}{2}\right)l_{3}^{2}\right.$$
$$\left.+\left(\sqrt{2}c_{i7}\cos\frac{\theta}{2}+\sqrt{2}c_{i8}\cos\frac{\theta}{2}-c_{i9}\sin\frac{\theta}{2}\right)m_{5}^{4}\right\}^2;$$

$$a_{5}^{4(2)}=\frac{\left(l_{5}^{4}\sin\frac{\theta}{2}-m_{5}^{4}\cos\frac{\theta}{2}\right)^2}{E_1-E_{3}^{2}};$$

$$a_i^{(2)}=\sum_{k=2,3}\frac{1}{E_i-E_k}\left\{\left(\sqrt{2}c_{i6}\sin\frac{\theta}{2}-\sqrt{2}c_{i8}\sin\frac{\theta}{2}+c_{i9}\cos\frac{\theta}{2}\right)l_k\right.$$
$$\left.+\left(\sqrt{2}c_{i7}\cos\frac{\theta}{2}+\sqrt{2}c_{i8}\cos\frac{\theta}{2}-c_{i9}\sin\frac{\theta}{2}\right)m_k\right\}^2$$
$$\times(i=6,...,9).$$

The work was supported in part by the Polish Committee for Scientific Research through Grant No. 2 PO3B 14210.

*E-mail: freiman@ilt.kharkov.ua
**E-mail: an_je@int.pan.wroc.pl

[1] M. Tinkham and M. W. P. Strandberg, Phys. Rev. **95**, 937 (1955).
[2] J. C. Burford and G. M. Graham, J. Chem. Phys. **49**, 763 (1968).
[3] V. V. Sumarokov, Yu. A. Freiman, V. G. Manzhelii, and V. A. Popov, Fiz. Nizk. Temp. **6**, 1195 (1980) [Sov. J. Low Temp. Phys. **6**, 580 (1980)].
[4] A. Jeżowski, Yu. A. Freiman, A. M. Tolkachev, V. P. Azarenkov, V. G. Manzhelii, and E. A. Kosobutskaya, Fiz. Nizk. Temp. **6**, 1484 (1980) [Sov. J. Low Temp. Phys. **6**, 723 (1980)].
[5] Yu. A. Freiman and A. Jeżowski, Fiz. Nizk. Temp. **10**, 649 (1984) [Sov. J. Low Temp. Phys. **10**, 340 (1984)].
[6] Yu. A. Freiman, A. Jeżowski, and V. V. Sumarokov, J. Phys. C, Solid State Phys. **19**, 5309 (1986).
[7] V. S. Ostrovskii, V. V. Sumarokov, and Yu. A. Freiman, Fiz. Nizk. Temp. **12**, 199, 975 (1986) [Sov. J. Low Temp. Phys. **12**, 116, 552 (1986)].
[8] G. M. Graham, J. S. M. Harvey, and H. Kiefte, J. Chem. Phys. **52**, 2235 (1970).
[9] R. Simoneau, J. S. M. Harvey, and G. M. Graham, J. Chem. Phys. **54**, 4819 (1971).
[10] V. A. Pavloshchuk, Yu. A. Pikus, and L. I. Shanskii, Optika i Spectroskopiya **49**, 867 (1980) [Opt. Spectrosc. (USSR) **49**, 474 (1980).
[11] I. M. Pritula and L. V. Khashchina, Fiz. Nizk. Temp. **18**, 1035 (1992) [Sov. J. Low Temp. Phys. **18**, 727 (1992)].
[12] A. Jeżowski, P. Stachowiak, J. Mucha, Yu. A. Freiman, and V. V. Sumarokov, High Temperatures-High Pressures **29**, 423 (1997).
[13] H. K. Jemieson and A. S. Hallis-Hallet, Proc. LT-10, Vol. 4, p. 158, VINITI, Moscow (1967).
[14] T. G. Blocker, C. L. Simmons, and F. G. West, J. Appl. Phys. **40**, 1154 (1969).
[15] Yu. A. Freiman, A. Jeżowski, Z. Litwicki, A. P. Brodyanskii, and E. V. Manzhelii, Proc. LT-21; Czech. J. Phys. **46**, 2101 (1996).
[16] M. E. Lines and M. A. Bösch, Comments Solid State Phys. **11**, 73 (1983).
[17] A. P. Brodyanskii and Yu. A. Freiman, Sov. J. Low Temp. Phys. **11**, 538 (1985).
[18] J. H. Van Vleck, *Theory of Electric and Magnetic Susceptibilities* (Oxford Press, Oxford, 1932).
[19] H. E. Stanley, *Introduction to Phase Transitions and Critical Phenomena* (Clarendon Press, Oxford, 1971).
[20] Yu. A. Freiman, S. M. Tret'yak, A. Jeżowski, and A. P. Brodyanski (to be published).
[21] P. J. von Ranke, V. K. Pecharsky, K. A. Gschneider Jr., and B. J. Korte, Phys. Rev. B **58**, 14436 (1998).

This article was published in English in the original Russian journal. Reproduced here with stylistic changes by the Translation Consultant.

Deposition of mass-selected ions in neon matrices: CS_2^+ and $C_6F_6^+$

M. Lorenz and V. E. Bondybey*

Institut für Physikalische und Theoretische Chemie der Technische Universität München, Lichtenbergstraße 4, 85747 Garching, Germany

(Submitted May 15, 2000)
Fiz. Nizk. Temp. **26**, 1044–1052 (September–October 2000)

Infrared and visible absorption spectra and laser-induced fluorescence (LIF) and excitation spectra are obtained for several simple cations deposited from a mass-selected ion beam. In the present preliminary study we demonstrate successful and clean mass selection by presenting spectra of samples obtained by depositing the isotopic $^{34}S^{12}C^{32}S^+$ ion in natural isotopic abundance, and analyzing its spectrum. Spectra of $C_6F_6^+$ deposited from a 20 eV ion beam exhibit quite different inhomogeneous line profiles, suggesting that even the relatively low kinetic energy results in considerable damage to the solid. Analysis of the spectra indicates that the Jahn–Teller-distorted vibrational structure in the doubly degenerate ground state of $C_6F_6^+$ is strongly perturbed in the newly formed sites, which are presumably of lower symmetry. A 33–46 cm^{-1} splitting of the origin and other totally symmetric bands in emission is tentatively attributed to the spin–orbit splitting in the $^2E_{1g}$ ground state. © *2000 American Institute of Physics.* [S1063-777X(00)02109-5]

1. INTRODUCTION

One of the major aims of the matrix isolation technique has been the preparation, stabilization, and spectroscopic characterization of radicals, ions, clusters and similar highly reactive, transient species.[1,2] While there are many methods for generating these reaction intermediates and transients, most of them share the same shortcomming, in that the species of interest are not prepared in pure form, but in a more or less complex mixture with a variety of other species. Since the early days, an obvious solution to this problem has frequently been considered: isolating the desired ions or molecules by means of mass selection. While conceptually it appears simple, implementation of this method has for a variety of reasons proved to be quite elusive.[3,4]

In the first place, only for relatively few species it is easy to generate ion beams of enough intensity to accumulate a sufficient concentration for their spectroscopic characterization. Another difficulty lies in the fact that in order to mass select the ions, they typically have to be accelerated to rather high energies, and to slow them down sufficiently for successful deposition is not a trivial task. Even if their energy can be reduced to 10–20 eV, an ion with this energy striking a matrix whose atoms are bound by few meV will produce a lot of damage, can vaporize hundreds of atoms, penetrate deep into the matrix,[5] and react with impurities and other species present in the solid,[6] thus defeating the major aim of matrix isolation. A final problem lies in the space charge resulting from accumulation of the charged species in the nonconducting rare gas matrix.[3] This may result in stray electric fields deflecting the molecular ion beam and further complicating the ion deposition.

In spite of the problems outlined above, there has been steady progress in this field in the last decade, indicating that the problems are not insurmountable. Several different groups have now reported studies in which mass-selected species have been successfully deposited and characterized spectroscopically. Very recently, we have completed the construction of an apparatus for investigation of mass-selected species in our laboratory and have succeeded in obtaining infrared and visible absorption spectra and laser-induced fluorescence excitation and resolved emission spectra of mass-selected ions. In the present paper we will first give a very short review of the existing approaches to mass-selected matrix studies and compare our experimental setup with those previously reported. We will then briefly present our preliminary results for individual isotopic species of the cations CS_2^+ and $C_6F_6^+$.

2. MASS-SELECTION STUDIES IN RARE GAS MATRICES

The first successful studies of mass-selected species in the matrix were reported some ten years ago almost simultaneously by several groups. Rivoal and coworkers have modified an apparatus in Lausanne originally intended for gas phase cluster studies, and interfaced it to a cryostat for matrix spectroscopy.[7,8] In the earliest experiments aimed at deposition of mass selected Ag_3^+ and Ni_3^+ clusters the currents were apparently too low for optical detection, but over the following few years the apparatus was steadily improved by changing the experimental parameters and source geometry.[5,9] The cluster ions were produced by means of sputtering with a 10 mA primary beam of 20 keV Kr^+ ions, analyzed in a quadrupole mass filter, and deposited with krypton matrix gas on a sapphire window. The ions were directed to the window with the help of an accelerating field and an electrostatic lens, and after deposition were neutralized by electrons from a tungsten filament. While in the early experiments fragmentation presented some problem, after further refinements it was possible to observe the UV absorption spectra of neutral silver clusters up to $n=39$.[10,11]

Lindsay, one of the investigators in the above study, Lombardi, and coworkers then constructed a new apparatus at the City College of New York, employing first a Wien

velocity filter in place of the quadrupole mass spectrometer. Even though this filter had the disadvantage of relatively low mass resolution, this represented no problem in studies aimed at M_n^+ metal clusters, where only clusters with varying values of n have to be separated. They are using the same CORDIS ion sputter source as Rivoal, Harbich *et al.* Over the following years, these workers have reported series of interesting studies of the absorption and resonance Raman spectra of numerous metal dimers and small clusters, including V_2,[12] W_2,[13] Ta_2,[14] Hf_2,[15] Re_2,[16] Co_2,[17] Zr_3,[18] Ta_4,[19] Ni_3,[20] Nb_3,[21] Rh_2,[22] Ru_2,[23] Hf_3,[24] and Pt_2.[25]

Another apparatus for mass-selected studies was developed at Michigan State by Leroi and Allison, who used a quadrupole filter from a modified residual gas analyser.[26] In their early studies they were able to reproduce the LIF spectrum of the CS_2^+ ion in solid argon, but only the parent carbon disulfide and diatomic CS could be detected in the infrared, an observation which the authors explained in terms of neutralization of the ion accompanied by fragmentation to CS+S.[3] These authors have more recently reported that the ion yield could be greatly enhanced by adding small quantities (0.1%) of CO_2 to the matrix gas, which then traps the electrons and suppresses the ion–electron recombination.[27] They then succeeded in recording the infrared spectra of several ions, including CF_3^+,[28] CS_2^+,[29] and CO_2^+,[27] in solid argon and neon matrices.

A whole series of highly successful investigations of mass-selected species in the matrix is due to Maier and coworkers, who used the technique to investigate numerous carbon chain species, which are of considerable importance in astrophysics and for interstellar chemistry. They generate the carbon chain molecules in a hot-cathode discharge source, using suitable precursor molecules, usually acetylene or its derivatives diluted by helium or argon.[4,30,31] The accelerated ions are focused by electrostatic lenses, and after selection in a quadrupole mass filter they are guided onto the matrix surface. The deposited mass selected species were then investigated in solid neon matrices by visible or UV absorption spectroscopy using a waveguide absorption technique. The spectra obtained in this way for the $H–C_k–H^+$ ion[32,33] and the $H–C_{2n}–CN^+$, and $NC–C_{2n}–CN^+$ ions[34] provide information complementary to our LIF studies on the same systems.[35,36] Recently, they used an electron impact source to produce the anions of the above mentioned linear chain molecules. After characterization of the anions, an electron was photo-detached and the corresponding neutral species were studied.[37,38] They also used sputtering of a graphite target to generate and deposit ionic $C_n^{\pm}$ cluster species and recorded their spectra. Particularly exciting are their observations and assignment of the electronic absorption spectra of neutral and anionic carbon clusters, C_n and C_n^-.[39–41] In their spectra of the anions they detected a whole series of close coincidences with frequencies of the so-called diffuse interstellar bands, which provided first really solid evidence for solving the long-standing mystery of their origin.[42,43]

Quite recently, Moskovits and coworkers started to use a mass-selection apparatus similar to Lindsay's setup to study transition metal clusters. In the beginning, they examined the direct synthesis of metal cluster complexes by deposition of mass-selected iron clusters with excess CO as ligand.[44] Using resonance Raman spectroscopy, they were later able to characterize Ag_5,[45] Ag_3, and Fe_3 (Ref. 46) in solid argon.

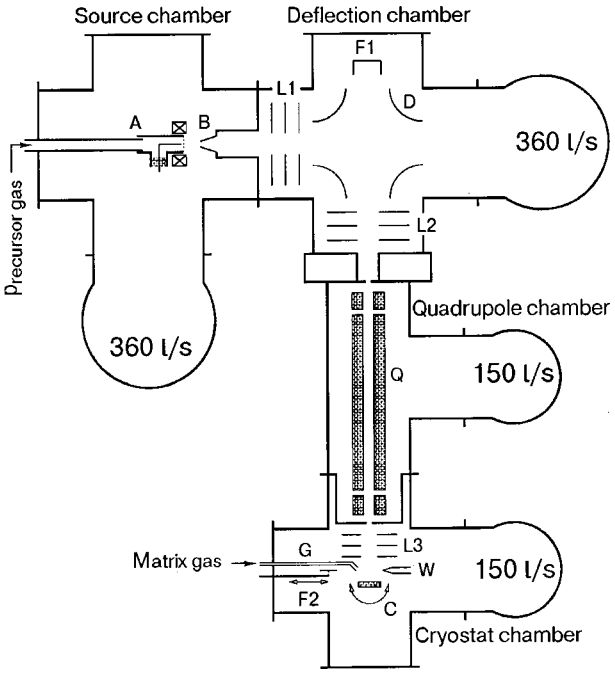

FIG. 1. Schematic of the experimental apparatus for mass-selected matrix studies, with microwave discharge ion source (A), skimmer (B), first electrostatic lens (L1), deflection unit (D), first Faraday cup (F1), second lens (L2), 12mm triple stage quadrupole mass filter (Q), final lens (L3), rotatable cold surface (C), matrix gas inlet (G), movable Faraday plate (F2) and the tungsten filament (W).

3. EXPERIMENTAL

The apparatus constructed in our laboratory is similar to Maiers setup[4]—a schematic drawing is shown in Fig. 1. We have also decided to use a quadrupole mass filter, which, unlike time-of-flight filters, for instance, allows both pulsed and cw operation. The ion source in the present experiment was a 12 mm Swagelok T piece, with the precursor gas flowing through the collinear sections, and with 50 W of 2.45 GHz microwave power being applied to a needle electrode via the perpendicular arm. A ring-shaped magnet surrounding the Swagelok is used to confine the charged species produced in the discharge. The discharge products from the source, held at +20 V, pass through a grid and are accelerated towards a 2 mm skimmer held at −20 V. The pressure in the source chamber, evacuated by a 360 l/s turbomolecular pump, is $10^{-4}–10^{-2}$ mbar.

The ionic species exiting the skimmer into the deflection chamber are focused with the help of an einzel-lens L1 and deflected 90° in a quadrupole electric field. A second lens, L2, then focuses the ions upon the entrance apperture of a quadrupole mass filter, with the undeflected neutrals being pumped by a second 360 l/s pump. A commercial triple-stage HIDEN HAL/3F quadrupole filter with 12 mm rods has a specified mass range up to 500 amu, resolution <1 amu, and a transmission of up to 30% when the resolution is decreased. The custom modified filter has 7 mm entrance and exit appertures, and is differentially pumped by a 150 l/s pump. The mass-selected ion beam is focused onto the ma-

trix by means of a lens L3 and deposited simultaneously with the matrix gas, neon in the present case. The substrate, a silver coated copper plate is held at ≈7 K by a LEYBOLD RDG 580 closed-cycle refrigerator.

To maintain overall neutrality of the matrix and to avoid building up space charges and stray fields, the matrix was sprayed by electrons from a hot tungsten filament held at −100 V. We experimented with alternating the ion and electron deposition, but, in the end, continuous operation proved to be most efficient, with optimal results being obtained with the electron current being about five times the ion current.

In order to optimize the experiment, the ability to measure the ion current is essential. For this purpose, one Faraday cup permitting measurement of the total ion current is located in the deflection chamber. A second detector, close to the cold surface, allows measuring the mass-selected ion current. The weak currents are amplified by a FEMTO DLPCA 100 current amplifier and digitized in the quadrupole control unit. Currents as low as 100 fA can be easily detected, and we obtain mass spectra with signal:noise better than 10000:1. With the mass filter set to the desired mass, all the experimental parameters can be adjusted for maximum current. With our microwave discharge source we could produce for both CS_2^+ and $C_6F_6^+$ currents of mass-selected ions of up to 2 nA.

After deposition, the matrix is rotated 120° and then the matrices are characterized spectroscopically using a BRUKER IFS 120 HR Fourier transform spectrometer, equipped with beamsplitters and detectors for the 500–30000 cm^{-1} spectral range. IR absorption spectra are measured with a liquid nitrogen cooled MCT (mercury–cadmium telluride) detector at a resolution of 0.06 cm^{-1}, whereas all other spectra were recorded with 0.5 cm^{-1} resolution. Laser excitation spectra are measured using an Ar^+ laser pumped power stabilized dye laser operating with a stilbene-3 dye. The total emission of the sample is detected with a PMT (and appropriate optical filters) connected to a lock-in amplifier. Laser induced fluorescence spectra are measured with the FT spectrometer using the same detector at a resolution of 0.5 cm^{-1}.

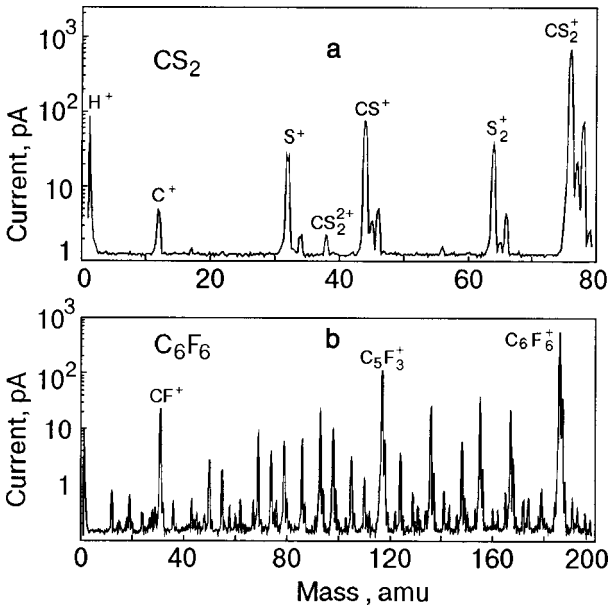

FIG. 2. Mass spectra obtained from our discharge source for the ions investigated in this work: CS_2 (a) and C_6F_6 (b).

4. RESULTS AND DISCUSSION

In our initial experiments we have investigated several ions whose matrix spectra are well known from previous studies. These ions can be durably trapped in rare gas matrices, since their electron affinity, i.e., 10.07 eV for CS_2^+, is much smaller than the ionization potential of the rare gas, 21.56 eV in the case of neon. To produce the ions, we have employed a microwave discharge through a low-pressure precursor gas, either pure or diluted with an inert buffer gas. In the first place, the mass spectrum of the ions emanating from the discharge was repeatedly recorded, and the source conditions were optimized for the ion of interest.

A typical mass spectrum obtained using CS_2 is presented in the Fig. 2a, which shows the ion current on a logarithmic scale versus the selected ion mass. After some optimization, the strongest peak is indeed the parention, CS_2^+, accompanied with ^{13}C and ^{34}S isotopic satellites. Also present is a number of easily identifiable fragments, in particular S_2, CS, S, and C. Typically the most intense mass peaks from the source corresponded to an ion current of about 1–2 nA.

In Fig. 3 we present an infrared spectrum of a sample resulting from a 3 h deposition of 1.5 nA current of ions with mass 76 amu. In spite of the nearly a factor of 10 shorter deposition time than in the experiments of Leroi *et al.*, a weak sharp peak at 1206.92 cm^{-1}, very close to the 1207.1 cm^{-1} frequency assigned by them to the ν_3 asymmetric stretching vibration of CS_2^+ in solid neon,[29] is clearly observable in the spectrum. In contrast with their study, we find in our samples little evidence of either the CS fragment at 1273.7 cm^{-1} or of the CS_2^- anion at 1159.4 cm^{-1}. If present at all, their concentrations relative to that of the CS_2^+ cation must be at least a factor of ten lower than in the earlier experiments. We have therefore no information as to the identity of the negatively charged species maintaining neutrality of the matrix. The absence of CS suggests that disso-

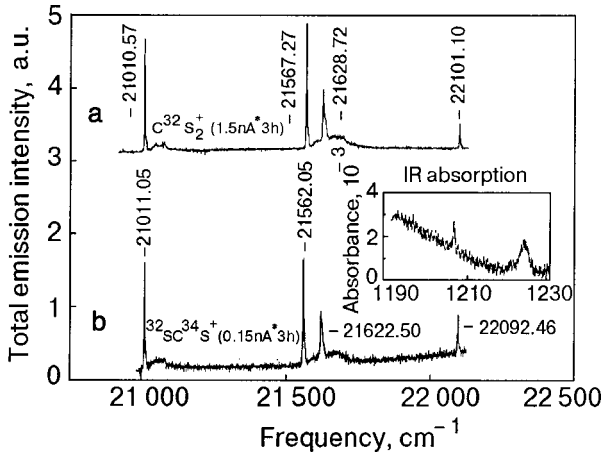

FIG. 3. Partial excitation spectra of the mass-selected $^{12}C^{32}S_2^+$ (a) and $^{34}S^{12}C^{32}S^+$ (b) ions in a solid neon matrix. The inset shows the infrared absorption spectrum of the latter ion.

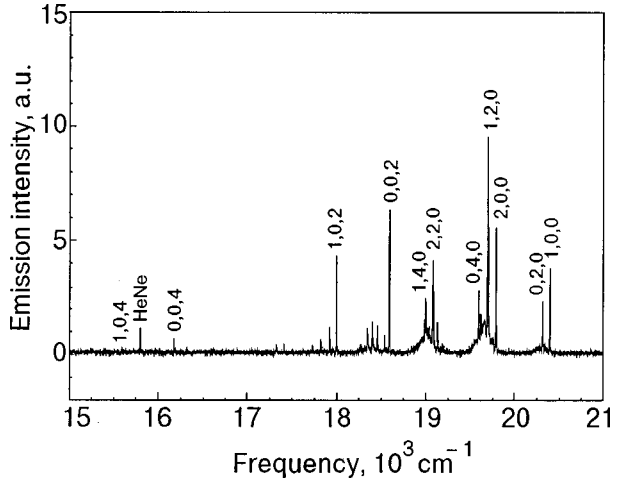

FIG. 4. Laser-induced fluorescence spectrum of the mass-selected $^{12}C^{32}S_2^+$ molecular ion excited at 21567 cm^{-1} (1,0,0).

ciative recombination of the CS_2^+ cation with an electron does not occur to any appreciable extent in our study.

The presence of CS_2^+ is then unambiguously confirmed by the LIF experiments. Figure 3a shows a total excitation spectrum of the matrix obtained by scanning a laser directed onto the matrix sample over the spectral range near the origin of the well known $A^2\Pi_u \leftrightarrow X^2\Pi_g$ CS_2^+ transition.[47,48] The spectrum shows clearly the (0,0,0) origin band at 21010.57 cm^{-1}, as well as several excited vibrational levels, the (1,0,0), (0,2,0) Fermi resonance doublet at 21567.27 and 21628.72 cm^{-1}, and the (2,0,0) level at 22101.0 cm^{-1}.

The remaining, and most important question which has to be answered is whether the observed CS_2^+ are really due to the ion deposition, or whether they could be due to neutral CS_2 from the source reaching the matrix and being ionized by the electrons from the tungsten filament, or by the ions from the molecular beam. This question is unambiguously resolved by a separate experiment (Fig. 3b), where the mass filter was tuned to mass 78 rather than 76, and ions of 0.15 nA current were deposited again over 3 hours. One obtains a spectrum very similar to Fig. 3a, but with the bands distinctly shifted to 21011.05, 21562.05, 21622.50, and 22092.46 cm^{-1}. These are clearly attributable to the $^{34}S^{12}C^{32}S^+$ molecular ion, present in a natural isotopic abundance in our sample.

A resolved fluorescence spectrum of CS_2^+ is shown in Fig. 4, and a similar spectrum was also recorded for the isotopic $^{34}S^{12}C^{32}S^+$ cation, with the observed bands and their assignments listed in the Table I. The measured frequencies are generally in good agreement with previous studies, but in view of the higher signal-to-noise in the present work, a number of new bands have been detected. The most prominent features in the emission spectrum are ''Fermi polyads'' due to the near resonance between ν_1 and $2\nu_2$. While the assignments of the first two polyads, that is the resonant (1,0,0), (0,2,0) levels and the levels involving the $2\nu_1$ overtone: (2,0,0), (1,2,0), (0,4,0), are quite unambiguous, for the higher overtones the spectra become more complex, and more levels are detected than expected. Some of this complexity probably arises from the Renner–Teller splitting in the degenerate $X^2\Pi_g$ state, or is caused by additional resonances involving the ν_3 asymmetric stretching mode.

TABLE I. Observed bands of mass selected CS_2^+ in solid neon (all values in cm^{-1}).

(ν_1,ν_2,ν_3)	$^{32}S^{13}C^{32}S^+$	$^{32}S^{12}C^{32}S^+$	$^{32}S^{12}C^{32}S^+$	$^{34}S^{12}C^{32}S^+$
	from Ref. 48		this work	
(2,0,0)	22063	22114	22101.1	22092.5
(0,2,0)	21601	21639	21628.7	21622.5
(1,0,0)	21541	21578	21567.3	21562.0
(0,0,0)	21011	21016	21010.6	21011.0
(1,0,0)	20402	20398	20392.9	20398.5
(0,2,0)	20325	20318	20312.9	20317.4
?			19935.7	
(2,0,0)	19809	19792	19788.3	19797.4
(1,2,0)	19710	19700	19695.6	19710.1
(0,4,0)	19627	19600	19595.4	19604.2
(3,0,0)	19218	19188	19202.1?	19197.2 ?
(2,2,0)	19101	19082	19076.6	19094.3
(1,4,0)	19019	18996	18992.7	19009.0
(0,6,0) ?	18912		18863.0	
(0,0,2)	18671	18598	18592.8	18598.6
(1,0,2)	18080		17994.2	18006.0
(0,0,4)			16170.3	
(1,0,4)			15589.7	

A strong band at 18592.98 cm^{-1} is clearly the overtone of the asymmetric stretching vibration, yielding, a value of $2\nu_3'' = 2417.75\,\text{cm}^{-1}$. This band is again the origin of a series of polyads due to combinations with ν_1'' and $2\nu_2''$. Combining the $2\nu_3$ value from the electronic spectrum with the infrared fundamental $\nu_3'' = 1206.92\,\text{cm}^{-1}$ gives $x_{3,3}'' = -1.955\,\text{cm}^{-1}$. Such negative anharmonicity is quite common for asymmetric vibrations of symmetric molecules, which often have a partial quartic oscillator character, since odd terms are not possible in the potential energy expansion. Similar but even larger negative anharmonicity was also found in the excited CS_2^+ $A^2\Pi_u$ state. Using this anharmonic term, one can predict the next overtones to be $3\nu_3'' \approx 3632.49$ and $4\nu_3'' \approx 4851.14\,\text{cm}^{-1}$. While the third overtone should, just like the fundamental, be inactive, a strong band is observed at 16170.34 cm^{-1}, close to 16159.43 cm^{-1} where the emission into the (0,0,4) level is predicted.

In Table I we also list the frequencies measured for the

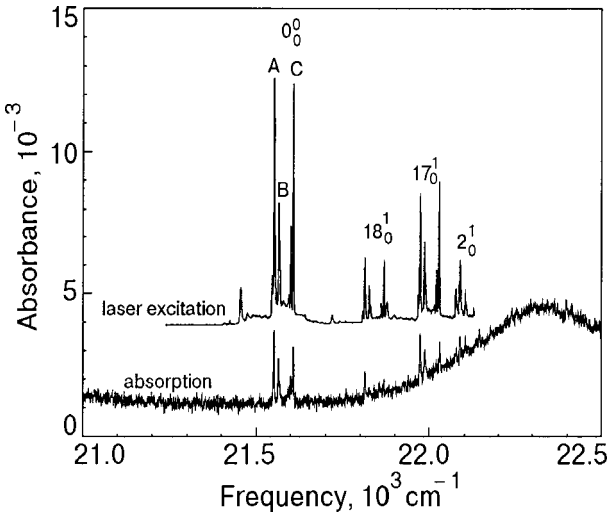

FIG. 5. Laser excitation (top) and absorption (bottom) spectrum of the hexafluorobenzene radical cation, $C_6F_6^+$. Note the presence of several additional, spectrally shifted sites besides the bands due to the main site A.

isotopic $^{34}S^{12}C^{32}S^+$ ion. In the previous studies both normal $^{12}C^{32}S_2^+$ as well as the isotopic $^{13}C^{32}S_2^+$ ions were investigated.[47,48] Based on the isotopic shifts it was concluded that in both electronic states involved in the transition, the ν_1 and $2\nu_2$ levels are almost perfectly mixed. Even though one would expect the symmetric stretching vibration ν_1 to exhibit no ^{13}C isotopic shift, $\rho \approx 1.0$, while for ν_2 an isotopic parameter $\rho \approx 1.034$ can be predicted, both ν_1 and $2\nu_2$ exhibited almost identical shifts just midway between these two values. Basically the same conclusion can be reached in the present work based on the observed ^{34}S isotopic shifts. Strictly speaking, $^{34}S^{12}C^{32}S^+$ is no longer a symmetric $D_{\infty h}$ molecule, and therefore the odd overtones, for instance the ν_3 and $3\nu_3$ levels, could also in principle appear directly in the spectrum. Unfortunately, due to the relatively low isotopic abundance of ^{34}S the spectra of the mixed isotopomer exhibit a somewhat lower signal-to-noise ratio, and these levels were not detected.

Another previously well-known ion which we have now investigated with our new experimental apparatus is $C_6F_6^+$, the hexafluorobenzene cation. It is known that it possesses a fully allowed π-π^* transition in the visible, and is known to fluoresce in matrices with quantum yield close to unity.[49] To produce the ion, we have again employed a microwave discharge through a pure parent C_6F_6 at a pressure of about 10^{-3} mTorr. One of the problems of such an approach is the extensive fragmentation of the parent, resulting in a very complex mass spectrum. As shown in Fig. 2b, after optimization the parent ion is the strongest peak in the spectrum, but a large number of fragments and other reaction products is observed, with just about any C_nF_m ion, with n and m ranging up to at least 8, being present.

In Fig. 5 the absorption spectrum of a sample resulting from 4 h deposition with the mass filter set to 186 amu is compared with the corresponding excitation spectrum. This latter was obtained by monitoring the intensity of the sample fluorescence while scanning the exciting laser in this spectral region. A very strong emission clearly attributable to $C_6F_6^+$ is indeed observed, but both the absorption and laser excitation spectra exhibit some interesting differences when compared with the previous studies, where the cation was produced by *in situ* 1216 A Lyman-α vacuum-UV radiation photoionization of the parent hexafluorobenzene. While the photoionized spectra exhibited essentially a single site and a narrow inhomogeneous distribution, the ion-beam deposited samples contain, besides the ''major'' $C_6F_6^+$ site A with origin at 21551.77 cm^{-1}, numerous other sites, which exhibit appreciable spectral shifts, both to higher and lower energies.

Some time ago we have similarly compared the spectra of several ionic species prepared in our laboratory by *in situ* photolysis of the parent neutrals in neon matrices, with the corresponding species deposited by Maier and coworkers from mass-selected ion beams.[32,33] While the ionization produced matrices yielding well defined, sharp lines, the ion beam deposition resulted in broad, structured bands with widths exceeding 150 cm^{-1}. At that time we explained this difference by inhomogeneous broadening due to damage to the neon matrix caused by the impact of the energetic, $\approx$60 eV, ions. The present investigation seems to confirm this interpretation. While the *in situ* photolysis produces a single site with origin at 21551.77 cm^{-1}, even though in our case the energy of the ions is believed to be $\leqslant$20 eV, their deposition results in about a dozen discrete sites, whose origins span a range of more than 200 cm^{-1}, from 21409.43 to 21640.44 cm^{-1}. In one experiment, on the other hand, where the energy of the deposited ions was lowered, the subsidiary sites almost disappeared, and the ''main'' site which was observed and investigated in the previous studies was dominant.

In Table II we list the observed transitions of $C_6F_6^+$ both for the ''main'' site A and for the two strongest ''new'' sites B and C, which are blue-shifted by 12.9 and 55.3 cm^{-1}, respectively. In Fig. 6, a comparison of the spectra and frequencies of the ''main'' site A with those of the new sites B and C reveals, that while the progression in the totally symmetric mode, ν_2, is essentially identical for the three sites, and also identical with the known gas phase frequencies, the other levels involving the Jahn–Teller active modes ν_{18} and ν_{17} (Ref. 50) exhibit strong perturbations. Thus the 288.8 cm^{-1} ν_{18} level is, in both of the strongest perturbed sites, split into two components, both of them blue-shifted to about 295 and 305 cm^{-1}, respectively. Similarly, ν_{17}, which occurs at 417.2 cm^{-1} in the main site, is shifted to 432.8 and 440.9 cm^{-1} in the two other sites. This applies also to their combination and overtone bands. In general, the vibrational levels involving the Jahn–Teller active modes are, in all the new sites, strongly shifted and sometimes split into several components, and new absorptions appear. Also the 0–0 band, and each of the bands of the strong, totally symmetric ν_2 progression which is seen up to $\nu_2=3$, exhibit in the spectra of the new sites a broader satellite band, shifted in emission by $\approx$33 and 46 cm^{-1}, respectively.

A tentative interpretation of these observations is that when produced by *in situ* photolysis of the parent, the $C_6F_6^+$ cation is in an unperturbed site with relatively high symmetry. When, however, the ion is deposited in the matrix from the gas phase with kinetic energies of $\approx$20 eV, lower-symmetry sites, perhaps with nearby vacancies, are produced and populated, which strongly affect the Jahn–Teller distor-

TABLE II. Observed bands of mass selected $C_6F_6^+$ in solid neon (''main'' site A and perturbed sites B and C, all values in cm^{-1}).

Mode	from Ref. 49	A	B	C
ν_2'	540	537.4	537.5	
ν_{17}'	426	422.5	420.8	424.0
ν_{18}'	265	263.9	263.2	263.5
0–0 X_1	21558	21551.8	21565.3	21607.0
0–0 X_2			32.8	46.1
ν_{18}	289	288.8	294.7	296.9
ν_{18a}			305.0	308.3
ν_{17}	417	417.2	432.8	440.9
$\nu_{17}+\nu_{18}$	498	497.9	500.9	503.0
$2\nu_{18}$	508	508.8		
		529.9	528.6	541.1
ν_2	554	553.1	553.6	554.7
		560.3	560.4	560.5
			567.2	
$\nu_2 X_2$			585.5	599.1
		688.2	710.2	707.6
$3\nu_{18}$	699	698.5	721.9	731.4
	759	758.4		
	770	770.0		
$2\nu_{17}$	797	797.3	814.7	816.2
		801.2		823.8
	826	825.9		
		830.1		
$\nu_2+\nu_{18}$	843	842.6	848.9	851.9
$\nu_2+\nu_{18a}$			859.0	862.7
$4\nu_{18}$	919	919.3		
$\nu_2+\nu_{17}$	972	971.2	986.8	995.4
$\nu_2+2\nu_{18}$	1052	1052.0		
$2\nu_2$	1107	1106.5	1107.0	1108.5
$2\nu_2 X_2$			1141.0	1153.1
ν_{16}	1226	1225.0	1246.5	
$\nu_2+3\nu_{18}$	1253	1252.2	1274.8	1286.2
	1280	1278.8		
		1310.1		
$\nu_2+\nu_{17}+2\nu_{18}$ (?)	1324			
$\nu_2+2\nu_{17}$	1352	1350.7		
$2\nu_2+\nu_{18}$	1397	1396.0	1402.3	
$2\nu_2+\nu_{18a}$			1412.5	
$\nu_2+4\nu_{18}$	1474	1473.3		
$2\nu_2+\nu_{17}$	1526	1524.9		
$2\nu_2+2\nu_{18}$	1605	1604.6		
$3\nu_2$	1661	1659.6	1660.2	?
	1682	1681.4		
ν_{15}	1698	1694.1	1696.2	1706.6
	1734	1732.9		
	1805	1805.2		
		1966.5		
	2172	2165.2		
	2220	2219.9		
$\nu_{15}+\nu_2$	2250	2248.9		
	2432			

tion, perturb the related vibrational structure, and relax the selection rules. An interesting question involving the doubly degenerate ground state of $C_6F_6^+$ and similar cations is the magnitude of the spin–orbit splitting. Several older theoretical works suggested that this is probably small,[51] but there is little *a priori* evidence on this point. Compared with the spin–orbit constants in a number of small compounds of first–row elements, the observed 33–46 cm^{-1} separation of the two components of the origin band, as well as of the other totally symmetric levels, would seem to be of the right order of magnitude to be assigned to the spin–orbit splitting of the degenerate X^2E_{1g} ground state of the $C_6F_6^+$ cation.

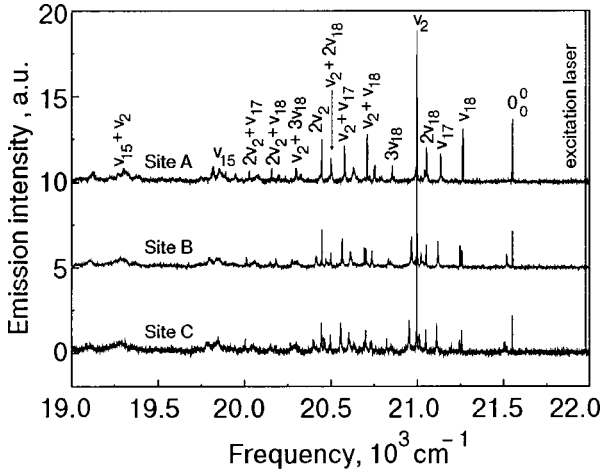

FIG. 6. Comparison of the LIF spectrum of the main site A with those of two of the ''perturbed'' sites, denoted B and C. For ease of comparison, the spectra of these sites were shifted to make the 0–0 origins overlap. Note the splitting of the spectral lines, as well as the presence of broader satellite bands near the 0–0 origin and other totally symmetric bands.

If one accepts this assignment, then, considering that the magnitude of the splitting changes by some 30% between the two sites examined, the question arises as to how much of this is intrinsic, free $C_6F_6^+$ splitting, and how much is due to the asymmetric environment. In other words, one might ask if one sees an extra component because the selection rules are relaxed, and a level which is not accessible in a symmetric site becomes visible when the site symmetry is lowered, or because the initially degenerate and unresolvable levels were split by the asymmetry. An unambiguous answer to these question will require additional study. It should be noted that the spin–orbit splitting was neglected in most previous treatments of substituted benzene cations. Strictly speaking, however, the spin-orbit and Jahn–Teller interactions are not independent of each other, and if both splittings are non-negligible, both would have to be simultaneously considered in a rigorous treatment of the X^2E_{1g} ground-state vibrational structure.

CONCLUSION

In the present manuscript we present preliminary results obtained with a new apparatus for deposition of mass-selected ions in low-temperature matrices. With this apparatus we obtain infrared and visible absorption and fluorescence and fluorescence excitation spectra of mass-selected ions. We demonstrate the successful and clean mass selection by presenting spectra of samples obtained by depositing the isotopic $^{34}S^{12}C^{32}S^+$ ion in natural isotopic abundance. Experiments with $C_6F_6^+$ demonstrate that deposition of ions with high kinetic energy from the gas phase produces a quite different inhomogeneous line profile and results in a variety of ''perturbed'' sites, presumably due to nearby defects and vacancies. The emission spectra of the perturbed sites are characterized by appreciable shifts and doubling of the vibrational levels of the degenerate X^2E_{1g} ground state, which may be due to a combination of the spin–orbit splitting and the Jahn–Teller effect.

We gratefully acknowledge the Deutsche Forschungsgemeinschaft, which contributed essentially to funding this project, as well as the Fond der Chemischen Industrie for generous support.

*E-mail: bondybey@ch.tum.de

[1] E. Whittle, D. A. Dows, and G. C. Pimentel, J. Chem. Phys. **22**, 1943 (1954).
[2] V. E. Bondybey, A. M. Smith, and J. Agreiter, Chem. Rev. **96**, 2113 (1996).
[3] M. S. Sabo, J. Allison, J. R. Gilbert, and G. E. Leroi, Appl. Spectrosc. **45**, 535 (1991).
[4] J. P. Maier, Mass Spectrom. Rev. **11**, 119 (1992).
[5] S. Fedrigo, F. Meyer, D. M. Lindsay, J. Lignieres, J. C. Rivoal, and D. Kreisle, J. Chem. Phys. **93**, 8535 (1990).
[6] T. M. Halasinski, J. T. Godbout, J. Allison, and G. E. Leroi, J. Phys. Chem. **100**, 14865 (1996).
[7] P. Fayet and L. Wöste, Z. Phys. D: At., Mol. Clusters **3**, 177 (1986).
[8] J. C. Rivoal, C. Grisolia, J. Lignieres, D. Kreisle, P. Fayet, and L. Wöste, Z. Phys. D: At., Mol. Clusters **12**, 481 (1989).
[9] S. Fedrigo, W. Harbich, and J. Buttet, J. Chem. Phys. **99**, 5712 (1993).
[10] W. Harbich, S. Fedrigo, and J. Buttet, Z. Phys. D: At., Mol. Clusters **26**, 138 (1993).
[11] W. Harbich, Y. Belyaev, R. Kleiber, and J. Buttet, Surf. Rev. Lett. **3**, 1147 (1996).
[12] Z. Hu, B. Shen, Q. Zhou, S. Deosaran, J. R. Lombardi, D. M. Lindsay, and W. Harbich, J. Chem. Phys. **95**, 2206 (1991).
[13] Z. Hu, G. Jian, J. R. Lombardi, and D. M. Lindsay, J. Chem. Phys. **97**, 8811 (1992).
[14] Z. Hu, B. Shen, J. R. Lombardi, and D. M. Lindsay, J. Chem. Phys. **96**, 8757 (1992).
[15] Z. Hu, G. Jian, J. R. Lombardi, and D. M. Lindsay, J. Phys. Chem. **97**, 9263 (1993).
[16] Z. Hu, G. Jian, J. R. Lombardi, and D. M. Lindsay, J. Chem. Phys. **101**, 95 (1994).
[17] J. Dong, Z. Hu, R. Craig, J. R. Lombardi, and D. M. Lindsay, J. Chem. Phys. **101**, 9280 (1994).
[18] H. Haouari, H. Wang, R. Craig, J. R. Lombardi, and D. M. Lindsay, J. Chem. Phys. **103**, 9527 (1995).
[19] H. Wang, R. Craig, H. Haouari, J. Dong, Z. Hu, A. Vivoni, J. R. Lombardi, and D. M. Lindsay, J. Chem. Phys. **103**, 3289 (1995).
[20] H. Wang, H. Haouari, R. Craig, J. R. Lombardi, and D. M. Lindsay, J. Chem. Phys. **104**, 3420 (1996).
[21] H. Wang, R. Graig, H. Haouari, Y. Liu, J. R. Lombardi, and D. M. Lindsay, J. Chem. Phys. **105**, 5355 (1996).
[22] H. Wang, H. Haouari, R. Craig, Y. Liu, J. R. Lombardi, and D. M. Lindsay, J. Chem. Phys. **106**, 2101 (1997).
[23] H. Wang, Y. Liu, H. Haouari, R. Craig, J. R. Lombardi, and D. M. Lindsay, J. Chem. Phys. **106**, 6534 (1997).
[24] H. Wang, Z. Hu, H. Haouari, R. Craig, Y. Liu, J. R. Lombardi, and D. M. Lindsay, J. Chem. Phys. **106**, 8339 (1997).
[25] H. Wang, Y. Liu, H. Haouari, R. Craig, J. R. Lombardi, and D. M. Lindsay, J. Phys. Chem. A **101**, 7036 (1997).
[26] J. R. Gilbert, G. E. Leroi, and J. Allison, Int. J. Mass Spectrom. Ion Phys. **107**, 247 (1991).
[27] J. T. Godbout, T. M. Halasinski, G. E. Leroi, and J. Allison, J. Phys. Chem. **100**, 2892 (1996).
[28] T. M. Halasinski, J. T. Godbout, G. E. Leroi, and J. Allison, J. Phys. Chem. **98**, 3930 (1994).
[29] T. M. Halasinski, J. T. Godbout, J. Allison, and G. E. Leroi, J. Phys. Chem. **100**, 14865 (1996).
[30] D. Forney, M. Jakobi, and J. P. Maier, J. Chem. Phys. **90**, 600 (1989).
[31] J. P. Maier, Chem. Soc. **26**, 21 (1997).
[32] P. Freivogel, J. Fulara, D. Lessen, D. Forney, and J. P. Maier, Chem. Phys. **189**, 335 (1994).
[33] J. Fulara, P. Freivogel, D. Forney, and J. P. Maier, J. Chem. Phys. **103**, 8805 (1995).
[34] D. Forney, P. Freivogel, J. Fulara, and J. P. Maier, J. Chem. Phys. **102**, 1510 (1995).
[35] J. Agreiter, A. M. Smith, and V. E. Bondybey, Chem. Phys. Lett. **241**, 317 (1995).
[36] A. M. Smith, J. Agreiter, and V. E. Bondybey, Chem. Phys. Lett. **244**, 379 (1995).
[37] M. Grutter, M. Wyss, J. Fulara, and J. P. Maier, J. Phys. Chem. A **102**, 9785 (1998).
[38] M. Grutter, M. Wyss, and J. P. Maier, J. Chem. Phys. **110**, 1492 (1999).
[39] P. Freivogel, M. Grutter, D. Forney, and J. P. Maier, J. Chem. Phys. **107**, 4468 (1997).
[40] M. Tulej, D. A. Kirkwood, G. Maccaferri, O. Dopfer, and J. P. Maier, Chem. Phys. **228**, 293 (1998).
[41] M. Grutter, M. Wyss, E. Riaplov, and J. P. Maier, Chem. Phys. **111**, 7397 (1999).
[42] M. Tulej, D. A. Kirkwood, M. Pachkov, and J. P. Maier, Astrophys. J. **506**, 69 (1998).
[43] D. A. Kirkwood, H. Linnartz, M. Grutter, O. Dopfer, C. Motylewski, M. Pachkov, M. Tulej, M. Wyss, and J. P. Maier, Faraday Discuss. **109**, 109 (1998).
[44] S. Fedrigo, T. L. Haslett, and M. Moskovits, J. Am. Chem. Soc. **118**, 5083 (1996).
[45] T. L. Haslett, K. A. Bosnick, and M. Moskovits, J. Chem. Phys. **108**, 3453 (1998).
[46] T. L. Haslett, K. A. Bosnick, S. Fedrigo, and M. Moskovits, J. Chem. Phys. **111**, 6456 (1999).
[47] V. E. Bondybey, J. H. English, and T. A. Miller, J. Chem. Phys. **70**, 1621 (1979).
[48] V. E. Bondybey, J. H. English, J. Chem. Phys. **73**, 3098 (1980).
[49] V. E. Bondybey and T. A. Miller, J. Chem. Phys. **73**, 3035 (1980).
[50] T. J. Sears, T. A. Miller, and V. E. Bondybey, J. Chem. Phys. **74**, 3240 (1981).
[51] H. M. McConnel, J. Chem. Phys. **34**, 13 (1961).

This article was published in English in the original Russian journal. Reproduced here with stylistic changes by the Translation Consultant.